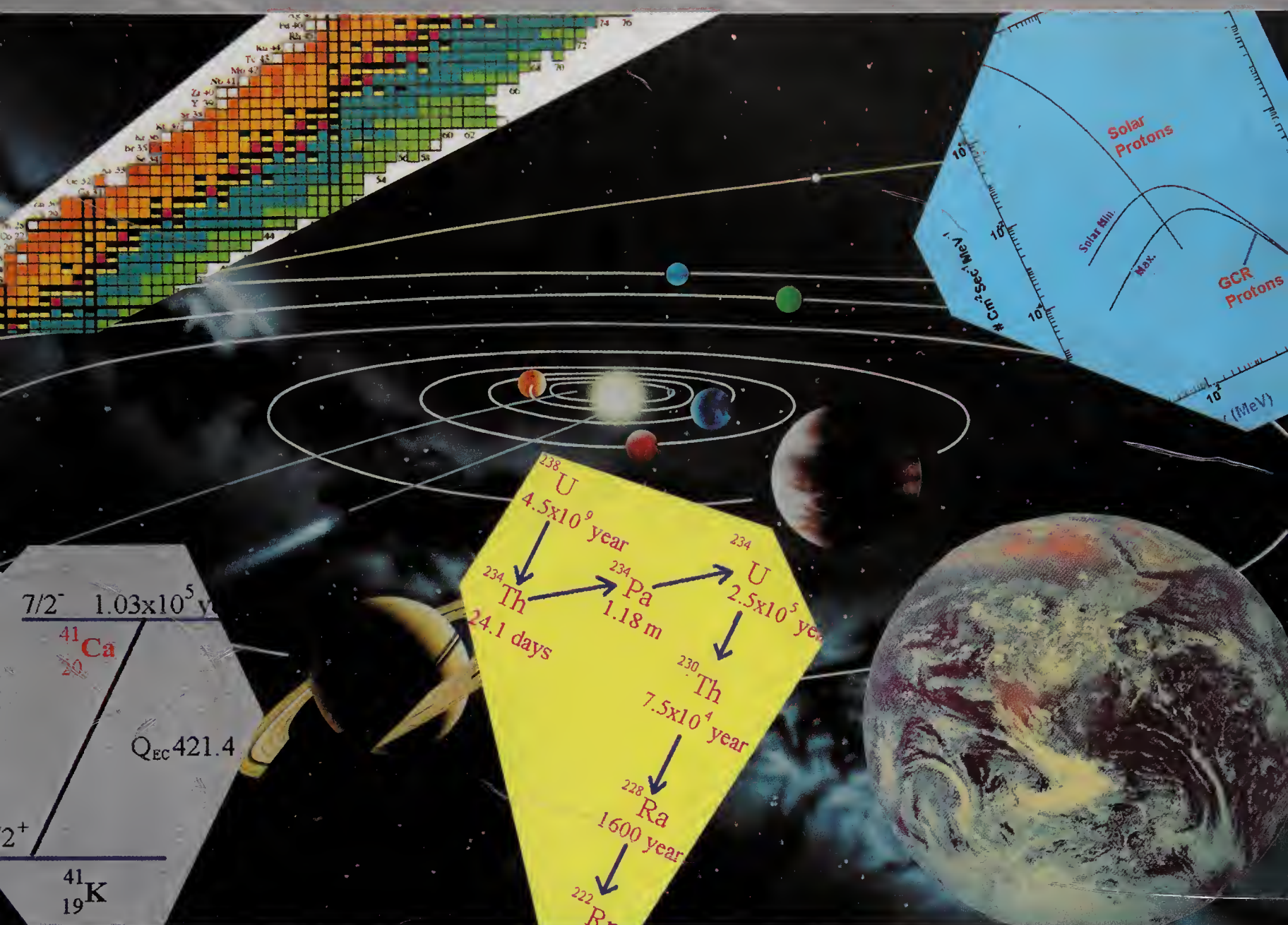



Isotopes in the Solar System



*Proceedings of the International Conference
PRL, Ahmedabad, India, November 1997*

Editors: J N Goswami and S Krishnaswami

Indian Academy of Sciences
Bangalore, India



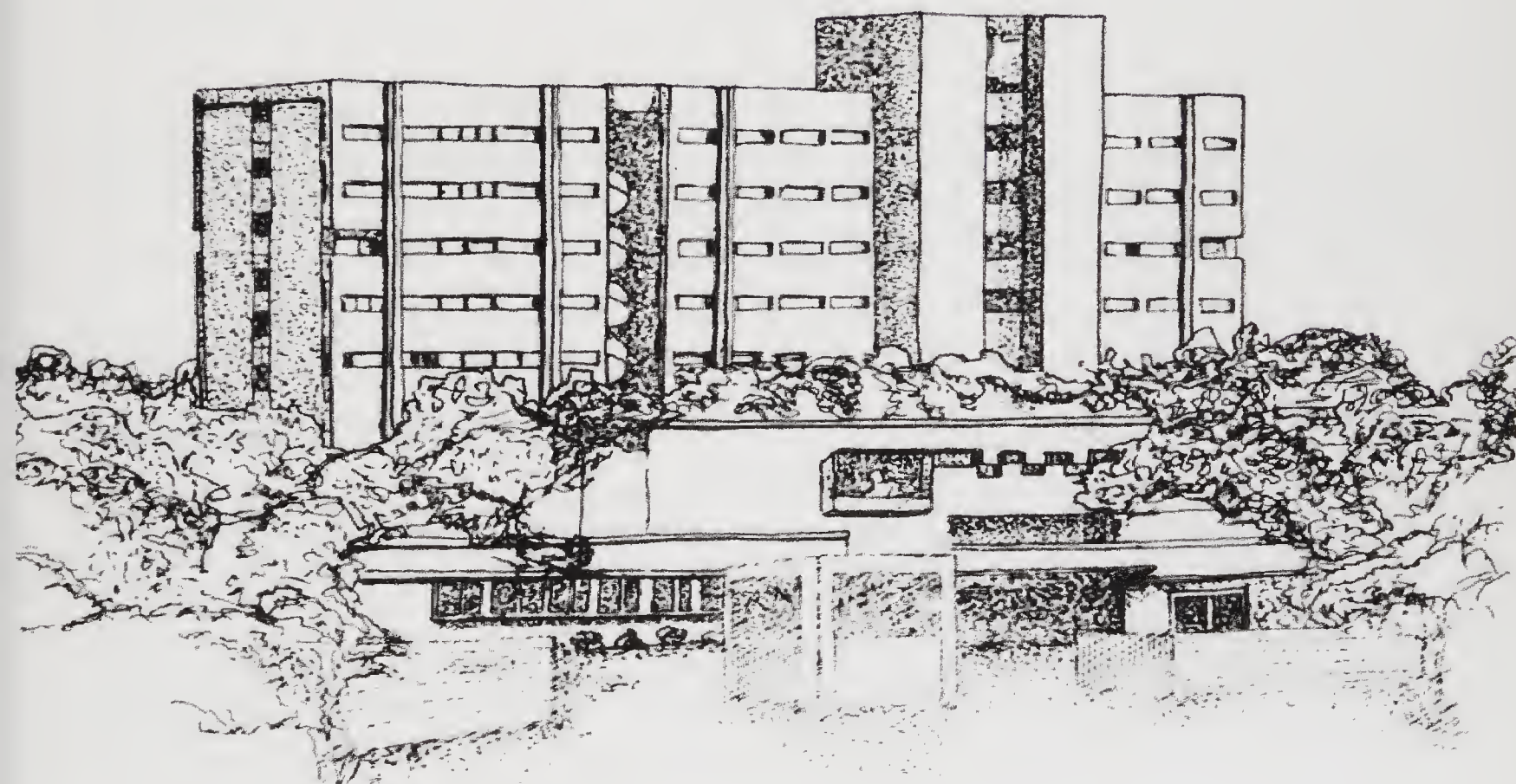
Digitized by the Internet Archive
in 2018 with funding from
Public.Resource.Org

<https://archive.org/details/isotopesinsolars00unse>

Isotopes in the Solar System

*Proceedings of the International Conference
PRL, Ahmedabad, India, November 1997*

Proceedings of the
International Conference on
Isotopes in the Solar System



Golden Jubilee
Physical Research Laboratory
Ahmedabad, India

1947 - 1997

COVER PICTURE: Planetary systems and examples of extinct, primordial and stable isotopes used as tracers to understand their evolutions. Energetic solar and galactic cosmic ray particles also contribute to the production of some of the isotopes in the Solar System.

© 1999 by the Indian Academy of Sciences.

Reprinted from *Proceedings of the Indian Academy of Sciences (Earth and Planetary Sciences)*
Volume 107, Number 4, December 1998.

Typeset and printed at Thomson Press (I) Ltd., Faridabad 121 007 for the Indian Academy of Sciences.

Contents

Editorial	
<i>V K Gaur</i>	1
Foreword	
<i>J N Goswami and S Krishnaswami</i>	3
Cosmic ray produced isotopes in terrestrial systems	
<i>D Lal</i>	7
Astronomical and terrestrial causes of physical, chemical and biological changes at geological boundaries	
<i>N Bhandari</i>	17
Geologic and tectonic evolution of the Himalaya before and after the India-Asia collision	
<i>Kewal K Sharma</i>	31
Silicate and carbonate weathering in the drainage basins of the Ganga-Ghaghara-Indus head waters: Contributions to major ion and Sr isotope geochemistry	
<i>S Krishnaswami and Sunil K Singh</i>	49
On the interpretation of the oceanic variations in $^{87}\text{Sr}/^{86}\text{Sr}$ as recorded in marine limestones	
<i>Youngsook Huh and John M Edmond.</i>	59
Ice-core records of global climate and environment changes	
<i>Robert J Delmas</i>	73
Speleothems as high-resolution paleoenvironment archives: Records from northeastern China	
<i>T L Ku and H C Li</i>	87
Stable isotope variations in a coral (<i>Favia speciosa</i>) from the Gulf of Kutch during 1948-1989 A.D.: Environmental implications	
<i>S Chakraborty and R Ramesh</i>	97
Application of ^{226}Ra , ^{228}Ra , ^{223}Ra , and ^{224}Ra in coastal waters to assessing coastal mixing rates and groundwater discharge to oceans	
<i>Willard S Moore.</i>	109
^{210}Pb in the ocean: A pilot tracer for modeling particle reactive elements	
<i>Ernst Maier-Reimer and Gideon Henderson.</i>	117
Determination of indium in natural waters by flow injection inductively coupled plasma mass spectrometry	
<i>D S Alibo, H Amakawa and Y Nozaki</i>	125

Contents

Nitrogen isotopic studies in the suboxic Arabian Sea <i>S W A Naqvi, T Yoshinari, J A Brandes, A H Devol, D A Jayakumar, P V Narvekar, M A Altabet and L A Codispoti</i>	133
On laboratory studies of grains from outside the solar system <i>U Ott</i>	145
The triggered origin of the solar system <i>Harri A T Vanhala</i>	157
Short-lived nuclides in the early solar system <i>J N Goswami</i>	167
The I-Xe chronometer <i>C M Hohenberg, R H Brazzle, O V Pravdivtseva and A P Meshik</i>	179
Noble gas components in planetary atmospheres and interiors in relation to solar wind and meteorites <i>K Marti and K J Mathew</i>	191
Studies of modern and ancient solar energetic particles <i>R C Reedy</i>	199
Interpretation of cosmogenic nuclides in meteorites on the basis of accelerator experiments and physical model calculations <i>R Michel and S Neumann</i>	207
Photographs of the Conference	225
List of Participants	229

Editorial

Seminal questions concerning the evolution of the Solar System and, in particular, of the planet earth and its climatic history, can now be pointedly addressed by investigating the isotopic records preserved in the earth, the moon and meteorites, thanks to the progressive refinement of experimental techniques and the new development of Accelerator Mass Spectrometry. To take just one example, the use of isotopic tracers has led to the delineation of past climates and of the dynamics of one of the major reservoirs of our planet, the Ocean system.

The papers contained in this special volume, highlight new and potentially illuminating areas of research which can better characterize and quantify the processes taking place in the earth and in planetary systems. Generally, most of these have been selected from the presentations made at the International Conference on **'Isotopes in the Solar System'**, held at the Physical Research Laboratory, Ahmedabad in November 1997. They expose new results obtained from the study of isotopic records preserved in samples of meteorites, terrestrial rocks, sea sediments, ice cores, glaciers, corals, cave deposits and in river, ocean and ground waters. In Earth Sciences, paleoclimate studies, particularly the signatures of rapid climatic changes recorded in glaciers and deep sea sediments, and the role of oceanic and atmospheric circulations in contributing to these abrupt changes, continue to be a topic of intense research. On a longer time scale, the impact of mountain building, especially of the voluminous Himalayan orogeny and associated chemical weathering, in influencing global climate and the chemical and isotopic make up of sea water is hotly debated. It is well known that rivers, glaciers and the atmosphere are

the primary pathways for the transfer of materials from continents to oceans. Recent evidence gathered from isotopic mass balance considerations, however, suggest that direct discharge of subsurface water into coastal regions may be an important source of water and material flux to the sea. The magnitude of this flux and its environmental consequence warrant further study. The application of the longer-lived cosmic ray produced isotopes to study surficial processes on Earth has gained considerable impetus after the development of accelerator mass spectrometry that allows rapid analysis of minute quantities of radioactivity in terrestrial samples. In the field of solar system studies, the possibility of a triggered origin of the Solar System is supported by recent results obtained from the studies of now-extinct short-lived nuclide records in primitive meteorites and numerical simulation studies of assisted collapse of molecular cloud fragments to form a Sun-like star. The evolution of planetary atmospheres on the Earth and Mars is another area of active interest in the field of planetary science. Furthermore, new possibilities are now offered by the isotopic records preserved in the interstellar grains of diamond, silicon, carbide and graphite found in meteorites to attempt a better understanding of the processes of stellar nucleosynthesis.

Papers in this issue discuss most of these aspects, and should prove valuable to researchers involved in isotopic studies in the field of Earth and Planetary Sciences as well as to graduate students and other scientists who may be interested in acquainting themselves with the contemporary scene in this field of research.

V K Gaur
Editor

Foreword

The unique “isotopic signatures” that characterise the various Earth and Planetary reservoirs make “Isotope Cosmo-Geochemistry” a powerful tool to study the past and contemporary physical, chemical and dynamical processes governing the evolution of the planet Earth and other Solar System objects. New ideas coupled with major advances in the detection and measurement of these isotopic signatures have led to significant strides in this field over the past couple of decades. Research in “Isotope Geochemistry” in India was initiated in the mid 1950s with a focus on the applications of Cosmic Ray produced isotopes to understand the time scales of atmospheric and marine processes and studies of Sr-isotopes to characterise crustal silicates. Over the years, the scope of studies in this newly emerging area has been considerably expanded through the use of additional isotope tracers in diverse fields of research, such as, the early evolution of the solar system objects, cosmic ray pre-history, origin and evolution of the continental flood basalts, geochemical cycles of elements, geomorphology, ocean circulation, palaeoclimate and catastrophic events in the Earth’s history.

This special issue of the Proceedings of the Indian Academy of Sciences (Earth and Planetary Sciences) contains some of the important papers (three plenary and sixteen invited) presented at the International Conference on “**Isotopes in the Solar System**” held at the Physical Research Laboratory at Ahmedabad in November 1997. These papers demonstrate the unique power of isotopes in the study of some of the dramatic transformations that have taken (or are taking) place in the extra-terrestrial and terrestrial settings. The first five contributions cover topics in isotope geology and geochemistry, followed by several papers on palaeoclimate records on different time scales and on the chemistry and dynamics of the river-ocean system. A series of papers dealing with isotopic studies of meteorites that have a direct bearing on the origin and early evolution of the solar system, pre-solar processes and cosmic ray prehistory completes the volume.

The article “Cosmic ray produced isotopes in the terrestrial system” by **D Lal** is a brief summary of current researches in this field with emphasis on the major advances made recently, thanks mainly to the newly developed Accelerator Mass Spectrometry

(AMS) technique that allows precise measurements of minute quantities of long-lived cosmogenic isotopes in terrestrial samples. This new technique has opened up several novel applications of cosmogenic nuclides as tracers for quantitative studies in Earth and Planetary Sciences, which hitherto could not be made using conventional techniques. Chemical and biological changes at geological boundaries and their probable causes is the central theme of the paper by **N Bhandari**, who reviews the salient features of various chemical and isotopic tracers in samples representing the Cretaceous/Tertiary, the Permo/Triassic and the Eocene/Oligocene boundaries from Indian sites. The results attest to an extra-terrestrial impact as the cause for the extinction of species at the K/T boundary, while terrestrial causes appear to be responsible for the biological changes observed at the P/T boundary. Analysis of K/T sections in the Deccan inter-trappeans coupled with their chronology further suggest that the major phase of eruption of the voluminous Deccan trap predate the K/T boundary event by ~ 2 Ma; this rules out Deccan volcanism as the major cause for extinction observed at this boundary.

The study of past climate and its variability continues to be an intriguing subject, of considerable interest among scientists, as it is a topic of direct relevance to the continued wellbeing and survival of mankind. The availability of source and process specific isotopic and elemental tracers along with highly sensitive techniques for their measurements have yielded excellent sets of high-resolution palaeoclimatic data from several types of archives. The review by **R J Delmas** provides an overview of the global climate and environmental changes retrieved from the Greenland and Antarctic ice cores. These studies provide a framework for investigating the teleconnections in climate change between the Northern and the Southern Hemispheres, an essential ingredient for a better understanding of the global climate system. The paper by **T L Ku and H C Li** demonstrates the utility of speleothems (a cave limestone deposit) as a high-resolution palaeoclimate recorder. Through the measurements of oxygen and carbon isotopes and trace elements, these authors have been able to reconstruct regional changes in precipitation,

temperature and vegetation in northeastern China. **S Chakraborty and R Ramesh** discuss the oxygen and carbon isotope records in a coral from the Gulf of Kutch, and conclude that $\delta^{18}\text{O}$ variations in it can be used to qualitatively reconstruct the regional rainfall variations.

One of the most conspicuous transformations of the Earth's surface during the Cenozoic is the uplift of the Himalayan mountain belt. **K K Sharma** provides an extensive review of the spatial and temporal evolution of the Himalaya both in terms of geology and tectonics. Has this uplift influenced changes in the global climate through enhanced aluminosilicate weathering and drawdown of atmospheric CO_2 ? This is a contentious issue. From the synthesis of global data on fluvial Sr and $^{87}\text{Sr}/^{86}\text{Sr}$, which is often used as a proxy for silicate weathering, **Y Huh and J M Edmond** conclude that there is no obvious climatic influence on weathering rates from the Tropics to the high Arctic and that the flux of dissolved load and CO_2 consumption for the Himalayan rivers are comparable to those of the Americas. **S Krishnaswami and Sunil K Singh** address the issue of carbonate-vs-silicate weathering in determining the Sr isotope composition of the head-waters of the Ganga. Through a comparison of $^{87}\text{Sr}/^{86}\text{Sr}$ and Sr/Ca in river waters, carbonates and silicates and inter-relation between Sr isotope composition and silicate derived cations in rivers, they argue that silicate weathering exerts a dominant control on the $^{87}\text{Sr}/^{86}\text{Sr}$ of these rivers.

Four papers in the volume are devoted to chemical and isotopic studies of sea-water. **W S Moore** through his studies of Ra isotopes in coastal waters off South Carolina brings out the importance of submarine groundwater discharge to the sea and suggests a possible approach to estimate its magnitude. The role of groundwater discharge to the oceans in contributing to the water and chemical budgets has been a topic of interest among hydrologists for some time. The approach presented in this paper shows a way to probe this issue. **E Maier-Reimer and G Handerson** discuss the basic requirements for successful modeling of particle reactive tracers in the ocean using ^{210}Pb as a test case. The ^{210}Pb distribution they obtain through a coupled general circulation-biogeochemical cycle model, is consistent with direct observations. **D S Alibo, M Amakawa and Y Nozaki** present two methods for the determination of indium in natural waters by flow injection inductively coupled plasma mass spectrometry. Their results from the Atlantic and the Pacific show that the inter-oceanic variations by and large mimic the behaviour of Al and that particle scavenging plays an important role in the distribution of indium in sea water. **S W A Naqvi et al** present data on the nitrogen isotope composition of various species of nitrogen (molecular N_2 , nitrate and nitrous oxide) and $\delta^{18}\text{O}$ in N_2O in the

suboxic water column of the Arabian Sea and suggest that microbially mediated reduction of NO_3^- to N_2 (denitrification) in the oxygen minimum zone greatly affects the natural isotopic abundances. They also observe that coupling between nitrification and denitrification is an important mechanism for N_2O production.

Of late, the isotopic studies of meteorites has progressed at a very rapid pace and contributed significantly to our current understanding of the origin and evolution of the early solar system. In fact laboratory studies of interstellar dust is now possible, thanks to the identification of diamond, silicon carbide and graphite grains in samples of primitive meteorites. Isotopic studies of these grains have confirmed their interstellar origin and provide new insight into the stellar environments in which they formed. Finally, isotopic studies of meteorites and lunar samples provide the only window to look at the intensity and composition of energetic particles of solar and galactic origin that have been present in the interplanetary space for aeons. All these aspects are discussed in a series of seven papers in the current volume. **U Ott** reviews the source and origin of interstellar grains found in meteorites and discusses new results that provide additional information on the origin of interstellar diamonds. **H Vanhala** presents results obtained from numerical simulation studies that suggest the possibility of a triggered origin of the solar system. The time scale for the collapse of the protosolar cloud to form the Sun, inferred from isotopic studies of meteorites, could be accommodated in this model. The presence of short-lived nuclides in the early solar system is discussed at length by **J N Goswami**, who considers the various suggestions regarding the source(s) of these nuclides and concludes that the current experimental data are consistent with their stellar origin. The time scales for the protosolar cloud collapse, for the formation of some of the first solar system solids and for thermal metamorphism and differentiation of meteorite parent bodies in the early solar system, that can be inferred from the data on short-lived nuclides in meteorites, are also discussed. The validity of the I-Xe dating technique to infer relative time scales of the early solar system processes is the theme of the paper by **C M Hohenberg et al**. They present recent experimental data to show that this dating approach can give meaningful information on the time scale for secondary processes such as aqueous alteration, thermal metamorphism, and shock, experienced by the meteorites on their parent bodies. **K Marti and K J Mathew** summarize the presently available data for noble gas isotopic compositions in solar wind, meteorites and planetary atmospheres and their possible interrelations, using Xe isotopes. The usefulness of the noble gas isotopic composition in understanding the processes affecting the evolution of

planetary atmosphere has also been discussed in this paper.

The last two papers in the volume present the progress made in understanding the energetic particle environment in the interplanetary space from studies of their interaction records in lunar samples and meteorites. **R C Reedy** reviews the data on the intensity of the contemporary solar energetic particles gathered from spacecraft observations, and compares them with those obtained from isotopic studies of lunar samples, that provide similar data, averaged over time scales of thousands to millions of years. Suggestions for further refinement of this data set to confirm the trends seen in the long-term behaviour of the solar activity are also presented. **R Michel and S Neumann** discuss the progress made in laboratory simulation studies of cosmic ray interactions with meteoroids in space and in analytical studies that attempt to model such interactions. Both these aspects are important for the interpretation of cosmogenic isotope data in meteorites in terms of cosmic ray intensity and their spatial and temporal variations. The need for further studies of pertinent nuclear reaction cross sections has been emphasized in both the papers.

The broad canvas of topics included in this volume amply demonstrates the wide scope of application of the isotopic records preserved in the Earth and

Planetary materials, to gain a quantitative understanding of the various processes operating in the planet Earth and other solar system objects during different epochs in their evolutionary history. It is hoped that the contents of this volume will provide an impetus to students and scientists alike in specific areas in Earth and Planetary sciences and serve as a meaningful source of current research for pursuing further work in these areas. We are grateful to all the contributors to this volume and also to the international panel of reviewers for their diligent and painstaking review of the manuscripts. We are grateful to Prof. V K Gaur, Editor-in-Chief, Proc. Indian Academy of Sciences, (EPS), for advice and encouragement received during the preparation of this volume. We thank Mr. P G Thomas, Mr. K R Nambiar, Mr. A D Shukla and Ms. K K Marhas of the Physical Research Laboratory for help during the various stages of its preparation, and the staff of the Indian Academy of Sciences for a commendable job in bringing out this volume within a short period of time. We gratefully acknowledge the financial assistance received from the Dept. of Space and the Dept. of Science and Technology, Govt. of India, for supporting this endeavour.

J N Goswami
S Krishnaswami
 Guest Editors

Cosmic ray produced isotopes in terrestrial systems

D LAL

Scripps Institution of Oceanography, Geosciences Research Division, UCSD 0220, La Jolla, CA 92093, USA
e-mail: dlal@ucsd.edu

Continuing improvements in the sensitivity of measurement of cosmic ray produced isotopes in environmental samples have progressively broadened the scope of their applications to characterise and quantify a wide variety of processes in earth and planetary sciences. In this article, I will concentrate on the new developments in the field of nuclear geophysics, based on isotopic changes produced by cosmic rays in the terrestrial systems. This field, which is best described as cosmic ray geophysics, caught roots with the discovery of cosmogenic ^{14}C on the Earth by Willard Libby in 1948, and grew rapidly at first, but slowed down during the '60s and '70s. In the '80s, there was a *renaissance* in cosmic ray produced isotope studies, thanks mainly to the developments of the accelerator mass spectrometry technique capable of measuring minute amounts of radioactivity in terrestrial samples. This technological advance has considerably enhanced the applications of cosmic ray produced isotopes and today we find them being used to address diverse problems in earth and planetary sciences.

I discuss the present scope of the field of cosmic ray geophysics with an emphasis on *geomorphology*. I must stress here that this is the decade in which this field, which has been studied passionately by geographers, geomorphologists and geochemists for more than five decades, has at its service nuclear methods to introduce numeric time controls in the range of centuries to millions of years.

1. Introduction

Our knowledge of the past climates and biogeochemical cycles depends on our capability to properly read and interpret the terrestrial proxy records. A prerequisite in these studies is the availability of suitable methods to correctly determine the rates of natural processes, and the chronology of the events. This task, it must be stressed here, is mostly not of dating events; more often it is of determining rates at which different geophysical reservoirs evolve through time by interactions with other reservoirs. As an example, consider the case of a rock mass ejected in a volcanic event, which survives partly or wholly through terrestrial processes. The age of the "rock", i.e. the time since the magma cooled down, is of interest in several problems and can be determined using (several) nuclear dating methods. But there occur changes in the rock due to a host of energetic processes to which the rock is subjected in its lifetime, by being

exposed to the environment. First, its surface weathers by the action of chemical and biological processes. The weathered surface may erode or serve as a host for accretion of exotic biological/chemical substances. The matrix of the rock continuously undergoes changes due to radioactive disintegrations of radionuclides present in the rock. Furthermore, nuclear interactions induced by cosmic radiation incident on the rock produce nuclides, some of which were not originally present in the rock. Similar is the case of oceans which formed a couple of hundred of million years ago. They have continuously evolved through time in their physical and chemical makeup. The evolutionary histories of rocks, and of oceans through time are of great importance for understanding Earth system processes. Note here that such terms as "age" of the atmosphere, or "age" of the ocean, do not have much meaning. This is so because the entity we are looking at has changed drastically since it formed. Strictly speaking, one cannot therefore assign an

Keywords. Cosmic rays; cosmogenic nuclides; nuclear geophysics; accelerator mass spectrometry (AMS); geomorphology.

“age” to them. To study the evolutionary history of the Earth, suitable tracers are needed which can throw light on the processes to which they are subjected, in addition to radioactive isotopes which can date specific events, such as sedimentation.

It is now being increasingly recognized that cosmic ray produced isotopic changes can be used to answer questions which relate to the evolution of the outer layers of the Earth—the atmosphere, the oceans, the cryosphere, and the lithosphere. There are a number of reasons why cosmic ray produced isotopes, also termed as “cosmogenic” isotopes serve as unique tracers:

- The flux of galactic cosmic rays, and therefore the production rates of cosmogenic isotopes on the Earth have essentially been constant through geological time;
- several cosmogenic stable and radioactive nuclei of widely different half-lives can be measured in materials naturally exposed through geochemical cycles in spite of their low production rates;
- the source functions of the cosmogenic isotopes produced in the atmosphere and in rocks/ice/oceans can be deduced fairly accurately.

The history of growth of the cosmogenic tracer field parallels that of the development of methods of determining isotopic composition of matter. The second half of the 1950s marked the beginning of studies of cosmogenic isotopes in the solar system, of ^3He in meteorites (Bauer 1947; Huntley 1948) and of ^{14}C and ^3He on the Earth (Anderson *et al* 1947; Libby *et al* 1949; Grosse *et al* 1951). These studies provided new insights into planetary processes and forced a rapid development of sensitive methods to measure ^{14}C and other cosmic ray produced isotopes. By the end of the sixties, the field of cosmogenic isotopes had already assumed an important stature, with discovery and studies of more than twenty stable and radioactive isotopes (Arnold *et al* 1961a,b; Honda and Arnold 1967) in meteorites and on the Earth (Lal and Peters 1962, 1967). These studies firmly established the value of cosmogenic nuclides as tracers for diverse processes in planetary sciences; however, the pace of these studies began to diminish because there were no real surprises or fresh excitement. These studies had become routine! In the case of meteorites, every new meteorite was analyzed when the sample became available. Application of cosmogenic nuclides to study terrestrial processes had also become routine, e.g. fall-out of nuclides in rains was measured at several sites. Studies of cosmogenic nuclide concentrations in the atmosphere were essentially stopped because of the cessation of air sampling programs, which were primarily taken up to sample fission products released in nuclear explosions. Measurements of ^{10}Be in marine sediments, which became accepted to be the only reliable method for dating sediments in million year

range, were however difficult since they involved processing hundreds of grams of sediment (cf. Amin *et al* 1966, 1975) and were continued by one or two groups, nevertheless, in view of its uniqueness for dating old sediments. A major new finding in the late sixties was the application of the ^{10}Be method for dating manganese nodules, which were found to have much higher ^{10}Be concentrations than the marine sediments (Somayajulu 1967), by virtue of their very slow rates of growth, $\sim \text{mm Ma}^{-1}$.

2. The '80s: A renaissance in the field of cosmic ray geophysics

The slow pace of work in the field of cosmic ray geophysics changed to an upsurge in the '80s with the development of Accelerator Mass Spectrometry (AMS), which made it considerably easier to measure long-lived cosmic ray produced radioisotopes in extra-terrestrial and terrestrial samples. AMS relies on the use of electrostatic tandem accelerators for particle identification, by accelerating isotopes of interest to MeV energies as negative ions. Two independent researches by Nelson *et al* (1977) in Canada, and by Bennett *et al* (1977) in the US, established the usefulness of the technique for detection of ^{14}C at natural levels. The central idea of using a mass-spectrometer to identify atoms of isotopes before they decay (and thus increasing detection sensitivity for the long-lived isotopes) was first enunciated by Muller (1977), who was however unsuccessful in his attempts to demonstrate its feasibility since he worked with positive ions and faced severe problems of interference, which are minimal with negative ions.

The AMS technique works efficiently for several nuclides (^{14}C , ^{41}Ca , ^{36}Cl , ^{26}Al , ^{10}Be and ^{129}I), permitting detection of $\sim 10^6$ atoms in each case (cf. Elmore and Phillips 1987), provided the isotope/element ratio is $\geq 10^{-14}$. This gave a gain factor of $1/10^6\lambda$ over isotope detection by the decay-counting method; here the disintegration constant, λ , is expressed in (min^{-1}) to correspond to the detection limit of approximately one dpm (disintegration per minute) by the counting method. The 4–6 orders of magnitude higher measurement sensitivity meant a large reduction in sample sizes, from (10–100) g to (1–10) mg, and in turn reopening a host of investigations carried out earlier using the decay-counting method, for a more detailed study of terrestrial and planetary processes. The decrease in the sample size meant:

- Economy on precious samples, e.g. the extraterrestrial and air-filter samples;
- making measurements with small sample sizes which were not possible earlier, e.g., ice core samples to delineate temporal variations in depositional fluxes of various nuclides.

Table 1. A select list of useful cosmogenic nuclides with half-lives exceeding ~ 1 year.

Isotope(s)	Half-life (year) (s = stable)	Main targets ^{a)}
³ H ^{b)}	12.3	O, Mg, Si, Fe (N, O)
³ He, ⁴ He	s	O, Mg, Si, Fe (N, O)
¹⁰ Be ^{b)}	1.6×10^6	O, Mg, Si, Fe (N, O)
¹⁴ C ^{b)}	5730	O, Mg, Si, Fe (N)
²⁰ Ne, ²¹ Ne, ²² Ne	s	Mg, Al, Si, Fe
²² Na ^{b)}	2.6	Mg, Al, Si, Fe (Ar)
²⁶ Al	7.1×10^5	Si, Al, Fe (Ar)
³² Si ^{b)}	~ 150	(Ar)
³⁶ Cl ^{b)}	3.0×10^5	Fe, Ca, K, Cl (Ar)
³⁶ Ar, ³⁸ Ar	s	Fe, Ca, K
³⁹ Ar ^{b)}	269	Fe, Ca, K (Ar)
⁴⁰ K	1.3×10^9	Fe
³⁹ K, ⁴¹ K	s	Fe
⁴¹ Ca	1.0×10^5	Ca, Fe
⁵³ Mn	3.7×10^6	Fe
⁵⁴ Mn	312 days	Fe
⁵⁵ Fe	2.7	Fe
⁵⁹ Ni	7.6×10^4	Ni, Fe
⁶⁰ Fe	1.5×10^6	Ni
⁶⁰ Co	5.27	Co, Ni
⁸¹ Kr ^{b)}	2.1×10^5	Rb, Sr, Zr (Kr)
⁷⁸ Kr, ⁸⁰ Kr, ⁸² Kr, ⁸³ Kr	s	Rb, Sr, Zr
¹²⁹ I ^{b)}	1.6×10^7	Te, Ba, La, Ce (Xe)
^{124–132} Xe	s	Te, Ba, La, Ce, I

^{a)} Elements from which most production occurs; those in parentheses are the targets for production in the Earth's atmosphere.

^{b)} Atmospheric cosmogenic isotopes.

- making adequate number of measurements to characterize geochemical reservoirs of interest, e.g. marine sediments and soil profiles;
- measuring concentrations of cosmogenic nuclides produced *in situ* in terrestrial solids.

Today, with the availability of the AMS, temporal variations in several long-lived radioisotopes can be quantitatively assessed in a wide range of sample types. In table 1, a list of isotopes of half lives ≥ 1 year which are produced from major target elements in the Earth's *atmosphere*, and in *common rocks*, are presented. Among the long-lived radioisotopes, ¹⁴C, ⁴¹Ca, ³⁶Cl, ²⁶Al, ¹⁰Be and ¹²⁹I have been extensively studied using the AMS in meteorites, in lunar samples and on the Earth; ongoing improvements in techniques would hopefully add the radionuclides ⁵⁵Fe, ³²Si, ⁵⁹Ni, ⁶⁰Fe and ⁵³Mn to this list in the near future!

Alongside the AMS development, substantial improvements were made in the sensitivity of conventional mass spectrometers for measurements of ³He and ²¹Ne (Craig and Poreda 1986; Kurz 1986; Marti and Craig 1987), permitting their measurements at levels of 10^5 – 10^6 atoms, thus achieving sensitivity similar to those of long-lived radioisotopes using AMS.

The AMS technique has now made it possible to measure several *atmospheric cosmogenic nuclides* (see

table 1) with ease. The most noteworthy impacts of this development have been towards the use of ¹⁴C and ¹⁰Be as tracers. These can now be measured practically in all samples exposed on the Earth's surface with great ease; in about 1 mg of modern carbon from the carbon cycle reservoirs for ¹⁴C, and in about 10–100 mg of modern soils and lake/marine sediments for ¹⁰Be. While radiocarbon allows a study of the past 40 ka, ¹⁰Be takes one back to about 5–7 Ma.

The applications of atmospheric ¹⁴C are vast indeed, however, no comprehensive review detailing all its applications exists to date. Next to atmospheric ¹⁴C, ¹⁰Be is the most employed tracer. Its most important attribute is its half-life, 1.5 Ma. None of the nuclides in the U-Th series have half-lives in the million years range. ¹⁰Be finds unique applications in dating soils and sedimentary deposits (Ku *et al* 1982; Bourles *et al* 1984; Barg *et al* 1997). For a critical discussion of the attributes and limitations of ¹⁰Be, reference is made to Lal (1998); and to some earlier broad reviews on ¹⁰Be (Morris 1991; McHargue and Damon 1991).

Data on time series of ¹⁴C/¹²C and ¹⁰Be are available for lake/marine sediments, tree rings, varves and corals (for ¹⁴C), and in marine sediments/manganese nodules and ice cores (for ¹⁰Be). These constitute invaluable data sets relevant to Earth's climatic history, past cosmic ray fluxes, solar activity and geomagnetic field intensity (Stuiver and Braziunas 1993; Yiou *et al* 1997; Finkel and Nishiizumi 1997).

The time series of ¹⁰Be and ³⁶Cl in polar ice have been measured back to ~ 50 ka BP (cf. Baumgartner *et al* 1996; Finkel and Nishiizumi 1996; Yiou *et al* 1996). These data are of immense value for understanding past changes in the atmospheric circulation and cosmic ray intensities.

These developments also opened up the field of nuclear geomorphology, merely by the fact that it has now become possible to measure the concentrations of several stable and radioactive isotopes produced *in situ* in terrestrial rocks and sediments. We will examine below the central premises on which this application is based, and briefly summarize the developments to date.

3. The scope of the cosmogenic *in situ* nuclides in earth sciences

A great variety of surface materials get “labelled” as a result of nuclear interactions of cosmic ray particles. The list is long for both the materials and the “nuclides”. As an illustration, some of the nuclides which are produced from cosmic ray interactions in common target nuclei present in typical surficial materials are given in table 1. The production rates increase exponentially with decreasing pressure in the atmosphere, with a characteristic mean pressure change of 160 g cm^{-2} .

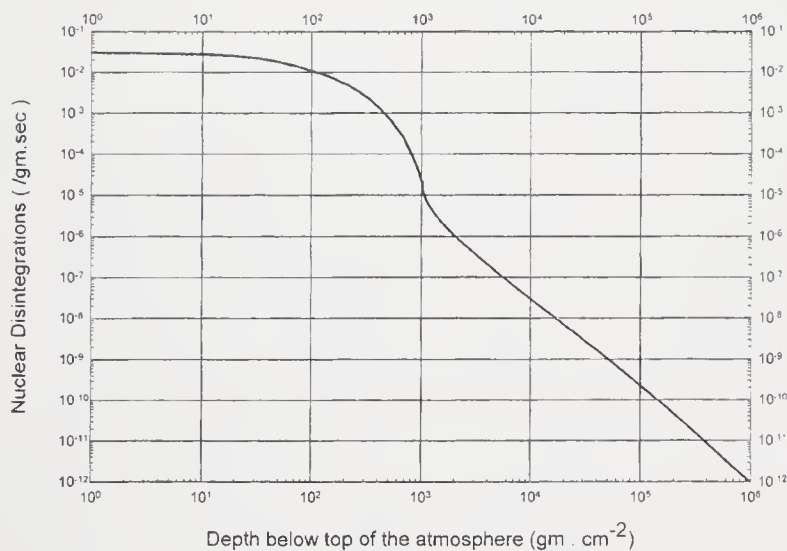


Figure 1. The approximate rate of all nuclear disintegrations due to the cosmic radiation, involving emission of one or more nucleons from the target nucleus, are plotted as a function of depth from the top of the atmosphere. The inflection at 1000 g cm^{-2} depth (sea level) represents a transition in the particle type in the cosmic radiation producing the nuclear disintegration, from nucleons at depths $< 1000 \text{ g cm}^{-2}$ to muons at greater depths.

The approximate latitude-averaged rates of nuclear disintegrations in the atmosphere, and at underground depths (below sea level) to a depth of 10^6 g cm^{-2} (about 3 km of rock) are presented in figure 1. The nature of the cosmic ray particles changes with depth in the atmosphere due to the growth and absorption of the nuclear cascade and the decay of pions into muons (Lal and Peters 1967; Lal 1988). The dominant mode of absorption of the secondary cosmic radiation is an exponential with depth (g cm^{-2}) in the atmosphere, and a power law underground. In the atmosphere, neutrons produce most of the nuclear disintegrations, while the muons, and the neutrons produced in interactions of muons are the interacting particles at underground depths. With our capability to measure $\sim 10^5$ – 10^6 atoms, nuclear disintegration rates $> 10^{-11} \text{ g}^{-1} \text{ sec}^{-1}$ can in principle be determined in natural samples exposed to cosmic radiation. This statement rests on the fact that deeper samples integrate cosmic ray exposure over longer periods of

time. Near surface samples have effective cosmic ray exposure ages of 10^4 – 10^6 years (Nishiizumi *et al* 1993). Deeper samples could be expected to have exposure ages of $> (10^7$ – $10^8)$ years.

The *in situ* produced cosmogenic nuclides which can be detected with the presently available techniques are listed in table 2 for several rock minerals. In polar ice, cosmic rays interactions with oxygen produce the isotopes, ^3H (half-life = 12.3 year), ^{14}C and ^{10}Be . As ice accumulates or ablates, the concentrations of these nuclides change in their traversal through the upper few meters (Lal *et al* 1987a, 1990).

The accumulation of the various nuclides in a rock horizon depends on its exposure history, specifically the geometry of exposure of the top meter or so of the surface. We have noted that the cosmic ray production rates decrease by a factor of “e” for shielding by about 160 g cm^{-2} . Thus, for example, in an eroding rock, the concentration of an *in situ*-produced nuclide owes itself to cosmic ray exposure during a period of time in which the rock erodes by a thickness of about 160 g cm^{-2} (about half a meter in a typical rock). The faster the erosion rate, the smaller the net accumulation of a nuclide in the rock; in other words, the effective period of cosmic ray exposure (or the near surface dwell time) depends directly on the erosion rate of the rock surface. Besides, the accumulation of a radioactive nuclide would also depend on its half-life; the steady state value will be reached earlier for nuclides with shorter half lives. The accumulation of a stable nuclide would, on the other hand, depend only on the erosion rate. In table 3, we have listed the effective near-surface dwell times for rocks eroding at different rates in the bracket (10^{-5} – 10^{-1}) cm per year. The accumulation time lies in the range of a few hundreds to a few million years for the cases discussed.

Since the effective steady state “exposure ages” of rocks is dependent on the erosion rate and the half life of the nuclide used as time marker, this value is independent of the total dwell time of the rocks in a given setting. It therefore becomes necessary to understand properly the implications of the estimated exposure ages in relation to the geological context. (For a

Table 2. *Cosmogenic nuclides of interest in some selected minerals.*

Mineral	Principal target elements	Cosmogenic nuclides of interest									Remarks
		^3He	^{21}Ne	^{39}Ar	^{14}C	^{36}Cl	^{26}Al	^{10}Be	^{53}Mn	^{81}Kr	
Diamond	C	✓									Ne isotopes possible in bort diamonds.
Garnet	Mg, Al, Si, O, Fe	✓	✓	✓	✓		✓	✓	✓		–
Ilmenite	Fe, Ti, O	✓	✓	✓	✓	✓	✓	✓	✓		–
Magnetite	Fe, O	✓	✓	✓	✓	✓	✓	✓	✓		–
Quartz	Si, O	✓	✓		✓		✓	✓			^3He leakage may be important.
Sphene	Ca, Ti, Si, O	✓	✓	✓	✓	✓	✓	✓			–
Zircon	Zr, Si, O	✓	✓		✓		✓	✓	✓		Radiogenic production of some nuclides may be important.

Table 3. *Effective exposure durations[†] (years), the effective surface dwell periods for steadily eroding rock surfaces.*

Nuclide	Principal target elements in rocks	Half-life (years)	Effective exposure duration (years) for different erosion rates (cm year ⁻¹)				
			10 ⁻⁵	10 ⁻⁴	10 ⁻³	10 ⁻²	10 ⁻¹
³⁹ Ar	Fe, Ca, K	269	3.9 × 10 ²	3.9 × 10 ²	3.9 × 10 ²	3.6 × 10 ²	2.3 × 10 ²
¹⁴ C	O, Mg, Si, Fe	5730	8.3 × 10 ³	8.2 × 10 ³	7.3 × 10 ³	3.5 × 10 ³	5.5 × 10 ²
⁸¹ Kr	Rb, Sr, Zr	2.1 × 10 ⁵	2.9 × 10 ⁵	2.0 × 10 ⁵	5.0 × 10 ⁴	5.8 × 10 ³	5.9 × 10 ²
³⁶ Cl	Fe, Ca, K, Cl	3.1 × 10 ⁵	4.2 × 10 ⁵	2.5 × 10 ⁵	5.2 × 10 ⁴	5.8 × 10 ³	5.9 × 10 ²
²⁶ Al	Si, Al, Fe	7.1 × 10 ⁵	8.7 × 10 ⁵	3.8 × 10 ⁵	5.6 × 10 ⁴	5.9 × 10 ³	5.9 × 10 ²
¹⁰ Be	O, Mg, Si, Fe	1.5 × 10 ⁶	1.6 × 10 ⁶	4.7 × 10 ⁵	5.8 × 10 ⁴	5.9 × 10 ³	5.9 × 10 ²
⁵³ Mn	Fe	3.73 × 10 ⁶	2.8 × 10 ⁶	5.3 × 10 ⁵	5.9 × 10 ⁴	5.9 × 10 ³	5.9 × 10 ²
³ He, ²¹ Ne	Mg, Si, Fe (O for ³ He)	stable	2.8 × 10 ⁶	5.9 × 10 ⁵	5.9 × 10 ⁴	5.9 × 10 ³	5.9 × 10 ²

[†] Based on rock density of 2.7 g cm⁻³, and 160 g cm⁻² for the mean absorption length for cosmic radiation.

discussion of this aspect of cosmogenic *in situ* studies, reference is made to Lal (1995), where a method has been suggested to report “transformed” exposure ages that correspond to the value which would have been obtained if the nuclide used had been stable).

3.1 Basic premises and special features underlying the use of cosmogenic nuclides in geomorphology

An important element in any quantitative geomorphic studies is the measurement of time elapsed between two *definable states of a system*; the various key processes of the system can then be characterized. Briefly, geomorphic studies require carrying out very detailed field work and learning how to read the proxy records of processes, and finally using some “clock” which can introduce numeric time control in the evolution of a given geomorphic system. In the absence of the availability of direct methods, estimates of geomorphic parameters have been made using the time-honored geophysical and geochemical mass balance techniques, with tectonic, hydro-geochemical and climatic constraints. Such techniques yield spatial and temporal averages, which are extremely useful. However, understanding geomorphic processes necessarily involves a detailed study of the full range of processes and their rates.

A number of nuclear methods, based on several radioactive nuclei which serve as reliable clocks, are presently available for dating the formation ages of igneous rocks, rates of accumulation of sediments, and measuring the time elapsed since a “molecule” has been isolated from one of the geospheres (e.g. formation of tree rings and formation of authigenic minerals). However, no radiometric method was available until recently for measuring time scales of processes which alter the shape or form of the Earth’s surface, e.g. landslides, glacial scour, erosion and fragmentation of rocks and aggradation. The reason for this shortcoming is obvious. All the nuclear techniques to date characterized the evolution of the rock from a fixed point in time, irrespective of its subsequent physical siting in the system, e.g. emplacement of an igneous rock on

the earth’s surface from a volcanic event (the parent-daughter relations are initialized in a molten rock and the accumulation of daughter nuclides within the rock which allows the determination of the age of the rock does not depend on the geometry of exposure of the rock on the earth’s surface). Similar is the case of isolation of an object from a dynamic chemical reservoir, e.g. the formation of a tree ring or a foraminifer shell in the ocean (the ¹⁴C/¹²C ratios in these samples are fixed at a certain value in the living organism that is representative of the reservoir wherefrom they derived the carbon and is nearly independent of the time when they were formed), or the burial of sediments (certain radionuclides are incorporated in the sediments as they accumulate and remain immobile with time, e.g. ¹⁰Be in marine sediments).

In all these examples the evolution of the sample matrix with respect to the relevant nuclides occurs within the volume of the sample, and is a function of time only, since the “agency” responsible for the “changes” is present within the sample.

On the other hand if the “agency” responsible for the change is extraneous to the sample, it is possible to decipher the setting in which it evolves as the changes recorded by the sample will be dependent on this setting. This requirement is met adequately in the case of interaction of cosmic radiation with terrestrial samples. The direct production of nuclides in terrestrial matter by cosmic rays depends on the altitude/latitude of the sample as well as its shape. This is a direct manifestation of the fact that as the cosmic ray particles penetrate through matter, they lose energy in the nuclear reactions they produce. Consequently, the rate of nuclear transmutations at any point within an object depends on its physical and chemical state, its location, and its shape. Thus, we see that in contrast to *in situ* nuclear transformations due to radioactivity, *in situ* cosmogenic transformations are dependent on the setting in which they were exposed to cosmic rays. The *in situ* cosmogenic isotopes can therefore reveal information on the exposure history of a sample.

The determination of cosmogenic isotopic changes in rocks/sediment requires care and state-of-the-art measurements, as discussed earlier. Three radionuclides, ^{36}Cl , ^{26}Al and ^{10}Be , that are also produced in significant amount by cosmic ray interactions in the atmosphere (Lal and Peters 1967) are of some concern (as an environmental source) in studies of their *in situ* cosmogenic production in rocks. These nuclides are removed from the atmosphere by wet precipitations and can get incorporated in the rock mass by adsorption. In the *in situ* parlance, these potentially interfering atmospheric nuclides are designated as “garden variety”, to distinguish them from those produced “*in situ*” in rocks by cosmic radiation.

The task of studying cosmogenic *in situ* isotopes is a challenging one, since the cosmic ray intensity is appreciably decreased at sea level and at mountain altitudes due to its absorption in the atmosphere. The atmosphere represents a thickness equivalent to thirteen nuclear interaction mean-free paths ($1 \text{ mfp} = 80 \text{ g cm}^{-2}$). The latitude-averaged rates of nuclear disintegration at an altitude of 3 km and at sea level are approximately 1.5×10^{-2} and 1.5×10^{-3} times the value at the top of the atmosphere, respectively. In surficial rock and soil samples, the range in concentrations of *in situ* ^{10}Be and ^{26}Al are rather small, of the order of $(1-10) \times 10^6$ atoms g^{-1} (SiO_2) (cf. Nishiizumi *et al* 1993) compared to their typical concentrations $> 10^{10}$ atoms g^{-1} , in meteorites. Nevertheless, the task of measuring the small concentrations of the *in situ* cosmogenic radionuclides free of “garden variety” counterparts is feasible.

Experimentally, developments in the extraction of a small number of atoms, $\sim 10^6-10^7$ atoms, from terrestrial rocks have been very successful, leading to unambiguous measurements of ^{10}Be and ^{26}Al signals due to cosmogenic *in situ* production at concentrations of $\geq 10^5$ atoms g^{-1} (Nishiizumi *et al* 1989, 1993). This is made possible by measuring the nuclides in quartz, which is present in most common rock types (excluding basalts), and can be cleansed off any garden-variety nuclides by treatment with strong acids (Lal and Arnold 1985). Other minerals can presumably serve as well, e.g. olivines of grain size $\geq 0.5 \text{ mm}$ (Nishiizumi *et al* 1990). Attempts to use the ubiquitous minerals magnetite and ilmenite, in acidic and basic rocks, are now being made (Lal, Vogt and Elmore, unpublished).

Theoretically, the application of the cosmogenic nuclides as tracers in geomorphology is straightforward. Analytical models show considerable sensitivity to geomorphic parameters; the suite of available stable and radioactive nuclei, with their (cosmic ray) source functions, seem ideal for studying geomorphic processes (Lal 1991; Nishiizumi *et al* 1993). A prerequisite in applications of these nuclides is a knowledge of their source functions. The *in situ* production rates of ^{10}Be and ^{26}Al have been measured in Sierra Nevada rocks

with glacial polish, which assures that their surface has not eroded since their free exposure (after excavation from depths by glacier erosion) to cosmic radiation (Nishiizumi *et al* 1989). The *in situ* production rates of ^{36}Cl have also been determined fairly accurately (Dep *et al* 1994; Phillips *et al* 1996).

Despite our good command of the techniques of measurements of ultra-low isotope concentrations, we have yet to learn how to realistically model the measured nuclide concentrations. Tracers are not a panacea; they are at best merely tools. Even if a model is not realistic, there would still be an output, which would however have no semblance with reality. The task of delineating geomorphic processes is that of observing nature in space, at the *present time*, and translating this into a model for the *past*. Tests or constraints can be put on models by examining several cosmogenic nuclides of different half-lives.

3.2 An overview of ongoing studies of geomorphic processes

In geomorphic studies, which bear some semblance to studies of cosmogenic nuclides in meteorites, one of the model outputs is the exposure ages of rocks. But the analogy stops here. The terrestrial rocks undergo appreciable erosion, and in most cases, except for rocks brought to a new setting in the recent past, as due to outcropping of a deep-seated rock by glacier action, or a meteorite impact, or exposing a previously shielded rock surface in a moraine setting, appreciable surface losses occur. The rock surfaces may also be in an erosion equilibrium with production, which occurs when $\mu\epsilon > \lambda$; here λ is the nuclide disintegration constant, ϵ is the average surface erosion rate, and μ is the reciprocal of the mean absorption length for cosmic rays in the rock. In this case, the effective exposure duration of the rock, i.e. the effective number of years of surface exposure given by the ratio of measured isotope concentration and surface production rate, is much smaller than its total surface dwell time.

For testing the usefulness of this nuclear dating method, some trials were made recently by Nishiizumi *et al* (1993) by measuring the concentrations of *in situ* cosmogenic nuclides ^{10}Be and ^{26}Al in the following natural samples listed in increasing order of complexity:

- (i) Low erosion rock surfaces from several locations in Antarctica;
- (ii) typical rock surfaces exposed at temperate and high latitudes;
- (iii) cosmic ray shielded rocks suddenly exposed on the surface due to the impact of a meteorite;
- (iv) cosmic ray shielded rocks exposed by glacier scour, with evidence of no subsequent erosion, as evidenced by the presence of glacial polish;
- (v) aggradation on a surface;

- (vi) glacial moraines;
- (vii) eroding bedrocks;
- (viii) alluvial fans; and
- (ix) marine terraces.

Context (iv) provided a direct determination of cosmic ray production rates of ^{10}Be and ^{26}Al in the Sierra Nevada ranges (Nishiizumi *et al* 1989). Using these results along with cosmic ray data, the latitude/altitude variation in the production rates of these nuclides could be estimated (Lal 1991). Measured erosion rates, based on ^{10}Be and ^{26}Al , for rocks collected from diverse geographical settings, are given by Nishiizumi *et al* (1993). The lowest erosion rate rock surfaces were discovered by Nishiizumi *et al* (1991a) in Antarctica (context (i)), with erosion rates $< 2 \text{ mm Ma}^{-1}$. Note that these represent the first direct measurements of rock erosion rates at the surfaces sampled. Before the development of the nuclear method under discussion, erosion rates could be deduced only on a gross basis for a watershed, based on material balance considerations for the dissolved and particulate fluvial transports.

The results of analyses of other geomorphic samples in deep-seated cosmic ray shielded rocks exposed due to the impact of the Canyon Diablo iron meteorite (Nishiizumi *et al* 1991b), producing the Meteor Crater (context iv), and aggradation at the Sherwin Till site (Nishiizumi *et al* 1993), which was buried by a thick layer of volcanic ash about 0.73 Ma ago (context (iv)), were very exemplary. The time of impact of the Canyon Diablo meteorite was estimated $\sim 50 \text{ Ma}$ ago. From studies of ^{10}Be and ^{26}Al in the Till, some limits could be placed on the accumulation rate of sediment at the Till, $\sim (1-3) \times 10^{-3} \text{ cm year}^{-1}$. Further measurements are needed to determine more precisely the aggradation rates.

Several examples of potential and present geomorphic studies involving dating of surfaces are also summarized by Cerling and Craig (1994); these are: *glaciation, erosion rates, Inselbergs, Kopjes and ancient erosion surfaces, volcanic events, alluvial deposits, ice ablation rates, ages of meteor craters, desert pavement, cataclysmic floods, the final riddle of Sphinx and other archaeological studies*.

It would be also appropriate to cite here a few special studies which clearly underscore the fact that whatever applications have been made to date, mark the beginning of a long, exciting road of adventures in geomorphology. We begin by citing two new cosmogenic *in situ* methods which promise information on both "surface erosion rates" and "exposure age". It was mentioned earlier that the definition of "exposure age" has first to be understood implicitly in context to the geological setting. Cosmogenic *in situ* nuclides give the effective surface exposure age, which is quite different from the time since a rock was emplaced at surface, e.g. excavated in a meteoritic impact. The effective surface exposure age is dependent on the

surface erosion rate, ϵ , and only when $\epsilon = 0$, does it equal the emplacement age (for a detailed discussion of this problem, see Lal 1995). Therefore the geologic context is very important, which is a prerequisite to make these studies useful. Most of the isotopes in table 1 are produced by spallation of the target nuclei by high energy neutrons. In the case of ^{36}Cl , it is also produced in the capture of thermal neutron by ^{35}Cl . The production rate of neutron produced ^{36}Cl shows a transition at a depth of about 100 g cm^{-2} . Dep *et al* (1998) show that this feature, in contrast to spallation nuclides whose production rates decrease exponentially with depth with a characteristic absorption, allows one to determine both rock erosion rate and exposure age. Another interesting case is of production of ^{36}Cl in calcium by muons at underground depths. Stone *et al* (1994) discuss the various ^{36}Cl production mechanisms and take advantage of the depth variant change in ^{36}Cl production rate to determine the exposure histories of the calcite formations.

The *in situ* produced nuclide ^{14}C has been successfully used to determine ice ablation (Lal *et al* 1990) and accumulation rates (Lal *et al* 1997). This nuclide is produced in the ice, primarily in the spallation of oxygen by energetic cosmic ray neutrons. The contribution from this source generally far exceeds the ^{14}C trapped in the ice during bubble closing (Jull *et al* 1994). The special attraction of this tracer is that one can use it to determine both ablation and past ice accumulation rates, for which no other direct methods are available. In cases where layer thicknesses can be determined, accumulation rates can be determined using ice flow models.

The geomorphic studies have continued to grow to date, addressing other questions where the cosmogenic nuclides could be harnessed to provide some numeric time controls. New findings that rock surfaces erode at very low rates in the dry valleys of Antarctica $\sim 1 \text{ mm Ma}^{-1}$ (Nishiizumi *et al* 1991a), that diamonds are irradiated to cosmic radiation within depths of $\sim 1 \text{ m}$ in the alluvium (Lal *et al* 1987b), that the last glacial maximum in the Wind River Range (feeding the Fremont Lake basin) occurred at $21,700 \pm 700 \text{ year BP}$, and lasted 5900 year (Gosse *et al* 1995), that earthquake recurrence dates in the Owens Valley can be found from a measurement of concentrations of *in situ* produced ^{10}Be and ^{26}Al in the Sierra Nevada alluvial fans (Bierman *et al* 1995), that from a study of *in situ* ^{10}Be and ^{26}Al in cave-deposited river sediments, one can determine downcutting rates of the New River, Virginia (Granger *et al* 1997), that formation ages of terraces in the Indus Valley can be deduced from ^{10}Be , ^{26}Al measurements in the polished rock surfaces in the terraces (Burbank *et al* 1996; Sharma *et al* 1998), provide selected examples of rapid development in this area.

The field of nuclear geomorphology is in its infancy. It is expected to grow further, limited only in its

applications by the availability of techniques for determining isotopic changes produced by the cosmic radiation. But I must hasten to remark that *isotopes* by themselves cannot reveal terrestrial processes or history. They can be utilized as remarkable tools, only when we understand Earth systems well enough to construct appropriate theoretical models which are consonant with the workings of nature.

4. Concluding remarks

As a result of advances in our understanding of phenomena of modern physics, we are now able to estimate, with a fair degree of confidence, the time it takes to erode away a mountain, and several critical time scales in geomorphic processes. We see that the history of slow, imperceptible changes in the face of the Earth are recorded ingeniously by nature in its diverse solids, e.g. rocks, sediments and ice sheets. Thus, the field of geomorphology, one of the oldest, has now come alive and assumed a new stature by the realization that several diagnostic isotopes which are continually produced in the rock matrix by the galactic cosmic radiation, can be used to unravel the history of solids.

Acknowledgements

I take this opportunity to express my grateful thanks to several of my colleagues, who with their theoretical and experimental abilities, helped speedy development of the field of cosmogenic *in situ* isotopes to its present status. I am indebted to J N Goswami and S Krishnaswami for helpful discussions and critical comments on an earlier version of this manuscript. I also thank R Morgan for his technical contributions in the preparation of this exposition.

References

- Amin B S, Kharkar D P and Lal D 1966 Cosmogenic ^{10}Be and ^{26}Al in marine sediments; *Deep Sea Res.* **13** 805–824
- Amin B S, Lal D and Somayajulu B L K 1975 Chronology of marine sediments using the ^{10}Be method: intercomparison with other methods; *Geochim. Cosmochim. Acta.* **39** 1187–1192
- Anderson E C, Libby W F, Weinhouse S, Reid A F, Kirschenbaum A D and Grosse A V 1947 Natural radio carbon from cosmic radiation; *Phys. Rev.* **72** 931–936
- Arnold J R, Honda M and Shedlovsky J P 1961a Radioactive species produced by cosmic rays in the Aroos iron meteorite; *Geochim. Cosmochim. Acta* **23** 219–232
- Arnold J R, Lal D and Honda M 1961b Record of cosmic ray intensity in meteorites; *J. Geophys. Res.* **66** 3541–3546
- Barg E, Lal D, Southon J R, Caffee M W, Finkel R C and Pavich M J 1997 Beryllium geochemistry in soils: evaluation of $^{10}\text{Be}/^9\text{Be}$ ratios in authigenic minerals as a basis for age models; *Chem. Geol.* **140** 237–258
- Bauer C A 1947 Production of helium in meteorites; *Phys. Rev.* **72** 354–355
- Baumgartner S, Beer J, Suter M, Dittrich-Hannen B, Clausen H and Johnsen S J 1996 Chlorine 36 fallout in the Summit Greenland Ice core project ice core; *J. Geophys. Res.* **102** C26659–C26662
- Bennett C L, Beukens R P, Clover M R, Gove H E, Liebert R B *et al* 1977 Radiocarbon dating using electrostatic accelerators: negative ions provide the key; *Science* **198** 508–510
- Bierman P R, Gillespie A R and Caffee M W 1995 Cosmogenic ages for earthquake recurrence intervals and debris flow fan deposition, Owens Valley, California; *Science* **270** 447–450
- Bourles D, Raisbeck G M, Yiou F, Loiseaux J M, Lieuvain M, Klein J and Middleton R 1984 Investigation of the possible association of ^{10}Be and ^{26}Al with biogenic matter in the marine environment; *Nucl. Instr. Meth.* **B5** 365–370
- Bourles D, Raisbeck G M and Yiou F 1989 ^{10}Be and ^9Be in marine sediments and their potential for dating; *Geochim. Cosmochim. Acta* **53** 443–452
- Burbank D W, Leland J, Fielding E, Anderson R S, Brozovic N, Reid M R and Duncan C 1996 Bedrock incision, rock uplift and threshold hill slopes in the Northwest Himalayas; *Nature* **379** 505–510
- Cerling T E and Craig H 1994 Geomorphology and *in situ* cosmogenic isotopes; *Ann. Rev. Earth Planet. Sci.* **22** 273–317
- Craig H and Poreda R J 1986 Cosmogenic ^3He in terrestrial rocks: the summit lavas of Maui; *Proc. Natl. Acad. Sci.* **83** 1970–1974
- Dep L, Elmore D, Lipschutz M, Vogt S, Phillips F and Zreda M 1994 Depth dependence of cosmogenic neutron capture produced ^{36}Cl in a terrestrial rock; *Nucl. Instr. Meth.* **B92** 301
- Dep L, Elmore D, Vogt S, Sharma P, Bourgeois M and Dunne A 1998 Erosion corrected ages of Quaternary geomorphic events using cosmogenic ^{36}Cl in rocks (preprint)
- Elmore D and Phillips F M 1987 Accelerator mass spectrometry for measurement of long lived radioisotopes; *Science* **236** 543–550
- Finkel R C and Nishiizumi N 1997 Beryllium 10 concentrations in the Greenland Ice Sheet Project 2 ice core from 3–40 ka; *J. Geophys. Res.* **102** C26699–C26707
- Gosse J C, Klein J, Evenson E B, Lawn B and Middleton R 1995 Beryllium-10 dating of the duration and retreat of the last Pinedale Glacial sequence; *Science* **268** 1329–1333
- Granger D E, Kirchner J W and Finkel R C 1997 Quaternary downcutting rate of the New River, Virginia measured from differential decay of cosmogenic ^{26}Al and ^{10}Be in cave-deposited alluvium; *Geology* **25** 107–110
- Grosse A V, Johnston W H, Wolfgang R L and Libby W F 1951 Tritium in nature; *Science* **113** 1–2
- Honda M and Arnold J 1967 Effects of cosmic rays on meteorites; *Handb. der Phys.* **XLV1/2** 613–631
- Huntley H E 1948 Production of helium by cosmic rays; *Nature* **161** 356
- Jull A J T, Lal D, Donahue, D J, Mayewski P, Loria C, Raynaud D, Petit J 1994 Measurements of cosmic-ray-produced ^{14}C in firn and ice from Antarctica; *Nucl. Instr. Meth.* **B92** 326–330
- Ku T L, Kusakabe M, Nelson D E, Southon J R, Korteling R G, Vogel J and Nowikow I 1982 Constancy of oceanic deposition of ^{10}Be as recorded in manganese crusts; *Nature* **299** 240–242
- Kurz M 1986 Cosmogenic ^3He in terrestrial igneous rocks; *Nature* **320** 435–439
- Lal D and Peters B 1962 Cosmic ray produced isotopes and their applications to problems in geophysics; In *Progress in Elementary Particle and Cosmic Ray Physics* (eds) J G Wilson and S A Wouthuysen (North Holland Pub. Co.) **VI** pp. 1–74
- Lal D and Peters B 1967 Cosmic ray produced activity on the earth; *Handb. der Phys.* **46** 551–612

- Lal D and Arnold J R 1985 Tracing quartz through the environment; *Proc. Indian Acad. Sci. (Earth Planet. Sci.)* **94** 1–5
- Lal D, Nishiizumi K and Arnold J R 1987a *In situ* cosmogenic ^3H , ^{14}C and ^{10}Be for determining the net accumulation and ablation rates of ice sheets; *J. Geophys. Res.* **92** B4947–B4952
- Lal D, Nishiizumi K, Middleton R and Craig H 1987b Cosmogenic ^{10}Be in Zaire alluvial diamonds: implications for ^3He contents of diamonds; *Nature* **328** 139–141
- Lal D 1988 *In situ*-produced cosmogenic isotopes in terrestrial rocks; *Ann. Rev. Earth Planet. Sci.* **16** 355–388
- Lal D, Jull A J T, Donahue D J, Burtner D, and Nishiizumi K 1990 Polar ice ablation rates based on *in situ* cosmogenic ^{14}C ; *Nature* **346** 350–352
- Lal D 1991 Cosmic ray tagging of erosion surfaces: *in situ* production rates and erosion models; *Earth Planet. Sci. Lett.* **104** 424–439
- Lal D 1995 On cosmic ray exposure ages of terrestrial rocks; a suggestion; *Radiocarbon* **37** 889–895
- Lal D, Jull A J T, Burr G S and Donahue D J 1997 Measurements of *in situ* ^{14}C concentrations in Greenland Ice Sheet Project 2 ice covering a 17-kyr time span: implications to ice flow dynamics; *J. Geophys. Res.* **102** C26505–C26511
- Lal D 1998 Cosmogenic ^{10}Be : a critical view of its widespread dominion in geosciences; *Proc Indian Acad. Sci. (Earth Planet. Sci.)* in press
- Libby W F, Anderson E C and Arnold J R 1949 Age determination by radiocarbon content: world-wide assay of natural radiocarbon; *Science* **109** 227–228
- Marti K and Craig H 1987 Cosmic ray produced neon and helium in the Summit lavas of Maui; *Nature* **325** 335–337
- McHargue L R and Damon P E 1991 The global beryllium-10 cycle; *Rev. Geophys.* **29** 141–158
- Morris J D 1991 Applications of cosmogenic ^{10}Be problems in earth sciences; *Ann. Rev. Earth Planet. Sci.* **19** 313–350
- Muller R A 1977 Radioisotope dating with a cyclotron; *Science* **196** 489–494
- Nelson D E, Koertling R G and Stott W R 1977 Carbon-14: direct detection at natural concentrations; *Science* **198** 507–508
- Nishiizumi K, Winterer E L, Kohl C P, Klein J, Middleton R, Lal D and Arnold J R 1989 Cosmic ray production rates of ^{10}Be and ^{26}Al in quartz from glacially polished rocks; *J. Geophys. Res.* **94** C17907–C17915
- Nishiizumi K, Klein J, Middleton R and Craig H 1990 Cosmogenic ^{10}Be , ^{26}Al and ^3He in olivine from Maui lavas; *Earth Planet. Sci. Lett.* **98** 263–266
- Nishiizumi K, Kohl C P, Arnold J R, Klein J and Fink D 1991a Cosmic ray produced ^{10}Be and ^{26}Al in Antarctic rocks: exposure dating and erosion history; *Earth Planet. Sci. Lett.* **104** 440–454
- Nishiizumi K, Kohl C P, Shoemaker E M, Arnold J R, Klein J, Fink D and Middleton R 1991b *In situ* ^{10}Be , ^{26}Al exposure ages at Meteor Crater, Arizona; *Geochim. Cosmochim. Acta* **55** 2699–2703
- Nishiizumi K, Kohl C P, Arnold J R, Dorn R, Klein J, Fink D, Middleton R and Lal D 1993 Role of *in situ* cosmogenic nuclides ^{10}Be and ^{26}Al in the study of diverse geomorphic processes; *Earth Surface Proc. and Landforms* **18** 407–425
- Phillips F M, Zreda M G, Elmore D and Sharma P 1996 A re-evaluation of cosmogenic ^{36}Cl production rates in terrestrial rocks; *Geophys. Res. Lett.* **23** 949–952
- Sharma K K, Gu Z Y, Lal D, Caffee M W and Southon J 1998 Late Quaternary morphotectonic evolution of the upper Indus Valley profile; A cosmogenic radionuclide study of river polished surfaces; *Curr. Sci.* **75** 366–371
- Somayajulu B L K 1967 Beryllium-10 in a manganese nodule; *Science* **156** 1219–1220
- Stone J, Allan G L, Fifield L K, Evans J M and Chivas A R 1994 Limestone erosion measurements with cosmogenic chlorine-36 in calcite; preliminary results from Australia; *Nucl. Instr. Meth.* **B92** 311–316
- Stuiver M and Braziunas T F 1993 Sun, ocean, climate and atmospheric $^{14}\text{CO}_2$: an evaluation of causal and spectral relationships; *The Holocene* **3** 355–363
- Yiou F, Raisbeck G M, Baumgartner S, Beer J, Hammer C, Johnsen S, Jouzel J, Kubik P W, Lestringuez J, Stievenard M, Suter M and Yiou P 1997 Beryllium 10 in the Greenland Ice Project ice core at Summit, Greenland; *J. Geophys. Res.* **102** C26783–C26794

Astronomical and terrestrial causes of physical, chemical and biological changes at geological boundaries

N BHANDARI

Physical Research Laboratory, Navrangpura, Ahmedabad 380 009, India
e-mail: bhandari@prl.ernet.in

The boundary horizons of the Cretaceous-Tertiary (Um Sohryngkew River section, Meghalaya and Anjar section, Kutch), the Permo-Triassic (Guling, Lalung, Ganmachidam and Attargoo sections, Spiti valley) and the Eocene-Oligocene (Tapti River section, Gujarat) have been identified in the sedimentary records of the Indian subcontinent. These sections have been studied for geochemical anomalies. The results are discussed in the framework of extra-terrestrial and terrestrial causes proposed to explain the physical, chemical and mineralogical observations at these boundaries. A critical analysis suggests that although the astronomical causes, particularly the bolide impacts, can easily explain the geochemical and physical changes, the terrestrial causes (volcanism) may have played a significant role in creating the biological stress observed in fossil records (mass extinction) at or near some of these boundaries.

1. Introduction

There are numerous extraterrestrial causes proposed to explain the observed physical, chemical and biological changes observed at various geological boundaries and, at the same time, there are some terrestrial causes which can do so equally effectively. Cratered surfaces of planets and satellites, meteor streams, fall of meteorites and strewn field of tektites suggest massive impacts of interplanetary bodies on the Earth in the past, which through a series of physico-chemical processes can result in mass extinctions associated with the geological boundaries. The presence of heavily shocked minerals and chemical enrichment of platinum group elements in approximately meteoritic proportions at some of the boundary horizons of sedimentary records corroborates the impact scenario.

The major source of bolides is the Earth-crossing asteroids and comets (Weissman 1982; Wetherill and Shoemaker 1982). A number of asteroids belonging to the Apollo-Amor families are known to intercept the orbit of the Earth. In addition comets from the Oort's cloud, which are loosely bound to the solar system by a weak gravitational field, can occasionally get deflected into planetary crossing orbits in the inner solar

system. Several mechanisms, capable of periodically deflecting comets from the Oort's belt are known to exist. These include the passage of the solar system through giant molecular clouds, gravitational perturbation by nearby stars or by any invisible solar companion or by Planet X which is effective in deflecting comets from Kuipers belt (Clube and Napier 1986; Davis *et al* 1984; Hills 1986). In addition to these processes by which the minor objects of the solar system can strike the Earth, a plausible mechanism by which the flux of extra solar material can periodically increase is due to the carousel-like motion of the solar system through the spiral arms of our galaxy. Besides the bolide impacts, several other astronomical mechanisms have been proposed which are capable of producing mass extinction. These include supernovae explosions (Ellis and Schramm 1995) or collision of neutron stars in the vicinity (within 10 kpc) of the Earth. The accompanying bursts of neutrinos and intense particle fluxes can give rise to radiation overdose and thermal neutron (Yayanos 1983) and muon induced transmutations can result in disruption of food chain. These are cited as possible pathways resulting in mass extinction. An alternative mechanism is that the intense radiation destroys the

Keywords. Geological boundaries; Deccan volcanism; bolide impacts; mass extinction; geochemical anomalies.

protective ozone layer thereby exposing both the marine and terrestrial organisms to the potentially lethal solar ultraviolet radiation, ultimately damaging the fabric of life on the Earth. Other extra-terrestrial hypotheses include accumulation of dark matter within the Earth which periodically generates heat (Abbas and Abbas 1998) and, in turn, can give rise to continental flood basalt volcanism resulting in extinctions.

On the other hand, there are several terrestrial processes like volcanism and sea level changes which are equally effective in bringing about drastic biological changes as observed in the sedimentary records. The prime candidate is flood basalt volcanism, which through a chain of physico-chemical processes culminating in climatic changes can provide severe stress, adequate to bring about mass extinction (McLean 1985). Eustatic changes in sea water also provide an effective mechanism for bringing about extinction of near shore species.

2. Evidence from extinction horizons

More than thirteen geological boundaries have been studied in detail for isotopic, chemical and mineralogical signatures in terrestrial sediments (see Rampino and Haggerty 1996; Shukla and Bhandari 1997 for a summary).

Physical evidence such as the presence of tektites, shocked quartz and other minerals, chemical anomalies e.g. high concentration of platinum group and other diagnostic elements and abrupt isotopic excursions of $\delta^{13}\text{C}$ and $\delta^{18}\text{O}$ have been documented at some of these boundaries. For understanding the physico-chemical processes responsible for extinctions at various boundaries, it is important to distinguish between global and local effects. The studies indicate that every extinction is unique and the imprints of these markers at different boundaries are not identical, making it difficult to invoke a single process responsible for all of them. There are large craters formed on the Earth without accompanying mass extinctions and there are extinctions where it has not been possible to identify a crater large enough to be responsible for the extinction. Kyte (1988) has mentioned that six stratigraphic boundaries (Cenomanian-Turonian, Callovian-Oxfordian, Early-Mid Jurassic, Permian-Triassic, Frasnian-Famennian and Proterozoic-Cambrian) may possibly be of impact origin whereas there are other boundaries where signatures of impact exist with negligible or no indication of extinction. Among the known (~ 130) impact craters listed by Grieve (1991) there are nine big craters (including Chicxulub) having sizes ranging from 55 to 200 km and ages varying between 33 and 1970 Ma. Among the twenty four well defined extinction peaks in the genus-level data (Raup and Sepkoski 1988), impact signatures are

found only in the case of five extinction boundaries (Pliocene, 2.3 Ma; Late Eocene, 33.7 Ma; K/T, 65 Ma; Triassic-Jurassic, 205 Ma and Frasnian-Famennian, 367 Ma (Rampino and Haggerty 1996)). Thus it is clear that large impacts are not responsible for all the observed extinctions. Similarly the synchronicity of major volcanic episodes and extinction events seen at several boundaries suggests a causal relation between them. But whereas some extinction events are closely related in time with major volcanic episodes, there also exist extinctions without concomitant volcanic activity as well as major volcanic episodes without extinctions. It is, therefore, unlikely that there is a general theory of extinction; rather it appears that there are several mechanisms capable of producing stress on life and some time they operate collectively and can result in mass extinctions. Evidence for causes other than bolide impact and volcanism, discussed above have not emerged from the observations at various boundaries carried out so far. A variety of evidences for impact have been found at the K/T boundary (table 1) but such a detailed work has not been done on other boundaries.

We will now summarize the work done on Indian sections on K/T, P/T and E/O boundaries within the framework of the impact and volcanic hypotheses. The Indian sedimentary records provide crucial evidences since India was geographically placed in a special position at the time of K/T and P/T transitions. Firstly, the Deccan flood basalt episodes occurred in central and western India during or close to the K/T boundary event. During this period, India was located outside the fallout zone of the Chicxulub ejecta (Alvarez 1995). Thus by comparing the Indian and other sedimentary records, the volcanic and impact signatures can be easily isolated. At the P/T transition time, India was located close to the Falkland island in the southern hemisphere where Rampino (1995) has proposed a large impact structure, which may have been responsible for this most severe extinction in Earth's history. Thus, in the context of the distribution of impact ejecta fallout, unlike the northern hemispheric sites (China, Alps etc.), India was located in a more favourable location.

3. Cretaceous-Tertiary boundary

The Alvarez hypothesis (Alvarez *et al* 1980) that an extraterrestrial object of the size ~ 10 km diameter hit the Earth which caused the mass extinction at the Cretaceous-Tertiary boundary was proposed to explain the presence of anomalously high concentration of iridium at the KTB. Their model envisages that a series of physico-chemical processes are triggered by such a large impact which include dust and aerosol loading of the atmosphere, blocking of sun light,

Table 1. Major observations at Cretaceous-Tertiary boundary (for sources of observations, see Shukla and Bhandari 1997 (table 3) and references therein).

Biological signatures	
<ul style="list-style-type: none"> • Global extinction of a large number of marine and land species. About 50% of genera and ~15% of families are believed to have become extinct. Whether the extinction is gradual, stepwise or sudden is still debated. • Extinction is believed to be selective. Differences in extinction between planktonic and benthic foraminifera have been observed. It has been suggested that extinction showed some latitudinal dependence and was mainly confined to tropics. • Near disappearance of pollens and plants. At the base of the K/T boundary <i>Micula murus</i> zone has been identified. 	
Geological signatures	
<ul style="list-style-type: none"> • Deccan flood basalts. Large scale ($> 10^6 \text{ km}^3$) flood volcanism in central and western India. It has been argued that the bulk of the basalts erupted within a Ma around KTB. However, $^{40}\text{Ar}/^{39}\text{Ar}$ ages show that the major peak of Deccan eruptions predated KTB by more than 1 Ma and its duration was more than 3 Ma (68 to 63 Ma). • Chicxulub Crater: (a) Chicxulub crater (diameter ~200 km) in the Yucatan peninsula has been identified as the crater formed at the K/T boundary. (b) The age of crater rocks is $64.98 \pm 0.05 \text{ Ma}$, same as the age of tektites from Haitian KTB site. (c) Apart from the 65 Ma resetting age, the zircons from various K/T sites (Colorado, Beloc and Saskatchewan) also give ages of ~545 Ma similar to the age of Chicxulub platform, indicating that it is the only large impact crater that formed at KTB (d) The geometry of the crater and the ejecta indicates that the bolide hit from southeast direction at a low angle (20 to 30°) and the ejecta was thrown in a northwesterly direction. • Sea level changes causing regression and transgression are believed to be the main factors in causing extinctions at KTB. A sharp drop of 100 m prior to KTB and an equally rapid rise thereafter have been observed in various sections. 	
Chemical and isotopic signatures	
<ul style="list-style-type: none"> • Global occurrence of enhanced level of iridium with orders of magnitude higher concentration above the background. In some sections, the Ir peak is super-imposed on a broad hump whereas a few sections show multiple Ir peaks. • Presence of amino acids (α-amino isobutyric acid), probably of extraterrestrial origin below and above the KTB but not in the KTB layer. It has been suggested that these amino acids are derived from cometary sources. • A sharp decrease in $\delta^{13}\text{C}$ at and above the K/T boundary attributed to planktonic extinction, indicative of stranglove ocean, followed by planktonic boom. • Excursions in $\delta^{18}\text{O}$ values indicating changes in sea water temperature of several degrees before and after the KTB. A slow cold wave is followed by a sudden warm epoch. • A marginal increase in strontium isotopic ratio ($^{87}\text{Sr}/^{86}\text{Sr}$) attributed to enhanced weathering due to impact induced acid rain. • Enrichment in N and S isotopic ratios ($^{15}\text{N}/^{14}\text{N}$, $^{34}\text{S}/^{32}\text{S}$) attributed to interaction of acid rain with organic matter in case of N and an anoxic event in case of S. • Fullerenes (C_{60}, C_{70}) have been detected at various KTB sites with estimated mean global C_{60} concentration at the KTB to be $\sim 1.4 \text{ ng cm}^{-2}$. • $^{187}\text{Os}/^{186}\text{Os}$ ratio is found to be ~ 1 in the K/T clay, similar to the value in meteorites or the Earth's mantle whereas the crustal value for this ratio is ~ 10. • A 2.5 mm fragment separated from the K/T clay horizon of a mid-Pacific core shows high concentration of Fe, Cr and Ir, characteristic of chondrites and is suspected to be the fragment of the bolide responsible for K/T impact. Almost pure micron size iridium nuggets from Chicxulub impact melt have also been isolated. 	
Mineralogical and other features	
<ul style="list-style-type: none"> • Presence of shocked grains of quartz, zircons and chromites. This is a strong evidence in favour of the impact hypothesis. • Spherules and microtektites have been reported from K/T sites. These include sanidine spherules and others having composition of potassium feldspar, glauconite, pyrite etc. Glasses with shapes resembling those of microtektites have been found from Beloc section near Haiti which have been dated to be $65.01 \pm 0.08 \text{ Ma}$. • Discovery of nanometer sized diamonds favour impact hypothesis. The Ir to nanometer size diamond ratio is similar to the value observed in case of C2 type chondrites and the carbon isotopic ratio does not favour a terrestrial origin. The horizon containing the diamonds had fifty one amino acids out of which eighteen are found in carbonaceous chondrites only. Based on C and N isotopic ratios in diamonds, an impact or plasma origin has been proposed. • Meteoric spinels (usually 2–10 microns), rich in nickel, have been found at the K/T boundary showing a prominent peak where the iridium enhancement is observed. These are believed to be produced in the atmosphere during the entry of the bolide. • Presence of soot in the boundary clay provides an evidence of large scale forest fires which could have contributed to blocking of sunlight. 	
Environmental signatures	
<ul style="list-style-type: none"> • A severe temperature fluctuation, a slow cold wave (-6°C) followed by a severe heat pulse ($+10^\circ\text{C}$). The cold wave is believed to be due to blanketing of sunlight by soot, dust and sulphuric acid aerosols and the heat wave is due to green house effect resulting from release of large amounts of CO_2 as a consequence of impact on carbonate rocks. Based on analysis of palaeosol carbonates, it has been found that the CO_2 concentration of the atmosphere at the time of KTB was about 800–1200 ppm. 	

Table 2. *Estimates of atmospheric loading (g) at K/T and P/T boundaries (adopted from Shukla and Bhandari 1997).*

Source	CO ₂	SO ₄ ⁻	HCl	NO	Soot from forest fires	Ejecta dust
a) K/T boundary						
Impact platform	$2.7-9 \times 10^{18}$	$0.38-3 \times 10^{19}$	—	3.15×10^{18}	10^{17}	10^{19}
Bolide	1.4×10^{17}	$3-300 \times 10^{14}$	—	2.7×10^{15}		
Deccan volcanism	2.2×10^{19}	1.7×10^{19}	2.7×10^{17}			
Total	$\sim 2.6 \times 10^{19}$	4.25×10^{19}	2.7×10^{17}	3.15×10^{18}	10^{17}	10^{19}
g cm ⁻²	5.2	8.3	0.05	0.62	0.014	2
b) P/T boundary						
Siberian volcanism	2.93×10^{19}	2.26×10^{19}	?	3.6×10^{19}	?	?

cessation of photosynthesis, significant temperature excursions, acid rain, destruction of ozone layer etc., finally leading to mass extinction. The role of acid rain (*aqua morta*) in bringing about extinction, particularly in the marine ecosystems, is very significant (Prinn and Fegley 1987; Sigurdsson *et al* 1992). The estimated aerosol loading of the atmosphere at K/T and P/T boundary times from various sources is summarised in table 2.

The questions which are now being debated in an impact scenario relate to (1) whether the bolide was a comet or an asteroid; and (2) the role of impact on extinction. The shape of the iridium peak can distinguish between asteroidal and multiple cometary impacts, provided that there is no post-depositional redistribution of iridium due to diffusion, biturbation etc. A sharp peak would indicate a single asteroidal impact whereas a broad peak or multiple peaks would indicate (multiple) cometary impacts. The answer to the second question rests on the evidence of extinction being in a single stage and sudden (years) or in multiple stages and gradual over prolonged period of time (million years). A sudden extinction will be consistent with an asteroidal impact. On the other hand, if the extinction is gradual or in several stages, then multiple impacts of cometary nuclei would be favoured. At the same time, however, the role of other causes of extinction such as multiple and protracted volcanic episodes should be considered. The collective effect of impacts and volcanism can be devastating. The suddenness of the final extinction may indicate that impact may be more important compared to volcanism for the terminal phase of extinction.

3.1 Results from the Indian sections

Deccan volcanism was active in central and western India at the time of K/T transition. Fossil data from intertrappeans in Krishna-Godavari basin (Raju *et al* 1991; 1995) and dating of basalt flows (Venkatesan *et al* 1996 a,b) show a prolonged period of volcanic activity over about three to six million years for the active phase of Deccan volcanism. The Deccan erup-

tions started around 67–68 Ma ago and continued till about 61 Ma ago. Vandamme *et al* (1991) have proposed that the peak Deccan activity occurred over a short span of time (≤ 0.5 Ma), coinciding with the KTB age. There may have been an increase in frequency of volcanic episodes at some locations around 65 Ma but if we consider the whole of the Deccan region, the limited data on ages of Deccan basalts suggest that the maximum activity occurred at 67 Ma, predating KTB by 2 Ma or more (Venkatesan *et al* 1996a,b). Also the duration of the peak Deccan activity was not as brief as the K/T transition. The data base on ages of basalts throughout the Deccan, their magnetism and fossil records of intertrappeans have to be enlarged significantly to draw statistically meaningful conclusions.

To explain the near simultaneity of both impact and volcanic events, it has been suggested that Deccan volcanism was triggered by an impact through pressure relief melting in the asthenosphere, as is believed to have occurred on the Moon which generated the lunar mare (Alt *et al* 1988; Rampino and Caldeira 1993). Sutherland (1996) has discussed the possibility of a chance coincidence of impact and volcanism at the KTB and the two events may not have been causatively linked. In this context, it was realised that K/T sections from Indian subcontinent should provide useful clues in understanding the role of Deccan volcanism as its effects would be more pronounced in its proximity. Several intertrappean (IT) samples (lava ash, clay, marl etc.) from several localities (Anjar, Takli, Padwar, Bargi, Chui hill, Bhachao etc.), belonging to Deccan province and a marine section in Um Sohryngkew River Basin in Meghalaya were therefore analysed to ascertain the Ir levels in these samples (Bhandari *et al* 1993a,b; 1995; 1996). The iridium concentration in all the samples, except for Anjar and Um Sohryngkew River sections, discussed below, range between 8 pg g^{-1} and 120 pg g^{-1} . These values are too low by orders of magnitude compared to the concentration of iridium observed at different KTB horizons (e.g. 5000 pg g^{-1} to 187000 pg g^{-1}) in various marine sites all over the globe. The tholeiitic basalts, which constitute

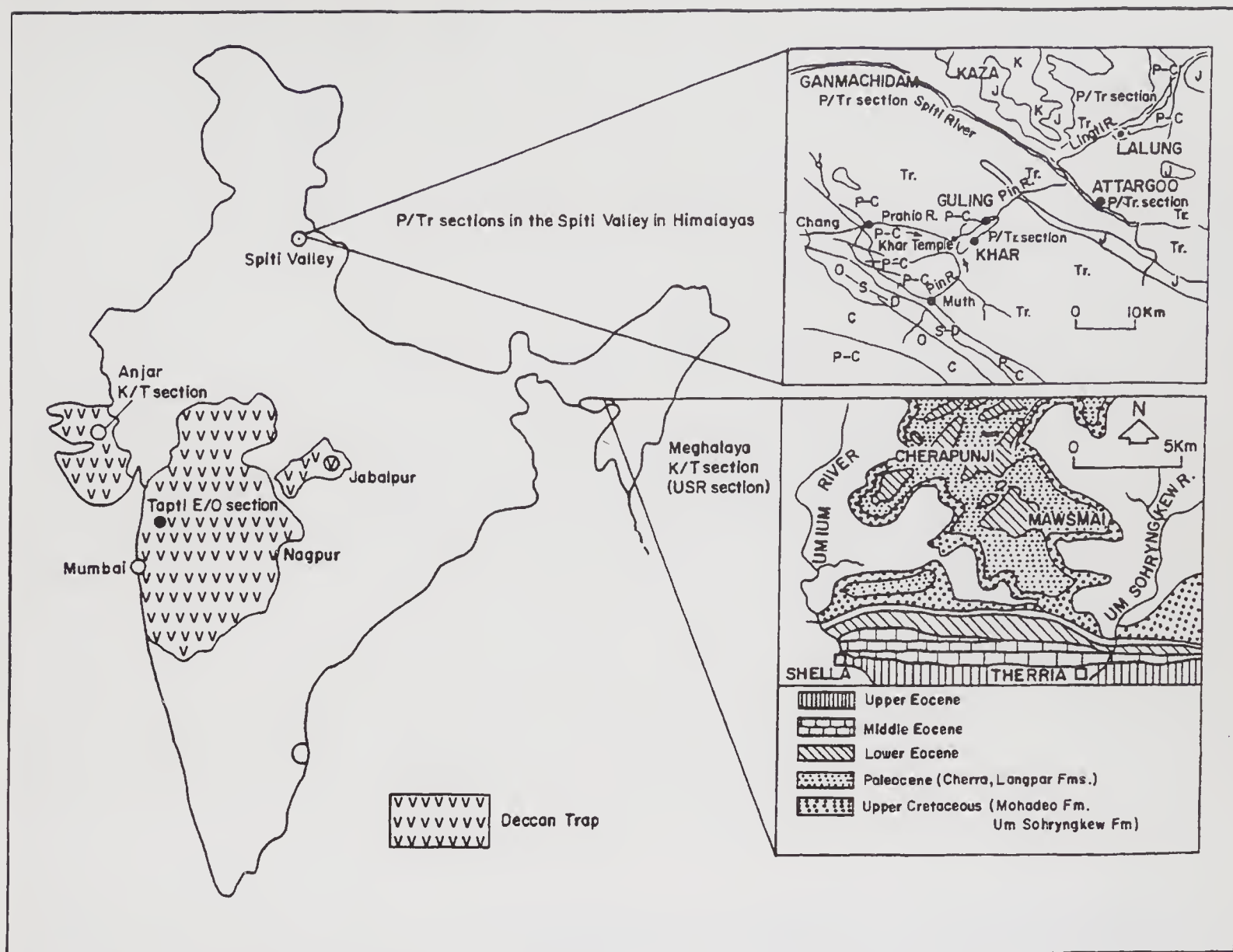


Figure 1. Sites of Indian E/O (Tapti River), K/T (Anjar and Um Sohryngkew River) and P/Tr (Spiti) boundary sections and the Deccan Plateau.

99.9% of the Deccan lava flows, have low concentration of iridium ($\leq 10 \text{ pg g}^{-1}$) and the iridium contribution due to Deccan, calculated assuming some reasonable partition coefficients between vapour and solid phases, falls short by more than an order of magnitude to account for its global inventory in the K/T boundary layer (Orth *et al* 1990; Bhandari *et al* 1994).

3.1.1 Um Sohryngkew river section

A marine K/T section from the Um Sohryngkew River basin, Meghalaya in eastern India (Pandey 1990; Garg and Jain 1995) was studied for geochemical anomalies. In this section Maastrichtian-Danian sequence is continuous and a 1.5 cm thick limonitic layer, rich in Ir, Os and the other siderophile elements characteristic of the KTB, has been observed (Bhandari *et al* 1994 and references therein). The Ir profile in this section, shows a broad (30 to 70 cm) band of modest Ir concentration ($\sim 100 \text{ pg g}^{-1}$), ten times higher than the background levels (10 pg g^{-1}), both below and

above the KTB. Superimposed on this broad band, there is a sharp Ir peak ($\sim 12000 \text{ pg g}^{-1}$) coincident with KTB (figure 2). It may be argued that the broad band of iridium is due to post depositional mobility, although there is no evidence of mixing due to bioturbation or any other mechanism in this section. The flux of iridium in this section is similar to that generally found elsewhere and does not show any extra iridium from the Deccan volcanism which occurred in the near vicinity. Ni-rich spinels have recently been found at the base of the iridium layer in this section (Robin *et al* 1997). They are believed to provide an unequivocal imprint of a cosmic bolide (Robin *et al* 1992).

Recently, from the geometry of impact (angle, velocity, palaeogeographic locations), Alvarez (1996) modelled the Chicxulub fallout ejecta debris and concluded that impact ejecta would not reach India, since it was located in the "forbidden zone". Although iridium and meteoric spinels have been found in Meghalaya section, there is as yet no evidence of the presence of shocked quartz and other minerals which are physical markers of the ejecta debris.

3.1.2 Anjar Intertrappean section

The volcano-sedimentary sequence in the coastal land section near Anjar, Kutch (Bhandari *et al* 1995, 1996) is an exception to the low iridium bearing intertrappeans of Deccan and shows three well separated Ir-rich layers within the third intertrappean (IT-3) bed (figure 2). The flows above and below the Ir layer have been dated using the ^{40}Ar - ^{39}Ar method (Venkatesan *et al* 1996a). The plateau ages of the lower flow (FIII) underlying the IT containing Ir-rich layer are found to be 65.2 ± 0.6 Ma and 64.9 ± 0.8 Ma whereas the overlying flow (FIV) gives a plateau-like age of 65.7 ± 0.7 Ma. These ages are similar to the age of KTB obtained from dating microtektites found in marine KTB sediments (Izett *et al* 1991) and the age of 64.98 ± 0.1 Ma obtained by dating melt glass from Chicxulub crater (Swisher *et al* 1992). The flows IV, V, VI and VII show reverse magnetic polarity (Kusumgar, pers. commn. 1996) whereas the secondary magnetic imprints on FI, II and III are too intense to reliably provide the direction of the primary magnetic polarity. Considering the chronology and magnetic polarity, we tentatively place flows IV, V and VI in magnetic chron 29R, during which the KTB layer is known to have been emplaced. The sediments in IT-3 generally have a high value of iridium (about 100 pg g^{-1}) and there are three thin patchy layers, separated by 25–32 cm, roughly in the middle of this bed, which show a large enhancement of Ir and Os, the maximum values being 1270 pg g^{-1} and 1410 pg g^{-1} respectively. These values are similar to the concentrations found in several other continental K/T sections and lower than concentrations found in most marine sections. The integrated amount of iridium in the Anjar section is comparable to and not higher than the fallout at any other place on the globe. This result indicates that the Deccan volcanism contributed only a negligible amount to the global iridium inventory at KTB. If the Ir-rich layers of the Anjar represent the K/T Boundary, then in the light of the observations summarised above, some conclusions can be drawn about the relation between Deccan and KTB. Firstly, the results show that Deccan volcanism was active before, during and after the KTB transition. Secondly, the extraterrestrial impact did not trigger Deccan volcanism. Both these results are consistent with the chronological framework developed by Venkatesan *et al* (1996a, b). These observations do not support the models of impact induced volcanism (Alt *et al* 1988) as well as simultaneity of impact and Deccan volcanism (Rampino and Caldeira 1993). The location of the KTB layer within the Anjar intertrappeans provide a high resolution time sequence because of the fast sedimentation rate, free from the uncertainties in absolute chronology and points to the possibility of multiple iridium events, provided that there is no post-depositional redistribution of iridium.

The Anjar section also provides important criteria to test some other hypotheses. Chatterjee and Rudra (1996) have proposed that there was another impact near the Indo-Seychelles border at the KTB time. The slightly oval shaped structure, named Shiva Crater (about $600 \times 450 \times 12$ km in size) would require a bolide 40 km in diameter, much bigger than the Chicxulub impactor. According to this hypothesis, this impact was so energetic that it created the Carlsberg Ridge and triggered the rifting of the Indian Plate. From the shape of the crater, Chatterjee and Rudra (1996) suggested that the bolide came from south west. If it were so, Anjar, being in the vicinity of the impact point and located in the immediate ejecta fallout zone, should have some evidence of impact debris. We have not found any evidence of ejecta debris at Anjar, as has been found around Chicxulub crater. If the sediments around the iridium layers at Anjar were deposited at the KTB time, as appears likely, then the absence of these markers at Anjar rules out another impact of a larger magnitude at the proposed site of the Shiva Crater. The same argument can be extended to another proposed crater near Bombay high (Negi *et al* 1993) based on a gravitational anomaly, although its dimensions are much smaller and large ejecta debris is not expected.

4. Permo-Triassic boundary

The Permian-Triassic (P/T) mass extinction was the most catastrophic in the geological record where as many as 90% of the marine fauna and 70% of the terrestrial vertebrates became extinct (Raup and Sepkoski 1986; Sepkoski 1992; Erwin 1994). Significant floral extinctions are also observed around this boundary (Retallack 1995). U/Pb dating of zircons from the Chinese section date the P/T boundary at 251.4 ± 0.3 Ma (Bowring *et al* 1998). The boundary is quite complex and palaeontological controls as well as preservation of evidence is relatively poor. However geochemical, isotopic and palaeontological studies have been carried out in many sections e.g. Austrian Carnic Alps (Holser *et al* 1989); China (Clark *et al* 1986; Zhou and Kyte 1988); India (Bhandari *et al* 1992); Italy (Wignall and Twitchett 1996); Russia (Alekseev *et al* 1983). Most of these sections are not complete and some horizons at or near the boundary are missing (Sweet *et al* 1992; Kapoor 1992). In some of them, claystone, mudstone or pyrite bands have been found at the P/T boundary. Based on the palaeontological data, Erwin (1994, 1996) suggests a short duration of about 2 Ma for this extinction but recent studies of the Chinese sections (Bowring *et al* 1998) favour catastrophic extinction over a still shorter duration of 1 Ma or less, with catastrophic addition of light carbon, giving a $\delta^{13}\text{C}$ excursion over an even shorter period of 165 ka. Important biological, geological, chemical and

Table 3. Major observations at Permo-Triassic boundary (modified from Shukla and Bhandari 1997).

Biological signatures
<ul style="list-style-type: none"> • Global extinction of about 90% of marine fauna and 70% of terrestrial vertebrates. This is the most severe extinction event in the Phanerozoic. • Near disappearance of Permian flora.
Geological signatures
<ul style="list-style-type: none"> • Siberian ood basalts: ^{40}Ar–^{39}Ar ages of basalts range between 253 Ma and 247 Ma. The volume is estimated to be $(2 \times 10^6 \text{ km}^3)$. It has been suggested that the bulk of the basalts erupted within a period of less than 1 Ma around P/T Boundary. • Pyroclastic volcanism in south China (1000 to 4000 km^3). • Sea level changes: rapid regression and transgression. About 280 m fall in sea level is estimated. The scenario envisages two regressions followed by a rapid transgression in the early Triassic.
Chemical and isotopic signatures
<ul style="list-style-type: none"> • Two small peaks of iridium ($< 120 \text{ pg g}^{-1}$) have been found at several locations. • A positive europium anomaly has been found in Lalung and Guling sections in Spiti, India. • A sharp decrease in $\delta^{13}\text{C}$ at P/T Boundary for a period of 165 ka. • Excursions in $\delta^{18}\text{O}$ values indicating changes in sea water temperature of several degrees before and after the P/T transition. • Enrichment in S isotopic ratios ($^{34}\text{S}/^{32}\text{S}$) attributed to an anoxic event. • A marked shift in Sr isotopes. • Strong anoxia in the world oceans, both at high and low palaeolatitudes in the late Permian. Records from the deep sea sections indicate a totally stratified ocean for a period of about 20 Ma which included a 12 Ma super-anoxic period.
Mineralogical and other features
<ul style="list-style-type: none"> • Presence of hematite in Permian and Triassic sediments except at the P/T Boundary where iron occurs as pyrite indicating highly anoxic conditions during the transition. The data are also supported by U concentration profile across the boundary. • Presence of quartz with planar deformation features in Australian and Antarctic PTB sections.

isotopic signatures found at P/T boundary are summarised in table 3. The most significant geologic event around this time was the Siberian volcanism (253 to 247 Ma), but its peak activity occurred over a short time scale of about 1 Ma (Renne and Basu 1991; Venkatesan *et al* 1997). Highly anoxic conditions prevailed in the oceans around the time of PTB (Isozaki 1997). The search for a chemical marker having a global nature, like Ir found at KTB, has so far not yielded any clues. The range of Ir values observed across the P/T boundary in various sections range from a few pg g^{-1} to just over a hundred pg g^{-1} (table 3) and therefore impact of a chondrite or iron meteorite is ruled out. A lot of effort for the search of impact signatures in sediments deposited at the PTB have been made and there is some indication of the presence of planar deformation features in quartz (Retallack *et al* 1998) but more work needs to be done to confirm that an impact has occurred at the boundary.

4.1 Clues from the Indian sections in Spiti valley

The Permo-Triassic boundary at Guling and Lalung in the Spiti valley is marked by a thin (about 2 cm) limonitic layer, which separates the Permian black shales from the Triassic limestone containing the *Otoceras*-*Opiceras* zone. A field trip carried out in

September 1997 revealed that this limonitic layer is not confined to Guling and Lalung sections but is present through out Spiti (at Attargoo, Ganmachidam, Losar etc.) and possibly also in Lahaul valley. Figure 3 shows the Permian shales, limonitic layer and the Triassic limestones in the Attargoo section. The limonitic layer seems to extend to Guryul Ravine in Kashmir also. Thus it can be taken as a regional, if not global, marker of the P/T boundary. According to Singh *et al* (1995), it is even more widespread, extending all the way from Kashmir to China.

Chemical analysis of Lalung and Guling sections in Spiti by Bhandari *et al* (1992), where the limonitic layer, described above, exists at the Permian-Triassic interface, shows a small Ir enhancement at the boundary (70 pg g^{-1}) and another minor Ir peak ($\sim 114 \text{ pg g}^{-1}$) about 70 cm below the boundary (table 3). These Ir levels are similar to the values observed in Carnic Alps by Holser *et al* (1989) and in Chinese sections by Zhou and Kyte (1988) both of which, unlike India, Australia and Antarctica, were located in the northern hemisphere. However, the boundary sample of the limonitic layer at Spiti shows a very high Eu concentration and the chondrite normalised REE patterns shows a positive Eu anomaly of $(\text{Eu}/\text{Eu}^*)_{\text{max}}$ equal to 1.9 (Eu* is the interpolated concentration based on its neighbouring elements Sm and Gd). The Eu anomaly is also associated with a high value of Sb

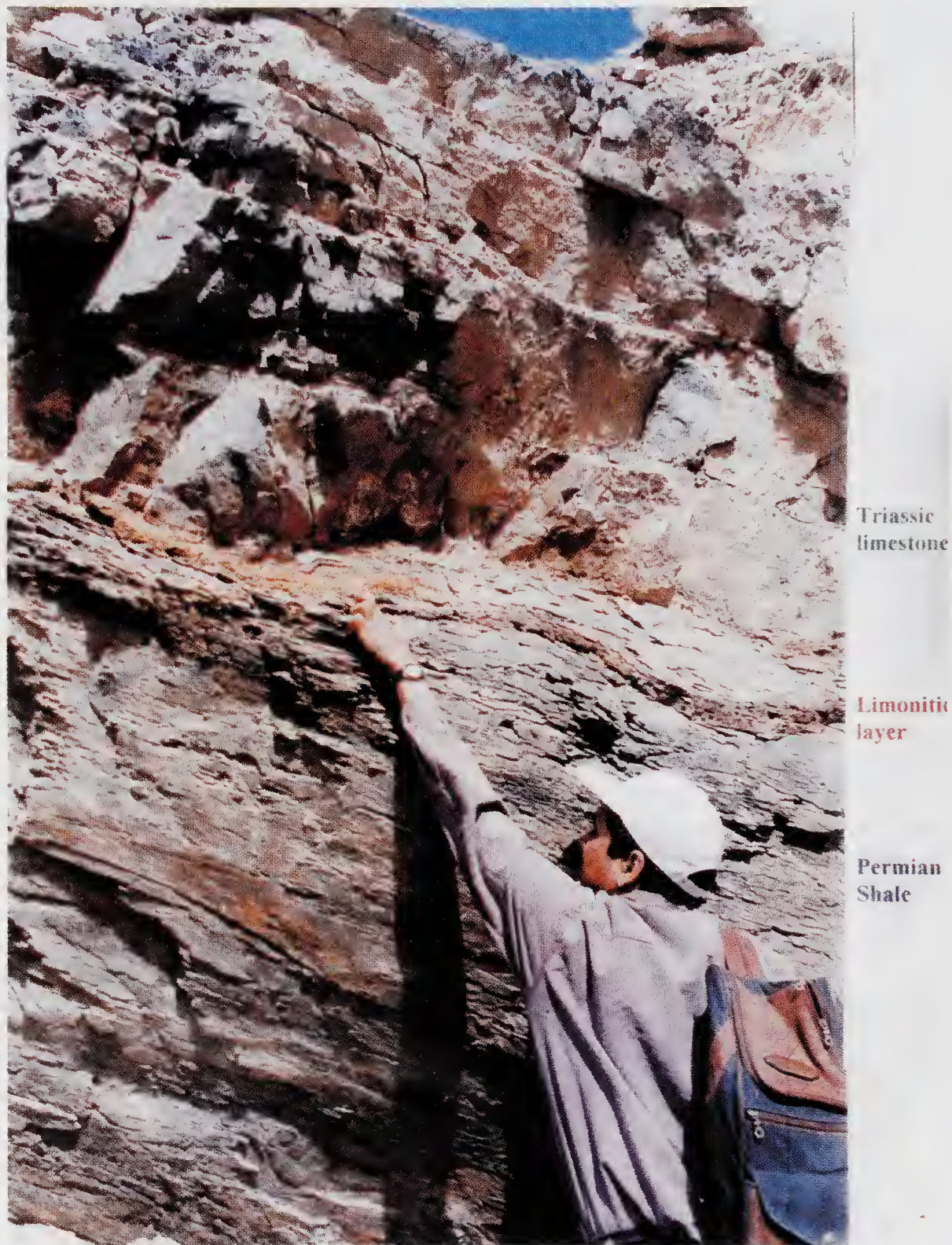


Figure 3. The Permian-Triassic section of Attargoo, showing the limonitic layer at the boundary of Permian black shales and the Triassic Limestone.

and Zn. Bhandari *et al* (1992) have discussed various terrestrial and extra-terrestrial causes which can give rise to the positive Eu anomaly and absence of iridium enrichment observed at the P/T boundary of Spiti valley. Among the terrestrial sources, it has been pointed out that volcanogenic sediments and interaction of hydrothermal solutions with felsic volcanic rocks could give rise to a positive Eu anomaly. Among the extraterrestrial objects, differentiated rocks like lunar anorthosites exhibit a high positive Eu anomaly and have very low Ir values. Thus if an impact were responsible for the P/T event, the observations

would be consistent with a bolide of a differentiated achondritic body.

Recently, Retallack *et al* (1998) has found some quartz grains having planar deformation features (PDF) in the P/T section near Sydney, Australia which can possibly be due to impact. Similar damaged quartz were found in the P/T section of Victoria Land, Antarctica. These PDF quartz are associated with $\delta^{13}\text{C}$ anomaly indicative of P/T extinction.

Siberian flood basalts have the largest subaerial exposure in the Phanerozoic and are associated with mafic intrusions which contain sulphide ores. The

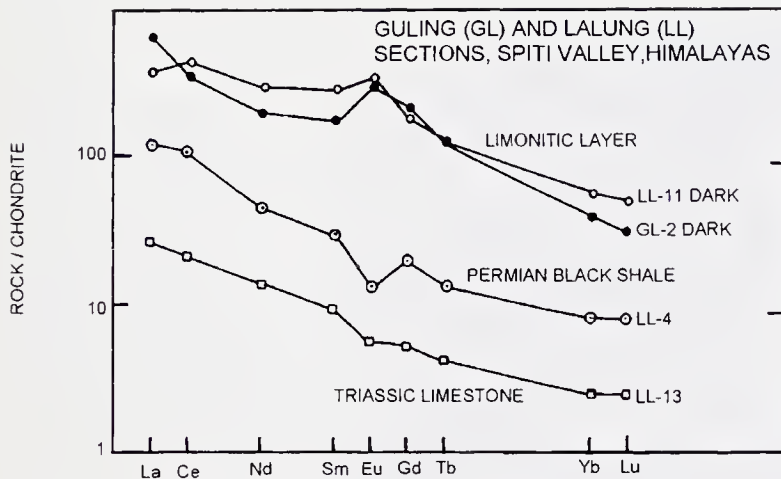


Figure 4. Chondrite normalized REE patterns from Guling and Lalung P/T boundary sections, Spiti. A positive Eu anomaly has been observed in the limonitic layer at the boundary (Bhandari *et al* 1992).

eruptions were both explosive and sulphur rich which would have injected a large amount of SO_2 and volcanic dust in the atmosphere causing acid rain and global cooling. The estimated sulphate loading of the atmosphere is given in table 2. Campbell *et al* (1992) mention several features of Siberian volcanism which could bring about global cooling through SO_2 emissions and have argued in favour of Siberian volcanism as the main cause of P/T extinction through climatic stress. This scenario is supported by Courtillot *et al* (1996) who also prefers Siberian volcanism to be dominantly responsible for the P/T extinction. The isotopic and geochemical studies of Alpine and the Chinese sections (Holser *et al* 1989; Clark *et al* 1986; Zhou and Kyte 1988) suggest a strong regression-transgression event occurring with mass extinction at the PTB and also favour a volcanic scenario based on geochemical arguments.

In the scenario that is emerging, various observations could be visualised as follows. Siberian traps pro-

duced sufficient sulphate aerosols in the stratosphere which resulted in rapid global cooling. This initiated ice cap accumulation causing a marine regression leading to sub-aerial exposure of the continental shelves. It also explains the observed excursions in C, S and Sr isotopes. Mantle derived CO_2 and SO_2 being light in C and S contributed to the negative anomalies in $\delta^{13}\text{C}$ and $\delta^{34}\text{S}$. When the Siberian volcanism ceased, a rapid transgression followed and climate recovery took place due to the green house effect of volcanic gases like CO_2 . Thus anoxia, volcanism and sea level regression, all three may have played an important role in P/T extinction. If $\delta^{13}\text{C}$ was added suddenly and catastrophically, then the possibility of an impact of a differentiated meteorite, low in Ir and having Eu anomaly has to be considered.

5. Late Eocene/Oligocene boundary

Mid-Eocene to Oligocene was an eventful time with several minor events of faunal and floral extinctions beginning at 40 Ma, punctuated by two impacts, though not accompanied by extinction, and a large scale volcanism in Ethiopia, culminating in a large sea level drop and major ice advance. The Eocene/Oligocene boundary is dated at 33.7 ± 0.2 Ma. Bottomley *et al* (1997) have dated the Popigai impact crater in Siberia (100 km diameter) and came to the conclusion that its age (35.7 ± 0.2 Ma) is similar to the Chesapeake Bay crater (85 km diameter, 35.3 ± 0.2 Ma) off the Coast of Virginia in USA. Therefore, the two impacts occurred almost simultaneously, at most within a few hundred thousand years. Such a quick succession of impacts is not expected from any statistical consideration from the known orbital populations of comets or asteroids. Only a large number of comets, if deflected from the Oorts cloud belt by some

Table 4. Major observations in the Late Eocene.

Biological signatures
<ul style="list-style-type: none"> Several minor extinctions in the Late Eocene and at the E/O Boundary.
Geological signatures
<ul style="list-style-type: none"> Chesapeake Bay Crater (85 km diameter), on the coast of Virginia in USA. The age of the Crater is 35.3 ± 0.2 Ma. Popigai Crater in Siberia (100 km diameter). The age of the Crater is 35.7 ± 0.2 Ma. Strewn field of North American Tektites (Georgian Tektites and Bediasites in Texas), attributed to the Chesapeake Bay crater. Large scale volcanism ($0.5 \times 10^6 \text{ km}^2$) in Ethiopia at 30 Ma much after the E/O boundary dated at 33.7 Ma.
Chemical and isotopic signatures
<ul style="list-style-type: none"> Excess ^3He and high $^3\text{He}/^4\text{He}$ over a prolonged period (~ 2.5 Ma) preceding and following the formation of the impact craters. Excess iridium at 35.7 ± 0.4 Ma. Nickel-rich spinels peaking at 35.7 ± 0.4 Ma but also distributed above and below the peak in lower concentration. Shocked quartz. Microtektites, microkrystites and clinopyroxene spherules. Sharp $\delta^{13}\text{C}$ and $\delta^{18}\text{O}$ excursions at the Eocene-Oligocene-boundary.

gravitational perturbations, can give rise to a comet shower, resulting in multiple impacts over a short period of time. Recent results based on the profiles of ^3He (Farley *et al* 1998), Ni-rich spinels (Pierrard *et al* 1998), shocked quartz (Clymer *et al* 1996), microtektites, microkrystites (Glass *et al* 1985) and iridium (Montanari *et al* 1993) in the Massignano section, Italy, favour a relatively prolonged period of impact of cometary debris during the Late Eocene (Farley *et al* 1998; Pierrard *et al* 1998).

The Ethiopian volcanism occurred much later at 30 ± 1 Ma ago (Hofmann *et al* 1997) and therefore could not have been responsible for the observed extinctions or climatic changes observed during Mid to late Eocene. In India, two sections (Tapti and Kutch) have been identified where Eocene/Oligocene boundary may be continuous. The E/O boundary is globally marked by large $\delta^{18}\text{O}$ and $\delta^{13}\text{C}$ excursion Sn (Zachos *et al* 1992; Miller *et al* 1988). The Kutch section shows similar $\delta^{18}\text{O}$ and $\delta^{13}\text{C}$ excursions and therefore appears to be continuous near the E/O boundary (Sarangi *et al* 1998). The fossil records show that the Tapti section may be continuous for a longer period from Mid-Eocene through the E/O boundary (Shukla *et al* 1999). In the mid-Eocene, some microtektite-like objects have been found in the Tapti section and search for iridium enhancement and other geochemical signatures of impacts is now in progress in our laboratory.

6. Summary

We have described the main features of the two most severe extinction events (K/T and P/T) in the geologic history of the Earth. Based on the evidences summarised here, it is clear that there are very few similarities in physical, chemical and biological markers observed at P/T and K/T boundaries. The situation is even more exclusive when other boundaries are taken into consideration. It therefore appears unlikely that there is a single mechanism which could explain all the extinctions observed over the geological history of the Earth. Hypotheses involving multiple causes, therefore, appear more plausible although McLaren and Goodfellow (1990) and Rampino and Haggerty (1996) have argued for an impact theory of extinction whereas Courtillot *et al* (1986) and McLean (1985) have advanced the volcanic hypothesis. It is possible that sometimes volcanism and impact occur together increasing the severity of climatic stress (Sutherland 1996). Erwin (1994; 1996) has advanced a multi-causal scenario where anoxia, aerosol loading, sea level regression, etc. have contributed to the P/T extinction in some measures. There are no physical or chemical evidences yet which would show that the other astronomical causes, like supernovae, dark matter accumulation, collision of neutron stars etc, had been responsible for the extinctions although such

events must have occurred over geological times. The search for consequences of such phenomena in the geological records must therefore continue. Physical effects of many of these astronomical processes must be recorded not only on the Earth but also on the Moon and other planets. For example, if accumulation of dark matter can give rise to periodic volcanism on the Earth, as has been proposed by Abbas and Abbas (1998), other celestial bodies like Mars and Moon must also exhibit periodic volcanism. As there is no evidence for it, such processes have probably played only a minor role, if at all, and can be ruled out. Similarly evidence for supernovae explosions, in the form of their radiation effects and debris should be present on other planetary bodies. It should be possible to confirm such processes by suitable studies.

Acknowledgements

The work reviewed here is based on a collaborative effort by several colleagues, specially Drs. P N Shukla, K Pande, A D Shukla, and J Pandey to whom I am grateful for discussions and suggestions. The field trip to Spiti and a part of the work described here was done under IGCP 386. This article is based on a large amount of literature which could not be cited due to space limitations and I wish to acknowledge the contributions made by many scientists to the understanding of the boundary problems.

References

- Abbas S and Abbas A 1998 Volcanogenic dark matter and mass extinctions; *Astroparticle Physics* **8** 317–320
- Alekseev A S, Barsukova L D, Kolesov G M, Nazarov M A and Grigoyan A G 1983 Permian-Triassic boundary event: geochemical investigation of the Trans Caucasia; *Lunar Planet. Sci.* (abstract) **14** 7–8
- Alt D, Sears J M and Hyndmann D W 1988 Terrestrial Maria: The origins of large basalt plateaus, hot spot tracks and spreading ridges; *J. Geol.* **96** 647–662
- Alvarez L W, Alvarez W, Asaro F and Michel H V 1980 Extraterrestrial cause of the Cretaceous/Tertiary extinction; *Science* **208** 1095–1108
- Alvarez W, Claeys P and Kieffer S W 1995 Emplacement of Cretaceous-Tertiary boundary shock quartz from Chicxulub Crater; *Science* **269** 930–934
- Alvarez W 1996 Trajectories of ballistic ejecta from the Chicxulub Crater; *Geol. Soc. Am. Spl. Pap.* **307** 141–150
- Bhandari N, Gupta M, Pandey J and Shukla P N 1994 Chemical profiles in K/T boundary section of Meghalaya, India: Cometary, asteroidal or volcanic; *Chem. Geol.* **113** 45–60
- Bhandari N, Gupta M and Shukla P N 1993a Deccan volcanic contribution of Ir and other trace elements near the K/T boundary; *Chem. Geol.* **103** 129–139
- Bhandari N, Shukla P N and Castagnoli G C 1993b Geochemistry of some K/T sections in India; *Paleogeog. Paleoclimatol. Paleoecol.* **104** 199–211
- Bhandari N, Shukla P N and Azmi R J 1992 Positive europium anomaly at the Permo-Triassic boundary, Spiti, India; *Geophys. Res. Lett.* **19** 1531–1534

- Bhandari N, Shukla P N, Ghevariya Z G and Sundaram S M 1995 Impact did not trigger Deccan volcanism: Evidence from Anjar K/T boundary intertrappean sediments; *Geophys. Res. Lett.* **22** 433–436
- Bhandari N, Shukla P N, Ghevariya Z G and Sundaram S M 1996 K/T boundary layer in Deccan intertrappeans at Anjar, Kutch; *Geol. Soc. Am. Spec. Pap.* **307** 417–424
- Bottomley R, Grieve R, York D and Masaitis V 1997 The age of the Popigai impact event and its relation to events at the Eocene/Oligocene boundary; *Nature* **388** 367–368
- Bowring S A, Erwin D H, Jin Y G, Martin M W, Davidek K and Wang W 1998 U/Pb zircon geochronology and tempo of the End-Permian mass extinction; *Science* **280** 1039–1045
- Campbell I H, Czamanske K, Fedorenko V A, Hill R I and Stepanov V 1992 Synchronism of the Siberian traps and the Permian-Triassic boundary; *Science* **258** 1760–1763
- Chatterjee S and Rudra D K 1996 K/T events in India: Impact, rifting, volcanism and Dinosaur extinction; *Memoirs of the Queensland Museum* **39** 489–532
- Clark D L, Wang C Y, Orth C J and Gilmore J S 1986 Conodont survival and low iridium abundance across the Permian-Triassic boundary in South China; *Science* **233** 984–986
- Clube S V M and Napier W M 1986 Giant comets and the galaxy: Implications of the terrestrial record; In *The galaxy and the solar system* (eds) R Smoluchowski, J N Bahcall and M S Matthews (Tucson, Arizona: The University of Arizona Press) pp. 260–285
- Clymer A K, Bice D M and Montanari A 1996 Shocked quartz from the late Eocene: Impact evidence from Massignano, Italy *Geology* **24** 483–486
- Courtillot V, Besse J, Vandamme D, Montigny R, Jaeger J J and Cappetta H 1986 Deccan flood basalts at the Cretaceous-Tertiary boundary; *Earth Planet. Sci. Lett.* **80** 361–374
- Courtillot V, Jaeger J J, Yang Z, Feraud G and Hofmann C 1996 The influence of continental flood basalts on mass extinctions: Where do we stand? *Geol. Soc. Am. Spec. Pap.* **307** 513–525
- Davis M, Hut P and Muller R A 1984 Extinction of species by periodic comet showers; *Nature* **308** 715–717
- Ellis J and Schramm D 1995 Could a supernova explosion have caused a mass extinction? *Proc. Nat. Acad. Sci. USA* **92** 235–238
- Erwin D H 1994 The Permo-Triassic extinction; *Nature* **367** 231–236
- Erwin D H 1996 The mother of mass extinctions; *Scientific Am.* **275** 56–62
- Farley K A, Montanari A, Shoemaker E M, and Shoemaker C S 1998 Geochemical evidence for a comet shower in the Late Eocene; *Science* **280** 250–253
- Garg R and Jain K P 1995 Significance of terminal Cretaceous calcareous nannoplankton marker *Micula prinsii* at the Cretaceous-Tertiary boundary in the Um Sohryngkew section, Meghalaya, India; *Curr. Sci.* **69** 1012–1017
- Glass B P, Burns C A, Crosbie J R and Dubois D L 1985 Late Eocene North American microtektites and Clinopyroxene-bearing spherules; *Proc. Lunar Planet. Sci. Conf., J. Geophys. Res.* **D90** 175–196
- Grieve R A F 1991 Terrestrial impacts: The record in the rocks; *Meteoritics* **26** 175–194
- Hills J 1986 Deflection of comets and other long-period solar companions into the planetary system by passing stars; In *The galaxy and the solar system* (eds) R Smoluchowski, J N Bahcall and M S Matthews, (Tucson, Arizona: The University of Arizona Press) pp. 397–408
- Hofmann C, Courtillot V, Feraud G, Rochette P, Yirgu G, Ketefo E and Pik R 1997 Timing of the Ethiopian flood basalt event and implications for plume birth and global change; *Nature* **389** 838–841
- Holser W T, Schonlaub H P, Attrep M, Boeckelmann K, Klein P, Magaritz M, Orth C J, Feninger A, Jenny C, Kralik M, Mauritsch H, Pak E, Schramm J M, Stattegger K and Schmoller R 1989 A unique geochemical record at the Permian-Triassic boundary; *Nature* **337** 39–44
- Isozaki Y 1997 Permo-Triassic boundary superanoxia and stratified Superocean: Records from deep sea; *Science* **276** 235–238
- Izett G A, Dalrymple G B and Snee L W 1991 ^{40}Ar - ^{39}Ar age of Cretaceous-Tertiary boundary tektites from Haiti; *Science* **252** 1539–1542
- Kapoor H M 1992 Permo-Triassic boundary of the Indian subcontinent and its intercontinental correlation; In *Permo-Triassic events in the Eastern Tethys* (eds) W C Sweet, Y Zunyi, J M Dikins and H Yin, Cambridge University Press, pp. 21–36
- Kyte F T 1988 The extraterrestrial component in marine sediments: description and interpretation; *Palaeoceanography* **3** 235–247
- McLaren D J and Goodfellow W D 1990 Geological and biological consequences of giant impacts; *Ann. Rev. Earth Planet. Sci.* **18** 123–171
- McLean D M 1985 Deccan traps mantle degassing in the terminal Cretaceous marine extinction; *Cretaceous Res.* **6** 235–259
- Miller K G, Feigenson, M D, Kent D V and Olsson R K 1988 Upper Eocene to Oligocene isotope ($^{87}\text{Sr}/^{86}\text{Sr}$, $\delta^{18}\text{O}$, $\delta^{13}\text{C}$) standard section; *Deep Sea Drilling Project Site* **522** 223–233
- Montanari A, Asaro F, Michel H V and Kennet J P 1993 Iridium anomalies of Late Eocene age at Massignano (Italy) and ODP sites 689B (Maud Rise, Antarctic); *Palaios* **8** 420–437
- Negi J G, Agrawal P K, Pandey O P and Singh A P 1993 A possible K-T boundary bolide impact site offshore near Bombay and triggering of rapid Deccan volcanism; *Phys. Earth Planet. Inter.* **76** 189–197
- Orth C J *et al* 1990 Iridium abundance patterns across bio-event horizons in the fossil record; In *Global catastrophes in Earth History; Geol. Soc. Am. Spl. Pap.* **247** 45–60
- Pandey J 1990 Cretaceous/Tertiary boundary, iridium anomaly and foraminifer breaks in the Um Sohryngkew River section, Meghalaya; *Curr. Sci.* **59** 570–575
- Pierrard O, Robin E, Rocchia R and Montanari A 1998 Extraterrestrial Ni-rich spinel in Upper Eocene sediments from Massignano, Italy; *Geology* **26** 307–310
- Prinn R G and Fegley B 1987 Bolide impacts, acid rain, and biospheric traumas at the Cretaceous-Tertiary boundary; *Earth Planet. Sci. Lett.* **83** 1–15
- Raju D S N, Ravindran V N, Dave A, Jaiprakash B C and Singh J 1991 K/T boundary events in the Cauvery and Krishna-Godavari basins and the age of Deccan volcanism; *Geoscience J.* **12** 177–190
- Raju D S N, Jaiprakash B C, Kumar A, Saxena R K, Dave A, Chatterjee T K and Mishra C M 1995 Age of Deccan Volcanism across KTB in Krishna-Godavari basin: New evidences; *J. Geol. Soc. India* **45** 229–233
- Rampino M R 1995 *Catastrophes: Impact of comets and asteroids in future climates of the world: A modelling perspective* (ed) A Henderson-Sellers (Elsevier) pp. 95–147
- Rampino M R and Caldeira 1993 Major episodes of geological change correlations, time structure and possible causes; *Earth Planet. Sci. Lett.* **114** 215–227
- Rampino M R and Haggerty B M 1996 Impact crises and mass extinctions: a working hypothesis; *Geol. Soc. Am. Spec. Pap.* **307** 11–30
- Raup D M and Sepkoski J J 1986 Periodic extinction of families and genera; *Science* **231** 833–836
- Raup D M and Sepkoski J J 1988 Testing for periodicity of extinction; *Science* **241** 94–96
- Renne P R and Basu A R 1991 Rapid eruption of the Siberian trap flood basalts at the Permo-Triassic boundary; *Science* **253** 176–179

- Retallack G J 1995 Permian-Triassic crisis on land; *Science* **267** 77–80
- Retallack G J, Seyedolali A, Krull E S, Holser W J, Ambers C P and Kyte F T 1998 Search for evidence of impact at the Permian-Triassic boundary in Antarctica and Australia; *Geology* **26** 979–982
- Robin E, Bonte P H, Forget L, Jehanno C and Rocchia R 1992 Formation of spinels in cosmic objects during atmospheric entry: A clue to the Cretaceous-Tertiary boundary event; *Earth Planet. Sci. Lett.* **108** 181–190
- Robin E, Rocchia R, Bhandari N and Shukla P N 1997 Cosmic Imprints in the Meghalaya K/T section; *International Conf. on Isotopes in the Solar System*, Physical Research Laboratory, Ahmedabad (abstracts) 95–96.
- Sarangi S, Sarkar A, Bhattacharya S K and Ray A K 1998 Isotopic evidence of a rapid cooling and continuous sedimentation across the Eocene-Oligocene boundary of Wagapadhar and Waior, Kutch; *J. Geol. Soc. India* **51** 245–248
- Sepkoski J J 1992 A compendium of marine fossil families; *Milwaukee Public Museum Contributions in Biology and Geology* **51** 1–125
- Shukla P N and Bhandari N 1997 Physical, chemical and biological changes at geological boundaries: Causes, consequences and clues based on the study of Indian sections; *Palaeobotanist* **46** 41–62
- Shukla A D, Shukla P N, Shukla S, Satyanarayana, Pandey J and Bhandari N 1998 Event horizons in the Eocene-Oligocene section, Tapti River, India (in preparation).
- Sigurdsson H, D'Hondt S and Carey S 1992 The impact of Cretaceous/Tertiary bolide on evaporite terrain and generation of major sulphuric acid aerosol; *Earth Planet. Sci. Lett.* **109** 543–559
- Singh T, Tiwari R S, Vijaya and Ram-Awtar 1995 Stratigraphy and palynology of Carboniferous-Permian-Triassic succession in Spiti valley, Tethys Himalaya, India; *J. Paleontol. Soc. India* **40** 55–76
- Sutherland F L 1996 The Cretaceous/Tertiary-boundary impact and its global effects with reference to Australia AGSO; *J. Aust. Geol. Geophys.* **16** 567–585
- Sweet W C, Zunyi Y, Dickins Y M and Yin H (eds) 1992 *Permo-Triassic events in the eastern Tethys* Cambridge University Press, pp. 1–8
- Swisher C C, Nishimura J M G, Montanari A, Margolis S V, Claeys P, Alvarez W, Renne P, Pardo E C, Maurrasse F J M R, Curtis G H, Smit J and Williams M O 1992 Coeval Ar/Ar ages of 65 million years ago from Chicxulub crater melt rock and Cretaceous-Tertiary boundary tektites; *Science* **257** 954–958
- Vandamme D, Courtillot V, Besse J and Montigny R 1991 Palaeomagnetism and age determinations of Deccan traps: Results of a Nagpur-Bombay traverse and review of earlier work; *Rev. Geophys.* **29** 159–190
- Venkatesan T R and Pande K 1996a A review of $^{40}\text{Ar}/^{39}\text{Ar}$ ages from western ghats, Deccan trap province, India: Implications for K/T events; In, *Deccan Basalts* (Nagpur: Gondwana Geological Society) pp. 321–328
- Venkatesan T R, Pande K and Ghevariya Z G 1996b $^{40}\text{Ar}/^{39}\text{Ar}$ ages of Anjar Traps, western Deccan Province (India) and its relation to Cretaceous-Tertiary boundary events; *Curr. Sci.* **70** 990–996
- Venkatesan T R, Kumar A, Gopalan K and Al'Mukhamedov A I 1997 $^{40}\text{Ar}/^{39}\text{Ar}$ age of Siberian basaltic volcanism; *Chem. Geol.* **138** 303–310
- Weissman P R 1982 Terrestrial impact rates for long and short period comets; *Geol. Soc. Am. Spec. Pap.* **190** 15–24
- Wetherill G W and Shoemaker E 1982 Collision of astronomically observable bodies with the Earth; *Geol. Soc. Am. Spec. Pap.* **190** 1–13
- Wignall P B and Twitchett R J 1996 Oceanic anoxia and the end Permian mass extinction; *Science* **272** 1155–1158
- Yayanos A A 1983 Thermal neutrons could be a cause of biological extinctions 65 Myr ago; *Nature* **303** 797–800
- Zhou L and Kyte F T 1988 The Permian-Triassic boundary event: A geochemical study of three Chinese sections; *Earth Planet. Sci. Lett.* **90** 411–421
- Zachos J C, Breza J R and Wise S W 1992 Early Oligocene ice sheet expansion on Antarctica: Stable isotope and sedimentological evidence from Kerguelen plateau; *South. Indian Ocean Geol.* **20** 569–573

Geologic and tectonic evolution of the Himalaya before and after the India-Asia collision

KEWAL K SHARMA

*Wadia Institute of Himalayan Geology, Gen. Mahadev Singh Road, Dehra Dun 248 001, India
e-mail: wihg@iasdl01.vsnl.net.in*

The geology and tectonics of the Himalaya has been reviewed in the light of new data and recent studies by the author. The data suggest that the Lesser Himalayan Gneissic Basement (LHGB) represents the northern extension of the Bundelkhand craton, Northern Indian shield and the large scale granite magmatism in the LHGB towards the end of the Palaeoproterozoic Wangtu Orogeny, stabilized the early crust in this region between 2–1.9 Ga. The region witnessed rapid uplift and development of the Lesser Himalayan rift basin, wherein the cyclic sedimentation continued during the Palaeoproterozoic and Mesoproterozoic. The Tethys basin with the Vaikrita rocks at its base is suggested to have developed as a younger rift basin (~ 900 Ma ago) to the north of the Lesser Himalayan basin, floored by the LHGB. The southward shifting of the Lesser Himalayan basin marked by the deposition of Jaunsar-Simla and Blaini-Krol-Tal cycles in a confined basin, the changes in the sedimentation pattern in the Tethys basin during late Precambrian-Cambrian, deformation and the large scale granite activity ($\sim 500 \pm 50$ Ma), suggests a strong possibility of late Precambrian-Cambrian Kinnar Kailas Orogeny in the Himalaya. From the records of the oceanic crust of the Neo-Tethys basin, subduction, arc growth and collision, well documented from the Indus-Tsangpo suture zone north of the Tethys basin, it is evident that the Himalayan region has been growing gradually since Proterozoic, with a northward shift of the depocentre induced by N-S directed alternating compression and extension. During the Himalayan collision scenario, the 10–12 km thick unconsolidated sedimentary pile of the Tethys basin (TSS), trapped between the subducting continental crust of the Indian plate and the southward thrusting of the oceanic crust of the Neo-Tethys and the arc components of the Indus-Tangpo collision zone, got considerably thickened through large scale folding and intra-formational thrusting, and moved southward as the Kashmir Thrust Sheet along the Panjal Thrust. This brought about early phase (M1) Barrovian type metamorphism of underlying Vaikrita rocks. With the continued northward push of the Indian Plate, the Vaikrita rocks suffered maximum compression, deformation and remobilization, and exhumed rapidly as the Higher Himalayan Crystallines (HHC) during Oligo-Miocene, inducing gravity gliding of its Tethyan sedimentary cover. Further, it is the continental crust of the LHGB that is suggested to have underthrust the Himalaya and southern Tibet, its cover rocks stacked as thrust slices formed the Himalayan mountain and its decollement surface reflected as the Main Himalayan Thrust (MHT), in the INDEPTH profile.

1. Introduction

“Geology of the Himalayas” by Gansser (1964) was the first regional attempt to synthesize the knowledge gained in the past one century on the world’s highest and the youngest mountain, followed by Le Fort

(1975, 1989). With developments in the concept of plate tectonics, the Himalaya believed to be a classic example of the continent-continent collision related mountain belt (Dewey and Bird 1970), the attention of many researchers was focused to understand the collision mountain building processes. Large geochemical,

Keywords. Collision tectonics; crustal growth; Himalayan evolution.

geochronological, isotopic and geophysical data base generated in the past two decades provides a good understanding of the geology of the Himalayan mountain and a better constrained model of its geodynamic evolution.

Despite the fact that many gaps in the understanding of the Himalayan geology and its tectonic evolution, have been filled, there are still many grey areas in the understanding of the Himalaya. Some of these are:

- (i) The stratigraphy of the Lesser Himalayan sedimentary units and their response to changes in tectonics within the basin and the surrounding regions,
- (ii) the status of the 2.5 Ga Rampur-Bhowali volcanics (Bhat and Le Fort 1992; Bhat *et al* 1998) and associated sediments of the Lesser Himalayan basin,
- (iii) the relationship of the Lesser Himalayan Sedimentaries (LHS) and the Lesser Himalayan Crystallines (LHC) which cover the LHS as thrust sheets,
- (iv) time and space relationship of the rocks of the lower and upper crystalline thrust sheets of the LHC,
- (v) did the LHS and the LHC rocks, during their long geological history from Archaean?-Palaeoproterozoic till their collision induced Himalayan deformation and metamorphism, remain as such without any change? or do they show any evidence of pre-Himalayan orogeny?,
- (vi) status of Vaikrita/Tibetan slab/Higher Himalayan Crystallines (HHC) *vis-a-vis* the Tethyan sedimentary sequences (TSS) and the LHC,
- (vii) the limit to which the Archaean-Proterozoic continental crust of the Indian shield extends under the Ganga Alluvium and the Himalaya, and
- (viii) the nature of the continental crust that lies beneath the Himalaya and South Tibet, observed as a reflecting surface in the INDEPTH profile (Zhao *et al* 1993).

The present paper is an attempt to answer some of these questions and discuss the current status of the geologic and the tectonic evolution in the light of new observations and data from the NW Himalaya (Himachal, Garhwal, Kumaun) and Central (Nepal) Himalaya. The NW Himalaya, being a less squeezed section than the Central (Nepal) and the NE Himalaya, has been the main focus in this paper.

2. Divisions of the Himalayas

The Himalayas from south to north are divided into five well-known and generally accepted lithotectonic units (figure 1).

The Sub or Outer Himalaya forms low altitude hills limited between the Main Frontal Thrust (MFT) in the south and the Main Boundary Thrust (MBT) in the north. It preserves the record of the post-collision sediments produced by weathering and erosion of the debris of the rising Himalayan front, carried and deposited by rivers in the fore-deep basin called the Murree-Siwalik Basin.

The Lesser or Lower Himalaya, limited between the MBT in the south and the Main Central Thrust-Vaikrita (MCT-V) in the north, comprises records of marine sediments of Proterozoic to Cambrian age and some sedimentary records of transgressing shallow sea during Permian, Upper Cretaceous and Middle Eocene. The LHS are covered by two thrust sheets of low to medium grade metasediments (Jutogh-Almora and Chail-Ramgarh). The sediments of the Lesser Himalayan basin in general provide information in terms of tectonic changes in the basin and associated magmatism and its surrounding regions during Proterozoic and Phanerozoic.

The Great or Higher Himalaya, limited by MCT in the south and Tethyan Detachment Fault (TDF) in the north, is represented by the high grade Precambrian crystallines, Cambro-Ordovician (500 ± 50 Ma) granites/orthogneisses and the Tertiary leucogranites.

The Tethys Himalaya is confined between the TDF in the south and the Indus-Tsangpo Suture (ITS) in the north. It comprises Late Precambrian to Phanerozoic (Palaeozoic-Mesozoic) marine sediments deposited in the Tethyan Sea that extended up to the Lesser Himalaya during the Vendian-Cambrian Cycle (Shah 1991).

The Trans-Himalaya or Indus-Tsangpo suture zone comprises the obducted slices of the oceanic crust of the Neo-Tethys, deep-sea trench sediments, subduction and collision related island arc magmatic rocks, the arc derived accretionary prism related sediments and the post-collision Kargil molassic sediments.

3. Geology of the Himalayas

Various aspects of the Himalayas can be covered under this heading, however, the author has preferred to discuss only some important aspects of the geology.

The Lesser Himalayan Basin sedimentaries (LHS). In view of the general paucity of fossils, difficulty to assign reliable stratigraphic ages due to sheared contacts, scarcity of the dependable isotopic numbers capable of resolving the age problems together with the confusion created by multiplicity of names assigned to similar lithologies in the adjoining areas, the LHS were considered as the most confused sequence of the Himalaya (Gansser 1981). No consensus has yet emerged to build a reliable time stratigraphy of the LHS, and the confusion still exists in recent literature (Shanker *et al* 1989; Valdiya 1995; Virdi 1995). Under

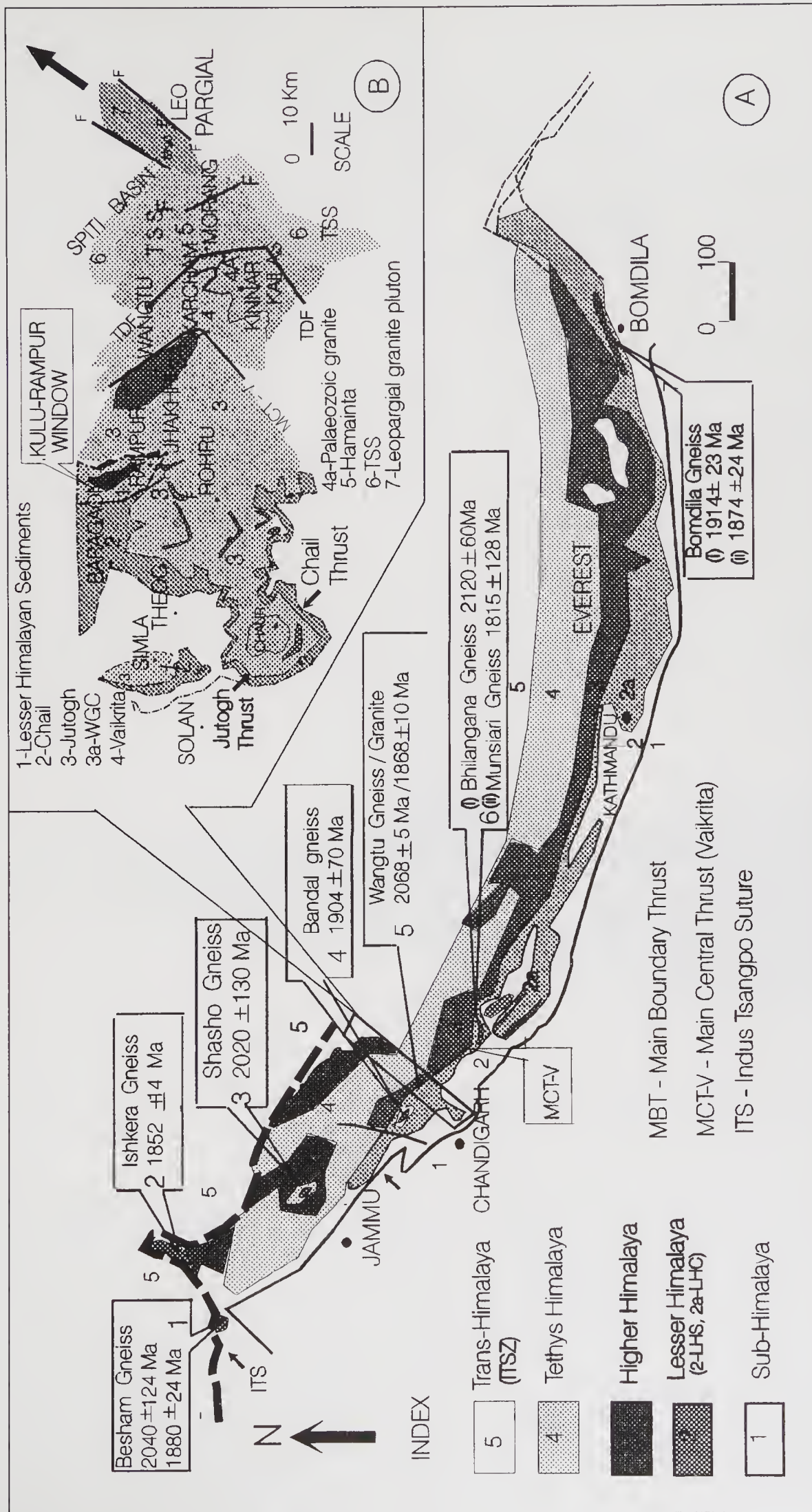


Figure 1. A: - Geological map showing divisions and litho-tectonic units of the Himalaya and ages of LHC slices along MCT-V, Sources of age data: 1 - Treloar and Rex (1990); 2 - Zeitler *et al* (1989); 3 - Bhanot *et al* (1988); 4 - Frank *et al* (1977); 5 - Singh *et al* (1993); 6 - (i) Raju *et al* (1984); (ii) Trivedi *et al* (1982); 7 - (i) Dikshitulu *et al* (1995); (ii) Rao (1998). B - Geological map along Satluj Valley showing LHC (Chail and Jutogh and HHC thrust sheets, TDF and Leopargial pluton north of it).

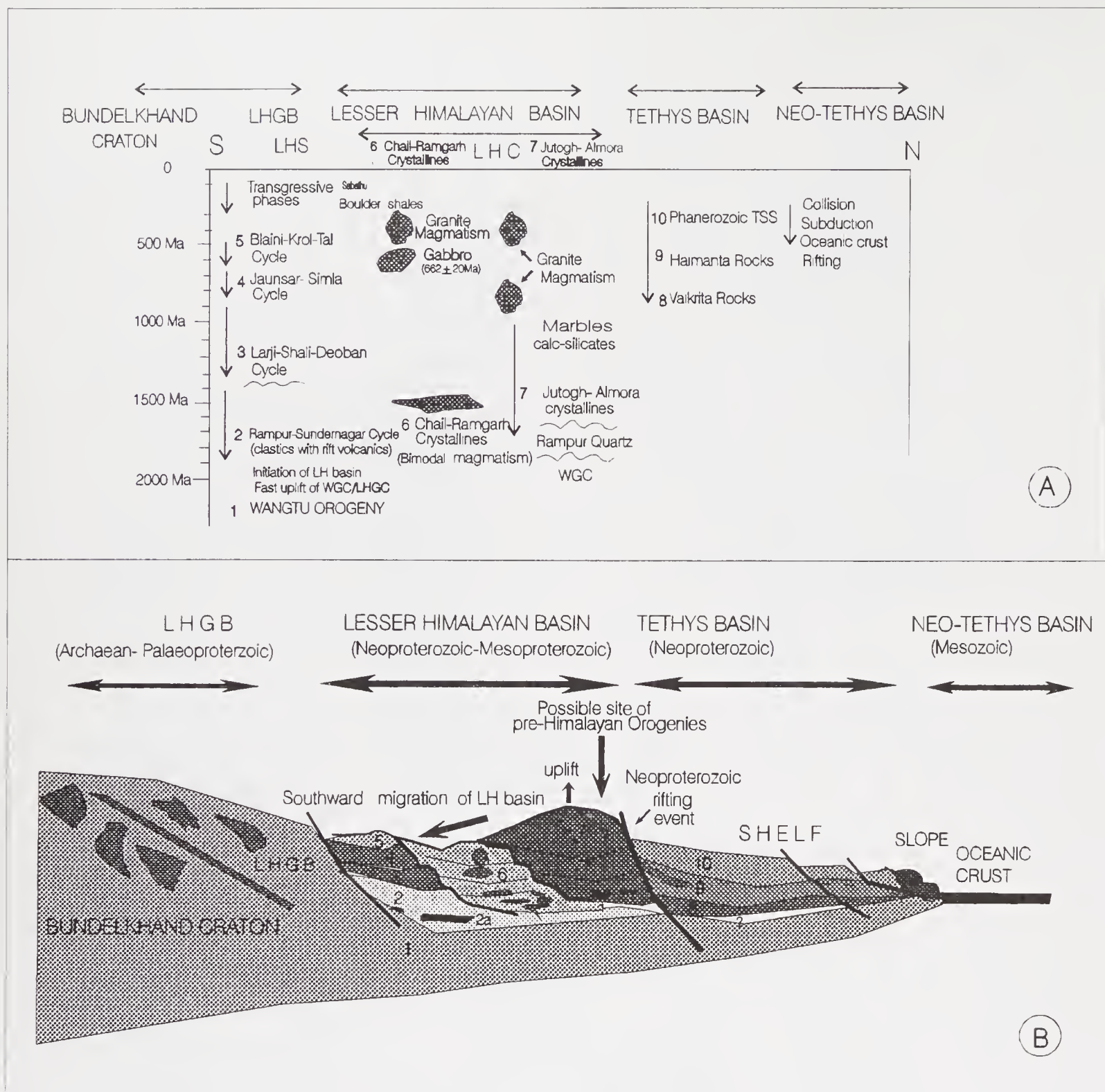


Figure 2. Time and space relationship of various sedimentary basins developed in the Himalayan region since Proterozoic (pre-Himalayan collision scenario).

the circumstances, the author considers the division of the LHS on the basis of sedimentary cycles as a fairly reasonable approach, and recognizes four sedimentary cycles (Rampur-Sundernagar cycle, Larji-Shali-Deoban cycle, Jaunsar-Simla cycle and Blaini-Krol-Tal cycle) given in figure 2. In view of the age controversy the earliest (Rampur-Sundernagar) cycle needs elaboration.

It is now generally accepted that the white quartzite (Rampur Formation) with penecontemporaneous tholeiitic volcanics (green beds or Rampur metavolcanics) and green (fuchsite) quartzites marking the basal sequence in the Kulu-Rampur Window (KRW),

represents the oldest unit of the LHS. The quartz dominated lithologies with a high degree of mineralogical and textural maturity and the associated rift related tholeiitic volcanics (Ahmad and Tarney 1991; Bhat and Le Fort 1992) in the lower part of the sequence suggest that the Lesser Himalayan sedimentation began in a rift basin and the terrain to the south exposed largely the granitic rocks (Bundelkhand craton; Sharma 1998). This is followed by a thick sequence of alternating bands of grey to white quartzite, metavolcanics and grey to green phyllites (Bhalan Fm) in the KRW (Sharma 1977). Similar lithostratigraphic units are widely exposed in the

Lesser Himalaya in Himachal Pradesh (Sundernagar group; Srikantia 1977), Garhwal-Kumaun (Berinag quartzite, Damtha group, Valdiya 1980), Nepal, Sikkim and Bhutan sectors (Valdiya 1995; Virdi 1995). The increasing argillaceous content in the younger sequences of Bhalan-Sundernagar-Dhamtha rocks suggests the deepening of the rift basin with time. This sedimentary sequence is called the Rampur-Sundernagar/Berinag-Damtha cycle. On a regional scale, similar lithostratigraphy has been recognized in the rift related volcano-sedimentary basins in the Proterozoic (Aravalli, Bijawar, Gwalior) surrounding the Bundelkhand craton (Ahmed and Tarney 1994; Sharma 1998; Sinha-Roy *et al* 1998).

Rampur-Mandi-Bhimal-Bhowali metavolcanics, dated 2.5 Ga using the Sm-Nd method (Bhat and Le Fort 1992; Bhat *et al* 1998), has surprised many (Valdiya 1995) and is not supported by the geological setting and other isotopic ages. The Bandal granite (1905 ± 70 Ma; recalculated with new λ value from Frank *et al* 1977), believed to intrude the Manikaran quartzite-volcanic unit (Sharma 1977), is indeed a multi-phase orthogneissic complex having sheared contact with quartzites and is similar to the Wangtu Gneissic Complex (WGC) exposed in the adjoining Satluj valley. The recent data from the WGC suggesting Palaeoproterozoic Wangtu Orogeny (discussed later), together with U-Pb dating of detrital zircon grains (between 1.87 Ga and 2.6 Ga) from the Lesser Himalayan sequences (Parrish and Hodges 1996), suggest their depositional age to be less than 1.87 Ga. The author considers the lower age limit for the sediments of the Rampur-Sundernagar cycle and its deeper facies equivalents (Chail-Ramgarh Gp) having bimodal magmatism (granite, porphyry, mafic volcanics, gabbro) to be around 1900 Ma (Trivedi and Pande 1993; Ahmad *et al* 1996).

The *Larji-Shali-Deoban* cycle that follows unconformably the Rampur-Sundernagar cycle rocks, represents carbonate dominating sequence with prolific development of the stromatolite assemblage suggesting Lower Riphean i.e. 1200-900 Ma age and stable shelf environment for their deposition (Raha 1980; Valdiya 1980; Tewari 1989). The Pb-Pb age of ca 1,000 Ma for the syn-diagenetic galena (Raha *et al* 1978) also constraints the carbonate sequence to be older than 1,000 Ma. The comparative lithologies are known from the Sirban limestone in Pakistan, Great limestone from Jammu, Larji-Shali from Himachal, Deoban-Gangolihat from Garhwal-Kumaun region, Dhading in Nepal and Buxa in Bhutan forming the key stratigraphic horizon in the Lesser Himalaya.

The carbonate sequence is followed by dominantly clastic sediments known as the Jaunsar-Simla groups (Srikantia and Sharma 1971; Kumar and Brookfield 1989), hence the *Jaunsar-Simla* cycle. The Simla group is considered as turbiditic sediment (Srikantia and Sharma 1971; Bhargava 1976; Valdiya 1980); shelf-

mud transition zone tidal flat complex (Singh and Meerajudin 1980) and as a large muddy delta built out into a basin formed by collapse of the Shali carbonate platform (Kumar and Brookfield 1989). The Nagthat quartzites in parts of the Mussoorie and Korgai synclines is considered as shore to proximal inner shelf deposits (Ghosh 1991).

Another sequence of clastics-carbonates-clastics rocks that lie with an unconformity over the Jaunsar-Simla rocks is termed the *Blaini-Krol-Tal* cycle. The sedimentation of this cycle took place in a much confined basin than the Inner Carbonate basin (Deoban-Shali) and accordingly has a restricted occurrence between Krol Hills in Himachal to Nainital in Kumaun. The discovery of conodonts (Azmi *et al* 1981), trilobites and other body fossils from Tal (Singh and Rai 1983; Kumar *et al* 1987) provide a more definite time control from Late Precambrian to Early Cambrian for the Blaini-Krol-Tal cycle. The Sr_i ratio of 0.7093 in the carbonaceous shales associated with phosphorites at the base of Tal closely corresponds to the world seawater record during Cambrian (Sharma *et al* 1992) and is significant to understand the tectonics of that time (discussed later).

A few transgressive phases during Lower Permian (Boulder Slate), upper Cretaceous shelly limestone and Eocene Sabathu Fm (Valdiya 1995; Virdi 1995; Mathur 1997) in the Lesser Himalaya suggest that the region has been a positive area for most of the time since Early Cambrian.

Metasediments of the Lesser Himalayan Crystallines (Chail-Ramgarh/Jutogh-Almora). The Lesser Himalayan sedimentary sequences in most places are covered by thrust sheets of low and medium grade crystalline (metasedimentary and magmatic) rocks known as Jutogh-Almora and Chail-Ramgarh (figure 1). The relationship between the LHS, the LHC and the HHC has been attempted, since a clear understanding of their composition and age is fundamental requisite to the better understanding of the crustal structure of the Himalayan Orogen.

The *Chail thrust sheet* in the Himachal Pradesh and the *Ramgarh thrust sheet* in the Garhwal-Kumaun region brings the low grade metasediments along the Chail/Ramgarh Thrust to lie over the LHS in the NW Himalaya. The author supports earlier workers (Saraswat *et al* 1970; Virdi 1981) who consider Chail rocks to have distinct lithology, grade of metamorphism (biotite-garnet grade) and tectonic position than the overlying Jutogh Thrust Sheet. The Chail thrust sheet is best exposed between Mandi and Kulu in the Beas valley, Baragaon and Dutt Nagar in the Satluj valley (surrounding the Kulu-Rampur Window) and below the Jutogh Thrust Sheet in the Simla and Chaur regions. Earlier, Sharma (1977) preferred to include Chail rocks of the Kulu-Rampur Window in the Jutogh Thrust Sheet (Khamrada Member), and Bhargava and Bassi (1994) in the Kulu Thrust Sheet.

The Chail rocks have dominantly pelitic (phyllite, schist) lithology with mylonitic orthogneisses in the lower part and occasional quartzitic and carbonaceous bands in the upper part. The mylonitic gneisses best developed in the Satluj valley between Baragaon and Nirath have yielded Rb-Sr whole rock isochron age of 1445 ± 75 Ma, which with two more samples added from the mylonitic gneisses (figure 1b) collected from Jhakhari (north of the KRW) together define a combined isochron age of 1495 ± 63 Ma with initial ratio of 0.7429 ± 84 Ma (Kumar 1986). To me, this age represents a strong thermal imprint on 1900 Ma granitic rocks associated with Ramgarh crystallines from the Kumaun region.

In the Garhwal-Kumaun region, the low grade rocks of the lower thrust sheet are known as Ramgarh Group and comprise of mylonitic quartz porphyry, porphyritic granite, phyllites, quartz wackes, metasiltstone, carbonaceous slates and phyllites with occasional crystalline limestone (Valdiya 1980). Collectively the lower thrust sheet of the Lesser Himalayan Crystallines may be called the *Chail-Ramgarh thrust sheet*. Rb-Sr dating ($\sim 1888 \pm 46$ Ma) of cogenetic quartz porphyry and associated granites (Trivedi and Pande 1993) from Amritpur area closely associated with mafic volcanism (flows and dykes), suggests the magmatic event to be Palæoproterozoic. The gabbro body, a plutonic phase of rift related Garhwal volcanics, from this sequence has been dated around 1900 Ma (Ahmad *et al* 1996). Further, the author considers the Chail rocks with bimodal magmatism to be metamorphosed deeper facies equivalent of the rocks of the Rampur-Sundernagar cycle of the LHS (figure 2). In this context it may be mentioned that earlier workers expressed their inability to differentiate between the Chail and the Berinag sequences (Fuchs 1982; Valdiya 1988) and between the Ramgarh succession and the Rautgarha Fm (Valdiya 1980).

The Jutogh-Almora thrust sheet. Generally a medium grade (garnet-staurolite) metasedimentary sequence (schists, quartzites, marble, calc-silicates, etc.), with bands of orthogneisses, amphibolites and occasional granite intrusives exposed around Chaur, Simla and in the Satluj valley, represents the rocks of the Jutogh Thrust Sheet (JTS) in the Himachal Himalaya. It forms a continuous sheet between Chaur and Karcham (figure 1b). The unfoliated intrusive granite phase (530 ± 40 Ma) around Chaur at the higher structural level and the biotite orthogneisses (1100 ± 50 Ma and 930 ± 115 Ma; Kumar 1986) interbedded with the Jutogh rocks at the lower structural level suggest two distinct magmatic events. Subsequently, zircon fractions from the biotite orthogneisses dated by U-Pb technique (912 ± 6 Ma and Pb loss at later event ca. 500 Ma) confirmed two magmatic episodes in the Jutogh Thrust Sheet in the Chaur area recognised by Rb-Sr dating. In the Satluj valley, the JTS is exposed around Jhakhari and

Karcham (figure 1b) and are represented by garnet-staurolite bearing schists alternating with bands of grey quartzites and amphibolites. The author, in an underground adit recently put up for hydro-electric project, near Karcham, observed that the highly foliated granitic gneisses of WGC grade into 30–50 m thick white quartzite unit, however, a local thrust separates the quartzites from the overlying Jutogh sequence of alternating schist, grey quartzite and amphibolites. A hot water ($\sim 80^\circ\text{C}$) spring located near the thrust contact suggests its deep seated nature. The author supports the views of the earlier workers (Bhargava and Ameta 1987; Bhargava *et al* 1991) that the WGC acts as basement for the relatively thinner unit of Rampur quartzite. Further east the JTS is thrust over by high grade (kyanite-sillimanite) Vaikrita (HHC) rocks.

In the Garhwal-Kumaun region the metamorphic rocks of the crystalline thrust sheet are known as the Almora Group, a structural rather than a true stratigraphic unit (Valdiya 1980). It comprises garnetiferous mica schist, micaceous quartzite with occasional carbonaceous/graphitic schists intruded by 565 ± 22 Ma old batholithic body of Champawat granodiorite (Valdiya 1980; Trivedi *et al* 1984). In view of the associated amphibolites in the lower part and the granitic rocks (with limited age data) in its upper part, the Jutogh-Almora crystallines are considered to be either contemporary or relatively younger than the Chail-Ramgarh crystallines.

Wangtu Gneissic Complex. A domal upwarp in the JTS, between Chaura and Karcham in the Satluj valley, with its deeper part exposed around Wangtu (Wangtu Dome, Berthelsen 1951) comprises dominantly of coarse and fine grained gneisses alternating with kyanite-sillimanite bearing schists, quartzites, calc-silicates and amphibolites. The author prefers to call this distinct lithology of the basal part of the JTS (figure 1b) dominating in metasediments, amphibolites and orthogneisses intruded by coarse and fine grained granites and associated pegmatite-aplite phase, as the Wangtu Gneissic Complex (WGC). Petro-mineralogical and geochemical studies carried out by the author suggest that the fine and coarse grained gneisses in layered parallel arrangement with high grade schists, quartzites, calc-silicates and amphibolites are genetically related to the fine and coarse grained porphyritic granites which intrudes them, except for a dominant pegmatite phase associated with the latter. The granitic rocks of the WGC are meta-aluminous to paraluminous in composition and the melts for both the suits were derived from similar source rocks (Rao *et al* 1995). The fractionated REE patterns of these rocks are similar to Proterozoic granitic rocks and suggest derivation of the magma from deeper crustal level, also supported by low Sr_i ratio of 0.705 of the granitic melt.

The younger (fine grained) granite phase intruding the gneisses defines a well spread six point isochron

giving age of 1895 ± 64 Ma with initial Sr ratio of 0.7046 ± 72 (Sharma *et al* 1993). Earlier, the fine and coarse grained gneisses from Tapri to Chaura, representing the peripheral part of the WGC, were collected by the author and dated by Rb-Sr technique as 2025 ± 86 Ma (Kumar 1986). The U-Pb dating of zircon fractions confirmed older ages for the gneisses (2068 ± 5 Ma) and younger ages (1866 ± 10 Ma) for the post-tectonic granites (Singh *et al* 1993). The lower intercept on the concordia diagram at 48 ± 28 Ma suggests lead loss during the Himalayan Orogeny.

The metapelites with sillimanite-kyanite-K-feldspar \pm muscovite assemblage, interlayered with quartzites, calc-silicates, ortho-amphibolites, fine and coarse grained gneisses indicate that the WGC reached the higher side of the sillimanite zone of Barrovian-type metamorphism. The involvement of the sillimanite and kyanite along with micaceous minerals in the tight folding associated with Proterozoic deformation suggest peak metamorphism to be pre- to syn-tectonic in nature. Further, the presence of sillimanite-kyanite bearing schistose xenoliths noticed in the fine grained gneisses (2068 ± 5 Ma) and orthogneiss xenolith in younger granite phase suggests that the early stage intrusion of the granite magma followed the peak metamorphism during Palaeoproterozoic. The author relates Palaeoproterozoic deformation, metamorphism and granite magmatism to the Wangtu Orogeny. The presence of cordierite, superimposed on the sillimanite-kyanite-K-feldspar assemblage, has also been noticed indicating lower temperature and lower pressure metamorphic conditions reached during exhumation of the rocks. This together with the presence of unrotated large xenoliths of orthogneisses and amphibolites in the younger (1860 ± 10 Ma) granites-pegmatites supports the "passive" or "permitted" emplacement of volatile rich end stage melts. Similar studies by the author in the Kulu-Rampur Window suggest that the Bandal granite exposed in the core of the tectonic window and believed to be intrusive in LHS (Sharma 1977), is indeed a gneissic basement (Bandal Gneissic Complex-BGC) having similar geochemical signature as in the granitic rocks of the WGC. Such a scenario supports orogeny related rapid uplift and fast removal of its cover rocks. The upwelling plume, further induced decompression/extension in the WGC and caused development of Lesser Himalayan rift basin and mafic magmatism.

It may be important to record that the rocks of the WGC preserve upper amphibolite (sillimanite-kyanite) grade assemblage in an area about 1 km^2 , presently exposed in the core of the Wangtu Dome. Somehow, this area escaped the effects of Himalayan deformation (Tertiary), which is commonly present in the peripheral part of the dome and its core part remained as tectonically resistant enclave. The superimposed younger (Tertiary?) metamorphism, in the marginal part of the WGC and the overlying Jutogh

metasediments, is of greenschist to lower amphibolite grade.

A colossal pile of metamorphics and mylonitic gneisses, best exposed near Munsiri in the Kumaun region, is known as Munsiri Fm (Valdiya 1980). According to the author, the Munsiri Fm compares with Wangtu Gneissic Complex and the Almora Group metasediments and granitoids with the Jutogh Group. This is substantiated by Palaeoproterozoic (1860 Ma) age of orthogneiss from the base of the Almora Nappe, Askot klippe, Munsiri and other places in the Kumaun Himalaya (Trivedi *et al* 1984).

The widespread occurrences of Palaeoproterozoic (2000 ± 100 Ma) orthogneisses, associated with metasediments and amphibolites all along the 2500 km length of the Himalaya (figure 1a) suggest the granite magmatism in the Lesser Himalaya to be a regional phenomena. Further, the orthogneiss occurrences aligned along the MCT represent the scraped slices of an extensive Lesser Himalayan Gneissic Basement (LHGB) that underthrusts the Himalaya and the Southern Tibet (see discussion).

The Tethyan Basin. The 10–15 km thick pile of Phanerozoic Tethyan sedimentary sequences (TSS) (Srikantia 1981; Gaetani *et al* 1986; Fuchs 1987; Bhargava 1998) and the underlying late Precambrian-early Palaeozoic rocks called Haimanta Fm/Phe Fm/Annapurna Fm/North Col Fm are generally considered the deposits of the Tethys basin. The author suggests sedimentary protoliths for the Vaikrita/Tibetan slab (HCC) rocks to represent the basal part of the Tethyan basin. The sedimentation in the rifted Tethyan basin, north of the Lesser Himalayan basin, is suggested to have begun in Neoproterozoic (~ 900 Ma), as evident from the detrital zircon grains of 960 Ma age from the metasandstones within HHC (Parrish and Hodges 1996), the quartz dominated lithology with tholeiitic volcanics in the lower part of the Vaikrita Group and the changes in the sedimentation pattern in the Lesser Himalayan basin.

The Phanerozoic Tethyan sedimentary sequences (TTS) have been discussed in detail by earlier workers. The present author would like to draw attention to changes in the Tethys basin which caused termination of deeper flyschoid sedimentation and shallowing of the basin during late Precambrian, absence of late Cambrian and early Ordovician sequence in the Kashmir-Zaskar region (Shah *et al* 1991), deformation (Baig *et al* 1988; Kumar *et al* 1978), early Palaeozoic (500 ± 50 Ma) magmatism (Sharma 1997) and the occurrence of Ordovician conglomerates of fluvial nature (Bagati 1991), suggesting a significant orogeny related tectonic activity on the regional scale during late Precambrian-Cambrian (Bhargava 1980; Valdiya 1995, Sharma 1997).

The Higher Himalayan Crystallines (HHC). There is sufficient lithological and isotopic data to suggest that the Neoproterozoic Vaikrita Group rocks, late

Precambrian-Cambrian Haimanta rocks and the Phanerozoic TSS rocks, along with their associated magmatic suits, represent more or less a complete sequence of the sedimentary pile of the Tethyan basin. In the Satluj valley, the author considers the Vaikrita Group lithology to correspond to original sediments dominating in quartz with interbedded basic lava flows in the lower part, dominantly argillaceous in the middle part and carbonaceous shales, marly shales with impure limestone bands in the upper part. The psammo-pelitic lithology of the upper part of the Vaikrita Group, corresponds closely to the lower part of the Haimanta particularly in its carbonaceous content. The transitional zone between the Vaikrita and the Haimanta in the Satluj valley is intruded by lower Ordovician (477 ± 29 Ma) granite (Kumar 1986). Such granitic rocks are also known from the Tibetan slab of the Nepal Himalaya and described as orthogneisses (Le Fort *et al* 1986). By far the most extensive tract of metamorphosed rocks seen within the Himalayas is to the south of Indus-Tsangpo Suture Zone. The widely exposed HHC in the Himalaya show strong similarity in its bulk lithology, early Palaeozoic granitic (orthogneisses) activity and the post Himalayan collision metamorphic history and deformation patterns (S-vergent tight to isoclinal folds and other thrust related structures). The migmatites and the Lower Ordovician orthogneisses intruded by small plutons and network of Miocene leucogranites, dominate in the uppermost part of the HHC.

The structural and metamorphic studies on the HHC rocks from Zaskar and Nepal sectors of the Higher Himalaya suggest three phases (M1, M2, M3) of metamorphism (Pognente and Benna 1993; Searle and Rex 1989). The first phase of metamorphism (M1: $T = 550\text{--}680^\circ\text{C}$ and $P = 8\text{--}10$ Kbar) is early Barrowian-type and is attributed to subduction and crustal thickening during India-Eurasia collision. In the middle and the upper levels of the HHC, the most common assemblage of quartz-plagioclase-orthoclase-biotite-garnet-sillimanite in the gneisses and migmatization and the formation of concordant garnet-orthoclase-sillimanite-bearing leucosomes is related to peak metamorphism (M2 phase, $T = 650\text{--}750^\circ\text{C}$ and $P = 4\text{--}7$ Kbar). A relatively lower temperature and lower pressure ($T = 600\text{--}700^\circ\text{C}$ and $P = 2\text{--}4$ Kbar) M3 phase metamorphism is characterized by the formation of andalusite-cordierite-orthoclase-bearing discordant leucosomes which cross cut M2 leucosomes in the upper part of the HHC. Similar observations have been made by the author and his associates on the Vaikrita rocks from the Satluj valley and estimated temperatures from 590°C to 700°C during metamorphism (Chawla 1995).

Tethyan Detachment Fault (TDF). Studies in south Tibet revealed the existence of a number of normal faults in the Tethyan sequence (Burg *et al* 1984), north of the Higher Himalayan Crystallines (HHC). Subse-

quently, the evidence suggesting normal detachment faulting of weakly to unmetamorphosed Tethyan sequence (Haimanta and TSS) against the mid-crustal high grade rocks of the HHC has been discussed from Zaskar, NW Himalaya (Herren 1987; Searle and Rex 1989; Patel *et al* 1993), Annapurna in Nepal (Brown and Nazarchuk 1993), Gyirong-Lhozha-La Kang segment in south Tibet (Burchfiel *et al* 1992) and very recently from Besham-Banna area in north Pakistan (Vince and Treloar 1996). These workers emphasized the role of the extensional tectonics in the TSS, contemporary to compressional tectonics active in the HHC and south of it. Burchfiel *et al* (1992) estimated nearly 10 km of vertical displacement and 35 km of northward horizontal extension across the normal detachment fault along the profile at Qomolangma (Everest) in south Tibet, while Herren (1987) estimates vertical displacement and horizontal extension of the order of 19 km and 16 km, respectively, in the Zaskar region of NW Himalaya. The sense of shear indicators recognised in a zone (Burg *et al* 1984; Herren 1987; Burchfiel *et al* 1992) suggests northward normal faulting of the hanging wall (Tethyan) rocks, whereas Patel *et al* (1993) have recognized an earlier phase of top-to-south thrusting of the hanging wall (TSS) of the Zaskar shear zone followed by northward normal faulting. Since the overlying Tethyan sedimentary sequence with its low grade basal unit (Haimanta) detached and glided down northward and are juxtaposed with the high grade mid-crustal rocks of the HHC, this detachment is referred by a regional name "Tethyan Detachment Fault" (TDF), instead of local names.

In Satluj valley, the present author observed that the contact zone between the HHC and the Haimanta Fm is marked by 1–2 km thick shear characterized by low angle ductile S-C fabrics, and also by brittle deformation (both high and low angle normal faults), indicating NE-directed extension (figure 1b). Across TDF, the F1 and F2 folding patterns in the HHC and the Haimanta rocks are similar with possible difference in the timing of their development due to the movement of two successive thrust sheets. The rocks north of the TDF show additional north dipping normal fault-generated structures, such as north-vergent folds, north dipping high and low angle faults, asymmetrical drag folds and S-C fabrics indicating northward sense of shearing. Low angle structures are related to normal detachment faulting along the TDF, whereas the high angle faults are later and have superposed on the earlier low angle structures. The northvergent mesoscopic to large megascopic tight folds observed in the northern part (Spilu-Pooh area) represent the gravity gliding related third generation folds (F3) developed during south dipping back thrusting, along which the Haimanta rocks were thrust over the domal upwarp in the high grade Vaikrita rocks (figure 1b). Similarly, the large north-facing

recumbent fold of the Annapurna, with a lateral extent of more than 200 km and an inverted limb up to 25 km (Colchen *et al* 1986) is also attributed to the gravity gliding.

Further, in the Satluj valley section, the basal unit (Haimanta) of the TSS has been metamorphosed to kyanite-staurolite grade in the core of a large south-directed thrust related recumbent fold developed during the southward movement of the Kashmir Thrust Sheet. Similar south vergent folds (F1) in the hanging wall have also been reported from the Zaskar and the Nyalam and Gyirong areas of south Tibet and are believed to predate the north-dipping normal faults (Burchfiel *et al* 1992; Patel *et al* 1993). Small plutons of the Tertiary leucogranite and the network of aplite-pegmatite veins intrude the Palaeozoic granite, locally called the Kinnar Kailas granite, in the upper part of the HHC. If the leucogranites of the Satluj valley, like all other Himalayan leucogranites, are Oligo-Miocene (29–18 Ma) in age, then the timing of the normal detachment faulting and associated ductile S-C mylonitic fabric and low angle faults in leucogranite represent a closely spaced and interrelated events. Intensive sericitization and chloritization of large kyanite blades in the Haimanta rocks observed near Morang and Kah in the Satluj valley is attributed to hydrothermal activity during intrusion of the leucogranite and the associated aplite-pegmatites. The Oligo-Miocene age of leucogranite intrusion constraints the southward thrusting and associated metamorphism of the Haimanta rocks, along with the thrusting of the KTS along Panjal Thrust, to be an earlier event, possibly during the mid-Eocene (45 ± 5 Ma). The leucogranite bodies are generally confined to the uppermost part of the HHC, i.e. the zone of normal detachment fault, and north of it. The aplite-pegmatite veins of the leucogranite in Satluj valley are folded along with the F2 folds in HHC. Elsewhere in the Himalaya leucogranite-aplite-pegmatite veins are also folded along with the northvergent folds developed as a consequence of north-dipping low angle normal faulting against the HHC (Burchfiel *et al* 1992). Later, these veins are offset by north-dipping high angle normal faults. Thus, the leucogranites generation, emplacement and crystallization are short time span events and contemporary to the initial stage of the detachment faulting. The development of northvergent folds, back thrust and regional synclinal fold in the Haimanta rocks in the Satluj valley (see figure 4a) is attributed to the northward dipping normal detachment faulting and gliding of the TSS rocks over the rapidly exhuming HHC. The high angle faulting and the N-S faulting are the subsequently developed structural features.

Leucogranite magmatism in HHC. In addition to a thick zone of anatectic melting resulting migmatites in the upper structural level of the HHC, leucogranite plutons of various dimensions intrude in the upper

most part the HHC and the basal part of the Haimanta rocks and some time through the upper Palaeozoic and Mesozoic sequences (Guillot *et al* 1993). In some cases (as the Leopargial pluton) they occur as far as 30 km towards north (figure 1b). Two distinct belts of the leucogranite plutons have been recognised in the Higher Himalayan region, (i) the southern belt (which is restricted to the contact zone of the HHC and the base of the Haimanta rocks and (ii) the northern belt confined to the Tso Morari Dome and the Lhagoi-Kangri belt (Tu *et al* 1981; Sharma 1997). The granites of the southern belts have been studied in detail. Characterized by remarkable uniformity in mineralogical and major-element composition, the leucogranites show very strong heterogeneity in Rb/Sr isotopic systematics. Sr, Pb, Nd and O isotopic data for some of the leucogranites (Le Fort 1981) corroborates field and laboratory data, suggesting derivation of anatectic melts from a crustal sedimentary source. The age data on a number of granite bodies from the southern belt suggest the time of granite emplacement and crystallization between 29 and 18 Ma (Le Fort 1981). The mineral age data from the granite bodies and the rocks of the HHC vary between 18 and 11 Ma and are interpreted to suggest the time of rapid exhumation and fast cooling of the HHC. U-Pb ages of zircon/monazite of 15.1 ± 0.5 Ma from Lhagoi-Kangri pluton and 9.8 ± 0.7 Ma and 9.2 ± 0.1 Ma for Maja pluton (Scharer *et al* 1986) suggest the granite plutons of the northern belt to be younger than the plutons of the southern belt.

The extensive occurrences of leucosome in the gneisses, in the upper part of the HHC, resulting into migmatites is attributed to the partial melting (~ 6 vol%) of the pelitic and quartzo-feldspathic source rocks by muscovite breakdown during the climax of the M2 metamorphism (Pognente and Benna 1993). The large volume of leucogranite melts that emplaced in the uppermost part of the HHC and north of it during Oligo-Miocene (29–18 Ma) is difficult to account for by fluid-absent muscovite breakdown reaction in pelites and quartzo-feldspathic rocks. Alternatively, biotite breakdown is necessary, as it can yield up to 50 vol% of granitoid melts. Crystallization experiments either in the fluid-absent or at low H₂O suggest that a major amount of the melt is produced by fluid-absent biotite breakdown in pelitic system at approximately 850°C (Clemens and Vielzeuf 1987) and only a small extent of melting occurs at 800°C temperature involving biotite \pm sillimanite \pm plagioclase \pm quartz = garnet \pm K-feldspar \pm liquid (Le Breton and Thompson 1988). In order to generate a still larger volume of the anatectic melts necessary to produce plutons of the size of Leopargial, Manaslu, Makalu and Kula Kangri, the availability of H₂O or temperature of 850°C is necessary. Since, there is no evidence that the HHC at the present level of erosion in the Himalaya has attained a temperature higher

than 750°C, the only other candidate to produce large volumes of leucogranite melt is H₂O. The presence of H₂O in the leucogranite melt is evident from the bulk composition of the Leo Pargial granite and other Himalayan leucogranites which are close to the minimum melt in the system Ab-An-Or-Qtz-H₂O, further supported by the presence of primary inclusions of H₂O ± CO₂ in the ratio of 70:30 in quartz from Leopargial leucogranite (Choubey *et al* 1992) in the Satluj valley. This would require wet anatexis to produce such melt.

Further, taking a clue from the arguments of Le Breton and Thompson (1988) that at comparable temperature and water contents, and from comparable protoliths, large amounts of melts are produced at low pressure than at high pressure, would imply that the sudden change in the pressure in the HHC can also accelerate melting. The detachment-controlled decompression in the HHC, under going peak (M2) metamorphism and migmatization, caused by northward gliding of more than 15–20 km thick pile of thickened and thrust stacked TSS rocks from the HHC would accelerate leucogranite melt generation.

Sedimentation and magmatism in the Indus-Tsangpo suture zone (ITSZ). The Indus-Tsangpo suture zone (ITSZ) that lies to the north of the Tethys Himalaya, is a highly complicated accretionary prism zone, comprising various components of the oceanic crust, deep marine trench sediments, magmatic rocks of the island arc, arc-trench gap sediments, back-arc sequences and so on. Five petro-tectonic assemblages characteristic of subduction-collision zone (Condie 1982) have been recognized and studied in detail by many workers from the ITSZ (Sharma 1991, 1991a; and references therein).

The bimodal volcanics (subaerial tholeiitic flows and rhyolites; Bhat *et al* 1981) from Kashmir (Panjal Traps) and Zaskar (Phe volcanics; Nanda *et al* 1978) represent cratonic rift assemblage, and the platform shelf deposits of the Tethys basin which merge northward with continental slope deposits called the Lamayuru flysch in Ladakh (Sinha and Upadhyay 1994) and Triassic flysch (Gyirong Group) in the Lhasa (Cao 1991) represent the cratonic assemblages constituting the passive margin of the Indian plate. The oceanic assemblages occur in two or three linear belts of ophiolitic melanges tectonically emplaced in the arc and the arc-trench interface (Sharma 1994). In the Lhasa sector, the complete section of the ophiolitic melange (Yarlung Zangbo ophiolite), with associated upper Jurassic, deep marine radiolarian cherts is exposed (Cao 1991; Mei 1991). Cao (1991) strongly feels that there are two different kinds of oceanic crust units recognised within Zangbo suture zone, the major one is obducted Yarlung Zangbo ophiolite of Upper Jurassic to pre-Albian age, while the subordinate one is a younger oceanic crust of Albian to Early Cenomanian age forming the basement for the Congdu trench

sediments. The occurrences of blueschist mostly associated with obducted ophiolitic masses (Jan 1991, 1991a) and its amphiboles dated around 98 Ma (K-Ar) suggest that the subduction related blueschist metamorphism took place during Cretaceous (Honegger *et al* 1989). Other subduction related petro-tectonic assemblages include, low-K tholeiitic volcanic arc (Dras-Kohistan island arc), basic igneous complexes, i.e. Kargil igneous complex in Ladakh (Sharma and Choubey 1991) and Chilas complex in Kohistan (Jan and Jabeen 1991), and calc-alkaline (syn- to post-collision) granite magmatism and volcanism and the boninitic (high-Mg tholeiite) Shyok/Chalt volcanics of the backarc basin (Petterson *et al* 1991; Sharma 1991b).

The effects of collision started showing up in the petro-tectonic assemblages since middle Eocene (~ 50 Ma), at least in the Ladakh sector, where arc-trench gap basin started shallowing and migration towards north. The uplift of the Ladakh range influenced the sedimentation and provided large volumes of volcanic-plutonic rock debris to this vanishing marine basin which changed to completely continental in Upper Oligocene (Nanda and Sahni 1990). The molassic deposition derived from Ladakh arc continued in the two linear basins to the south and north of the uplifted Ladakh Range (Sharma 1991c). The information on collision related assemblages are limited from Kohistan and Lhasa sectors. According to Cao (1991), the Qiuwu Molasse of Eocene age overlies unconformably the Gangdise granitoids and indicates that the collision occurred prior to their deposition.

4. Discussion

Pre-collision tectonic evolution of the Himalaya. The tectono-magmatic evolution of the Wangtu Gneissic Complex (WGC) in particular and the Lesser Himalayan Gneissic Basement (LHGB) in general, compares closely with the tectono-magmatic evolution of the Bundelkhand craton, northern part of the Indian shield closest to the Himalaya. The U-Pb and Pb-Pb age of 2656 ± 0.9 Ma from LHC (Parrish and Hodges 1996) closely correspond to one of the three (2.7 Ga) Archean events (3.4 Ga, 3.0 Ga, 2.7 Ga) of granitic activity from Bundelkhand craton (Sharma 1998), suggesting a strong possibility of Archean crustal components in the LHGB. It is now well established that the stabilization of the Bundelkhand craton and its relicts in Aravalli, marked by enormous activity of late-tectonic granite magmatism in a narrow time span (~ 2.5 ± 0.1 Ga), coincided with the Archean-Proterozoic Boundary (Weidenbeck *et al* 1996). The large scale granite magmatism and the stabilization of the LHGB around 2 ± 0.1 Ga in the Himalayan region, followed the Wangtu Orogeny and is attributed to northward younging of the collision

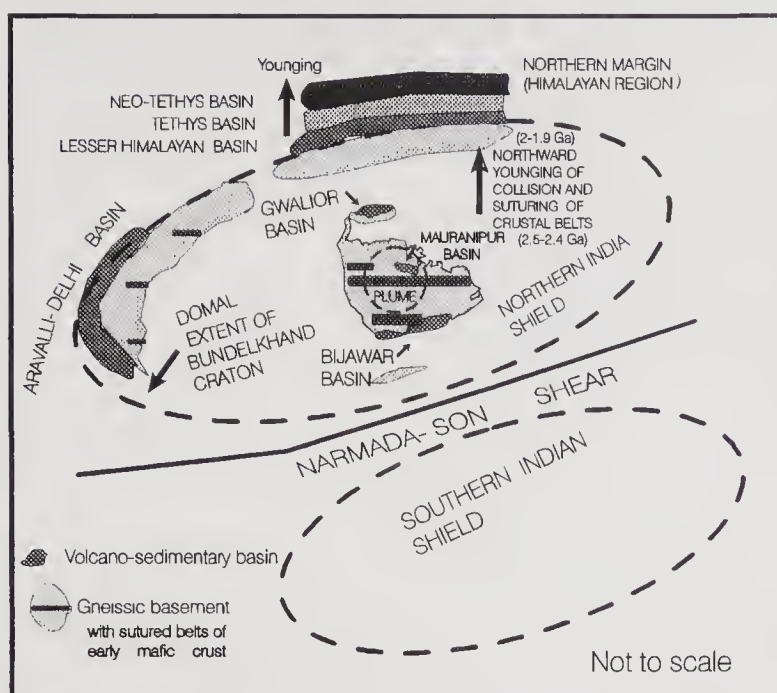


Figure 3. Sketch showing evolution of Bundelkhand craton and its northern margin extending in the Himalayan region (pre-Himalayan collision scenario).

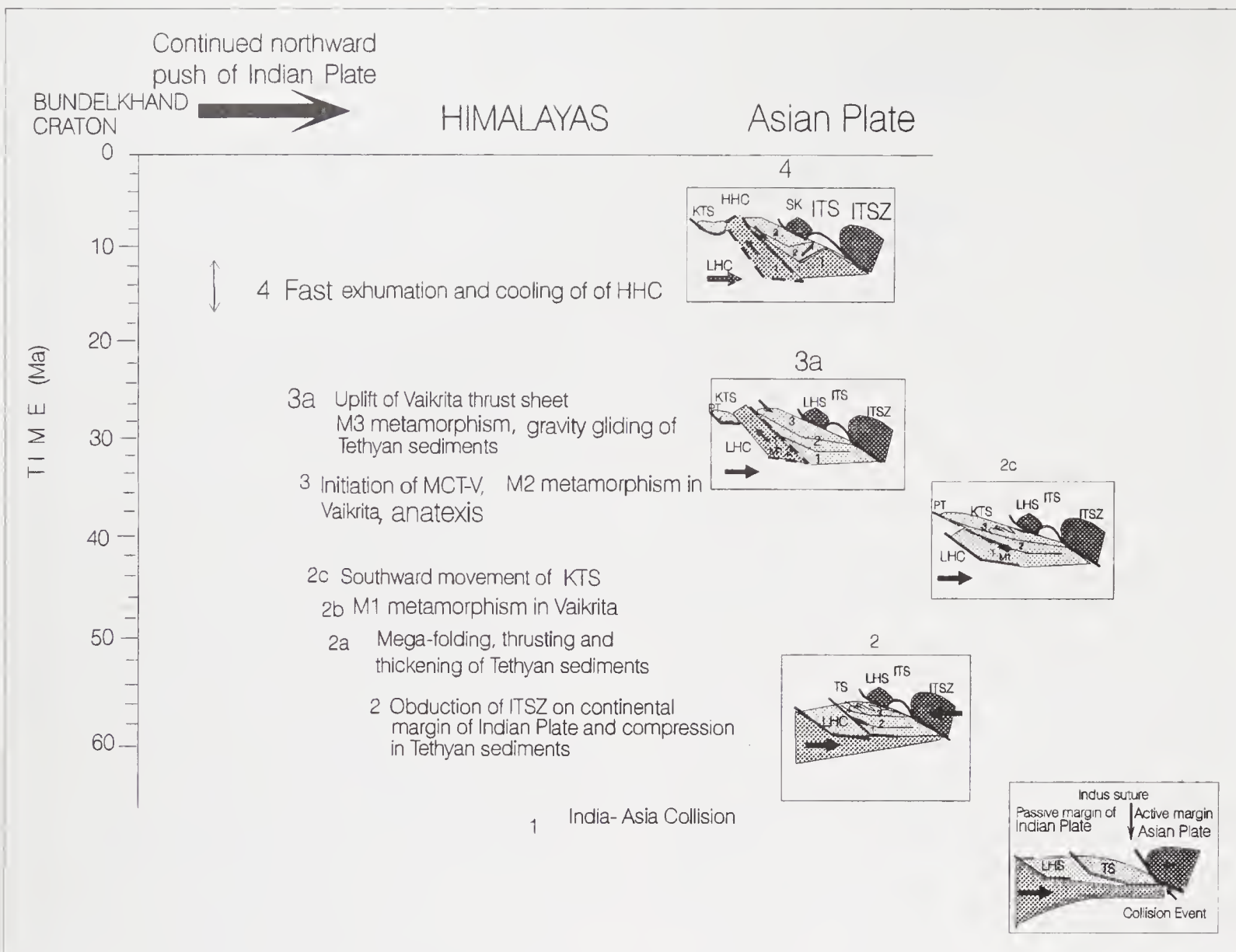
and suturing (figure 3) of Archaean crustal belts. All the three regions (Bundelkhand craton, the Aravalli and the Lesser Himalaya) witnessed rapid uplift, passive emplacement of pegmatites in WGC and quartz veins in the Bundelkhand craton and fast erosion, suggesting a change over from compressional to extensional environment culminating in the development of rift basins such as Bijawar, Gwalior, Aravalli and the Lesser Himalaya. This is attributed to the upwelling of mantle plume causing doming of the Bundelkhand craton, its rifting and mafic magmatism in the northern Indian shield (figure 3). The sedimentation in the rifted Lesser Himalayan basin began with Rampur-Sundernagar cycle on the eroded surfaces of the granitic crust which provided clean-washed matured quartz to form thick quartzite interbedded with tholeiitic volcanics, and continued through Palaeoproterozoic-Mesoproterozoic forming the LHS and the LHC sequences with associated granitic magmatism (figure 2). The Tethyan basin evidently developed to the north of the Lesser Himalaya during Neoproterozoic (~ 900 Ma), floored by gneissic basement and the rocks of the Lesser Himalayan basin, as evident from the mixed population of detrital zircon grains of ages older than 960 Ma from impure meta-sandstone within the HHC (Parrish and Hodges 1996). ϵNd value and Sm-Nd ratio of the gneissic rocks of the HHC (Parrish and Hodges 1996) support their derivation from two different sources having distinct signatures. The possibility of a rifting event, that could control fault-bounded development of the Tethyan basin and deposition in it, is quite strong. The author believes that it is along such a fault that the 10–12 km thick pile of the Phanerozoic TSS could be deposited under gradually subsiding shallow basin conditions, without the basin getting filled. The

presence of the mixed population of the detrital zircons from the metasandstones (HHC) in Nepal, derived from the Palaeoproterozoic and Mesoproterozoic granitoids of LHC and, the Lesser Himalayan sequences (LHS and LHC), suggest that the Lesser Himalaya became a positive topography for erosion, soon after the intrusion of 950 Ma granites exposed in the Chaur area and elsewhere. The widespread granite magmatism of 1400–950 Ma in the LHC (Chail, Jutogh), mylonitic gneisses in Chail (~ 1400 Ma) and reactivation of uranium mineralization in Rampur quartzite (~ 1200 Ma) and the presence of tholeiites, having distinct geochemical signatures than the Garhwal volcanics of the Lesser Himalayan basin interbedded with the impure quartzites in the basal part of the Neoproterozoic Vaikrita Group, not only supports the rift related nature of the Vaikrita basin but also suggests rapid uplift and fast erosion of the Lesser Himalayan rocks. It seems to be a compression related uplift and erosion before the rifting event, as it was accompanied by granite magmatism followed by removal of at least a few kilometers of the cover rocks and the southward shifting of the Lesser Himalayan basin, where sedimentation of Jaunsar-Simla and Blaini-Krol-Tal cycles (Outer Carbonate Belt) continued in a confined basin.

Some workers (Baig *et al* 1988; Bhargava and Bassi 1994; Valdiya 1995), on the basis of field data, strongly argued in favour of the late Precambrian-Cambrian orogeny. The geological observations from the Kinnar Kailas area in Satluj valley by the author, together with syn-collisional geochemical signatures of the Ordovician granites from the Kashmir, Tso Morari and Satluj valley (Sharma 1997) are in favour of the late Precambrian-Cambrian orogeny in the Himalaya called the Kinnar Kailas Orogeny which terminated sedimentation in the Lesser Himalayan basin. In this connection it may be pertinent to mention that the highly radiogenic strontium bearing gneisses of the LHGB, exposed along the present Himalayan Crystalline Axis, have strongly influenced the Sr-evolution pattern of the ocean water since 40 Ma and particularly during the past 20 Ma (Himalayan Orogeny) through Himalayan rivers (Krishnaswami *et al* 1992; Sharma 1993). Similar trends observed in the evolution curve of the ocean water around Late Precambrian-Cambrian (Burke *et al* 1982) and corroborated by Sr isotopic data from the Cambrian black shales of the Tal basin ($\text{Sr}_i = 0.709$; Sharma *et al* 1992), suggest that the Himalayan like situation created, exposing Palaeoproterozoic granites of the Lesser Himalaya, during the Kinnar Kailash Orogeny. This aspect needs to be looked into carefully with detailed studies.

The scenario that prevailed in the Lesser Himalayan region during Proterozoic-Phanerozoic, prior to the Himalayan collision, is illustrated in figures 2 and 3.

Post-collision tectonic evolution of the Himalaya. The rise of the Himalayan mountains is attributed to



the continued NE-SW compression, active even after the collision of India with Asia. The compressional regime in the Himalaya progressively shifted from north to south, as evident from the southward propagation of the thrust sheets, northward dip of the major thrusts and faults demarcating various lithotectonic units, presence of southvergent mega-folds, crystalline nappes and klippes with their rootzones in the north and the well-outlined windows of Lesser Himalayan sedimentaries under the crystalline thrust sheets. It is believed that nearly 2,000 km of convergence occurred since Eocene as indicated by studies of sea floor magnetic anomalies and palaeomagnetism on the Lhasa and Ladakh block (Patriat and Achache 1984). This has been taken up by some workers as combination of intracontinental thrusting, homogeneous crustal thickening and the lateral expulsion of the material along strike slip fault systems developed in the Asian Plate. However, crustal shortening, of the order of 500 km, in the Himalaya and 150–200 km in the Lesser Himalaya, based on the known structural outlines (Gansser 1981), seems to be a reasonable estimate.

It is now well established that India continued its northward movement at a reduced speed after its first collision with Asia in the NW Himalaya 60–65 Ma ago (Smith *et al* 1994). One of the factors responsible for the reduction in speed could be the bouyancy effect caused by the subducting lighter Indian continental crust under the denser rocks of the Indus suture zone (ISZ). An attempt has been made to model various events in chronological order (figure 4). The southward thrusting of the denser rocks of the ISZ on the shelf rocks of the Indian passive margin as Spongton Nappe took place during Mid-Eocene, ca. 50 Ma ago. Evidently, it suggests that the sedimentary cover rocks (TSS) of the subducting India continental crust were under tremendous compression. This caused large scale folding, intra-formational thrusts and nappes (Nimalling-Tsarp Nappe, Steck *et al* 1993) of the TSS and their southward movement as Kashmir Thrust Sheet. Obviously the contact zone between the Vaikrita and Haimanta rocks, profusely intruded by a large batholithic body of Lower Palæozoic Kinnar Kailas granite was preferred for thrusting. It was during its southward thrusting that the basal unit of

the KTS was deformed, metamorphosed and a small amount of leucogranite magma generated during mid-Eocene (47 ± 3 Ma) in the lower Swat region, N. Pakistan (Smith *et al* 1994). The thrust loading of the thickened TSS and the Haimanta rocks (more than 20 km thick pile) over the Vaikrita rocks caused the Barrovian-type M1 metamorphism and transformed them into the early stage of the HHC. Somehow, the southward movement of the KTS was arrested sometime around Oligocene-Miocene, possibly due to locking of the Panjal Thrust. Thus, the compression got shifted to a new site at the base of the Vaikrita along the suggested Neoproterozoic fault which separated the Tethyan Basin from the Lesser Himalayan Basin. This resulted in the peak (M2) metamorphism and an *in situ* anatexis (migmatization) in the HHC and the development of an incipient thrust (future MCT) at the base of the Vaikrita. Experimental structural studies suggest initiation of a thrust along an older fault during compression (Dubey and Bhat 1986; Ramsay and Huber 1987).

During the continued compression, the HHC Thrust Sheet possibly moved over a ramp causing fast exhumation. The thickened pile (more than 20 km thick) of comparatively cool and unconsolidated Tethyan rocks, notwithstanding the upward thrust movement of the hot Vaikrita (HHC) slab, started gliding northward against the HHC, thus causing normal faulting (extension) of Haimanta and TSS rocks along the TDF. Under such a situation, the upper part of the HHC, which was already undergoing partial melting, accentuated leucogranite melt generation due to the extension-induced decompression, as discussed earlier. The extension in the zone of detachment and north of it provided the required space for the diapiric rise and "*in situ*" ballooning of the magma (Guillot *et al* 1993) and the crystallization of the leucogranite plutons. The Oligo-Miocene age (29–18 Ma) of the Leucogranite plutons in the Higher Himalayan region (southern belt) constraints the timing of the gravity gliding and detachment faulting. The low angle ductile shearing of the leucogranites and the involvement of the pegmatite veins in the gravity gliding related northvergent folds (Burchfiel *et al* 1992), indicate that the region was still at depth and in the ductile regime. Such a scenario suggests contemporaneity between the compressional regime necessary to cause southward thrusting and rapid exhumation of the HHC on the one hand, and the extension causing normal detachment faulting of the TSS north of it. In fact, the compression in the HHC and extension in the TSS were more or less simultaneously active during this period. The rapid exhumation and fast cooling of the HHC after granite intrusion between 18–11 Ma period is evident from the coexisting mineral ages. This clearly points to the fact that various compression and extension related events took place in a short time span. The studies on the Leopargial granite pluton from Satluj

valley support this observation. The thermobarometry of feldspar from Leopargial leucogranite in the Satluj valley suggests that the feldspars of the pluton crystallized around 746°C at a depth corresponding to 5 kbar pressure (Gupta and Kumar 1993) and was in equilibrium with the P-T conditions of the surrounding rocks undergoing peak M2 metamorphism ($T = 650\text{--}750^\circ\text{C}$, $P = 4\text{--}7$ kbar). This together with field observations and the fluid inclusion studies on primary inclusions in quartz and feldspar of the granite and pegmatites from Leopargial pluton indicating lower fluid trapping temperature ($370\text{--}460^\circ\text{C}$) and pressure (1.5–2.5 Kbar) suggest that the pluton emplaced and crystallized quite rapidly under the environment of abrupt change from compression to extension.

Further, the possibility of temperature higher than the M2 metamorphism (about 850°C) in the HHC, being reached at the deeper level (below the present level of erosion) during Miocene cannot be ruled out. This caused large scale involvement of biotite in melting, thus, producing large volumes of the leucogranite magma to satisfactorily explain the higher proportion of the leucogranite magma emplacement north of the TDF. Such a possibility is strongly supported by the suggested presence of magma under the Tibetan plateau during INDEPTH studies (Nelson *et al* 1996). It is of interest to note that the Indian continental crust farther north of ITSZ and under south Tibet is in a partially molten state with tectonic slices of the mafic lower crust (Nelson *et al* 1996). This observation supports the authors suggestion that temperature higher than 850°C was reached at the deeper level (below the present level of erosion) in the HHC and north of it during Miocene, thus involving biotite melting in order to produce large volumes of leucogranite magma. The younger ages of the granite plutons (less than 10 Ma) from the northern belt, in comparison to the southern belt, and the presence of magma farther north under Tibet, strongly support the views of the author.

The continued northward push of the Indian plate after the collision, resulted stacking of various thrust slices of the metasedimentary cover rocks (Jutogh-Munsiari and Vaikrita group) of the underthrusting LHGB, thus producing double-normal thickness of the crust under the Himalaya. Various geophysical studies including the deep seismic reflection (INDEPTH), substantiate geological observations suggesting large scale structural imbrications and stacking of thrust slices (figure 5). The most conspicuous 'mid-crustal' reflection visible on the INDEPTH seismic profile (Zhao *et al* 1993) is marking the active thrust fault called the Main Himalayan Thrust (MHT). In the opinion of the author, the MHT along which the Indian crust is now underthrusting south Tibet and the upper crust that underlies MHT (figure 5), is in fact the Palaeoproterozoic LHGB forming the

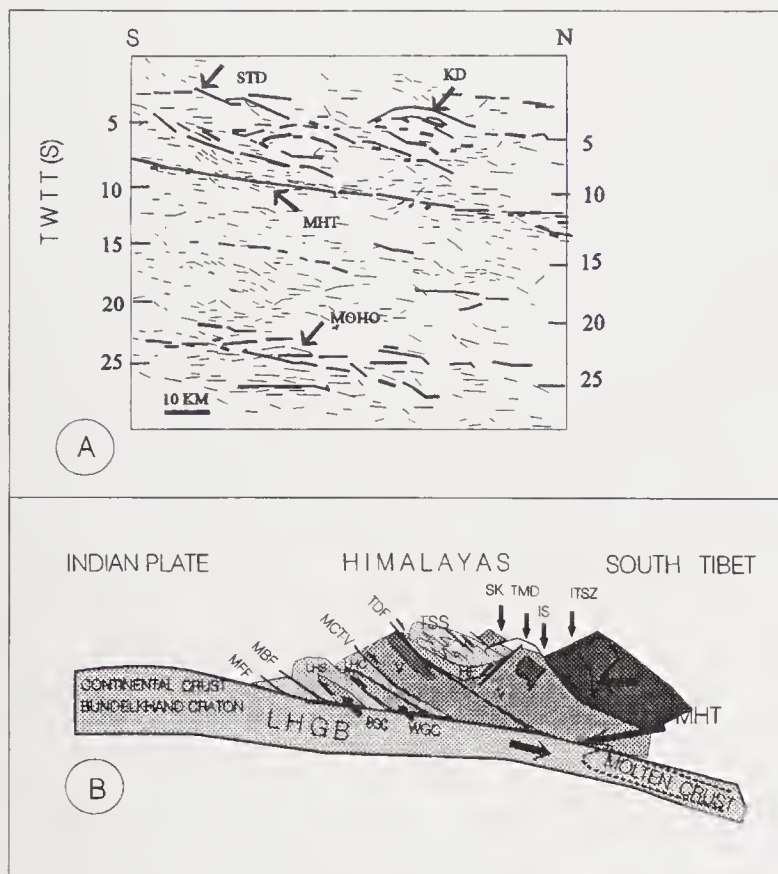


Figure 5. A: – INDEPTH seismic structure under Himalaya and South Tibet; B: – The geological profile of the Himalaya along the Satluj valley.

decollement surface. The seismic reflectors such as Main Central Thrust (MCT), South Tibet Detachment (STD) and Kangmar Dome (KD) noticed at a shallower level than the MHT, in the INDEPTH profile (figure 5A), match closely with the MCT-V, Tethyan Detachment Fault (TDF) and Tso Morari Dome (TDM) mapped by the author in the Satluj valley section (figure 5B), NW Himalaya. Further an important unnamed thrust, shown between MBT and MCT (Zhao *et al* 1993), corresponds closely with the Jutogh Thrust in the Satluj valley which separates the LHC from the LHS.

5. Conclusions

- The Lesser Himalayan Gneissic Basement (LHGB) represents the northern extension of the Bundelkhand craton, Northern Indian shield and stabilized around 2,000 Ma ago, following the N-S compression related Palaeoproterozoic Wangtu Orogeny in the Himalayan region. The LHGB, underwent rapid uplift and the fast erosion soon after the orogeny, i.e. the compressional regime soon changed to the extensional (very much similar to the Himalayan situation), and caused development of rift-related Lesser Himalayan basin around 1900 Ma ago.
- The Vaikrita Group, supported by the presence of detrital zircon of mixed ages and as young as 970 Ma, represents Neoproterozoic (900 ± 50 Ma) sequence. It forms the basal part of the sedimentary

pile of the Tethys basin, followed by the Haimanta (late Precambrian-early Palaeozoic) in the middle part and the TSS (Phanerozoic) in the upper part. The Tethyan sedimentary sequences were deposited in a fault controlled rift-related basin developed on the Palaeoproterozoic-Mesoproterozoic LHS/LHC floor. The compression related tectonic readjustment in the Lesser Himalayan region is suggested during Neoproterozoic (the Lesser Himalayan Orogeny) which caused deformation of deeper facies equivalents of the LHS and changed them to the LHC, granite magmatism (1000–900 Ma), uplift of the Lesser Himalayan sequences and southward shift of the Lesser Himalayan basin where in the Jaunsar-Simla and Blaini-Krol-Tal cycles (Outer Carbonate Belt) were deposited in a relatively confined basin. This region, again witnessed possibly the Kinnar Kailas Orogeny in the Late-Precambrian-Cambrian time.

- During the Himalayan Orogeny, the Vaikrita Group rocks (HHC) absorbed the maximum compression caused due to the India-Asia collision and the continued northward push of the Indian plate. The large scale folding and stacking of the thrust slices of the TSS resulted in thickening of the Tethyan sedimentary pile (> 15 km), sufficient to cause Barrovian metamorphism (M1) in the basal sequences (Vaikrita). The Kashmir Thrust Sheet (locally metamorphosed) moved southward along Panjal Thrust and is the first thrust sheet to move in the Himalaya, followed by the HHC along the MCT-V. Geologically the Lesser Himalaya (between MBT and MCT-V) is a distinct lithotectonic (Archaean, Palaeoproterozoic, Mesoproterozoic) entity than the Higher Himalaya (Neoproterozoic) and the Main Central Thrust (MCT-V) represents a deep crustal thrust that separates them.
- The peak metamorphism (M2 phase) and the remobilization in the HHC during the Himalayan Orogeny is attributed to compression caused by the northward movement of the Indian Plate and the resistance offered by the Asian Plate and the lighter crust of the former to underthrust the heavier rocks of the ITSZ (buoyancy effect). The accumulation of the stresses at the base of the Vaikrita, caused initiation of thrust (Future MCT-V) at the site of the boundary fault separating it from the Lesser Himalayan sequences.
- The ramp related rapid uplift of the HHC around Miocene (18–11 Ma), marks M3 metamorphism in it during its exhumation and contemporary gravity gliding of the thickened TSS over the hot and the fast exhuming HHC. This produced decompression induced leucogranite melts which emplacement in successive phases [southern belt plutons (29–18 Ma), northern belt plutons (15–10 Ma) and active magmatism under Tibet], possibly related to the rate of movement of the Indian Plate.

- The LHGB, the northern extension of the Bundelkhand craton, underthrusts the Himalaya and south Tibet and its cover rocks (LHS, LHC, HHC, TSS) stacked as thrust slices, formed the Himalayan Mountain and its decollement surface as the Main Himalayan Thrust, observed in the INDEPTH profile.

6. Problems for future study

Many issues raised in this paper, regarding the distinct entity of the Vaikrita (HHC) *vis-a-vis* LHGB and LHC, and the role they played in the formation of the Neoproterozoic Tethyan basin and possible signatures of the Lesser Himalayan Orogeny during Mesoproterozoic and the Kinnar Kailas Orogeny during late Precambrian-Cambrian, might stimulate some workers to look into the pre-collision geology in detail. In addition, the author considers the following questions to be answered for better understanding of the Himalayan collision mountain.

- Since when did the Central Crystalline Axis (CCA) become a positive area during the Himalayan Orogeny and to what extent could it rise. Did the CCA uplift only in the last 40 Ma as suggested by Sr-evolution curve or did it influence and contribute to the geological development of the surrounding regions during the late Precambrian-Cambrian (Kinnar Kailas Orogeny) including the equally strong change in Sr-evolution curve of the seawater during that time.
- When did the first topography, to form hills and ranges, come into being? Is the mature topography of the Lesser Himalaya an indication of its being old (Pre-Himalayan Orogeny related) and exposed since a long time?
- The pattern of uplift and erosion in the Himalaya and Tibet and the role it played in achieving the status of being the highest mountain and the highest plateau of planet Earth. In what way did the isotopic clocks, sedimentation, or vegetation based exhumation/uplift rates calculated for different time spans and different sectors of the Himalaya, correspond to a more precise, cosmic ray produced isotope based erosion/incision rates in the Himalaya.
- The precise timing of the glacial epochs in the Himalaya and when the last snow cover disappeared from various sectors of the Himalaya.

Acknowledgements

The author expresses his thankfulness to the Director, Wadia Institute of Himalayan Geology, Dehra Dun for the facilities and the cooperation to carry out researches in the Himalaya. The financial assistance

provided by the Department of Science and Technology to the author under various projects sanctioned on Ladakh, Mandi-Jaspa and Bundelkhand, is gratefully acknowledged. Special thanks are due to the research staff, who worked with the author from time to time. The suggestions given by Drs. Talat Ahmed, M I Bhat, A K Dubey, N S Virdi and Surendar Kumar and an anonymous reviewer greatly helped to improve this manuscript. My thanks to Ms Kalpana Negi who helped to produce the computer diagrams for this paper.

References

- Ahmad T and Tarney J 1991 Geochemistry and petrogenesis of Garhwal volcanics: implications for evolution of the north Indian lithosphere; *Precambrian Res.* **50** 69–88
- Ahmad T and Tarney J 1994 Geochemistry and petrogenesis of late Archaean Aravalli volcanics basement enclaves and granitoids Rajasthan; *Precambrian Res.* **65** 1–23
- Ahmad T, Trivedi J R and Mukherjee P K 1996 Rb-Sr age of Kepsar-Thayeli gabbroic body Garhwal Himalaya: implications for Paleo-Proterozoic basic-acidic bimodal magmatism in Himalaya; *Proc. 7th National Symposium on Mass Spectrometry* Bombay (abstract) 478–479
- Azmi R J, Joshi M N, and Juyal K P 1981 Discovery of the Cambro-Ordovician conodonts from the Mussoorie Tal phosphorite and its significance in correlation of the Lesser Himalaya; In *Contemporary Geoscientific Researches in Himalaya* (eds) A K Sinha, Bishan Singh and Mahendra Pal Singh, Dehra Dun **1** pp. 245–350
- Bagati T N 1991 Evolution of the Tethyan sedimentary basin in the western Himalaya; In *Sedimentary basins of India: Tectonic context* (eds) S K Tandon, C C Pant and S M Casshyap (Nainital: Gyanoday Prakasha) pp. 218–235
- Baig M S, Lawrence R D and Snee L W 1988 Evidence for late Precambrian to early Cambrian orogeny in northwest Himalaya, Pakistan; *Geol. Mag.* **251** 83–86
- Berthelsen A 1951 A geological section through the Himalaya: a preliminary report; *Bull. Geol. Soc. Denmark* **12** 102–104
- Bhargava O N 1976 Geology of the Krol Belt and associated formations; *Mem. Geol. Surv. India* **106** 167–234
- Bhargava O N 1980 Pre-Tertiary orogenies in the Himalaya: a review of various evidences; *Geol. Rundschau* **69** 811–823
- Bhargava O N and Ameta S S 1987 The Rampur window revisited; In *Proc. National Seminar on Tertiary Orogeny*, pp. 11–24
- Bhargava O N, Bassi U K and Sharma R K 1991 The crystalline thrust sheets, age of metamorphism, evolution and mineralization of the Himachal Himalaya; *Indian Minerals* **45** (1 & 2) 1–18
- Bhargava O N and Bassi U K 1994 The Crystalline Thrust Sheets in the Himachal Pradesh and the age of amphibolite facies metamorphism; *J. Geol. Soc. India* **43** 343–352
- Bhargava O N 1998 Geological account of the Tethyan rocks in the Spiti Valley: their comparison with Tethyan successions in other parts of the Himalaya; *J B Auden Lecture 29th June 1998 Wadia Institute of Himalayan Geology, Dehra Dun* pp. 1–35
- Bhat M I, S M Zainuddin and A Rais 1981 Panjal trap chemistry and the birth of Tethys; *Geol. Mag.* **118** 4367–4375
- Bhat M I and Le Fort P 1992 Sm-Nd age and petrogenesis of Rampur metavolcanic rocks NW Himalaya: Late Archaean relics in the Himalayan belt; *Precambrian Res.* **56** 191–210
- Bhat M I, Claesson S, Dubey A K and Pande K 1998 Sm-Nd age of the Garhwal-Bhowali volcanics western Himalayas:

- vestiges of the late Archaean Rampur flood basalt province of the northern Indian craton; *Precambrian Res.* **87** 217–231
- Brown R L and Nazarchuk J H 1993 Annapurna detachment in the Greater Himalaya of central Nepal; In *Himalayan Tectonics* (eds) P J Treloar and M P Searle *Geol. Soc. Spl. Publ.* **74** 461–473
- Burchfiel B C, Zhiliang C, Hodges K V, Yuping L, Royden L H, Changrong D and Jiene X 1992 The South Tibetan Detachment System Himalayan Orogen: Extension contemporaneous with the parallel to shortening in a collisional mountain belt; *Geol. Soc. Am. Spl. Pap.* **269** 1–41
- Burg J P, Brunel M, Gasais D, Chen G M and Liu G H 1984 Deformation of leucogranites of the crystalline main central sheet in southern Tibet; (China) *J. Structural Geol.* **6** 535–542
- Burke W H, Dension R E, Hetheington E A, Kocprick R B, Nelson H F and Otto J B 1982 Variation of seawater $^{87}\text{Sr}/^{86}\text{Sr}$ throughout Phanerozoic time; *Geology* **10** 516–519
- Cao R-L 1991 Sedimentology of trench-arc sediments and its relation to ophiolite obduction; In *Geology and Geodynamic Evolution of the Himalayan Collision Zone* (ed) K K Sharma *Phys. Chem. Earth* **17** (2) pp. 237–268
- Chawla H S 1995 Petrochemical and mineralogical studies of Akpa granite and its associated rocks of Kinnaur district Himachal Pradesh India; *Unpublished Ph D thesis*, H N B Garhwal University, Srinagar, 173pp.
- Choubey V M, Sharma K K, Rameshwar Rao D and Sharma R 1992 Geochemical and fluid inclusion studies of Leopargial leucogranite, Kinnaur District, Himachal Pradesh, India; *J. Him. Geol.* **3** 2155–2161
- Clemens J O and Vielzenf D 1987 Constraints on melting and magma production in the crust; *Earth Planet. Sci. Lett.* **86** 287–306
- Colchen M, Le Fort P and Peacher A 1986 Annapurna, Manasu Ganesh Himalaya; *notice de la con monologiqu on 1/200,000* bilingual edition, French-English, C.N.R.S. Paris.
- Condie K C 1982 *Plate tectonics and crustal evolution* second edition, Pergamon Press, pp. 1–310
- Dewey J F and Bird J M 1970 Mountain belts and the new global tectonics; *J. Geophys. Res.* **75** 2625–2647
- Dikshitulu G R, Pandey B K, Krishna V and Dhanaraju R 1995 Rb-Sr systematics of granitoids of the Central Gneissic Complex Arunachal Himalaya: implications on tectonism stratigraphy and source; *J. Geol. Soc. India* **45** 51–56
- Dubey A K and Bhat M I 1986 The role of reactivation of pre-rift basement listric faults in the structural evolution of the Himalaya: an experimental study; *Curr. Trends Geol.* **9** 265–290
- Frank W, Thoni M and Purtscheller F 1977 Geology and petrography of Kulu-south Lahul area; *Sci Terre Himalaya CNRS* **268** 147–166
- Fuchs G R 1982 Explanations of the geologic-tectonic map of the Himalaya; *Geol. Surv. Austria, Wien*, pp. 1–50
- Fuchs G R 1987 The geology of southern Zaskar (Ladakh) – evidence for the autochthony of the Tethys zone of the Himalaya; *Jahrb. Geol. B-A* **130** 465–491
- Gaetani M, Casnedi R, Fois E, Garzanti E, Jadoul F, Nicora A and Tintori A 1986 Stratigraphy of the Tethys Himalaya in Zaskar, Ladakh; *Riv. It. Paleont. Strat. Milano* **91** 443–478
- Gansser A 1964 *Geology of the Himalaya*, (London: Intersci. Publishers, John Wiley and Sons Ltd.) pp. 1–289
- Gansser A 1981 The geodynamic history of the Himalaya; In *Zagros-Hindukush-Himalaya Geodyn. Evol.* (eds) H K Gupta and F M Delany *Am. Geophys. Union, Washington DC* **3** 111–121
- Ghosh S K 1991 Source rock characteristics of the Late Proterozoic Nagthat Formation, NW Kumaun Lesser Himalaya, India; *J. Geol. Soc. India* **38** 485–495
- Guillot S, Peacher A, Rochette P and Le Fort P 1993 The emplacement of the Manaslu granite of central Nepal: field and magnetic susceptibility constraints; In *Himalayan Tectonics* (eds) P J Treloar and M P Searle *Geol. Soc. Spl. Publ.* **74** 413–428
- Gupta L N and Kumar R 1993 Petrography and chemistry of Yangthang granite; *J. Him. Geol.* **4**(1) 15–26
- Herren E 1987 Zaskar shear zone: Northeast-southwest extension within the Higher Himalayas (Ladakh India); *Geology* **15** 409–413
- Honnegger K, Le Fort P, Moneta G and Zimmerman J L 1989 The blueschists along the Indus suture zone in Ladakh, N W Himalaya; *J. Met. Geol.* **7** 57–72.
- Jan M Q 1991 High-P metamorphic rocks from the Himalaya and their tectonic implication – a review; In *Geology and Geodynamic Evolution of the Himalayan Collision Zone* (ed) K K Sharma *Phys. Chem. Earth* **18** (1 & 2) 329–343
- Jan M Q 1991a Petrology and geochemistry of the southern amphibolites of the Kohistan arc N Pakistan; In *Geology and Geodynamic Evolution of the Himalayan Collision Zone* (ed) K K Sharma *Phys. Chem. Earth* **17**(2) 71–92
- Jan M Q and Jabeen N 1991 A review of mafic-ultramafic plutonic complexes in the Indus suture zone of Pakistan; In *Geology and Geodynamic Evolution of the Himalayan Collision Zone* (ed) K K Sharma *Phys. Chem. Earth* **17**(2) 93–114
- Krishnaswami S, Trivedi J R, Sarin M M, Ramesh R and Sharma K K 1992 Strontium isotopes and rubidium in the Ganga-Brahmaputra river system: Weathering in the Himalaya fluxes to the Bay of Bengal and contributions to the evolution of oceanic $^{87}\text{Sr}/^{86}\text{Sr}$; *Earth Planet. Sci. Lett.* **109** 243–253
- Kumar R and Brookfield M E 1989 Sedimentary environments of the Simla Group (Upper Precambrian), Lesser Himalaya and their palaeotectonic significance; *Sediment. Geol.* **52** 27–43
- Kumar S 1986 Rb-Sr geochronological studies of some granitic rocks of Himachal and Kashmir Himalayas, India; *Unpublished Ph.D. thesis* Punjab University, Chandigarh 200pp
- Kumar G, Joshi A and Mathur V K 1987 Redlichid trilobites from the Tal formation, Lesser Himalaya, India; *Curr. Sci.* **56** 659–663
- Kumar R, Shah A N and Bingham D K 1978 Positive evidence of a Precambrian tectonic phase in central Nepal, Himalaya; *J. Geol. Soc. India* **19** 519–522
- Le Breton N and Thompson A B 1988 Fluid-absent (dehydration) melting of biotite in metapelites in the early stages of crustal anatexis; *Contrib. Mineral Petrol.* **99** 226–237
- Le Fort P 1975 Himalayas: the collided range present knowledge of the continental arc; *Am. J. Sci.* **A275** 1–44
- Le Fort P 1981 Manaslu leucogranite: a collisional signature of the Himalaya, a model for its genesis and emplacement; *J. Geophys.* **86** 10545–10568
- Le Fort P, Debon F, Pecher J, Sonet J and Vidal P 1986 The 500 Ma magmatic event in alpine southern Asia, a thermal episode at Gondwana Scale; *Sciences de la Terre, Memoire* **47** 31–42
- Le Fort P 1989 The Himalayan orogenic segment; In *Tectonic evolution of the Tethys region* (ed) A M C Sengor (Kluwer Academic Publishers) pp. 289–386
- Mathur N S 1997 A comparative study of the lower Tertiary biostratigraphic sequences in the northwestern Himalaya and their palaeogeographic significance; In *Geodynamic Domain in Alpine Himalayan Tethys* (ed) A K Sinha, IGCP (Special Publication, Oxford & IBA, New Delhi) pp. 125–158
- Mei Hou-Jun 1991 The ophiolites of the Qinghai-Xizang Tibet plateau and the Cenozoic rift magmatism in the Qing-Zang terrain; In *Geology and Geodynamic Evolution of the Himalayan Collision Zone* (ed) K K Sharma *Phys. Chem. Earth* **17**(2) 195–219
- Nanda A C and Sahni A 1990 Oligocene vertebrates from the Ladakh Molasse Group, Ladakh Himalaya: palaeobiogeographic implications; *J. Him. Geol.* **1** 1–10

- Nanda M M, Singh M P and Sinha P K 1978 On the volcanics of the Zaskar valley, Ladakh-J & K; *Rec. Geol. Surv. India* **110** 194–202
- Nelson K D and 27 others 1996 Partially molten middle crust beneath southern Tibet, Synthesis of Project INDEPTH results; *Science* **274** 1684–1687
- Parrish R R and Hodges K V 1996 Isotopic constraints on the age and provenance of the Lesser and Greater Himalayan sequences, Nepalese Himalaya; *Geol. Soc. Am. Bull.* **108** 904–911
- Partiat P and Achache J 1984 India-Eurasia collision chronology has implications for crustal shortening and driving mechanism of plates; *Nature* **311** 615–621
- Patel R C, Singh S, Asokan A, Manickavasagam R M and Jain A K 1993 Extensional tectonics in the Himalaya orogen, Zaskar, NW India; In *Himalayan Tectonics* (eds) P J Treloar and M P Searle *Geol. Soc. Spl. Publ.* **74** 445–459
- Petterson M G, Windley B F and Luff I W 1991 The Chalt volcanics Kohistan N. Pakistan: High-Mg tholeiitic and low-Mg calc-alkaline volcanism in a Cretaceous island arc; In *Geology and Geodynamic Evolution of the Himalayan Collision Zone* (ed) K K Sharma *Phys. Chem. Earth* **17** 219–230
- Pognente U and Benna P 1993 Metamorphic zonation magmatization and leucogranites along the crust transect of eastern Nepal and Tibet: record of an exhumation history; In *Himalayan Tectonics* (eds) P J Treloar and M P Searle; *Geol. Soc. Spl. Publ.* **74** 323–340
- Raha P K, Chandy K C and Balasubramanyan M N 1978 Geochronology of Jammu limestone, Udhampur Dist., Jammu, India; *J. Geol. Soc. India* **185** 93–95
- Raha P K 1980 Stromatolite zonation in Jammu limestone, Udhampur Dist., Jammu; *Geol. Surv. India Misc. Pub.* **44** 134–171
- Rao D R, Sharma K K and Gopalan K 1995 Granitoid rocks of Wangtu Gneissic Complex Himachal Pradesh: An example of *in situ* Fractional Crystallisation and Volatile Action; *J. Geol. Soc. India* **46** 5–14
- Rao P S 1998 Kameng orogeny (1.8–1.9 Ga) from the isotopic evidence on the Bomdila orthogneisses, Kameng sector (NEFA) India; *13 HKTI Workshop Abstract Volume* Peshawar, April 20th–22nd, 159–162
- Raju B N V, Chhabria T, Prasad R N, Mahadevan T M and Bhalla N S 1982 Early Proterozoic Rb-Sr isochron age for central Crystalline rocks Bhilangana valley, Garhwal Himalaya; *Him. Geol.* **12** 196–205
- Ramsay J G and Huber M I 1987 *The techniques of modern structural geology* (London: Academy Press) pp. 309–700
- Saraswat A C, Balakrishnan S P and Vardharaju H N 1970 On the extension of Jutogh and Chail series in to Mahasu, Dist. H.P. and adjoining Uttarkashi District of U.P.; *Pub. Centre Advanced Studies in Geology* Punjab Univ., Chandigarh **7** 68–71
- Scharer U, Xu R H and Allegre C J 1986 U(Th)-Pb systematics and age of Himalayan leucogranites, South Tibet; *Earth Planet. Sci. Lett.* **77** 35–48
- Searle M P and Rex A J 1989 Thermal model for the Zaskar Himalaya; *J. Metamor. Geol.* **7** 127–134
- Shah S K 1991 Stratigraphic setting of the Phanerozoic rocks along the northern boundary of the Indian plate; In *Geology and Geodynamic Evolution of the Himalayan Collision Zone* (ed) K K Sharma *Phys. Chem. Earth* **18**(1 & 2) 317–328
- Shah S K, Parch S K and Raina A K 1991 Late Cambrian trilobites from Himalaya; *J. Palaeontol. Soc. India* **36** 89–102
- Shanker R, Kumar G and Saxena S P 1989 Stratigraphy and sedimentation in Himalaya: A reappraisal; *Geol. Surv. India Spl. Publ.* **26** 1–60
- Sharma K K and Choubey V M 1991 Kargil igneous complex an obducted base of Dras island arc; In *Geology and Geodynamic Evolution of the Himalayan Collision Zone* (ed) K K Sharma *Phys. Chem. Earth* **17**(2) 155–171
- Sharma K K 1991 *Geology and Geodynamic Evolution of the Himalayan Collision Zone*; *Phys. Chem. Earth* (U.K.: Pergamon Press) **17**(2) pp 1–194
- Sharma K K 1991a *Geology and Geodynamic Evolution of the Himalayan Collision Zone*; *Phys. Chem. Earth* (U.K.: Pergamon Press) **18**(1 & 2) pp. 195–446
- Sharma K K 1991b Petrochemistry and tectonic environment of Dras, Shyok, Khardung and Chushul volcanics of Indus suture zone, Ladakh: A comparative study; In *Geology and Geodynamic Evolution of the Himalayan Collision Zone* (ed) K K Sharma *Phys. Chem. Earth* **17**(2) 133–154
- Sharma K K 1991c Tectonomagmatic and sedimentation history of Ladakh collision zone: a synthesis. In: *Geology and Geodynamic Evolution of the Himalayan Collision Zone*, (Ed.) K K Sharma *Phys. Chem. Earth* **17** (2) 133–154
- Sharma K K, Rao D R, Azmi R J, Gopalan K and Pantulu G V C 1992 Precambrian-Cambrian boundary in the Tal Formation of Garhwal Lesser Himalaya: Rb-Sr age evidence from black shales underlying phosphorites; *Curr. Sci* **62** 528–530
- Sharma K K 1993 Influence of Himalayan style continental collision and weathering on strontium isotopes in sea water; *J. Him. Geol.* **4** 111–119.
- Sharma K K, Rao D R, Gopalan K and Swaraman T V 1993 Rb/Sr isochron age of Early Proterozoic granites from Wangtu gneissic complex, Kinnaur Himalaya; *Proc. 6th National Symposium on Mass Spectrometry, Dehra Dun* 501–503
- Sharma K K 1994 Ophiolites of different tectonic setting in Himalayan collision zone: an example from Ladakh; In *Geology of South Asia-I* Proc. GEOSAS-I Islamabad Pakistan, pp. 136–140
- Sharma K K 1997 Granite plutons in domal uplifts in the northern margin of the Indian plate, NW Himalaya; In *Geology in South Asia-II* (eds) N P Wijayananda, P G Cooray P and Mosley *Geological Survey and Mines Bureau, Sri Lanka Prof. Paper* **7** 27–40
- Sharma K K 1998 Geological evolution and crustal growth of the Bundelkhand craton and its relicts in the surrounding regions, N. Indian Shield; In: *Indian Precambrian* (Ed) B S Poliwal (Jodhpur, India: Scientific Publishers) 33–43
- Sharma V P 1977 Geology of the Kulu-Rampur belt, Himachal Pradesh; *Mem. Geol. Surv. India* **106** 235–407
- Sinha A K and Upadhyay R 1994 Tectonic setting and pre-orogenic sedimentation in the Indus-Tsangpo Yarlung suture zone of Ladakh Himalaya, India; *J. Southeast Asian Earth Sci.* **9** 435–450
- Singh I B and Rai V 1983 Fauna and biogenic structures in Krol-Tal succession (Vendian-Early Cambrian) Lesser Himalaya: Their biostratigraphic and palaeoecological significance; *J. Palaeontol. Soc. India* **28** 67–90
- Singh S, Sjöberg H, Classon S, Gee D and Jain A K 1993 New U-Pb Proterozoic data from Chor-Wangtu granitoids of Himalayan crystalline belt from Himachal, India; In *Seminar on Himalayan Geology and Geophysics* WIHG, Dehradun pp. 55–56
- Singh I B and Meerajudin 1980 Some sedimentological observations on the Chhaosa Formation (Simla Slates) in the Simla Hills; *Him. Geol.* **8** (2) 683–700
- Sinha-Roy S, Malhotra G and Mohanty M 1998 Geology of Rajasthan; *Geol. Soc. India, Bangalore* pp. 1–278
- Smith H A, Chamberlain C P and Zeitler P K 1994 Timing and duration of Himalayan metamorphism within the Indian plate, Northwest Himalaya, Pakistan; *J. Geol.* **102** 493–508
- Srikantia S V and Sharma R P 1971 Simla Group – A reclassification of the Chail Series, Jaunsar Series and the Simla Slates in the Simla Himalaya; *J. Geol. Soc. India* **12** 234–240
- Srikantia S V 1977 The Sundernagar Group: its geology correlation and significance as stratigraphically the deepest

- sediment in the Peninsular or Lesser Himalaya; *J. Geol. Soc. India* **18** 7–22
- Srikantia S V 1981 The lithostratigraphy, sedimentation and structure of the Proterozoic and Phanerozoic formations of Spiti basin in the Higher Himalaya of H.P.; *Misc. Publ. Geol. Surv. India* **412** 218–228
- Steck A, Spring L, Vannay J C, Masson H, Stutz E, Bucher H, Marchant R and Tietche J C 1993 Geological transect across the Northwestern Himalaya in eastern Ladakh and Lahul (A model for the continental collision of India and Asia) *Eclogae Geologicae Helvetiae* **86** 219–163
- Tewari V C 1989 Upper Proterozoic-lower Cambrian Stromatolites and Indian stratigraphy; *Him. Geol.* **13** 143–180
- Treloar P J and Rex D C 1990 Cooling and uplift histories of the crystalline thrust stack of the Indian plate internal zones west of Nanga Parbat, Pakistan Himalaya; *Tectonophysics* **180** 323–349
- Trivedi J R, Gopalan K and Valdiya K S 1984 Rb-Sr ages of granitic rocks within the Lesser Himalayan nappes, Kumaun, India; *J. Geol. Soc.* **25** 641–654
- Trivedi J R and Pande K 1993 ^{87}Rb - ^{87}Sr chronology of the Amritpur granite Kumaun Lesser Himalaya; *Proc. 6th National Symposium on Mass Spectrometry* Bombay (abstract) 486–488
- Tu G C, Zhong Y Q, Zhao Z H and Wang Z G 1981 Characteristics and evolution of granites of southern Xizang; In *Geology and Ecological studies of Qinghai-Xizang plateau* (Beijing: Science Press) **1** 353–362
- Valdiya K S 1980 *Geology of the Kumaun Lesser Himalaya* (Dehradun: Wadia Institute of Himalayan Geology) pp 291
- Valdiya K S 1980 The two intracrustal boundary thrusts of the Himalaya; *Tectonophysics* **66** 323–348
- Valdiya K S 1988 Tectonics and evolution of the Central sector of the Himalaya; *Phil. Trans. Royal. Soc. London* **326A** 157–175
- Valdiya K S 1995 Proterozoic sedimentation and Pan-African geodynamic development in the Himalaya; *Precambrian Res.* **74** 35–55
- Vince K J and Treloar P J 1996 Miocene north-vergent extensional displacements along the Main Mantle Thrust, NW Himalaya, Pakistan; *J. Geol. Soc. London* **153** 677–680
- Virdi N S 1981 Chail metamorphics of the Himachal Lesser Himalaya; In *Current Trends in Geology: Metamorphic Tectonites of the Himalaya* (ed) P S Saklani, Today and Tomorrows Printers and Publishers, New Delhi **4** pp. 89–100
- Virdi N S 1995 Proterozoic sedimentological cycles and the geotectonic evolution of the southern margin of the Proto-Tethys: evidence from the western Himalaya; *Indian J. Petrol. Geol.* **4** 245–73
- Wiedenbeck M, Goswami J N and Roy A B 1996 Stabilization of the Aravalli craton of northwest India at 2.5 Ga: an ion microprobe zircon study; *Chem. Geol.* **129** 325–340
- Zeitler P K, Sutter J F, Williams I S, Zartman R and Tahirkheli R A K 1989 Geochronology and temperature history of the Nanga Parbat-haramosh Massif, Pakistan; *Geol. Soc. Amer.* (special paper) **232** 1–22
- Zhao W, Nelson K D and Project INDEPTH team 1993 Deep seismic reflection evidence for continental underthrusting beneath southern Tibet; *Nature* **366** 557–559

Silicate and carbonate weathering in the drainage basins of the Ganga-Ghaghara-Indus head waters: Contributions to major ion and Sr isotope geochemistry

S KRISHNASWAMI and SUNIL K SINGH

Physical Research Laboratory, Navrangpura, Ahmedabad 380 009

e-mail: swami@prl.ernet.in

The role of silicate and carbonate weathering in contributing to the major cation and Sr isotope geochemistry of the headwaters of the Ganga-Ghaghara-Indus system is investigated from the available data. The contributions from silicate weathering are determined from the composition of granites/gneisses, soil profiles developed from them and from the chemistry of rivers flowing predominantly through silicate terrains. The chemistry of Precambrian carbonate outcrops of the Lesser Himalaya provided the data base to assess the supply from carbonate weathering. Mass balance calculations indicate that on an average $\sim 77\%$ (Na + K) and $\sim 17\%$ (Ca + Mg) in these rivers is of silicate origin. The silicate Sr component in these waters average $\sim 40\%$ and in most cases it exceeds the carbonate Sr. The observations that (i) the $^{87}\text{Sr}/^{86}\text{Sr}$ and Sr/Ca in the granites/gneisses bracket the values measured in the head waters; (ii) there is a strong positive correlation between $^{87}\text{Sr}/^{86}\text{Sr}$ of the rivers and the silicate derived cations in them, suggest that silicate weathering is a major source for the highly radiogenic Sr isotope composition of these source waters. The generally low $^{87}\text{Sr}/^{86}\text{Sr}$ (≤ 0.720) and Sr/Ca ($\sim 0.2 \text{ nM}/\mu\text{M}$) in the Precambrian carbonate outcrops rules them out as a major source of Sr and $^{87}\text{Sr}/^{86}\text{Sr}$ in the headwaters on a basin-wide scale, however, the high $^{87}\text{Sr}/^{86}\text{Sr}$ (~ 0.85) in a few of these carbonates suggests that they can be important for particular streams. The analysis of $^{87}\text{Sr}/^{86}\text{Sr}$ and Ca/Sr data of the source waters show that they diverge from a low $^{87}\text{Sr}/^{86}\text{Sr}$ and low Ca/Sr end member. The high Ca/Sr of the Precambrian carbonates precludes them from being this end member, other possible candidates being Tethyan carbonates and Sr rich evaporite phases such as gypsum and celestite. The results of this study should find application in estimating the present-day silicate and carbonate weathering rates in the Himalaya and associated CO_2 consumption rates and their global significance.

1. Introduction

It is well recognised that the high $^{87}\text{Sr}/^{86}\text{Sr}$ and Sr concentration of rivers draining the Himalaya, particularly the Ganga-Brahmaputra (G-B) have significantly influenced the Sr isotope evolution of the oceans since the Cenozoic (Palmer and Elderfield 1985; Palmer and Edmond 1989; Richter *et al* 1992; Krishnaswami *et al* 1992). The source(s) contributing to the high $^{87}\text{Sr}/^{86}\text{Sr}$ of these rivers remains controversial, though many recent studies have addressed this topic as it has relevance to atmospheric CO_2

budget and global change (Edmond 1992; Krishnaswami *et al* 1992; Palmer and Edmond 1992; Derry and France-Lanord 1996; France-Lanord and Derry 1997; McCauley and DePaolo 1997; Quade *et al* 1997; Harris *et al* 1998; Blum *et al* 1998). The high $^{87}\text{Sr}/^{86}\text{Sr}$ of silicates (granites, gneisses and metasediments) in the drainage basins of these rivers have led to the suggestion (Edmond 1992; Krishnaswami *et al* 1992; Harris 1995) that they exert dominant control over the $^{87}\text{Sr}/^{86}\text{Sr}$ of rivers flowing through them. Palmer and Edmond (1992) based on the observation that the major ion chemistry of the G-B rivers is mainly regulated by

Keywords. Sr isotopes; major ions; silicate weathering; Himalayan rivers.

carbonate weathering (Sarin *et al* 1989; 1992) proposed that carbonates enriched in radiogenic strontium during metamorphism is responsible for their high $^{87}\text{Sr}/^{86}\text{Sr}$. Recently Quade *et al* (1997) from Sr isotope measurements in carbonates from paleosoles and river particulate matter have attested to the suggestion that carbonates are an important contributor to the high $^{87}\text{Sr}/^{86}\text{Sr}$ of these rivers. Besides this, data on Sr isotope composition of carbonates from the Himalaya are sparse. Sarkar *et al* (1996) have reported $^{87}\text{Sr}/^{86}\text{Sr}$ in a few samples of carbonates from the Krol-Tal formations, Derry and France Lanord (1996) have quoted values of ≈ 0.710 – 0.714 for marbles from the Higher Himalayan Crystallines and Tethyan Sediments and ≈ 0.8 (with low Sr) for samples from the Lesser Himalaya.

Precambrian carbonates of the Lesser Himalaya are one of the most extensive carbonate deposits of the Himalaya through which many of the source waters of the Ganga-Ghaghara-Indus flow. Studies on the chemical and Sr isotope composition of these carbo-

nates (Singh *et al* 1998) have provided insight into their role in contributing to the Sr isotopic budget of these rivers. These results and available data on the chemistry and $^{87}\text{Sr}/^{86}\text{Sr}$ of silicates from the drainage basins of the Ganga-Ghaghara source waters have been synthesised in this manuscript to determine their controls on the major ion chemistry and Sr isotope composition of these waters.

2. The data set

2.1 Source waters and lithology of their drainage basins

The source waters of the Ganga (Bhagirathi, Alaknanda and Bhilangna), the Ghaghara (Kali, Sarju, Ramganga) all originate in the Higher Himalaya and Tibet. Granites, gneisses and metasediments (Gansser 1964) are the dominant lithology of their drainage basins in this region. Presence of marbles along with

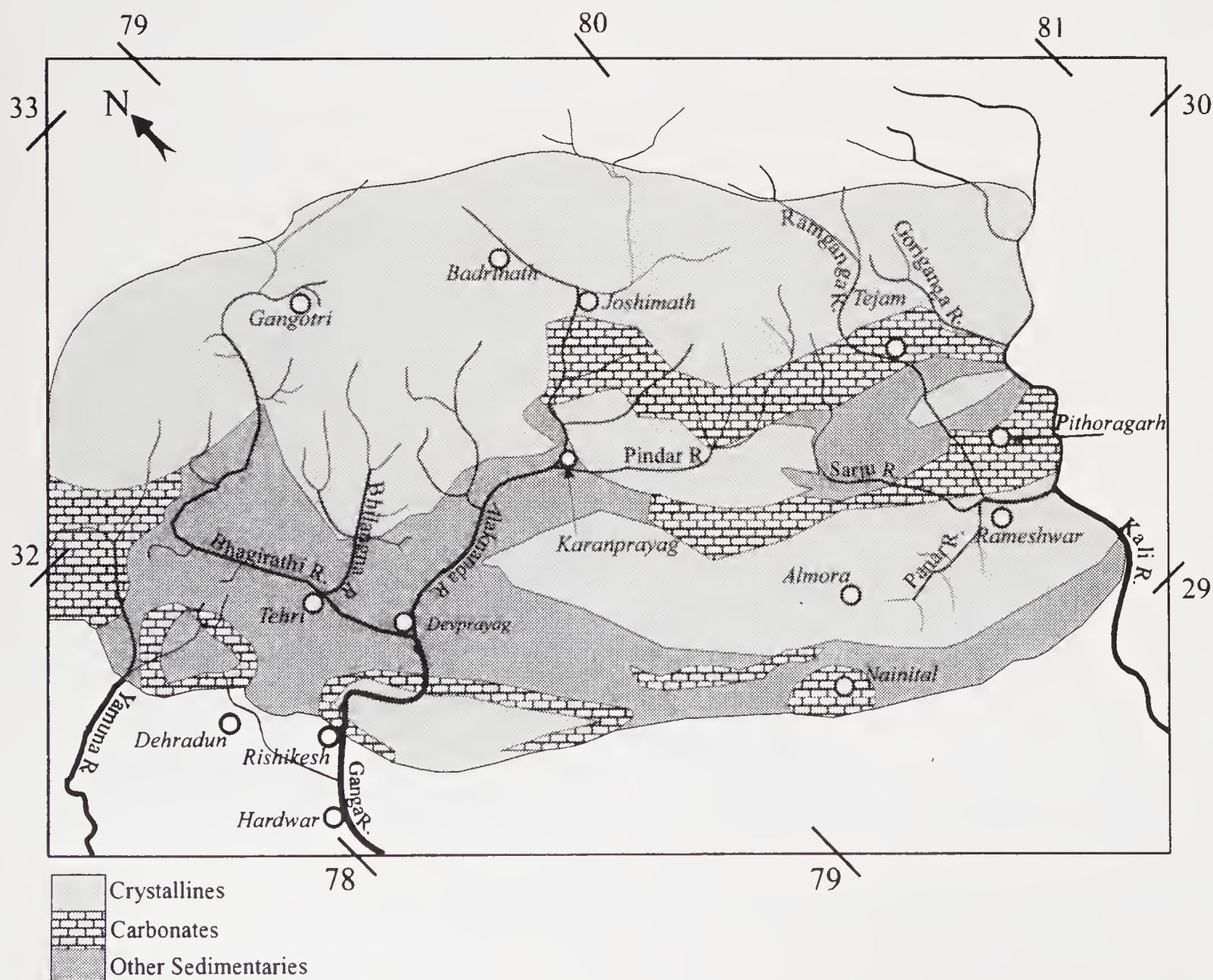


Figure 1. The source waters of the Ganga-Ghaghara and a broad lithological map of their drainage basins.

crystallines and calc-silicates have been reported in the drainage basins of the Alaknanda, Kali and Goriganga (Gansser 1964). Tethyan sediments containing carbonates are exposed in the Higher Himalaya and Tibet, in the drainage basins of Kali and Sutlej. A large fraction of the drainage basins of the source waters of the Ganga-Ghaghara and the Indus lie in the Lesser Himalaya, where in addition to the crystallines, Precambrian carbonates and sedimentaries constitute a major component of their lithology (Valdiya 1980). The chemical weathering in the Lesser Himalaya is likely to be more intense than in the Higher Himalaya because of relatively higher temperature, rainfall and the availability of more biogenic soil CO_2 . Figure 1 shows a broad lithological map of the drainage basins of the Ganga-Ghaghara source waters.

2.2 Contributions of silicate weathering to major ion chemistry

The major ion chemistry of the source waters and their Sr isotopic composition are presented in some of our earlier publications (Krishnaswami *et al* 1992; Sarin *et al* 1992; Pande *et al* 1994; Trivedi *et al* 1995). The primary sources of major ions to these source waters are (i) atmospheric deposition, (ii) dissolution of evaporites and (iii) weathering of silicates and carbonates. To determine the silicate component of major cations and Sr in river waters it is necessary to apportion them into various sources. It is estimated from the available data on the chemical composition of rain, snow and glacier ice that atmospheric deposition on an average contributes about 15% of Na and K each to the source waters of the Ganga (Sarin *et al* 1992; Krishnaswami *et al* 1998); the supply to individual streams/ivers, however, could be different from the average estimated above. The dissolution of evaporites (halites and gypsum) can be an important source for Na and Ca in rivers. One approach to calculate the contribution of Na to rivers from atmospheric deposition and halite dissolution is to assume that it equals the chloride concentration in them (Sarin *et al* 1989, Krishnaswami *et al* 1998). Based on the above approach the silicate component of sodium and potassium in the source waters of the Ganga, Ghaghara and Indus (Sutlej, Beas, Chandra, Bhaga and Dharcha) can be calculated as:

$$(\text{Na}_s + \text{K}_s) = (\text{Na}_r - \text{Cl}_r) + 0.85 \text{K}_r \quad (1)$$

where the subscript *s* and *r* refer to silicate and river. These calculations show that on an average $\sim 77\%$ of Na and K (range 53 to 90%) in these waters is of silicate origin (figure 2). The validity of these calculations requires that there are no alkaline/saline deposits containing carbonates/bicarbonates and sulphates of sodium along the drainage basins of these source waters, a condition very likely to be met for the rivers considered in this study. Estimation of silicate com-

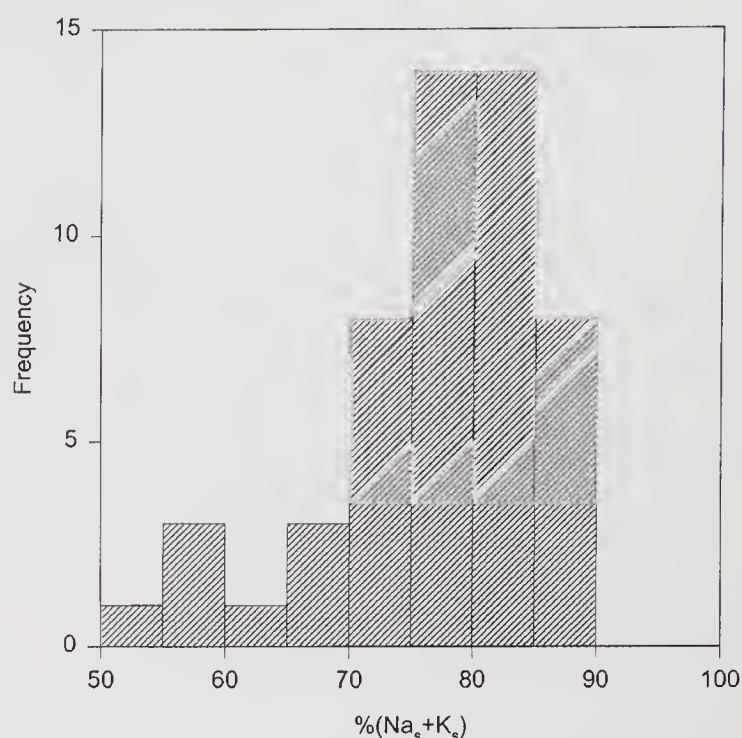


Figure 2. The fraction of silicate (Na + K) in the head waters of the G-G-I system. On an average silicate (Na + K) accounts for $\sim 77\%$ of their abundance in the rivers.

ponents of Ca and Mg (Ca_s and Mg_s) in these waters is a more difficult task and rely on a few simplifying assumptions which can be contentious. Calcium is supplied to rivers from the weathering of silicates and carbonates and dissolution of evaporites whereas the sources of Mg are silicates and carbonates. The silicate component of Ca and Mg in rivers can be derived if the ratio of (Ca/Na) and (Mg/Na) released to solution during silicate weathering can be ascertained. It is possible to place some constraints on these ratios (i) by assuming that they are the same as their abundance ratio in granites/gneisses of the Lesser Himalaya. This requires that Ca(Mg) and Na weather congruently from granites/gneisses, a condition which may be difficult to satisfy as silicate rocks generally weather incongruently; (ii) from the Ca(Mg) and Na abundances in granites/gneisses and in soils developed from them (Krishnaswami *et al* 1998). This approach would yield a time averaged value for (Ca/Na) and (Mg/Na) ratio released to solution; and (iii) by assuming that they are the same as those measured in rivers flowing predominantly through silicate terrains. In this case, minor abundances of carbonates and gypsum in the drainage basin can be important as they weather more easily relative to silicate rocks and thus can contribute to Ca and Mg budget of the rivers. In such cases, the (Ca/Na) and (Mg/Na) measured in the rivers is likely to be higher than those released from silicates.

The mean Ca/Na abundance ratio ($\mu\text{mole}/\mu\text{mole}$) in granites/gneisses and metasediments of the Higher and Lesser Himalaya are in the range of 0.32 ± 0.29 to 0.46 ± 0.28 (Krishnaswami *et al* 1998). The (Ca/Na) ratio released to rivers during the weathering of these silicates would be 0.45 ± 0.3 if they weather

congruently. The (Ca/Na) solution ratio, calculated (Krishnaswami *et al* 1998) from the soil profile data (Gardner and Walsh 1996) is 0.47 ± 0.08 nearly identical to those in the silicates. The measured (Ca/Na) in Jola gad, a tributary of Bhilangana draining predominantly silicate terrain is 1.15 (Sarin *et al* 1992, Singh *et al* 1998). Thus, the three approaches discussed above yield values in the range of 0.45–1.15 for Ca/Na ratio released to rivers from silicates during their weathering. Using a value of 0.7 ± 0.3 for Ca/Na solution ratio, the silicate Ca in the G-G-I source waters is estimated to range between 2% and 61% with a mean of 16% (Krishnaswami *et al* 1998). This compares with the reported value of $\sim 17\%$ for the G-B river system calculated based on Sr isotopic mass balance and Sr/Ca ratios in granites and carbonates (McCauley and DePaolo 1997).

The Mg/Na solution ratio determined from their abundances in granites/gneisses and from the Jola gad waters are similar and centre around ~ 0.5 , much higher than that calculated from the soil profile data, 0.05–0.17 (Krishnaswami *et al* 1998). Considering these, the silicate Mg in the source waters have been calculated using a Mg/Na solution ratio of 0.3 ± 0.2 . Thus, the sum of silicate Ca and Mg in these source waters, $(Ca_s + Mg_s)$, equals that of silicate Na, $[(Ca_s + Mg_s)/Na_s = (1 \pm 0.35)]$.

The foregoing discussions have brought out some of the difficulties associated with the precise determination of Ca_s and Mg_s to the source waters of the G-G-I river systems. The approaches described above, however, provide reasonable estimates of Ca_s and Mg_s in these rivers. The fraction of silicate derived cations in these rivers, $(\Sigma Cat)_s$ is given by (Krishnaswami *et al* 1998)

$$(\Sigma Cat)_s = \frac{(Na_s + K_s + Ca_s + Mg_s)}{(Na_r + K_r + Ca_r + Mg_r)} = \frac{[(Na_r - Cl_r) \times 2 + 0.85K_r]}{[Na_r + K_r + Ca_r + Mg_r]} \quad (2)$$

The term, $(Na_r - Cl_r) \times 2$ equals the sum of silicate Na, Ca and Mg. Figure 3 presents the $(\Sigma Cat)_s$ in the G-G-I source waters in the form of histograms taking into consideration $\pm 1\sigma$ uncertainty in the $(Ca_s + Mg_s)$ estimation. These calculations though have been carried out for all the source waters analysed by our group (Sarin *et al* 1992; Pande *et al* 1994; Trivedi *et al* 1995; Krishnaswami *et al* 1998), they are likely to be more reliable for the larger streams/rivers which integrate contributions from different silicate lithologies. These estimates show that on an average the $(\Sigma Cat)_s$ in the G-G-I source waters is $\sim 30\%$, a significant part of which is contributed by Na and K. The silicate (Ca + Mg) in these waters average only about 15%–20% of their measured concentrations, much unlike (Na + K) which is predominantly of silicate origin. These calculations suggest that the bulk of (Ca + Mg)

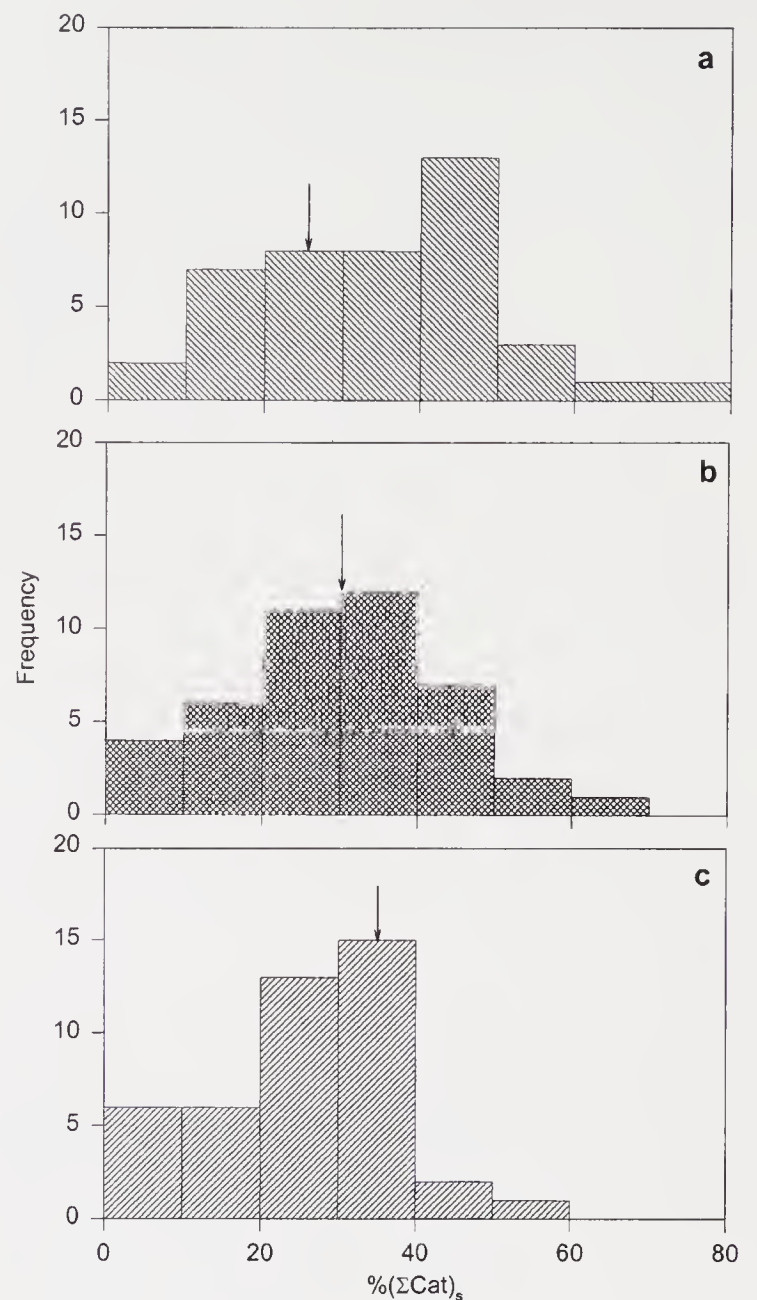


Figure 3. $(\Sigma Cat)_s$ in the head waters of G-G-I system. Three histograms are shown. (a) $(Ca_s + Mg_s) = 0.65Na_s$; (b) $(Ca_s + Mg_s) = Na_s$; and (c) $Ca_s + Mg_s = 1.35Na_s$. Figures (a) and (c) are calculated by considering $\pm 1\sigma$ uncertainty in the estimates of $(Ca_s + Mg_s)$. On an average, $(\Sigma Cat)_s$ accounts for $\sim 30\%$ of the total cations in the source waters (figure b). The arrow represents the mean of the distribution.

in these waters have a non-silicate source, carbonates and evaporites for Ca and carbonates for Mg.

2.3 Ca and Mg from carbonate weathering

The weathering of carbonates (limestone/dolomite) releases both Ca and Mg to rivers. Precambrian carbonate outcrops are abundant in the Lesser Himalaya along the drainage basins of the source waters of the G-G-I river systems (figure 1). The sources of Mg to rivers are silicates and carbonates, therefore the difference between the Mg concentration in rivers and the silicate Mg, calculated by the method described earlier, provides an estimate of carbonate magnesium, Mg_c , in these rivers. A similar approach to derive carbonate calcium, Ca_c , renders the results ambiguous

as Ca can also be supplied by the dissolution of gypsum. Use of SO_4 concentration in rivers as an index of gypsum derived Ca is also fraught with problems as SO_4 in rivers can be derived from two sources, dissolution of gypsum and oxidation of pyrites. Thus, from the available data it is not possible to quantitatively apportion the measured Ca in rivers among its three primary sources. An upper limit of carbonate Ca can, however, be estimated by assuming that there is no supply of Ca from gypsum i.e., Ca budget in these source waters is governed by only two sources, silicates and carbonates, analogous to that of Mg. The upper limit of $(\text{Ca}_c + \text{Mg}_c)$ in these rivers, thus estimated range between 43% and 98% of their measured concentration (Krishnaswami *et al* 1998). These results also show that the $(\text{Ca}_c + \text{Mg}_c)$ component in the Alaknanda and the source waters of the Ghaghara and the Indus is generally higher relative to that in the Bhagirathi and the Bhilangna, broadly consistent with the lithologies of their drainage basins (figure 1).

2.4 Sr and $^{87}\text{Sr}/^{86}\text{Sr}$ budget of G-G-I source waters

The relevance of silicate weathering in the Himalaya and the associated CO_2 consumption to long term global change (Raymo and Ruddiman 1992) has prompted the search for suitable "proxies" to characterise silicate weathering. In this context identifying the major source(s) for the high $^{87}\text{Sr}/^{86}\text{Sr}$ in the G-G-I source waters has gained significance. It has been suggested that the weathering of Precambrian granites/gneisses (Krishnaswami *et al* 1992), leucogranites (Edmond 1992) and metasediments (Harris 1995) can all serve as sources to the highly radiogenic Sr isotopic composition of these waters. In addition, the dominant control of carbonate weathering on the major ion chemistry of these waters has led Palmer and Edmond (1992) to hypothesise that metamorphosed carbonates enriched in radiogenic Sr could also be an important contributor to the high $^{87}\text{Sr}/^{86}\text{Sr}$ of these rivers. Considering that most of the G-G-I source waters flowing along the Himalaya (east to west) have high $^{87}\text{Sr}/^{86}\text{Sr}$ with moderate Sr concentration (Krishnaswami *et al* 1992; Pande *et al* 1994; Trivedi *et al* 1995) for silicates and/or carbonates to be an important source it is required that (i) they have $^{87}\text{Sr}/^{86}\text{Sr}$ sufficiently high to account for the measured values in the rivers; (ii) they contribute significantly to the Sr budget of the rivers; and (iii) they occur widespread all along the Himalaya. The silicates, granite/gneisses and metasediments by and large satisfy the above requirements. They are ubiquitous all along the Himalaya. The $^{87}\text{Sr}/^{86}\text{Sr}$ of granites/gneisses from the Lesser Himalaya is quite radiogenic with typical values in the range of 0.71 to 1.0 (figure 4). The mean whole rock $^{87}\text{Sr}/^{86}\text{Sr}$ for this range, ≈ 0.78 , overlaps with the highest $^{87}\text{Sr}/^{86}\text{Sr}$ measured in the source waters, 0.7986 ± 0.0008 for the

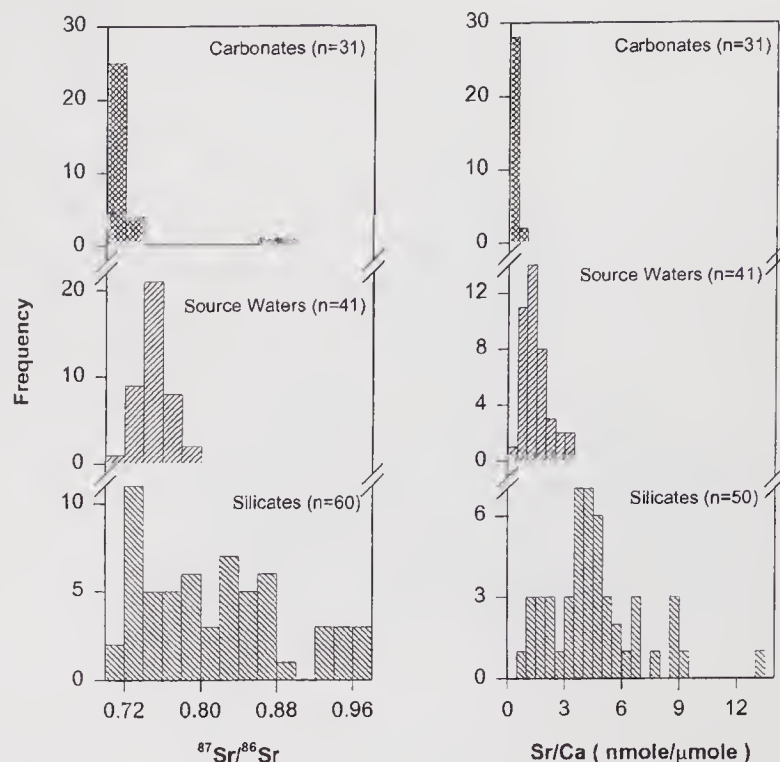


Figure 4. Comparison of $^{87}\text{Sr}/^{86}\text{Sr}$ and Ca/Sr in G-G-I source waters, silicates (granites/gneisses) and Precambrian carbonate outcrops of the Lesser Himalaya. The data show that the bulk of the carbonates have $^{87}\text{Sr}/^{86}\text{Sr}$ and Ca/Sr much less than those measured in the head waters (Singh *et al* 1998). Granites/gneisses having $^{87}\text{Sr}/^{86}\text{Sr} > 1.0$ though reported, they are excluded from the histogram.

Jola gad (Krishnaswami *et al* 1992). The whole rock Sr/Ca of the LH granites/gneisses are in the range of 0.85 to 25.5 (figure 4) which bracket the values measured in source waters (Singh *et al* 1998). Thus, the whole rock $^{87}\text{Sr}/^{86}\text{Sr}$ and Sr/Ca of silicates seem adequate to dominate the Sr concentration and its isotopic compositions in source waters, however, better understanding of the effects of their incongruent weathering is needed to assess more quantitatively their role on the riverine Sr isotope budget. The control of silicate weathering on the Sr isotope composition of rivers is evident from the plot (figure 5) of $^{87}\text{Sr}/^{86}\text{Sr}$ vs $(\Sigma\text{Cat})_s$, the fraction of silicate derived cations. The data in figure 5 show a strong positive correlation ($r^2 = 0.56$) reflecting the control of silicate weathering on the $^{87}\text{Sr}/^{86}\text{Sr}$ of the source waters.

The silicate component of Sr in these source waters can be estimated following the procedure adopted for the major ions. The Sr/Na abundance ratio (mole) in the HH and LH granites and gneisses are 1.68 ± 0.72 and 1.22 ± 0.65 respectively (Krishnaswami *et al* 1998). The soil profile data yield values in the range of 2.5 to 2.9 for Sr/Na solution ratio, which compares with the measured Sr/Na molar ratio of 1.96 in the Jola gad waters. Following the assumptions employed for major ions, the Sr/Na ratio (molar) released to rivers during silicate weathering would be in the range of 1.2–2.9; for calculations a value of 2.0 ± 0.8 have been used (Krishnaswami *et al* 1998). The fraction of silicate Sr in the various source waters range between

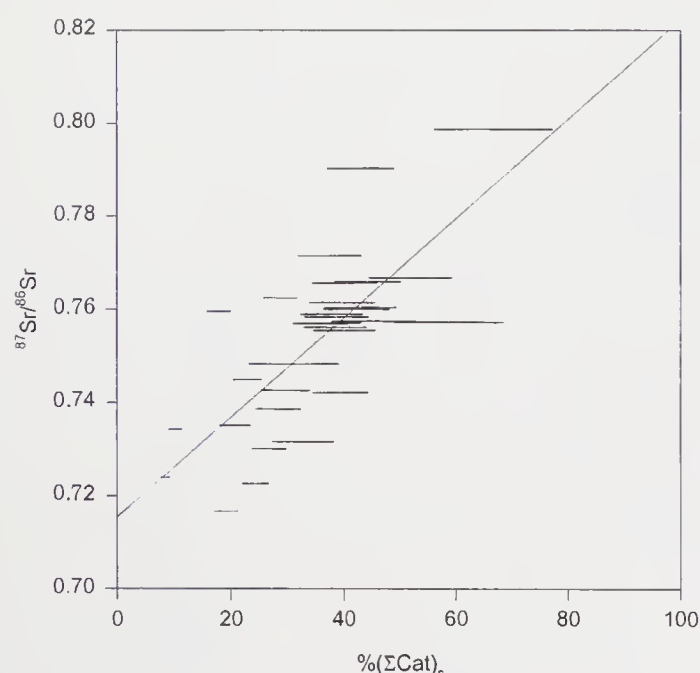


Figure 5. Variation of the measured $^{87}\text{Sr}/^{86}\text{Sr}$ in G-G-I source waters with their calculated $(\Sigma\text{Cat})_s$. There is an overall positive correlation between the two ($r^2 = 0.56$) suggesting that silicate weathering is an important source for the highly radiogenic $^{87}\text{Sr}/^{86}\text{Sr}$ of the rivers. The bars represent the range in $(\Sigma\text{Cat})_s$ calculated by considering $\pm 1\sigma$ uncertainty.

2% and 100% with the Bhilangna, Bhagirathi and their tributaries having higher Sr_s component, 30%–100% relative to the Kali, Sutlej, Chandra and Bhaga, which have $\leq 10\%$. The average Sr_s component in G-G-I source waters is 40%. McCauley and Depaolo (1997) have estimated the silicate Sr contribution to the G-B rivers to be 39% based on Sr isotopic mass balance assuming a two component system, silicates and carbonates.

In addition to silicates, another source which could control the Sr concentration and its isotopic composition in rivers is carbonates. The detailed studies of chemical and isotopic composition of Precambrian carbonate outcrops from the Lesser Himalaya (Singh *et al* 1998) provide necessary data to test their role on the Sr budget and $^{87}\text{Sr}/^{86}\text{Sr}$ of the source waters. The important findings are (i) these carbonates show definite evidence of alteration such as low Sr concentration with enriched $^{87}\text{Sr}/^{86}\text{Sr}$; (ii) the Sr/Ca ratio (mole) in them are only 0.04 to 0.64, with a mean of 0.2 ± 0.15 significantly lower than those in source waters (figure 4); and (iii) their $^{87}\text{Sr}/^{86}\text{Sr}$ are generally < 0.72 , though there are a few samples with much higher values, ~ 0.85 (figure 4). These findings have led to the conclusion (Singh *et al* 1998) that these extensive exposures of Precambrian carbonate outcrops are unlikely to be a major contributor to the high $^{87}\text{Sr}/^{86}\text{Sr}$ of the source waters on a basin-wide scale, though they could be important for particular streams. This conclusion is not unexpected considering that for these carbonates to be important on a large scale their $^{87}\text{Sr}/^{86}\text{Sr}$ has to be considerably enriched all along the Himalayan range drained by the G-G-I source waters.

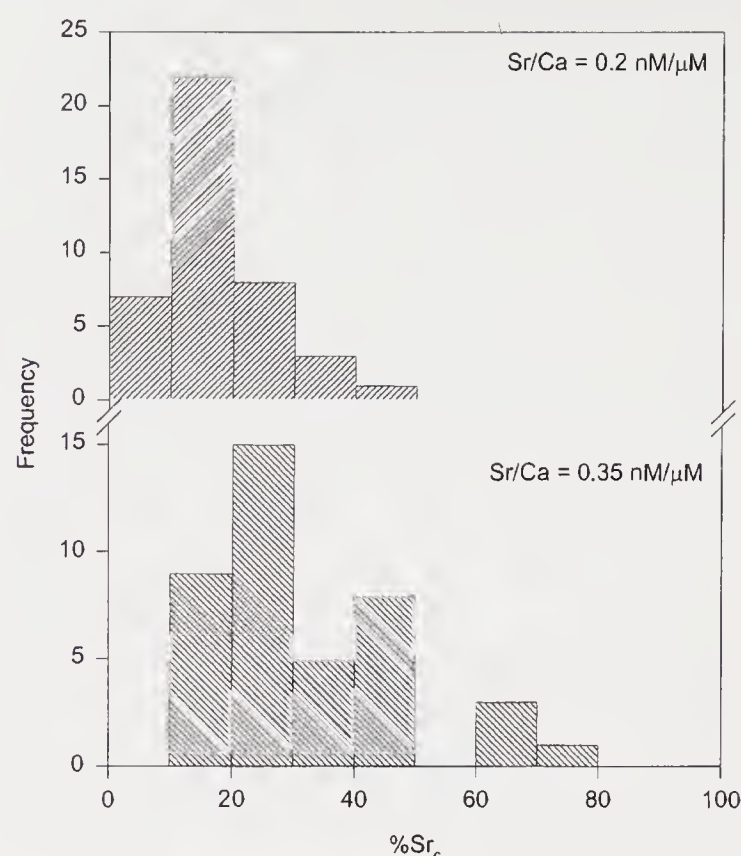


Figure 6. Carbonate Sr component in the G-G-I source waters. The values are upper limits and are calculated by assuming that all the Ca in the headwaters is of carbonate origin and Sr/Ca in the carbonates as 0.2, their mean abundance ratio in Precambrian carbonate outcrops (a) and 0.35, 1σ over the mean abundance ratio in carbonates (b).

How important are these carbonates in regulating the Sr budget of the source waters? This question can be addressed by estimating the carbonate Sr in them. The primary sources of Sr to rivers are silicates, carbonates and evaporites. As discussed earlier, it is not possible to estimate the evaporite contribution to major ions (and Sr) from the available data; however an *upper limit* on the carbonate Sr can be derived by assuming that (i) *all* Ca in the rivers is of carbonate origin; and (ii) the Sr/Ca ratio in the carbonates is $0.20 \pm 0.15 \text{ nM}/\mu\text{M}$, the mean value measured in the Precambrian carbonate outcrops (Singh *et al* 1998). The results (figure 6) show that the carbonate Sr can account for a maximum of 6 to 44% (mean 18%) of measured riverine Sr. (The limit would increase to 11 to 77%, (mean 31%) if the Sr/Ca ratio in the carbonates is taken as 0.35). A more realistic estimate of carbonate Sr can be calculated based on the carbonate Ca component of rivers (Krishnaswami *et al* 1998) which equals the difference between the measured Ca in them and their calculated silicate Ca. The results of these calculations yield a value of 5% to 42% (mean 15%) for the carbonate Sr contribution. The contribution of silicate and carbonate Sr in the source waters are compared in figure 7. The data, inspite of substantial uncertainty, show that in most of the source waters the silicate Sr component exceeds that of the carbonate Sr, exceptions being some of the tributaries of the Ghaghara and the Indus, where

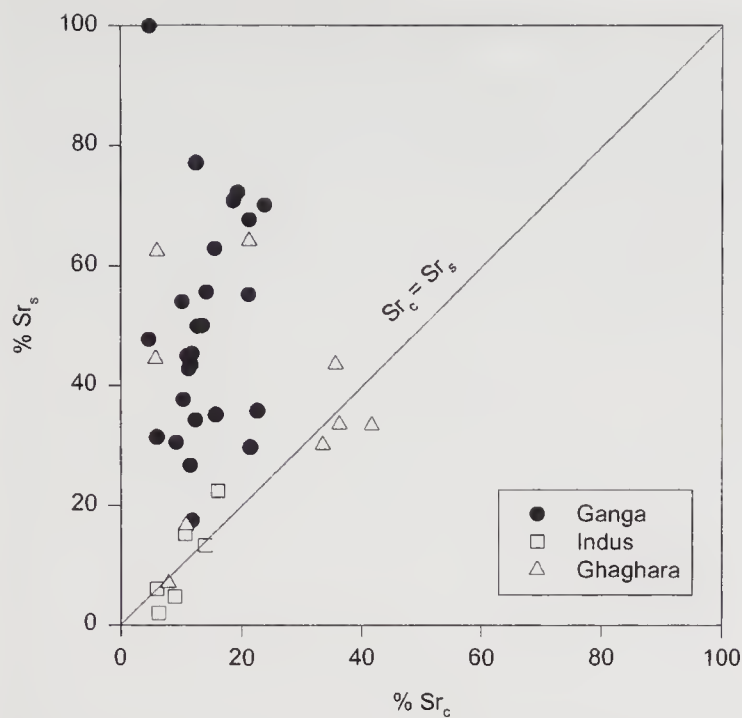


Figure 7. Scatter plot of Sr_s vs Sr_c (Sr_c calculated using $Sr/Ca = 0.2$). The silicate Sr exceeds the carbonate Sr in a majority of the headwaters. The data for the Ganga, Ghaghara and the Indus headwaters are shown by separate symbols. In Kali, Gori (Ghaghara system), Sutlej, Beas, Chandra, Bhaga, Dharcha (Indus system) $Sr_s \approx Sr_c$ (see text for calculations).

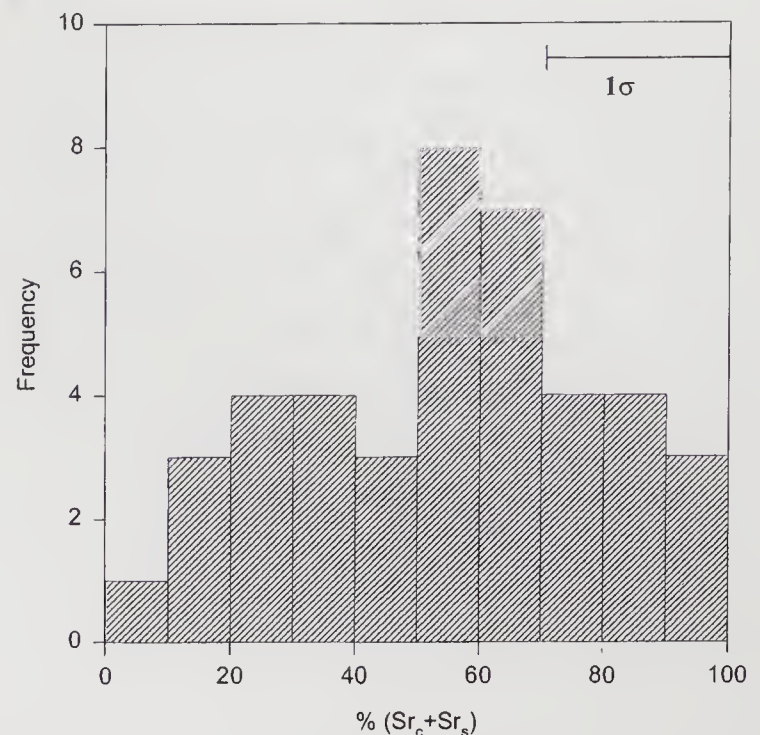


Figure 8. The sum of silicate and carbonate Sr contributions to the Sr budget of the G-G-I source waters. The data show that only in a few of the head waters, the Sr budget can be balanced based on the approaches discussed in the text. Samples with $(Sr_s + Sr_c)$ contribution $> 70\%$ can be made to balance the budget by considering 1σ uncertainty.

$Sr_s \approx Sr_c$. Thus the extensive outcrops of the Precambrian carbonate deposits of the Lesser Himalaya do not seem to be a major source for both Sr concentration and $^{87}Sr/^{86}Sr$ in the source waters on a large scale, they could, however, be still important for particular streams.

Can the silicates and the Precambrian carbonates account for Sr balance in the source waters? The fraction of riverine Sr that is supplied from the weathering of silicates and Precambrian carbonates is presented in figure 8 which show that only in a few of the source waters the Sr budget can be balanced if input is solely from these sources. It is possible to balance Sr budget in a few more rivers in which the sum of silicate and carbonate Sr contribution exceeds 70% by considering 1σ uncertainties associated with the estimates (figure 8). It is seen from this exercise that in a number of source waters, particularly Kali, Gori (Ghaghara system), Sutlej, Beas, Chandra, Bhaga and Dharcha (Indus system) it is difficult to account for their measured Sr if the two end members chosen (silicates and Precambrian carbonates) are its only sources and if the approaches used for estimating their contributions are valid. These calculations point to the need for another source for balancing the Sr budget in some of these source waters. The analysis of Sr isotope data of these rivers also seems to suggest this inference. The plot of $^{87}Sr/^{86}Sr$ vs Ca/Sr in the source waters (figure 9; note that unlike in earlier discussions where the Sr/Ca abundance ratios were compared, in figure 9 Sr isotope ratios are plotted as a function of Ca/Sr , following the conventional

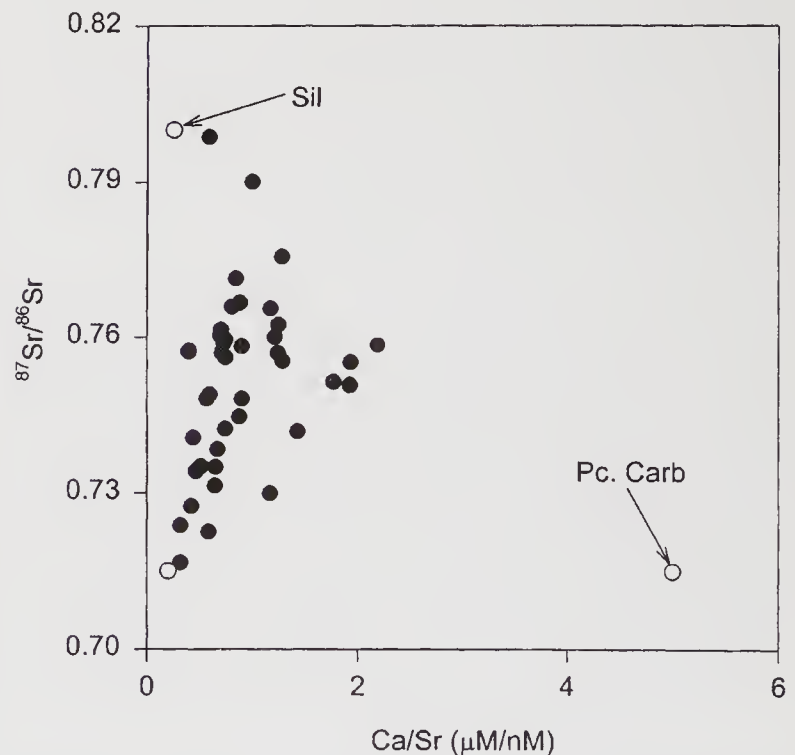


Figure 9. Plot of measured $^{87}Sr/^{86}Sr$ vs Ca/Sr in the headwaters. The end member values for silicates (Sil: $^{87}Sr/^{86}Sr = 0.8$; $Ca/Sr = 0.2 \mu M/nM$) and Precambrian carbonates (Pc. Carb: $^{87}Sr/^{86}Sr = 0.715$; $Ca/Sr = 5$) are also given. The data fan out from a low $^{87}Sr/^{86}Sr$ and low Ca/Sr end member. Possible candidates for this end member are Tethyan carbonates and Sr rich evaporite phases.

mixing diagrams) shows that the data fan out from a low Ca/Sr and low $^{87}Sr/^{86}Sr$ end member, similar to the trend in the $^{87}Sr/^{86}Sr$ vs $1/Sr$ plot (Singh *et al* 1998) suggesting the need for more than two end

members to explain the data. The low $^{87}\text{Sr}/^{86}\text{Sr}$ and Ca/Sr (i.e. high Sr) end member is commonly taken to be carbonates. The results of Singh *et al* (1998) and those presented in this study (figure 9) suggest that the extensive outcrops of Precambrian carbonates of the Lesser Himalaya because of their relatively lower Sr abundance (i.e. high Ca/Sr) are not the low $^{87}\text{Sr}/^{86}\text{Sr}$ and low Ca/Sr end member. Possible candidates for this end member are the Tethyan carbonates (present in the drainage basins of some of the Ghaghara and Indus source waters) and/or evaporites rich in Sr (gypsum, celestite etc.). Very recently, Blum *et al* (1998) based on the chemical and Sr isotope study of Raikhot watershed from the Higher Himalayan crystallines have suggested that weathering of vein calcites contributes to their high $^{87}\text{Sr}/^{86}\text{Sr}$. These vein calcites are inferred to have high $^{87}\text{Sr}/^{86}\text{Sr}$ (~ 0.8) and Ca/Sr ~ 5 (Blum *et al* 1998) and thus preclude them from being the end member with low $^{87}\text{Sr}/^{86}\text{Sr}$ and low Ca/Sr (figure 9).

3. Summary

Studies on the silicate weathering rates in the Himalaya and associated CO_2 consumption have gained considerable importance recently because of their possible influence on long term global change. Such studies naturally require "ideal proxies" to derive silicate weathering rates and its temporal variations. Sr isotope though have proved to be informative in this context, proper interpretation of $^{87}\text{Sr}/^{86}\text{Sr}$ in rivers needs better understanding of the various sources contributing to the Sr budget and their magnitudes. The major emphasis of this manuscript has been to estimate the contributions of silicates and carbonates to the major ion and Sr budget of the G-G-I source waters. The results show that on an average about a third of the major cations in these rivers is of silicate origin and that silicates exert a dominant control on their high $^{87}\text{Sr}/^{86}\text{Sr}$. Precambrian carbonate outcrops, a major component of the lithology of the head waters in the Lesser Himalaya, though may contribute to the high $^{87}\text{Sr}/^{86}\text{Sr}$ in particular streams, they are unlikely to be important for the Sr budget and the high $^{87}\text{Sr}/^{86}\text{Sr}$ of the headwaters on large, basin-wide scale. The Sr budget of many of the headwaters is difficult to balance if its supply is only from the two sources, granites/gneisses and Precambrian carbonates from the Lesser Himalaya, the data, therefore, indicate the need for an additional Sr rich source with low $^{87}\text{Sr}/^{86}\text{Sr}$.

Acknowledgements

This work is a synthesis of our continuing investigations on the major ion and Sr isotope geochemistry of

the rivers draining the Himalaya. Discussions with Drs. M M Sarin and J R Trivedi who have contributed significantly to these investigations over the years have been very helpful and productive. We thank Mr. Tarun K Dalai for his help with the synthesis and Prof. J Edmond and an anonymous reviewer for comments on an earlier version of the manuscript.

References

- Blum J D, Gazis C A, Jacobson A D and Chamberlain C P 1998 Carbonate versus silicate weathering in Raikhot watershed within the High Himalayan crystalline series; *Geology* **26** 411–414
- Derry L A and France-Lanord C 1996 Neogene Himalayan weathering history and river $^{87}\text{Sr}/^{86}\text{Sr}$: impact on marine Sr record; *Earth Planet. Sci. Lett.* **142** 59–74
- Edmond J M 1992 Himalayan tectonics, weathering processes, and the strontium isotope record in marine limestone; *Science* **258** 1594–1597
- France-Lanord C and Derry L 1997 Organic carbon forcing of the carbon cycle from the Himalayan erosion; *Nature* **390** 65–67
- Gansser A 1964 *Geology of the Himalayas* (London: Interscience) 287pp
- Gardner R and Walsh N 1996 Chemical weathering of metamorphic rocks from low elevations in the Himalaya; *Chem. Geol.* **127** 161–176
- Harris N 1995 Significance of weathering Himalayan metasedimentary rocks and leucogranites for the Sr isotope evolution of seawater during early Miocene; *Geology* **23** 795–798
- Harris N, Bickle M, Chapman H, Fairchild I and Banbury J 1998 The significance of Himalayan rivers for silicate weathering rates: evidence from Bhote Kosi tributary; *Chem. Geol.* **144** 205–220
- Krishnaswami S, Trivedi J R, Sarin M M, Ramesh R, and Sharma K K 1992 Strontium isotope and rubidium in the Ganga-Brahmaputra river system: Weathering in the Himalaya, Fluxes to Bay of Bengal and contribution to the evolution of oceanic $^{87}\text{Sr}/^{86}\text{Sr}$; *Earth Planet. Sci. Lett.* **109** 243–253
- Krishnaswami S, Singh S K and Dalai T K 1998 Silicate weathering in the Himalaya: Role in contributing to major ions and radiogenic Sr to the Bay of Bengal; In *Proc. INSA Symposium on "Present trends and future directions in ocean sciences"* (in press)
- McCauley S E and DePaolo D J 1997 The marine $^{87}\text{Sr}/^{86}\text{Sr}$ and $\delta^{18}\text{O}$ records, Himalayan Alkalinity Fluxes and Cenozoic climate models; In *Tectonic Uplift and Climate Change* (ed) W F Ruddiman (New York, USA: Plenum Press) pp. 428–467
- Palmer M R and Edmond J M 1989 The strontium isotope budget of the modern ocean; *Earth Planet. Sci. Lett.* **92** 11–26.
- Palmer M R and Edmond J M 1992 Controls over the strontium isotope composition of river water; *Geochim. Cosmochim. Acta* **56** 2099–2111
- Palmer M R and Elderfield H 1985 Sr isotope concentration of sea water over the past 75 Myr; *Nature* **314** 526–528
- Pande K, Sarin M M, Trivedi J R, Krishnaswami S and Sharma K K 1994 The Indus river system (India-Pakistan): Major ion chemistry, Uranium and Strontium isotopes; *Chem. Geol.* **116** 245–259
- Quade J, Roe L, DeCelles P G and Ojha T P 1997 The late Neogene $^{87}\text{Sr}/^{86}\text{Sr}$ Record of Lowland Himalayan Rivers; *Science* **276** 1828–1831

- Raymo M E and Ruddiman W F 1992 Tectonic forcing of late Cenozoic climate; *Nature* **16** 117–122
- Richter M, Rowley D B and DePaolo D J 1992 Sr evolution of sea water: The role of tectonics; *Earth Planet. Sci. Lett.* **109** 11–23
- Sarin M M, Krishnaswami S, Dilli K, Somayajulu B L K and Moore W S 1989 Major ion chemistry of the Ganga-Brahmaputra river system: Weathering processes and fluxes to the Bay of Bengal; *Geochim. Cosmochim. Acta* **53** 997–1009
- Sarin M M, Krishnaswami S, Trivedi J R and Sharma K K 1992 Major ion chemistry of the Ganga source waters: Weathering in the high altitude Himalaya; *Proc. Indian Acad. Sci. (Earth Planet. Sci.)* **101** 89–98
- Sarkar A, Roy A, Ghatak G S and Bhattacharya S K 1996 Strontium isotope study of Krol-Tal carbonates: Implication to the Strontium isotope flux of Himalayan Rivers; *Indian J. Geol.* **68** 255–262
- Singh S K, Trivedi J R, Pande K, Ramesh R and Krishnaswami S 1998 Chemical and strontium, oxygen, and carbon isotopic compositions of carbonates from the Lesser Himalaya: Implications to the strontium composition of the source waters of the Ganga, Ghaghara and Indus rivers; *Geochim. Cosmochim. Acta.* **62** 743–755
- Trivedi J R, Pande K, Krishnaswami S and Sarin M M 1995 Sr isotopes in rivers of India and Pakistan: A reconnaissance study; *Curr. Sci.* **69** 171–178
- Valdiya K S 1980 *Geology of the Kumaun Lesser Himalaya* (Dehradun: Wadia Institute of Himalayan Geology) pp. 391

On the interpretation of the oceanic variations in $^{87}\text{Sr}/^{86}\text{Sr}$ as recorded in marine limestones

YOUNGSOOK HUH and JOHN M EDMOND

*Department of Earth, Atmospheric and Planetary Sciences, Massachusetts Institute of Technology,
Cambridge, Massachusetts, 02139, USA
e-mail: yhu@mit.edu*

The present published inventory of fluvial Sr and $^{87}\text{Sr}/^{86}\text{Sr}$ data, combined with new information from the big rivers of Eastern Siberia (a combined total of $\sim 1,000$ measurements), is used to investigate the probable origin of the large rise in the marine isotopic ratio, recorded in limestones, over the last ~ 20 million years. With the exception of the data from the Ganga-Brahmaputra all measurements fall on what is proposed to be called the “Wickman trend”, essentially a mixing line between the limestone sink for Sr, with the integrated marine ratio, and the flux from the weathering of average continental crust. However, time-variations along this trend, i.e. changes in relative weathering intensity, cannot explain the observations from limestones. They can only be caused by very high and radiogenic fluxes of Sr as are occurring from the present Himalayan orogeny, lying far above the Wickman trend and caused by metamorphic remobilization of radiogenic Sr during underthrusting and subsequent unroofing associated with the collision of India with Eurasia. In general the variations in the ratio are therefore caused by specific tectonic events, not by general climatic variations in the intensity of aluminosilicate weathering.

1. Introduction

1.1 The record

In a classic early paper Wickman (1948) proposed that since ^{87}Rb is strongly enriched relative to Sr in continental igneous rocks as compared to mantle basalts, i.e., is what is now called an incompatible element, the fluvial weathering yield of the resulting radiogenic daughter ($t_{1/2} = 47 \times 10^9$ year), ^{87}Sr , should determine the oceanic $^{87}\text{Sr}/^{86}\text{Sr}$ value. Therefore this should increase monotonically with time, assuming early formation of the continental crust. This ratio could then be used as a dating tool for “soft” rocks formed in the marine environment that incorporate Sr into their lattice sites and exclude Rb, i.e., limestones, evaporites, etc. While it was soon shown that Wickman’s estimate of the crustal Rb enrichment was much too high the dating potential, even with a time resolution greatly reduced from the original

estimate, attracted some interest. The first test of the hypothesis was made by Gast (1955) who found that continental limestone values were constant within (considerable) measurement error over the past ~ 500 Ma as was the contemporary seawater value. The important result was that marine limestones sample the “whole ocean value” of the ratio. This has been confirmed by many subsequent studies. The oceanic residence time of Sr is ~ 2.5 Ma ($90\mu\text{M}$ and 0.7091 in the oceans; $0.89\mu\text{M}$ and 0.7119 flow-weighted average in rivers; Palmer and Edmond 1989), biological effects are minimal and non-fractionating and hence the oceans are isotopically homogeneous.

Peterman *et al* (1970) extended this work with significantly increased precision and developed a catenary relationship with high $^{87}\text{Sr}/^{86}\text{Sr}$ values in the latest Precambrian and the Recent (~ 0.7090) and oscillations about lower values in the interim with pronounced minima in the mid-Permian and

Keywords. Sr isotopes; aluminosilicate weathering; Siberia; rivers.

the Late Jurassic (~ 0.7068), i.e. completely contrary to Wickman's original suggestion (figure 1a). Veizer and Compston (1974, 1976) greatly developed this record back to the Archean (figure 1b, c). However, since the "half life" of shallow water limestones with respect to weathering is ~ 150 Ma, the availability of samples drops off very steeply with time. In addition, secondary diagenetic effects can disturb the record due to addition of Sr from other sources with distinctive Rb/Sr ratios, different ages and hence widely differing $^{87}\text{Sr}/^{86}\text{Sr}$ values. Thus the older part of the record showed a very broad spread (~ 0.0015) at a given time interval and aliasing, i.e. features determined by the sporadic sampling of a continuously varying signal.

The situation changed dramatically with the development of a very high resolution record for the Phanerozoic (Burke *et al* 1982; figure 1d) derived mainly from core samples that could be

"stacked" to give a synthetic, continuous stratigraphic column of limestones over the past 550 Ma. This approach showed in detail the oscillations hinted at previously. Thus the use of the ratio in chrono-stratigraphy became a possibility, the resolution depending on its time-rate of change. At a more fundamental level the question of the interpretation of the oscillations in terms of geologic and environmental processes came to the fore. As a result of this break-through, with its stratigraphic and geochemical implications, a large effort has gone into further refining the record. Initially work was directed at the continuous carbonate sections recovered by the Deep Sea Drilling Programs from the last ~ 50 Ma. Extension has depended on shallow water macro-fossils from various localities and has resulted in a detailed description of the evolution of the oceanic ratio over the past ~ 900 Ma (figure 2).

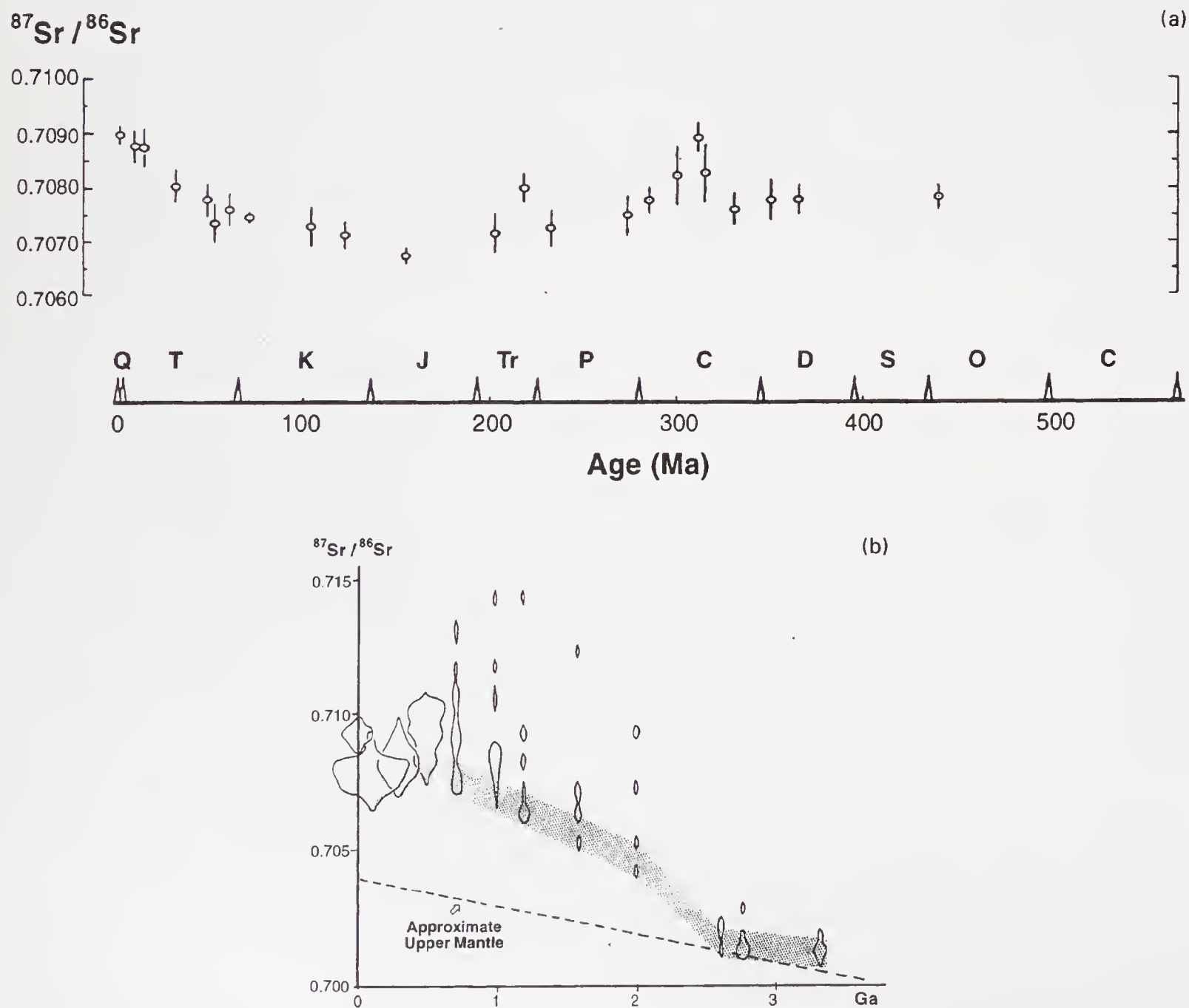


Figure 1(a-b). (Continued)

(c)

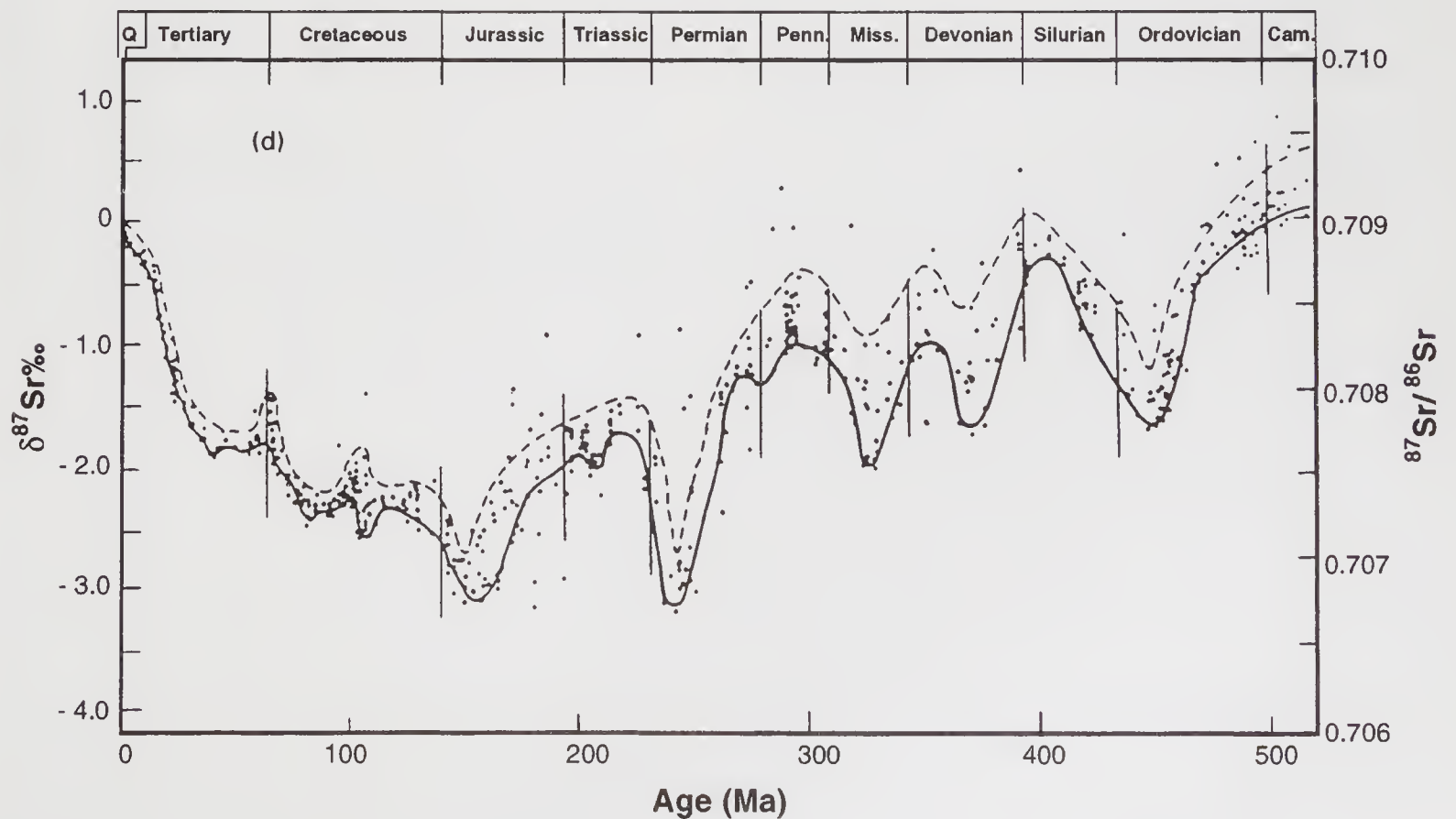
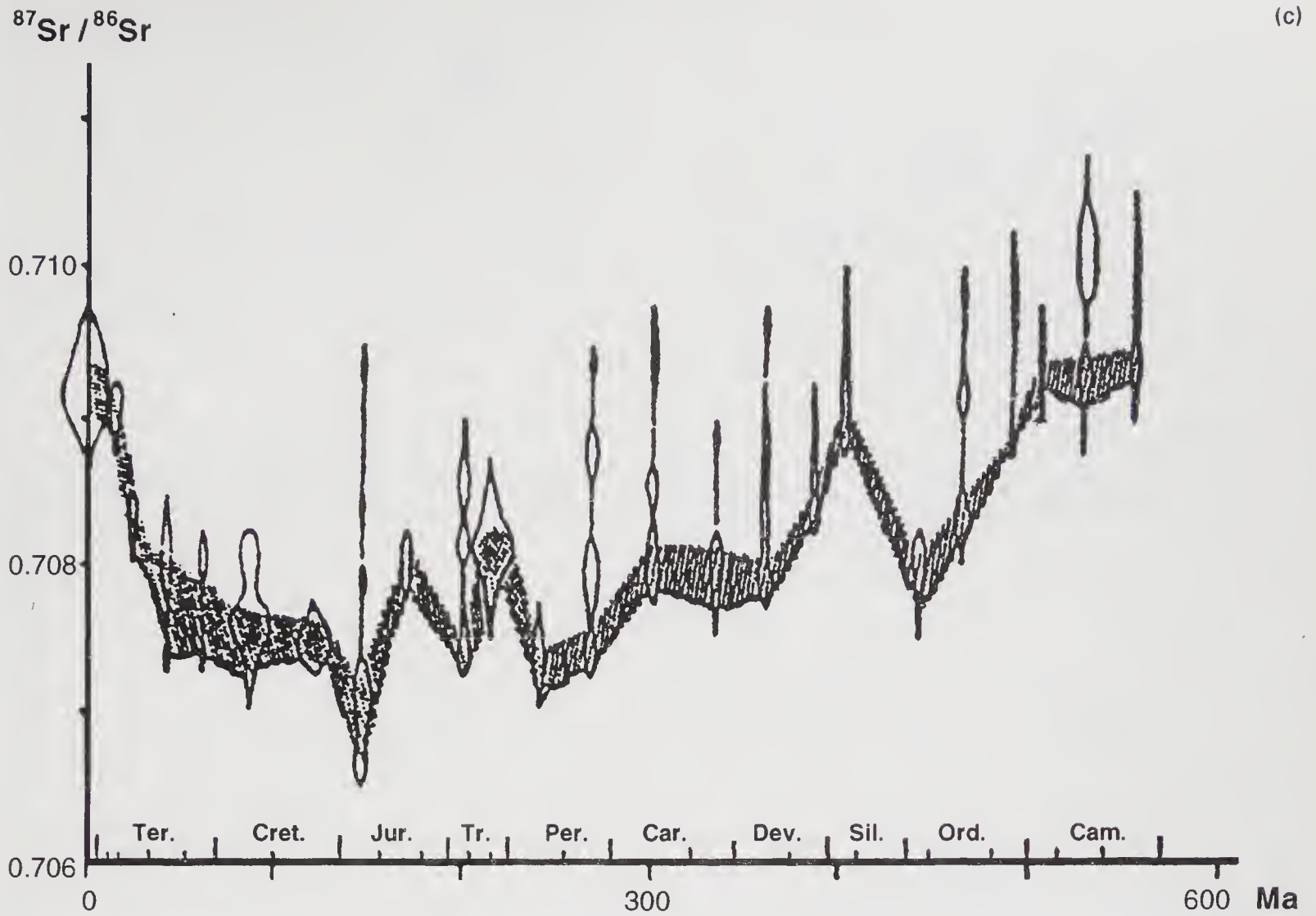


Figure 1(a–d). Illustrative summary of the evolution of the basic information on the $^{87}\text{Sr}/^{86}\text{Sr}$ ratio in seawater as recorded in marine limestones. (a) The original curve from Peterman *et al* (1970; error bars are purely instrumental); (b, c) from Veizer and Compston (1974, 1976; error ellipses encompass the range in measurements for a given age with the least radiogenic values used to define the curves); (d) the “Burke curve” from Burke *et al* (1982; again, within the measurement envelope, the least radiogenic values are generally assumed to be the best estimates).

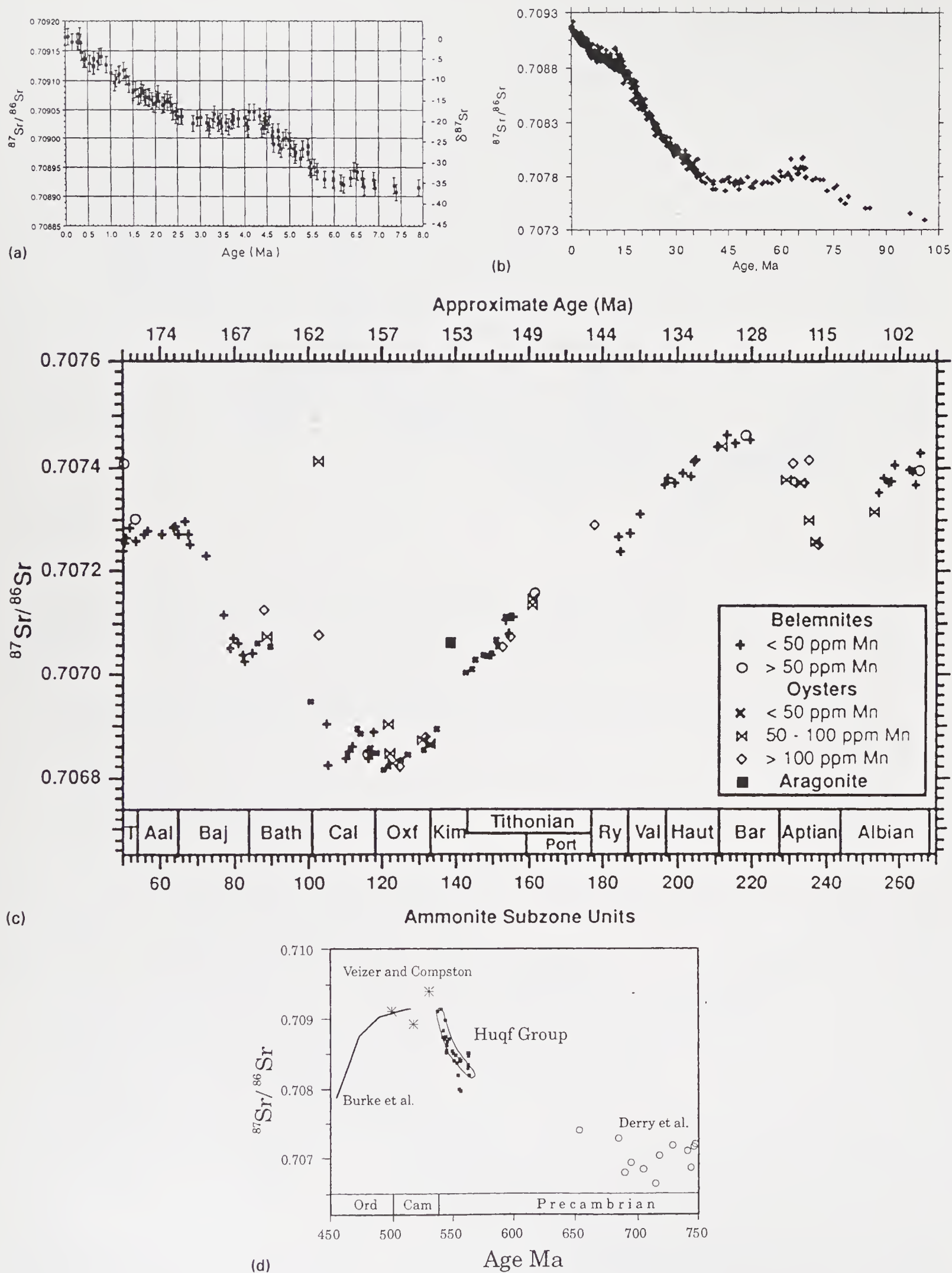


Figure 2. Some examples of high-resolution Sr isotopic data for the past 750 Ma. (a) Hodell *et al* (1990); (b) Rea (1992); (c) Jones (1994); (d) Burns *et al* (1994).

A synthesis of all the data back to the Early Jurassic has been made (Jones 1994) correcting for inter-laboratory measurement bias, uncertainties in the stratigraphic ages and suspected diagenetic effects. A formal statistical analysis of the record back to 450 Ma has been made by Smalley *et al* (1994) in order to constrain its use in dating. Thus the validity of the original “Burke curve” is now secure and has been refined to what is probably the maximum extent feasible given the difficulties of carbonate preservation.

1.2 Interpretation

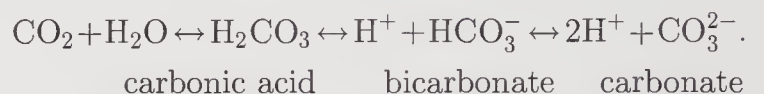
Since the publication of the Burke curve the case has consistently been made that the variations in the marine $^{87}\text{Sr}/^{86}\text{Sr}$ ratio reflect changes in the intensity of weathering of continental aluminosilicate rocks, i.e. a revival of Wickman’s original hypothesis (Berner and Rye 1992 and references therein). This was given support by the observation that the flux of Sr and its isotopic composition ($\sim 125\mu\text{M}$, 0.7035) associated with deep sea hydrothermal activity (unknown to Wickman) is quite constant in the contemporary ocean with a contribution of \sim one third to the overall total oceanic isotopic budget (Palmer and Edmond 1989). Thus the mantle flux, slowly varying as it is known to be, acts as a “fly-wheel” to stabilize the system. This stabilization effect is accentuated by the incorporation of Sr into marine limestones, the major sink for the element. The memory of past changes in the oceanic ratio, whatever the cause, is damped since the fluvial flux from the weathering of continental limestone deposits and the diagenetic flux from marine sediments act to integrate past variations (the time averaged value is ~ 0.708) and are together responsible for at least another one third of the flux to the ocean (Brass 1976). These two sources, hydrothermal activity and limestone weathering, result in a combined, relatively stable, base-line input with a net ratio of ~ 0.7065 , as is seen in the Permian and Jurassic minima. This leaves the dissolution of ancient Rb-rich aluminosilicate rocks as the “master variable” in determining the observed rapid changes in the marine isotopic record. The validity of this interpretation underpins all recent discussions of the evolution of the Earth surface environment since the $^{87}\text{Sr}/^{86}\text{Sr}$ record is the only existing, well-defined potential index of changes in weathering processes associated with long term global climatic and tectonic variations.

The argument for climatic stability is quite straight forward (Walker *et al* 1981). Solar radiation is deposited on the Earth in two major ways: absorption of the UV, predominantly in the stratosphere by O_3 , and deposition of the energy in the visible range on the surface there to be re-radiated in the IR, directly or as latent heat release from evaporated H_2O , with

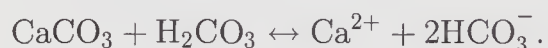
ultimate return to space. The major atmospheric absorber in the IR is water vapor, the dominant “greenhouse” gas. The partial vapor pressure of water, $p_{\text{H}_2\text{O}}$, is strongly constrained by thermal equilibration with the oceanic reservoir through the Clausius-Clapeyron relationship:

$$\frac{d \ln P}{dT} = \frac{\Delta H_{\text{vap}}}{RT^2}$$

where T is temperature and ΔH_{vap} is the latent heat of vaporization. This is completely validated by the meteorological observations between 0° and 75° latitude and in all seasons (Webster 1994). Since this function has an approximately exponential relationship to sea surface temperature, the system is very sensitive to the atmospheric variations in other IR-absorbing molecules, the suite of polyatomic greenhouse gases. While contemporary anthropogenic activities are adding a plethora of these species to the atmosphere, over geologic time scales CO_2 is the only one for which the variations can be of any significance. This becomes clear from an examination of the weathering-tectonic cycle. Atmospheric CO_2 reacts with water vapor to form carbonic acid:



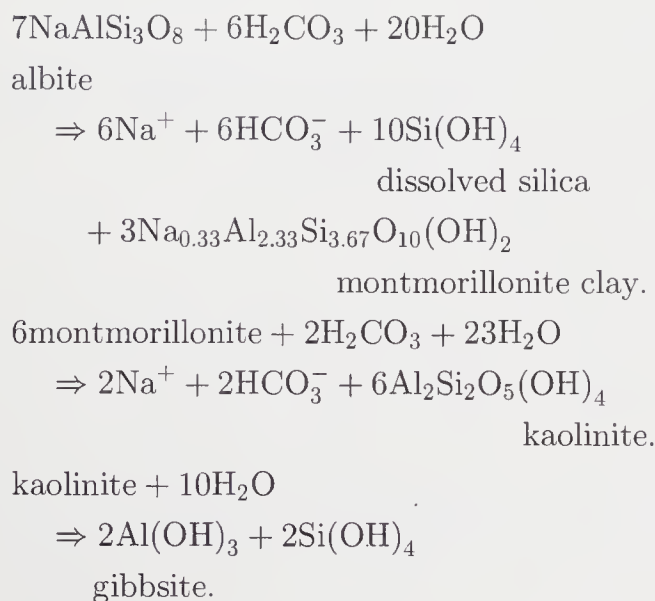
This reaction series constitutes the predominant source of protons for weathering reactions save for minor contributions from volcanically derived H_2SO_4 and HCl . Weathering of the simple evaporitic salts, NaCl and CaSO_4 , is by congruent dissolution reactions that do not involve external reactants save for water as the passive medium. Dissolution of limestones, dolomites and other carbonate-containing rocks, does involve protons: e.g.



However, this reaction is rapidly reversible on geologic time-scales because of inorganic precipitation, usually of the soluble phase aragonite, from seawater as it becomes supersaturated due to the accumulation of the fluvial inputs. This process is observed over all of geologic time, although at different scales, from Archean carbonate platforms (Grotzinger 1989) to the contemporary Bahaman Banks. Over the last 600 Ma biogenic formation of calcitic and aragonitic shells and other structural components has been the dominant removal mechanism. Dolomites ($\text{CaMg}[\text{CO}_3]_2$) are formed by secondary diagenetic processes acting on marine platform carbonates in hypersaline lagoonal environments (Sun 1994). The only other significant carbonate phase is siderite, FeCO_3 , which forms in anoxic environments that generate Fe^{2+} and thus is usually associated with black shales.

For aluminosilicate weathering the overall reaction cycle is more problematic. Using albite as a simple

example:



These reactions can be viewed, very simply, as a progressive cation exchange of protons produced by carbonic acid dissociation for ions contained in the quenched, disequilibrium, high temperature igneous and metamorphic phases to produce minerals such as clays much closer to thermodynamic stability under earth-surface conditions. Structural re-arrangements result in the additional loss of Si to solution. Thus, in the absence of carbonates and evaporites, the fluvial ratios of cations (in equivalents) to bicarbonate and silica are diagnostic of weathering processes (Edmond *et al* 1995). The regeneration mechanism that closes this *aluminosilicate* weathering cycle is the “Urey reaction”:



This formulation, while thermodynamically favored, is in effect a shorthand statement of the fact that *any* cation-poor aluminosilicate phase, i.e. a weathered clay, will react with carbonates at intermediate to elevated temperatures to give a calc-silicate plus free CO_2 . Ironically, the reaction proceeds in a water-saturated environment in the same thermal regime as the “oil maturation window” 120–150°C, with the result that many super-giant gas fields identified seismically as “bright spots” have turned out, upon drilling, to be dominantly composed of CO_2 (Hunt 1979). Thus the return flux of CO_2 necessary to sustain weathering is from metamorphic processes in orogenically active zones with a smaller, primary mantle input from seafloor hydrothermal systems, hot-spot volcanism and andesitic volcanoes on active margins.

The control on atmospheric $p\text{CO}_2$ and hence on global temperature is then through the Clausius-Clapeyron relationship and the Arrhenius rate law:

$$k = Ae^{(-\Delta H/RT)}.$$

Increased CO_2 leads to warming; this increases $p\text{H}_2\text{O}$ (at $\sim 6\% \text{ } ^\circ\text{C}^{-1}$ at tropical temperatures) and hence

water vapor transport and precipitation and therefore weathering rates through the increase in the availability of the reaction flux medium, H_2O , and the rising ambient temperature. A contemporary example of this effect is the El Niño phenomenon. The resulting accelerated consumption of the excess CO_2 brings the system back into balance through the negative feedback effect; the $p\text{CO}_2$ – $p\text{H}_2\text{O}$ interaction acts as a global thermostat preventing “runaway”. Much emphasis has been placed on the apparent necessity for a rather exact balance in this overall cycle given that the observed fluvial flux of bicarbonate “fixed” by aluminosilicate weathering is sufficient to completely deplete the inventory of atmospheric CO_2 on time scales much less than 1 Ma (Berner and Caldeira 1997). Thus the average silicate weathering index assumed to be provided by the $^{87}\text{Sr}/^{86}\text{Sr}$ ratio is crucial to an understanding of the means by which the Earth has remained a habitable (oceanic) environment over geologic time escaping the “icehouse” and “greenhouse” fates of Mars and Venus, respectively.

Validating this index can only be done based on the one natural “experiment” available, the fluvial weathering rate of the contemporary continents as a function of climate. Terrains representative of most of geologic time in terms of geology, elevation, relief and climate are presently active in all latitude zones on the Earth’s surface. Yet the interpretation of the fluvial flux of Sr and the associated isotopic ratio is complicated by several factors. Even in basins mapped as entirely composed of basement or metamorphic rocks, residual outliers of the original platform cover, carbonates, evaporites and detrital sediments, can dominate the fluvial signal since the simple salts and the massive carbonates and carbonate cements are usually high in Sr, with the integrated marine isotopic ratio, making it difficult to extract the primary signal of the *net* sink for CO_2 in these circumstances. The detrital sediments, in the absence of their reactive cements (calcite, dolomite, siderite, organics), do not contribute significantly to the dissolved load by weathering at outcrop because they are mechanically incompetent. However they do weather, sometimes intensively, during subsequent storage in flood plains; the magnitude of this contribution to the net fluvial flux is difficult to quantify although the effect on the mineralogy and $\delta^{18}\text{O}$ isotopic composition of the residual components is clear (France-Lanord *et al* 1996, Johnsson *et al* 1988). The crystalline aluminosilicate minerals themselves weather at greatly differing rates in the general order, quartz \ll mica $<$ K-feldspar \ll Ca/Na-feldspar \ll Mg/Fe-minerals. Oxidative weathering of reduced facies containing Fe^{2+} , e.g. basalts and sulfides, or organic carbon, provides an alternative source of protons and can accelerate dissolution; however this is usually a local process associated with sulfide mineralisation or with accessory minerals such as biotite and with black shales.



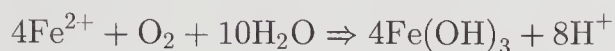
organics



reduced Fe

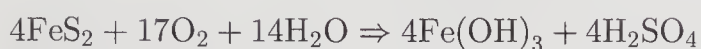
reduced Fe

(soluble).



oxidized Fe

(insoluble).



pyrite

sulfuric acid.

This reaction complex is of much greater importance in the weathering of shales and of ultramafic as opposed to granitic terrains since the former are dominated by Fe/Mg-silicates and hydrothermal sulfide ore deposits; while these are areally quite specific and easily identified geologically, e.g. black shales, flood basalt provinces, accreted island arcs, active margin volcanics, where present they can dominate the fluvial chemistry of large basins due to their reactivity.

The very strong contrast in weathering rates (several orders of magnitude) between the Na/Ca and K-containing minerals leads to an effective fractionation of the Sr isotopes during dissolution reactions since Sr follows Na/Ca and Rb substitutes for K in igneous and metamorphic processes. In rocks of mantle origin, basalts, ultramafics and most granites, the initial non-radiogenic isotopic ratio (~ 0.703) is preserved in the rapidly weathering Na/Ca phases since they effectively exclude the large-radius, radioactive, parent ion Rb from their structures during primary crystallization. River sands produced in more differentiated terrains are usually composed of quartz and K-mica, i.e. a large proportion of the radiogenic Sr is exported from the drainage in the mechanical load since Rb is accommodated in the K-sites. The average crustal ratio is ~ 0.725 but with a very wide range, depending on rock type and age, from ~ 0.704 for ultramafics to > 0.9 for old potassic granites.

The net fluxes from basaltic hydrothermal systems and from carbonates are likely to be quite stable, or continuously varying, in time; they are high but with relatively constant isotopic ratios. The aluminosilicate source from continental weathering spans the isotopic range from mantle values to extremely radiogenic ratios, generally with an Sr flux inversely proportional to $^{87}\text{Sr}/^{86}\text{Sr}$ (Palmer and Edmond 1989).

2. The fluvial flux and isotopic ratio

2.1 The data set

The published data sets usable for analysis consist of Sr- $^{87}\text{Sr}/^{86}\text{Sr}$ measurements on rivers world-wide, in

all environments and at all basin scales (figure 3); the number of analyses at hand, including recent reports from the Himalaya and the new data presented here for eastern Siberia, is $\sim 1,000$. These data have been accumulated over the last ~ 20 years and so their quality increases dramatically with time. However, since the few time series available (Palmer and Edmond 1989; Edmond *et al* 1995) show that the

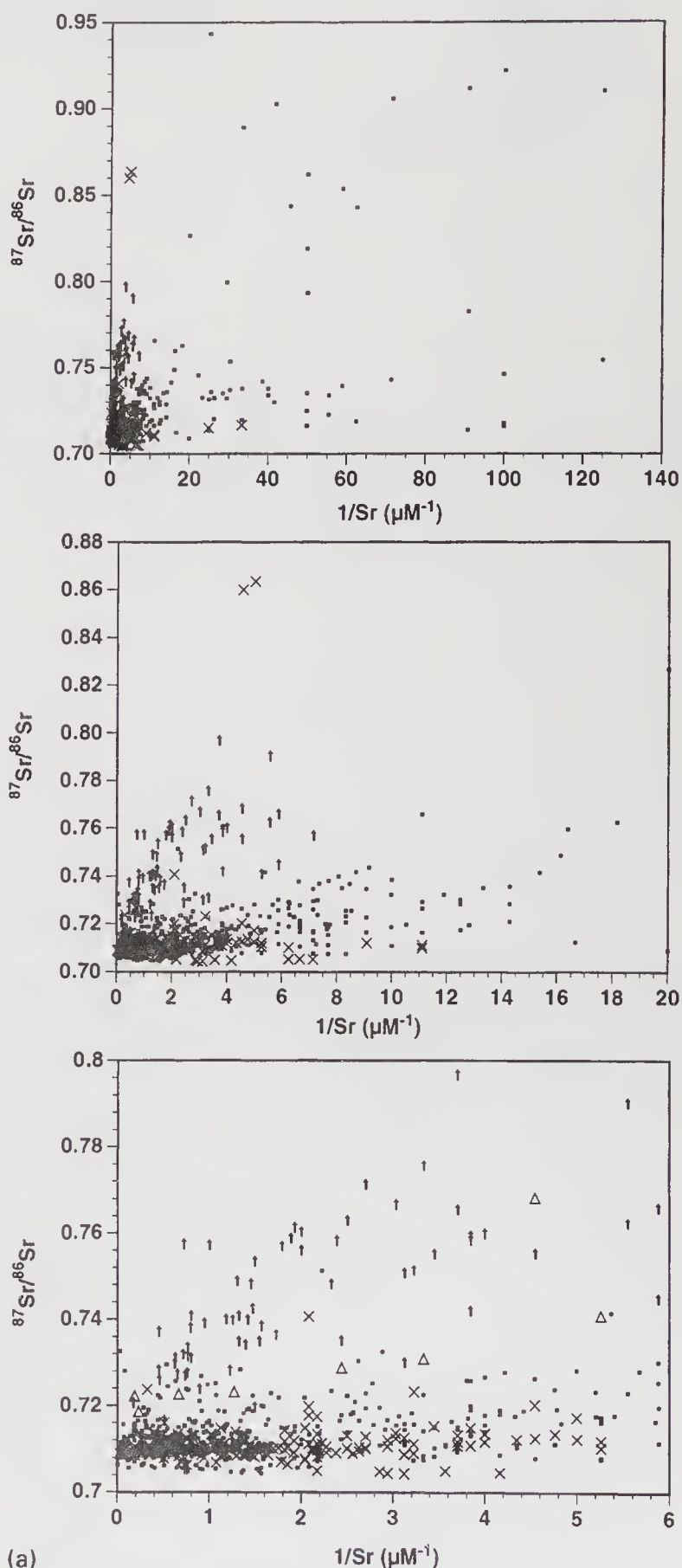


Figure 3(a). (Continued)

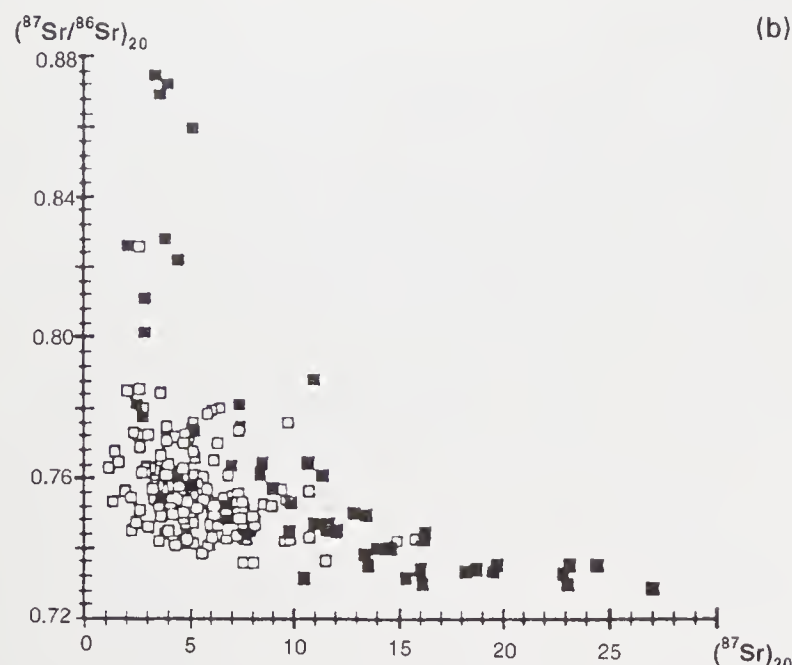


Figure 3. (a) The existing fluvial $\text{Sr}-^{87}\text{Sr}/^{86}\text{Sr}$ data set. \uparrow – Himalayan rivers; X – Siberian rivers; \bullet – Other rivers. Data from Brass 1976; Fisher and Stueber 1976; Wadleigh *et al* 1985; Albarède and Michard 1987; Goldstein and Jacobsen 1987; Palmer and Edmond 1989 1992; Ingram and Sloan 1992; Krishnaswami *et al* 1992; Négrel *et al* 1993; Blum *et al* 1994; Pande *et al* 1994; Cameron *et al* 1995; Trivedi *et al* 1995; Zhang *et al* 1995; Yang *et al* 1995; Huh *et al* 1998a,b; Huh and Edmond 1998. (b) The compilation of initial ratios for the Himalayan metamorphic rocks (adjusted to an assumed age of 20 Ma; Harris 1995).

ratio can change in the third place seasonally, data quality is not a serious limitation. Generally, the river discharge is not included with the published measurements; however, fluxes can be calculated using compilations of average runoff in the particular basins since these, in fact, are regional contour maps of actual long-term hydrologic measurement series not easily available in the literature (UNESCO 1979). The combination of point determinations, in time, of the elemental and isotopic values with decadal averages of the basin runoff results in uncertainties in net transport that are difficult to quantify; optimistically, the fluvial flux of Sr to the ocean is known to about 25% and the ratio to ~ 0.0005 .

Unfortunately there exists a substantial body of reported isotopic data without the associated Sr concentrations; these cannot be used in the type of analysis presented here. In addition the data for the dissolved load (Na, K, Mg, Ca, Cl, SO_4 , alkalinity, Si) are often incomplete making the relationship between the Sr concentrations and isotopic compositions to the geology, topography and climate of the various basins difficult to establish. However, broad trends emerge in this $\text{Sr}-^{87}\text{Sr}/^{86}\text{Sr}$ global data set which can be interpreted, at least qualitatively.

The entire published fluvial data set (as of 1998) is presented in figure 3 at various levels of resolution. There are several features that are immediately apparent.

- (b) 1. The overwhelming proportion of the data ($\geq 70\%$) plots in the domain of marine limestones, i.e. high Sr, ratios ~ 0.7085 .
2. There is a positive “main linear trend” from this nexus to more radiogenic values at progressively lower concentrations; the scatter in this trend increases markedly at very low Sr. It can be regarded as a mixing line between continental basement, with all its heterogeneity, and the much more homogeneous limestones.
3. There is a subsidiary, undersampled, negative trend to less radiogenic values; this represents mafic rocks in their various manifestations.
4. There is a striking, strongly positive trend to very radiogenic values with high Sr concentrations; all these samples are from the Himalayan orogen, with no important exceptions.

Thus the factors required to explain the marine isotopic record reside in (2) and (4), since features (1) and (3) are probably quite constant in time. Feature (2) can be regarded as the “normal Wickman trend”, the variable contribution of aluminosilicate weathering to the limestone “buffer” flux. Note that the Sr concentrations fall off very rapidly with increase in the ratio. Feature (4) is unique to the Himalayas, the transport of radiogenic Sr in high concentrations.

The Wickman trend encompasses all the data from “normal” terrains, i.e. excluding flood basalt provinces, occluded island arcs, greenstone belts and the Himalaya, but including at least 75% of the continental area presently undergoing active weathering. Therefore, at the present state of knowledge, it can be assumed as the datum line over at least the period of the Phanerozoic limestone record and is the basis for the argument that the Sr isotopic ratio in limestones is an index of the severity of continental weathering. However, the isotope ratio in the rivers defining the trend increases only at the expense of steeply decreasing Sr concentrations. Thus it is difficult to develop a mass balance variation sufficient to explain the large oscillations observed in the limestone record based on the Wickman trend alone.

Beginning with the brief suggestion by Armstrong (1971) that the oscillations are correlated with continental-scale glaciations it has been assumed that glacial processes increase the weathering rates of aluminosilicate rocks and therefore the fluvial flux of radiogenic Sr. Recent data from Eastern Siberia demonstrate that, at least in a periglacial environment dominated by ice action at all scales, this is not the case. An extensive survey has been carried out of all the significant rivers east of Lake Baikal and their tributaries (~ 300 samples; figure 3a). The data fall into three distinct groupings; a steeply rising relationship to relatively radiogenic values, > 0.720 , a horizontal trend at ~ 0.7085 and a decreasing trend to ~ 0.7045 . The first relationship is from the basement

rocks of the Aldan Shield and Trans-Baikal Highlands that constitute the southern rim of the Lena basin; it is not comparable in scale to the Himalayan feature but demonstrates an insignificant contribution from carbonates. There is also a component from the extensive exposures of detrital sediments to the east, in particular the Verkhoyansk and Cherskiy Ranges. The second is from the undeformed platform cover of marine Cambrian to Tertiary age found in many of the basins and is consistent with the observed dominance of marine limestones and evaporites in these sequences. The third is from the basaltic terrains found throughout the region as greenstone belts, occluded arc volcanics and extinct active margins associated with old collision zones to the east.

When compared to the global data set it can be seen that the Siberian data are not remarkable (figure 3a). In addition there are no striking features in the calculated denudation rates (figure 4); these are comparable to those from similar regimes in lower latitudes (Huh and Edmond, in press; Huh *et al* 1998a, b).

The important observation is that there is no obvious climatic influence on weathering rates in any of the diverse environments for which data are available, from the Tropics to the high Arctic (figure 4). The fluxes of Sr and its isotopes are not affected by climatic influences on the weathering regimes.

By a process of elimination, based as it is on a global data set, the only currently active environment producing radiogenic Sr in sufficient flux to generate the Tertiary rise in the marine ratio is the Himalayan orogeny, specifically the Ganga-Bramaputra basins. However the mechanisms by which this flux is maintained are rather controversial. This unique feature of the Himalayan weathering regime was first identified in pioneering work by Krishnaswami *et al* (1992). Given the strong signal in the major ion data characteristic of carbonate dissolution it was proposed initially that hydrothermally altered limestones in the Tethyan sedimentary sequence were responsible for the flux (Palmer and Edmond 1989). There is abundant evidence for fluid alteration in these rocks. The ancient Archean Indian plate is being underthrust to great depths beneath the south Asian margin in the collision zone. Heated formation waters could extract highly radiogenic Sr from unstable Rb-sites in these rocks and emplace it in recrystallized limestones higher in the section producing a source labile to weathering. However, there are two flaws in this argument: from thermodynamic considerations the Sr concentrations in these altered rocks should be low; it also seems unlikely that such alteration should be ubiquitous in the range as is required by the fluvial measurements.

An alternative hypothesis, based on geochronological work using Rb/Sr summarized by Harris (1995; figure 3b), is that during the partial melting of the underthrust crust which produces the Central Crys-

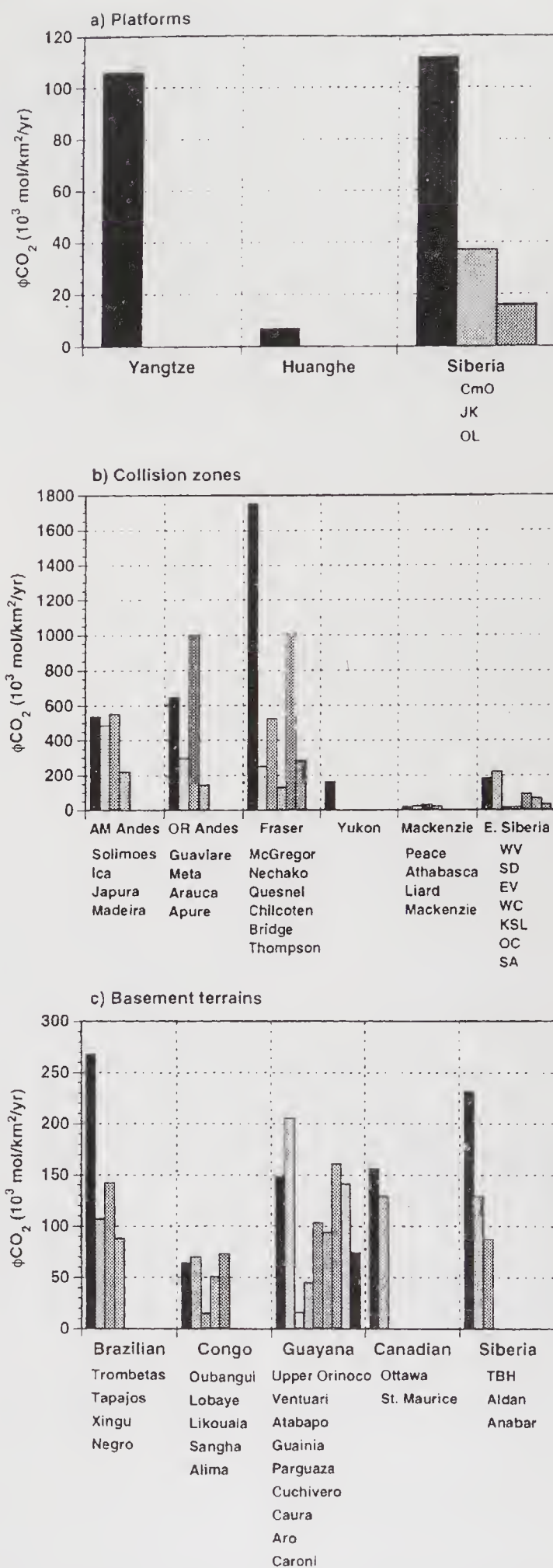


Figure 4. The calculated values for the CO_2 consumption rates by aluminosilicate weathering (ϕCO_2) from the various terrains from which data are available. Note the complete lack of a correlation with latitude for any of the environments studied to date (Huh *et al* 1998a,b; Huh and Edmond, in press).

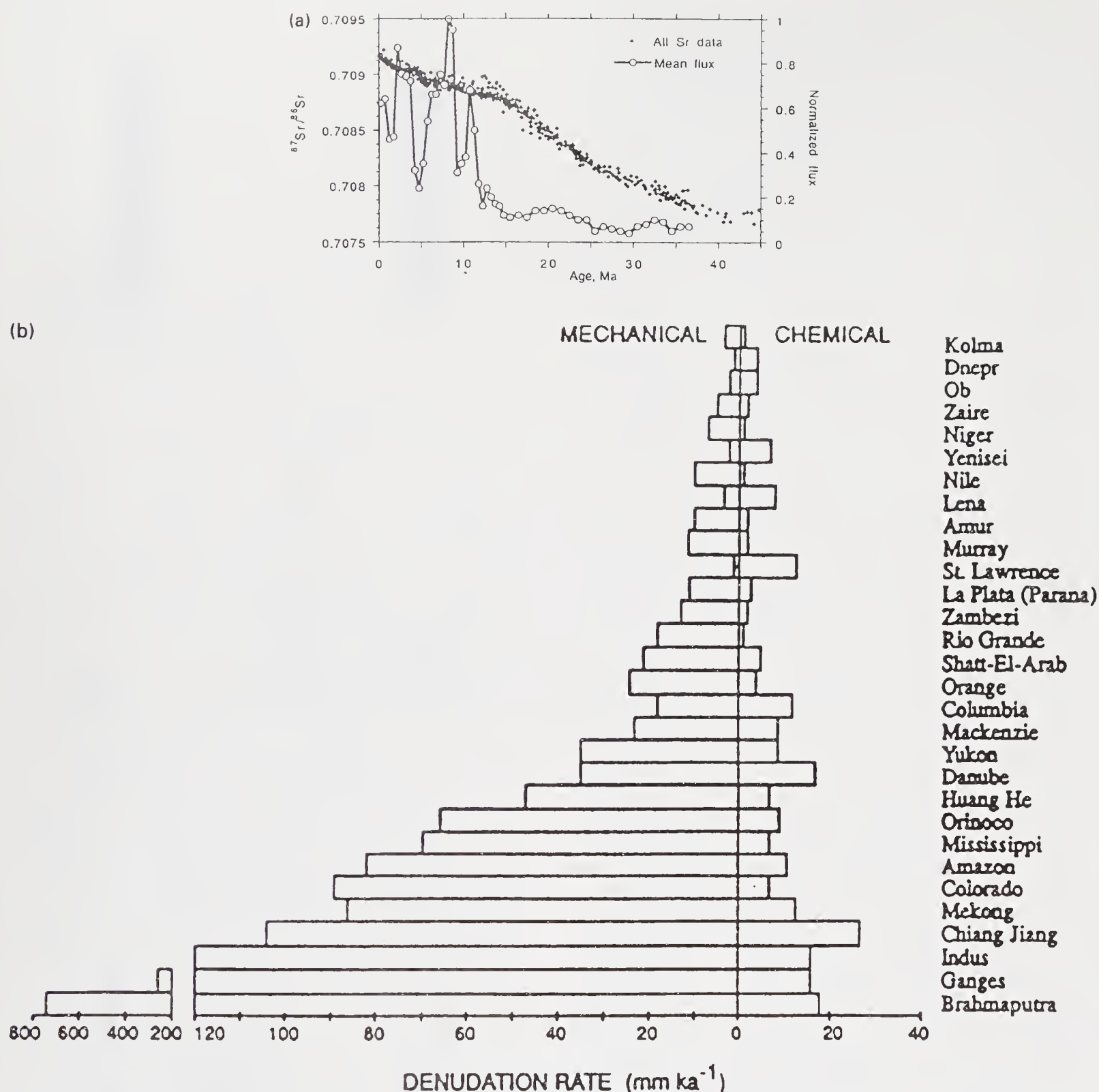


Figure 5. (a) The relationship between the evolution of the marine Sr isotopic ratio and the sedimentation rates in the Bengal Fan as determined by drilling (Rea 1992); (b) the global relationship between mechanical and chemical weathering (Summerfield and Hulton 1994).

talline Zone, characteristic of the *entire* Himalayan range, there was large-scale remobilization of radiogenic Sr from the refractory K-minerals into the labile Na/Ca-phases. Rapid weathering of these rocks following back-thrusting to very great elevations and subsequent erosional unroofing would then produce the observed Sr concentration and isotopic signatures.

Discrimination between these two conflicting end-member interpretations depends entirely on the field observations, geological and fluvial. Evidence for the metamorphic redistribution of radiogenic Sr within the crystalline rocks is abundant throughout the

range and can be considered secure. A comparable prevalence of meta-carbonates with high *concentrations* of radiogenic Sr has not been demonstrated. The most comprehensive survey is that reported by Singh *et al* (1998). They analyzed over 30 limestones from a variety of formations outcropping in the headwaters of the Ganga, Ghaghara and Indus rivers in the Lesser Himalaya. The isotope ratios cluster around ~ 0.714 with a few outliers with very high values, ~ 0.88 . In all cases the Sr concentrations are low. The associated fluvial ratios, mean ~ 0.75 , lie in the range reported for the crystalline rocks and are significantly more

radiogenic than the carbonate values. Assuming that *all* the Ca in the rivers is from carbonates then their contribution of Sr to the Ganga headwaters, based on the concentration-isotopic balance, is between 6 and 40% depending on the tributary. Clearly these are maximum values. By contrast Harris *et al* (1998), based on a few river samples from the Bhote Kosi, a minor tributary of the Ganga to the east of Nepal, calculated that the contribution of radiogenic Sr from carbonates is dominant. Their fluvial values ($n = 7$) fall in the range 0.7123–0.7693 with a non-flow weighted average of ~ 0.720 , normal for the range as a whole. Leachates from the bedload, presumed to represent carbonates, give a range of 0.7123–0.7920, average ~ 0.720 . Thus their values are comparable to those from the much larger data set analyzed by Singh *et al* (1998). Their leachate values are generally much lower than parallel measurements of the total bulk samples suggesting the possibility of “contamination” by the partial dissolution of the aluminosilicates.

In a different approach to the problem Richter *et al* (1992) combined the data from the Himalaya proper, but also the Tibetan Plateau, with estimates of the historical Sr fluxes based on measurements of the rates of accumulation of detrital sediments. The latter come from seismic and drilling data from the various foreland basins and deep sea fans. They assumed that 25% of the Sr associated with bulk mechanical erosion is released to solution. The impression of a relationship between mechanical and chemical denudation rates, while common, is not borne out by observation (Rea 1992; Summerfield and Hulton 1994; figure 5). In fact the chemical denudation rate of the Himalaya is at least a factor of 50 less than the mechanical. Reconstruction of the solute flux from the preserved detrital load is not possible with present understanding. In addition the Tibetan Plateau, the source of many of the rivers included in this particular study, Yangtze, Mekong, Irrawadi, Salween, is an elevated continental margin composed in the main of platform carbonates and evaporites; vide the $^{87}\text{Sr}/^{86}\text{Sr}$ for the Brahmaputra/Tsangpo in Tibet north of the range, ~ 0.710 , $2\mu\text{M}$. All of these values fall on the Wickman trend and, hence, are not capable of markedly influencing the oceanic ratio.

Intensive investigations of the sediments of the Bengal Fan (summarized in France-Lanord *et al* 1996 and Derry and France-Lanord 1997) demonstrate that the detrital flux has been predominantly from the Central Crystalline Belt for at least the last 20 m.y. The measured isotopic composition of Sr in the minerals of this huge sedimentary pile is consistent with this interpretation. Relating these observations to contemporary observations of the river fluxes is complicated by the fact that much of the chemical, as opposed to mechanical, weathering appears to occur during sediment storage in the subsiding foredeep (Sarin *et al* 1989; France-Lanord *et al* 1996). The

widespread occurrence of saline and alkaline soils in the Gangetic plain attests to this. This process probably leads to a sequestration of silica. However, comparing the available fluvial data for the Himalayan range at face value with those of the active margins of the Western Americas (Amazon, Orinoco, Frazer, Mackenzie, Yukon), it is clear that the chemical flux, *per length of arc*, is not remarkable (figure 4; Edmond and Huh 1997; Huh and Edmond 1998a, b; Huh and Edmond, in press). The dissolved load transport and CO_2 consumption rates calculated for the Himalayan rivers (Ganga, Brahmaputra, Indus) are comparable to those of the Americas (Edmond and Huh 1997). What is very distinctive is the flux of radiogenic Sr (figure 3), especially from the Ganga-Brahmaputra, for the reasons argued here.

3. Conclusions

This review of all the available data for fluvial Sr and its isotopic ratio ($\sim 1,000$ determinations) shows that there are two trends, the “normal” Wickman relation, essentially a mixing line, and the much more accentuated trend developed for the Himalayan rivers that drain the *Central Crystalline Belt*, not the Central Asian uplift as a whole. It therefore appears that, given the slow variation in time of the oceanic hydrothermal flux from the mantle and of the erosion/deposition of carbonates and evaporites, the major swings in the $^{87}\text{Sr}/^{86}\text{Sr}$ ratio of seawater must be the result of discrete geologic *events*. In the contemporary world only the crustal “subduction” of the ancient Indian Plate and the resulting remobilization of the radiogenic Sr developed in the refractory K-minerals into more labile Ca/Na aluminosilicate phases can explain the enormous rise in the isotopic ratio over the last 20 Ma. Determination of the “initial ratio” in the Ca/Na-feldspars in the roots of ancient collision zones, e.g. the Pan-African (figure 2), would help to substantiate this conclusion. In any case there is no such thing as “average crustal weathering” any more than there is “average continental crust”. Particular rocks weather, with their individual properties and in their changing environments. The marine $^{87}\text{Sr}/^{86}\text{Sr}$ evolution, and perhaps the $^{187}\text{Os}/^{186}\text{Os}$ record (Peucker-Ehrenbrink *et al* 1995), are the only tools presently available to unravel this profound problem.

Acknowledgements

This paper is dedicated to the memory of Aruna Lal as an early pioneer of women in the physical sciences not only in India, where her role was very important, but even in California, and to Professor Lal himself and to the many colleagues that he has inspired at TIFR and PRL. Their collective friendship and complete

generosity to us and their intellectual influence upon us, especially JME, continues to be profound. Over the decades we have had a hard time scampering to keep up. This work was supported by the National Science Foundation grants EAR-9304843, EAR-9627613 and OCE-9616599.

References

- Albarède F and Michard A 1987 Evidence for slowly changing $^{87}\text{Sr}/^{86}\text{Sr}$ in runoff from freshwater limestones of southern France; *Chem. Geol.* **64** 55–65
- Armstrong R L 1971 Glacial erosion and the variable isotopic composition of strontium in seawater; *Nature* **230** 132–133
- Berner R A and Caldeira K 1997 The need for mass balance and feedback in the geochemical carbon cycle; *Geology* **25** 955–956
- Berner R A and Rye D M 1992 Calculation of the Phanerozoic strontium isotope record of the oceans from a carbon cycle model; *Am. J. Sci.* **292** 136–148
- Blum J D, Erel Y and Brown K 1994 $^{87}\text{Sr}/^{86}\text{Sr}$ ratios of Sierra Nevada stream waters: Implications for relative mineral weathering rates; *Geochim. Cosmochim. Acta* **58** 5019–5025
- Brass G W 1976 The variation of marine $^{87}\text{Sr}/^{86}\text{Sr}$ ratio during Phanerozoic time: interpretation using a flux model; *Geochim. Cosmochim. Acta* **40** 721–730
- Burke W H, Denison R E, Heatherington E A, Koepnick R B, Nelson H F and Otto J B 1982 Variation of seawater $^{87}\text{Sr}/^{86}\text{Sr}$ throughout Phanerozoic time; *Geology* **10** 516–519
- Burns S J, Haudenschild U and Matter A 1994 The strontium isotopic composition of carbonates from the Late Precambrian (~561–540 Ma) Huqf Group of Oman; *Chem. Geol.* **111** 269–282
- Cameron E M, Hall G E M, Veizer J and Krouse H R 1995 Isotopic and elemental hydrogeochemistry of a major river system: Fraser River, British Columbia, Canada; *Chem. Geol.* **122** 149–169
- Derry L A and France-Lanord C 1997 Himalayan weathering and erosion fluxes: climate and tectonic controls; In, *Tectonic Uplift and Climate Change* (ed) W F Ruddiman (Plenum Press) pp. 289–312
- Edmond J M and Huh Y 1997 Chemical weathering yields from basement and orogenic terrains in hot and cold climates; In, *Tectonic Uplift and Climate Change* (ed) W F Ruddiman, Plenum Press, pp. 329–351
- Edmond J M, Palmer M R, Measures C I, Grant B and Stallard R F 1995 The fluvial geochemistry and denudation rate of the Guayana Shield in Venezuela, Colombia and Brazil; *Geochim. Cosmochim. Acta* **59** 3301–3325
- Fisher R and Stueber A M 1976 Strontium isotopes in selected streams within the Susquehanna River basin; *Water Resources Res.* **12** 1061–1068
- France-Lanord C, Derry L and Michard A 1996 Evolution of the Himalaya since Miocene time: isotopic and sedimentological evidence from the Bengal Fan; In *Himalayan Tectonics* (eds) P J Treloar and M P Searle, (Geological Society Special Publication) pp. 603–621
- Gast P W 1955 Abundance of ^{87}Sr during geologic time; *Geol. Soc. Am. Bull.* **66** 1449–1454
- Goldstein S J and Jacobsen S B 1987 The Nd and Sr isotopic systematics of river-water dissolved material: Implications for the sources of Nd and Sr in seawater; *Chem. Geol.* **66** 245–272
- Grotzinger J P 1989 Facies and evolution of Precambrian carbonate depositional systems: Emergence of the modern platform archetype; In *Controls on Carbonate Platform and Basin Development*, (The Society of Economic Paleontologists and Mineralogists) pp. 79–106
- Harris N 1995 The significance of weathering Himalayan metasediments and leucogranites for the Sr-isotope evolution of seawater during the Early Miocene; *Geology* **23** 795–798
- Harris N, Bickle M, Chapman H, Fairchild I and Bunbury J 1998 The significance of Himalayan rivers for silicate weathering rates: evidence from the Bhote Kosi tributary; *Chem. Geol.* **144** 205–220
- Hodell D A, Mead G A and Mueller P A 1990 Variations in the strontium isotopic composition of seawater (8 Ma to present): Implications for chemical weathering rates and dissolved fluxes to the oceans; *Chem. Geol.* **80** 291–307
- Huh Y and Edmond J M 1998 The fluvial geochemistry of the rivers of Eastern Siberia III: Tributaries of the Lena and Anabar draining the basement terrain of the Siberian Craton and the Trans-Baikal Highlands; *Geochim. Cosmochim. Acta* (in press)
- Huh Y, Tsoi M-Y, Zaitsev A and Edmond J M 1998a The fluvial geochemistry of the rivers of Eastern Siberia I: Tributaries of the Lena River draining the sedimentary platform of the Siberian Craton; *Geochim. Cosmochim. Acta* **62** 1657–1676
- Huh Y, Panteleyev G, Babich D, Zaitsev A and Edmond J M 1998b The fluvial geochemistry of the rivers of Eastern Siberia II: Tributaries of the Lena, Omoloy, Yana, Indigirka, Kolyma, and Anadyr draining the collisional/accretionary zone of the Verkhoyansk and Cherskiy ranges; *Geochim. Cosmochim. Acta* **62** 2053–2075
- Hunt J M 1979 *Petroleum Geochemistry and Geology* (Freeman, San Francisco), pp. 617
- Ingram B L and Sloan D 1992 Strontium isotopic composition of estuarine sediments as paleosalinity-paleoclimate indicator; *Science* **255** 68–72
- Johnson M J, Stallard R F and Meade R H 1988 First-cycle quartz arenites in the Orinoco River basin, Venezuela and Colombia; *J. Geol.* **96** 263–277
- Jones C E 1994 Strontium isotopic variations in Jurassic and Cretaceous seawater; *Geochim. Cosmochim. Acta* **58** 3061–3074
- Krishnaswami S, Trivedi J R, Sarin M M, Ramesh R and Sharma K K 1992 Strontium isotopes and rubidium in the Ganga-Brahmaputra river system: Weathering in the Himalaya, fluxes to the Bay of Bengal and contributions to the evolution of oceanic $^{87}\text{Sr}/^{86}\text{Sr}$; *Earth Planet. Sci. Lett.* **109** 243–253
- Négre P, Allègre C J, Dupré B and Lewin E 1993 Erosion sources determined by inversion of major and trace element ratios and strontium isotopic ratios in river water: The Congo Basin case; *Earth Planet. Sci. Lett.* **120** 59–76
- Palmér M R and Edmond J M 1989 The strontium isotope budget of the modern ocean; *Earth Planet. Sci. Lett.* **92** 11–26
- Palmer M R and Edmond J M 1992 Controls over the strontium isotope composition of river water; *Geochim. Cosmochim. Acta* **56** 2099–2111
- Pande K, Sarin M M, Trivedi J R, Krishnaswami S and Sharma K K 1994 The Indus river system (India-Pakistan): Major-ion chemistry, uranium and strontium isotopes; *Chem. Geol.* **116** 245–259
- Peterman Z E, Hedge C E and Tourtelot H A 1970 Isotopic composition of strontium in seawater throughout Phanerozoic time; *Geochim. Cosmochim. Acta* **34** 105–120
- Peucker-Ehrenbrink B, Ravizza G and Hofmann A W 1995 The marine $^{187}\text{Os}/^{186}\text{Os}$ record of the past 80 million years; *Earth Planet. Sci. Lett.* **130** 155–167
- Rea D K 1992 Delivery of Himalayan sediment to the Northern Indian Ocean and its relation to global climate, sea level, uplift and seawater strontium; *Geophys. Monogr.* **70** 387–402

- Richter F M, Rowley D B and DePaolo D J 1992 Sr isotope evolution of seawater: the role of tectonics; *Earth Planet. Sci. Lett.* **109** 11–23
- Sarin M M, Krishnaswami S, Dilli K, Somayajulu B L K and Moore W S 1989 Major ion chemistry of the Ganga-Brahmaputra river system: Weathering processes and fluxes to the Bay of Bengal; *Geochim. Cosmochim. Acta* **53** 997–1009
- Singh S K, Trivedi J R, Pande K, Ramesh R and Krishnaswami S 1998 Chemical and strontium, oxygen, and carbon isotopic compositions of carbonates from the Lesser Himalaya: Implications to the strontium isotope composition of the source waters of the Ganga, Ghaghara, and the Indus rivers; *Geochim. Cosmochim. Acta* **62** 743–755
- Smalley P C, Higgins A C, Howarth R J, Nicholson H, Jones C E, Swinburne N H M and Bessa J 1994 Seawater Sr isotope variations through time: a procedure for constructing a reference curve to date and correlate marine sedimentary rocks; *Geology* **22** 431–434
- Summerfield M A and Hulton N H 1994 Natural controls of fluvial denudation rates in major world drainage basins; *J. Geophys. Res.* **99** 13871–13883
- Sun S Q 1994 A reappraisal of dolomite abundance and occurrence in the Phanerozoic; *J. Sed. Res.* **A64** 396–404
- Trivedi J R, Pande K, Krishnaswami S and Sarin M M 1995 Sr isotopes in rivers of India and Pakistan: A reconnaissance study; *Curr. Sci.* **69** 171–178
- UNESCO 1979 Discharge of the Selected Rivers of the World, Imprimeries Louis-Jean, Gap, France
- Veizer J and Compston W 1974 $^{87}\text{Sr}/^{86}\text{Sr}$ composition of seawater during the Phanerozoic; *Geochim. Cosmochim. Acta* **38** 1461–1484
- Veizer J and Compston W 1976 $^{87}\text{Sr}/^{86}\text{Sr}$ in Precambrian carbonates as an index of crustal evolution; *Geochim. Cosmochim. Acta* **40** 905–914
- Wadleigh M A, Veizer J and Brooks C 1985 Strontium and its isotopes in Canadian rivers: Fluxes and global implications; *Geochim. Cosmochim. Acta* **49** 1727–1736
- Walker J C G, Hays P B and Kasting J F 1981 A negative feedback mechanism for the long-term stabilization of Earth's surface temperature; *J. Geophys. Res.* **86** 9776–9782
- Webster P J 1994 The role of hydrological processes in ocean-atmosphere interactions; *Rev. Geophys.* **32** 427–476
- Wickman F E 1948 Isotope ratios, a clue to the age of certain marine sediments; *J. Geol.* **56** 61–66
- Yang C, Telmer K and Veizer J 1995 Chemical dynamics of the St. Lawrence riverine system: $\delta \text{D}_{\text{H}_2\text{O}}$, $\delta^{18}\text{O}_{\text{H}_2\text{O}}$, $\delta^{13}\text{C}_{\text{DIC}}$, $\delta^{34}\text{S}_{\text{Sulfate}}$, and dissolved $^{87}\text{Sr}/^{86}\text{Sr}$; *Geochim. Cosmochim. Acta* **60** 851–866
- Zhang J, Takahashi K, Wushiki H, Yabuki S, Xiong J and Masuda A 1995 Water geochemistry of the rivers around the Taklimakan Desert (NW China): Crustal weathering and evaporation processes in arid land; *Chem Geol.* **119** 225–237

Ice-core records of global climate and environment changes

ROBERT J DELMAS

Laboratoire de Glaciologie et Géophysique de l'Environnement du CNRS, associated to Université Joseph Fourier (Grenoble-1), B.P. 96, 38402 Saint Martin d'Hères-Cedex, France
e-mail: delmas@glaciog.ujf-grenoble.fr

Precipitation accumulating on the Greenland and Antarctic ice sheets records several key parameters (temperature, accumulation, composition of atmospheric gases and aerosols) of primary interest for documenting the past global environment over recent climatic cycles and the chemistry of the pre-industrial atmosphere. Several deep ice cores from Antarctica and Greenland have been studied over the last fifteen years. In both hemispheres, temperature records (based on stable isotope measurements in water) show the succession of glacial and interglacial periods. However, detailed features of the climatic stages are not identical in Antarctica and in Greenland. A tight link between global climate and greenhouse gas concentrations was discovered, CO₂ and CH₄ concentrations being lower in glacial conditions by about 80 and 0.3 ppmv, respectively, with respect to their pre-industrial levels of 280 and 0.65 ppmv. Coldest stages are also characterized by higher sea-salt and crustal aerosol concentrations. In Greenland, contrary to Antarctica, ice-age ice is alkaline. Gas-derived aerosol (in particular, sulfate) concentrations are generally higher for glacial periods, but not similar in both the hemispheres. Marine and continental biomass-related species are significant in Antarctica and Greenland ice, respectively. Finally, the growing impact of anthropogenic activities on the atmospheric composition is well recorded in both polar regions for long-lived compounds (in particular greenhouse gases), but mostly in Greenland for short-lived pollutants.

1. Introduction

Year after year, over millennia and millennia, snow has been accumulating on the Antarctic and Greenland ice sheets. By compaction, deposited snow progressively transforms into firn and ultimately to ice (figure 1). During this process, an array of various atmospheric parameters are recorded, forming a unique archive of great value for climatic and environmental studies (e.g. Delmas 1992). Information preserved in polar ice caps can be retrieved by ice core drilling and analysis. Vostok, GRIP (GReenland Ice core Project) and GISP2 (Greenland Ice Sheet Project 2) have been the most famous recent operations carried out by the international community of glaciologists, and a wealth of climate-related data have been obtained from several ice cores drilled during the past two decades at various polar sites (figure 2).

Several measurements are performed on the ice cores. Palæotemperature reconstruction is based on water isotope fractionation processes taking place in the atmospheric water cycle (Craig 1961; Dansgaard 1964). It has been demonstrated experimentally that the "isotopic temperature" (isotope composition of ice) reflects mainly the mean annual temperature at the precipitation site. Water stable isotopes measured on ice cores are therefore used as proxies for palæotemperature.

Secondly, past atmospheric gas composition can be obtained by analyzing the air bubbles entrapped in ice during the slow transformation of firn into ice. This process occurs typically between about 50 and 120 meter depth (depending on accumulation rate and temperature, Raynaud *et al* 1993). For long-lived gases like greenhouse gases, their measured composition in the ice can be taken as their global value.

Keywords. Palæoclimatology; ice core; Antarctica; Greenland; global change.

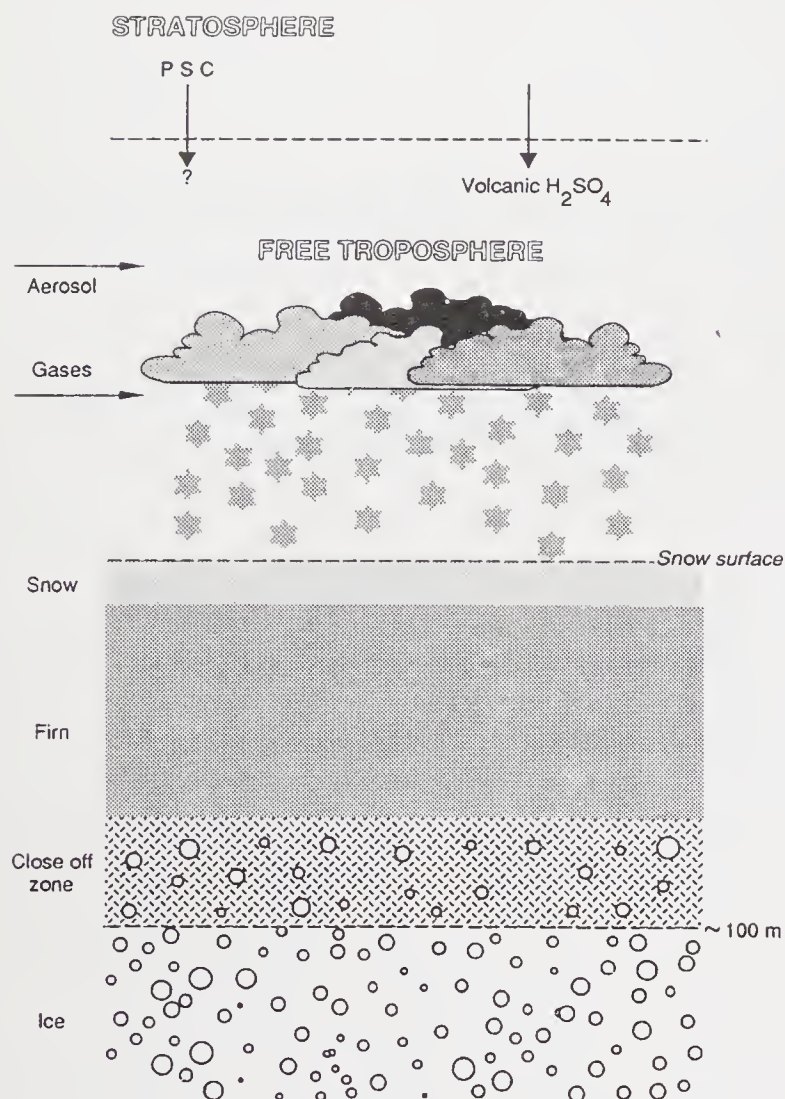


Figure 1. Schematic graph showing the formation of ice records. Atmospheric particulate impurities (aerosols) are mainly scavenged at cloud level and "wet-deposited" to the ground. Post-deposition effects can modify their initial composition. Firn is a porous material formed by sintering of the snow crystals. The transformation of firn into ice is a slow process which takes centuries to millennia, depending on local temperature and snow accumulation rate. During this process air bubbles are entrapped. PSC = Polar Stratospheric Cloud. (From Delmas 1992.)

Thirdly, atmospheric particulate species (aerosols) and some soluble gases, mostly collected at cloud level by the snowflakes (or also possibly dry-deposited on the ground), are also buried together with the snow and ice layers and stored nearly unchanged in the polar ice sheets for several thousand years. However, it should be stressed that caution must be exercised when interpreting ice core chemical data to derive atmospheric information, due to possible perturbations during their transfer to the ice. This caution is valid for all the three kinds of information mentioned above.

After an introduction to glaciological methods, this paper will review major information obtained from ice cores about

- long-term natural variations of the global environment,
- anthropogenic atmospheric pollution. Ice cores document a wide variety of atmospheric parameters for

various climatic conditions. On the basis of ice core data, it is therefore possible to compare man-induced and climate-induced atmospheric composition changes. We will see that in many cases, the anthropogenic effect exceeds the natural fluctuation range. For instance, the present-day atmospheric levels of two major greenhouse gases (CO_2 and CH_4) are unprecedented over the last 400 ka. This may be the most important information provided, up to now, to Global Change science by polar ice core researchers.

2. Methods

2.1 Isotope measurements

Mass-spectroscopic measurements of thousands of ice samples are necessary to obtain detailed palæotemperature profiles. Water isotope (HDO and $(\text{H}_2^{18}\text{O})$ concentrations (called δD or $\delta^{18}\text{O}$) are expressed in permil units with respect to SMOW reference (SMOW = Standard Mean Ocean Water). For years, the empirical linear relationships linking δD (or $\delta^{18}\text{O}$) of present polar snow to mean annual temperature of the study area have been used to reconstruct palæotemperatures. The theoretical basis of the method was first established by Dansgaard (1964) and later regularly improved by various authors (Lorius and Merlivat 1977; Dansgaard and Oeschger 1989). Deuterium excess d ($d = \delta\text{D} - 8\delta^{18}\text{O}$, according to Dansgaard 1964) is a parameter related to the geographical location where water vapor originated. The validity of using the observed current relationships for palæotemperature reconstruction was supported for years by comparing various other proxy data with ice-core results. During the last three decades, most deep ice-core isotope profiles have been interpreted by climatologists in terms of past temperature records on the basis of simple isotopic models. However, most recently, temperature measurements in the GRIP bore hole (Johnsen *et al* 1995a) showed that the temperature warming when passing from LGM (Last Glacial Maximum) to modern climate conditions was probably double (i.e. about 20°C) than previously estimated from isotope measurements. GCM (General Circulation Model) analysis is currently being used to obtain a better estimate of glacial/interglacial temperature changes from Greenland and Antarctic ice cores (Krinner *et al* 1997). In the wake of important palæoclimatic data obtained from the recent Greenland and Antarctic deep ice cores, Jouzel *et al* (1997) have assessed the validity of temperature reconstruction from water isotopes in ice cores. Despite disagreements among some data sets, calculation estimates and modelling, the authors conclude that the use of the isotope palæothermometer appears justified.

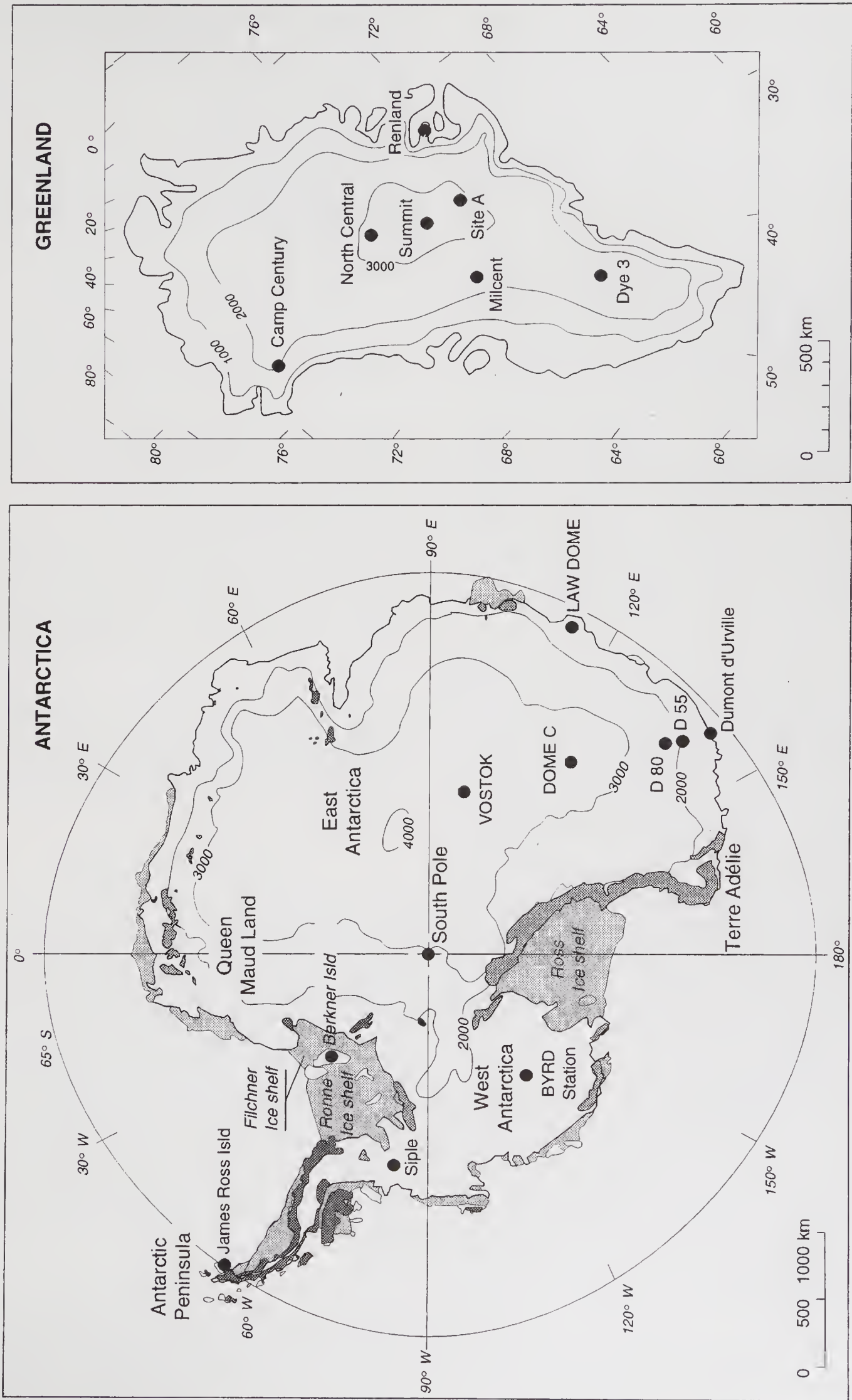


Figure 2. Map of the two major polar ice sheets (Greenland and Antarctica) with indication of the most important drilling sites.

For the measurement of radioactive isotopes produced by atmospheric nuclear tests, low level α , β , or γ counting techniques have to be used. Accelerator Mass Spectrometry (AMS) technology made it possible to obtain detailed ^{10}Be profiles from just a few kg (or even less) ice samples. ^{10}Be data are used for calculating past snow accumulation rates and solar cycle fluctuations (see McHargue and Damon 1991, for a review).

2.2 Electric conductivity measurements (ECM)

It is worth mentioning about the ECM of ice cores. This nondestructive technique, which has to be carried out at low temperatures ($< -15^\circ\text{C}$), is a good proxy of the acidity of the ice (Hammer 1980). It is most frequently used in the field for detecting acid spikes of volcanic origin and for discriminating along deep ice cores the glacial (alkaline in Greenland, slightly acidic in the Antarctic) from the acidic interglacial ice layers. It is a direct current (dc) method. More recently, an ac method, called the dielectric profiling technique (DEP), has been developed by Moore and Paren (1987). It responds both to the acid and salt content of the ice (Moore *et al* 1989).

2.3 Measurements of trace constituents

Polar ice is an extremely pure material and its analysis needs great care and sophisticated analytical techniques. The total amount of gas which can be extracted from polar ice is of the order of 0.1 ml g^{-1} at STP, less when the ice was formed at high elevation sites, more at low elevation. Concentrations of major soluble ions (e.g. sulfate or nitrate) are frequently in the micro or sub-micro equivalent per liter range. In most cases, the use of clean rooms for sub-sampling operations is essential for obtaining reliable data. Gas entrapped in air bubbles can be recovered either by melting ("wet method") or by crushing ("dry method") the ice. 50 g-ice samples (or less) are sufficient for gas chromatography measurements of greenhouse gases. Methods for recovering and analyzing palæo-atmosphere samples for CO_2 have been critically reviewed recently by Wilson and Long (1997).

For major ionic species down to the sub-ppb level, ion chromatography is most commonly used. Atomic absorption, and more recently ICP-MS, allows one to measure ppt levels of elements. Microparticle counting is used to determine the insoluble fraction. Continuous flow measurement methods suitable for rapid field determinations of a few soluble species (calcium, ammonium, hydrogen peroxide, formaldehyde) have been developed recently (Fuhrer *et al* 1993; Sigg *et al* 1994).

2.4 Establishing the ion balance of soluble impurities

The ice samples have generally to be melted before being analysed. Therefore the initial chemical com-

pounds from which the ions originate are difficult to establish. In practice some assumptions can be made and it is possible to learn about their sources provided that all ionic species have been determined. When a great number of samples is measured, the interpretations become more certain.

The ion balance (i.e. Σ cations = Σ anions, concentrations expressed in $\mu \text{ eq. l}^{-1}$) of pre-industrial polar precipitation can be written, if we consider only major ions:

$$\begin{aligned} &[\text{H}^+] + [\text{Na}^+] + [\text{Mg}^{++}] + [\text{Ca}^{++}] + [\text{NH}_4^+] \\ &= [\text{SO}_4^{--}] + [\text{NO}_3^-] + [\text{Cl}^-] + [\text{HCO}_3^-]. \end{aligned} \quad (1)$$

This equation is useful to interpret the chemical composition of Holocene Antarctic ice. Additional ions may have to be introduced in equation (1), in particular for Greenland snow: in present pre-industrial climatic conditions, light carboxylic acids may contribute to ice acidity whereas, for glacial ages, carbonates contributed by crustal dust are overwhelming in the ion balance of the ice, which is, in this case, alkaline.

In any case, for present times, the results obtained from Antarctica and Greenland ice sheets demonstrate clearly that the chemistry of snow is not fundamentally different in both polar regions: gas-derived acids are dominant, H_2SO_4 in Antarctica, HNO_3 in Greenland.

2.5 Dating

The age of the ice is a key parameter in palæoclimatic studies. Generally, the accuracy of the dating decreases with depth. Three methods, frequently in combination, are commonly used to date the snow and ice layers (Hammer 1989).

2.5.1 Seasonal variations

The concentrations of most species (except gases) in snow exhibit marked seasonal variations which can be used for dating purposes. It is the case of water stable isotopes, but also of chemical species such as acids, hydrogen peroxide, sea salt, dust etc. However, due to the possible reworking of deposited snow by wind and to the migration processes which may affect soluble species in the firn layers, seasonal variations are sometimes blurred. Moreover, due to thinning of ice layers, they tend to vanish progressively with depth. In this respect, seasonal variations of insoluble dust survive the longest. In any case, seasonal variations are difficult to observe at sites with low accumulation rates ($< 5 \text{ g cm}^{-2} \text{ a}^{-1}$) and the method therefore fails in central Antarctic areas.

2.5.2 Reference horizons

Special levels linked to large volcanic eruptions (Hammer 1980), atmospheric nuclear tests or even natural phenomena (e.g. ^{10}Be peaks), are frequently used as time markers (Stauffer 1989). The limit and

the precision of the method are dictated by the knowledge of the 'age' of the event horizons. This method is particularly useful to compare the time scale of deep ice cores.

2.5.3 Ice modelling

Deep ice cores are generally dated using steady state models of the ice sheets which provide an approximate depth-age relationship (Reeh 1989). Over the Holocene (i.e. the last 10,000 years), the accuracy of the method is satisfactory, but glaciologists are less confident in the dating of ice-age ice, in particular owing to the uncertainty in past snow accumulation rates (the key parameter for central polar area models). For instance, the two-dimensional ice flow model used for the Vostok ice core provided a time scale with an uncertainty of 20 ka at 220 ka BP (Jouzel *et al* 1993).

When the accumulation is high as in Greenland, dating is easier. A comparison of several dating methods (visual stratigraphy, oxygen isotope variations, ECM, volcanic signals, laser-light scattering from dust and major ion chemistry) is given by Meese *et al* (1997) for establishing the depth-age scale of the recent GISP 2 ice core. The ice at 2800 m is dated at 110 ka B.P., with an estimated error ranging from 1 to 10% in the top 2500 m and averaging 20% below.

Note that the age of the air contained in the bubbles is markedly younger than the age of the ice in which it is enclosed, since bubble close-off occurs in depth, well after snow deposition, as earlier mentioned. Dating of air entrapped in polar ice is therefore a complex issue (e.g. Raynaud *et al* 1993).

3. Natural changes

3.1 Vostok studies

The study of polar ice has given a new insight into the past history of global climate changes over the past few hundred thousand years. In particular, measurements on the Vostok ice core has lead to important advances in understanding past climate and environmental changes over glacial-interglacial cycles. In this respect, the initial temperature profile of Vostok Station, spanning a full glacial-interglacial cycle and later improved and extended, can be used as a pattern (Lorius *et al* 1985).

Drillings were initiated in 1970 by the Arctic and Antarctic Research Institute of Leningrad, USSR at this East Antarctic site (78° 28' S, 106° 48' E, elevation: 3490 m, mean annual temperature: -55°C). In the ensuing three decades, the drilling has considerably progressed and the operation has become international (Russian-American-French cooperation). It is estimated that presently about 300 m of ice are still to be drilled, but the lake detected under the ice sheet at this location prevents the completion of the drilling to

the bed rock. From 160 ka studied and published in 1987 (Jouzel *et al* 1987; Genthon *et al* 1987), the records were first extended in 1993 back to 220 ka (Jouzel *et al* 1993; Jouzel *et al* 1996), which represents two full ice ages and even the end of the preceding interglacial. The analyses already carried out on the recent cores indicate that the Vostok ice record is now covering four full glacial and interglacial climatic stages, i.e. about 426 ka (Petit *et al* 1997). The chronology correlates satisfactorily with oceanic records.

The 1987 Vostok record offered for the first time the opportunity to demonstrate the link between continental temperature and the orbital geometry of the Earth: the role of astronomical forcing as being the initial cause of the pleistocene glacial-interglacial cycles ("Milankovitch theory", Berger 1988) was fully confirmed. In particular, spectral analysis demonstrates that the Vostok isotope record is dominated, aside from the 100 ka eccentricity cycle, by a strong signal of about 40 ka, corresponding to precession of the equinoxes. The axial tilt cycle (slightly above 20 ka) was also observed.

Data show that interglacial periods have a relatively short duration in comparison to glacial ages. During the latter, temperature fluctuates significantly in accordance with the various cycles mentioned earlier. The penultimate glacial period (PGP), lasting from about 140 to 200 ka B.P., appears to have been more uniformly cold than the last glacial maximum (LGM). The strong correlation between both CO₂ and CH₄ concentrations and climate over the last

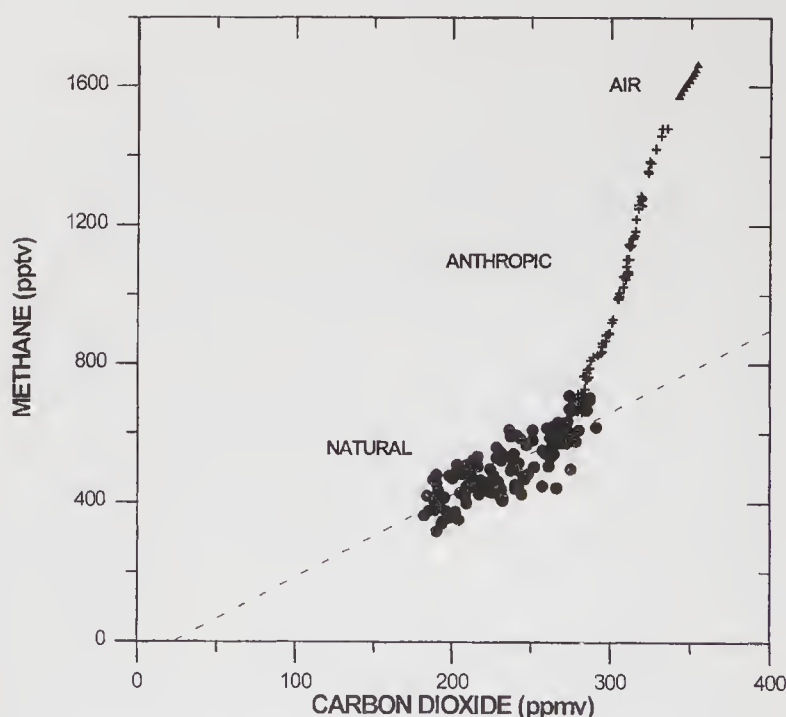


Figure 3. Co-variability of carbon dioxide and methane atmospheric concentrations in pre- and industrial conditions as reconstructed from Antarctic ice cores (solid circles: Vostok data; crosses: Law Dome data). Recent atmospheric data from Amundsen-Scott Station (South Pole; solid triangles) are also reported. Stippled straight line has been calculated using Vostok data only.

glacial-interglacial cycle (Barnola *et al* 1987; Chappellaz *et al* 1990) is remarkable. CO₂ and CH₄ concentrations were found to be low (190–200 and 0.35 ppmv, respectively) in cold stages and high (260–280 and 0.65 ppmv, respectively) in the warm stages. These figures have been roughly confirmed from the recently extended Vostok records (Barnola *et al* 1991; Raynaud *et al* 1993; Jouzel *et al* 1996): CO₂ concentrations are low from 140 to 190 ka B.P., with values similar to those observed for the second part of LGM. Also similar, or even sometimes slightly lower than during the LGM, the lowest methane concentrations are observed only for the last stage of PGP. A linear correlation links pre-industrial CO₂ and CH₄ concentrations over the entire study period (figure 3).

A major feature of the ice-age ice at Vostok is its high content of continental dust and sea-salt aerosol as shown by the concentration patterns of insoluble dust particles (Petit *et al* 1990), sodium and calcium (Legrand *et al* 1988). This effect had already been reported a decade earlier at other polar sites (Cragin *et al* 1977). The changes measured in ice depend on several factors (emission rates, meridional transport, atmospheric transformation, deposition mechanism) which all may have changed in the past in relation with climate. GCM simulations are now frequently used to interpret the experimental data (Genthon and Armengaud 1995).

In the Southern Hemisphere, the atmospheric circulation has not been so dramatically modified as in the Northern Hemisphere (see below). Most recent investigation (Basile *et al* 1997) shows that over the last glacial and interglacial periods, the dominant source of dust for East Antarctica was always the southern part of South America, as suggested previously by Delmas and Petit (1994). The geographical extent of this source was strongly modulated by sea-level changes. Despite the high inputs of crustal dust in glacial conditions, Vostok ice remained acidic all along the study time periods (Legrand *et al* 1988).

Concentrations of ions related to the major global S and N cycles have been determined. Nitrate deposition in Vostok snow increased during glacial periods in relation with crustal dust inputs (Legrand *et al* 1988). Regarding the sulfur cycle, the authors concluded from ice core data that marine biogenic DMS (dimethylsulphide) emissions around Antarctica were enhanced during cold climatic stages (Legrand *et al* 1991, 1992a), a suggestion which needs further confirmation.

The two marked peaks of ¹⁰Be concentrations around 35 and 60 ka B.P. were interpreted as reflecting changes in global production of cosmogenic radioisotopes (Raisbeck *et al* 1987).

3.2 GRIP and GISP information

GRIP (Greenland Ice core Project, European; Stauffer 1993) and GISP2 (Greenland Ice Sheet Project,

American) started both in 1989 at Summit, central Greenland. The drilling reached the bedrock in summer 1992 and 1993, respectively.

The isotope measurements from both the ice cores confirmed that the climate of the Northern Hemisphere was frequently unstable (Dansgaard *et al* 1993; GRIP Project Members 1993). Rapid variations are observed for glacial ages and climatic transitions (Johnsen *et al* 1992). For instance, 22 interstadials were found over the last glacial period (Dansgaard *et al* 1993). More surprisingly, drastic climate variations were also observed for part of the last interglacial (called “Eemian” 140–110 ka B.P., a relatively warm period, often suggested as an analog to our present climate after a greenhouse warming). However, this climatic interpretation of the variations observed in GRIP for interglacial climatic conditions became questionable following the publication of the results obtained in GISP2. Both data sets are in excellent agreement up to 2700–2750 m depth, but for the bottom 10% of the core isotope records differ markedly (Taylor *et al* 1993; Grootes *et al* 1993; Jouzel *et al* 1994) (figure 4). It is probable that these differences result from flow deformation occurring in ice layers located in the last hundred meters, close to the bedrock (Johnsen *et al* 1995b).

GRIP and Vostok time scales correlate very satisfactorily over the last ~ 100,000 years. The agreement is less convincing for the older climatic periods due to the glaciological disturbances mentioned earlier. In spite of all the difficulties encountered on the deepest part of these two recent Greenland cores, these analyses have provided a wealth of high quality palaeoenvironmental information gathered from the upper hundreds of meters. In addition to climatic phenomena, GRIP and GISP results revealed the relative importance of continental biological processes for atmospheric composition in comparison with Antarctica where the influence of marine biogenic activity is dominant. Measurements show that emissions from boreal forest fires and vegetation play a major role in atmospheric chemistry (Legrand *et al* 1992b, 1995). Continuous measurements of ammonium along the core revealed long-term changes of ammonia emissions from soil and vegetation in the Northern Hemisphere (Fuhrer *et al* 1996). Temperature changes, identified primarily by isotope measurements, are therefore reinforced by the additional information linked to biogeochemical cycles. This is particularly important in the Northern Hemisphere where seesaw processes are observed. The concentration of compounds like methane, which depends mainly on soil humidity (Blunier *et al* 1995), astonishingly mimics temperature variations (Chappellaz *et al* 1993, figure 5). The concentration of formate seems to be closely linked with the extent of vegetation at mid to high northern latitudes (Legrand and De Angelis 1995).

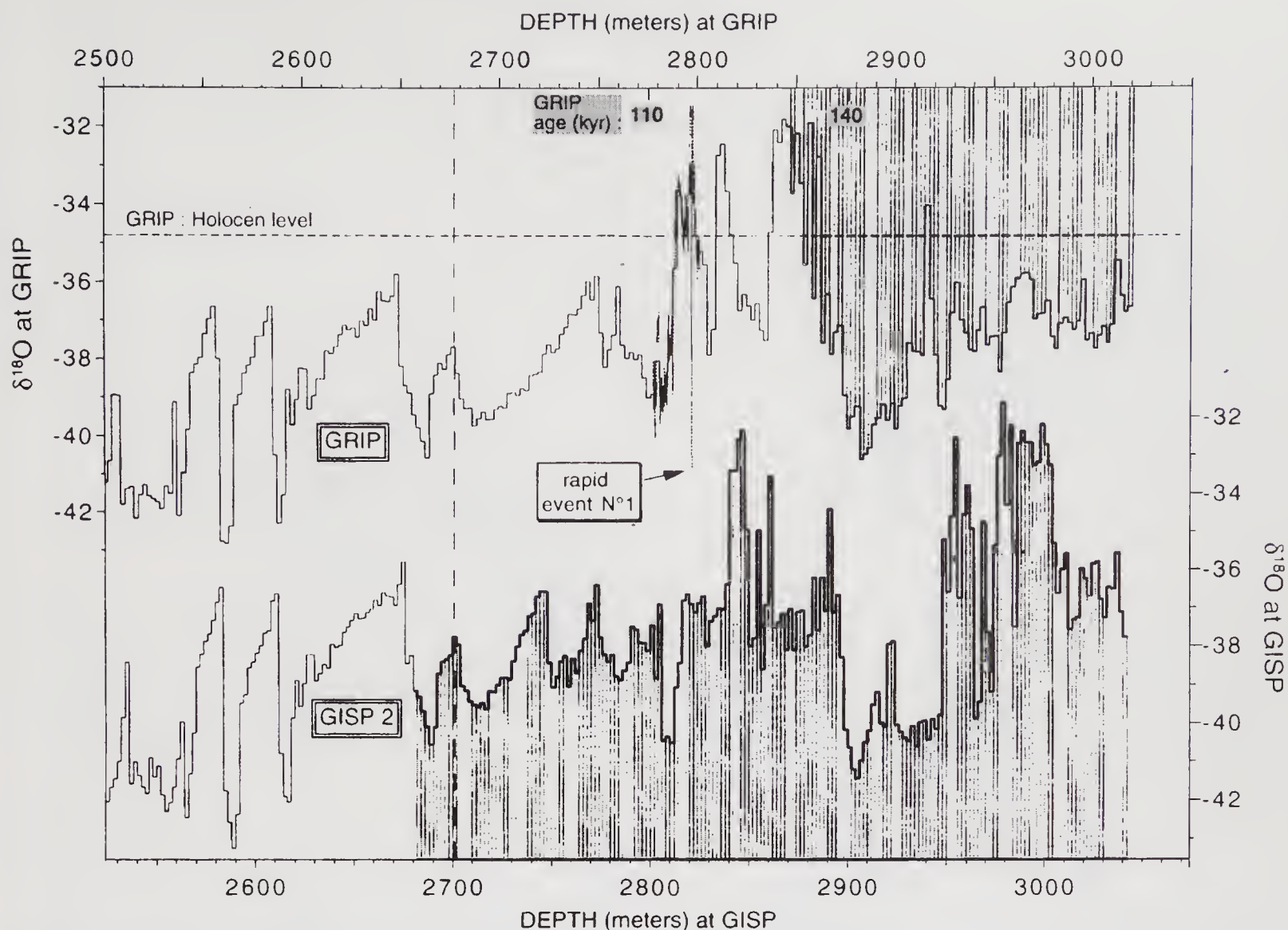


Figure 4. Comparison of the water isotope records in the deepest part of GRIP and GISP 2 ice cores (from Jouzel *et al* 1994). Discrepancies appear below 2700m depth (note that the depth scales are slightly shifted for a better comparison of the profiles). Hatched areas correspond to depths for which tilted ice layers are observed. A rapid climatic event is recorded at about 2790m (GRIP project members 1993).

Regarding marine biogenic activity, sulfate and methanesulfonate (MSA) measurements are not in agreement with Antarctic data. In particular, high MSA values are not observed in glacial conditions (Mayewski *et al* 1994; Legrand *et al* 1997). Marine biogenic activity, responsible for the relatively high sulfate content of Antarctic precipitation, has a weaker influence in the North. On the other hand, volcanic sulfate is probably a more important contribution in Greenland than in the Antarctic. Eruptions of global concern have been detected by ECM along the Eurocore and GRIP cores at Summit (Clausen *et al* 1995) as well as on the GISP core (Zielinski *et al* 1994). More intense volcanic activity seem to follow the glacial/interglacial transition.

Very large amounts of alkaline dust were transported in the glacial atmosphere and deposited in Greenland. This is a confirmation of previous studies at Camp Century and Dye 3 (Cragin *et al* 1977). Sr and Nd isotope measurements (Biscaye *et al* 1997) indicate that LGM dust originates from East Asia. This suggests that the general atmospheric circulation

was most probably shifted southward by the considerable expansion of the Laurentide ice sheet during the ice age (Mayewski *et al* 1994). This dust input changes markedly the chemical and physical properties of the ice corresponding to cold periods. It can be deduced from these observations that the general chemical properties of the northern hemisphere atmospheric aerosol were also significantly different from those of the present. The only major species which does not exhibit concentration changes over climatic stages in Greenland is nitrate. Up to now, no plausible explanation has been proposed for explaining this peculiar feature of nitrate deposition.

Detailed ^{10}Be measurements along the GRIP core (Yiou *et al* 1997) have shown that concentration changes of this cosmogenic radioisotope are primarily linked to snow accumulation changes, as in Antarctica. However, a solar and geomagnetic modulation is also detected, as also possibly primary cosmic ray variations. The most recent of the two peaks found in the Vostok core is well recorded in GRIP about 38 ka B.P.

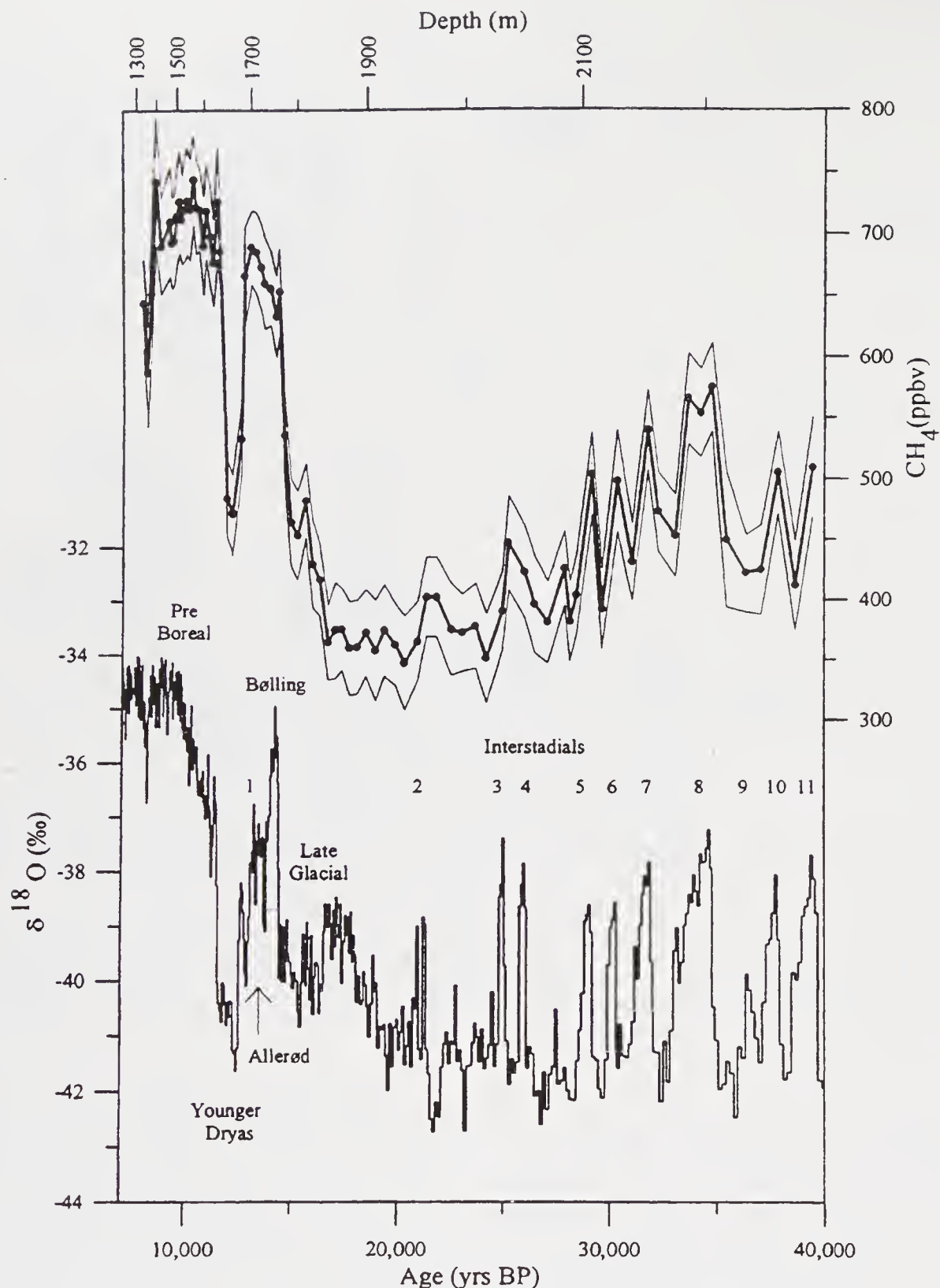


Figure 5. GRIP ice core: methane concentration changes (in ppbv with error envelope) remarkably mimic the typical seesaw climatic profile ($\delta^{18}\text{O}$ in ‰) observed for the last 40 ka (from Chappellaz *et al* 1993).

4. Changes due to anthropic activities

We will examine separately the cases of global and hemispheric pollutions (long-lived and short-lived species, respectively).

4.1 Long-lived species

The atmospheric concentrations of several long-lived trace gases are currently increasing due to anthropo-

genic emissions. Monitoring programmes to document these trends started only recently. Consequently, ice core data are invaluable for reconstructing the pre-industrial levels and documenting in detail the sources and sinks controlling their atmospheric concentrations. In particular, the concentration changes of greenhouse gases are clearly recorded in the air bubbles encapsulated in ice from both polar regions. The studies are now extending back to the last millennia, in order to better define the natural variability in

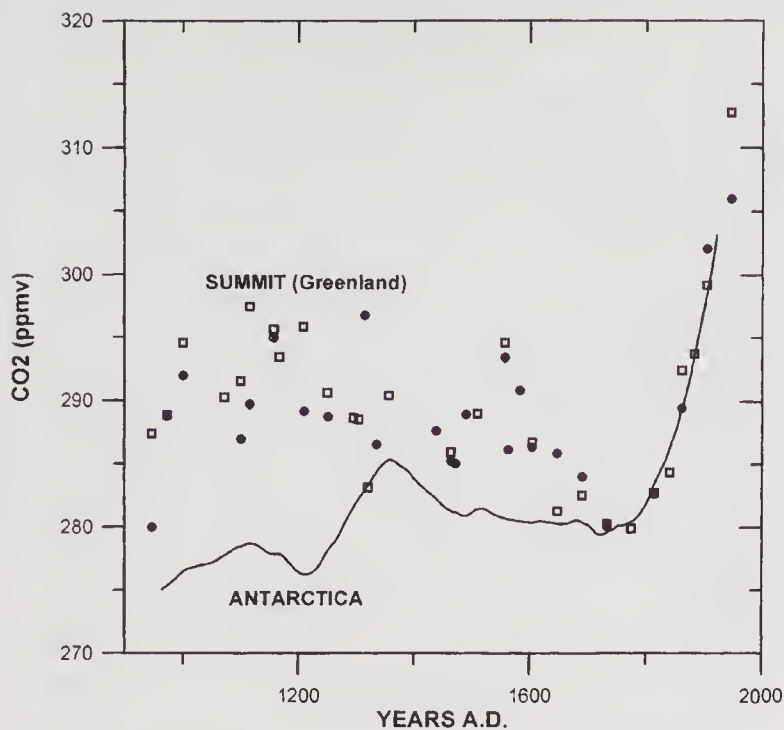


Figure 6. Carbon dioxide concentrations over the last 1000 years measured in Greenland ice cores (Eurocore and GRIP) by two different laboratories: LGGE Grenoble (squares) and Physikalisches Institut Bern (solid circles). Antarctic profile (continuous line) was obtained from Antarctic ice cores. Figure modified from Barnola *et al* 1995.

present climatic conditions, characterize the very beginning of the anthropogenic impact and assess the interhemispheric difference.

Greenhouse-gas concentrations over the last thousand years are shown in figure 6. In Greenland, preindustrial concentrations of CO_2 (Barnola *et al* 1995) and CH_4 (Blunier *et al* 1993; Nakazawa *et al* 1993) during the 18th century are found to be 280 and 0.73 ppmv (0.67–0.68 in Antarctica), respectively. During the last millennium, prior to the 17th century, CO_2 concentrations show fluctuations in the range 275–285 ppmv.

Note that detailed descriptions of the CO_2 and CH_4 concentration increases linked to human activity have been obtained at Law Dome, a very high accumulation coastal Antarctic site (Etheridge *et al* 1992; Etheridge *et al* 1996).

It is important to emphasize that: 1) the present-day greenhouse-gas concentrations are outside the range of natural variation reconstructed from ice core studies, and 2) the changes due to human activities have occurred in less than two centuries, contrary to natural ones which take millennia. This is illustrated by figure 3: the co-variation of the CO_2 and CH_4 concentrations have been radically modified when passing from pre-industrial (the last 220 ka) to industrial conditions (the last two hundred years). It is amazing that the increases of the atmospheric concentration of these two gases are so tightly linked for the industrial period; their anthropogenic origins and sinks are quite different. A reason for the observed correlation could just be their dominant link to global population growth.

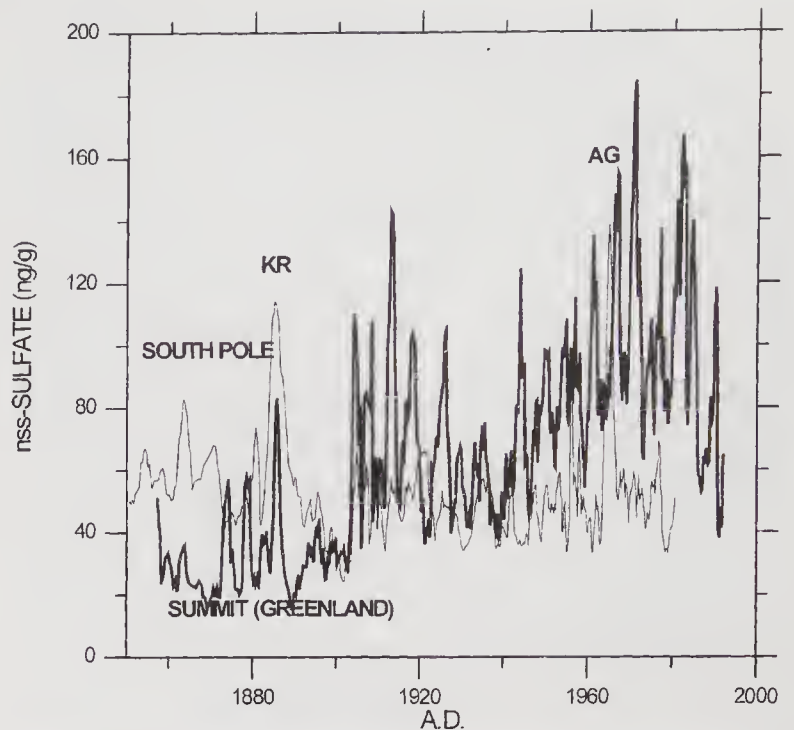


Figure 7. Non-sea-salt sulphate concentration changes since 1860 A.D. at Summit (Greenland; Legrand *et al* 1997) and at South Pole (Kirchner 1988). Dating of snow layers at South Pole may be uncertain by a few years between the two volcanic markers Krakatau (KR 1883, recorded in both polar regions) and Agung (AG 1963, recorded at South Pole only). Anthropogenic pollution is recorded only in Greenland and visible from about the turn of this century.

4.2 Short-lived species

For species having atmospheric residence times of the order of weeks to months, the impact of pollution is limited to the hemisphere where the pollutants are emitted.

The cases of sulphate and nitrate in Greenland were documented for more than a decade (Neftel *et al* 1985; Mayewski *et al* 1986). More detailed measurements have been performed in Greenland during the Eurocore, GRIP and GISP2 operations at Summit. As an example, the GRIP sulphate profile of the last 150 years, compared to the South pole sulphate record, is presented in figure 7. It shows that the anthropogenic contribution started to be significant during the first decade of this century, but the record is blurred by several volcanic eruptions having occurred at that time. At present, since about 20 years, this pollution shows a decreasing trend due to measures taken to reduce the sulphur content of fossil fuels. At South Pole, only natural fluctuations are recorded. Nitrate exhibits a steadily growing trend since about forty years, in relation with the still rising NO_x northern hemisphere emissions but this record could be different from the true atmospheric variations due to possible post-deposition changes affecting this gaseous species in the firn. Unfortunately, the ice does not record all the species that would be required to fully estimate the oxidation capacity of the past atmosphere, in particular the most important ones O_3 and OH radical, except H_2O_2 (Neftel *et al* 1984; Sigg and Neftel 1991;

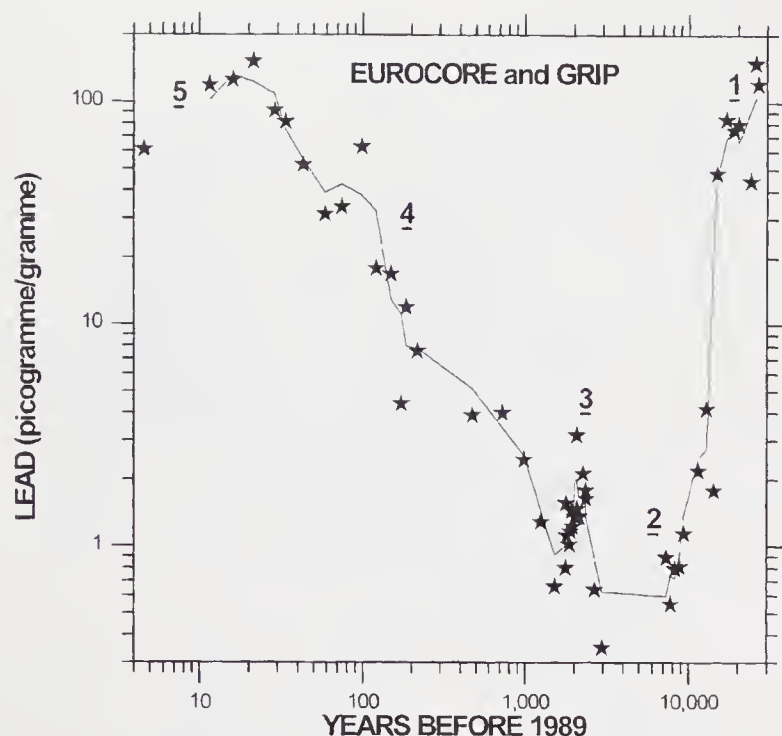


Figure 8. Lead in Summit (Greenland) snow and ice over the last 30000 years. Several stages are identified. 1: last ice age; 2: Holocene; 3: impact of ancient roman and greek pollutions; 4: industrial revolution; 5: most recent decades with increasing use of unleaded gasoline. Data are from Hong *et al* (1994; 1996a,b) and Candelone *et al* (1995).

Anklin and Bales 1997). On the other hand, related species CO (Haan *et al* 1996), HCOH (Staffelbach *et al* 1991) and overall CH₄ (Khalil and Rasmussen 1985; Khalil and Rasmussen 1989; Raynaud *et al* 1993) and NO₃ (see above) are now available with a variable degree of confidence for the pre-industrial and industrial times.

Metals such as Pb, Cu, Zn, Cd, Hg are naturally present in primary aerosol (mainly continental dust). They may have a gas-derived aerosol fraction linked to biological processes. These metals, in particular atmospheric lead produced from alkyl Pb additives used as antiknock agents in automobile and aircraft gasoline, have been intensively studied in polar snow in relation with ecological and health problems they can cause on a local scale. Surprisingly, this type of pollution is not recent: the analysis of the upper part of the GRIP ice core demonstrated that mining activities during Greek and Roman times have had also a marked influence on the atmospheric cycle of lead (Hong *et al* 1994) and copper (Hong *et al* 1996a). Regarding the intrinsic level of this pollution, it can be shown (figure 8) that very high values were already reached during the ice age, quite comparable to anthropogenic levels, due to enhanced crustal dust transport to Greenland in very cold climatic conditions. Isotope measurement is a powerful tool to unravel the respective contributions of the various source regions of this metal (Rosman *et al* 1993). The identification of automobile lead was reinforced by subpicogramme level analysis of the degradation products of organolead compounds (Lobinski *et al* 1993).

5. Concluding remarks

This paper must be considered as a general rapid survey of the palaeoenvironmental information which has been extracted from recent polar ice cores. Only the most striking features have been reported.

Recent ice core data obtained in Antarctica (Vostok) and Greenland (Summit cores) have made it possible to investigate the teleconnections existing between climate changes in the Northern and Southern Hemispheres and therefore to better understand the climatic system on the global scale. In addition to climatic parameters, polar ice provides additional information linked to the continental and marine atmospheric environments.

This effort must be amplified, since polar regions, in particular the Antarctic, are composed of distinct geographical areas representative of various climatic zones. It could be mentioned also that the Holocene time period is relatively less documented than the last ice ages. The study of just one or two ice cores is insufficient to picture with certainty the situation prevailing over a whole polar ice sheet. International deep drilling operations are currently being developed at several Greenland (e.g. North-GRIP) and Antarctic (EPICA [European Project for Ice Coring in Antarctica, Lorius and Jouzel 1996] in East Antarctica, WAISCORE [West Antarctic Ice Sheet CORE] in West Antarctica, Dome Fuji etc.) sites for a better coverage of these vast remote continents.

Some pending questions should be further investigated: a typical example is the nature and origin of nitrate in polar regions. Nitrate is a major constituent of polar ice impurities. Moreover, this compound is linked to the oxidation capacity of the atmosphere. In addition, ice core research should be aimed at two immediate goals: 1) a better understanding of the transfer function linking ice records to atmospheric composition, and 2) an increase of the number of compounds or elements determined in the ice samples:

1. On the Central Antarctic Plateau, where several ice coring operations have been carried out or are being planned for future, marked postdeposition effects have been discovered recently for atmospheric acid gases like HCl, HNO₃, and MSA (Wagnon *et al* in press), making the current interpretation of ice core data of these species uncertain. Laboratory experiments are also recommended to investigate the physico-chemical interactions between gaseous species and ice surfaces at low temperature. Regarding CO₂, there are still discussions about the accuracy of the ice records, in particular for Greenland ice where air bubble composition may be slightly modified in depth. More work is in progress about this critical issue.
2. The determination of a larger number of trace species in polar ice is possible, using the new and

powerful analytical techniques such as liquid or gas chromatography, or mass spectrometry (e.g. ICP-MS; GC-MS). In addition to major greenhouse gases, other gases should also be investigated, e.g. hydrocarbons involved in the tropospheric ozone formation or OCS, a major gaseous species of the atmospheric sulphur cycle.

The organic fraction of the impurities deposited in ice is a domain which is nearly unexplored: organic compounds could be used to document marine and continental biogenic activity in past climatic conditions.

Polar ice has already provided invaluable information about the global climatic system, but not yet revealed all its secrets.

References

- Anklin M and Bales R C 1997 Recent increase in H_2O_2 concentration at Summit, Greenland; *J. Geophys. Res.* **102** 19099–19104
- Barnola J M, Raynaud D, Korotkevich Y S and Lorius C 1987 Vostok ice core provides 160,000-year record of atmospheric CO_2 ; *Nature* **329** 408–414
- Barnola J M, Pimienta P, Raynaud D and Korotkevich Y S 1991 CO_2 -climate relationship as deduced from the Vostok ice core: A re-examination based on new measurements and re-evaluation of the air dating; *Tellus* **43B** 43–90
- Barnola J M, Anklin M, Porcheron J, Raynaud D, Schwander J and Stauffer B 1995 CO_2 evolution during the last millennium as recorded by Antarctic and Greenland ice; *Tellus* **47B** 264–272
- Basile I, Grousset E F, Revel M, Petit J-R, Biscaye P E and Barkov N I 1997 Patagonian origin of glacial dust deposited in East Antarctica (Vostok and Dome C) during glacial stages 2, 4 and 6; *Earth Planet. Sci. Lett.* **146** 573–589
- Berger A 1988 Milankovitch theory and climate; *Rev. Geophys.* **26** 624–657
- Biscaye P E, Grousset F E, Revel M, Van der Gaast S, Zielinski G E, Vaars A and Kukla G 1997 Asian provenance of glacial dust stage 2 in the GISP 2 ice core Summit Greenland; *J. Geophys. Res.* **102** 26765–26782
- Blunier T, Chappellaz J A, Schwander J, Barnola J-M, Despert T, Stauffer B and Raynaud D 1993 Atmospheric methane record from a Greenland ice core over the last 1000 years; *Geophys. Res. Lett.* **20** 2219–2222
- Blunier T, Chappellaz J, Schwander J, Stauffer B and Raynaud D 1995 Variations in atmospheric methane concentration during the Holocene epoch; *Nature* **374** 46–49
- Candelone J-P, Hong S, Pellone C and Boutron C F 1995 Post-industrial revolution changes in large scale atmospheric pollution of the Northern Hemisphere by heavy metals as documented in central Greenland snow and ice; *J. Geophys. Res.* **100** 16605–16616
- Chappellaz J, Barnola J-M, Raynaud D, Korotkevich Y S and Lorius C 1990 Ice core record of atmospheric methane over the past 160000 years; *Nature* **345** 127–131
- Chappellaz J, Blunier T, Raynaud D, Barnola J M, Schwander J and Stauffer B 1993 Synchronous changes in atmospheric CH_4 and Greenland climate between 40 and 8 kyr BP; *Nature* **366** 443–445
- Clausen H B, Hammer C U, Christensen J, Schott-Hvidberg C, Dahl-Jensen D, Legrand M and Steffensen J P 1995 1250 years of global volcanism as revealed by central Greenland ice cores; In *Ice Core Studies of Biogeochemical Cycles* NATO ASI Series (ed) R. Delmas **I30** pp. 175–194
- Craig H 1961 Isotopic variations in meteoric waters; *Science* **133** 1702–1703
- Cragin J H, Herron M M, Langway Jr. C C and Klouda G 1977 Interhemispheric comparison of changes in the composition of atmospheric precipitation during the late cenozoic area; In *Polar Oceans* (ed) M J Dunbar, Calgary Arctic Institute of North America pp. 617–631
- Dansgaard W 1964 Stable isotopes in precipitation; *Tellus* **16** 436–468
- Dansgaard W and Oeschger H 1989 Past environmental long-term records from the Arctic; In *The Environmental Record in Glaciers and Ice Sheets* (eds) H Oeschger and C C Langway Jr. (John Wiley and Sons Ltd., Dahlem Konferenzen) pp. 287–318
- Dansgaard W, Johnsen S J, Clausen H B, Dahl-Jensen D, Gundestrup N S, Hammer C U, Hvidberg C S, Steffensen J P, Sveinbjörnsdottir A E, Jouzel J and Bond G 1993 Evidence for general instability of past climate from a 250-kyr ice-core record; *Nature* **364** 218–220
- Delmas R J 1992 Environmental information from ice cores; *Rev. Geophys.* **30** 1–21
- Delmas R J and Petit J-R 1994 Present Antarctic aerosol composition a memory of ice age atmospheric dust?; *Geophys. Res. Lett.* **21** 879–882
- Etheridge D M, Pearman G I and Frazer P J 1992 Changes in tropospheric methane between 1841 and 1978 from a high accumulation rate Antarctic ice core; *Tellus* **44B** 282–294
- Etheridge D M, Steele L P, Langenfelds R M, Francey R J, Barnola J-M and Morgan V I 1996 Natural and anthropogenic changes in atmospheric CO_2 over the last 1000 years from air in Antarctic ice and firn; *J. Geophys. Res.* **101D** 4115–4128
- Fuhrer K, Neftel A, Anklin M and Maggi W 1993 Continuous measurements of hydrogen peroxide formaldehyde calcium and ammonium concentrations along the new GRIP ice core from Summit (Central Greenland); *Atmosph. Envir.* **27A** 1873–1880
- Fuhrer K, Neftel A, Anklin M, Staffelbach T and Legrand M 1996 High resolution ammonium ice core record covering a complete glacial-interglacial cycle; *J. Geophys. Res.* **101D** 4147–4164
- Genthon C, Barnola J M, Raynaud D, Lorius C, Jouzel J, Barkov N I, Korotkevich Y S and Kotlyakov V M 1987 Vostok ice core climatic response to CO_2 and orbital forcing changes over the last climatic cycle; *Nature* **329** 414–418
- Genthon C and Armengaud A 1995 GCM simulations of atmospheric tracers in the polar latitudes South Pole (Antarctica) and Summit (Greenland) cases; *Sci. Tot. Envir.* **160/161** 101–116
- GRIP Project Members 1993 Climate instability during the last interglacial period recorded in the GRIP ice core; *Nature* **364** 203–207
- Grootes P M, Stuiver M, White J W C, Johnsen S and Jouzel J 1993 Comparison of oxygen isotope records from the GISP2 and GRIP Greenland ice cores; *Nature* **366** 552–554
- Haan D, Martinerie P and Raynaud D 1996 Ice core data of atmospheric carbon monoxide over Antarctica and Greenland during the last 200 years; *Geophys. Res. Lett.* **23** 2235–2238
- Hammer C U 1980 Greenland ice sheet evidence of post glacial volcanism and its climatic impact; *Nature* **288** 230–235
- Hammer C U 1989 Dating by physical and chemical seasonal variations and reference horizons; In *The Environmental Record in Glaciers and Ice Sheets* (eds) H Oeschger and C C Langway Jr. (John Wiley and Sons Ltd., Dahlem Konferenzen) pp. 99–121
- Hong S, Candelone J P, Patterson C C and Boutron C F 1994 Greenland ice evidence of hemispheric pollution for lead two

- millennia ago by Greek and Roman civilizations; *Science* **265** 1841–1843
- Hong S, Candelone J-P, Patterson C C and Boutron C F 1996a History of ancient copper smelting pollution during roman and medieval times recorded in Greenland ice; *Science* **272** 246–249
- Hong S, Candelone J P and Boutron C F 1996b Changes in natural lead, copper, zinc and cadmium concentrations in central Greenland ice from 8250 to 149100 years ago their association with climatic changes and resultant variations of dominant source contributions; *Earth Planet. Sci. Lett.* **143** 233–244
- Johnsen S J, Clausen H B, Dansgaard W, Fuhrer K, Gundestrup N S, Hammer C U, Iversen P, Jouzel J, Stauffer B and Steffensen J P 1992 Irregular glacial interstadials recorded in a new Greenland ice core; *Nature* **359** 311–313
- Johnsen S J, Dahl-Jensen D, Dansgaard W and Gundestrup N S 1995a Greenland temperatures derived from GRIP bore hole temperature and ice core isotope profiles; *Tellus* **47B** 624–629
- Johnsen S J, Clausen H B, Dansgaard W, Gundestrup N S, Hammer C U and Tauber H 1995b The Eem stable isotope record along the GRIP ice core and its interpretation; *Quatern. Res.* **43** 117–124
- Jouzel J, Lorius C, Petit J R, Genthon C, Barkov N I, Kotlyakov V M and Petrov V M 1987 Vostok ice core a continuous isotope temperature record over the last climatic cycle 160000 years; *Nature* **329** 403–408
- Jouzel J *et al* 1993 Extending the Vostok ice core record of palaeoclimate to the penultimate glacial period; *Nature* **364** 407–412
- Jouzel J, Lorius C, Johnsen S and Grootes P 1994 Climate instabilities Greenland and Antarctic records; *C.R. Acad. Sci. Paris* **319** 65–67
- Jouzel J *et al* 1996 Climatic interpretation of the recently extended Vostok ice records; *Clim. Dyn.* **12** 513–521
- Jouzel J *et al* 1997 Validity of the temperature reconstruction from water isotopes in ice cores; *J. Geophys. Res.* **102** 26471–26487
- Khalil M A K and Rasmussen R A 1985 Causes of increasing methane depletion of hydroxyl radicals and the rise of emissions; *Atmos. Envir.* **19** 397–407
- Khalil M A K and Rasmussen R A 1989 Temporal variations of trace gases in ice cores; In *The Environmental record in glaciers and ice sheets* (eds) H Oeschger and C C Langway Jr. (John Wiley and Sons Ltd., Dahlem Konferenzen) pp. 193–205
- Kirchner S 1988 *Chimie de la neige NaCl NO₃ SO₄ à la Station Pôle Sud* Thesis, Univ. of Grenoble France, pp. 250
- Krinner G, Genthon C and Jouzel J 1997 GCM analysis of local influences on ice core δ signals; *Geophys. Res. Lett.* **24** 2825–2828
- Legrand M R, Lorius C, Barkov N I and Petrov V N 1988 Vostok (Antarctica) ice core atmospheric chemistry changes over the last climatic cycle 160000 years; *Atmosph. Envir.* **22** 317–331
- Legrand M, Feniet-Saigne C, Saltzman E S, Germain C, Barkov N I and Petrov V N 1991 Ice-core record of oceanic emissions of dimethylsulphide during the last climate cycle; *Nature* **350** 144–146
- Legrand M, Feniet-Saigne C, Saltzman E S and Germain C 1992a Spatial and temporal variations of methanesulfonic acid and non sea salt sulphate in Antarctic ice; *J. Atmos. Chem.* **14** 245–260
- Legrand M, De Angelis M, Staffelbach T, Neftel A and Stauffer B 1992b Large perturbations of ammonium and organic acids content in the Summit-Greenland ice core fingerprint from forest fires?; *Geophys. Res. Lett.* **19** 473–475
- Legrand M and De Angelis M 1995 Origins and variations of light carboxylic acids in polar precipitations; *J. Geophys. Res.* **100** 1445–1462
- Legrand M, De Angelis M, Cachier H and Gaudichet A 1995 Boreal biomass burning over the last 80 years recorded in a Summit-Greenland ice core; In *Ice Core Studies of Biogeochemical Cycles* (ed) R Delmas, NATO ASI Series **130** pp. 355–368
- Legrand M, Hammer C U, De Angelis M, Savarino J, Delmas R J, Clausen C and Johnsen S J 1997 Sulphur derived species methanesulfonate and SO₄ over the last climatic cycle in the GRIP (central Greenland) ice core; *J. Geophys. Res.* **102** 26663–26679
- Lobinski R, Boutron C F, Candelone J P, Hong S, Szpunar-Lobinska J and Adams F 1993 Speciation analysis of organolead compounds in Greenland snow at the femto-gram-per-gram level by capillary gas chromatography/atomic emission spectrometry; *Analyt. Chem.* **65** 2510–2515
- Lorius C and Merlivat L 1977 Distribution of mean surface stable isotope values in East Antarctica observed changes with depth in a coastal area in Isotopes and Impurities; In *Snow and Ice, Proc. IUGG Symp. Grenoble 1975* IAHS Publ. **118** pp. 127–137
- Lorius C, Jouzel J, Ritz C, Merlivat L, Barkov N I, Korotkievitch Y and Kotlyakov V N 1985 A 150000 year climatic record from Antarctic ice; *Nature* **316** 591–596
- Lorius C and Jouzel J 1996 European Project for Ice Coring in Antarctica (EPICA) In *The Oceans and the Poles* (ed) G Hempel (Gustav Fischer Verlag) pp. 263–277
- Mayewski P A, Lyons W B, Spencer M J, Twickler M, Dansgaard W, Koci B, Davidson C I and Honrath R E 1986 Sulphate and nitrate concentrations from a South Greenland ice core; *Science* **232** 975–977
- Mayewski P A *et al* 1994 Changes in atmospheric circulation and ocean ice cover over the North Atlantic during the last 41000 years; *Science* **263** 1747–1751
- McHargue L R and Damon P E 1991 The global beryllium-10 cycle; *Rev. Geophys.* **29** 141–158
- Meese D A, Gow A J, Alley R B, Zielinski G A, Grootes P M, Ram M, Taylor K C, Mayewski P A and Bolzan J F 1997 The Greenland Ice Sheet Project 2 depth-age scale methods and results; *J. Geophys. Res.* **102** 26411–26423
- Moore J C and Paren J G 1987 A new technique for dielectric logging of Antarctic ice cores; *J. Phys.* **48** 155–160
- Moore J C, Mulvaney R and Paren J G 1989 Dielectric stratigraphy of ice a new technique for determining total ionic concentrations in polar ice cores; *Geophys. Res. Lett.* **16** 1177–1180
- Nakazawa T, Machida T, Tanaka M, Fujii Y, Aoki S and Watanabe O 1993 Differences of the atmospheric CH₄ concentration between the Arctic and Antarctic regions in pre-industrial/pre-agricultural era; *Geophys. Res. Lett.* **20** 943–946
- Neftel A, Jacob P and Klockow D 1984 Measurements of hydrogen peroxide in polar ice samples; *Nature* **311** 43–45
- Neftel A, Beer J, Oeschger H, Zürcher F and Finkel R C 1985 Sulphate and nitrate concentrations in snow from South Greenland 1895–1978; *Nature* **314** 611–612
- Petit J-R, Mounier L, Jouzel J, Korotkievich Y S, Kotlyakov V M and Lorius C 1990 Palaeoclimatological and chronological implications of the Vostok core dust record; *Nature* **343** 56–58
- Petit J-R *et al* 1997 Four climate cycles in Vostok ice core; *Nature* **387** 359–360
- Raisbeck G M, Yiou F, Bourles D, Lorius C, Jouzel J and Barkov N I 1987 Evidence for two intervals of enhanced ¹⁰Be deposition in Antarctic ice during the last glacial periods; *Nature* **326** 273–277
- Raynaud D, Jouzel J, Barnola J M, Chappellaz J, Delmas R J and Lorius C 1993 The ice record of greenhouse gases; *Science* **259** 926–934

- Reeh N 1989 Dating by ice flow modeling a useful tool or an exercise in applied mathematics? In *The Environmental Record in Glaciers and Ice Sheets* (eds) H Oeschger and C C Langway Jr. (John Wiley and Sons Ltd., Dahlem Konferenzen) pp. 141–159
- Rosman K J R, Chisholm W, Boutron C F, Candelone J-P and Görlach U 1993 Isotopic evidence for the source of lead in Greenland snows since the late 1960s; *Nature* **362** 333–335
- Sigg A and Neftel A 1991 Evidence for a 50% increase in H₂O₂ over the past 200 years from a Greenland ice core; *Nature* **311** 557–559
- Sigg A, Fuhrer K, Anklin M, Staffelbach T and Zurmühle D 1994 A continuous analysis technique for trace species in ice cores; *Envir. Sci. Technol.* **28** 204–209
- Staffelbach T, Neftel A, Stauffer B and Jacob D 1991 A record of the atmospheric methane sink from the formaldehyde in polar ice cores; *Nature* **349** 603–605
- Stauffer B 1989 Dating of ice by radioactive isotopes; In *The Environmental Record in Glaciers and Ice Sheets* (eds) H Oeschger and C C Langway Jr. (John Wiley and Sons Ltd., Dahlem Konferenzen) pp. 123–139
- Stauffer B 1993 The Greenland Ice Core Project; *Science* **260** 1766–1767
- Taylor K C, Hammer C U, Alley R B, Clausen H B, Dahl-Jensen D, Gow A J, Gundestrup N S, Kipfstuhl J, Moore J C and Waddington E D 1993 Electrical conductivity measurements from the GISP2 and GRIP Greenland ice cores; *Nature* **366** 549–552
- Wagnon P, Delmas R J and Legrand M 1999 Loss of volatile acid species from upper firn layers at Vostok Antarctica; *J. Geophys. Res.* in press
- Wilson A T and Long A 1997 New approaches to CO₂ analysis in polar ice cores; *J. Geophys. Res.* **102** 26601–26606
- Yiou F, Raisbeck G M, Baumgartner S, Heer J, Hammer C, Johnsen S, Jouzel J, Kubik P W, Lestringuez J, Stievenard M, Suter M and Yiou P 1997 ¹⁰Be in the Greenland Ice Core Project ice core at Summit, Greenland; *J. Geophys. Res.* **102** 26783–26794
- Zielinski G A, Mayewski P A, Meeker L D, Whitlow S, Twickler M S, Morrison M, Meese D A, Gow A and Alley R B 1994 Record of volcanism since 7000 B.C. from the GISP2 Greenland ice core and implications for the volcano-climate system; *Science* **64** 948–952

Speleothems as high-resolution paleoenvironment archives: Records from northeastern China

T L KU and H C LI

Department of Earth Sciences, University of Southern California, Los Angeles, CA 90089-0740, USA
e-mail: rku@usc.edu

The isotopic compositions of oxygen and carbon and trace concentrations of magnesium and strontium in speleothems formed in limestone caves respond to climate changes outside the caves. Measurements of these properties on a stalagmite from Shihua Cave near Beijing, China, allowed reconstruction of the regional changes in precipitation, temperature and nature of vegetation. Over the last ~ 500 years, there were fourteen precipitation cycles with a periodicity of 30–40 years, which may well reflect fluctuations in the strength of the East Asian summer monsoons reaching northeastern China. Relative to the mean temperature of this time interval, the period 1620–1900 AD was cold and periods 1520–1620 and 1900–1994 were warm. Over the last ~ 3000 -years, about eight wet/cool-dry/warm climatic cycles of 300–400 years duration occurred, the latest wet/cool half cycle corresponding to the Little Ice Age. The $\delta^{13}\text{C}$ record registers the anthropogenic activities of fossil fuel CO_2 combustion in recent decades and regional deforestation between 13 and 16 centuries when Beijing was bustling with palatial constructions and being developed into the world's most populated city.

1. Introduction

The climate in China, particularly over its eastern lowland (< 2000 m), is strongly affected by the monsoon system. Much of eastern China during the winter months is under the influence of the Siberian High which produces an outflow of cold, dry air off the Asian continent. With the onset of summer, warm, moist, and unstable air moves inland from the anticyclones over the tropical and subtropical western Pacific and Indian Oceans (figure 1). These maritime air masses associated with the summer monsoons bring over 75% of the annual precipitation in eastern China. The amount of precipitation depends on the monsoon strength. Stronger summer monsoons would push the maritime air masses further inland. Precipitation occurs mostly at the polar frontal zone which typically stays in southeastern China in the spring, moves toward the Yangtze drainage basin during early summer and then reaches northeastern China during July and August. Shifts in the timing, position, strength and persistence of the monsoon may lead to so-called “flood-in-north

and drought-in-south” (and vice versa) conditions. For instance, in the central-eastern and southern coasts of China, especially in the Yangtze drainage basin, the heavy rainfall period from mid-June to mid-July, called “Meiyu” (Plum Rain), is associated with small depressions passing seawards along a quasi-stationary front. In this Meiyu front, huge, stationary and persistent thunderstorms are initiated and sustained by upper tropospheric divergence and lower tropospheric convergence in the southwest monsoon. The development of the Meiyu front depends strongly on the strength of the summer monsoons. If the summer monsoon is too strong, the rain belt moves quickly into northern China, and there will be an empty Meiyu, and the Yangtze valley will suffer from drought (Zhu 1954; Tao 1984; Domros and Peng 1988). The ability to identify recognizable pattern(s) of the monsoon variability over time in eastern China, a region among the world's most densely populated, is thus of great value.

As the active period of the summer monsoon closely coincides with the rainy season in China, the amount

Keywords. Speleothem; paleoclimate; high-resolution; oxygen isotopes; carbon isotopes; trace metals.

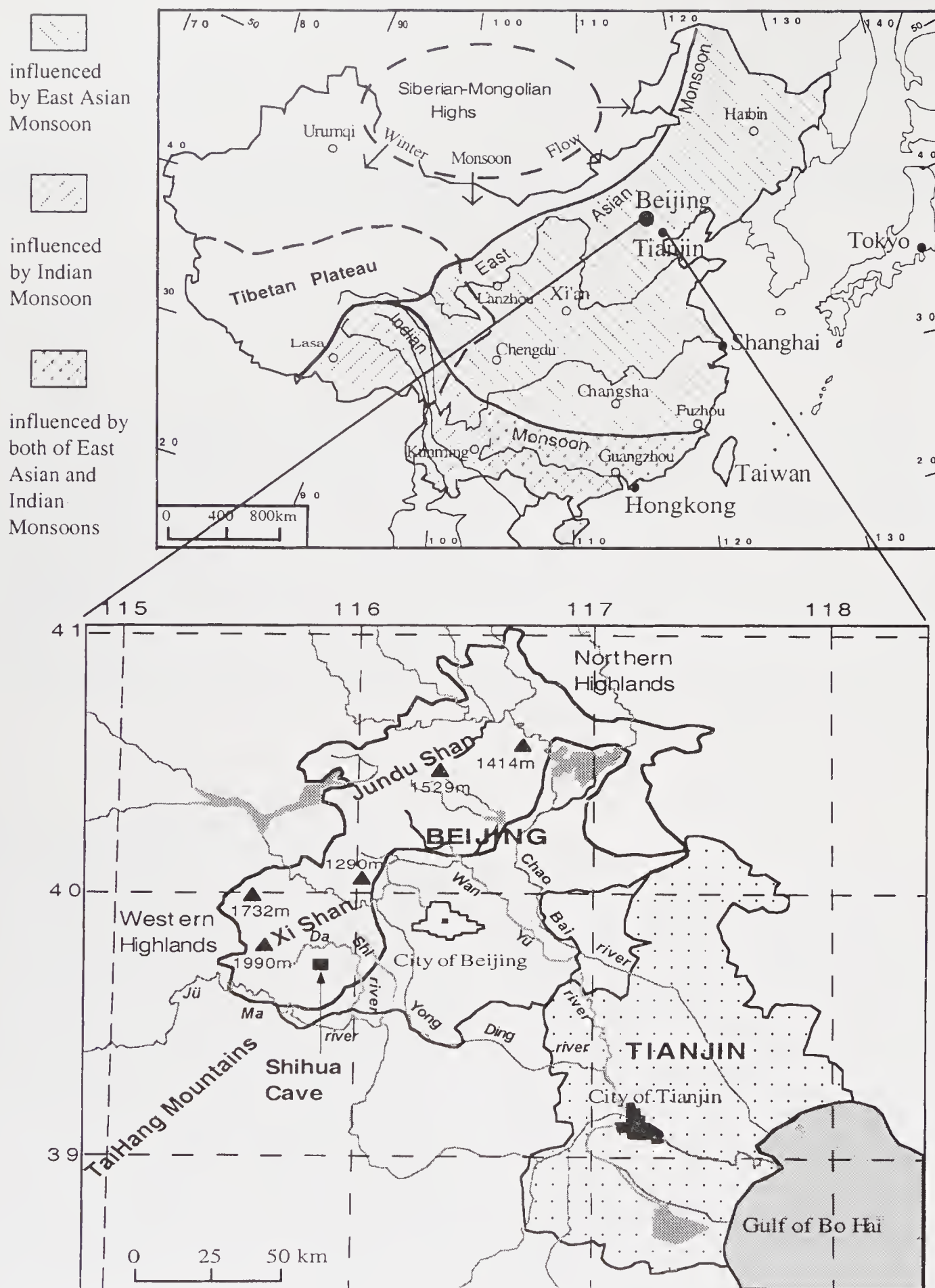


Figure 1. Maps showing: (1) climatic regimes in China under the influence of East Asian and Indian summer monsoons and Siberian winter monsoon associated with the Siberian-Mongolian High, and (2) the location of Shihua Cave near Beijing where stalagmite S312 was collected.

of rainfall can be viewed as an indicator of the monsoon strength. Instrumental records of precipitation in Beijing, Tianjin, Shanghai and Hong Kong over the last 100 years have all exhibited interannual-

to-decadal cyclic changes. Spectral analyses show periodicities of approximately 35, 22 and 11 years, besides the quasi-biennial oscillations in all records. The 35-year periodicity, known as the Brückner cycle,

was recognized in 1890 by the Swiss professor, E. Brückner, from his detailed investigations of rivers, lakes, harvests and vintages in Europe (Lamb 1977). Snitnikov (1957) also noted a recurrent fluctuation in the levels of the water bodies throughout a vast region of Asia with periods of 20–45 years. Reconstructing drought and flood charts in China for the last 500 years using historical data from year-books, diaries and gazettes, Chinese scientists found a 36-year cycle in the eastern part of the Yangtze River and southwest China, and a 22-year cycle in the central part of the Yangtze River and north-eastern China (Wang and Zhao 1981). However, due to the relatively short instrumental records (few extending beyond 100 years) and lack of precision in the descriptive data, the afore-mentioned periodicities have been considered unstable in space and time (Burroughs 1992). Verifying their existence over times longer than a mere century is important not only for retracing the regional drought/flood conditions but also for understanding the physical significance and predictive value of the monsoonal rain.

Limestone cave deposits (speleothems), particularly in the form of stalagmites, can effectively record climatic variability occurring at different time scales over the Holocene and late Pleistocene. They are among the most widely distributed in continental environments, and are amenable to precise dating by lamination counting and uranium series ($^{230}\text{Th}/^{234}\text{U}$ and ^{210}Pb) dating. Earlier attempts to read their $\delta^{18}\text{O}$ signals at time intervals of > 1000 years (Hendy and Wilson 1968; Harmon *et al* 1978) enabled paleotemperatures to be studied (Gascoyne 1992). More recently, efforts to extract higher-resolution climatic information from this natural archive have been carried out, aided by the ever-improving techniques in micro-sampling (Quinn *et al* 1996), lamination counting (Baker *et al* 1993; Shopov *et al* 1994), radiometric dating with ^{210}Pb (Baskaran and Iliffe 1993) and $^{230}\text{Th}/^{234}\text{U}$ (Li *et al* 1989) and small gas-volume stable isotope analysis. The high-resolution (down to subdecadal) speleothem $\delta^{18}\text{O}$ records allow reconstruction of paleo-precipitation as well as paleotemperature (Dorale *et al* 1992; Bar-Matthews *et al* 1997). Changes in the nature of vegetation cover above the caves, also a reflection of climatic variation, can be deciphered from the speleothem $\delta^{13}\text{C}$ records (Dorale *et al* 1992; Baker *et al* 1997). Furthermore, studies have shown the potential of Mg/Ca and/or Mg/Sr in speleothem as a paleotemperature indicator (Gascoyne 1983; Goede and Vogel 1991). In this paper, we report our study on a stalagmite from Shihua Cave in the outskirts of Beijing in northeastern China. From the time-series variations of $\delta^{18}\text{O}$, $\delta^{13}\text{C}$, Mg/Ca and Mg/Sr in the specimen, we have reconstructed the climatic and environmental changes for the last 3000 years.

2. Sample material, analysis and results

Shihua Cave ($115^{\circ}54'\text{N}$, $39^{\circ}48'\text{N}$) is located about 55 km southwest of Beijing, China, at an elevation of 200 m on the foothill of West Hill or Xi Shan (figure 1). Formed in carbonate rocks of mid-Ordovician age, the cave is 30 to 130 m below the present land surface. It is 7-level deep with the bottom 2 levels being submerged under water. The top 3 levels, open to the public, have a total passage length of 1900 m. Li *et al* (1996b) reported similar values of $\delta^{18}\text{O}$ (averaging $-9.4 \pm 0.3\text{‰}$ SMOW), δD ($-65.4 \pm 3.0\text{‰}$ SMOW) and ^3H (30.8 ± 4.5 TU) among local rain, shallow groundwater, river water, and drip and pool waters in the cave. In a δD vs. $\delta^{18}\text{O}$ plot, data points for these waters mostly fall close to the “meteoric water” line, showing little effects of evaporation and mixing with old groundwater. At present, it takes about one week’s time for the cave water dripping rate to respond to surface precipitation, and the ^3H measurements indicate a replacement time of water above the cave of about three years. The data set showed rapid transmission of isotopic signals of the precipitation outside the cave to its interior and pointed to the potential of stalagmites grown in the cave as a high-resolution recorder for regional changes in paleoenvironments.

Sample S312, a stalagmite of about 20 cm in height, was collected in November 1995 from level 3 deep within the Shihua Cave. The specimen was in growth position at the time of the collection. Its uppermost tip was receiving drip water and contained > 15 dpm g^{-1} of excess ^{210}Pb activities which decrease exponentially with depth in the uppermost 1.5 cm. Dating with ^{210}Pb , a method first attempted on speleothems by Baskaran and Iliffe (1993), and with ^{14}C (Li *et al* 1996a) confirmed the annual nature of laminae deposition within the sample, a conclusion also reached by other workers for stalagmite calcite (e.g., Baker *et al* 1993). Combining the results on lamination counting, ^{210}Pb and ^{14}C , Li *et al* (1996a) concluded that the top 13 cm of S312 accumulated continuously with an average growth rate of ~ 0.044 mm y^{-1} . The uppermost 2 cm representing approximately 500 years of record was sampled along the central growth-axis with a time resolution of roughly three years, using a computer-aided triaxial sampler (Quinn *et al* 1996). A total of 133 samples were then analyzed for their oxygen and carbon isotopic compositions using a VG Prism II mass spectrometer connected to an Autocarb device for reaction of powdered carbonate with 100% H_3PO_4 at 90°C . Between every five sample analyses, a working standard (USC Paleo-2) was run. Based on the reproducibility of the standard runs, we estimated one-sigma measurement errors at $\pm 0.15\text{‰}$ for $\delta^{18}\text{O}$ and $\pm 0.1\text{‰}$ for $\delta^{13}\text{C}$. To study the climatic record for the past ~ 3000 years, we further took 109 samples from S312 to a depth of 12.5 cm at coarser intervals of ~ 25 years. In addition to $^{18}\text{O}/^{16}\text{O}$ and $^{13}\text{C}/^{12}\text{C}$,

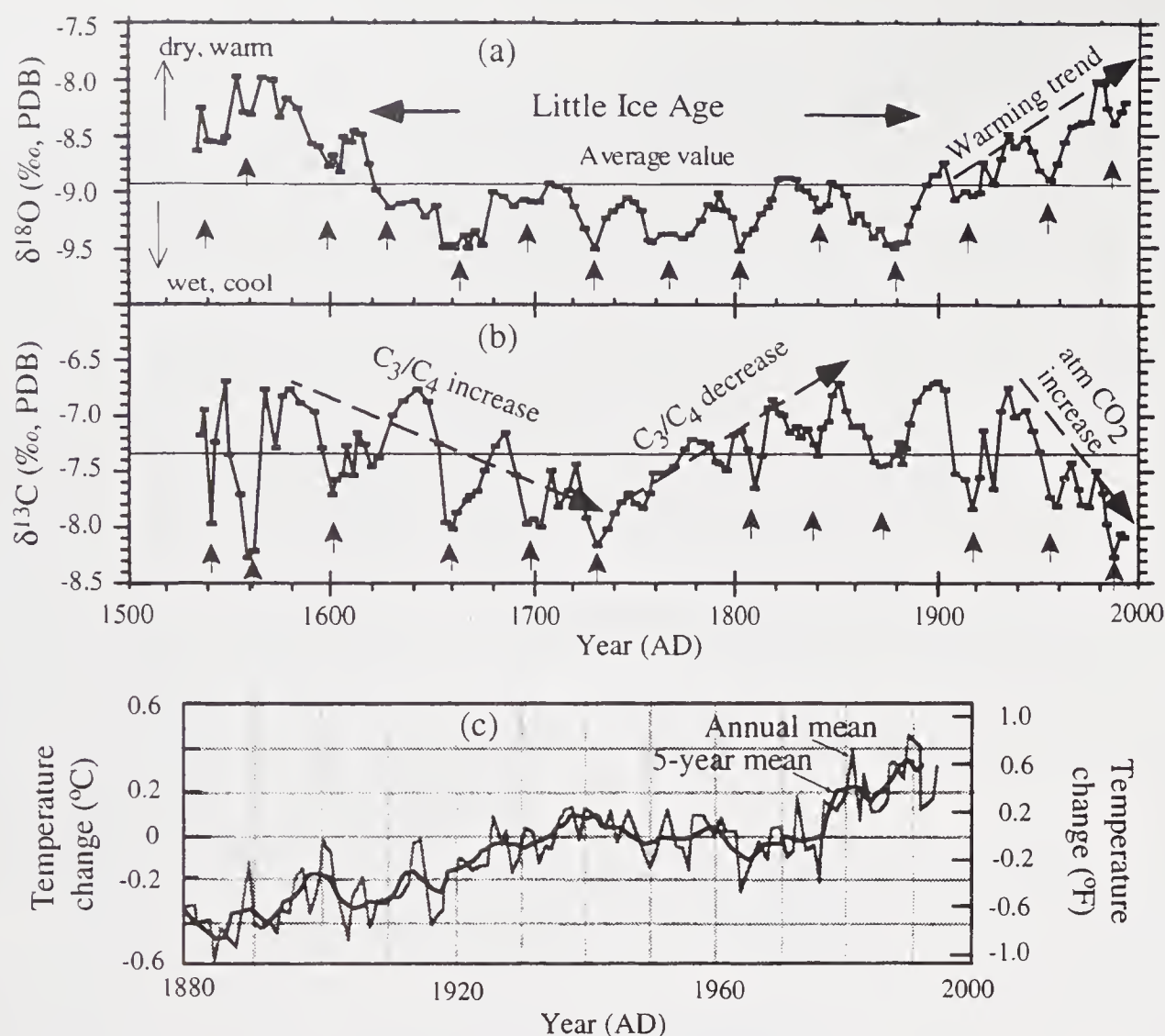


Figure 2. Plots showing variations of (a) $\delta^{18}\text{O}$ and (b) $\delta^{13}\text{C}$ in the topmost 2 cm of stalagmite S312. Short arrows mark the precipitation maxima deduced from the isotopic data. Horizontal lines represent the average values for the two records. Plots in (c) are from Strahler and Strahler (1997) showing the global temperature changes.

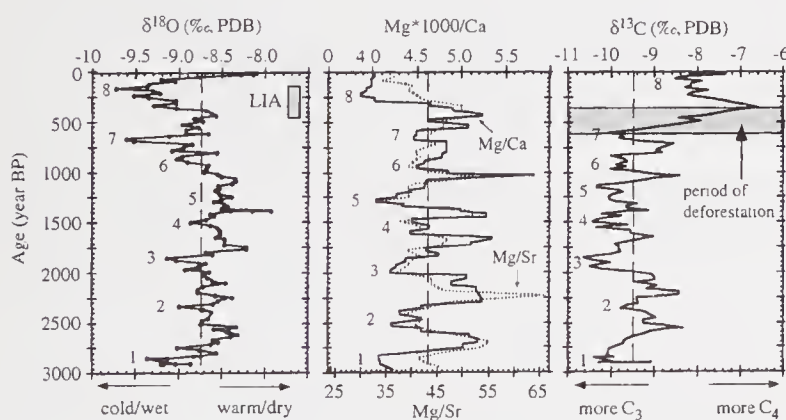


Figure 3. $\delta^{18}\text{O}$, Mg/Ca, Mg/Sr and $\delta^{13}\text{C}$ variations in the top 12.5 cm of stalagmite S312 measured at a resolution of ~ 25 years. All four records show approximately eight major cycles with their minima indicated by numerals 1 through 8. The vertical dashed lines represent the average values over the last 3000 years for $\delta^{18}\text{O}$, Mg/Ca and Mg/Sr. For $\delta^{13}\text{C}$, the dashed line shows the average value over the interval 3000–650 years BP. LIA in the $\delta^{18}\text{O}$ record stands for the Little Ice Age. The marked increase of $\delta^{13}\text{C}$ between 650 and 360 years BP attributable to deforestation activities near Beijing is indicated.

magnesium and strontium concentrations in these samples were determined to a precision of about $\pm 1\%$ using atomic absorption spectrophotometry.

Results of the oxygen and carbon isotopic analyses, reported in the conventional “ δ ” notation of per-mil difference from the PDB standard, are plotted against age in figures 2 and 3 for records of the past 500 years and 3000 years, respectively. The age assignment, based on a mean growth rate of 0.044 mm y^{-1} and taking the topmost sample to be of 1994 AD in age, has an overall uncertainty of about $\pm 10\%$ (Li *et al* 1996a). In figure 3 are also plotted the time variations in ratios Mg/Ca and Mg/Sr in the top 12.5 cm of S312. The numerical data for these plots have been tabulated in Li *et al* (1997a, 1997b) except for the $\delta^{18}\text{O}$ and Mg/Sr/Ca data sets in figure 2 which are available upon request from the authors.

3. $\delta^{18}\text{O}$ as precipitation and temperature proxy

$\delta^{18}\text{O}$ in a stalagmite is generally in isotopic equilibrium with $\delta^{18}\text{O}$ of the cave drip water and regional surface water (Yonge *et al* 1985; Dorale *et al* 1992; Gascoyne 1992; Bar-Matthews *et al* 1997), and this has also been the case for S312 (Li *et al* 1997a). Given that speleothems record $\delta^{18}\text{O}$ changes of local precipi-

precipitation, it is appropriate to examine the influence of climate change on the $\delta^{18}\text{O}$ of precipitation ($\delta^{18}\text{O}_p$) as $\delta^{18}\text{O}_p$ becomes lighter with increasing precipitation and decreasing air temperature.

Let us begin with the Rayleigh equation describing the oxygen isotope fractionation between water vapor in clouds and raindrops:

$$\delta^{18}\text{O}_v = (\delta^{18}\text{O}_o + 1000) f^{(\alpha-1)} - 1000 \quad (1)$$

where $\delta^{18}\text{O}_o$ and $\delta^{18}\text{O}_v$ are $\delta^{18}\text{O}$ of the vapor before and after condensation, respectively, f is the fraction of residual vapor, and α is the fractionation factor, defined as:

$$\alpha = (\delta^{18}\text{O}_p + 1000)/(\delta^{18}\text{O}_v + 1000). \quad (2)$$

Combining equations (1) and (2) with the observed temperature dependence of α , i.e., $\alpha \approx 1.0112 - 8.2678 \times 10^{-5}T^\circ\text{C}$ (Dansgaard 1964), we have:

$$\begin{aligned} \delta^{18}\text{O}_p &= \alpha(\delta^{18}\text{O}_o + 1000) f^{(\alpha-1)} - 1000 \\ &= ((1.0112 - 8.2678 \times 10^{-5}T)(\delta^{18}\text{O}_o + 1000) \\ &\quad \times f^{(0.0112 - 8.2678 \times 10^{-5}T)} - 1000). \end{aligned} \quad (3)$$

Thus $\delta^{18}\text{O}_p$ is seen to vary with f (the extent of rain-out from a vapor source: smaller f values resulting from larger amounts of precipitation), T (condensation temperature), and $\delta^{18}\text{O}_o$ (which depends on the source water and its evaporation temperature).

3.1 Influence of precipitation amount on $\delta^{18}\text{O}_p$ (f -dependence)

Equation (3) shows that $\delta^{18}\text{O}_p$ is inversely related to the amount of precipitation for a given source water, a relation borne out by observations made in the tropical and mid-latitude regions (Dansgaard 1964; Rozanski *et al* 1993), and by Bar-Matthews *et al* (1997) who showed that the $\delta^{18}\text{O}$ values of the seepage and drip water in Soreq Cave (Israel) are negatively correlated with the annual rainfall. This inverse relationship is hardly affected by changes in $\delta^{18}\text{O}_o$ and T , as seen by taking the derivative of equation (3) with respect to f , and noting that, since $\delta^{18}\text{O}_o \ll 1000$ and $\alpha > 1$, $d(\delta^{18}\text{O}_p)/df$ is always positive. It should be noted that individual $\delta^{18}\text{O}_p$ values may sometimes deviate from this relationship, as the Rayleigh formulation requires that the vapor-liquid system remains closed.

3.2 Influence of temperature on $\delta^{18}\text{O}_p$

Since α decreases with increasing vapor condensation temperatures, $\delta^{18}\text{O}_v$ is positively correlated to T irrespective of changes in f . On the other hand, as Li *et al* (1998) have pointed out, the $\delta^{18}\text{O}_p$ - T relationship is somewhat more complicated in that $d(\delta^{18}\text{O}_p)/dT$ switches from positive to negative values when f becomes ≥ 0.38 . This sign change may explain the observation (Rozanski *et al* 1993) that monthly aver-

aged $\delta^{18}\text{O}_p$ and temperature show positive correlations in certain regions (e.g., high-latitude belts) but negative correlations in others (e.g., Hong Kong and New Delhi). Based on the Rayleigh condensation model with isobaric cooling of precipitating air masses, Van der Straaten and Mook (1983) calculated that the slope of the $\delta^{18}\text{O}_p$ - T relationship should be about $0.6\text{‰}/^\circ\text{C}$ between 0 and 20°C . At all stations between 40°N and 60°N of the IAEA/WMO global network, the observed slopes range from 0.58 to $0.9\text{‰}/^\circ\text{C}$ (Dansgaard 1964; Rozanski *et al* 1993). Yonge *et al* (1985) showed that the $\delta^{18}\text{O}$ of dripwater is positively correlated with cave temperatures in the range -5° to 25°C , with a slope of $0.5\text{‰}/^\circ\text{C}$. In each of the caves from Mexico to Canada which they studied, the cave temperature is the same as the mean annual temperature above the cave. In tropical regions with temperatures 20° – 30°C , such a correlation is lacking, due to the dominating effect of precipitation amount (Rozanski *et al* 1993). Therefore, outside tropics and subtropics and perhaps arid regions of the world, a positive correlation between $\delta^{18}\text{O}_p$ and T should generally prevail.

3.3 Climatic inference of $\delta^{18}\text{O}_o$

The oxygen isotopic composition of the vapor source becomes progressively lighter with increasing latitude and altitude as the air mass carrying the vapor travels away from its origin in low-latitude oceans. Besides this distance-elevation effect, two other factors control $\delta^{18}\text{O}_o$; namely, the evaporation temperature and the $\delta^{18}\text{O}$ of the surface-ocean source water. These two factors are expected to vary substantially only over glacial-interglacial time scales, however. On shorter terms, $\delta^{18}\text{O}_o$ is modified by the frequency and magnitude of the rain-out along the vapor transport trajectory: the higher the frequency and extent of the rain-out, the lighter the $\delta^{18}\text{O}_o$. As seen from the temperature derivative of equation (3), $\delta^{18}\text{O}_o$ is not sensitive to local air temperature variations. For example, from the mean $\delta^{18}\text{O}$ of -10.28‰ for the summer rain in Beijing (Zhen *et al* 1983), we estimate that $\delta^{18}\text{O}_o$ ranges from -19.24‰ to -20.44‰ when temperature varies from 10°C to 25°C . As long as the vapor source remains stable, we can take the annual mean $\delta^{18}\text{O}_o$ at a given location as invariant. In eastern China, precipitation mostly occurs in the summer and the vapor source comes mainly from the western north Pacific.

In summary, $\delta^{18}\text{O}_p$ decreases with increasing precipitation. In “low- f ” regions of mid-to-high latitudes, $\delta^{18}\text{O}_p/dT$ ranges from 0.5 to $0.9\text{‰}/^\circ\text{C}$. This temperature effect more than offsets the calcite-water isotopic fractionation of $-0.23\text{‰}/^\circ\text{C}$ (O’Neil *et al* 1969). Drip water in many caves comes from surface precipitation. $\delta^{18}\text{O}$ of stalagmites formed in deep parts of caves (where temperature remains rather constant year round) reflect $\delta^{18}\text{O}_p$, so that calcite layers with

lighter $\delta^{18}\text{O}$ values form under relatively wet and cold conditions and those with heavier $\delta^{18}\text{O}$ values form under drier and warmer climate. If both precipitation and temperature increase or decrease during a given period, it will lead to a minimization of the $\delta^{18}\text{O}$ change in stalagmites. However, changes in annual precipitation (two to fourfold) are often greater than changes in annual temperature ($< 2^\circ\text{C}$). Therefore, averaged over decadal or longer time intervals, the temperature effect becomes more important than the precipitation effect. One may safely assume that, in the main, high-resolution (< 10 years) $\delta^{18}\text{O}$ records in stalagmites reflect changes in precipitation, whereas on coarser time scales (> 50 years), the stalagmite $\delta^{18}\text{O}$ records temperature variations.

4. Mg/Ca and Mg/Sr as paleotemperature proxy

The finding that distribution of magnesium between calcite and water is temperature-dependent (Katz 1973; Fuchtbauer and Hardie 1976; Gascoyne 1983) opens the possibility of assessing past changes in cave temperature, or the mean annual temperature above the cave, based on variations in the Mg content of calcitic speleothems (Gascoyne 1983; Goede and Vogel 1991). The homogeneous distribution coefficient, $D_{\text{Mg/Ca}}$, defined as:

$$D_{\text{Mg/Ca}} = \frac{(\text{Mg/Ca})_c}{(\text{Mg/Ca})_w} \quad (4)$$

where subscripts w and c refer to water and calcite, respectively, has a temperature coefficient B ($= \Delta D_{\text{Mg/Ca}} / \Delta T$) of $0.0011 \pm 50\%/^\circ\text{C}$ in the range $7^\circ\text{--}80^\circ\text{C}$ (Katz 1973; Fuchtbauer and Hardie 1976; Gascoyne 1983). If cave-water Mg/Ca is determined for a given location where the present-day temperature is known, past temperatures at the location can be derived from Mg/Ca ratios in a stalagmite sample, assuming that cave-water Mg/Ca ratio has remained constant. Since Sr/Ca does not show a temperature dependence in the calcite formation (Kinsman and Holland 1969; Katz *et al* 1972; Gascoyne 1983), it has been suggested that Mg/Sr is used to correct for variations in Mg/Ca due to factors other than temperature (Goede and Vogel 1991). However, this correction requires the assumption of constancy of Mg/Sr in water entering the cave over time.

5. $\delta^{13}\text{C}$ as paleoclimate proxy

The carbon isotopic composition of stalagmites reflects the $\delta^{13}\text{C}$ of soil CO_2 above a limestone cave and is affected by the relative abundance of C_3 and C_4 plants grown locally (Hendy 1971; Dorale *et al* 1992; Li *et al* 1997b; Bar-Matthews *et al* 1997). The C_3

(Calvin) and C_4 (Hatch-Slack) photosynthetic pathways fractionate carbon isotopes to different degrees. The C_3 plants, generally growing under wet and cool climatic conditions and including trees, most shrubs and herbs, and cool season grasses, have $\delta^{13}\text{C}$ values between -25‰ and -32‰ relative to the PDB standard. The C_4 plants, including maize, sorghum, prairie and savanna grasses which grow under relatively high temperature and high water-stress conditions, have $\delta^{13}\text{C}$ values ranging from -10‰ to -14‰ (Cerling 1984; Cerling *et al* 1989; Kelly *et al* 1991). Hence, at a given location, the C_3/C_4 plant ratio can be modulated by changes in climate and recorded by $\delta^{13}\text{C}$ in speleothems. Lighter $\delta^{13}\text{C}$ signals in speleothems indicate a higher C_3/C_4 plant ratio (hence in general wet and cool climatic conditions) and vice versa. On decadal or shorter scales, however, the relative proportion of C_3 and C_4 plants at a location is not expected to undergo large changes without human intervention. In this case, the variation of $\delta^{13}\text{C}$ in speleothem deposit is mainly influenced by the residence time and P_{CO_2} of seepage water and by the extent of CaCO_3 dissolution of the cave-limestone host rock. These factors are related to local precipitation. When rainfall increases, the stalagmite $\delta^{13}\text{C}$ will decrease because of: (1) less dissolution of the isotopically heavy CaCO_3 due to shortening of the residence time and reduced P_{CO_2} of the seepage water in the overlying limestone, and (2) an increase of cave water drip rate, reducing the degassing of the isotopically light CO_2 (Fischer *et al* 1996; Holmgren 1996; Dulinski and Rozanski 1990). Therefore, the $\delta^{13}\text{C}$ record of a speleothem may provide information not only on the paleovegetation over long time intervals (> 50 years), but also on the variability of precipitation on short time scales, such that wetter and cooler periods are registered by lighter $\delta^{13}\text{C}$ signals.

6. Data interpretation

The present-day temperatures inside Shihua Cave remain close to the annual mean surface temperature, around 13°C . At this temperature, calcites precipitating from the cave drip water under isotopic equilibrium will have a $\delta^{18}\text{O}$ (PDB) value of about -8.25‰ (Epstein *et al* 1953, O'Neil *et al* 1969), a value that is close to the post-1985 values of -8.19 to -8.39‰ found in S312 (figure 2). Our measurement results on S312 will be interpreted based on the theoretical considerations presented above with the implicit assumption that calcite-water isotopic equilibrium holds true.

6.1 The $\delta^{18}\text{O}$ records

The 500-year record (figure 2a) shows cyclic variations with a periodicity of 30–40 years which is similar

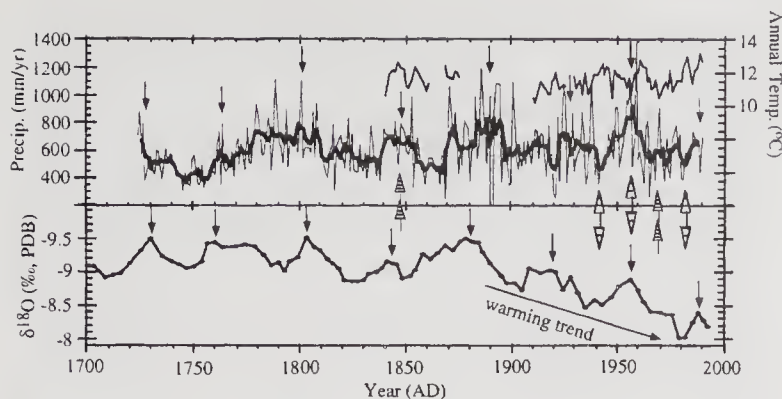


Figure 4. Comparisons of the $\delta^{18}\text{O}$ record in S312 with the instrumental records of temperature and precipitation in Beijing. The annual temperature record extends back to about 1840 AD, with data gaps. Data on annual precipitation for the last 260 years are filtered with 5-year running averages. Thin vertical arrows serve to guide the $\delta^{18}\text{O}$ -precipitation correlation, bearing in mind the uncertainties involved in the dating of S312. Double arrows of the same direction denote periods when both precipitation and temperature increased or decreased, suppressing the $\delta^{18}\text{O}$ change. Double arrows with opposite directions denote periods when precipitation and temperature changed in the opposite sense, enhancing the $\delta^{18}\text{O}$ change.

to those of the Brückner cycles and the historical description of drought-flood occurrences in north-eastern China, mentioned earlier. A recent analysis of the frost cycles in central and southern China also revealed such a cyclicity (Karlstrom 1997). We have discussed speleothem $\delta^{18}\text{O}$ as a proxy for precipitation on decadal and shorter time scales. This $\delta^{18}\text{O}$ -climate connection can be seen by directly comparing the $\delta^{18}\text{O}$ record in S312 with the instrumental records of precipitation and temperature in Beijing for the last 260 years (figure 4). The comparison shows good correlations considering the uncertainties in dating the stalagmite. Light $\delta^{18}\text{O}$ corresponds to high precipitation, consistent with our theoretical analysis. A comparison with the shorter (~ 100 -year) precipitation records in Tianjin and Shanghai shows the same (Ku *et al* 1998). The fourteen precipitation cycles over the last 500 years recorded in S312 may well reflect changes in the strength of the East Asian summer monsoons. On longer time scales of > 50 years, the $\delta^{18}\text{O}$ record is driven by temperature variations as dictated by the positive $\delta^{18}\text{O}_p$ -T correlation. The post-1880 AD trend toward heavier $\delta^{18}\text{O}$ (figures 2a and 4) serves to reflect the warming trend of global temperatures (figure 2c). Taking the mean $\delta^{18}\text{O}$ over the last 500 years as representing the average temperature for the period, we see that colder-than-average temperatures prevailed in Beijing between 1620 and 1900 AD (figure 2a), a period overlapping a part of the Little Ice Age in Europe. It is worth noting in figure 4 the opposite effects of precipitation and temperature on the $\delta^{18}\text{O}$ in stalagmites. As both increased (ca. 1845 AD) or decreased (ca. 1970 AD), the magnitude of stalagmite $\delta^{18}\text{O}$ changes was reduced. When temperature increased but precipitation decreased (ca. 1940 and 1980 AD), and vice versa

(ca 1960 AD), the stalagmite $\delta^{18}\text{O}$ changes tended to be enhanced. Extending to ~ 3000 yr BP for the top 12.5 cm of the specimen shows $\delta^{18}\text{O}$ to vary from -8.14 to -9.72 ‰ (figure 3). In this data set, $\delta^{18}\text{O}$ registers both precipitation and temperature variations. Relative to the mean value of -8.73 ‰, lighter $\delta^{18}\text{O}$ denotes wetter and colder climates. Figure 3 displays eight major climatic cycles over the past 3000 years each with a duration of 300–400 years. The lightest $\delta^{18}\text{O}$ peak (peak 8) occurred during the Little Ice Age. The $\delta^{18}\text{O}$ peaks find their equivalents in the Mg/Ca and $\delta^{13}\text{C}$ records.

6.2 The Mg/Ca and Mg/Sr records

The Mg/Ca and Mg/Sr distributions show similar cyclic patterns between them for the last 3000 years. These patterns in turn correspond to those delineated by $\delta^{18}\text{O}$, with Mg/Ca and Mg/Sr minima matching light $\delta^{18}\text{O}$ peaks (identified by numerals 1 through 8 in figure 3). The matching is expected, as both the Mg ratios and $\delta^{18}\text{O}_p$ are positively related to temperature. However, because $\delta^{18}\text{O}_p$ also depends on precipitation, the matching is not to be done quantitatively to include a comparison of amplitude changes.

In principle, we can estimate paleotemperature by measuring Mg/Ca in cave water and stalagmite calcites actively forming in Shihua Cave at different temperatures. Such a data set has yet to be gathered. For the purposes of the present discussion, we use the Mg ratios as a qualitative temperature proxy to complement the isotopic records as shown in figure 3. We note that applying a coefficient of $0.0011/^\circ\text{C}$ quoted earlier for $D_{\text{Mg/Ca}}$ to the Mg/Ca data of S312 would give long-term temperature fluctuations of less than $\pm 0.9^\circ\text{C}$ about the 3000-year mean for the cycles shown.

6.3 The $\delta^{13}\text{C}$ records

Similar to that of the $\delta^{18}\text{O}$ record, $\delta^{13}\text{C}$ generally exhibits a 30–40 year cyclic variation during the last 500 years (figure 2). The similarity is in accordance with our discussion that decadal or shorter-scale $\delta^{13}\text{C}$ signals record variability in precipitation; i.e., lighter $\delta^{13}\text{C}$ reflects higher precipitation which also brings about lighter $\delta^{18}\text{O}$ signals. For longer intervals, changes in vegetation cover in terms of C_3/C_4 plant ratio become the main cause for the $\delta^{13}\text{C}$ variation. In figure 2 we see two major periods of such vegetative changes. From about 1570 to 1730 AD the $\delta^{13}\text{C}$ trended toward lighter values, paralleling the long-term decline of $\delta^{18}\text{O}$. The climate during this interval was cool/wet favoring the growth of C_3 plants in the region. Between 1730 and 1850 AD, the $\delta^{13}\text{C}$ reversed toward an increasing trend even though temperature remained below the 500-year mean (as part of the Little Ice Age) as shown by the $\delta^{18}\text{O}$ record. We

suggest that the reduced C_3/C_4 plant ratio shown by the $\delta^{13}C$ change was the result of an increase of agricultural growth in the region where C_4 plants such as maize and sorghum were widely grown to meet the ever-burgeoning population in Beijing during the Qing Dynasty.

A most interesting feature of the $\delta^{13}C$ data shown in figure 2 is its opposite trend to that of $\delta^{18}O$ during the last fifty years or so. One cannot attribute the decrease of $\delta^{13}C$ from about 1940 to 1990 AD to changes in temperature or C_3/C_4 plant ratio. Rather, the decrease may well reflect the effect of enhanced fossil fuel CO_2 in the atmosphere on the $\delta^{13}C$ of soil CO_2 (Baskaran and Krishnamurthy 1993). Friedli *et al* (1986) measured the $\delta^{13}C$ in CO_2 extracted from Antarctic ice and found it to have decreased since about 1920 AD. Marino and McElroy (1991) analyzed the $\delta^{13}C$ in C_4 plant cellulose and also noted a recent long-term decline of $\delta^{13}C$ of atmospheric CO_2 . Direct time-series measurements of atmospheric CO_2 by Keeling *et al* (1989) have shown a decline of $\delta^{13}C$ while concentrations increased in recent decades, with an average $\delta^{13}C$ declining rate of -0.034‰ y^{-1} between 1956 and 1989. As summarized by Baskaran and Krishnamurthy (1993), enhanced fossil fuel CO_2 concentrations in the atmosphere have caused a decrease of $\delta^{13}C$ in the atmospheric CO_2 , and, over the last 30 to 70 years, the $\delta^{13}C$ changes in the atmospheric CO_2 have averaged around -0.03‰ y^{-1} . This effect is also recorded by stalagmite S312. In figure 2 we see that its $\delta^{13}C$ has decreased from -6.7 to -8.1‰ since 1940 AD, with a long-term declining rate of about -0.028‰ y^{-1} .

The 3000-year record of $\delta^{13}C$ is best understood in the context of the $\delta^{18}O$ and Mg/Ca/Sr records as interpreted above. In figure 3, the average “climatic condition” over the past three millennia is represented by the vertical dashed lines delineating the mean values for $\delta^{18}O$, Mg/Ca and Mg/Sr. Thus for $\delta^{18}O$, data points fall to the left of the dashed lines represent periods of cold and wet climate relative to the mean, and those to the right represent periods of relatively dry and warm climate. For the Mg ratios, data points fall to the left of the dashed line represent periods colder than the mean, and those to the right represent warmer periods. In these contexts, the general parallelism of the $\delta^{13}C$ record with respect to those of $\delta^{18}O$ and Mg ratios (figure 3) is understandable. This is because long-term $\delta^{13}C$ variations in speleothems reflect changes in C_3/C_4 ratio of vegetation cover, as cooler and wetter climates favor the growth of C_3 plants with lighter $\delta^{13}C$ values. However, a conspicuous deviation from the parallelism occurred during the last ~ 600 years (figure 3). In fact, there exists a clear demarcation in the $\delta^{13}C$ distribution. Between 3000 and 650 years BP, the $\delta^{13}C$ fluctuated around a mean value of -9.46‰ (shown by the dashed line in figure 3). Since 650 years BP, $\delta^{13}C$ has

jumped to a mean value of -8.05‰ . A 3.5‰ increase occurred from 650 to 360 years BP, an increase that is unprecedented in the $\delta^{13}C$ record shown and not corroborated by the $\delta^{18}O$ and Mg ratio records. In the early part of this period, $\delta^{18}O$, Mg ratio and $\delta^{13}C$ all increased. But when $\delta^{18}O$ and Mg ratio reached their respective peaks and began to show a return to wet/cool climate from 420 to 360 years BP, the increase of $\delta^{13}C$ continued reaching a value of -6.6‰ (figure 3). This increase of 3.5‰ in $\delta^{13}C$ cannot be caused by climate change alone; it must include an important anthropogenic component. The buildup of Beijing as the capital city of China began in great earnest at the dawn of the Yuan Dynasty (a.k.a. Genghis Khan), and culminated around the late Ming Dynasty (Skinner 1977; Sit 1995). Over a span of 300 years (ca. 1270–1579 AD), roughly coinciding with the 650–360 years BP period discussed here, Beijing more than tripled its size and nearly doubled its population from 410 to 706 thousands (the world’s largest). Demand for wood to meet these expansions led to vast deforestation in the Xi Shan and Jundu Shan – mountains to the city’s west and north (figure 1), particularly at Xi Shan (Ho 1985) where the Shihua Cave is located. The attendant soil conservation and flood problems had rendered Yong Ding River (figure 1) to bear nicknames such as Turbid River and Little Yellow River (Ho 1985). Apparently, a reduction of the C_3/C_4 plant ratio resulting from the deforestation has been recorded by the $\delta^{13}C$ in speleothem S312. As can be seen from figure 3, the relative abundance of C_3 and C_4 plants in the Xi Shan area has yet to return to the pre-deforestation conditions.

7. Summary and conclusions

Studies of the paleoclimate history of continental areas are important to our understanding of how terrestrial ecosystems and hydrologic systems respond to changes in the earth’s radiation budget. However, owing to the variable nature of continental processes, few archives of these processes are available, especially where the nature of these processes can be traced with a very high time-resolution (down to interannual). The speleothem deposits of limestone caves represent one such archive. This study has shown that a combination of isotopic (^{18}O and ^{13}C) and chemical (Mg/Sr/Ca) data sets obtained from the deposit can help decipher past changes in temperature, precipitation and nature of vegetation.

On decennial or shorter scales, $\delta^{18}O$ variations in a speleothem mainly reflect changes in precipitation, with lighter $\delta^{18}O$ corresponding to increased rainfall. Long-term (> 50 years) $\delta^{18}O$ variations primarily reflect fluctuations in temperature, with lighter $\delta^{18}O$ corresponding to colder temperatures. Information on climate provided by $\delta^{13}C$ is also time-scale dependent:

Long-term (> 50 years) records reflect changes in regional vegetation cover in terms of the relative abundance of C₃ and C₄ plants, whereas the variability in precipitation is registered by short-term records. In either case, wetter and cooler climates give rise to lighter $\delta^{13}\text{C}$ signals. The Mg/Ca and Mg/Sr ratios in speleothem calcites vary positively with temperature.

Observed $\delta^{18}\text{O}$ variations in stalagmite S312 indicate climate changes during the past 500 years in northeastern China as follows. Compared to the 500-year mean, temperatures in Beijing and Tianjin were lower between 1620 and 1900 AD, and higher during 1520–1620 AD and since 1900 AD. Superimposed on these long-term temperature trends are fourteen cycles (30–40 year duration) of precipitation changes, with wet periods centered around 1985, 1955, 1910, 1880, 1840, 1800, 1760, 1730, 1690, 1660, 1630, 1600, 1560 and 1530 AD. Historical records and data on $\delta^{13}\text{C}$ confirm these precipitation variations, which may well manifest the fluctuations in the strength of the East Asian summer monsoons. The 3000-year record of S312 shows eight major wet/cool – dry/warm climatic cycles of 300–400 years duration, the latest wet/cool half cycle corresponding to the Little Ice Age originally documented in Europe.

The $\delta^{13}\text{C}$ results indicate that stalagmite S312 has recorded not only the past variation of climate but also man's activity in affecting the environment and its ecosystems. The latter includes enhanced input of fossil-fuel CO₂ into the atmosphere and deforestation near Beijing when it was made the capital city of ancient China during the 13th to 16th centuries.

Acknowledgements

We are honored to be invited to present the work at the International Conference on 'Isotopes in the Solar System', on the occasion of the Golden Jubilee of the Physical Research Laboratory. The stable isotope measurements were made in the laboratory of Prof. Lowell D. Stott to whom we are most grateful. We acknowledge the assistance from our Chinese colleagues Prof. Zhao Shusheng, Mr. Li Tieyin and Mr. Lu Jinbo in the sample collection and Prof. Zhu Zhaoyu in the drafting of figures. The constructive comments of two anonymous reviewers are much appreciated. This study was supported by the US National Science Foundation under grant ATM-9615875.

References

- Baker A, Ito E, Smart P L and McEwan R F 1997 Elevated and variable values of ^{13}C in speleothems in a British cave system; *Chem. Geol.* **136** 263–270
- Baker A, Smart P L, Edwards R L and Farrant A 1993 Annual growth banding in a cave stalagmite; *Nature* **304** 518–520
- Bar-Matthews M, Ayalon A and Kaufman A 1997 Late Quaternary paleoclimate in the Eastern Mediterranean region from stable isotope analysis of speleothems at Soreq Cave, Israel; *Quat. Res.* **47** 155–168
- Baskaran M and Iliffe T M 1993 Age determination of recent cave deposits using excess ^{210}Pb -A new technique; *Geophys. Res. Lett.* **20** 603–606
- Baskaran M and Krishnamurthy R V 1993 Speleothems as proxy for the carbon isotope composition of atmospheric CO₂; *Geophys. Res. Lett.* **20** 2905–2908
- Burroughs W J 1992 *Weather Cycles: Real or Imaginary*, (Cambridge: Cambridge University Press) 521 p
- Cerling T E 1984 The stable isotopic composition of soil carbonate and its relationship to climate; *Earth Planet. Sci. Lett.* **71** 229–240
- Cerling T E, Quade J, Wand Y and Bowman J R 1989 Carbon isotopes in soils and paleosols as ecology and Paleoecology indicators; *Nature* **341** 138–139
- Dansgaard W 1964 Stable isotopes in precipitation; *Tellus* **16** 436–468
- Domros M and Peng G-B 1988 *The Climate of China* (New York: Springer-Verlag) 357p
- Dorale J A, Gonzalez L A, Reagan M K, Pickett D A, Murrell M T and Baker R 1992 A high-resolution record of Holocene climate change in speleothem calcite from Cold Water Cave, Northeast Iowa; *Science* **258** 1626–1630
- Dulinski M and Rozanski K 1990 Formation of $^{13}\text{C}/^{12}\text{C}$ isotope ratios in speleothems: A semi-dynamic model; *Radiocarbon* **32** 7–16
- Epstein S, Buchsbaum R, Lowenstam H A and Urey H C 1953 Revised carbonate-water isotopic temperature scale; *Bull. Geol. Soc. Amer.* **64** 1315–1326
- Friedli H, Lotscher H, Oeschger H, Siegenthaler U and Stauffer B 1986 Ice core record of the $^{13}\text{C}/^{12}\text{C}$ ratio of atmospheric CO₂ in the past two centuries; *Nature* **324** 237–238
- Fischer M J, Gale S J, Heijnis H and Drysdale R N 1996 Low latitude speleothem growth and climate; In: *Climate Change: The Karst Record* (ed) S E Lauritzen (Karst Water Institute Special Publication 2) pp. 26–29
- Fuchtbauer H and Hardie L A 1976 Experimentally determined homogeneous distribution coefficients for precipitated magnesium calcites: application to marine carbonate cements; *Abstr. Geol. Soc. Am. Annual Meeting* Denver, CO
- Gascoyne M 1992 Paleoclimate determination from cave deposits; *Quat. Sci. Rev.* **11** 609–632
- Gascoyne M 1983 Trace-element partition coefficients in the calcite-water system and their paleoclimatic significance in cave studies; *J. Hydrol.* **61** 213–222
- Goede A and Vogel J C 1991 Trace element variations and dating of a late Pleistocene Tasmanian speleothem; *Palaeogeogr. Palaeoclimat. Palaeoecol.* **88** 121–131
- Harmon R S, Thompson P, Schwarcz H P and Ford D C 1978 Late Pleistocene paleoclimates of North America as inferred from stable isotope studies of speleothems; *Quat. Res.* **9** 54–70
- Hendy C H 1971 The isotopic geochemistry of speleothems-I: The calculation of the effects of different models of formation on the isotopic composition of speleothems and their applicability as paleoclimatic indicators; *Geochim. Cosmochim. Acta* **35** 801–824
- Hendy C H and Wilson A 1968 Paleoclimate data from speleothem; *Nature* **219** 48–51
- Ho R-Z (chief editor) 1985 *Historical Maps of Beijing*, The Editorial Committee of Historical Maps of Beijing, Beijing Press, 127p
- Holmgren K 1996 The potential of speleothems in the reconstruction of southern African palaeoclimates – an example from Lobatse II Cave, Botswana; In: *Climate Change: The Karst Record* (ed) S E Lauritzen (Karst Water Institute Special Publication 2) pp. 62–64

- Karlstrom T 1997 Addendum I: Paleoclimate and the solar-insolation/tidal-resonance climate model; In *Proc. 13th Annual Pacific Climate (PACCLIM) Workshop* (ed) C M Isaacs and V L Tharp (Interagency Ecological Program, Technical Report 53, California Department of Water Resources) pp. 201–224
- Katz A 1973 The interaction of magnesium with calcite during crystal growth at 25–90°C and one atmosphere; *Geochim. Cosmochim. Acta* **37** 1563–1586
- Katz A, Sass E and Starinsky A 1972 Strontium behavior in the aragonite-calcite transformation: An experimental study at 40–98°C; *Geochim. Cosmochim. Acta* **36** 481–496
- Kelly E F, Amundson R G, Marino B D and DeNiro M J 1991 The stable isotope ratios of carbon in phytoliths as a quantitative method of monitoring vegetation and climatic change; *Quat. Res.* **35** 222–233
- Keeling C D, Bacastow R B, Carter A F, Piper S C, Timothy W P, Heimann M, Mook W G, and Roeloffzen H 1989 A three dimensional model of atmospheric CO₂ transport based on observed winds: 1. Analysis of observational data; *Am. Geophys. Un. Monogr.* **55** 165–236
- Kinsman D J J and Holland H D 1969 The co-precipitation of cations with CaCO₃-IV. The co-precipitation of Sr²⁺ with aragonite between 16°C and 96°C; *Geochim. Cosmochim. Acta* **33** 1–17
- Ku T-L, Li H-C and Stott L D 1998 Decadal climatic reconstruction from stable isotope records of speleothem in Shihua Cave, China: A summer monsoon domain; In *Proc. 14th Annual Pacific Climate (PACCLIM) Workshop* (eds) R C Wilson and V L Tharp (Interagency Ecological Program, Technical Report 53, California Department of Water Resources) pp. 45–58
- Lamb H H 1977 *Climatic History and the Future* (New York: Barnes & Noble) 740p
- Li H-C, Ku T L, Chen W-J, Jiao W-Q, Zhao S-S, Chen T-M, and Li T-Y 1996a Isotope studies of Shihua Cave, Beijing-II: Radiocarbon dating and age correction of stalagmite; *Seismology and Geology* **18** 329–338
- Li H-C, Ku T L, Zhao S-S, Liu T S, Jiao W-J, Yin J-H, Li T-Y, and Lu J-B 1996b Isotope studies of Shihua cave-I: δD , $\delta^{18}O$ and tritium activity of Shihua cave, Beijing; *Seismology and Geology* **18** 325–328 (in Chinese)
- Li H-C, Ku T L, Chen W-J, and Li T-Y 1997a Isotope studies of Shihua cave-III: Reconstruction of paleoclimate and paleo-environment of Beijing during the last 3,000 years from $\delta^{13}C$ and $\delta^{18}O$ records in stalagmite; *Seismology and Geology* **19** 77–86 (in Chinese)
- Li H C, Ku T L, Stott L D, Yuan D, Chen W and Li T 1997b Interannual-resolution $\delta^{13}C$ record of stalagmites as proxy for the changes in precipitation and atmospheric CO₂; *Carsologica Sinica* **16** 285–295 (in Chinese)
- Li H C, Ku T L, Stott L D and Chen W 1998 Application of interannual-resolution stable isotope records of speleothem: Climatic changes in Beijing and Tianjin, China during the past 500 years – the $-\delta^{18}O$ record; *Science in China* (Series D) **28** 181–186
- Li W-X, Lundberg J, Dickin A P, Ford D C, Schwarcz H P, McNutt R, and Williams D 1989 High precision mass spectrometric U-series dating of cave deposits and implications for paleoclimate studies; *Nature* **339** 534–536
- Marino B D and McElroy M B 1991 Isotopic composition of atmospheric CO₂ inferred from carbon in C₄ plant cellulose; *Nature* **349** 127–131
- O'Neil J R, Clayton R N and Mayeda T K 1969 Oxygen isotope fractionation in divalent metal carbonates; *J. Chem. Phys.* **51** 5547–5558
- Quinn T M, Taylor F W, Crowley T J and Link S M 1996 Evaluation of sampling resolution in coral stable isotope records: A case study using records from New Caledonia and Tarawa; *Paleoceanography* **11** 529–542
- Rozanski K, Arzguas-Araguas L and Gonfiantini R 1993 Isotopic patterns in modern global precipitation, In *Climate Change in Continental Isotopic Records* (ed) P K Swart *et al* (Amer. Geophys. Union, Monograph 78) pp. 1–36
- Shopov Y Y, Ford D C and Schwarcz H P 1994 Luminescent microbanding in speleothems: High resolution chronology and paleoclimate; *Geology* **22** 407–410
- Sit V F S 1995 Beijing: *The Nature and Planning of a Chinese Capital City* (John Wiley & Sons) 385p
- Skinner G W 1977 *The city in late imperial China*, (Stanford Univ. Press) 800p
- Snitnikov A V 1957 Variability in the general moistness of the continents of the Northern Hemisphere; *Zap. Geogr. Obs. S.S.S.R.* **16** new series, Akad. Nauk (in Russian)
- Strahler A H and Strahler A N 1997 *Physical Geography: Science and Systems of the Human Environment* (John Wiley & Sons) 637p
- Tao S 1984 The climate of China; In, *Physical Geography of China* (ed) S Tao (Beijing, China: Science Press) pp. 161
- Van der Straaten C M and Mook W G 1983 Stable isotope composition of precipitation and climatic variability; In *Paleoclimate and Paleowaters: A Collection of Environmental Isotope Studies* (International Atomic Energy Agency, Vienna) pp. 53–64
- Wang S-W and Zhao Z-C 1981 Droughts and floods in China, 1470-1979; In *Climate and History – Studies In Past Climates and Their Impact On Man* (eds) T M L Wigley, M J Ingram and G Farmer (Cambridge: Cambridge Univ. Press) pp. 271–288
- Yonge C J, Ford D C, and Gray J 1985 Stable isotope studies of cave seepage water; *Chem. Geol.* **58** 97–105
- Zhen S-H, Hou F-G and Ni B-L 1983 Studies on hydrogen and oxygen isotopes of meteoritic water in China; *Chinese Sci. Bull.* **13** 801–806 (in Chinese)
- Zhu C 1954 Southeast monsoon and rainfall in China; In *Collection of Scientific Papers in Meteorology* pp. 1919–1949 (Peking, Acad. Sinica)

Stable isotope variations in a coral (*Favia speciosa*) from the Gulf of Kutch during 1948–1989 A.D.: Environmental implications

S CHAKRABORTY and R RAMESH

Physical Research Laboratory, Navrangpura, Ahmedabad 380 009, India
e-mail: r.ramesh@prl.ernet.in

The stable isotopic analyses ($\delta^{18}\text{O}$ and $\delta^{13}\text{C}$) of a coral *Favia speciosa* spanning forty two years (1948–89 A.D.), collected from the Pirotan island (22.6°N, 70°E) in the Gulf of Kutch have been carried out to assess its potential for retrieving past environmental changes in this region. It is seen that the summer (minima) $\delta^{18}\text{O}$ variations in the coral CaCO_3 are negatively correlated with seasonal (summer) monsoon rainfall in the adjoining region of Kutch and Saurashtra and a qualitative reconstruction of historical rainfall variations in this region can be obtained by analyzing the $\delta^{18}\text{O}$ in this species of coral. The observed mean seasonal range of $\delta^{18}\text{O}$ variations is $0.34 \pm 0.17\text{‰}$ ($n = 42$), whereas the expected range calculated (from available SST and measured $\delta^{18}\text{O}$ of sea water) is $\sim 1.1 \pm 0.15\text{‰}$. The difference is due to the coarse resolution of sampling, which can be corrected. The seasonal range in $\delta^{13}\text{C}$ is $\sim 1\text{‰}$ and is explained by changes in: a) the light intensity related to the cloudiness during monsoons and b) phytoplankton productivity.

1. Introduction

To understand various climatic phenomena and their interlinkages it is essential to have a comprehensive data base both from regular meteorological observations and natural proxy records, which extend the data base back in time. In this context, isotopic analysis of corals is useful for monitoring historical changes of climate and physical properties of the surface ocean. The oxygen isotopic variations in coral skeletons have been shown to be useful for monitoring seasonal and annual temperature variations including El Niño in different oceanic regions (Weber and Woodhead 1972; Fairbanks and Dodge 1979; Dunbar and Wellington 1981; Druffel 1985; Charles *et al* 1997). Shen and Sanford (1990), and Cole and Fairbanks (1990) found that the $\delta^{18}\text{O}$ of corals from Tarawa Atoll (Republic of Kiribati) is also inversely related to local precipitation. Aharon (1991) investigated the isotopic records of corals, giant clams and calcareous algae of Great Palm Island and found that the coral $\delta^{18}\text{O}$ was con-

trolled both by temperature and salinity, modulated by rainfall. We (Chakraborty and Ramesh 1992; 1993; 1997) have shown that the seasonal amplitude in $\delta^{18}\text{O}$ of corals from Lakshadweep islands (Arabian Sea) reflects the monsoon induced sea surface cooling of 4°C.

The most characteristic feature of the Arabian Sea is the occurrence of south west (SW) summer monsoon associated with intense winds resulting in a large scale surface ocean circulation (Shetye *et al* 1990) and rainfall over the Indian subcontinent. During winter, the wind direction reverses leading to changes in the surface ocean currents. The SW monsoon causes upwelling of cool, nutrient rich water in several areas like the Somali basin and the west coast of India. In this paper we report $\delta^{18}\text{O}$ and $\delta^{13}\text{C}$ data of a coral collected from the Pirotan island (figure 1), Gulf of Kutch (northern Arabian Sea) and examine their utility as proxy records of SST and monsoon rainfall. Gulf of Kutch (figure 1, mean water depth ~ 30 m) is a shallow well-mixed region where the seasonal SST variations (figure 2) seem to be mainly controlled by

Keywords. Climate; monsoon; SST; stable isotopes; corals; Gulf of Kutch.

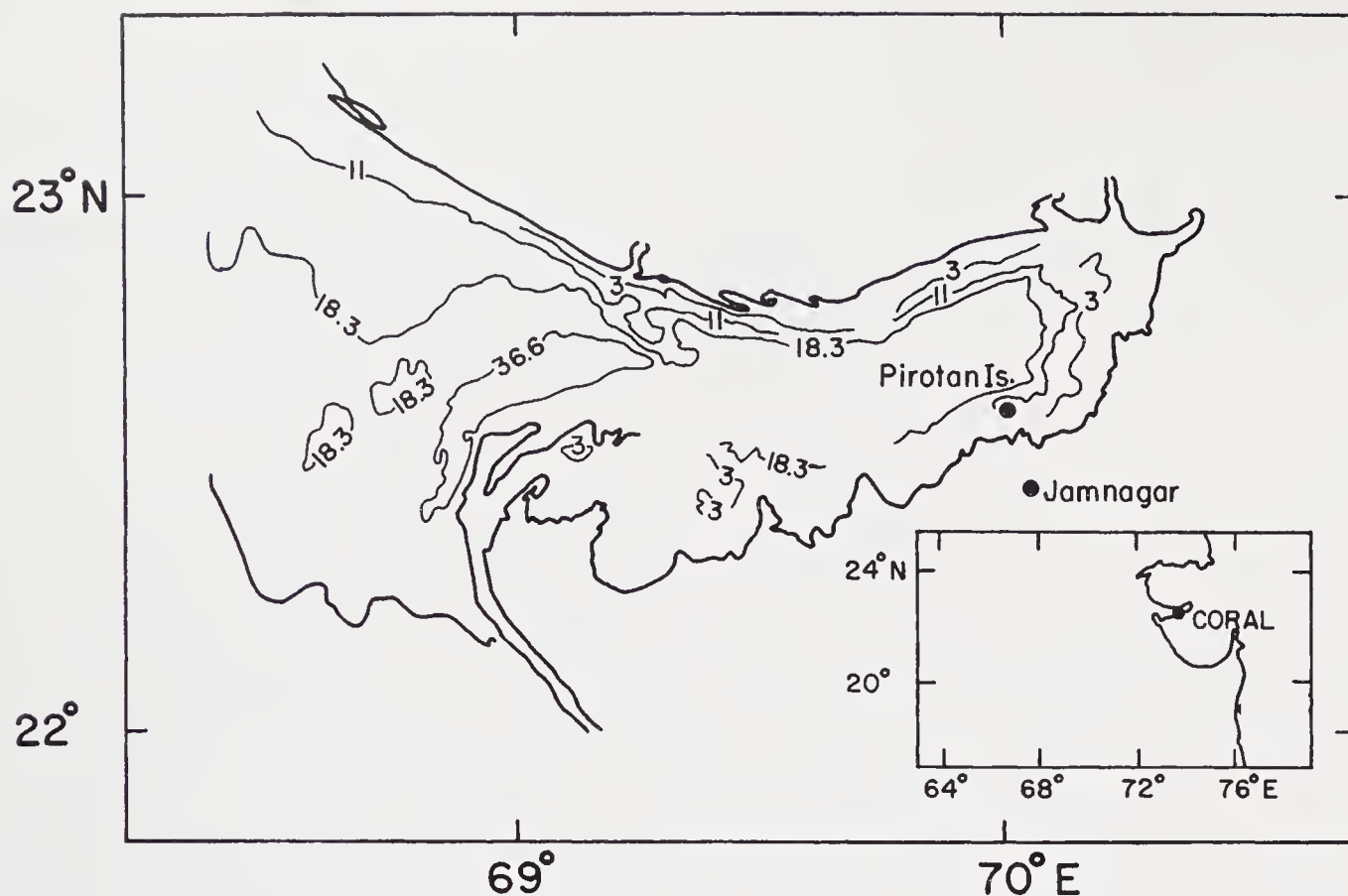


Figure 1. Sample location in the Gulf of Kutch. Contours show water depth in meters.

summer solar heating and winter cooling. Nevertheless, the cloud cover during the SW monsoon reduces the SST by about 2°C in the Gulf.

2. Methods

A live coral head, *Favia speciosa* was collected in June 1990 off the coast of Pirotan island situated in the Gulf of Kutch at a water depth of ~ 1 metre during low tide. The sample was washed with fresh water, dried and cut into a vertical section (~ 1 cm thick) along the growth axis. The annual bands (consisting of light and dark rings) were photographed using the standard X-ray technique (Wellington and Glynn 1983) and counted to determine the age, assuming that the latest band, which had only developed the light part, corresponds to 1990 (this band, however, was not analyzed for stable isotopes, as it was only partially formed and contained considerable organic matter). The annual band widths (i.e., growth rates) were measured from the X-ray positive using a hand lens fitted with a scale correct to 0.1 mm. Milligram quantities of calcium carbonate powder were removed from a radial strip by careful filing, taking 2 to 8 samples per annual band. The extracted powder was roasted under vacuum at 350°C for an hour to remove organic matter. Isotopic measurements were made using a VG 903 mass-spectrometer following standard techniques (Chakraborty and Ramesh 1997) and the results reported in δ notation with respect to PDB with a precision of 0.07‰ for both $\delta^{18}\text{O}$ and $\delta^{13}\text{C}$.

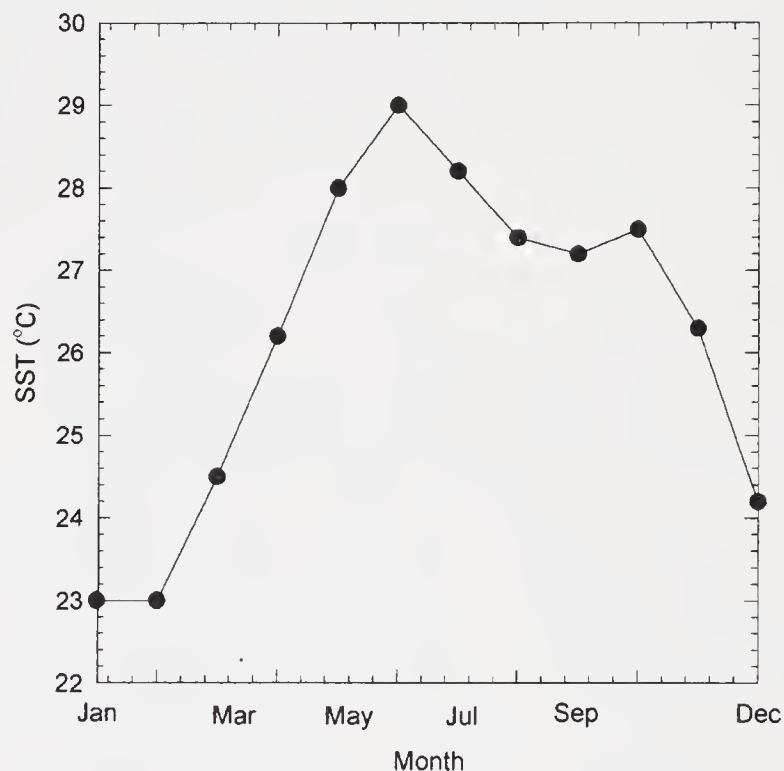


Figure 2. Seasonal sea surface temperature variations near the sample location (Sadler *et al* 1987).

3. Results and discussion

3.1 Growth rate

Table 1 shows the growth rate of the coral, which varies from $\sim 6\text{mm y}^{-1}$ in the early stages to $\sim 3\text{mm y}^{-1}$ during the late stages, with an overall mean growth rate of 3.5mm y^{-1} . Because of the

Table 1. Growth rate, oxygen and carbon isotope ratios in the coral. Underlined data indicate the minimum values in carbon and oxygen isotope ratios. If adjacent data points are indistinguishable within the analytical uncertainty ($\pm 0.07\text{‰}$), the minima in $\delta^{18}\text{O}$ are chosen to correspond with $\delta^{13}\text{C}$ minima. $\delta^{18}\text{O}$ and $\delta^{13}\text{C}$ are relative to V-PDB standard.

Year (A.D.)	Distance (mm)	$\delta^{18}\text{O}$ (‰)	$\delta^{13}\text{C}$ (‰)	Growth rate (mm y ⁻¹)	Rain (mm)	$\delta^{18}\text{O}$ range (‰)
1948	0.0	-4.08	-0.54	5.4	201	0.37
	1.7	<u>-4.15</u>	<u>-1.12</u>			
	3.3	-3.78	-0.36			
	4.4	-3.86	-0.44			
1949	5.4	-3.73	-0.71	8.3	536	0.69
	6.3	-4.27	-1.82			
	7.5	<u>-4.37</u>	<u>-2.14</u>			
	8.4	-4.36	-1.54			
	9.5	-4.42	-1.14			
	10.7	-4.25	-0.72			
	11.8	-3.82	-0.50			
	12.7	-3.84	-0.30			
1950	13.7	-3.69	-0.35	6.9	554	0.59
	15.4	-3.99	-0.22			
	17.0	-4.04	-0.23			
	18.8	<u>-4.28</u>	<u>-0.55</u>			
1951	20.6	-3.65	1.02	7.1	303	0.32
	22.6	-3.70	-0.09			
	24.5	-3.80	<u>-0.43</u>			
	26.2	<u>-3.97</u>	-0.29			
1952	27.8	-3.88	-0.20	4.2	392	0.52
	29.2	<u>-4.36</u>	<u>-1.72</u>			
	30.5	-4.40	-0.94			
1953	32.0	-4.10	-0.03	8.2	659	0.47
	34.0	-4.16	-0.99			
	35.0	<u>-4.57</u>	<u>-1.41</u>			
	36.3	-4.48	-1.41			
	38.6	-4.25	-0.54			
1954	40.2	-4.23	-0.26	3.8	526	0.45
	41.6	-4.68	-2.23			
	42.7	<u>-4.65</u>	<u>-2.52</u>			
1955	44.0	-4.20	-0.41	7.8	343	0.30
	45.7	-3.94	0.48			
	49.6	-4.23	-0.34			
	48.2	-4.24	-0.37			
	49.9	<u>-4.22</u>	<u>-0.81</u>			
	50.7	-4.03	-0.04			
1956	51.8	-3.99	0.02	3.5	710	0.20
	52.5	-4.07	-0.57			
	53.0	<u>-4.19</u>	<u>-0.56</u>			
	54.0	-4.07	-0.58			
1957	55.3	-3.75	<u>-0.59</u>	5.7	486	0.41
	57.2	-4.06	0.62			
	58.8	<u>-4.16</u>	0.35			
1958	61.0	-3.91	0.65	7.5	541	0.38
	62.5	-4.10	-0.05			
	63.8	-4.19	-0.42			
	65.1	<u>-4.29</u>	<u>-0.57</u>			
	66.6	-4.11	-0.26			
1959	68.5	-4.10	0.27	3.5	1241	0.43
	70.5	<u>-4.53</u>	<u>-0.58</u>			
1960	72.0	-4.25	0.00	5.1	290	0.29
	73.8	<u>-4.54</u>	<u>-1.34</u>			
	75.6	-4.42	-1.01			
1961	77.1	-4.27	0.04	5.2	785	0.07
	78.8	<u>-4.29</u>	<u>-0.77</u>			
	80.3	-4.22	-0.46			

(Continued)

Table 1. (Continued)

Year (A.D.)	Distance (mm)	$\delta^{18}\text{O}$ (‰)	$\delta^{13}\text{C}$ (‰)	Growth rate (mm y ⁻¹)	Rain (mm)	$\delta^{18}\text{O}$ range (‰)
1962	82.3	-3.98	-0.31	6.7	382	0.45
	83.9	<u>-4.40</u>	-0.26			
	85.6	<u>-4.23</u>	<u>-0.45</u>			
	87.5	-3.95	0.13			
1963	89.0	-3.73	0.12	5.0	351	0.43
	90.8	<u>-4.08</u>	<u>-0.66</u>			
	92.4	-4.16	-0.39			
1964	94.0	-3.85	0.54	6.4	491	0.15
	95.5	-3.90	-0.09			
	96.9	<u>-4.00</u>	<u>-0.81</u>			
	98.6	-3.98	-0.27			
1965	100.4	-3.70	0.19	3.0	415	0.47
	102.1	<u>-4.17</u>	<u>-0.98</u>			
1966	103.4	-3.92	-0.42	6.6	304	0.36
	105.2	-4.09	-0.03			
	106.7	-4.28	-0.15			
	108.2	<u>-4.20</u>	<u>-0.56</u>			
1967	110.0	-3.98	0.53	3.5	737	0.36
	111.9	<u>-4.34</u>	<u>-0.03</u>			
1968	113.5	-3.82	<u>-0.88</u>	3.3	319	0.12
	115.0	<u>-3.94</u>	0.94			
1969	116.8	-3.99	0.40	5.1	268	0.11
	118.2	-4.10	-0.06			
	120.2	<u>-4.01</u>	<u>-0.34</u>			
1970	121.9	-3.67	0.19	6.3	813	0.55
	123.8	<u>-4.22</u>	<u>-0.46</u>			
	125.5	-4.00	-0.50			
1971	128.2	-3.51	<u>-0.41</u>	4.6	418	0.23
	131.0	<u>-3.74</u>	-0.13			
1972	132.8	-3.65	<u>0.05</u>	4.3	212	0.19
	135.0	<u>-3.84</u>	0.22			
1973	137.1	-3.44	0.36	3.7	377	0.40
	139.2	<u>-3.84</u>	<u>-0.02</u>			
1974	140.8	-3.70	0.34	3.6	140	0.32
	142.7	<u>-4.02</u>	<u>-0.30</u>			
1975	144.4	-3.78	0.65	6.2	569	0.71
	145.8	-3.85	1.05			
	147.4	-4.24	<u>-0.14</u>			
	149.0	<u>-4.49</u>	-0.10			
1976	150.6	-4.35	0.32	3.8	520	0.10
	152.0	-4.43	-0.21			
	153.1	<u>-4.45</u>	<u>-0.48</u>			
1977	154.4	-4.30	0.21	5.6	529	0.26
	156.0	-4.41	0.06			
	157.2	<u>-4.54</u>	<u>-0.47</u>			
	158.8	-4.56	-0.22			
1978	160.0	-4.15	0.20	5.7	473	0.47
	161.5	-4.57	-0.01			
	162.9	<u>-4.62</u>	<u>-1.10</u>			
	164.3	-4.34	0.26			
1979	165.7	-4.28	0.52	4.3	974	0.70
	166.9	-4.94	-0.72			
	168.4	<u>-4.98</u>	<u>-0.73</u>			

(Continued)

Table 1. (Continued)

Year (A.D.)	Distance (mm)	$\delta^{18}\text{O}$ (‰)	$\delta^{13}\text{C}$ (‰)	Growth rate (mm y ⁻¹)	Rain (mm)	$\delta^{18}\text{O}$ range (‰)
1980	170.0	<u>-4.41</u>	<u>-0.28</u>	2.8	629	0.02
	171.5	-4.39	-0.24			
1981	172.8	-4.08	0.07	4.4	631	0.39
	174.4	<u>-4.47</u>	<u>-0.76</u>			
	175.6	-4.26	-0.37			
1982	177.2	-3.96	-0.06	2.2	365	0.18
	178.3	<u>-4.14</u>	<u>-0.26</u>			
1983	179.4	-3.96	0.57	4.7	626	0.17
	181.2	-4.03	-0.06			
	182.9	<u>-4.13</u>	<u>-0.29</u>			
1984	184.1	-3.69	0.65	4.4	388	0.19
	185.6	<u>-3.76</u>	<u>0.09</u>			
	187.3	-3.88	0.84			
1985	188.5	-3.77	0.75	2.5	268	0.17
	189.8	<u>-3.94</u>	<u>0.61</u>			
1986	191.0	-3.63	1.16	4.2	219	0.30
	192.8	-3.93	0.76			
	193.9	<u>-3.93</u>	<u>0.18</u>			
1987	195.2	-3.71	0.80	4.6	71	0.29
	196.4	-3.88	0.88			
	198.6	<u>-4.00</u>	<u>-0.02</u>			
1988	199.8	-3.74	0.77	6.1	718	0.47
	201.7	-3.85	0.49			
	203.9	<u>-4.21</u>	<u>0.00</u>			
1989	205.9	-3.90	<u>0.96</u>	3.1	529	0.19
	208.0	<u>-4.09</u>	1.57			

varying growth rate the number of subsamples per band for isotopic analyses also varied from 8 to 2. On an average about 7 sub-samples were taken from 2 annual bands. The sub-samples filed out had a finite width of ~ 1 mm, which could represent a time period of ~ 25 days in the best case (8 sub-samples per band) to ~ 3 months in the worst case (2 samples per band); it must be noted that ~ 1 to 2 mm gap was maintained between consecutive samples to avoid cross-contamination between them.

3.2 Oxygen isotopes

The oxygen ($\delta^{18}\text{O}$) and carbon ($\delta^{13}\text{C}$) isotopic data from annual bands of the coral sample are presented in figure 3(a and b). It is known that the $\delta^{18}\text{O}$ of biogenic marine CaCO_3 is determined by temperature and $\delta^{18}\text{O}$ of the water in which it grows (Shackleton 1967). Often, the $\delta^{18}\text{O}$ data for the sea water are not available and salinity can be used as a substitute, as the two are in general correlated (Craig and Gordon 1965). However, this relationship differs from region to region. COADS (Comprehensive Ocean Atmospheric Data Set) SST data (Sadler *et al* 1987) at 22.5°N , 70°E averaged over the past eighty years are shown in figure 2. The curve shows maximum SST (29°C) around June and minimum (23°C) around January–

February. A small trough during August–October shows a decrease in SST (2°C) probably because of cloud cover. An increase in SST would result in a decreased $\delta^{18}\text{O}$ value of the coral, as the temperature dependence of the fractionation factor is negative ($-0.24\text{‰ }^\circ\text{C}^{-1}$ for the species under consideration, Weber and Woodhead 1972). *Therefore we infer that coral $\delta^{18}\text{O}$ maximum must occur in January and minimum in June*, with a seasonal range of $\sim 1.44\text{‰}$ corresponding to the temperature range of 6°C . However, this has to be corrected for the $\delta^{18}\text{O}$ variations in sea water. We have also collected sea water samples from the coral location periodically and measured their $\delta^{18}\text{O}$ values (table 2). The mean winter (December to February) value is 0.68‰ while the mean summer (May–June) value is 0.92‰ (values relative to V-SMOW). Eventhough these values are the same within analytical precision ($\pm 0.15\text{‰}$), there appears to be a tendency towards higher $\delta^{18}\text{O}$ values during summer due to higher SST and consequent evaporation. Therefore we subtract $\sim 0.3\text{‰}$ from the calculated range of 1.44‰ . Thus the expected seasonal range in coral $\delta^{18}\text{O}$ is $\sim 1.1 \pm 0.15\text{‰}$. The observed mean seasonal $\delta^{18}\text{O}$ amplitude is $0.34 \pm 0.17\text{‰}$, as calculated from the data shown in table 1. The apparent discrepancy between the observed and calculated $\delta^{18}\text{O}$ amplitudes has been noted earlier by others

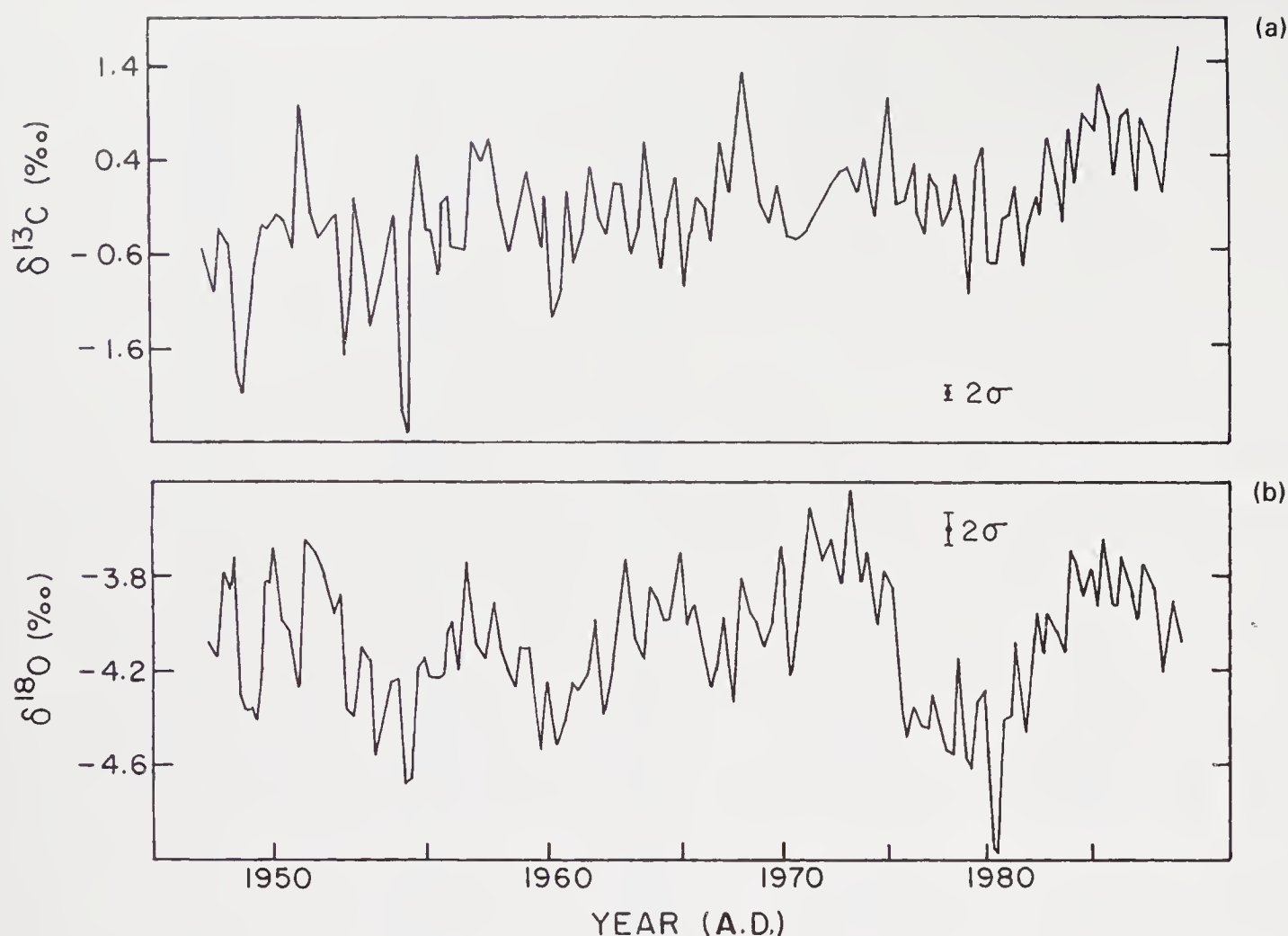


Figure 3. Carbon (a) and oxygen (b) isotopic records of the coral (*Favia speciosa*) for the period 1949–89 A.D.

Table 2. $\delta^{18}\text{O}$ of sea water (relative to V-SMOW standard) from the Gulf of Kutch.

Date of collection	$\delta^{18}\text{OSMOW}$ (‰)
24.11.92	0.75
21.12.92	0.61
18.01.93	0.76
17.02.93	0.63
05.05.93	0.93
10.06.93	0.91

Analytical uncertainty $\pm 0.15\%$.

(Emiliani *et al* 1978; Fairbanks and Dodge 1979; Leder *et al* 1991) and is explained in the present paper based on a model simulation, discussed in section 3.5.

3.3 Correlation with rainfall

Figure 4(a, b and c) respectively show annual minima in $\delta^{18}\text{O}$ and $\delta^{13}\text{C}$ of the coral (data underlined in table 1) and the monsoon (July to September) rainfall of Kutch and Saurashtra region for the period 1949–89 A.D. (India Meteorological Department's Records). Each annual minimum in $\delta^{18}\text{O}$ corresponds to June of that year, as explained in section 3.2. It can be seen that there is a negative correlation between $\delta^{18}\text{O}$ minima ($\delta^{18}\text{O}_m$, corresponding to the highest SST in the Gulf before commencement of the monsoon rains in Kutch) and the monsoon rainfall (figure 5). The

relationship between coral $\delta^{18}\text{O}$ and rainfall is given by:

$$\delta^{18}\text{O}_m = -3.906 - 6.498 \times 10^{-4} R$$

where R represents rainfall in mm. The correlation coefficient (r) is -0.56 ($n = 41$) significant at 0.01 level (P). In order to produce a change of 0.1% (detection limit) in coral $\delta^{18}\text{O}$ the rainfall has to change by ~ 150 mm. The magnitude of year to year variation in rainfall is ~ 340 mm (one standard deviation, calculated from data shown in table 1). This will cause a mean interannual change in the coral $\delta^{18}\text{O}$ of a magnitude 0.22% . However, the difference in rainfall between two consecutive years can be as large as -700 to $+950$ mm, as seen from the rainfall record for the period 1949–89 A.D. (table 1); therefore the change in coral $\delta^{18}\text{O}$ can be as large as $+0.46$ to -0.63% . Figure 3(b) shows that such variations are indeed observed during some years when the sampling resolution is high.

In addition, there is a long term cycle of 7- to 8-year period that can be discerned visually from figure 3(b). [Power spectral analysis is not carried out because of (a) non-uniform sampling interval and (b) standard FFT codes either interpolate the data or fill with zeroes, which might produce spurious spectra, especially when the sampling resolution is coarse, forced by the slow growth rate of the coral]. This could be

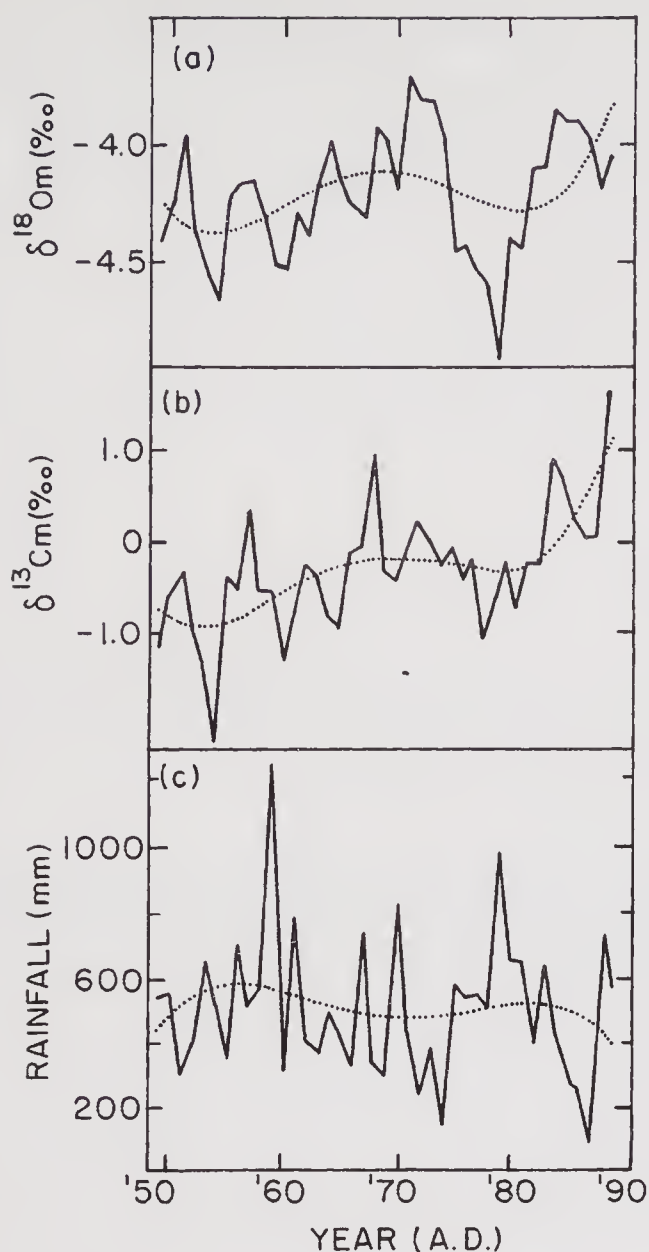


Figure 4. $\delta^{18}\text{O}$ minima (a), $\delta^{13}\text{C}$ minima (b) and monsoon rainfall (c) of the Kutch and Saurashtra region. The dotted curves are fourth order polynomials fitted to the data and indicate the long term trends.

due to a number of years of consistently increasing or decreasing rainfall. The consistently higher than normal rainfall during the late 70s is reflected as a dip in the coral $\delta^{18}\text{O}$ (figure 3b).

The dotted lines in figure 4(a, b and c) are fourth order regression lines through the data representing the trends. We used the trend lines to generate points of $\delta^{18}\text{O}$ and rainfall and found them to be correlated better: $r = -0.8$ ($n = 41$). This shows that while the long term changes in coral $\delta^{18}\text{O}$ can be used as a monsoon rainfall signal, seasonal variations tend to introduce noise in this signal. If the seasonal changes are removed by taking the average $\delta^{18}\text{O}$ of each year, this mean annual $\delta^{18}\text{O}$ is also found to be significantly correlated with monsoon rainfall over Kutch and Saurashtra ($r = -0.48$, $P < 0.01$). This observation is consistent with the theory of Shukla (1975) and observations of Shukla and Misra (1977) that the increase in SST in the Arabian Sea enhances the evaporation rate and hence the precipitation over Gujarat.

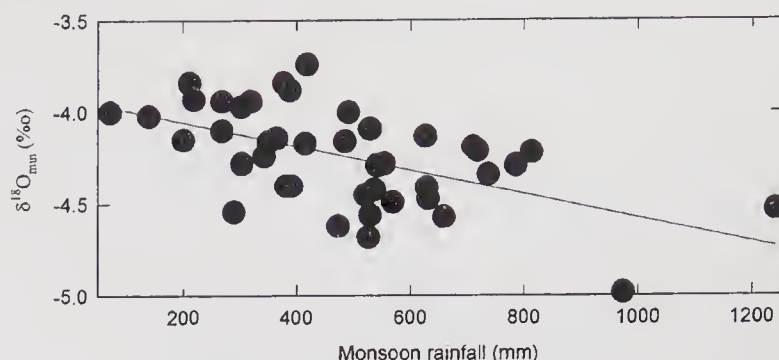


Figure 5. Correlation between monsoon rainfall and minima in $\delta^{18}\text{O}$.

3.4 Carbon isotopes

The $\delta^{13}\text{C}$ values show a long term increase of about 2‰ during the forty years of the coral growth, from a mean of ~ -1 ‰ during the early stages to the present day mean value of 1‰ (figure 3a). The cause of this long term trend is not clear. Growth rate related ^{13}C fractionation may be a likely cause, as suggested by McConnaughey (1989). In the earlier stages of growth, the mean growth rate is higher ($\sim 6 \text{ mm y}^{-1}$) whereas in the later stages, the mean growth rate is between 3 and 4 mm y^{-1} . This would contribute to the relative enrichment of ^{13}C during the later stages (figure 6). It is currently not possible to estimate the expected ^{13}C enrichment, as experimental data on photosynthesis rates of coral zooxanthellae and consequent ^{13}C enrichment are not available for any type of corals from the Arabian Sea region.

Like $\delta^{18}\text{O}$, $\delta^{13}\text{C}$ also shows annual oscillations with an average amplitude of about 1‰ (figure 3a). The minimum in $\delta^{13}\text{C}$ occurs during June–July, approximately at the same time when the minimum in $\delta^{18}\text{O}$ occurs, as can be seen from table 1. In fact, $\delta^{18}\text{O}$ and $\delta^{13}\text{C}$ are significantly positively correlated ($r = 0.56$). The reason for the minimum in $\delta^{13}\text{C}$ during June–July is probably the reduced rate of photosynthesis during this time of the year compared to the pre-monsoon (February to May) and post-monsoon (October to January) seasons. As is well known, photosynthesis discriminates against ^{13}C and makes the marine bicarbonate enriched in ^{13}C in seasons of high phytoplankton photosynthetic activity (McConnaughey 1989). Qasim (1982) has observed that, in general, the phytoplankton productivity is high in the Indian coastal regions of the northern Arabian Sea. The average surface productivity for this region is 18.86 , 7.0 and $25.12 \text{ gC m}^{-2} \text{ day}^{-1}$ for the pre-monsoon (March to May), monsoon (June to September) and post-monsoon months (November to January) respectively (table 8 of Qasim 1982). In addition, Madhupratap *et al* (1996) made a comprehensive set of measurements in the north eastern Arabian Sea, which indicate that winter (February) productivity ($807 \text{ mgC m}^{-2} \text{ d}^{-1}$) was higher than that during April–May ($310 \text{ mgC m}^{-2} \text{ d}^{-1}$) in the upper 120 m, near the

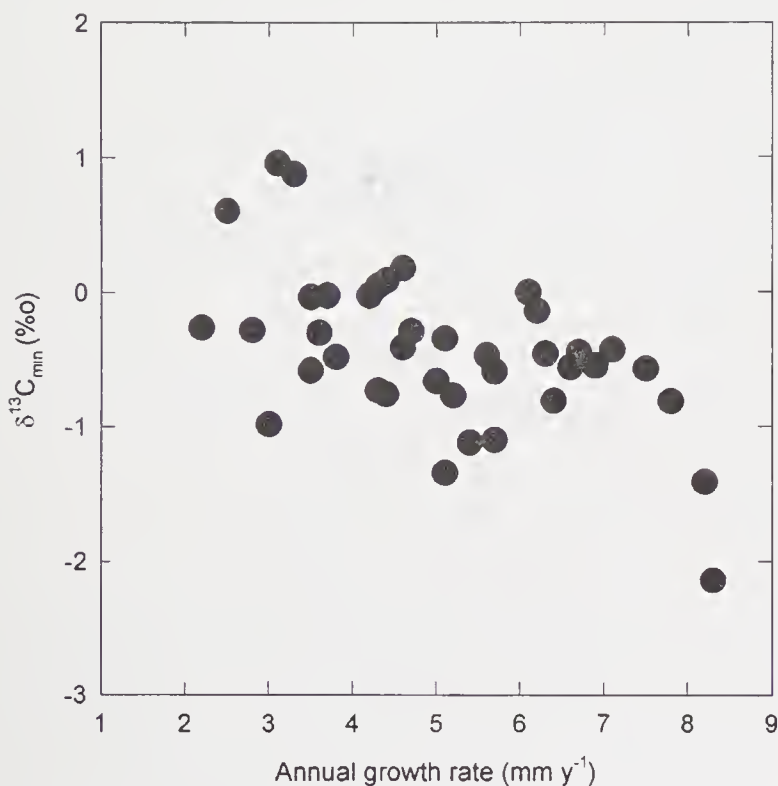


Figure 6. Correlation between coral growth rate and minima in $\delta^{13}\text{C}$.

Gulf of Kutch. The lowest biological productivity during the monsoon period, probably leads to the depletion of ^{13}C in the coral. A possible reason for the lower productivity during the monsoon season may be the cloud cover over the region, cutting off sun light. According to Fairbanks and Dodge (1979), reduced light intensity due to cloudiness reduces the coral $\delta^{13}\text{C}$.

3.5 Effect of sampling on the retrieval of the climatic signal

The retrieval of climatic information from the isotopic profiles of corals depends largely on the sampling resolution. Early attempts to link the coral $\delta^{18}\text{O}$ records to SST were not successful as observed by Goreau (1977) and Emiliani *et al* (1978). This apparent drawback of isotopic study was attributed to the sampling resolution problem by Fairbanks and Dodge (1979). They showed that with the analysis of as much as twelve sub-samples per annual band, they were able to recover the full seasonal amplitude of SST from the coral $\delta^{18}\text{O}$ measurements. The lesser the number of sub-samples per annual band, the greater the chances of missing the maxima and minima in the coral $\delta^{18}\text{O}$. Moreover, in the case of very narrow annual bands, it is difficult to get more than a few sub-samples per band for isotopic analyses. Furthermore, a sub-sample taken by filing or drilling has a finite width (say $\sim 1\text{ mm}$), which, in the case of a narrow band, can average the SST signal for a period of as much as six months. Thus depending on the coral growth rate (i.e., the skeletal extension rate) and the sampling interval, the measured seasonal $\delta^{18}\text{O}$ amplitude can be greatly

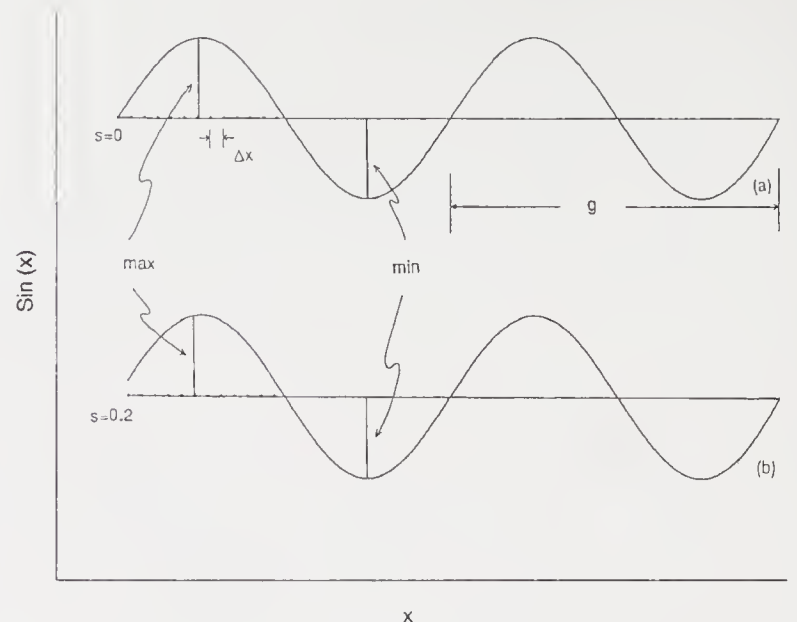


Figure 7. Illustration of sub-sampling the seasonal climatic signal; s is the distance from the origin of the first sample (phase). (a) $s = 0$, i.e., phase = 0 and (b) $s = 0.2$, or phase = 7.2° . Δx is the sampling interval and g stands for annual growth increment.

reduced compared to its actual value. To assess the magnitude of this reduction, we performed a simple computer simulation.

Since the annual $\delta^{18}\text{O}$ variations in a coral can be idealized, in the zeroth order approximation, to sinusoidal variations, we generated twenty cycles of a sine wave of unit amplitude and a (spatial) period of 10 mm. This would correspond to a $\delta^{18}\text{O}$ time series of a coral having a twenty year growth with an annual growth increment (g) of 10 mm. Implicit in our use of unit amplitude throughout the twenty cycles is that the seasonality in climate forcing did not change during this period (i.e., interannual variability is zero). Also the constant spatial period represents a uniform annual growth increment throughout the twenty years of the coral life span. We sub-sample this time series for different constant sub-sampling intervals ($\Delta x = 1, 2, 3, 4$ and 5 mm) and consider each sub-sample as a datum point. The maxima and minima in this sampled time series are identified (figure 7). The sum of the magnitudes of the maximum and minimum in each cycle is divided by two to obtain the mean amplitude for each cycle. Then the average of these mean amplitudes of the twenty cycles is calculated and is termed as the 'retrieved amplitude'. We establish a functional relationship between $\Delta x/g$ (reciprocal of the number of sub-samples per band) and A (the ratio of the retrieved amplitude to the actual amplitude). Obviously $A \leq 1$, because the sampling process tends to reduce the signal and at best can retrieve the actual amplitude. In practice, when the coral is collected, the annual cycle corresponding to the year of collection may not be complete. Hence the sampling may not commence at phase = 0 of the sine wave. Therefore the above exercise was repeated for different values of (a) s , the starting

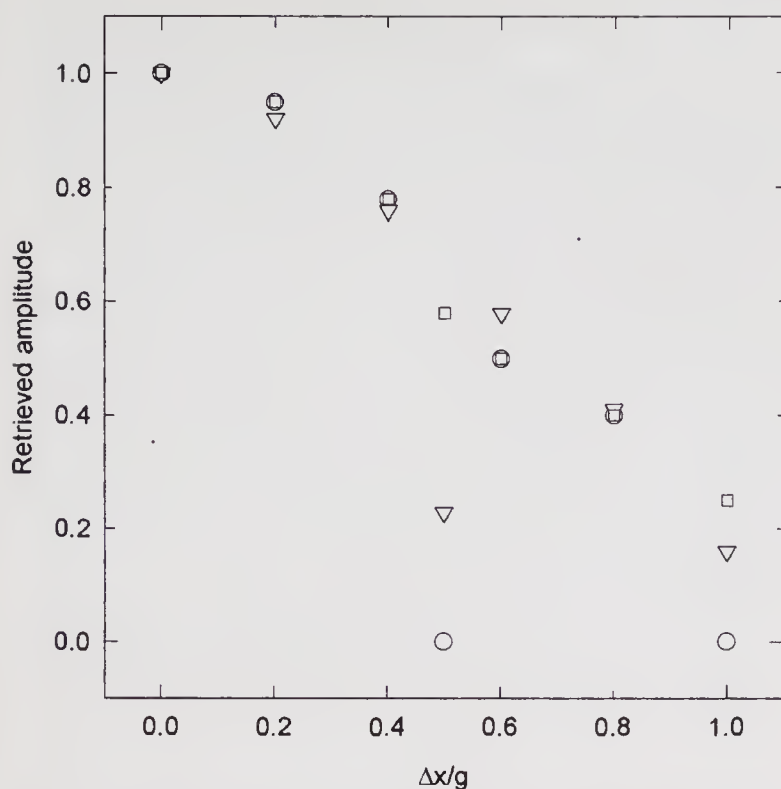


Figure 8. Variation of A (ratio of the retrieved amplitude to the true amplitude) as a function of $\Delta x/g$ [ratio of sampling interval to the constant (5 mm) annual growth increment]. Different symbols indicate different starting distances from the origin (s): Open circle $s = 0$; inverted triangle, $s = 0.2$; square, $s = 0.5$.

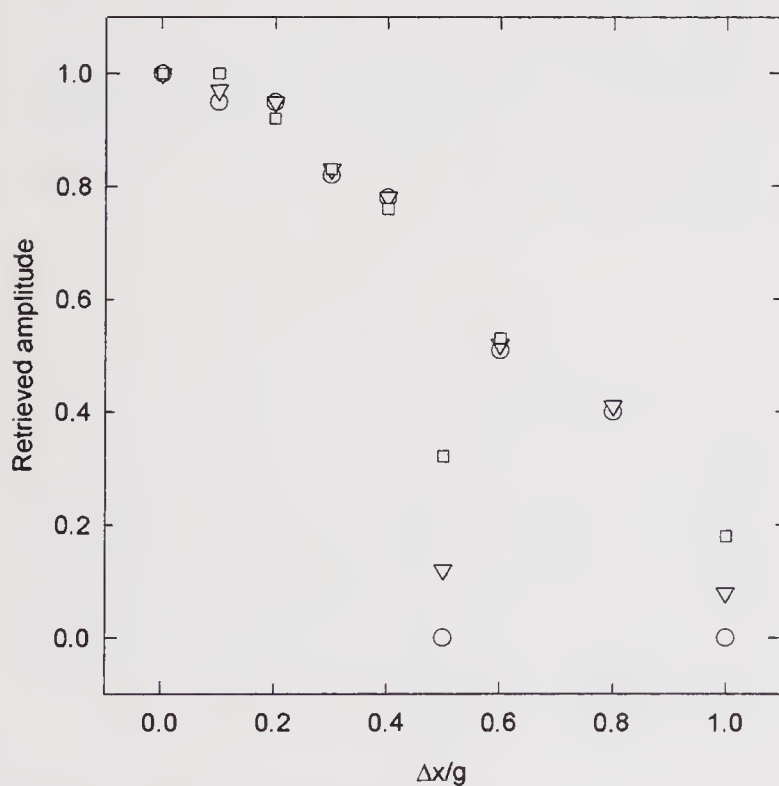


Figure 9. Same as figure 6, but for a constant growth increment (g) of 10 mm.

distance of the first sub-sampling point (i.e., different phases) and (b) g (but kept constant throughout the twenty year span, spatial periods of 5 and 10 mm).

Figures 8 and 9 show plots of A versus $\Delta x/g$ when $g = 5$ and 10 mm respectively. Circles denote the values of A for cases when $s = 0$ (sampling started with zero phase) and inverted triangles and squares

denote cases when the sampling started at phases of 14.4° and 36° ($s = 0.2$ and 0.5 mm from the origin) respectively.

It is obvious that when $\Delta x/g = 0$ (i.e., infinitely close sampling), we retrieve the full amplitude (i.e., $A = 1$) and when $\Delta x/g = 0.5$ or 1 (sampling interval = half or full spatial period), $A = 0$, if the sampling starts at origin (i.e., zero phase). This is seen in figures 8 and 9. For the rest of the values of $\Delta x/g$, A lies between 0 and 1. As $\Delta x/g$ increases, there is a general reduction in A . For example, when $\Delta x/g = 0.8$, 60% of the amplitude is lost. For the other cases when the sampling started with non-zero phase, the general trend is the same. However, for $\Delta x/g = 0.5$, we do get A values above zero. This is because the sample points do not lie on the zeroes of the sine curve, but slightly off the zeroes, providing some 'amplitude'. Further as the phase increases from 0 to 36° , the scatter in A increases around $\Delta x/g = 0.5$ and 1 . The higher the starting phase, the higher is the retrieved amplitude (at these two abscissae). If a reduction of 10% in the amplitude is acceptable, then $\Delta x/g$ must be at least ~ 0.3 , i.e., approximately a minimum of four sub-samples per annual band.

In another simulation (a first order approximation), we assumed that while there is no interannual climatic variability, the annual growth increment varies in a random fashion between 2.5 to 5 mm (similar to the growth rate variation in the Gulf of Kutch (GK) coral; growth rate varies due to, say, changes in nutrient supply). Since a simple sine function has a constant (spatial) period, a variable growth rate cannot be represented by such a function. To circumvent this, we generated single cycles of twenty sine functions of unit amplitude but with varying periods (2.5 to 5 mm). Then we made the composite function by putting the sine function in the same time sequence as their growth rates in the case of the GK coral. The end points of the cycles match because the value of the sine functions in a full cycle is zero at either end ($0, 2\pi$). This curve is then sampled as before to obtain A for different Δx (1, 2, 3 and 4 mm) and s ($0^\circ, 18^\circ$ and 45°) values. In this case $\Delta x/g$ is not a constant as g varies with time. Therefore we plot A versus $\Delta x/\underline{g}$ where \underline{g} is the average of all g 's (~ 4 mm). Figure 10 shows the results; the reduction in amplitude is more or less the same as in the earlier case of constant growth increments. For example, for $\Delta x/\underline{g} = 0.2$, A is 0.92 ± 0.07 , the same within the uncertainty as 0.95 for $\Delta x/\underline{g} = 0.2$ (constant \underline{g}). However a direct comparison is made difficult by the observation that even for the case when the sampling is done with zero phase, A is not zero for $\Delta x/\underline{g} = 0.5$ and 1 . This is understandable because the annual growth increment is varying and therefore even for $s = 0$, some amplitude is recovered for $\Delta x/\underline{g} = 0.5$ and 1 .

In addition to the sampling interval, another factor which reduces the retrieved amplitude is the

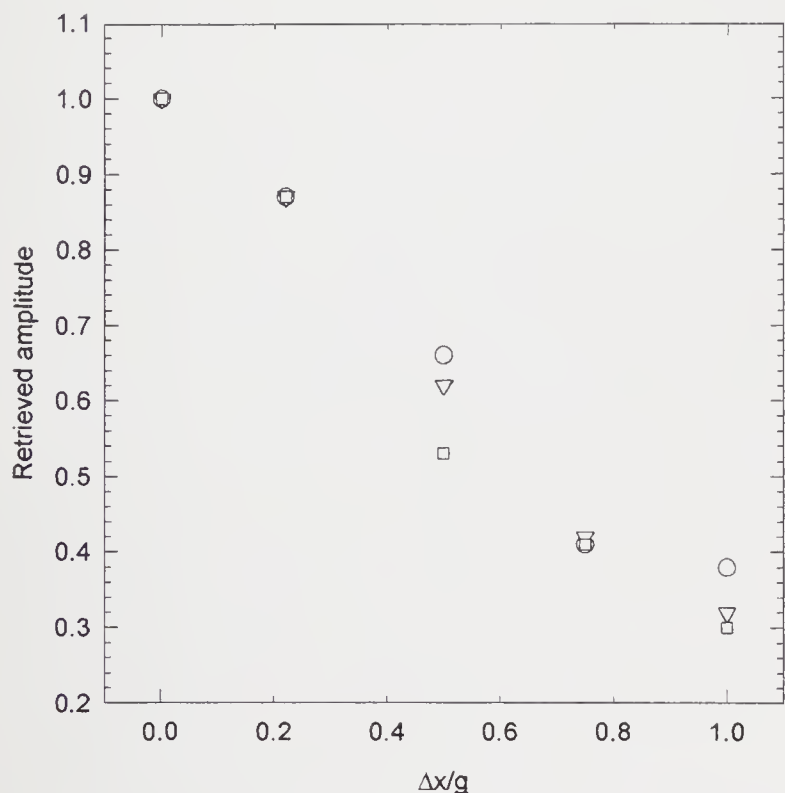


Figure 10. Same as figure 6, but for a variable growth increment ($g = 2.5$ to 5 mm).

averaging of the signal due to finite sub-sample thickness. We considered the effect of sampling thickness on the amplitude in the following way (second order approximation): we sampled the data generated for the variable growth increment case at different intervals, but now by averaging 1 mm around each sample. For this case the reduction in amplitude was found to be 40% for a $\Delta x/g$ value of 0.38, very similar to the value of $\Delta x/g$ in the GK coral. Using this we can compute the approximate magnitude of the actual seasonal $\delta^{18}\text{O}$ amplitude in the GK coral. The observed amplitude of $0.34 \pm 0.17\%$ can be considered to be 60% of the actual amplitude, therefore the actual amplitude would be $0.57 \pm 0.28\%$. This is about a factor of two less than the calculated amplitude of $1.1 \pm 0.15\%$. Considering the uncertainty in these estimates, it can be argued that the expected and observed $\delta^{18}\text{O}$ amplitudes are consistent within $\pm 2\sigma$ uncertainties. However, they could be genuinely different for reasons other than those considered above. These include: (i) The model does not consider year to year changes in $\delta^{18}\text{O}$ of sea water that may be caused by fresh water input (rainfall or run-off due to minor discharges from seasonal streams). (ii) The calculated coral $\delta^{18}\text{O}$ amplitude may be an over estimate as (a) the temperature coefficient for our sample may be different from that of the coral for which the value is reported by Weber and Woodhead (1972); we have used their value as this is the only available value in the literature for the genus *Favia*. However, there may be variations from species to species and from place to place. For instance McConnaughey (1989) reported temperature coeffi-

cients of 0.205 and 0.015 for *Pavona clavus* samples, one from Champion Island and the other from Punta Pitt, separated by 100 km; (b) we do not have the SST data in the exact location of the coral. The actual variations in SST may not be identical to what we have assumed. Further, the data (Sadler *et al* 1987) used by us is averaged over eighty years and does not contain any information on the year-to-year variability. The data were read off from contours spaced at 1°C intervals. In general, these data are compiled from records of ships that passed through the region. Whereas for the Pacific and Atlantic, there are more than 100 ship records, for the Indian Ocean there are only twenty five ship records. This may even be less for the Gulf of Kutch.

Notwithstanding the above possible uncertainties, we get a reasonably good agreement between the calculated and observed $\delta^{18}\text{O}$ amplitudes.

4. Conclusions

Coral $\delta^{18}\text{O}$ and summer monsoon rainfall are correlated, which can be used for qualitative reconstruction of historical rainfall records and also help understand the role of the Arabian SST in determining the inter-annual variability of monsoon rainfall over India. It is necessary that a very close sampling is done for the $\delta^{18}\text{O}$ analysis in order to retrieve the full seasonal cycle. The $\delta^{13}\text{C}$ variations in these corals could be used to substantiate past productivity/monsoon reconstructions, since they appear to be mainly controlled by cloudiness.

Acknowledgements

We thank M Bhaskaran and colleagues at CMFRI, Sika for assistance in sample collection; Ravi Bhushan, D N Yadav and R A Jani for help; M I Patel for guidance; S Krishnaswami and G B Pant for useful suggestions and encouragement. We thank referees P K Swart, S K Bhattacharya, M S Srinivasan and Rupa Kumar Kolli for comments and suggestions to improve the manuscript. This project was funded by the ID-GBP and partly by INSA.

References

- Aharon P 1991 Records of reef environment histories: Stable isotopes in corals, giant clams, and calcareous algæ; *Coral Reefs* 10 71–90
- Chakraborty S and Ramesh R 1992 Climatic significance of $\delta^{18}\text{O}$ and $\delta^{13}\text{C}$ variations in a banded coral (*Porites*) from Kavaratti, Lakshadweep islands; In, *Oceanography of the Indian Ocean* (ed) B N Desai (New Delhi: Oxford & IBH) pp. 473–478
- Chakraborty S and Ramesh R 1993 Monsoon induced sea surface temperature changes recorded in Indian corals; *Terra Nova* 5 545–551

- Chakraborty S and Ramesh R 1997 Environmental significance of carbon and oxygen isotope ratios of banded corals from Lakshadweep, India; *Quaternary International* **37** 55–65
- Charles C D, Hunter D E, Fairbanks R G 1997 Interaction between the ENSO and the Asian monsoon in a coral record of tropical climate; *Science* **277** 925–928
- Cole J and Fairbanks R G 1990 The southern oscillation recorded in the $\delta^{18}\text{O}$ of corals from Tarawa atoll; *Paleoceanography* **5** 669–683
- Craig H and Gordon L 1965 Deuterium and oxygen-18 variation in the ocean and the marine atmosphere; In *Stable isotopes in Oceanographic Studies and Paleotemperatures* (ed) E Tongiorgi (Spoleto) pp. 9–130
- Druffel E M 1985 Detection of El Niño and decade time scale time variability of sea surface temperature from banded coral records: Implications for the carbon dioxide cycle; In *The carbon cycle and atmospheric CO_2 natural variations Archean to Present* (eds) E T Sundquist and W S Broecker, Geophysical Monograph **32** (Washington DC: American Geophysical Union) pp. 111–112
- Dunbar R B and Wellington G M 1981 Stable isotopes in a branching coral monitor seasonal temperature variation; *Nature* **293** 453–455
- Emiliani C, Hudson J H, Shinn E A and George R Y 1978 Oxygen and carbon isotopic growth records in a reef coral from the Florida Keys and a deep sea coral from Blake Plateau; *Science* **202** 627–629
- Fairbanks R G and Dodge R E 1979 Annual periodicity of the $^{18}\text{O}/^{16}\text{O}$ and $^{13}\text{C}/^{12}\text{C}$ ratios in the coral *Montastrea annularis*; *Geochim. Cosmochim. Acta* **43** 1009–1020
- Goreau T J 1977 Coral skeleton chemistry: Physiological and environmental regulation of stable isotopes and trace metals *Montastrea annularis*; *Proc. R. Soc. London* **B196** 291–315
- Leder J J, Szmant A M and Swart PK 1991 The effect of prolonged bleaching on skeletal banding and stable isotopic composition *Montastrea annularis*; *Coral Reefs* **10** 19–27
- Madhupratap M, Prasanna Kumar S, Bhattathiri P M A, Dileep Kumar M, Raghukumar S, Nair K K C and Ramaiah K (1996) Mechanisms of biological response to winter cooling in the northern Arabian Sea; *Nature* **384** 549–552
- McConnaughey T 1989 ^{13}C and ^{18}O isotopic disequilibrium in biological carbonates I: Patterns; *Geochim. Cosmochim. Acta* **53** 151–162
- Qasim S Z 1982 Oceanography of the Northern Arabian Sea; *Deep Sea Res.* **9** 1041–1068
- Sadler J C, Lander M A, Hori A M and Oda L K 1987 Tropical marine climate atlas 2 *Indian Ocean and Atlantic Ocean* (University of Hawaii Department of Meteorology)
- Shackleton N J 1967 Oxygen isotope analyses and Pleistocene temperatures reassessed; *Nature* **215** 43–46
- Shen G T and Sanford C L 1990 Trace element indicators of climatic variability in reef building corals; In *Global Ecological Consequences of the 1982–83 El Niño–Southern Oscillation* (ed) P W Glynn (New York: Elsevier) pp. 255–284
- Shetye S R, Gouveia A D, Shenoi S S C, Sundar S, Michael G S, Almeida A M and Santanam K 1990 Hydrographic and circulation off the west coast of India during the Southwest monsoon 1987; *J. Mar. Res.* **48** 359–378
- Shukla J 1975 Effect of Arabian Sea surface temperature anomaly on Indian summer monsoon: A numerical experiment with the GFDL model; *J. Atmos. Sci.* **32** 503–511
- Shukla J and Misra B N 1977 Relationship between sea surface temperature and wind speed over the central Arabian Sea and monsoon rainfall over India; *Mon. Weather. Rev.* **105** 998–1002
- Weber J N and Woodhead P M J 1972 Temperature dependence of oxygen-18 concentration in reef coral carbonates; *J. Geophys. Res.* **77** 463–473
- Wellington G M and Glynn P W 1983 Environmental influences on skeletal banding in eastern Pacific (Panama) corals; *Coral Reefs* **1** 215–222

Application of ^{226}Ra , ^{228}Ra , ^{223}Ra , and ^{224}Ra in coastal waters to assessing coastal mixing rates and groundwater discharge to oceans

WILLARD S MOORE

*Department of Geological Sciences, University of South Carolina Columbia, SC 29208, USA
e-mail: moore@epoch.geol.sc.edu*

The fate of dissolved material delivered to the coastal ocean depends on its reactivity and the rate at which it is mixed offshore. To measure the rate of exchange of coastal waters, we employ two short-lived radium isotopes, ^{223}Ra and ^{224}Ra . Along the coast of South Carolina, shore-perpendicular profiles of ^{223}Ra and ^{224}Ra in surface waters show consistent gradients which may be modeled to yield eddy diffusion coefficients of $350\text{--}540\text{ m}^2\text{ s}^{-1}$. Coupling the exchange rate with offshore concentration gradients yields estimates of offshore fluxes of dissolved materials. For systems in steady state, the offshore fluxes must be balanced by new inputs from rivers, groundwater, sewers or other sources. Two tracers that show promise in evaluating groundwater input are barium and ^{226}Ra . These tracers have high relative concentrations in the fluids and low-reactivity in the coastal ocean. Applying the eddy diffusion coefficients to the offshore gradient of ^{226}Ra concentration provides an estimate of the offshore flux of ^{226}Ra . Measuring the concentrations of ^{226}Ra in subsurface fluids provides an estimate of the fluid flux necessary to provide the ^{226}Ra . These estimates indicate that the volume of groundwater required to support these fluxes is of the order of 40% of the surface water flow.

1. Introduction

Within the decay series of uranium and thorium are four radium isotopes (figure 1) derived from the decay of thorium parents. Because thorium remains tightly bound to particles while radium daughters are mobilized in the marine environment, sediments provide a continuous source of Ra isotopes to marine waters at rates set by the decay constants of the Ra daughters. Measurements of the Th isotope activities in the sediments and the distribution coefficient of radium between the sediments and water provide a means of quantifying the potential input of each Ra isotope to the ocean. With half-lives ranging from 3.6 days (^{224}Ra) to 11.4 days (^{223}Ra) to 5.7 years (^{228}Ra) to 1600 years (^{226}Ra), this quartet of isotopes can provide powerful constraints on ocean mixing and chemical exchange in the coastal ocean.

The short lived Ra isotopes are regenerated on a time scale of days to tens of days. On this period the longer

lived Ra isotopes can be considered stable with respect to radioactive generation and decay. Such differences in time scale coupled with similarities in source function give this quartet a unique potential to understand complex environments. For example Rama and Moore (1996) observed that the daily export of ^{226}Ra and ^{228}Ra from the North Inlet, SC, salt marsh was far in excess of the activities of these isotopes that could be produced and released from surface sediments in this system. They surmised that groundwater must supply the extra ^{226}Ra and ^{228}Ra to the system. Investigations of ^{223}Ra and ^{224}Ra in North Inlet revealed that these isotopes were also contributed by groundwater input. A model of the distribution of the Ra quartet in surface and subsurface waters revealed that much of the groundwater discharge must be directly to the tidal creeks.

Moore (1996) established that the activity of ^{226}Ra in the coastal ocean of the southeastern U. S. was primarily derived from groundwater discharge. Far

Keywords. Radium; groundwater; coastal processes.

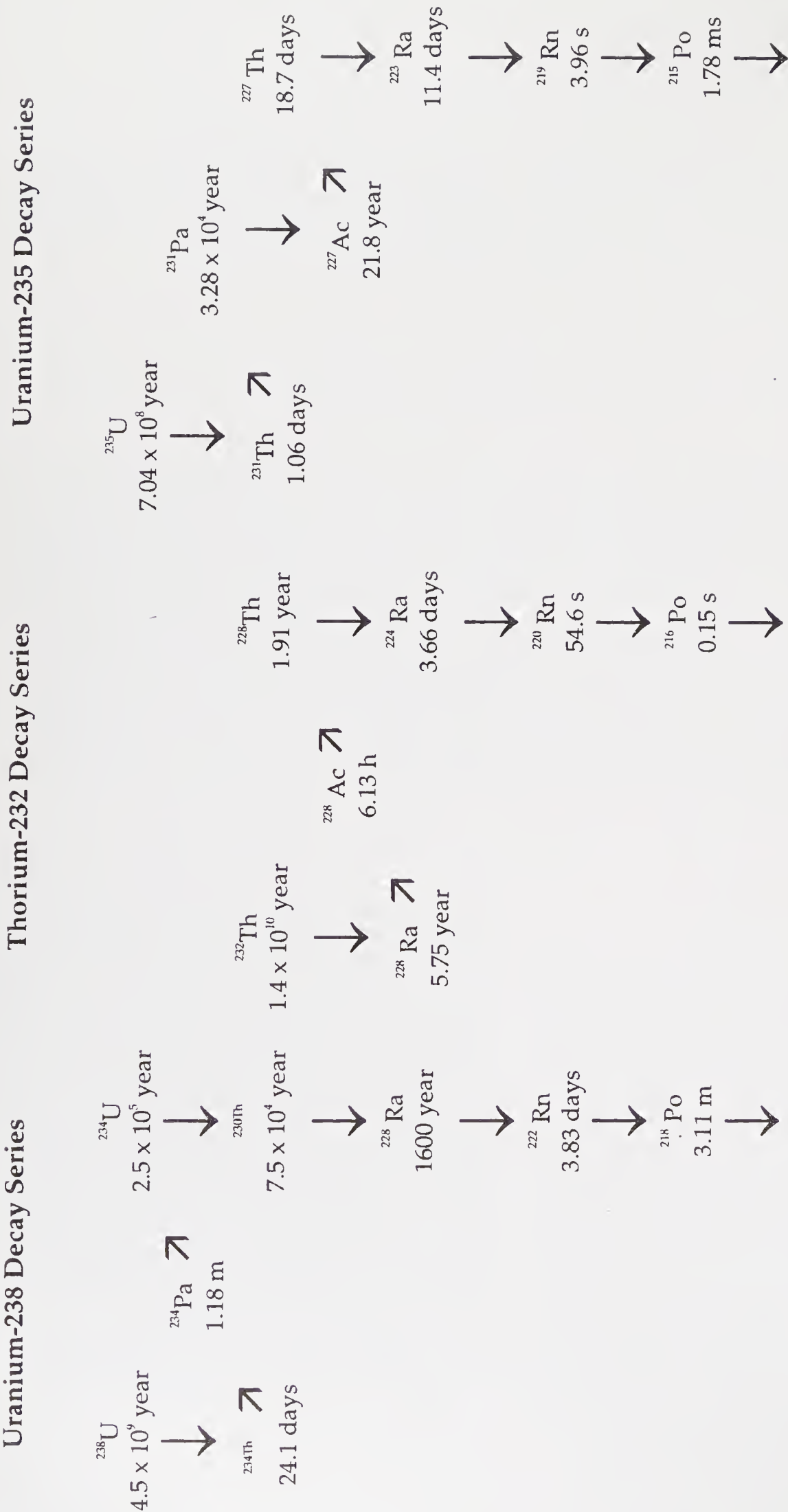


Figure 1. Isotopes of the Uranium and Thorium decay series showing the lineage of the Ra isotopes.

more ^{226}Ra was measured than could be explained from discharge of river water and associated particles. Moore (1996) used estimates of the residence time of near shore waters to calculate the flux of groundwater required to support the observed excess ^{226}Ra . The residence time estimate and hence the groundwater flux calculation can be improved using the short lived Ra isotopes. This is the focus of the present paper.

2. Methods

Large volume (100–500L) samples are pumped from the sea surface or depth into plastic drums. As most of the fine-grained particulate matter is restricted to the estuaries and marshes, the waters offshore are generally low in suspended inorganic materials. Therefore, these samples were not prefiltered. The volume is recorded and subsamples are collected for salinity, nutrient and trace metal analyses. The water is pumped through a column of manganese coated acrylic fiber (Mn-fiber) to quantitatively remove Ra (Moore 1976).

In the shipboard laboratory each sample of Mn-fiber is partially dried and placed in an air circulation system described by Moore and Arnold (1996). Helium is circulated over the Mn-fiber and through a 1.1 L scintillation cell where alpha particles from the decay of Rn and daughters are recorded by a photomultiplier tube (PMT) attached to the scintillation cell. Signals from the PMT are routed to a delayed coincidence system pioneered by Giffin *et al* (1963) and adapted for Ra measurements by Moore and Arnold (1996). The delayed coincidence system utilizes the difference in decay constants of the short lived Po daughters of ^{219}Rn and ^{220}Rn to identify alpha particles derived from ^{219}Rn or ^{220}Rn decay.

After the ^{223}Ra and ^{224}Ra measurements are complete, the samples are aged for 2–6 weeks to allow initial excess ^{224}Ra to equilibrate with ^{228}Th adsorbed to the Mn-fiber. The samples are measured again to determine ^{228}Th to correct for supported ^{224}Ra .

In a shore-based laboratory, Mn-fibers are leached with HCl in a Soxhlet extraction apparatus to quantitatively remove the long lived Ra isotopes. The Ra is precipitated with BaSO_4 . The precipitant is aged 2 weeks to allow ^{222}Rn and its daughters to equilibrate with ^{226}Ra . The samples are measured in a gamma-ray spectrometer to assess the activities of ^{226}Ra and ^{228}Ra (Moore 1984).

Samples reported in this paper were collected from the coastal ocean off North and South Carolina between 8th–18th July 1994. During this cruise we sampled five shore-perpendicular transects. The outer two transects (Cape Fear and Savannah) were sampled one time, the two adjacent transects (Myrtle Beach and Charleston) were sampled three times and the central transect (Winyah Bay) was sampled four times.

3. Results

Figure 2 shows the distribution of ^{226}Ra and ^{228}Ra in the surface water during the first pass across the study area when all five transects were sampled. Figure 3 shows the distributions of ^{223}Ra and ^{224}Ra during the first pass. During the period of investigation a strong pycnocline at 10 m depth effectively isolated the surface water from contact with the bottom. This pycnocline was not present over the inner shelf in <15 m water depths, allowing vertical mixing in the near-shore region.

The highest activities of each isotope occur on the inner shelf which is about 20 km wide with depths of 10–20 m. By contrast, the Gulf Stream which intersects the edge of the shelf, 80–100 km offshore, contains negligible activities of ^{223}Ra and ^{224}Ra and activities of ^{226}Ra and ^{228}Ra characteristic of the open Atlantic Ocean. Between the inner shelf and the Gulf Stream, the short lived Ra isotopes decrease in an exponential manner and the longer lived ^{226}Ra and ^{228}Ra decrease in a more linear fashion. However, within the study area there are clearly regions where the distribution does not conform exactly to this pattern. For example off Myrtle Beach, there are samples on the mid shelf, 20–40 km offshore, that have Ra activities similar to inner shelf samples.

The ^{228}Th measurements reveal a marked deficiency of ^{228}Th relative to its parent, ^{228}Ra . This indicates the rapid removal of Th from the water column. The low ^{228}Th activities also confirm our earlier assumption that little fine-grained detrital material is present in the samples.

4. Discussion

Pomeroy *et al* (1993) estimated mean cross-shelf advective velocities at the 20 m isobath for the South Atlantic Bight water column of 0.1 cm s^{-1} . Because the advective velocities were small and well below the limit of detection using current meters, they considered the flux to be essentially diffusive. Using a 40 km scale length, they estimated an eddy diffusion coefficient of the order $150 \text{ m}^2 \text{ s}^{-1}$ would be required to explain the decrease in freshwater across the shelf.

Ra tracers may be used to estimate eddy mixing of coastal waters across the shelf. Several groups have attempted to use the distribution of ^{228}Ra ($t_{1/2} = 5.7$ years) in continental shelf waters to determine horizontal mixing rates across the shelf (Kaufman *et al* 1973; Brewer and Spencer 1975; Lietzke and Lerman 1975). These one or two dimensional models assume that the distribution of ^{228}Ra is in steady state and that only radioactive decay and horizontal mixing between shelf and surface offshore waters change the ^{228}Ra activity. Moore (1987) concluded that such models are not generally applicable to ^{228}Ra along the

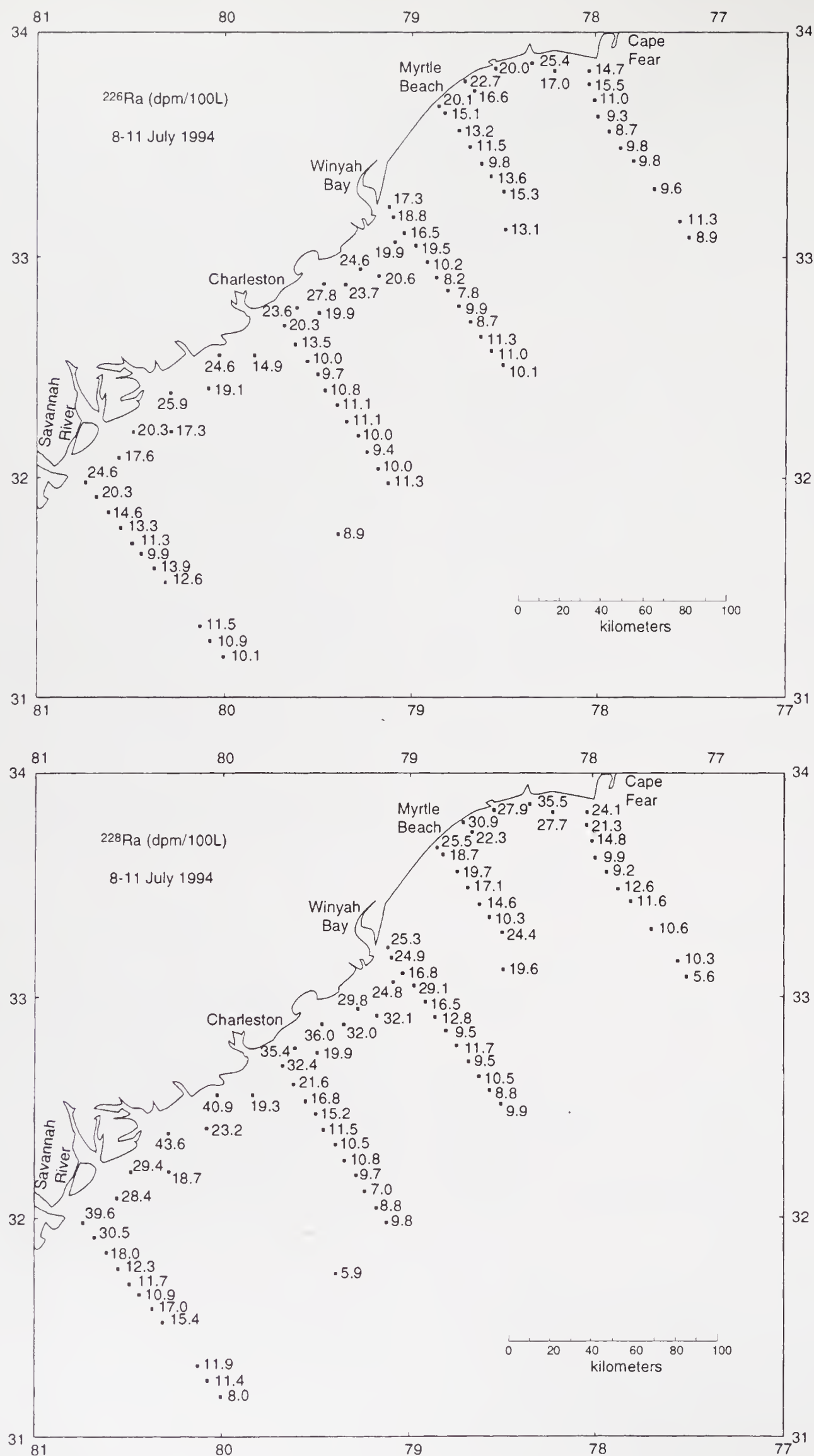


Figure 2. The distribution of ^{226}Ra and ^{228}Ra in the surface water of the South Atlantic Bight during the first pass.

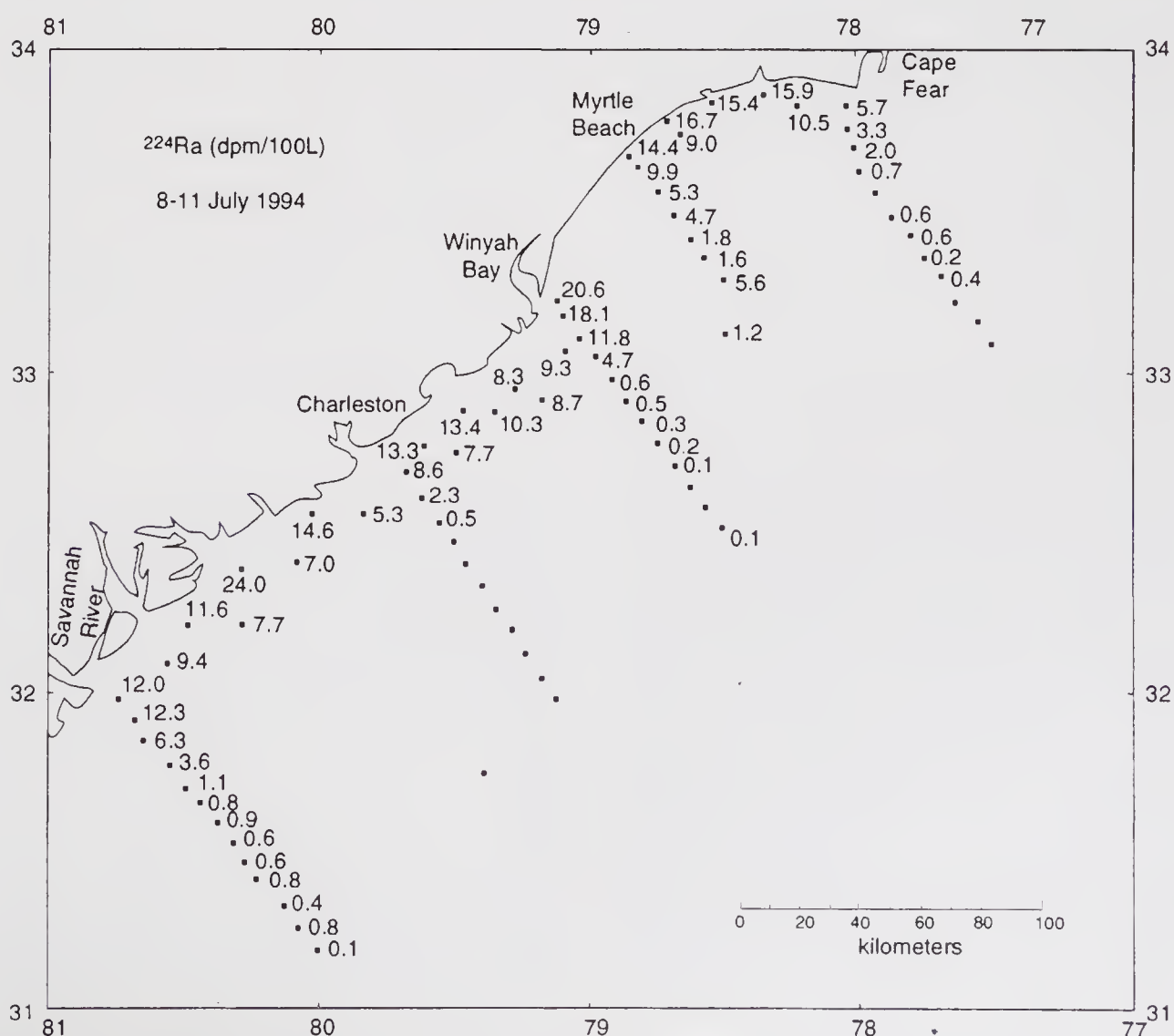
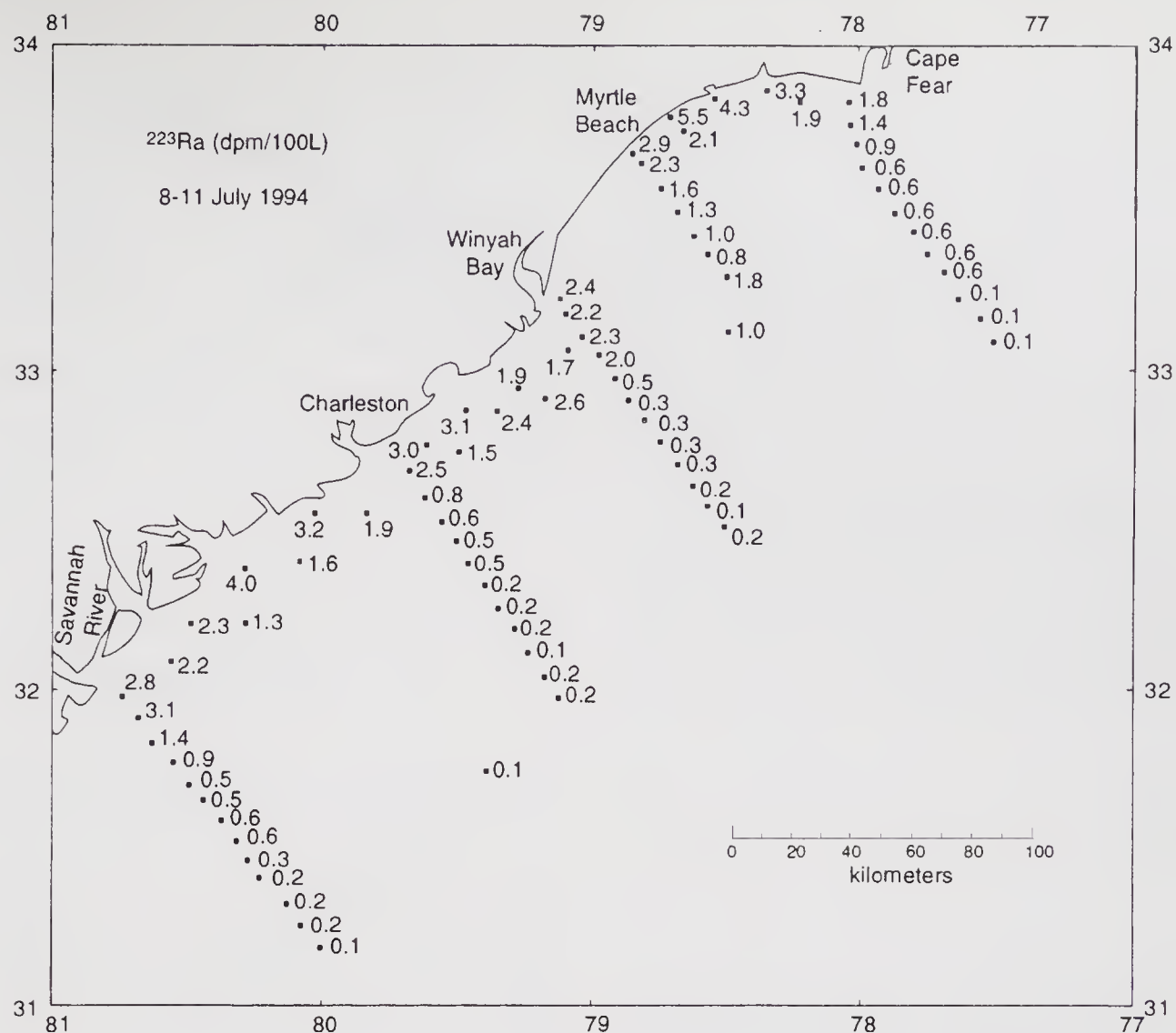


Figure 3. The distribution of ^{223}Ra and ^{224}Ra in the surface water of the South Atlantic Bight during the first pass.

southeastern U. S. coast because the distribution changes during the year and violates the steady state assumption. Torgersen *et al* (1996) used the distribution of ^{224}Ra in surface and deep waters of Long Island Sound to estimate horizontal mixing rates. They found that the distributions fit a horizontal eddy dispersion coefficient of $5\text{--}50\text{ m}^2\text{ s}^{-1}$ for mixing across the 8 km wide sound.

Although these horizontal mixing models may not be always applicable to ^{228}Ra , they should be applicable to ^{224}Ra and ^{223}Ra . The distribution of these isotopes may change seasonally; but, during periods of stable conditions, the distributions of these tracers should approximate steady state. The Ra distribution may be expressed by a simple one-dimensional horizontal diffusion model in which the distribution is in balance between eddy diffusion and radioactive decay

$$\frac{dA}{dt} = K_h \frac{\partial^2 A}{\partial x^2} - \lambda A. \quad (1)$$

At steady state,

$$A_x = A_0 \exp \left[-x \sqrt{\frac{\lambda}{K_h}} \right] \quad (2)$$

where A_x = activity at distance x from coast, A_0 = activity at distance 0 from coast, λ = decay constant, and K_h = horizontal eddy diffusion coefficient.

A plot of $\ln ^{223}\text{Ra}$ or $\ln ^{224}\text{Ra}$ as function of distance from the coast may be used to estimate K_h if the exchange is dominated by eddy diffusion rather than advection and if the system is steady state

$$\ln A_x = \ln A_0 - x \sqrt{\frac{\lambda}{K_h}}. \quad (3)$$

In this case the slope,

$$m = \sqrt{\frac{\lambda}{K_h}}. \quad (4)$$

Figure 4 is a plot of $\ln ^{223}\text{Ra}$ and $\ln ^{224}\text{Ra}$ vs distance across the shelf for the four occupations (passes) of the Winyah Bay transect. Here λ for ^{223}Ra is 0.0608 d^{-1} and for ^{224}Ra is 0.19 d^{-1} . The best fits to the $\ln ^{223}\text{Ra}$ profiles have an average slope of -0.036 km^{-1} and K_h of $47\text{ km}^2\text{ d}^{-1}$ ($540\text{ m}^2\text{ s}^{-1}$). For $\ln ^{224}\text{Ra}$ the average slope is -0.080 km^{-1} which yields a K_h of $30\text{ km}^2\text{ d}^{-1}$ ($350\text{ m}^2\text{ s}^{-1}$). No significant differences in slope for ^{223}Ra were found over a two week period, indicating that the distributions are approximately steady state. The ^{224}Ra distribution showed progressive decreases in slope during the study, suggesting that mixing was slower during the first two passes. The divergent behavior of the two tracers may also indicate that advection plays a role in the transport. Models that incorporate an advection component are currently being formulated.

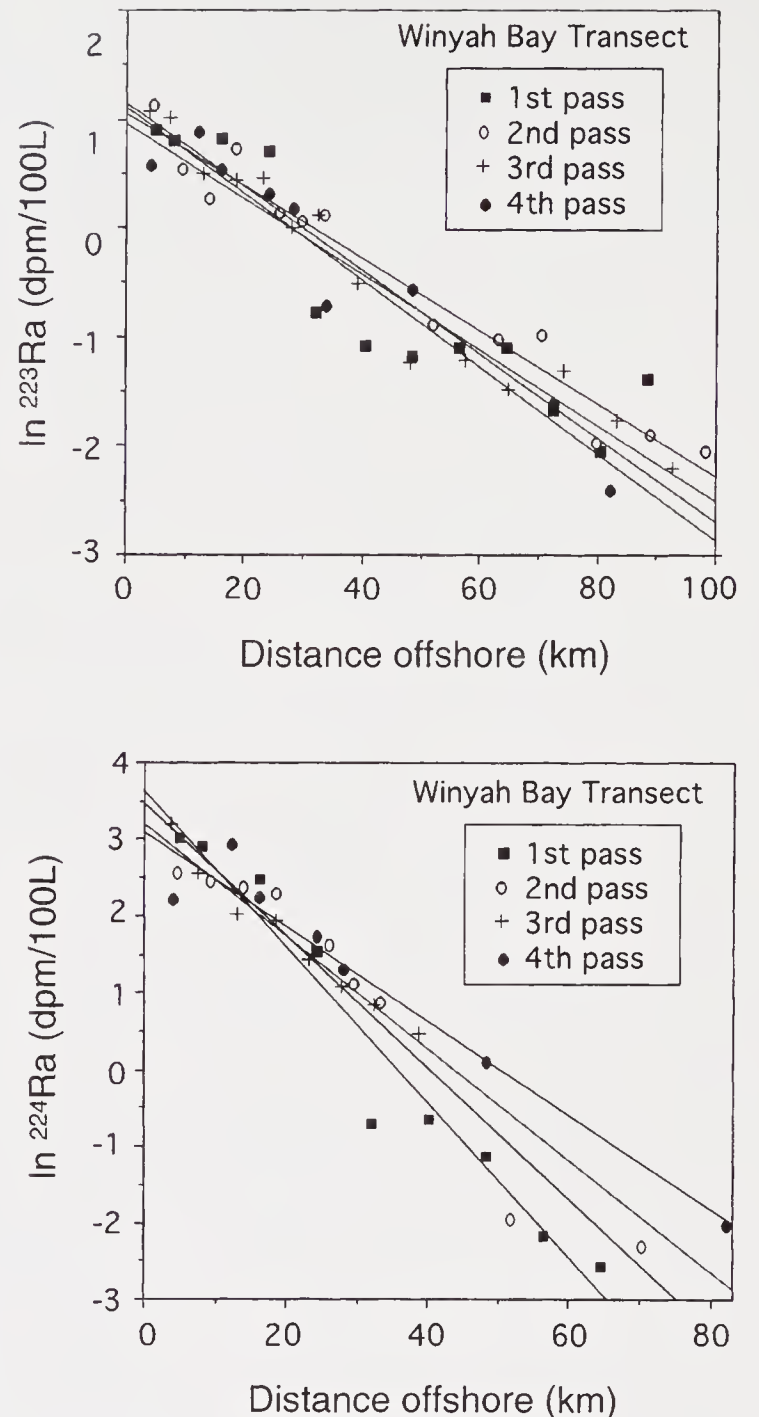


Figure 4. Plots of $\ln ^{223}\text{Ra}$ and $\ln ^{224}\text{Ra}$ activity vs. distance across the shelf for the four occupations of the Winyah Bay transect.

Values of K_h may be used in conjunction with concentration gradients across the shelf to estimate offshore fluxes. Figure 5 is a plot of the ^{226}Ra concentration across the Winyah Bay transect for all passes. Values on the inner shelf near Winyah Bay are quite variable, reflecting the position of the Winyah Bay plume. From 15 to 50 km offshore, the concentrations decrease in a roughly linear fashion from 17 to 9 dpm 100 L^{-1} . The gradient in this region is $2.3\text{ dpm m}^{-3}\text{ km}^{-1}$ or $2.3 \times 10^{-3}\text{ dpm m}^{-4}$. Multiplying by ^{223}Ra -based $K_h = 540\text{ m}^2\text{ s}^{-1}$ yields an offshore ^{226}Ra flux of $1 \times 10^5\text{ dpm m}^{-2}\text{ d}^{-1}$. Moore (1996) used an estimated 30-day residence time for water on the inner shelf and these ^{226}Ra data to calculate a ^{226}Ra flux of $7 \times 10^4\text{ dpm m}^{-2}\text{ d}^{-1}$, close to the value derived here. Using the ^{224}Ra -based K_h would have made the results

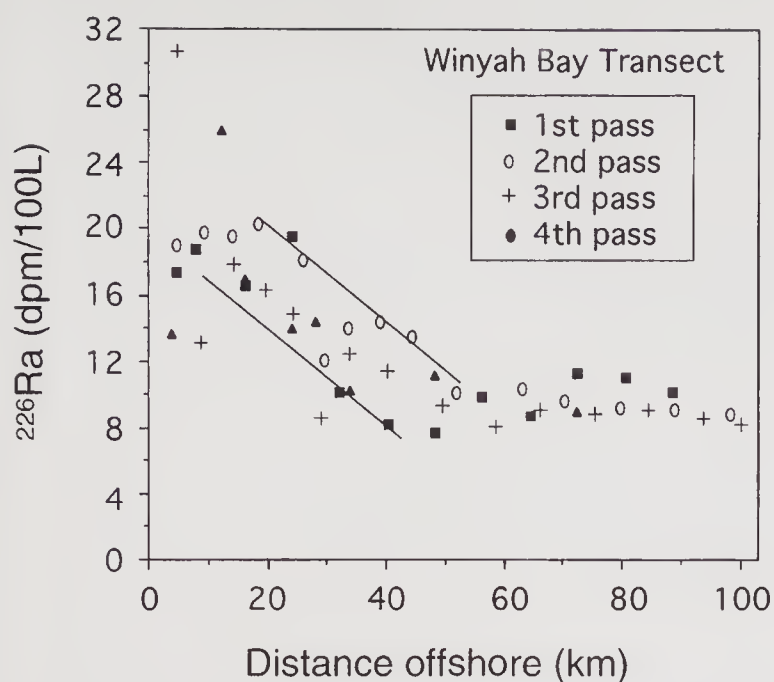


Figure 5. A plot of the ^{226}Ra activity vs. distance across the shelf for the four occupations of the Winyah Bay transect.

identical. Thus, these independent approaches yield similar results.

This example is presented to show how exchange rates estimated from short-lived tracers can be used to evaluate offshore fluxes. Because ^{226}Ra is not rapidly removed from the solution, the offshore gradient is caused by dilution due to mixing, not by biological or chemical removal. In this case fresh input must balance the loss by dilution. Measurements of the ^{226}Ra concentration in submarine groundwater coupled with computed offshore fluxes yield estimates of the discharge of submarine groundwater into the coastal ocean. For the ^{226}Ra fluxes given here, a volume of submarine groundwater of the order of 40% of the surface freshwater is required to explain the ^{226}Ra flux. The groundwater flux given here does not represent a flux of freshwater to the coast as the groundwaters responsible for the ^{226}Ra flux have a variable salinity.

This strategy can be extended to studies of other solutes entering the coastal ocean by submarine groundwater. If the average concentration of other solutes in submarine groundwater can be established, the estimate of groundwater input derived from the Ra studies provides flux estimates of the other solutes to the coastal ocean by submarine groundwater discharge. These fluxes may be important for nutrients, trace metals, and organic compounds.

5. Conclusions

Short-lived Ra isotopes provide a means of determining the exchange time of water across the continental

shelf. In the South Atlantic Bight exchange times of nearshore waters with the Gulf Stream are of the order of thirty days. Estimates of exchange times may be used in conjunction with measurements of dissolved components in the coastal ocean to derive fluxes of these components to the open ocean. These fluxes to the ocean must be balanced by fluxes of these components to coastal waters from rivers, groundwater or other sources.

Acknowledgements

I thank the officers and crew of the R/V Cape Hatteras as well as Jim Krest, Donnie Smoak, Jim Todd, Erin McGuinness, Ioanna Stergiades, and Stefka Nikolova for their help in sample collection and processing. Discussions with Rama and Tim Shaw helped me evaluate the importance of groundwater. This research was supported by the U. S. National Science Foundation.

References

- Brewer P G and Spencer D W 1975 Minor element models in coastal waters; in *Marine Chemistry in the Coastal Environment* (ed.) T Church (Washington, DC: American Chemical Society) pp. 80–96
- Giffin C, Kaufman A and Broecker W S 1963 Delayed coincidence counter for the assay of actinon and thoron; *J. Geophys. Res.* **68** 1749–1757
- Kaufman A, Trier R, Broecker W S and Feely H W 1973 Distribution of ^{228}Ra in the world ocean; *J. Geophys. Res.* **78** 8827–8848
- Lietzke T A, and Lerman A 1975 Effects of bottom relief in two-dimensional ocean eddy diffusion models; *Earth Planet. Sci. Lett.* **24** 337–344.
- Moore W S 1976 Sampling ^{228}Ra in the deep ocean; *Deep-Sea Res.* **23** 647–651
- Moore W S 1984 Radium isotope measurements using germanium detectors; *Nucl. Inst. Methods* **223** 407–411
- Moore W S 1987 ^{228}Ra in the South Atlantic Bight; *J. Geophys. Res.* **92** 5177–5190
- Moore W S 1996 Large groundwater inputs to coastal waters revealed by ^{226}Ra enrichments; *Nature* **380** 612–614
- Moore W S and Arnold R 1996 Measurement of ^{223}Ra and ^{224}Ra in coastal waters using a delayed coincidence counter; *J. Geophys. Res.* **101** 1321–1329
- Pomeroy L R, Blanton J O, Poffenhofer G A, Damm K L V, Verity P G, Windom H L and Lee T N 1993 Inner Shelf Processes; in *Ocean Processes: U. S. Southeast Continental Shelf* (ed.) D W Menzel (Washington, DC: U. S. Dept. Energy)
- Rama and Moore W S 1996 Using the radium quartet to estimate water exchange and groundwater input in salt marshes; *Geochim. Cosmochim. Acta* **60** 4645–4652
- Torgersen T, Turekian K K, Turekian V C, Tanaka N, DeAngelo E, and O'Donnell J 1996 ^{224}Ra distribution in surface and deep water of Long Island Sound. Sources and horizontal transport rates; *Cont. Shelf Res.* **16** 1545–1559

^{210}Pb in the ocean: A pilot tracer for modeling particle reactive elements

ERNST MAIER-REIMER¹ and GIDEON HENDERSON²

¹ *Max-Planck-Institut für Meteorologie, Bundesstr. 55, 20146 Hamburg, Germany*

² *Lamont-Doherty Earth Observatory, Palisades, N.Y, 10964, USA*

e-mail: maier-reimer@dkrz.de

We discuss the basic requirements for a successful modeling of ^{210}Pb in the ocean as a test tracer for at least other lead isotopes, but also of other elements that behave similarly to lead. With the aid of realistic models of the oceanic circulation and the major biogeochemical cycles in it, the result is a dynamically consistent model of lead cycling that reproduces observed profiles within 10%.

1. Introduction

Stable Pb-isotope ratios such as $^{207}\text{Pb}/^{204}\text{Pb}$ show spatial variability in the oceans. This is expected from the fact that the Pb-isotope composition of continental crust varies around the globe and as lead has a residence time in the oceans significantly shorter than the mixing time. The natural variation in Pb isotopes in the oceans has been observed by observations in manganese nodules and crusts (Abouchami and Goldstein 1995; von Blanckenburg 1996). And variation in Pb isotope ratios through geological time at a single site is also known to occur from studies of manganese crusts (Christensen *et al* 1997; O’Nions *et al* 1998). The Pb isotope ratio pattern in the ocean is controlled by the distribution of inputs of Pb to the ocean, the advection of Pb by ocean circulation, and the removal of Pb by scavenging onto sedimenting particles. The Pb isotope distribution in the past ocean therefore has the potential to provide information about the distribution of continental weathering in the past, ocean circulation in the past, and ocean-productivity in the past. But deconvolving these three effects from the Pb-isotope record is problematic. This problem is compounded by the fact that, in the modern ocean, Pb-isotopes are almost entirely controlled by anthropogenic aerosol contamination. This prevents us from using the modern as the key to the past in our attempts to understand the controls on

Pb-isotopes in the oceans. Lead also has a short lived isotope, ^{210}Pb , which is not significantly anthropogenically perturbed. In this study, we modelled the input, advection, and removal of ^{210}Pb in an ocean GCM in order to better understand the controls on the natural Pb distribution in the ocean. This study also represents an early attempt to introduce particle-reactive elements to an ocean GCM and may therefore be more widely applicable to the many elements which exhibit this behaviour in seawater.

^{210}Pb (half-life 22.3 years) is a decay product of the ^{238}U -series with intermediate products ^{234}Th , ^{234}Pa , ^{234}U , ^{230}Th (half-life 75,000 years) and ^{226}Ra (half-life 1600 years). The subsequent transitions (^{222}Rn , ^{218}Po , ^{214}Pb , ^{214}Bi , ^{214}Po) to ^{210}Pb are so fast that the decay of ^{226}Ra can be taken locally as source for ^{210}Pb . Another source is from eolian transport of ^{222}Rn (half-life 3.8 days) that emanates from continental crusts. The strength of this source is rather well established by the use of well calibrated atmospheric transport models (Preiss and Genthon 1997). In the ocean, lead tends to attach to biogenic particles and to become buried in sediments (Cochran *et al* 1990). Modeling ^{210}Pb as an isolated study would be a rather hopeless task: ocean circulation, particle fluxes and the distribution of ^{226}Ra , of which only sparse data are available, must be specified as input data. Ultimately, these input fields must be provided by precursor models that are validated individually. The present

Keywords. Lead isotopes; ^{210}Pb ; tracer; reactive elements; oceanic circulation.

study is based on the Hamburg model of the oceanic carbon cycle (HAMOCC3, Maier-Reimer 1993) which itself is based on a model of physical circulation (LSG, Maier-Reimer *et al* 1993).

From the applications of the model to date, we see a classification of tracers into four categories, listed in order of increasing importance of the role of circulation models for the interpretation of data:

- I) Dense data of the dynamically active tracers T, S, which determine velocity. A model like ours is of little value for an “explaining” description of the data; it is useful primarily for an estimate of the sensitivity of the circulation with respect to changing surface conditions. These hydrographic fields are, of course, the base of all modeling efforts. It is, however, an old dilemma dating from the time when the first diagnostic models were constructed by Sarkisyan (1969), that the available data (Levitus 1983) – collected over many decades – are not fully compatible with a plausible circulation pattern. Toggweiler *et al* (1989) pointed out that a purely prognostic run with their circulation model produced moderately realistic distributions of T, S, and radiocarbon, whereas their “robust diagnostic” run with internal restoring to observed hydrography produced a very unrealistic distribution of radiocarbon.
- II) Moderately sparse physical tracer data such as PO_4 (see below), ^{14}C from bombs and cosmic rays, CFC's, ^3H , ^3He from known sources provide a check of circulation. After determining the checks to be successful, the model can be taken for interpolation in space and time and for computation of inventories.
- III) Moderately sparse biogenic tracer data for PO_4 , alkalinity, ΣCO_2 , $\text{Si}(\text{OH})_4$, O_2 react on the circulation and weakly on biological parametrization. Once the physical circulation of the model is accepted, the model is applied to determine the strength of the biological pumping mechanism. Successful modeling of $\delta^{13}\text{C}$ and the depth of the lysocline is essential for constraining models of past circulation states by the sedimentary records.
- IV) Exotic tracers in our definition are, for example ^{39}Ar , ^3He from ridge crests, ^{32}Si from cosmic rays, lead isotopes, anthropogenic CO_2 , etc. They are characterized either by the sparseness of data or by the lack of knowledge about the sources or by the difficulties of the measurements. In this category models provide essential tools to interpret the data, either by narrowing the uncertainties of source and sink mechanisms, or even by questioning the reliability of data (e.g. Peng *et al* 1993).

2. The source from ^{226}Ra

Since Thorium is very quickly scavenged out from the water, the main source for Radium is deep sea-floor regions with low sediment accumulation rates; at locations with high accumulation rates, Th has partly entered sedimentary diagenesis below the bioturbated layer before releasing its decay product to the water column.

From GEOSECS we have available 845 data points for ^{210}Pb and 591 for ^{226}Ra . Reconstruction and mapping of the three-dimensional structure is, thus, not trivial. Standard procedures of objective mapping are

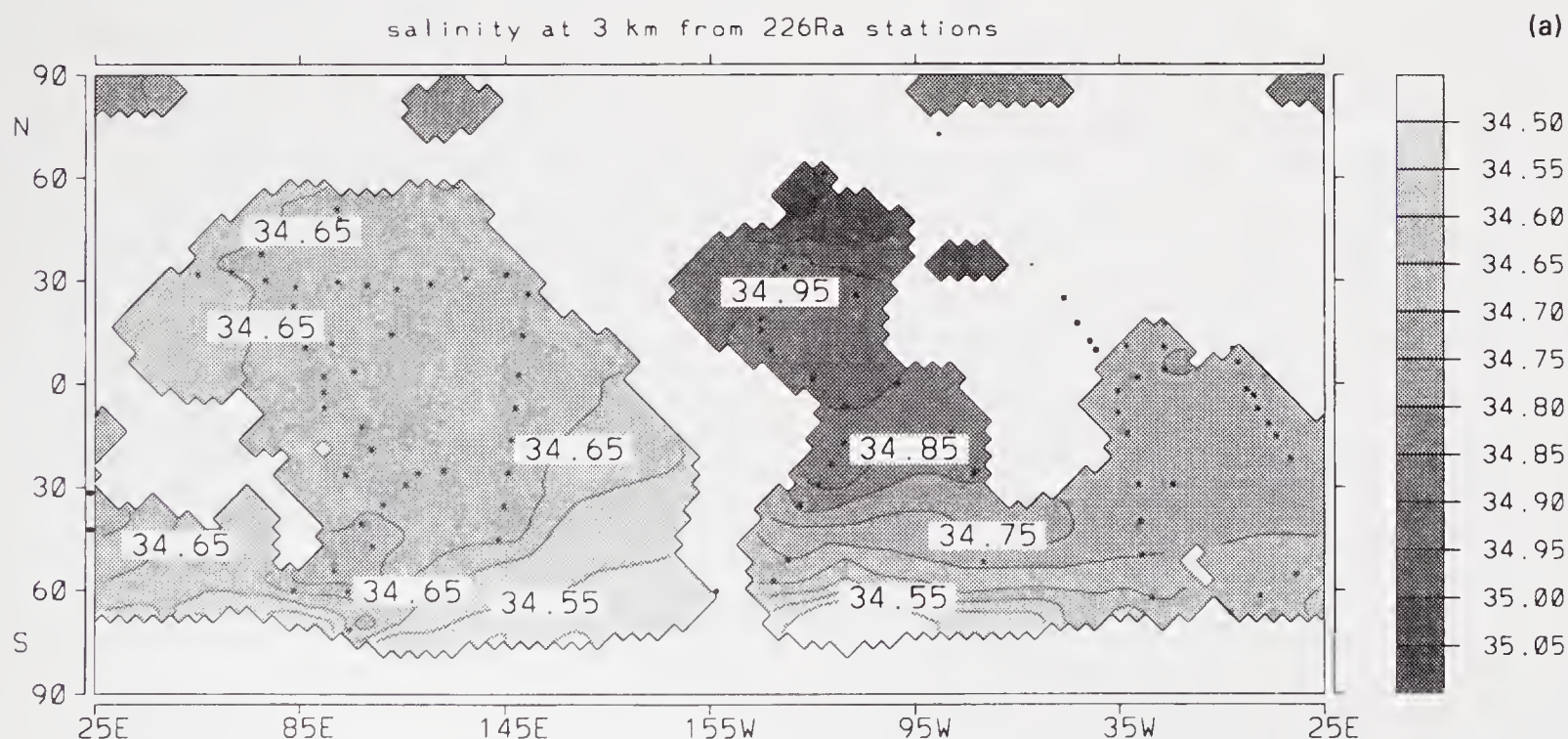


Figure 1(a). Reconstruction of salinity under the assumption that measurements were only available at stations where ^{226}Ra data exist.

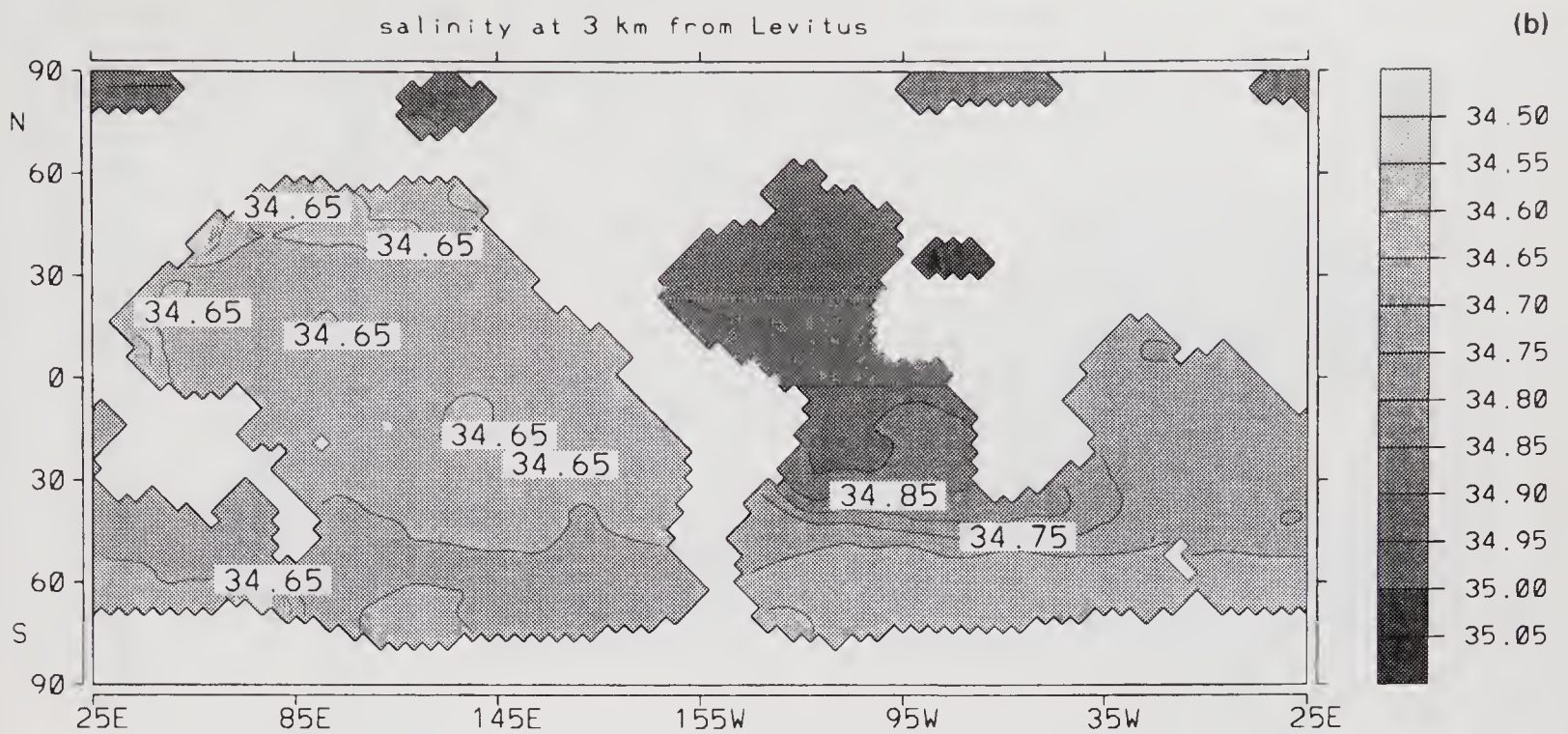


Figure 1(b). Salinity from the Levitus atlas interpolated on the grid of the model.

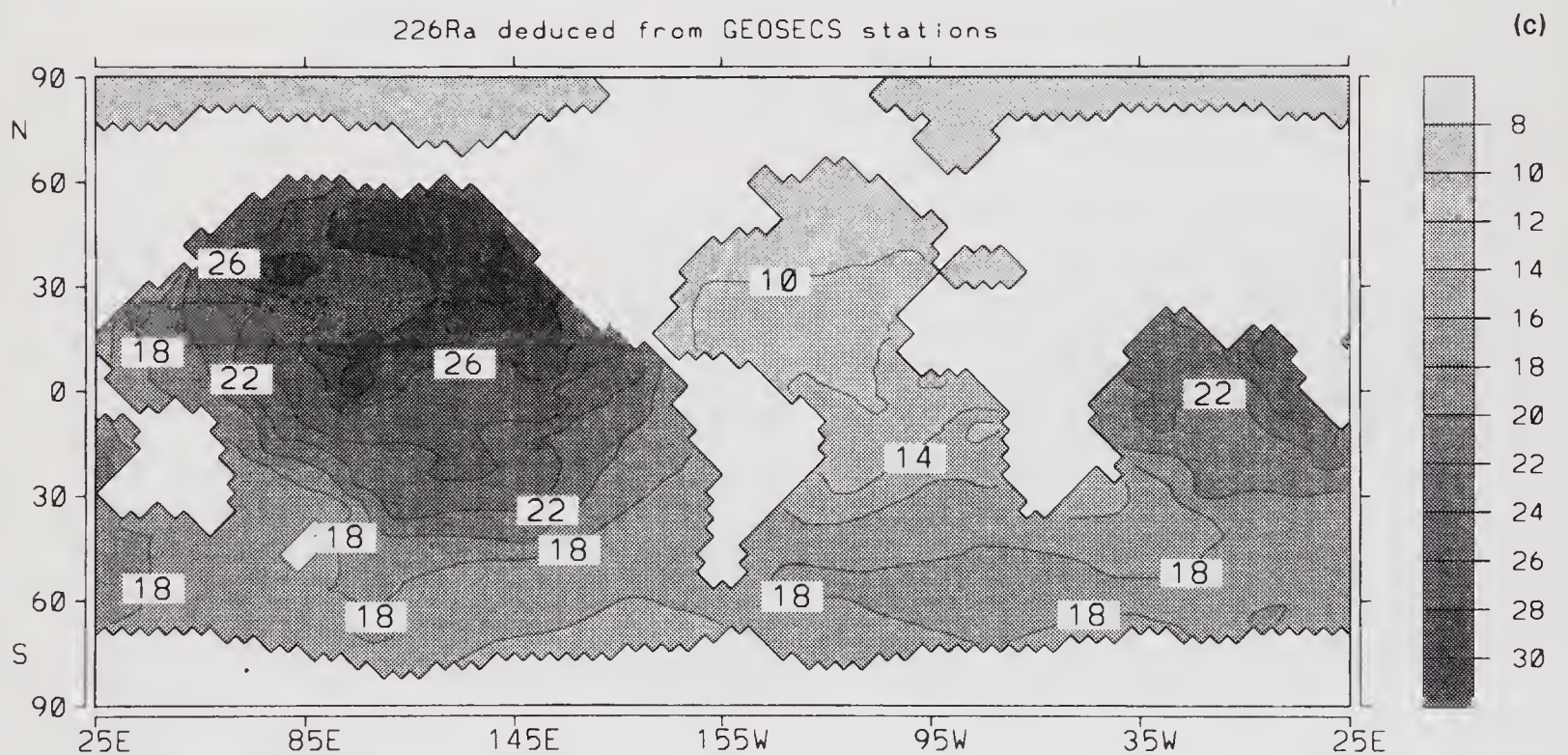


Figure 1(c). Reconstructed distribution of ^{226}Ra at 2 km depth. Units are dpm/100 kg.

more or less based on a concept of isotropic diffusion of the information into space. More realism may be expected from a technique by which the circulation field of a model, once it is accepted to represent essential aspects of the global circulation, is used as an interpolator. The observational information is propagated up- and downstream the models streamline. The space is filled up completely with information by the models diffusivity. Figure 1(a) displays a reconstruction of the salinity field in 1 km depth, based on the hypothetical assumption that salinity measurements were available only at those positions where ^{226}Ra measurements were made. The agreement with the

observed salinity distribution is, of course, not perfect; as a result from a GCM it would hardly be taken as acceptable. The dots indicate the positions of data. The global aspects such as the excess salinity of the Northern Atlantic relative to the rest of the deep ocean, however, are captured. In contrast, figure 1(b) displays the distribution of salinity from Levitus (1983) as interpolated onto the grid of our model. Obviously, the streamline interpolation gives a fair reproduction of the known field of salinity. Regional features like the spreading of Mediterranean water in the Atlantic (the centre of the plume is not matched by one of the stations), however, are underrepresented.

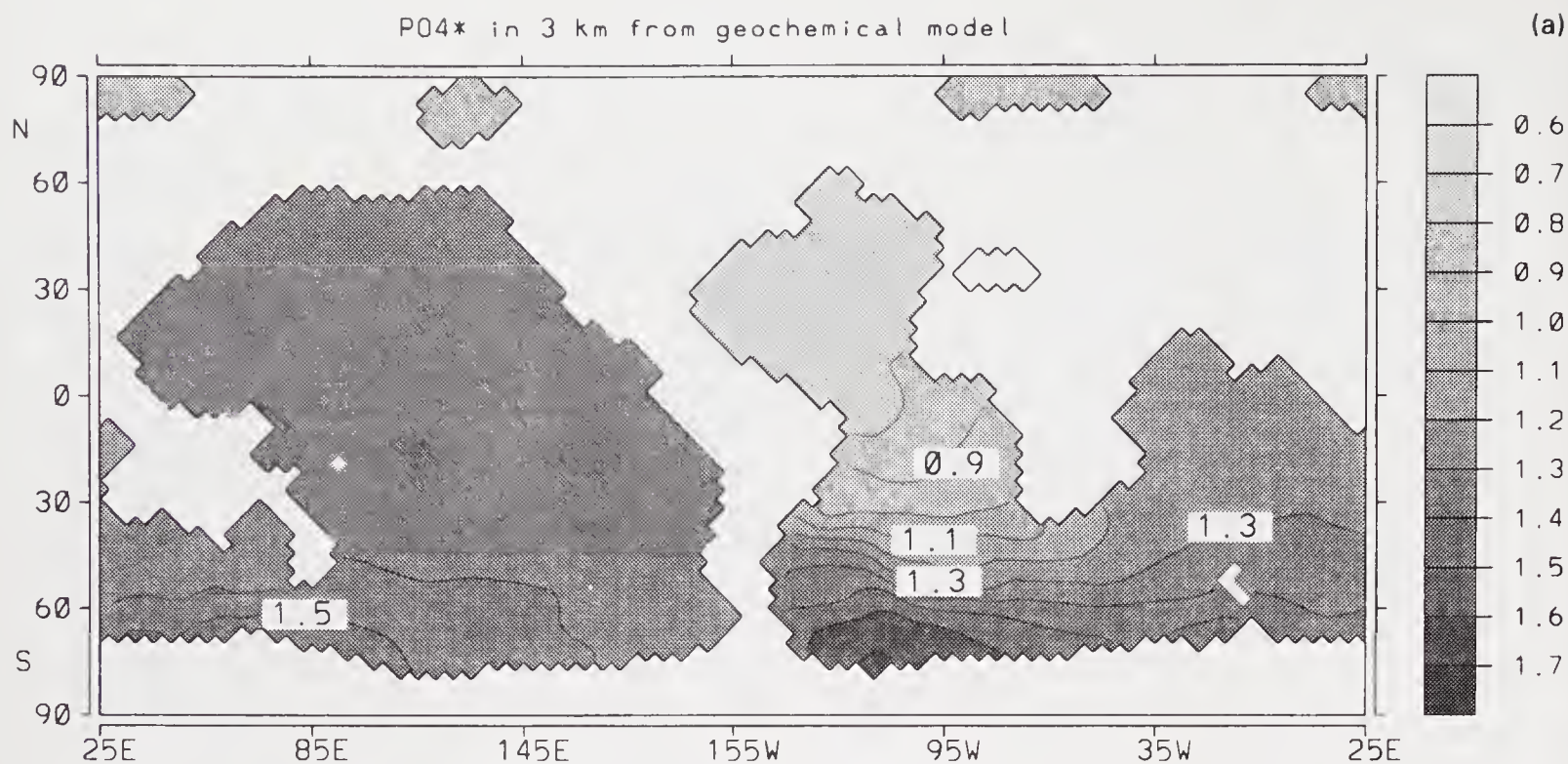


Figure 2(a). Distribution of the models PO_4^* at 3 km depth, the center depth of NADW. Note the homogeneous pattern in the Northern Pacific with 1/3 of NADW and 2/3 of Antarctic deep water.

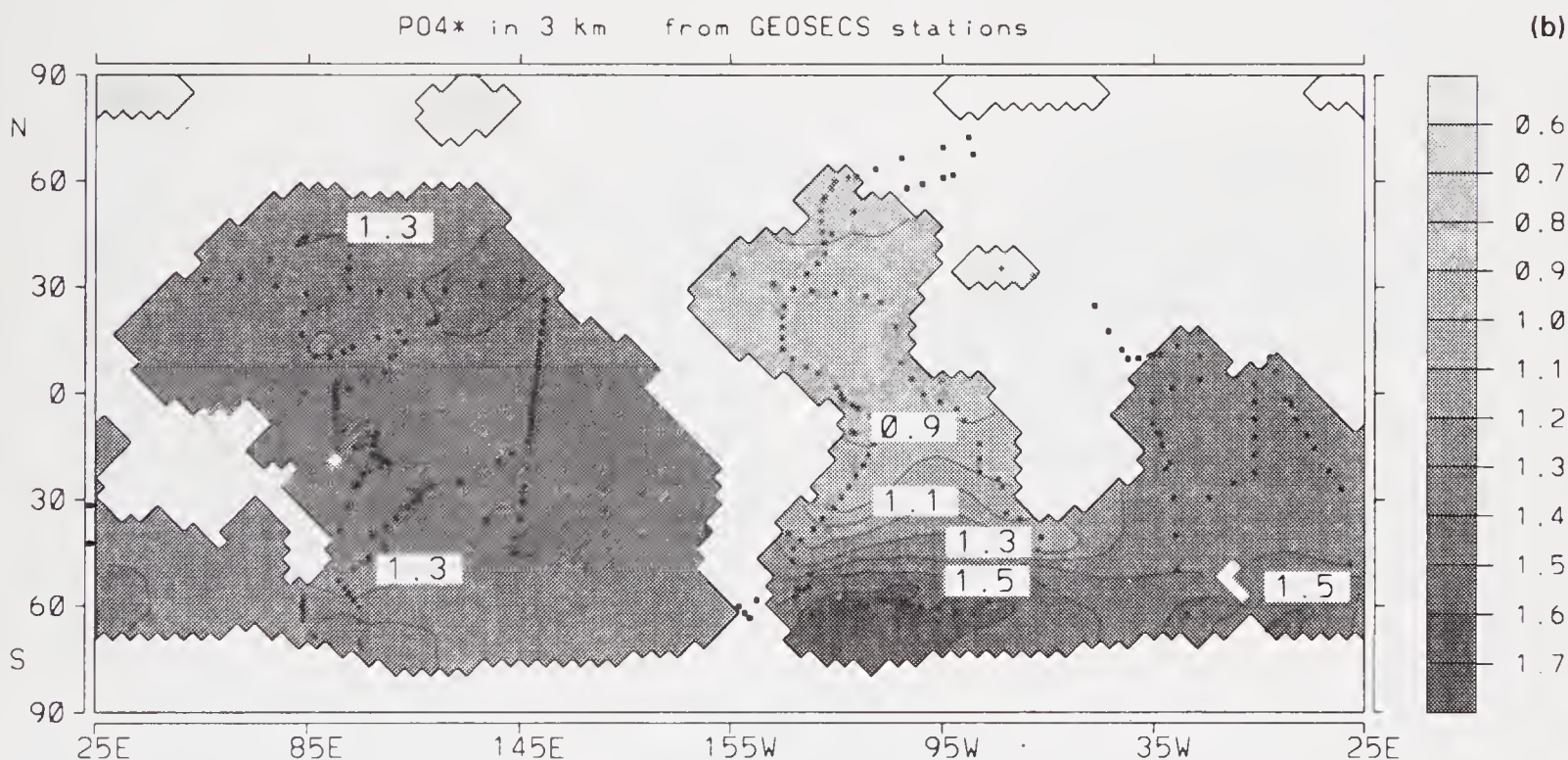


Figure 2(b). Reconstruction of PO_4^* from 10399 GEOSECS stations.

It may be expected that for a sparsely measured tracer like ^{226}Ra the representation of the real but unknown field has a similar degree of realism. Figure 1(c) displays the corresponding distribution of ^{226}Ra in 1 km depth.

The realism of the global deep circulation pattern is confirmed by the distribution of

$$\text{PO}_4^* = \text{PO}_4 + \text{O}_2/172 - 1.95\mu/l,$$

a combination of phosphate and oxygen that does not change during remineralization of sinking organic debris (Broecker *et al* 1991).

As compared with salinity, PO_4^* has the advantage that the magnitudes of the deep sea gradients are more than half the amplitude of the sea surface gradients. It enters the deep ocean in the regions of deep water formation in the Northern Atlantic and around Antarctica, primarily in the Weddell Sea. The distribution is characterized by the mixing between the low values of the northern endmember and the high values of the southern component. Fortunately (from the modeler's point of view), it reacts not very sensitively to the details of the biological production scheme; it can be considered, thus, as a predominantly

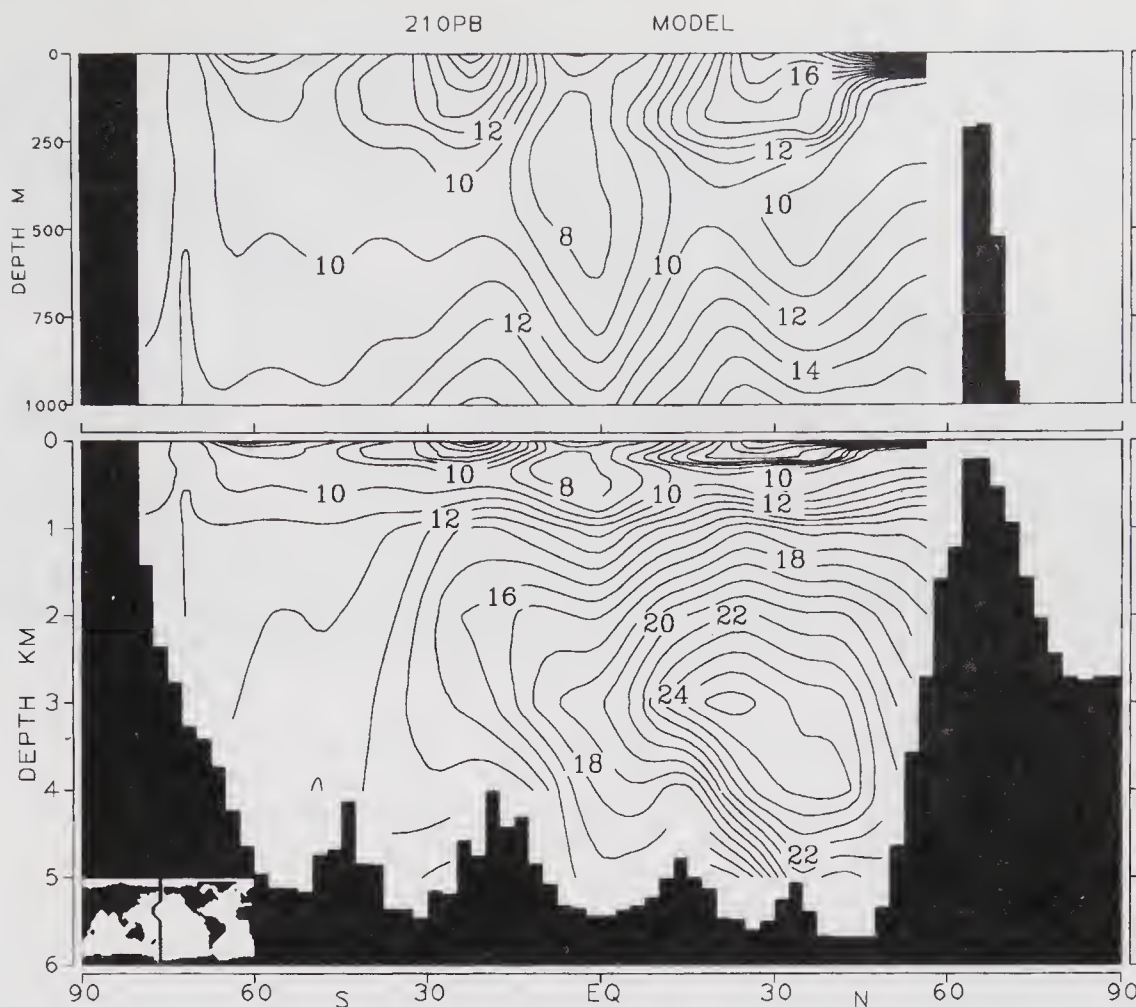


Figure 3. Section of ^{210}Pb in the Western Pacific as given in the ikon. Units are dpm/100 kg.

physical tracer which mirrors the model's deep circulation and mixing properties. Production is simulated by removal of phosphate from the surface with a globally uniform time constant of four months which is locally modified by temperature and mixing conditions. The time constant of four months was chosen to match realistic numbers of phosphate minima in the subtropical gyres (Maier-Reimer 1993). No restoring to observations is performed. Figure 2(a) shows the model's prediction of PO_4 at a depth horizon of 3 km, which can be directly compared with the corresponding figure from Broecker *et al* (1991), or with the result of the dynamic interpolation of 10399 GEO-SECS data with our circulation field. The quantitative simulations of the end member values (0.7 in the Northern Atlantic and 1.7 in the Weddell Sea) is to some extent dependent on the tuning process, but it turned out that this tracer is rather insensitive to the details of biological parameterization. The spreading and mixing into the regions far away from the deep water production represents an independent test of the model's deep circulation.

3. Simulation of ^{210}Pb

For ^{210}Pb the situation is more complex than for ^{226}Ra . Due to the short half-lifetime of 22.3 years, and due to affinity to sinking particles, the interpolation

along streamlines is inappropriate. The merit of the model now lies in the determination of the scavenging rates: as the carbon cycle model (Maier-Reimer 1993) from group III predicts realistic distributions of deep oxygen, phosphate, and alkalinity which are determined by the divergence of the fluxes of organic carbon and of calcareous shells, the model can be run in a prognostic mode, tuning the scavenging rates to match the few observed profiles of ^{210}Pb . The model predicts fluxes of organic material, opal, and calcareous shells. In order to minimize the number of free parameters we assume that ^{210}Pb scavenging depends only on the total mass flux of particles and is not affected by the chemistry of these particles. An additional scavenging mechanism is exerted in the deep sea by the contact of dissolved lead with sediment material, as postulated by Spencer *et al* (1981). The tuning of the scavenging rates was obtained in a series of 60-years simulation (3 half-life times), starting from a first guess simulation, where the sum of squares of discrepancies between available data and corresponding model values was minimized. The resulting rms error of individual stations is 1.8 dpm/100 kg, i.e. appr. 10% of typical absolute values.

We restrict our discussion of the results on a very few aspects here. Figure 3 shows the simulated distribution of ^{210}Pb along a section in the western Pacific (outlined in the ikon in the left bottom corner). The basic features of the surface maximum (due to eolian

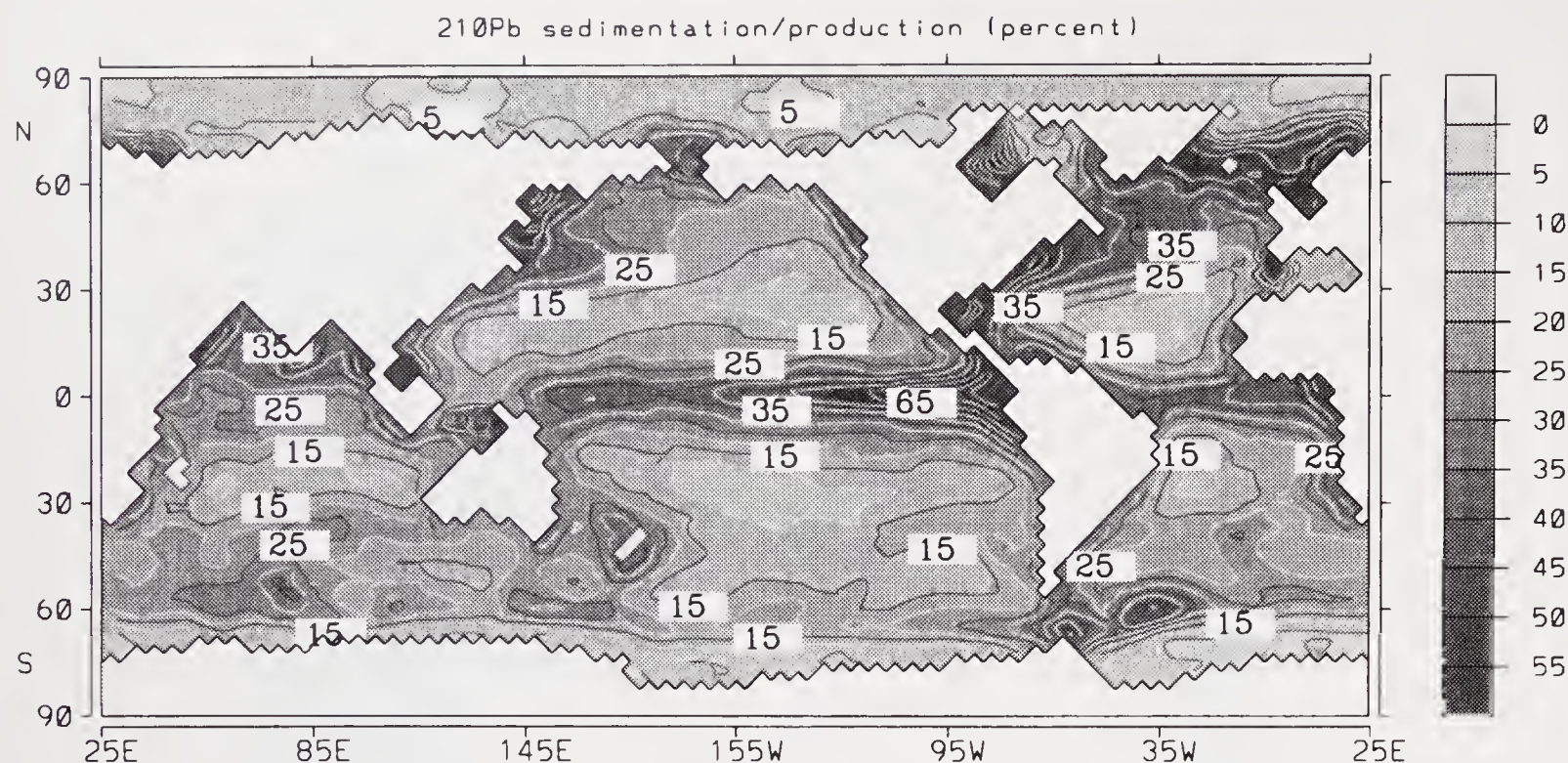


Figure 4. Sedimentation vs. depth-integrated production of ^{210}Pb .

input) and an intermediate maximum at appr. 3 km are reproduced well. The position and strength of the deep maximum – apparently at the same level as the alkalinity maximum – depends delicately on circulation properties, particle flux divergence, and the tuned scavenging rates.

Figure 4 shows the relationship of sedimentation to the depth integrated production. The figure clearly displays regions of high productivity where strong particle fluxes provide a rather high scavenging, and thus, sedimentation rate. In the subtropical gyres the sedimentation rate is rather low, and the production rate for ^{226}Ra is thus rather high. Again due to the low particle flux, the scavenging rate is rather small and most of the loss of ^{210}Pb is due to radioactive decay. Lateral advection (not discussed here) provides a smearing between these two extreme types of local dynamics.

A peculiar feature in figure 4 consists of the low values around Antarctica. This is partly due to the extremely low (except downstream of Australia and Patagonia) eolian input. On the other hand, the Southern Ocean is known to be the most prominent HNLC (high nutrient low chlorophyll) region of the World Ocean, i.e. the biological production is – for whatever reasons – much lower than would be expected from the nutrient supply. Candidates for an explanation of this behaviour are, e. g., unfavourable physical environmental conditions or the lack of iron as a micronutrient due to low dust input. This question is subject to an ongoing vivid scientific debate.

4. Conclusion

As the model provides a ^{210}Pb distribution close to that observed we have some confidence that it is

advecting and removing ^{210}Pb in a realistic manner. As the other Pb isotopes are expected to be advected and removed in a similar fashion, this provides the potential to investigate the natural stable Pb isotope distribution in the ocean with two of its three controls understood. This investigation will be the subject of future papers.

References

- Abouchami W and Goldstein S L 1995 A lead isotopic study of circum-antarctic manganese nodules; *Geochimica et Cosmochimica Acta* **9**
- Broecker W S, Blanton S, Smethie W M and Östlund G 1991 Radiocarbon decay and oxygen utilization in the deep Atlantic Ocean; *Glob. Biogeochem. Cycles* **5** 87–117
- Christensen J N, Halliday A N, Godfrey L V, Hein J R and Rea D K 1997 Climate and ocean dynamics and the lead isotopic records in Pacific ferromanganese crusts; *Science* **277** 913–918
- Cochran J K, McKibbin-Vaughan T, Dornblaser M M, Hirschberg D, Livingston H D and Buesseler K D 1990 ^{210}Pb scavenging in the North Atlantic and North Pacific oceans; *Earth Planet. Sci. Lett.* **97** 332–352
- Levitus S 1983 Climatological atlas of the World Ocean; *NOAA Prof. Paper No. 13*
- Maier-Reimer E 1993 Geochemical cycles in an ocean general circulation model – Preindustrial tracer distributions; *Glob. Biogeochem. Cycles* **7** 645–677
- Maier-Reimer E, Mikolajewicz U and Hasselmann K 1993 Mean circulation of the Hamburg LSG OGCM and its sensitivity to the thermohaline surface forcing; *J. Phys. Oceanogr.* **23** 731–757
- O'Nions R K, Frank M, von Blanckenburg F and Ling H-F 1998 Secular variation of Nd and Pb isotopes in ferromanganese crusts from the Atlantic, Indian and Pacific Oceans; *Earth Planet. Sci. Lett.* **155** 15–28
- Peng T H, Maier-Reimer E and Broecker W S 1993 Distribution of ^{32}Si in the World Ocean: Model compared to Observation; *Glob. Biogeochem. Cycles* **7** 463–474

- Preiss N and Genthon C 1997 Use of a new database of lead 210 for global aerosol model validation; *J. Geophys. Res. Atm.* **102** 25347–25357
- Sarkisyan A S 1969 Theory and computation of ocean currents; *US Dept. Comm. Springfield, VA*
- Spencer D W, Bacon M P and Brewer P G 1981 Models of the distribution of ^{210}Pb in a section across the north equatorial Atlantic Ocean; *J. Mar. Res.* **39** 119–138
- Toggweiler J R, Dixon K and Bryan K 1989 Simulations of radiocarbon in a coarse-resolution World Ocean model 1: Steady state prebomb distributions; *J. Geophys. Res.* **94** 8217–8242
- von Blanckenburg F, O’Nions R K and Hein J R 1996 Distribution and sources of preanthropogenic lead isotopes in deep ocean water from Fe-Mn crusts; *Geochim. Cosmochim. Acta* **60** 4957–4964

Determination of indium in natural waters by flow injection inductively coupled plasma mass spectrometry

DIA SOTTO ALIBO, HIROSHI AMAKAWA and YOSHIYUKI NOZAKI

*Marine Inorganic Chemistry Division, The Ocean Research Institute, University of Tokyo,
Nakano-ku, Tokyo 164, Japan
e-mail: nozaki@ori.u-tokyo.ac.jp*

Two methods have been developed to measure indium (In) in natural waters by flow injection inductively coupled plasma mass spectrometry (ICPMS). One is the isotope dilution technique using an ^{113}In enriched spike and the other utilizes natural yttrium present in the sample as an internal standard. In the former, optimization of the ^{113}In spike to minimize error is often difficult for samples in which In concentrations are variable, whereas in the latter method, a separate determination of Y in the sample is necessary and hence more sample is required. Using about 1 liter of a water sample, 200 fold preconcentration of In was performed by solvent extraction and back extraction technique and then introduced into the ICPMS to measure the $^{113}\text{In}/^{115}\text{In}$ or $^{115}\text{In}/^{89}\text{Y}$ ratios. The detection limits were 0.01–0.02 pmol kg $^{-1}$ for both methods.

Application of the methods to seawater samples yielded the concentrations of 0.06–0.15 pmol kg $^{-1}$ for the Pacific and 0.6–1.5 pmol kg $^{-1}$ for the Atlantic. The large inter-oceanic variation of In best resembles that of Al amongst the 3B group of elements in the periodic table. River and estuarine samples gave a more variable range of concentrations of 0.01–15 pmol kg $^{-1}$. Most of the In supplied by rivers is removed by scavenging in the estuarine mixing zone, suggesting that the fluvial input of In to the ocean is small.

1. Introduction

Although its crustal abundance is small (~ 0.1 ppm; Taylor 1964), indium is widely distributed in nature but never occurs uncombined. It has a low melting point (155°C) and tends to be enriched in zinc blende (up to $\sim 0.1\%$) making this mineral the main source of indium at present (Shaw 1952). The industrial demand of indium has increased dramatically over the last few decades, largely because the indium tin oxide alloy has been used in flat panel display devices and coatings (Roskill Information Services, Ltd. 1996). Other industrial uses of indium include plating, soldering, manufacturing semiconductors, etc. Very little is known about the behavior of In in the aqueous environment, including industrial sewage.

Since the 1980s, there has been a growing interest on the unique geochemical behaviors of the 3B group elements in the oceans (Hydes 1979; Murozumi and

Nakamura 1980; Orians and Bruland 1988a,b). For example, the dissolved Al concentrations in the north Pacific are extremely low, generally less than 1 nmol kg $^{-1}$ (Orians and Bruland 1985; Measures *et al* 1986), despite the fact that Al is a major component of crustal materials (8.3% by weight). Al exhibits marked (and the largest among the elements ever reported) inter-oceanic variations showing more than an order of magnitude higher concentrations in the Atlantic and Mediterranean waters than in Pacific waters. These oceanic distributions of dissolved Al appear to be controlled by complex mechanisms of the atmospheric and riverine inputs, removal by scavenging, release from bottom sediments, and advective transport of water masses (Measures 1995). Gallium also shows a complex distribution in the north Pacific which is affected by mechanisms similar to those of Al, although the continued scavenging by particulate matter and regeneration processes throughout the

Keywords. Indium; dissolved indium; ICPMS; isotope dilution method; oceanic distribution.

water column may be more important for Ga resulting in a systematic increase towards the bottom (Orians and Bruland 1988a and b). Thallium is unique in this group of elements having less variable concentrations of 59–80 pmol kg⁻¹ (Murozumi and Nakamura 1980; Flegal and Patterson 1985) irrespective of the location and depth in the oceans. Based on this observation, it has been suggested that thallium may be present as Tl⁺ rather than the thermodynamically predicted species of Tl(OH)3⁰, and hence it behaves conservatively similar to K⁺ (Flegal and Patterson 1985). However, this view is controversial because Tl could inadvertently take a pseudo-conservative type distribution like Ce (Li 1991). Thus, indium, being sandwiched by Ga above and Tl below in the periodic table, may be important for the better understanding of the comparative marine geochemistries of the 3B group elements.

Nevertheless, investigations on indium in the oceans have been few to date. Indium concentration in seawater was theoretically deduced to be less than 100 pmol kg⁻¹ (Baric and Branica 1969). The first report on indium concentration in seawater (Chow and Snyder 1969) gave values of 26–52 pmol kg⁻¹ for a vertical profile in the Pacific based on the isotope dilution thermal ionization mass spectrometry. The values, however, are highly uncertain due to a high blank in the measurements. In contrast, concentrations reported for four samples in the north Atlantic (Matthews and Riley 1970) based on neutron activation analysis ranged from 2.7 pmol kg⁻¹ at the surface to 0.9 pmol kg⁻¹ at 2000 m depth. Since these data were obtained when clean sampling and analytical techniques for seawater had not yet been well developed, confirmation is necessary before discussing their geochemical and oceanographic significance. Recently, Orians and Boyle (1993) described the method of In determination in natural waters using

inductively coupled plasma mass spectrometry (ICPMS), but they did not measure real natural samples. In this paper, we describe new sensitive ICPMS methods for the determination of indium in natural waters together with the data on river, estuarine and sea waters.

2. Methods

2.1 Instrumentation

Two inductively coupled plasma mass spectrometers were used in this study. One is the Yokogawa PMS 2000 ICPMS (Yokogawa Analytical Systems Inc.) with a typical sensitivity of ~20000 counts/s for 1 ppb Y solution. The other is a HP 4500 Series ICPMS (Hewlett Packard Inc.) which has a typical sensitivity of ~50000 counts/s for 1 ppb Tl solution. The former was used for the isotope dilution method and for the determination of Y necessary for the internal standard method. To avoid cross contamination, the latter was only used for the determination of indium in unspiked samples. The instrument operating conditions of these ICP mass spectrometers are given in table 1.

The ICPMS ion lens voltages were optimized using a 1 ppb solution of Y, Cs, and Tl. The lens voltages were varied to obtain maximum signals for ⁸⁹Y and ¹³³Cs because the masses investigated in the present study were within the range of 89 to 118.

2.2 Reagents and apparatus

High-purity water used in all experiments was prepared by deionization to 18 MW using a four-bowl Milli-Q Reagent Water System (Millipore Co. Ltd.) fed by water purified by reverse osmosis. The mixture

Table 1. ICPMS operating conditions.

	PMS2000	HP4500
1. Plasma conditions		
Detector voltage	2400 V	1210 V
Cooling chamber temperature	0°C	2°C
Argon gas flow rate:		
Plasma	14 ± 0.5 l min ⁻¹	15 ± 0.1 l min ⁻¹
Auxiliary	0.8 ± 0.2 l min ⁻¹	1.00 ± 0.01 l min ⁻¹
Carrier	0.81 ± 0.01 l min ⁻¹	0.85 ± 0.01 l min ⁻¹
2. Sampling Conditions		
Sample cone diameter	1.0 mm	1.0 mm
Skimmer cone diameter	0.45 mm	0.40 mm
Torch position	4.0 mm	0.5 mm
Peristaltic pump rate (solution up-take rate)	0.1 rps	0.1 rps
3. Data acquisition		
Dwell time per point	50 msec	100 msec
Data acquisition time	120 sec	5.56 sec
Scanning mass	89–118	89–118

of 65% HDEHP (bis(2-ethylhexyl) hydrogen phosphate) and 35% H₂MEHP (2-ethylhexyl dihydrogen phosphate) were purchased from TOKYO KASEI Co. Ltd. This was diluted in heptane to make the final concentration of 0.25M (65% HDEHP and 35% H₂MEHP) solution. The heptane and octyl alcohol used in the solvent extraction were of analytical grade purchased from WAKO PURE Chemical Industries Ltd. High-quality ultrapure 20% HCl, 68% HNO₃ and 20% ammonia (all TAMAPURE-AA-100 grade) were purchased from TAMA Chemicals Inc. and used without further purification.

The standard solutions of In, and Y were provided by SPEX Industries. The 1000 ppm solutions of In and Y were mixed together and diluted to make the 1 ppb monitoring standard solution. An indium oxide powder isotopically enriched in ¹¹³In (96.28%) was obtained from Oak Ridge National Laboratory, U.S.A.. The spike solution was prepared by dissolving the powder in 2M HNO₃ and then diluted to 14.49 ppb with 1% HNO₃. About 100 ng of the In spike was transferred to a Teflon beaker and heated to dryness. The residue was taken up in 5 µL of 1% HNO₃ and loaded on a Re single filament. Then, the isotopic ratio was determined by Finnigan MAT 262 thermal ionization mass spectrometer using a Re single filament. Measured ¹¹³In/¹¹⁵In ratio was 25.8552±0.0013 which agrees with the certified value within ±0.02%. The 1 ppb solution with the same isotopic composition as the spike was also prepared for monitoring mass fractionation in the isotope dilution method.

All glass labware used in the experiments, such as separatory funnels and beakers, were first cleaned with acetone and heptane, soaked in 8M HNO₃ for more than 2 days, and then thoroughly rinsed with Milli-Q water before use. The Teflon items, such as stopcocks detached from the separatory funnels and beakers, were first soaked in SCAT detergent in the supersonic bath, and then successively boiled in aqua regia and Milli-Q waters.

2.3 Water sampling and preparation

Seawaters were obtained from various depths in the western north Pacific during the R. V. Hakuho-Marui cruise (KH-94-3; the Leo Minor Expedition) in October, 1994. Seawater samples were collected using 10-121 Niskin (ordinary or lever action type) bottles mounted on a CTD-RMS (Conductivity, Temperature, Depth-Rosette Multi-Sampling System) array with the capacity of holding 12 or 24 bottles. Precautions against contamination were made as follows. The inside wall of all Niskin bottles was coated with Teflon, and the inner spring of ordinary-type Niskin bottles was replaced by a Dow Corning Silastic tube. (The lever-action type Niskin bottles do not have the inner spring.) The samplers were also thoroughly washed with 2% Extran MAO1 (Merck)

solution, 0.1M HCl solution and Milli-Q water, successively.

Aliquots of about 3 to 5 liters of seawater were transferred from the Niskin bottles to pre-cleaned polyethylene bottles or cubic containers. The filtration, when necessary, was done immediately after sampling using Millipore HF400 TS hollow fiber of 0.04 µm pore size. Both filtered and unfiltered samples were immediately acidified with 20% HCl (TAMAPURE-AA-100) to pH~1.5.

River waters were collected either from the riverside or a fishing boat. A 5l handmade polyethylene sampler with a bottom inlet controlled by a plastic stopcock was used. After sampling, the water was filtered through a 0.04 µm hollow fiber (Millipore HF400 TS) and acidified to pH~1.5 with 20% HCl (TAMAPURE-AA-100).

These water samples were transported to the ORI laboratory in Tokyo and stored until analysis.

2.4 Procedure

About 1l of the water sample was transferred in a separatory funnel and adjusted to pH 1.6 with ammonia. (For the isotope dilution method, an exact amount of ¹¹³In spike was added to the solution. The solution was thoroughly mixed and stored for more than 24 hours in order to reach isotopic equilibration.). The indium together with Y in the solution was then extracted into 20 ml of 0.25 M HDEHP/H₂MEHP in heptane. The aqueous solution was discarded and the organic phase was washed three times with 5 ml of 0.15 M HCl. Then, 10 ml of octyl alcohol was added to the organic phase to transform any dimeric HDEHP/H₂MEHP complexes to monomeric ones and thereby facilitate in the back-extraction. Indium was back-extracted into three successive 5 ml portions of 6 M HCl which was collected in a 50 ml separatory funnel. The HCl solution was washed with 3 ml heptane, and then transferred into a 30 ml Teflon beaker. The solution was evaporated to almost dryness (to a small drop of liquid) on a hot plate, and then diluted with 5 ml 1% HNO₃. The solution was then introduced into the Hewlett Packard HP 4500 ICPMS to measure the ¹¹⁵In/⁸⁹Y ratio. (For the isotope dilution method, the ¹¹³In/¹¹⁵In ratio was measured by the Yokogawa PMS 2000 ICPMS.) Since the masses, 113 and 115 are subject to interference from the isotopes of Cd and Sn, the mass numbers 110 for Cd and 117 for Sn were also monitored to correct for isobaric interferences. Alongside, a solution for procedural blank was also run. In the isotope dilution method, a standard solution with an In isotopic ratio similar to those of the samples was also measured to correct for mass discrimination due to the instrument.

For the internal standard method, the Y concentration in the sample was also determined using a

different 150–1000 ml aliquot by the previously published method (Shabani *et al* 1990). The chemical procedure is almost identical to the above except that In (25 ng) is added to the sample solution as a yield monitor at the beginning and Cd (25 ng) is added just before the ICPMS (Yokogawa PMS 2000) measurement to correct the stability of the instrument. The 1 ppb Y and In standard solutions were also run to monitor the mass fractionation.

Each sample and standard solution was repeatedly measured by ICPMS at least 3 times, and more if the relative standard deviation did not fall within the normal range.

2.5 Isotope dilution calculations

Although the isotope dilution method has various advantages in trace element analysis, one of the difficult tasks is to determine the amount of spike to be added to the sample. It has been demonstrated that the optimum isotopic ratio in the resultant mixture to minimize the uncertainty introduced by error propagation through the isotope dilution calculation is the geometric mean of the ratios of the spike and sample (Heumann 1988). For indium with the natural isotopic abundance of 4.38% ^{113}In and 95.62% ^{115}In , the optimum $^{113}\text{In}/^{115}\text{In}$ ratio is estimated to be 1.08 for the ^{113}In (96.28%) enriched spike. This implies that the best result would be obtained when approximately the same amount of the In spike as that present in the sample was added. However, for unknown samples, optimization of the In spike to be added is often difficult. The calculation of indium with normal isotopic composition in the sample (In_n) is made by the following equation,

$$\text{In}_n = \left(\frac{1 + R_n}{1 + R_{sp}} \right) \left(\frac{R_m - R_{sp}}{R_n - R_m} \right) \text{In}_{sp} \quad (1)$$

where In_n and In_{sp} are the moles of indium in the sample and spike, respectively, and R_n , R_{sp} , and R_m are the $^{113}\text{In}/^{115}\text{In}$ ratios in the sample, spike, and the mixture corrected for blank, mass discrimination of the instrument, and isobaric interferences. The error propagation depends upon the value of R_m . The practical target $^{113}\text{In}/^{115}\text{In}$ ratios may be set to 1–8 which corresponds to the error magnification within 1.5.

2.6 Isobaric interferences

In the isotope dilution method, interferences occur both at mass 113 by ^{113}Cd (12.2% of Cd) and at mass 115 by ^{115}Sn (0.34% of Sn). Although most Cd present in seawater sample is removed by the preconcentration step, it is used as a monitoring standard for the ICPMS and hence signals in the counts for Cd are generally seen. The contribution, however, is suitably corrected by using measured

counts at ^{110}Cd (12.5% of Cd) and the natural $^{113}\text{Cd}/^{110}\text{Cd}$ ratio. Interference at mass 113 is also possible from a molecular ion $^{97}\text{Mo}^{16}\text{O}^+$ (9.45% of Mo). Since most Mo isotopes have corresponding isobars of Sn, it is somewhat difficult to precisely estimate the interference. The contribution, however, is neglected by considering that Mo is removed by the preconcentration step and a fraction of molecular ions formed is generally small (Heumann 1988). On the other hand, Sn is contained in the sample and to a lesser extent in reagents. This Sn is not removed by the preconcentration step of solvent extraction and normally identified for its presence in the ICPMS measurements. Nevertheless, the contribution can be precisely corrected by using the counts for ^{117}Sn (7.57% of Sn) and the natural $^{115}\text{Sn}/^{117}\text{Sn}$ ratio (0.045). The correction typically ranged 10–20% of total counts at mass 115. Although $^{99}\text{Ru}^{16}\text{O}^+$ (12.7% of Ru) can interfere ^{115}In , we neglected this effect because the Ru concentration in seawater is extremely low (Koide *et al* 1986).

In the internal standard method, correction for the isobaric interference is needed only at mass 115. This was performed as described above. The isobaric interference for ^{89}Y is negligible in the determination of Y in seawater (Shabani *et al* 1990; Zhang 1995).

2.7 Procedural blanks and recovery

Blanks were generally measured simultaneously together with every five sample measurements. Determination of the blanks was done by simulating the experimental procedure on only the reagents, and therefore, the blank values are contributed by contaminants in the reagents used and those introduced during the pre-concentration, back-extraction, and evaporation procedures. The isotope dilution method gave an average value of $0.020 \pm 0.007 \text{ pmol kg}^{-1}$ ($n = 4$), while the internal standard method had a mean of $0.016 \pm 0.004 \text{ pmol kg}^{-1}$ ($n = 10$). These blanks comprise 10–20% of the In concentrations in Pacific seawater samples. The detection limits calculated as three times the standard deviations of the procedural blanks were $0.023 \text{ pmol kg}^{-1}$ and $0.012 \text{ pmol kg}^{-1}$ for the isotope dilution method and the internal standard method, respectively.

The internal standard method is based on the assumption that the recovery of In is equal to that of Y. This is most reliably attainable if the preconcentration step is quantitative for the two elements. This is tested by measuring the recovery of In added to seawater for the determination of Y for the internal standard method. Based on thirtyfour individual measurements using both filtered and unfiltered seawaters, the In recovery was found to be $99.0 \pm 1.5\%$. This is indistinguishable from the recovery of Y which was $99.1 \pm 1.0\%$ (Shabani *et al* 1990).

Table 2. Replicate measurements.

A. Isotope dilution method (Sample: Northwest Pacific, 5000 m)		
	<u>Date</u>	<u>In (pmol kg⁻¹)</u>
	July 22nd, 1995	0.185
		0.170
	August 11th, 1995	0.192
		0.191
		0.183
	Average:	0.184 ± 0.009
	% RSD:	4.79
B. Internal standard method (Sample: Sagami Bay, 5 m)		
	<u>Date</u>	<u>In (pmol kg⁻¹)</u>
	August 29th, 1996	0.080
		0.076
		0.076
		0.071
	Average:	0.076 ± 0.004
	% RSD:	4.87

Although not required, similar recovery for In is expected for the isotope dilution method.

2.8 Reproducibility and method comparison

Table 2 gives the data on replicate measurements by the two methods. The determinations by the isotope dilution method were made on five aliquots of unfiltered seawater from a 5000 m depth in the western north Pacific, while those by the internal standard method were based on 0.04 µm filtered seawater from a 5 m depth in Sagami Bay. Although the sample was analyzed at different times (July and August 1995) by the isotope dilution method, the results agreed with each other. There seems no significant difference in reproducibility between the two methods, since the relative standard deviations were approximately the same at ~5%.

Filtered seawater samples obtained from various depths of the Sagami Trough were measured by the two methods. The results are compared in table 3. The errors indicated are based on the standard deviation of repeated measurements of the same sample aliquots by ICPMS. The slightly higher individual errors in the isotope dilution method than in the internal standard method are ascribable to overspiking which resulted in the measured ¹¹³In/¹¹⁵In ratio of ~14. Nevertheless,

the results show a good agreement between the two methods. This also strongly suggests that the isotope equilibration required for the isotope dilution method is reached within one day.

These methods were applied to open seawater and river-estuarine waters of which implications are described below.

3. Results and discussion

3.1 Western Pacific profile

Figure 1 shows the vertical profile of In in the Izu-Ogasawara Trench which was obtained by the internal standard method together with yttrium, nutrients and hydrographic data. These water samples were not filtered and hence the data represent "acid-soluble" total concentration of In. The In concentration decreased from 0.14 pmol kg⁻¹ at the surface to 0.085 pmol kg⁻¹ at 499 m and then increased to a subsurface maximum of 0.14 pmol kg⁻¹ at 1500 m, where dissolved oxygen becomes minimum. From the subsurface maximum, the In concentration decreased with depth to nearly constant value around 0.05 pmol kg⁻¹ below 3500 m. Two data points within the trench are 0.070 and 0.055 pmol kg⁻¹, and there is no significant difference in the In concentration within and above the trench. The concentration levels of In are similar to those obtained previously in the western north Pacific based on the isotope dilution method (Amakawa *et al* 1996). The distribution pattern is different from those of Y (figure 1) and rare earth elements which show systematic increase with depth like dissolved Si (Zhang *et al* 1994).

3.2 Inter-oceanic comparison

The vertical profile of In in the western north Pacific showing a general decrease with depth suggests that In is categorized as one of the least soluble elements with the scavenged-type oceanic distribution (Nozaki 1997). This is inconsistent with the recent data which indicate that, like Th, about 40% of total indium is in particulate form (Alibo *et al* in preparation). On the other hand, it has recently been found that the north Atlantic waters have an order of magnitude higher concentrations of dissolved indium, ranging from 0.6–1.5 pmol kg⁻¹, than the Pacific waters and show a

Table 3. Comparison of the methods.

Sample	In (pmol kg ⁻¹)	RSD ^a %	In (pmol kg ⁻¹)	RSD ^a %	% Difference
	Isotope Dilution Method		Internal Standard Method		
T97-2 50m	0.123 ± 0.015	11.9	0.125 ± 0.012	9.5	2.1
T97-2 800m	0.113 ± 0.013	11.2	0.105 ± 0.004	3.5	7.4
T97-2 1500m	0.094 ± 0.006	6.5	0.093 ± 0.006	6.0	1.4

^a Relative standard deviation of repeated measurements by ICPMS.

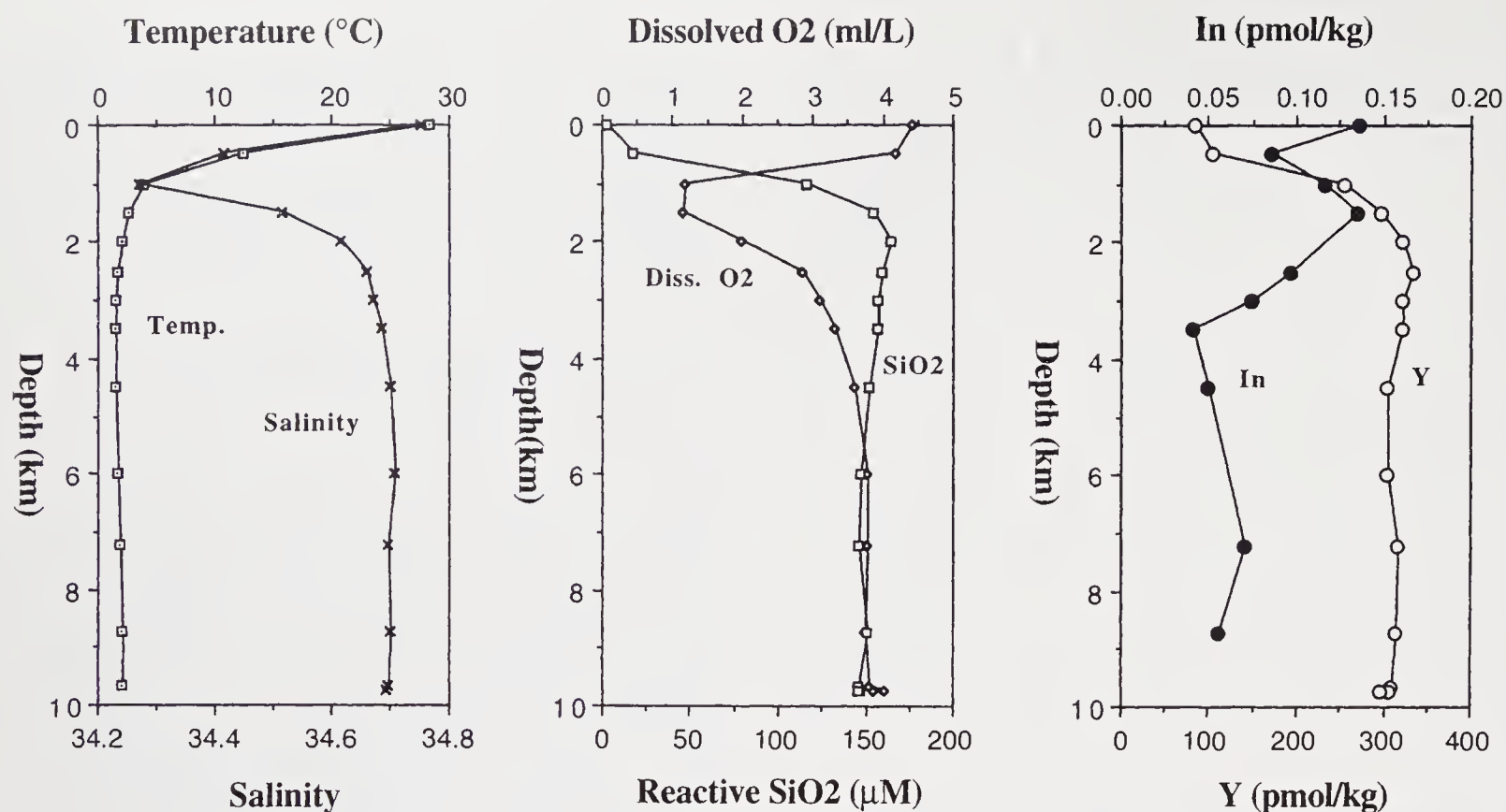


Figure 1. The depth profiles of temperature, salinity, dissolved oxygen, silica, and "acid-soluble" Y and In in the Izu-Ogasawara Trench (29°05'N, 142°51'E; water depth 9738 m) of the western north Pacific.

systematic increase in the In concentration with depth (Alibo 1997). The large inter-oceanic variation of In is similar to that of Al (Orlans and Bruland 1985), although details of their vertical profiles appears to be different. Measures (1995) utilized dissolved Al as an oceanographic tracer of water masses based on its large dynamic range (signal to noise ratio). Such application may be strengthened if scavenging by particles and mixing of water masses which modify the concentration of dissolved Al can be distinguished.

Simultaneous measurements of Al and In may help to resolve the two.

3.3 River and estuarine waters

Table 4 gives the data on the river and estuarine waters from Japan and Thailand measured by the internal standard method. The river waters have higher concentrations of indium than the seawater, but show considerable decrease in its concentration

Table 4. Indium concentrations in river and estuarine waters.

	Sampling date	Salinity	In (pmol kg ⁻¹) ^a
Japanese river			
Tonegawa	Oct. 22nd, 1995	0.1	8.87 ± 0.07
		16.4	1.00 ± 0.02
Tamagawa	Nov. 3rd, 1995	0.2	11.82 ± 0.14
		19.4	1.40 ± 0.01
Arakawa	Nov. 3rd, 1995	2.6	14.98 ± 0.05
		16.0	1.56 ± 0.03
Thai river			
Chao Praya	Jan. 21st, 1996	0.02	0.363 ± 0.006
	Jan. 20th, 1996	15.4	0.034 ± 0.004
Chao Praya	July 2nd, 1996	0.1	0.241 ± 0.005
		25.5	0.081 ± 0.006
Chao Praya	Nov. 14th, 1996	0.6	0.131 ± 0.008
		24.5	0.030 ± 0.001

^a Errors are based on the standard deviation of replicate ICPMS measurements.

during mixing with seawater. It is interesting to note that the Japanese rivers have higher In concentrations by an order of magnitude than the Thai river. In these Japanese rivers, anthropogenic Gd anomalies were found in all the samples presumably due to recent medical use in hospitals (Bau and Dulski 1996), whereas Thai samples did not show any Gd anomaly. Thus, although further study is necessary, it seems likely that In in the Japanese rivers may be derived both from natural and industrial sources.

The Chao Praya data with salinities higher than 15 ppt were obtained in the Gulf of Thailand. These In concentrations (table 4) are comparable with or even lower than those in open seawaters. This suggests that In supplied by rivers is largely removed by scavenging in the estuarine mixing zone and hence fluvial input to the ocean is small. Alternatively, like Al, the eolian input is likely to be a dominant source in the open ocean. Quantification of these sources must wait for future study.

4. Conclusion

We have developed two practical methods for the determination of indium in natural waters. Although the isotope dilution method is, in principle, regarded as one of the most accurate methods for the determination of trace metals in natural waters, improper spiking considerably magnifies the analytical error. This can happen when the In concentrations are extremely low, (e.g. Pacific deep waters) resulting in fewer net counts than ~100 or varies by more than an order of magnitude between samples (e.g. the river waters). There are also uncertainties introduced by isobaric interferences at masses 113 and 115, simultaneously, which can vary depending upon the condition of the experiments. The internal standard method needs quantitative preconcentration of In and Y which requires some skill in the chemical procedure. Nevertheless, once mastered, the correction for isobaric interferences in the internal standard method is simpler than in the isotope dilution method. Thus, if the water sample is not limited for use in the analysis, the internal standard method may be the preferred choice.

Indium concentrations in Pacific seawaters are extremely low presumably due to scavenging by particulate matter. There is a large variation in the In concentration between the north Atlantic and the Pacific, similar to that of Al. Although river waters have higher In concentrations than seawater, it is unlikely that riverine input is a significant source for In in the ocean.

Acknowledgements

We would like to thank Dr. Anond Snidvongs and the students of Chulalongkorn University for their help in

sampling in the Chao Praya river estuary. We also thank the staff and students of the geochemistry group at the Ocean Research Institute, University of Tokyo for collaboration in the river and seawater sampling. This work was supported by the Ministry of Education, Science, Sports and Culture, Japan under Grant-in-Aids to the University of Tokyo (P. I. Y. Nozaki).

References

- Alibo D S 1997 *The marine geochemistry of indium*; Master thesis, University of Tokyo, 72
- Amakawa H, Alibo D S and Nozaki Y 1996 Indium concentration in Pacific seawater; *Geophys. Res. Lett.* **23** 2473–2476
- Baric A and Branica M 1969 Behavior of indium in seawater (A preliminary study); *Limnol. Oceanogr.* **14** 796–798
- Bau M and Dulski P 1996 Anthropogenic origin of positive Gd anomalies in river waters; *Earth Planet. Sci. Lett.* **143** 245–255
- Chow T J and Snyder C B 1969 Indium content of seawater; *Earth Planet. Sci. Lett.* **7** 221–223
- Flegal A R and Patterson C C 1985 Thallium concentration in seawater; *Mar. Chem.* **15** 327–331
- Heumann K G 1988 Chemical analysis; in *Inorganic mass spectrometry* (eds) F Adams, R Gijbels and R Van Grieken (John Wiley and Sons, Inc., New York), pp. 301–376
- Hydes D J 1979 Aluminum in seawater: Control by inorganic processes; *Science* **205** 1260–1262
- Koide M, Stallard M, Hodge V F and Goldberg E D 1986 Preliminary studies on the marine chemistry of ruthenium; *Nether. J. Sea Res.* **20** 163–166
- Li Y-H 1991 Distribution patterns of the elements in the ocean: A synthesis; *Geochim. Cosmochim. Acta* **55** 3223–3240
- Matthews A D and Riley J P 1970 The occurrence of indium in seawater and some marine sediments; *Nature* **225** 1242
- Measures C I 1995 The distribution of Al in the IOC stations of the eastern Atlantic between 30°S and 34°N; *Mar. Chem.* **49** 267–281
- Measures C I, Edmond J M and Jickells T D 1986 Aluminium in the northwest Atlantic; *Geochim. Cosmochim. Acta* **50** 1423–1429
- Murozumi M and Nakamura S 1980 Isotope dilution mass spectrometry of copper, cadmium, thallium and lead in the marine environment; in *Isotope Marine Chemistry* (ed.) E D Goldberg et al Uchida-Rokkakuhou Pub. Tokyo pp. 439–471
- Nozaki Y 1997 A fresh look at element distribution in the north Pacific Ocean; *Eos Trans. AGU* **78** 221
- Orians K J and Boyle E 1993 Determination of picomolar concentrations of Ti, Ga and In in sea water; *Anal. Chim. Acta* **282** 63–74
- Orians K J and Bruland K W 1985 Dissolved aluminium in the Pacific Ocean; *Nature* **316** 427–429
- Orians K J and Bruland K W 1988a Dissolved gallium in the open ocean; *Nature* **332** 717–719
- Orians K J and Bruland K W 1988b The marine geochemistry of dissolved gallium: A comparison with the dissolved aluminium; *Geochim. Cosmochim. Acta* **52** 2955–2962
- Roskill Information Services Ltd 1996 The economics of indium, 6th edition
- Shaw D M 1952 The geochemistry of indium; *Geochim. Cosmochim. Acta* **2** 185–206
- Shabani M B, Akagi T, Shimizu H and Masuda A 1990 Determination of trace lanthanides and yttrium in seawater by inductively coupled plasma mass spectrometry after

- preconcentration with solvent extraction and back extraction; *Anal. Chem.* **62** 2709–2714
- Taylor S R 1964 Abundance of chemical elements in the continental crust: a new table; *Geochim. Cosmochim. Acta* **28** 1273–1285
- Zhang J 1995 The geochemistry of yttrium and lanthanides in sea water; Ph.D thesis, University of Tokyo, 160pp
- Zhang J, Amakawa H and Nozaki Y 1994 The comparative behavior of yttrium and lanthanides in the sea water of the north Pacific; *Geophys. Res. Lett.* **21** 2677–2680

Nitrogen isotopic studies in the suboxic Arabian Sea

S W A NAQVI¹, T YOSHINARI², J A BRANDES^{3,4}, A H DEVOL³, D A JAYAKUMAR¹,
P V NARVEKAR¹, M A ALTABET⁵ and L A CODISPOTI⁶

¹ *National Institute of Oceanography, Dona Paula, Goa 403 004, India*

² *Wadsworth Center, New York State Department of Health, and School of Public Health, State University of New York at Albany, P.O. Box 509, Albany, NY 12201, USA*

³ *School of Oceanography, University of Washington, Seattle, WA 98195, USA*

⁴ *Present Address: Geophysical Laboratory, Carnegie Institution of Washington, Washington, DC 20015, USA*

⁵ *Department of Chemistry and Biochemistry and Center for Marine Science and Technology, University of Massachusetts, Dartmouth, North Dartmouth, MA 02747, USA*

⁶ *Center for Coastal Physical Oceanography, Old Dominion University, Norfolk, VA 23529, USA*
e-mail: naqvi@csnio.ren.nic.in

Measurements of $^{15}\text{N}/^{14}\text{N}$ in dissolved molecular nitrogen (N_2), nitrate (NO_3^-) and nitrous oxide (N_2O) and $^{18}\text{O}/^{16}\text{O}$ in N_2O [expressed as $\delta^{15}\text{N}$ and $\delta^{18}\text{O}$, relative to atmospheric N_2 and oxygen (O_2), respectively] have been made in water column at several locations in the Arabian Sea, a region with one of the thickest and most intense O_2 minima observed in the open ocean. Microbially-mediated reduction of NO_3^- to N_2 (denitrification) in the oxygen minimum zone (OMZ) appears to greatly affect the natural isotopic abundances. The $\delta^{15}\text{N}$ of NO_3^- increases from 6‰ in deep waters (2500 m) to 15‰ within the core of the denitrifying layer (250–350 m); the $\delta^{15}\text{N}$ of N_2 concurrently decreases from 0.6‰ to 0.20‰. Values of the isotopic fractionation factor (ε) during denitrification estimated using simple advection-reaction and diffusion-reaction models are 22‰ and 25‰, respectively. A strong decrease in $\delta^{15}\text{N}$ of NO_3^- is observed from ~ 200 m (> 11 ‰) to 80 m (~ 6 ‰); this is attributed to the input of isotopically light nitrogen through nitrogen fixation. Isotopic analysis of N_2O reveals extremely large enrichments of both ^{15}N and ^{18}O within the OMZ, presumably due to the preferential reduction of lighter N_2O to N_2 . However, isotopically light N_2O is observed to accumulate in high concentrations above the OMZ indicating that the N_2O emitted to the atmosphere from this region cannot be very heavy. The isotope data from the intense upwelling zone off the southwest coast of India, where some of the highest concentrations of N_2O ever found at the sea surface are observed, show moderate depletion of ^{15}N , but slight enrichment of ^{18}O relative to air. These results suggest that the ocean-atmosphere exchange cannot counter inputs of heavier isotopes (particularly ^{18}O) associated with the stratospheric back flux, as proposed by previous workers. This calls for additional sources and/or sinks of N_2O in the atmosphere. Also, the N_2O isotope data cannot be explained by production through either nitrification or denitrification, suggesting a possible coupling between the two processes as an important mechanism of N_2O production.

1. Introduction

In spite of the great abundance of nitrogen in the earth's surface environment, photosynthetic production in the oceans is generally nitrogen limited

(Codispoti 1989). This is because molecular nitrogen (N_2), the dominant gaseous constituent of the atmosphere, has low chemical reactivity, and as such only a few organisms of the sea have the capability to utilize or "fix" it (Galloway *et al* 1995). Most organisms can

Keywords. Stable isotopes; nitrogen; oxygen; denitrification; Arabian Sea.

only make use of nitrogen in the combined forms, such as nitrate (NO_3^-) and ammonium (NH_4^+), which occur in much lower concentrations than N_2 , but can be assimilated with greater ease. Nitrogen in these forms occurs in a number of oxidation states ranging from -3 to $+5$. The speciation is strongly dependent on the redox potential of seawater determined mainly by the ambient oxygen (O_2) levels. The bulk of the oceanic water column is well-oxygenated, making NO_3^- the predominant species of combined nitrogen in the sea.

The inventory of combined nitrogen in the oceans is regulated by several processes. Inputs of nitrogen to the oceans occur mainly through river runoff, atmospheric deposition and nitrogen fixation, while its loss is principally through conversion of combined nitrogen into N_2 (Codispoti and Christensen 1985). This process, known as denitrification, takes place when the O_2 concentrations are close to zero and bacteria utilise NO_3^- instead of O_2 as an oxidant for decomposing organic matter (Richards 1965). Conditions conducive for denitrification commonly develop within the coastal sediments. In the water column, however, the oceanic currents supply enough O_2 at all depths to prevent the development of anoxia in most oceanic areas. However, there are three regions where some unusual oceanographic processes cause the O_2 demand to exceed its supply leading to an almost complete O_2 depletion (suboxia) at mid-depths (Deuser 1975). Two of these sites are located in the eastern tropical north and south Pacific, while the third is found in the Arabian Sea. Although these regions account for only $\sim 2\%$ of the total oceanic area, they are extremely important from the biogeochemical and climatic points of view. This is because the high and temporally variable rate of denitrification in these regions has the potential to greatly alter the oceanic combined nitrogen inventory. This in turn may cause variations in the rate of photosynthetic carbon fixation and thereby in the rate at which carbon dioxide (CO_2) is sequestered from the atmosphere. Thus the oceanic O_2 -deficient zones probably contribute very significantly to global climatic changes (McElroy 1983; Codispoti et al 1996a). Another important way in which these environments affect the atmospheric composition is through production of trace gases, particularly nitrous oxide (N_2O). The importance of N_2O owes to its capacity to strongly absorb the back radiation emitted by the earth in the infrared range and to the role it plays in the chemistry of stratospheric ozone depletion. Recent studies show that the oceans may account for about half of the total inputs of N_2O to the atmosphere from all natural sources, and that a large fraction of the oceanic efflux comes from the O_2 -deficient zones particularly the Arabian Sea (Codispoti and Christensen 1985; Law and Owens 1990; Naqvi and Noronha 1991; Bange et al 1996).

A considerable amount of work on nitrogen cycling in suboxic waters of the Arabian Sea, carried out over the past two decades, has established it to be globally significant (Naqvi 1994). However, these studies largely involved chemical and, to a lesser extent, biochemical measurements. Investigations on the natural abundance of stable isotopes in various dissolved nitrogen species have been initiated only recently (Yoshinari et al 1997; Naqvi et al 1998; Brandes et al 1998). This approach is based on the fact that the biogeochemical processes involve characteristic mass-dependent discriminations between various isotopes, and so the isotopic data can provide useful insights into the pathways of nitrogen transformations (Wada and Hattori 1991). A brief account of the progress made in this area is given here.

2. Material and methods

Isotopic measurements on three dissolved nitrogen species (N_2 , NO_3^- and N_2O) were made during four cruises of FORV *Sagar Sampada* (SS106, November 1992; SS119, April 1994; SS128, January 1995; and SS141, May 1996) and two cruises of ORV *Sagar Kanya* (SK87, September 1993; and SK103, June-July 1995) at the stations shown in figure 1. However, concurrent measurements on all these species were made only at one station (3204/SS119). While the

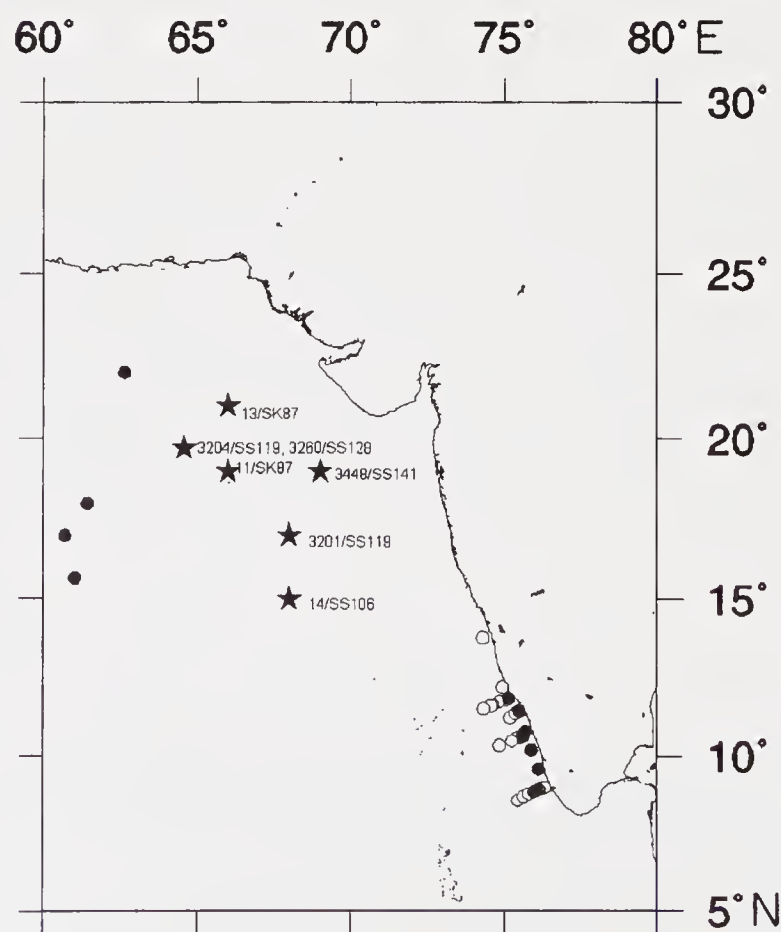


Figure 1. Station locations (open circles: surface N_2O concentration only; filled circles: surface N_2O concentration and isotopes; stars: vertical profiles).

$^{15}\text{N}/^{14}\text{N}$ ratio was measured in N_2 and NO_3^- , both $^{15}\text{N}/^{14}\text{N}$ and $^{18}\text{O}/^{16}\text{O}$ were determined in N_2O . In addition, routine hydrographic (temperature and salinity) and hydrochemical (dissolved O_2 and nutrients) data were collected during all the cruises.

Water samples for $^{15}\text{N}/^{14}\text{N}$ analysis in N_2 and/or NO_3^- were taken during SK87, SS119, SS128 and SS141 from 1.8-litre Niskin samplers mounted on the CTD (conductivity-temperature-depth) rosette. Utmost care was taken to avoid atmospheric contamination while sampling for N_2 . Sub-samples (200–250 ml) were drawn immediately after recovery into evacuated, HgCl_2 -poisoned 500-ml glass bottles. The N_2 extraction and analysis was done at the University of Washington using a Finnigan MAT 251 mass spectrometer (Brandes *et al* 1998). Reproducibility was within $\pm 0.05\%$. Subsamples (1 litre) for NO_3^- were stored after poisoning with 1 ml saturated HgCl_2 for analysis at the University of Washington following the method described by Brandes and Devol (1997). Briefly, it involved reduction of NO_3^- to NH_4^+ using Devardas alloy. The NH_4^+ was distilled and sorbed into an ion sieve. The sorbed material was then filtered onto quartz QM-A filters and sealed into evacuated quartz combustion tubes containing Cu and CuO. Ampoule contents were converted into N_2 with a micro-Dumas combustion method, extracted into liquid N_2 -cooled cold fingers containing molecular sieve and analysed for $^{15}\text{N}/^{14}\text{N}$ using a Finnigan MAT 251 mass spectrometer. The results, reproducible to $\pm 0.2\%$, were corrected for an isotopic shift of -0.9% to account for the reagent blank.

Samples for the N_2O isotope analysis were collected using specially modified 20-litre Go-flo samplers mounted on a hydrowire (during SS106 and SK87) or a CTD rosette sampler (during SS119 and SK103). The modified samplers enabled extraction of N_2O , without transferring the water to another vessel, with high-purity argon that was recirculated after removal of moisture and CO_2 and adsorption of N_2O on a molecular sieve (MS 5A) packed in stainless steel columns. Extraction was carried out for 90 minutes at an Ar flow rate of $\sim 1.5 \text{ l min}^{-1}$ (Yoshinari *et al* manuscript in preparation). After thermal desorption in the shore laboratory, N_2O was purified by gas chromatography and its isotopic composition ($^{15}\text{N}/^{14}\text{N}$ and $^{18}\text{O}/^{16}\text{O}$) measured at Woods Hole Oceanographic Institution by continuous-flow isotope-ratio monitoring using a Finnigan MAT 251 mass spectrometer (Yoshinari *et al* 1997). Reproducibility was better than $\pm 0.3\%$ for both isotopes.

Dissolved O_2 measurements were made with the Winkler titration technique during all cruises while nutrients were analysed using a Technicon Autoanalyser II on board *Sagar Sampada* and a Skalar 6-channel Analyser 5100/1 on board *Sagar Kanya* following standard methods (Grasshoff *et al* 1983). N_2O concentration was determined on board ships by head-

space extraction with helium followed by injection into a Perkin-Elmer 3920B gas chromatograph equipped with an electron capture detector (precision $\sim 4\%$).

3. Results and discussion

3.1 Nitrogen isotopic fractionation during denitrification

The reduction of NO_3^- to N_2 by denitrifying bacteria is believed to occur through the pathway (Payne 1973):



Nitrite (NO_2^-), the first intermediate of this reduction sequence, accumulates in the oceanic suboxic zones (Richards 1965). In the Arabian Sea, as in the eastern tropical Pacific Ocean (Cline and Richards 1972), the secondary nitrite maximum (SNM), located in the upper portion of the oxygen minimum zone (OMZ), is invariably associated with $\text{O}_2 < 0.1 \text{ ml l}^{-1}$, in contrast to the primary NO_2^- maximum commonly found at the base of the euphotic zone. Precise O_2 measurements carried out during a U.S. JGOFS cruise in the Arabian Sea revealed that the threshold O_2 levels required for the NO_2^- build-up lie between 0.01 and 0.02 ml l^{-1} (S W A Naqvi and L A Codispoti, unpublished data). Dramatic changes in water chemistry are seen once this threshold is crossed. An apparent spurt in denitrification activity causes a minimum in the vertical profile of NO_3^- (figure 2). Interestingly, while NO_2^- accumulates under these conditions, N_2O , the other major intermediate, shows an opposite trend (e.g., figures 2 and 3), indicating that the reduction of NO_2^- may be the rate limiting step. These microbially-mediated transformations leave a strong imprint on the isotopic composition of dissolved nitrogen species. This is because, of the two nitrogen isotopes with mass numbers of 14 and 15 (^{14}N and ^{15}N), NO_3^- ions containing the more abundant ^{14}N are preferentially

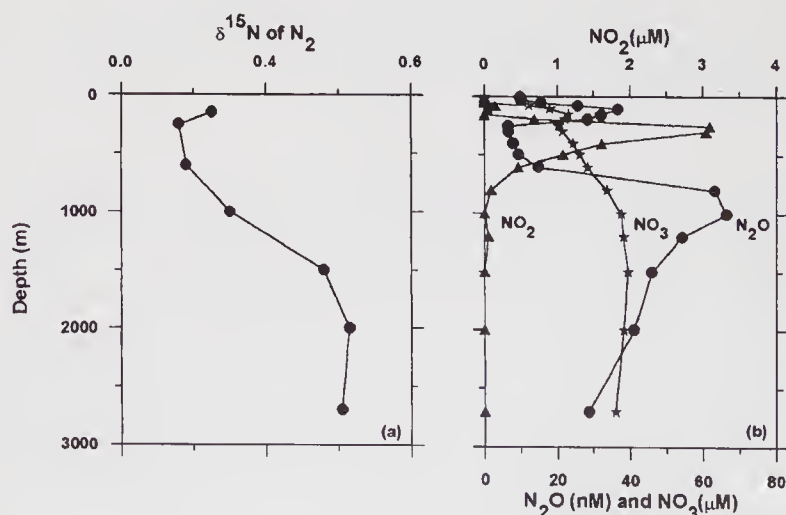


Figure 2. Vertical profiles of (a) $\delta^{15}\text{N}$ of N_2 (‰ relative to air) and (b) concentrations of NO_3^- (μM), NO_2^- (μM) and N_2O (nM) at Sta. 3448/SS141.

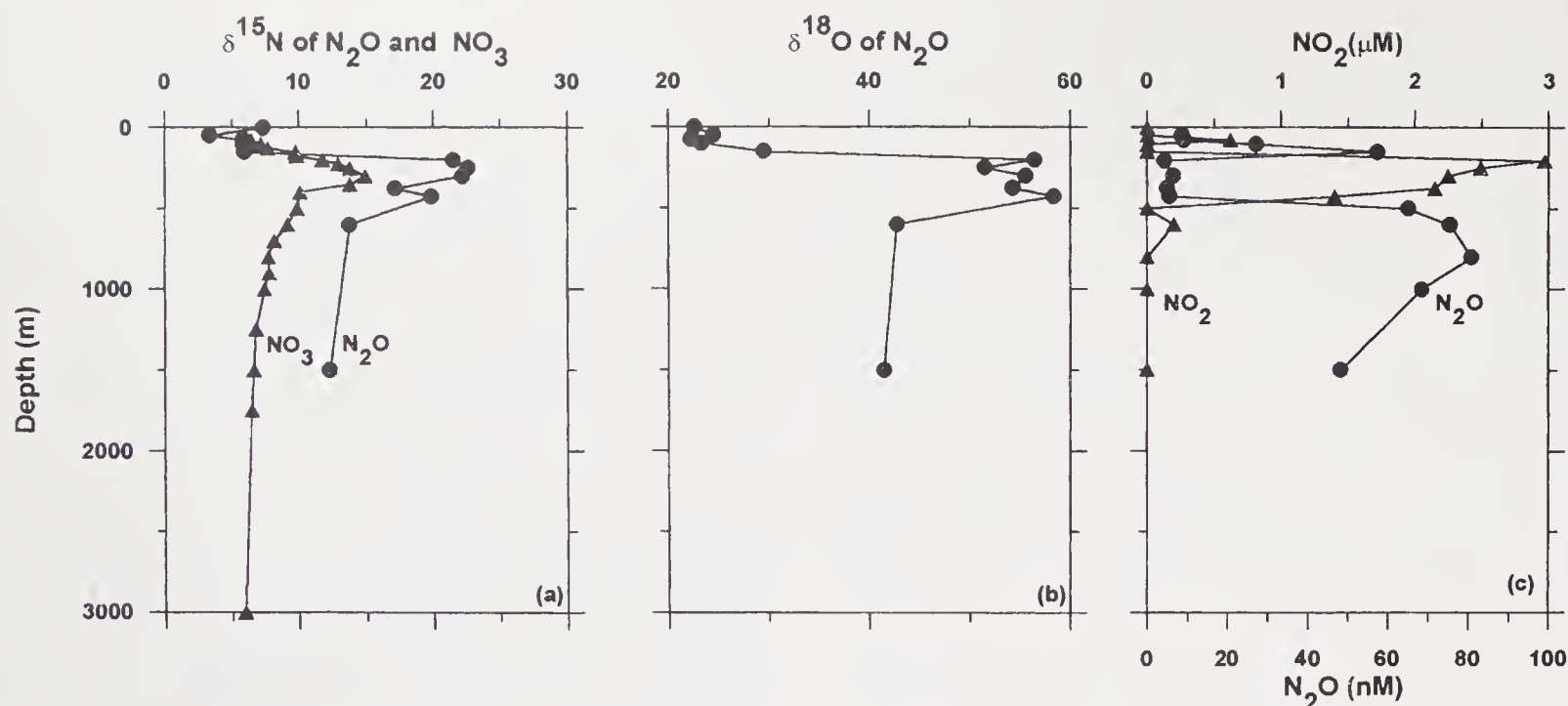


Figure 3. Vertical profiles of (a) $\delta^{15}\text{N}$ of NO_3^- and N_2O (‰ relative to air), (b) $\delta^{18}\text{O}$ of N_2O (‰ relative to air) and (c) concentrations of NO_2^- (μM , triangles) and N_2O (nM, circles) at Sta. 3201/SS119 (modified from Naqvi *et al* 1998).

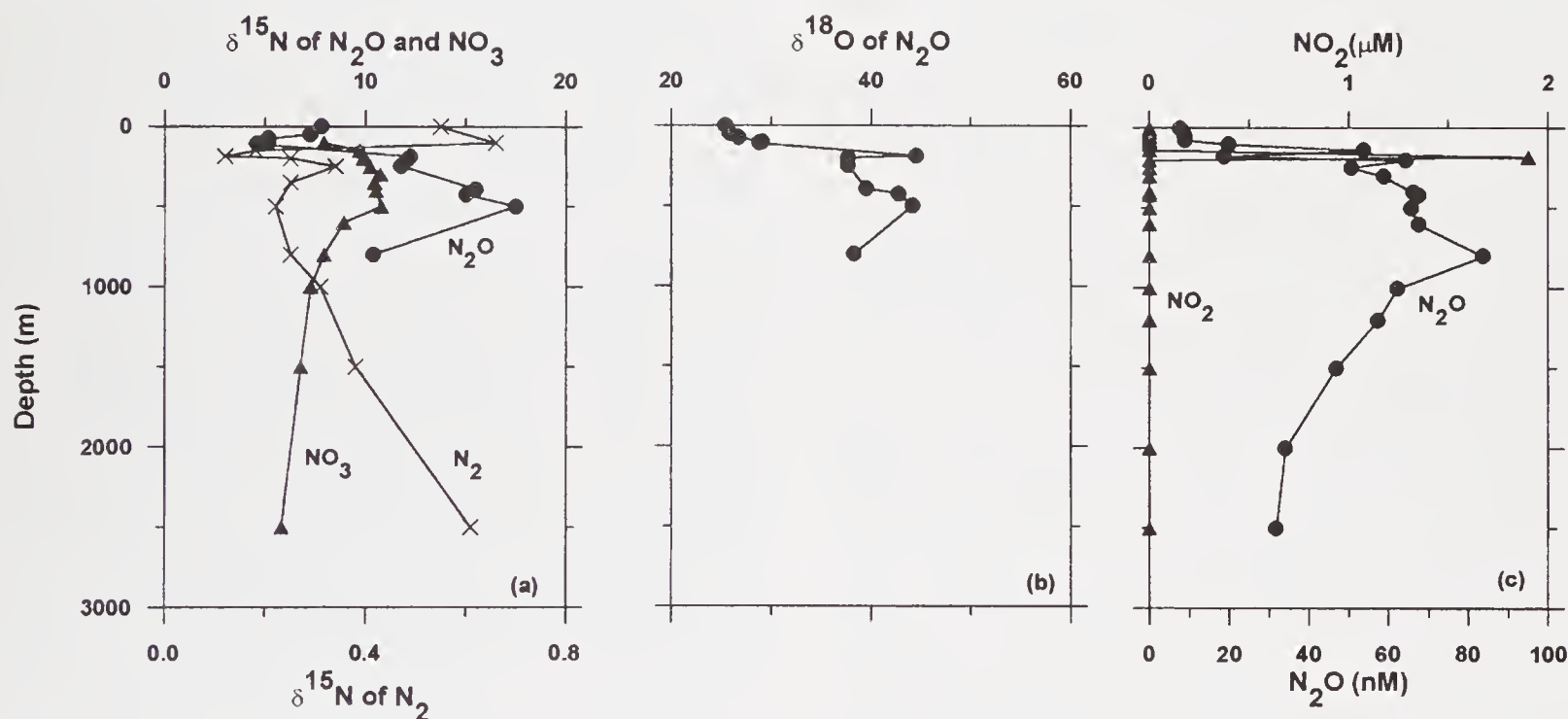


Figure 4. Vertical profiles of (a) $\delta^{15}\text{N}$ of N_2 , NO_3^- and N_2O , (b) $\delta^{18}\text{O}$ of N_2O and (c) concentrations of NO_2^- (μM , triangles) and N_2O (nM, circles) at Sta. 3204/SS119 (the $\delta^{15}\text{N}$ - NO_3^- profile at this site was obtained during SS128) (modified from Brandes *et al* 1998; Naqvi *et al* 1998).

reduced during denitrification, leaving the residual NO_3^- enriched with ^{15}N . On the other hand N_2 , the end product of denitrification, gets greatly enriched with ^{14}N . This is strikingly demonstrated by our results. The vertical profile of $\delta^{15}\text{N}$ of N_2 at the strongly nitrate reducing Sta. 3448/SS141, located in the northeastern Arabian Sea, exhibits a pronounced minimum coinciding with the SNM with values dipping below 0.2‰ (figure 2) (the $\delta^{15}\text{N}$ of N_2 in surface waters in this region, not determined at this station, is generally greater than 0.5‰). Interestingly at 150 m depth, where the NO_3^- concentration was

high ($23\mu\text{M}$) and NO_2^- was not detectable, the $\delta^{15}\text{N}$ was still quite low (0.25‰) i.e., only marginally higher than the minimal value but less than half of the values observed in waters outside the O_2 -deficient zone. Even at 1000 m depth the $\delta^{15}\text{N}$ was only 0.3‰. This indicates that the denitrification signature extends well outside the SNM. A similar pattern is also seen at Sta. 3204/SS119 (figure 4). This station had a thin, weakly-developed SNM associated with a minimum in $\delta^{15}\text{N}$ of N_2 (0.18‰) at 150-190 m. This was underlain by a layer with relatively high $\delta^{15}\text{N}$ of N_2 (maximum 0.39‰) which, going by its high salinity,

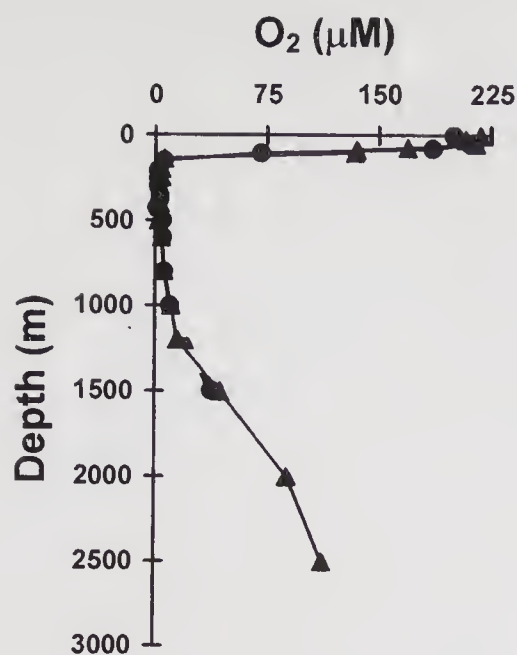


Figure 5. A comparison of vertical profiles of O_2 (μM) at Stas. 3201/SS119 (circles joined by dotted lines) and 3204/SS119 (triangles, joined by continuous lines) (modified from Naqvi *et al* 1998).

evidently originated in the Persian Gulf. The O_2 concentrations, as determined by the Winkler method, were not appreciably different from those at Sta. 3201/SS119 (figure 5). The association of a maximum in $\delta^{15}N$ of N_2 with the Persian Gulf salinity maximum layer shows that the former is a sensitive tracer of advection. Again the vertical extent of the $\delta^{15}N$ - N_2 minimum is much larger than the SNM. This would mean that substantial N_2 may be produced without the accumulation of NO_2^- or/and the rapid mixing results in the export of lighter N_2 out of the SNM.

The distribution of $\delta^{15}N$ of NO_3^- shows a good correspondence to that of secondary NO_2^- (figures 3, 4 and 6). Sharp increases in $\delta^{15}N$ of NO_3^- (up to 15‰) were observed within the SNM at Stas. 3201/SS119 (figure 3) and 13/SK87 (figure 6) with both maxima being thicker at the latter site. In contrast, at Sta. 3204/SS119 where the SNM was weakly developed, the extent of ^{15}N enrichment in NO_3^- was considerably smaller (figure 4). At all the three stations, significant ^{15}N enrichment in NO_3^- [relative to the average value of 5.7‰ for the oceanic subsurface waters (Altabet *et al* 1995)] persisted down to at least 1,500 m, consistent with the observed trends in $\delta^{15}N$ of N_2 .

These data on $\delta^{15}N$ of N_2 and NO_3^- can be used to compute the fractionation factor, $\epsilon_{denit} [= 10^3(1 - \alpha)]$, where α is the ratio between the rates of utilisation of $^{15}NO_3^-$ and $^{14}NO_3^-$, during denitrification using simple advection-reaction and diffusion-reaction models (Brandes *et al* 1998). In the first case, we ignore diffusion and the water mass is assumed to advect into the OMZ without undergoing any mixing in the vertical and horizontal directions. The isotopic distribution can then be modelled with a simple Rayleigh equation (Bender 1990):

$$\delta^{15}N-NO_3 = 10^3(\alpha - 1) \ln f_{NO_3} + (\delta^{15}N-NO_3)_{init} \quad (1)$$

where f_{NO_3} is the ratio between the observed and expected NO_3^- concentrations and $(\delta^{15}N-NO_3)_{init}$ gives the isotopic composition of the initial (unaltered) material. Values of f_{NO_3} were computed using the relationships between a nitrate tracer (NO) and potential temperature and the observed NO_3^- and NO_2^- concentrations (Naqvi *et al* 1990).

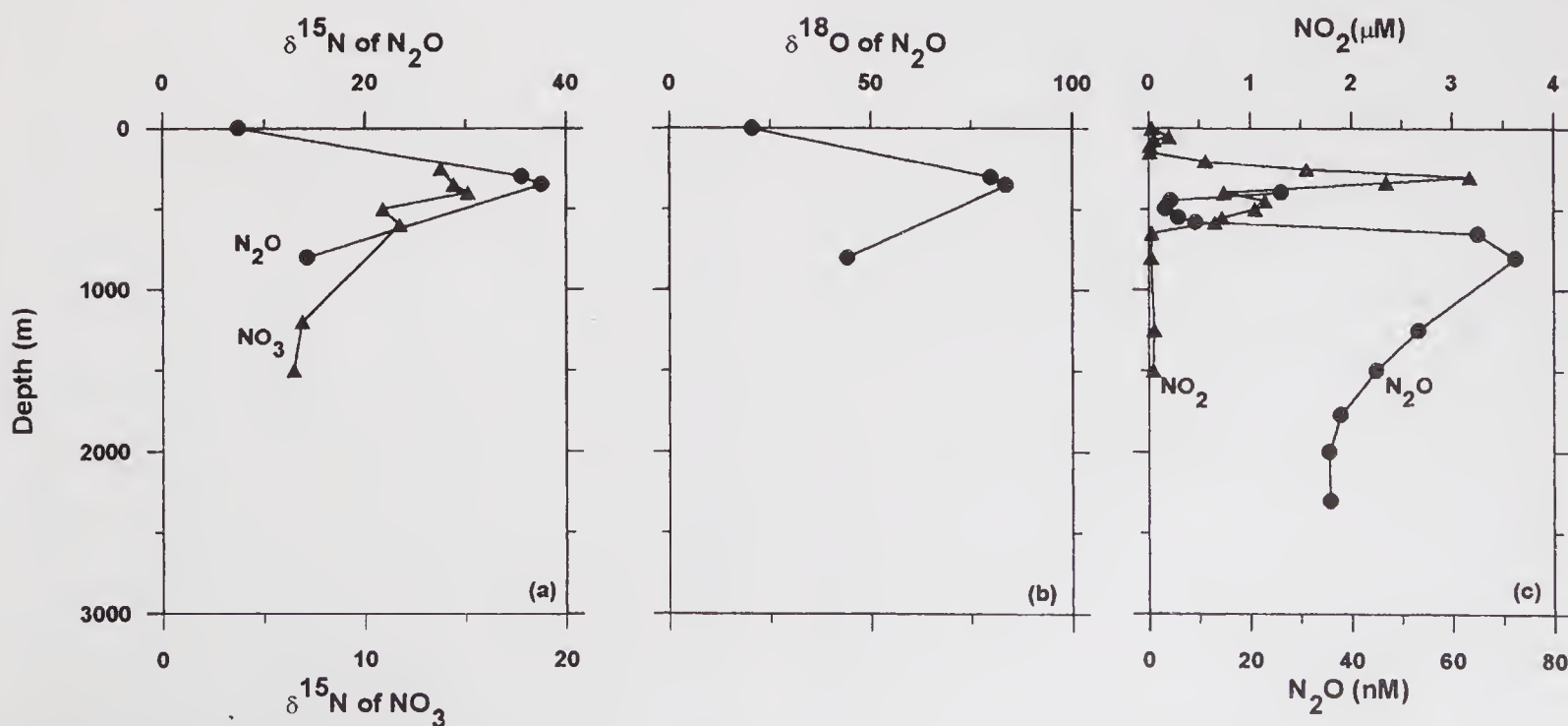


Figure 6. Vertical profiles of (a) $\delta^{15}N$ of NO_3^- and N_2O , (b) $\delta^{18}O$ of N_2O and (c) concentrations of NO_2^- (μM , triangles) and N_2O (nM, circles) at Sta. 13/SK87 (modified from Brandes *et al* 1998; Yoshinari *et al* 1997).

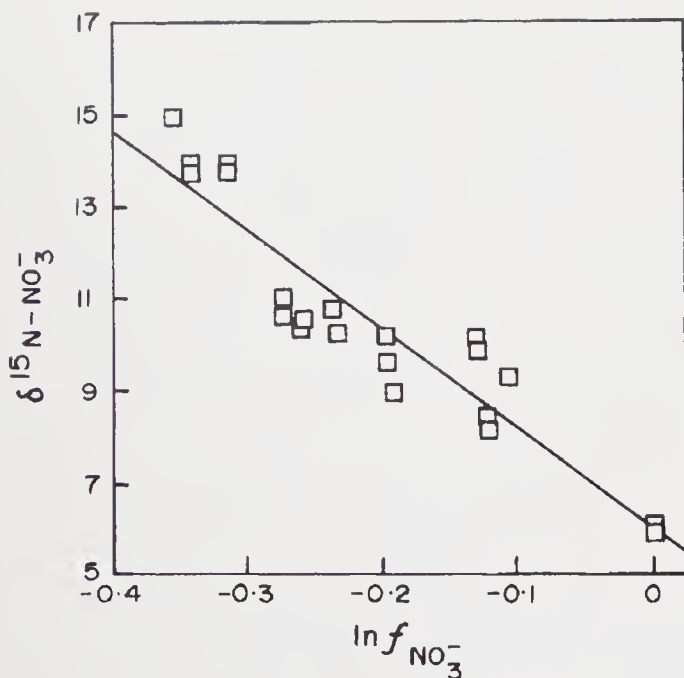


Figure 7. The $\delta^{15}\text{N}$ of NO_3^- (‰ relative to air) vs. the natural log of f , the ratio of measured to expected nitrate concentrations (pooled data from three stations). The line gives the least squares fit to the data (modified from Brandes *et al* 1998).

A plot of $\delta^{15}\text{N}$ - NO_3 versus $\ln f_{\text{NO}_3}$ for the depth range 200–600 m (figure 7) shows a good linear relationship between the two ($r^2 = 0.9$). The slope of the regression line yields a value of 22‰ for $\varepsilon_{\text{denit}}$, not too different from a similarly computed value (25‰) for the eastern tropical north Pacific (ETNP) (Brandes *et al* 1998).

The opposite extreme to the advection-reaction model is the reaction-diffusion model having no advective component. Such a model is expected to yield a larger fractionation factor than the advective model because the system being “open” allows the addition of new, unaltered material into the reaction region and the removal of old, altered material.

The reaction-diffusion equation is:

$$\partial[^{14}\text{NO}_3]/\partial t = J_{14\text{NO}_3} + K_d \partial^2[^{14}\text{NO}_3]/\partial x^2 \quad (2)$$

where J is the denitrification rate and K_d the horizontal eddy diffusivity along the 300 m isopycnal which was chosen because it lies close to the core of the denitrifying layer (Naqvi 1987); x increases from the edge to the centre of the denitrifying zone. For $^{15}\text{NO}_3^-$ the equation is:

$$\partial[^{15}\text{NO}_3]/\partial t = \alpha([^{15}\text{NO}_3]/[^{14}\text{NO}_3])J_{14\text{NO}_3} + K_d \partial^2[^{15}\text{NO}_3]/\partial x^2. \quad (3)$$

Because there is no exact analytical solution for these equations, the values of both ^{14}N and ^{15}N were calculated numerically using a tridiagonal matrix solution method (Press *et al* 1992). The boundary conditions were that the NO_3^- and $\delta^{15}\text{N}$ - NO_3 compositions at $x = 0$ were 28 μM (NO_3^- deficit = 0) and 6‰, respectively, and that there was no NO_3^- or isotopic flux out of the centre of the OMZ. Alternative

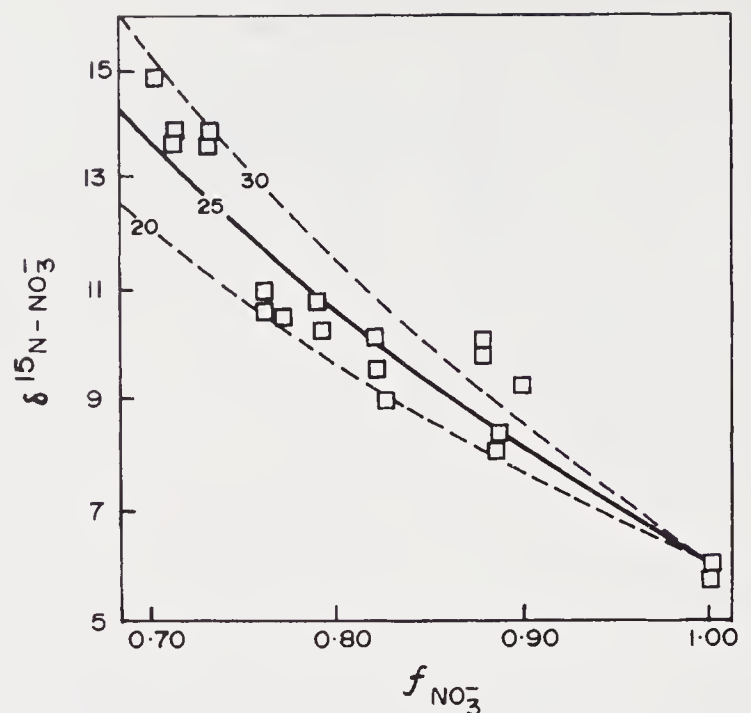


Figure 8. The $\delta^{15}\text{N}$ of NO_3 (‰ relative to air) vs. f , the ratio of measured to expected nitrate concentrations. Also plotted are the diffusion-reaction model results with the numbers denoting fractionation factors (modified from Brandes *et al* 1998).

boundary conditions, such as an interior concentration boundary condition, would change ε by no more than 2 (Brandes *et al* 1998).

The value of J was set at $1 \times 10^{-7} \mu\text{moles N l}^{-1} \text{sec}^{-1}$. Although this value is only 1/2 of the rate estimated by Naqvi and Shailaja (1993) from the ETS data, it gives realistic nitrate deficit given a x_E of 500 km, which is the minimum distance between the southern boundary of the suboxic zone at 12°N and the southernmost station located at 17°N . The value of K_d was taken as $1800 \text{ m}^2 \text{sec}^{-1}$ (Jenkins 1990). Using these parameters, NO_3^- concentrations dropped to $\sim 70\%$ of the initial values in the interior of the denitrification zone, in agreement with the observations (Naqvi 1987). With these values of J and K_d the best-fit to the data was obtained with a fractionation factor of 25‰ (figure 8), only slightly lower than a similarly calculated value of 30‰ for the ETNP (Brandes *et al* 1998). These values of ε are higher than those (15–20‰) derived from laboratory experiments of denitrification (Delwiche and Steyn 1970; Mariotti *et al* 1981), but lower than the estimate (30–60‰) of Cline and Kaplan (1975) derived from one-dimensional model fits to their ETNP data. However, the same data when fitted to the advection-reaction model described above yielded a value of ε (25‰) which compares very well with our results.

Although, the above models ignore either diffusion or advection, and a more realistic approach should simultaneously consider both of these, the results of the two models are not too divergent. More significantly, as the estimates from the Arabian Sea and ETNP are not very different, it would appear that the

fractionation factor is not strongly dependent on either the denitrification rate or the local hydrography of the region.

3.2 Nitrogen fixation

A very important aspect of the data is the strong decrease in $\delta^{15}\text{N}$ - NO_3 in near-surface waters (figures 3 and 4). At 200 m, for example, the value is $> 10\text{‰}$ but it declines to $\sim 6\text{‰}$ (close to the oceanic background) at 80 m. This trend is exactly opposite to that seen outside the OMZ (Sigman *et al* 1997). The observed decrease can only result from an input of light nitrogen to the surface waters. The two possible sources are unaltered NO_3^- horizontally advected from outside the central Arabian Sea, and nitrogen fixation. The known pattern of water circulation in the Arabian Sea (Naqvi 1987; Olson *et al* 1993) makes the first mechanism less likely, and so the most plausible mode of input of isotopically light NO_3^- to the surface layer appears to be nitrogen fixation.

If NO_3^- from 200 m at 11‰ is being upwelled to the surface, and all nitrogen is removed by primary producers at 70–80 m, one can estimate the amount of nitrogen reaching the surface ocean that originally came from nitrogen fixation (Brandes *et al* 1998). Assuming that the changes in isotopic composition below 80 m are due to dilution by remineralised nitrogen fixed at 0‰ , about 40% of the NO_3^- present at 80 m should have been derived from nitrogen fixation. Using the data on primary productivity in this region this translates into a nitrogen fixation rate of up to 6 Tg N y^{-1} ($1 \text{ Tg} = 10^{12} \text{ g}$) or about 25% of the denitrification rate. Thus, in spite of a high rate of nitrogen fixation, the Arabian Sea still serves as a net sink of combined nitrogen. This is consistent with the data on N:P ratios in this region (Codispoti 1997).

3.3 Dual isotopic composition of nitrous oxide

As stated earlier, the eastern boundary upwelling environments that contain O_2 -depleted waters are important for global N_2O cycling. This is because of the extreme sensitivity of the processes involved in N_2O production and consumption to minor changes in ambient O_2 levels in the low range ($< \sim 0.5 \text{ ml l}^{-1}$; Codispoti and Christensen 1985). An intense N_2O accumulation is found to occur as the O_2 concentrations approach, but do not reach, suboxia. However, under strongly nitrate reducing conditions, such as those found within the SNM, N_2O concentrations fall rapidly below saturation, evidently as a result of its reduction to N_2 (e.g., figures 2 and 3). Thus, the Arabian Sea contains sites, located in close proximity of each other, which act either as strong source or strong sink of N_2O (Naqvi and Noronha 1991). Why does a strong net accumulation of N_2O occur in the low- O_2 zones is an issue that has not been fully

resolved so far. This is because N_2O is an intermediate of both the oxidative and reductive sequences of the nitrogen cycle and can be produced both during nitrification and denitrification. The two pathways leave very different isotopic signatures: N_2O produced during denitrification is enriched with ^{15}N and ^{18}O while that formed during nitrification is depleted in these isotopes (e.g., Yoshida 1988; Wada and Hattori 1991; Yoshinari *et al* 1997). Hence measurements of the $^{15}\text{N}/^{14}\text{N}$ and $^{18}\text{O}/^{16}\text{O}$ ratios in N_2O dissolved in seawater are expected to provide insights into the mechanisms of its transformations. However, while substantial data have now been generated on the dual isotopic composition of N_2O in seawater, their interpretation has not been straightforward, and indeed often contradictory (Yoshida *et al* 1989; Kim and Craig 1990). The Arabian Sea contains several diverse biogeochemical environments and offers the most extreme conditions for N_2O cycling (Burkill *et al* 1993). The isotopic composition of N_2O in this region may therefore be helpful in improving the understanding of its transformations.

Data on the isotopic composition of N_2O at five stations (3201/SS119, 3204/SS119, 13/SK87, 11/SK87 and 14/SS106) are shown in figures 3, 4, 6, 9 and 10, respectively. The most prominent feature of the isotope profiles is the large enrichment of both ^{15}N and ^{18}O at all the stations, although the degree of enrichment varies considerably. As stated earlier, Stas. 14/SS106 and 3204/SS119 experienced mildly reducing conditions (thin SNM) while the other three stations were strongly nitrate reducing. These differences in redox conditions are reflected in the isotope data. The greatest enrichment is seen at Sta. 13/SK87; peak $\delta^{15}\text{N}$ and $\delta^{18}\text{O}$ values at this site (37.5 and 83.6‰ , respectively) are the highest reported yet from a natural environment (Yoshinari *et al* 1997). In contrast, the most southern Sta. 14/SS106 exhibited the least enrichment*. Preferential loss of lighter N_2O to N_2 within the SNM evidently leads to the observed enrichments of ^{15}N and ^{18}O in residual N_2O . The N_2O concentration minimum is embedded between two maxima, but the isotopic compositions of these N_2O -rich layers are very different. Going upward from the OMZ, the $\delta^{15}\text{N}$ and $\delta^{18}\text{O}$ values fall sharply across the oxic-suboxic boundary with the former generally lower than the tropospheric value (7‰ – Kim and Craig 1990) in the upper 150 metres. In contrast, although $\delta^{15}\text{N}$ and $\delta^{18}\text{O}$ also decrease below SNM, their levels remain much higher than the tropospheric values (20.7‰ for $\delta^{18}\text{O}$ – Kim and Craig 1990) in the

* Samples from Sta. 14/SS106 were analysed following an older method [combustion of N_2O to N_2 and CO_2 (Yoshinari and Koike 1994)]. It is possible that the oxygen isotope data at this station suffer from some contamination in CO_2 with traces of water leading to somewhat lower $\delta^{18}\text{O}$ values; this would, however, not affect the nitrogen isotope data.

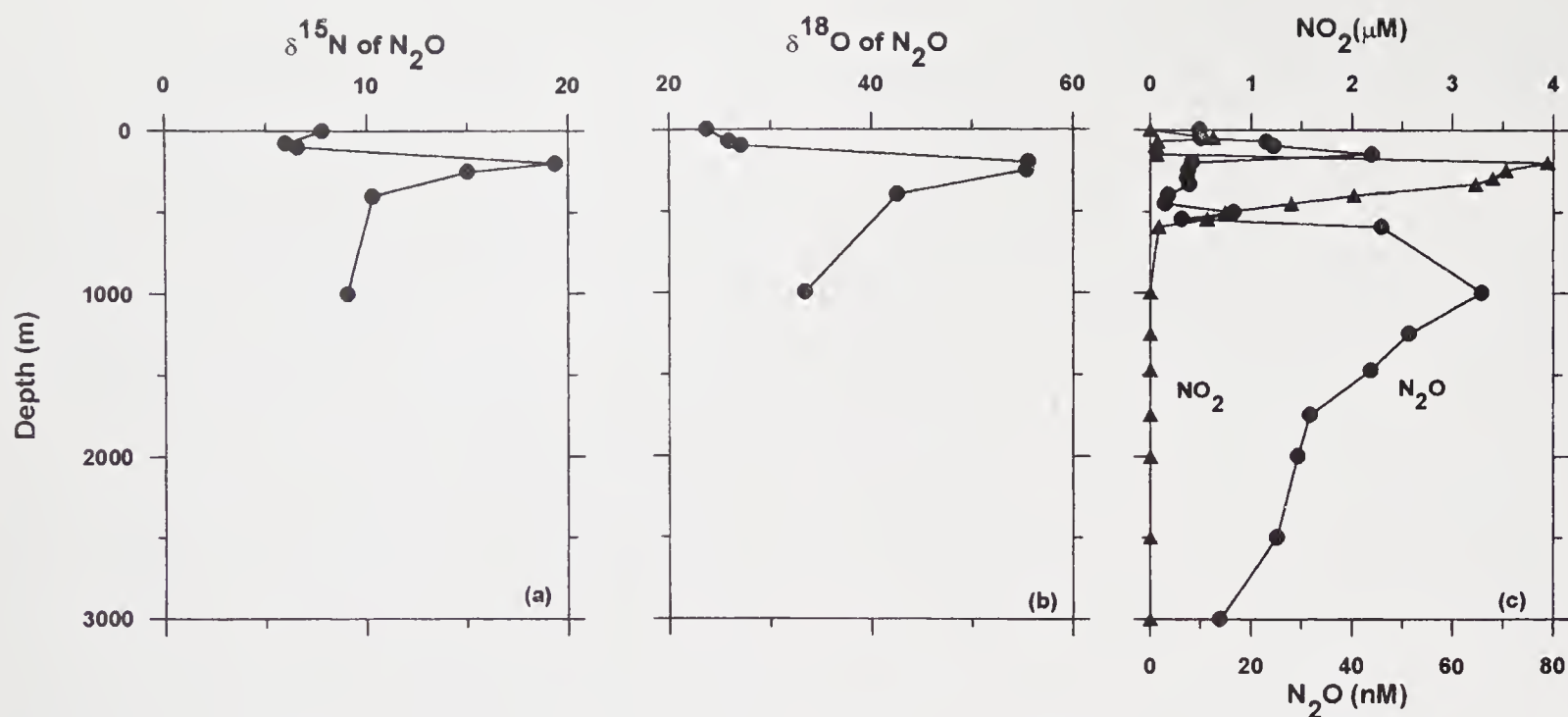


Figure 9. Vertical profiles of (a) $\delta^{15}\text{N}$ and (b) $\delta^{18}\text{O}$ of N_2O , and (c) concentrations of NO_2^- (μM , triangles) and N_2O (nM, circles) at Sta. 11/SK87 (modified from Yoshinari *et al* 1997).

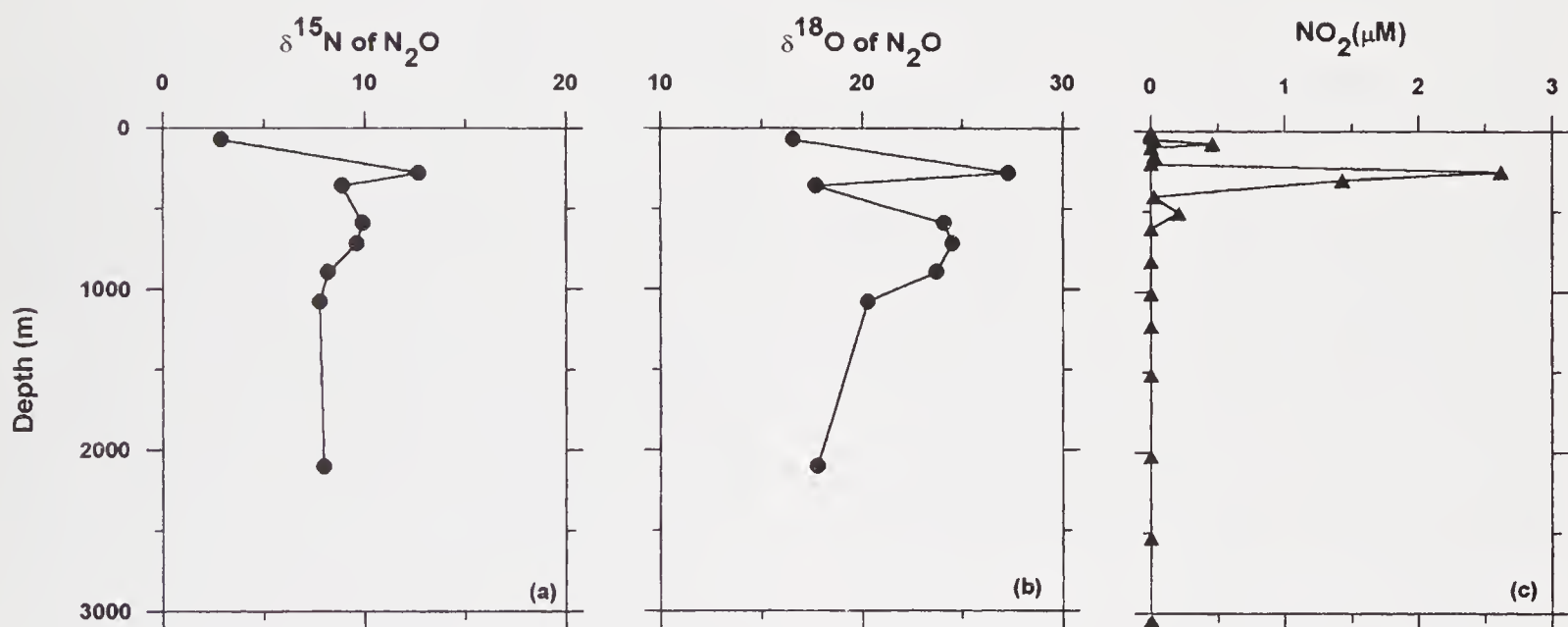


Figure 10. Vertical profiles of (a) $\delta^{15}\text{N}$ and (b) $\delta^{18}\text{O}$ of N_2O , and (c) concentration of NO_2^- (μM) at Sta. 14/SS106.

deep waters. Since the suboxic waters with huge enrichments of heavier isotopes are capped by a layer which has high concentrations of light N_2O , the N_2O escaping to the atmosphere in the region cannot be heavy. Thus the near-tropospheric isotopic values at the sea surface at the open ocean sites (mean \pm s.d. = $7.65 \pm 0.47\text{‰}$ for $\delta^{15}\text{N}$ and $23.45 \pm 1.35\text{‰}$ for $\delta^{18}\text{O}$; $n = 11$) probably reflect an active air-sea exchange. The fate of heavy N_2O is not known, but it is expected to be advected out of the region and contribute to the elevated $\delta^{15}\text{N}$ and $\delta^{18}\text{O}$ in N_2O observed outside the suboxic zones (Kim and Craig 1990).

An important aspect of the data is that the $\delta^{15}\text{N}$ of NO_3^- is consistently lower than that of N_2O at depths exceeding ~ 200 m, and higher at shallower depths

(figures 3 and 4). This indicates that the intense N_2O accumulation in the upper and lower parts of the OMZ may be through different mechanisms. Greater enrichment of $\delta^{15}\text{N}$ in N_2O relative to NO_3^- appears to be characteristic of denitrification as revealed by recent culture experiments (Altabet M A, unpublished data). It may arise from a combination of much lower N_2O concentration than the amount of denitrified nitrogen and large kinetic isotope fractionation associated with the reduction of N_2O to N_2 (Yoshida *et al* 1984). This pattern is the most pronounced within N_2O -depleted SNM at 3201/SS119. Its persistence even below SNM at 3201/SS119 and at depths exceeding ~ 200 m at 3204/SS119 suggests significant N_2O production through denitrification. This obser-

vation is consistent with the view that denitrification may lead to a net N_2O accumulation under certain conditions (Betlach and Tiedje 1981; Capone 1996). However, we also note that heavy isotope enrichment has also been observed, albeit to a lesser degree, in the more oxygenated deep waters of the Pacific Ocean by Kim and Craig (1990). It was attributed to partitioning of isotopes during nitrification by which the precursor species of N_2O [such as hydroxylamine (NH_2OH)] is enriched with ^{15}N and ^{18}O . But the problem with this mechanism is that it cannot explain the observed large increases in N_2O at O_2 levels approaching suboxia (Law and Owens 1990; Naqvi and Noronha 1991) over concentrations expected from linear relationships between N_2O production and O_2 utilisation commonly observed in the oceans (Yoshinari 1976; Elkins *et al* 1978). This obviously requires a reductive step in N_2O production. An alternative mechanism of the observed heavy isotope enrichment could be the consumption of N_2O within sediments (and in water in areas such as the Arabian Sea and eastern tropical Pacific) and subsequent transport of heavy N_2O to the ocean interior (Zafiriou 1990). Lastly, coupling of nitrification and denitrification through common intermediates/by-products may also influence the isotopic composition of N_2O (Zafiriou 1990; Naqvi and Noronha 1991; Naqvi 1991). Such a coupling should be especially important near the oxic-suboxic interface, and this could possibly account for the enigmatic isotopic trend seen in the upper layer of the Arabian Sea which defies conventional explanation. That is, while the lighter N_2O at depths less than $\sim 200\text{m}$ is apparently not produced by denitrification, the classical nitrification pathway ($\text{NH}_4^+ \rightarrow \text{NO}_2^- \rightarrow \text{N}_2\text{O}$) (Yoshida 1988) also cannot fully explain the observed data for two reasons. First, as stated earlier, the $\delta^{15}\text{N}$ values are much higher than that reported ($< -60\text{‰}$) by Yoshida (1988) for or the production of N_2O from NH_4^+ via NO_2^- by *Nitrosomonas europaea*¹. Secondly, what is more significant is that the observed $\delta^{18}\text{O}$ is much higher than the value for nitrification expected from $\delta^{18}\text{O}$ of H_2O and O_2 [assuming that one oxygen atom in NO_2^- is derived from H_2O and the other from dissolved O_2 (Yoshinari *et al* 1997) and using the data from GEOSECS station 416 (Ostlund *et al* 1987), the $\delta^{18}\text{O}$ of nitrification-derived N_2O should have been $< -3\text{‰}$]. Given the very abrupt decrease in O_2 below the surface mixed layer and the expected abundance of large particles at this level, it seems very plausible (Naqvi and Noronha 1991; Naqvi 1991) that an intermediate or by-product of nitrification such as NO enters the denitrification sequence and gets reduced to N_2O . As the oxygen atom of

NH_2OH , the probable precursor of NO (Ward and Zafiriou 1988), is derived from O_2 (Dua *et al* 1979) which is characterised by high $\delta^{18}\text{O}$ (Ostlund *et al* 1987), N_2O produced through this pathway is expected to be enriched in ^{18}O . Moreover, unlike N_2O , production of NO by nitrifying bacteria involves modest depletion of ^{15}N (Yoshida 1988). Thus, N_2O produced through this pathway is expected to be moderately depleted in ^{15}N , but enriched in ^{18}O , as observed.

Therefore, it may be concluded that, in conformity with previous suggestions (Zafiriou 1990; Naqvi 1991), there are probably several mechanisms of N_2O production in the ocean involving different isotopic fractionations. The relative contribution from various pathways is probably determined by the O_2 distribution and organic carbon availability, both of which vary in space and time. This not only brings about large spatial changes in N_2O production and consumption but, in response to temporal changes in the geographical extent and intensity of the O_2 minimum zones (Altabet *et al* 1995; Ganeshram *et al* 1995) the oceanic N_2O source strength may also vary greatly with time contributing to fluctuations in the atmospheric N_2O content as recorded in ice cores (Leuenberger and Siegenthaler 1992).

As stated earlier, the Arabian Sea is a region of high N_2O efflux to the atmosphere; the emission rate is particularly high in the three upwelling centres located off Somalia, Arabia and Southwest India (Bange *et al* 1996; de Wilde and Helder 1997; Naqvi *et al* 1998). Observations made off the southwest coast of India during the summer monsoon of 1995 yielded some of the highest N_2O levels reported from the sea. At twenty-three stations sampled during SK103 (figure 1) the surface concentrations and saturations were $11.2\text{--}62.5\text{ }\mu\text{M}$ (mean \pm s.d. = $28.5 \pm 14.7\text{ nM}$) and $193\text{--}953\%$ ($458 \pm 223\%$), respectively. These values were associated with intense upwelling as manifested by low sea surface temperatures (minimum 22.8°C) and high NO_3^- (maximum $16\text{ }\mu\text{M}$) which are comparable to those observed in the upwelling zones of the western Arabian Sea (Smith and Codispoti 1980; Codispoti *et al* 1996b). The $^{15}\text{N}/^{14}\text{N}$ and $^{18}\text{O}/^{16}\text{O}$ ratios in surface-water N_2O measured at eight of these stations together with those from eight open ocean stations are plotted versus percentage saturation in figure 11. The $\delta^{15}\text{N}$ and percentage saturation appear to be negatively correlated, with N_2O in upwelling waters of the southeastern Arabian Sea being the most depleted in ^{15}N . A few measurements (not included in figure 11) were also made in subsurface waters. The lowest $\delta^{15}\text{N}$ (0.8‰) was recorded at 26 m at $11^\circ 51'\text{N}$, $75^\circ 09'\text{E}$; the corresponding N_2O concentration and saturation were 115.6 nM and 1709% , respectively. Since this is the lowest $\delta^{15}\text{N}$ ever recorded from the oceanic water column, and because at such high concentrations the signatures of background N_2O would be almost

¹ One may question the applicability of these experimental results, conducted with a high ammonium concentration, to the substrate-limited natural environments, but it may be noted that N_2O emitted from the soils is quite depleted in both ^{15}N and ^{18}O (see figure 12).

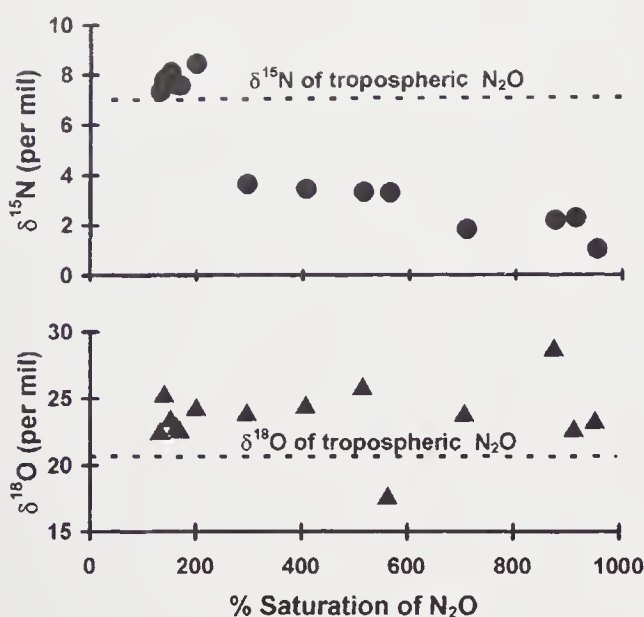


Figure 11. The $\delta^{15}\text{N}$ and $\delta^{18}\text{O}$ of N_2O as a function of N_2O saturation at sea surface (depth $< 5\text{m}$). Horizontal dashed lines indicate isotopic composition of N_2O in marine air (Kim and Craig 1990). Values with moderate saturation and $\delta^{15}\text{N}$ close to the atmospheric value are from the northern Arabian Sea; all others are from the coastal upwelling zone off SW India (modified from Naqvi *et al* 1998).

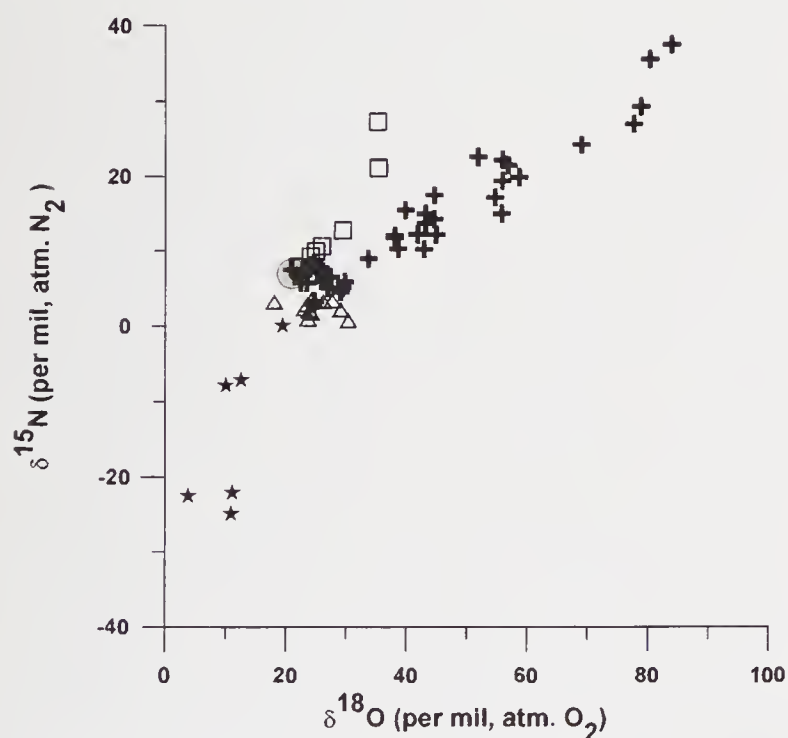


Figure 12. Comparison of isotope data from the Arabian Sea with representative data from other environments (Kim and Craig 1990; Rahn and Wahlen 1997) (stars: soil gas; triangles: upwelling zone off SW India; crosses: northern Arabian Sea; squares: stratosphere; circle: troposphere). Note that the tropospheric value does not fall on vectors joining the other end members (modified from Yoshinari *et al* 1997; Naqvi *et al* 1998).

completely erased, it can be taken to represent the end-member composition of N_2O produced in seawater. It is substantially lower than the $\delta^{15}\text{N}$ of tropospheric N_2O , but much higher than the expected $\delta^{15}\text{N}$ of N_2O produced through nitrification (Yoshida 1988). In contrast to $\delta^{15}\text{N}$, $\delta^{18}\text{O}$ did not exhibit a

discernible relationship with percentage saturation, and with the exception of one sample, all $\delta^{18}\text{O}$ values were consistently higher than the $\delta^{18}\text{O}$ of tropospheric N_2O .

The above observations have an important implication for the atmospheric N_2O budget. Isotopic analysis of stratospheric N_2O at 68°N has shown large enrichments of $\delta^{15}\text{N}$ and $\delta^{18}\text{O}$ (~ 21 and 35‰ , respectively) relative to the troposphere (Kim and Craig 1993). This trend has been confirmed by more recent observations at $33\text{--}48^\circ\text{N}$, albeit with somewhat smaller enrichments in the lower stratosphere, but the causative mechanism is still not fully understood (Rahn and Wahlen 1997; Cliff and Thiemens 1997; Yung and Miller 1997). However, the magnitude of ^{15}N and ^{18}O fluxes (~ 400 and $500\text{ TgN}\text{‰}\text{y}^{-1}$, respectively, obtained from the older data and about half as much from recent results) are such that these cannot be balanced by air-sea exchange, as proposed (Kim and Craig 1993; McElroy and Jones 1996). Even if, as an extreme case, the lowest observed $\delta^{15}\text{N}$ value from the ocean ($\sim 1\text{‰}$) is combined with the largest estimate of oceanic N_2O production ($11\text{ TgN}\text{y}^{-1}$) (Capone 1996), the air-sea exchange can counter no more than $66\text{ TgN}\text{‰}\text{y}^{-1}$ of the stratospheric ^{15}N flux. The reported ^{18}O fluxes are even more problematic since the observed opposite trends of ^{15}N and ^{18}O imply that the air-sea exchange will lead to an increase in the tropospheric ^{18}O inventory. The gravity of this issue is evident from the fact that on a $\delta^{15}\text{N}$ vs. $\delta^{18}\text{O}$ diagram constructed with the published data representing various planetary reservoirs of N_2O , the stratospheric composition conspicuously forms a "corner" (figure 12). Thus the tropospheric value, which does not fall on vectors joining the other end-members, cannot be explained by simple mixing between various reservoirs (Kim and Craig 1993). In view of these observations, it is imperative that more measurements be made on N_2O in the stratosphere and that emitted from different terrestrial reservoirs. If the published data are representative, however, then there ought to exist some hitherto poorly known sources and/or sink of N_2O that may be vital for tropospheric isotopic balance (Prasad 1994; McElroy and Jones 1996; Cliff and Thiemens 1997).

Acknowledgement

This research was funded by the Office of Naval Research (USA) through the US-India Fund. We are grateful to E Desa and B J Zahuranec for their encouragement and support; to the Department of Ocean Development (India) for making time on the research vessels available; and to C Nasolkar, V V S S Sarma, and M Kuhland for their technical assistance. This work is the NIO Contribution Number 2586.

References

- Altabet M A, Francois R, Murray D W and Prell W L 1995 Climate-related variations in denitrification in the Arabian Sea from sediment $^{15}\text{N}/^{14}\text{N}$ ratios; *Nature* **373** 506–509
- Bange H W, Rapsomanikis S and Andreae M O 1996 Nitrous oxide in coastal waters; *Global Biogeochem. Cycles* **10** 197–207
- Bender M L 1990 $\delta^{18}\text{O}$ of dissolved O_2 in seawater: A unique tracer of circulation and respiration in the deep sea; *J. Geophys. Res.* **95** 22243–22252
- Betlach M R and Tiedje J M 1981 Kinetic explanation for accumulation of nitrite, nitric oxide and nitrous oxide during bacterial denitrification; *Appl. Environ. Microbiol.* **42** 1074–1084
- Brandes J A and Devol A H 1997 Isotopic fractionation of oxygen and nitrogen in coastal marine sediments; *Geochim. Cosmochim. Acta* **61** 1793–1802
- Brandes J A, Devol A H, Jayakumar D A, Yoshinari T and Naqvi S W A 1998 Isotopic composition of nitrate in the central Arabian Sea and eastern tropical North Pacific: a tracer for mixing and nitrogen cycles; *Limnol. Oceanogr.* (in press)
- Burkill P H, Mantoura R F C and Owens N J P 1993 Biogeochemical cycling in the northwestern Indian Ocean: a brief overview; *Deep-Sea Res. II* **40** 643–649
- Capone D G 1996 A biologically constrained estimate of oceanic N_2O flux; *Mitt. Internat. Verein. Limnol.* **25** 105–114
- Cliff S S and Thiemens M H 1997 The $^{18}\text{O}/^{16}\text{O}$ and $^{17}\text{O}/^{16}\text{O}$ ratios in atmospheric nitrous oxide: a mass-dependent anomaly; *Science* **278** 1774–1776
- Cline J D and Richards F A 1972 Oxygen deficient conditions and nitrate reduction in the eastern tropical North Pacific Ocean; *Limnol. Oceanogr.* **17** 885–900
- Cline J D and Kaplan I R 1975 Isotopic fractionation of dissolved nitrate during denitrification in the eastern tropical North Pacific; *Mar. Chem.* **3** 271–299
- Codispoti L A 1989 Phosphorus vs. nitrogen limitation of new (export) production; *Productivity of the ocean: present and past* (eds) W Berger, V Smetacek and G Wefer (John Wiley and Sons) pp. 377–394
- Codispoti L A 1997 The limits to growth; *Nature* **387** 237–238
- Codispoti L A and Christensen J P 1985 Nitrification, denitrification and nitrous oxide cycling in the eastern tropical South Pacific Ocean; *Mar. Chem.* **16** 277–300
- Codispoti L A, Devol A, Minas A, Paerl H, Naqvi S W A, Christensen J, Becker P and Yoshinari T 1996a A revised oceanic combined nitrogen budget and its implications for exchange of carbon dioxide between the atmosphere and ocean; *Carib. J. Sci.* **32** 284–285
- Codispoti L A, Morrison J and Jones B 1996b The chemical hydrographic milieu of the U.S. JGOFS Arabian Sea Process Study; *EOS – Trans. Amer. Geophys. Union* OS23
- Delwiche C C and Steyn P L 1970 Nitrogen isotope fractionation in soils and microbial reactions; *Environ. Sci. Tech.* **4** 929–935
- Deuser W G 1975 *Reducing environments; Chemical Oceanography* (eds) J P Riley and G Skirrow (Academic Press) **3** 1–37
- de Wilde H P J and Helder W 1997 Nitrous oxide in the Somali Basin: the role of upwelling; *Deep-Sea Res. II* **44** 1319–1340
- Dua R D, Bhandari B and Nicholas D J D 1979 Stable isotope studies in the oxidation of ammonia to hydroxylamine by *Nitrosomonas europaea*; *FEBS Lett.* **106** 401–404
- Elkins J W, Wofsey S C, McElroy M B, Colb C E and Kaplan W 1978 Aquatic sources and sinks for nitrous oxide; *Nature* **275** 602–606
- Galloway J N, Schlesinger W H, Levy H, Michaels A and Schnoor J L 1995 Nitrogen fixation: anthropogenic enhancement – environmental response; *Global Biogeochem. Cycles* **9** 235–252
- Grasshoff K, Ehrhardt M and Kremling K 1983 *Methods of Seawater Analysis* (Verlag Chemie) pp. 419
- Ganeshram R S, Pederson T F, Calvert S E and Prell W L 1995 Large changes in oceanic nutrient inventories from glacial to interglacial periods; *Nature* **376** 755–758
- Jenkins W J 1990 Determination of isopycnal diffusivity in the Sargasso Sea; *J. Phys. Oceanogr.* **21** 1058–1061
- Kim K-R and Craig H 1990 Two isotope characterisation of N_2O in the Pacific Ocean and constraints on its origin in deep water; *Nature* **347** 58–61
- Kim K-R and Craig H 1993 Nitrogen-15 and oxygen-18 characteristics of nitrous oxide: a global perspective; *Science* **262** 1855–1857
- Law C S and Owens N J P 1990 Significant flux of atmospheric nitrous oxide from the northwestern Indian Ocean; *Nature* **346** 826–828
- Leuenberger M and Siegenthaler U 1992 Ice-age atmospheric concentration of nitrous oxide from an Antarctic ice core; *Nature* **360** 449–451
- Mariotti A, Germon J C and Petal H 1981 Experimental determination of nitrogen kinetic isotope fractionations: some principles; illustration for denitrification and nitrification processes; *Plant and Soil* **62** 413–430
- McElroy M B 1983 Marine biological controls of atmospheric CO_2 and climate; *Nature* **302** 328–329
- McElroy M B and Jones D B 1996 Evidence for an additional source of atmospheric N_2O ; *Global Biogeochem. Cycles* **10** 651–659
- Naqvi S W A 1987 Some aspects of the oxygen-deficient conditions and denitrification in the Arabian Sea; *J. Mar. Res.* **49** 1049–1072
- Naqvi S W A 1991 N_2O production in the ocean; *Nature* **349** 373–374
- Naqvi S W A 1994 Denitrification processes in the Arabian Sea; *Proc. Indian Acad. Sci. (Earth & Planet Sci.)* **103** 279–300
- Naqvi S W A and Noronha R J 1991 Nitrous oxide in the Arabian Sea; *Deep-Sea Res.* **38** 871–890
- Naqvi S W A and Shailaja 1993 Activity of the respiratory electron transport system and respiration rates within the oxygen minimum layer of the Arabian Sea; *Deep-Sea Res. II* **40** 687–695
- Naqvi S W A, Noronha R J, Somasundar K and Sen Gupta R 1990 Seasonal changes in the denitrification regime of the Arabian Sea; *Deep-Sea Res.* **37** 693–711
- Naqvi S W A, Yoshinari T, Jayakumar D A, Altabet M A, Narvekar P V, Devol A H, Brandes J A and Codispoti L A 1998 Budgetary and biogeochemical implications of N_2O isotope signatures in the Arabian Sea; *Nature* **394** 462–464
- Olson D B, Hitchcock G L, Fine R A and Warren B A 1993 Maintenance of the low-oxygen layer in the Arabian Sea; *Deep-Sea Res. II* **40** 673–685
- Ostlund H G, Craig H, Broecker W S and Spencer D 1987 *GEOSECS Atlantic, Pacific, and Indian Ocean Expeditions Shorebased Data and Graphics*, National Science Foundation **7** pp. 200
- Payne W J 1973 Reduction of nitrogenous oxide by microorganisms; *Bacteriol. Rev.* **37** 409–452
- Prasad S S 1994 Natural atmospheric sources and sinks of nitrous oxide I: An evaluation based on ten laboratory data; *J. Geophys. Res.* **99** 5285–5294
- Press W H, Flannery B P, Teukolsky S A and Vetterling W T 1992 *Numerical Recipes in C, The Art of Scientific Computing* (Cambridge University Press) pp. 996
- Rahn T and Wahlen M 1997 Stable isotope enrichment in stratospheric nitrous oxide; *Science* **278** 1776–1778
- Richards F A 1965 Anoxic basins and fjords; *Chemical Oceanography* (eds) J P Riley and G Skirrow, Academic Press **1** pp. 611–645

- Sigman D M, Altabet M A, Michener R, McCorkle D C, Fry B and Holmes R M 1997 Natural abundance-level measurement of the nitrogen isotopic composition of oceanic nitrate: An adaptation of the ammonia diffusion method; *Mar. Chem.* **57** 227–242
- Smith S L and Codispoti L A 1980 Southwest monsoon of 1979: Chemical and biological response of Somali coastal waters; *Science* **209** 597–600
- Wada E. and Hattori A 1991 *Nitrogen in the Sea: Forms, Abundances and Rate Processes* (CRC Press) pp. 208
- Ward B B and Zafiriou O C 1988 Nitrification and nitric oxide in the oxygen minimum of the eastern tropical North Pacific; *Deep-Sea Res.* **35** 1127–1142
- Yoshida N 1988 ^{15}N -depleted N_2O as a product of nitrification; *Nature* **335** 528–529
- Yoshida N, Hattori A, Saino T, Matsuo S and Wada E 1984 $^{15}\text{N}/^{14}\text{N}$ ratio of dissolved N_2O in the eastern tropical Pacific Ocean; *Nature* **307** 442–444
- Yoshida N, Morimoto H, Hirano M, Koike I, Matsuo S, Wada E, Saino T and Hattori A 1989 Nitrification rates and ^{15}N abundances of N_2O and NO_3 in the western North Pacific; *Nature* **342** 895–897
- Yoshinari T 1976 Nitrous oxide in the sea; *Mar. Chem.* **4** 189–202
- Yoshinari T and Koike I 1994 The use of stable isotopes for the studies of gaseous nitrogen species in the marine environment; *Stable Isotopes in Ecology and Environmental Science* (eds) K Lajtha and R Michener (Blackwell Scientific) pp. 114–137
- Yoshinari T, Altabet M A, Naqvi S W A, Codispoti L A, Jayakumar A, Kuhland M and Devol A 1997 Nitrogen and oxygen isotopic composition of N_2O from suboxic waters of the eastern tropical North Pacific and the Arabian Sea – measurement by continuous-flow isotope ratio monitoring; *Mar. Chem.* **56** 253–264
- Yung Y L and Miller C E 1997 Isotopic fractionation of stratospheric nitrous oxide: Is there a chemical source?; *Science* **278** 1778–1780
- Zafiriou O C 1990 Laughing gas from leaky pipes; *Nature* **347** 15–16

On laboratory studies of grains from outside the solar system

U OTT

Max-Planck-Institut für Chemie, Becherweg 27, D-55128 Mainz, Germany
e-mail: ott@mpch-mainz.mpg.de

An overview is given of the identified surviving presolar grains in primitive meteorites. Two of these phases are discussed in more detail: (a) Presolar silicon carbide, with special emphasis on heavy element isotopic compositions which trace the slow neutron capture process (s-process) of nucleosynthesis. It is argued that there are problems either with the grain or neutron capture cross section data or with current basic understanding of heavy element nucleosynthesis. (b) Presolar diamonds, where new developments are discussed concerning the origin of the (supernova) Xenon-HL component thought to be contained within them; in addition, arguments are presented in favor of diverse carrier phases for the various Xe components observed in diamond separates.

1. Introduction

The year of 1997 marks not only the 50th anniversary of PRL at Ahmedabad; it also marks the tenth anniversary of the first actual isolation from and identification in primitive meteorites of grains of presolar origin (Lewis *et al* 1987; Bernatowicz *et al* 1987; Zinner *et al* 1987), and thus of the availability of material of truly and undoubtedly interstellar origin for study in the laboratory. While 1987 was the year of identification and true isolation, the presence of grains in primitive meteorites whose origin lies outside the solar system and predates its formation had been suspected before. Hints had been seen in the isotopic compositions of the so-called planetary noble gases, especially in xenon and neon: the Xe-HL component, as it is called today, was first seen by Reynolds and Turner (1964) and first hints for Ne-E, virtually monoisotopic ^{22}Ne , were seen by Black and Pepin (1969). It was the quest for the carrier phases of these isotopically unusual noble gases that eventually, in 1987, led to the identification of presolar diamond and silicon carbide as well as to that of presolar graphite (Amari *et al* 1990). Isotopic analyses have thus been and still are instrumental in the search for surviving presolar grains in meteorites, with the large isotope abundance anomalies found in these grains the only

(possible) real proof of their presolar origin. In return, with the interstellar origin of the grains assured, the observed isotopic structures provide a variety of information, not obtainable in this detail by other means, on several highly interesting subjects: • details of the nuclear processes by which the chemical elements are synthesized in stars; • mixing during the life and during the explosion of stars; • circumstellar grain formation; • constraints on conditions in the interstellar medium and the early Solar System. The latter comes about because conditions must have allowed the survival of at least a fraction of the grains originally formed.

To celebrate the anniversary of the isolation of interstellar grains from meteorites, a conference has been held at the McDonnell Center for the Space Sciences at Washington University, St. Louis, where most of the work on single grains has been performed. The book produced as the result of that conference (Bernatowicz and Zinner 1997) contains contributions that cover virtually all aspects of research done on these fascinating objects over the last ten years, and the interested reader is referred to this book for details. In my contribution to this Conference proceedings I will give a short overview of the surviving grains of interstellar origin that have been isolated (section 2), together with a short summary of isotopic structures

Keywords. Presolar grains; isotope abundance anomalies; nucleosynthesis; s-process; r-process.

Table 1. *Types of presolar grains identified in meteorites.*

Phase	Abundance* [ppm]	Typical size [μm]	Isotopically anomalous elements	Stellar sources.
Graphite ^a	~ 10	$\sim 1\text{--}20$	C, N, O, Mg(Al), Si, K, Ca, Ti, noble gases	Novæ, supernovæ, AGB stars.
Diamond	~ 1400	~ 0.002	N, Sr, Te, Ba, noble gases	Supernovæ.
Silicon carbide ^b (SiC)	~ 14	$\sim 0.3\text{--}20$	C, N, Mg(Al), Si, Ca, Ti, Sr, Zr, Mo, Ba, Nd, Sm, Dy, noble gases	AGB stars (mainstream), supernovæ (Type X)
Corundum ^c (Al ₂ O ₃)	~ 0.01	$\sim 0.5\text{--}3$	O, Mg(Al)	Red Giants, AGB stars, supernovæ
Silicon nitride (Si ₃ N ₄)	≥ 0.002	~ 1	C, N, Mg(Al), Si	Supernovæ

* Listed abundances are from the compilation of Huss (1997) and refer to the CI meteorite Orgueil (exception: silicon nitride, where the number is for Murchison). Generally the abundances scale with the matrix fraction of the meteorites and decrease with increasing metamorphism (Huss 1997). Size ranges are from Zinner (1997) and may be biased against small grains.

^a Contains subgrains of: TiC, ZrC, MoC.

^b Contain subgrains of: TiC.

^c In addition one grain of spinel (MgAl₂O₄) and two of mixed spinel-corundum compositions have been found.

in the rarer grains (graphite, corundum, silicon nitride) and then focus on some of the research in which I have been personally involved: isotopic features in interstellar SiC with special emphasis on heavy element nucleosynthesis (section 3) and currently ongoing research on interstellar diamond (section 4). Some concluding remarks will be given in the final section (section 5).

2. An overview

2.1 Inventory of presolar grains

An overview of the various types of grains in meteorites for which a presolar origin has been proven without reasonable doubt is given in table 1 (assembled primarily from Zinner 1997 and Huss 1997). Note, however, that this does not imply that all meteoritic grains of a given type have a (proven) presolar origin. In the case of graphite, e.g., only the round grains show isotopic signatures indicative of a circumstellar origin (Amari *et al* 1990; Zinner *et al* 1995); while in the case of corundum only on the order of a per cent of the grains are arguably presolar (Nittler 1997). As far as the nanodiamonds are concerned, the nominally most abundant identified presolar phase (table 1), it has to be kept in mind that their presolar origin is inferred only from the presence in diamond separates of isotopically anomalous Xenon-HL the origin of which seems to be tied to a supernova (Clayton 1989, e.g.). The extension of the supernova association to the diamonds *per se* is not straightforward however, because with current techniques it is not possible to analyze single diamond grains even for the abundant elements (Zinner 1997) and there is, on the average, only one atom of (supernova) Xe-HL per several million diamond grains.

Elements with observed isotope abundance anomalies in the truly presolar grains are listed in the fourth column of table 1. Generally the anomalies are very large: for example, $^{12}\text{C}/^{13}\text{C}$ in both interstellar SiC grains and interstellar graphite grains ranges from ~ 0.02 to ~ 80 times the normal ratio of ~ 89 (Hoppe and Ott 1997; Hoppe *et al* 1995). Such variations are much larger than isotopic effects in other meteoritic phases where abundance anomalies have been detected, such as the Ca-Al-rich FUN inclusions (Begemann 1993; Zinner 1997).

With the exception of the rare corundum grains, all the grains listed in table 1 can have formed only in a reducing environment, where the ratio of carbon to oxygen was greater than one. This limits the possible stellar sources to a few types (Hoppe *et al* 1994; Hoppe and Ott 1997): (Red Giant) carbon stars, novæ, as well as, at the right time in their development, Wolf-Rayet stars and, with the right mixing between zones, supernovæ. Refinement is possible for specific cases with the help of the isotopic structures. The most clear-cut case is silicon carbide, with an origin from carbon stars indicated for the vast majority of grains and an origin from supernovæ for the rare grains of Type X (Hoppe and Ott 1997; Amari and Zinner 1997). Before discussing the isotopic structures in SiC and diamond in more detail in sections 3 and 4, a short summary of the features of graphite, corundum and silicon nitride is given below.

2.2 Rarer grains: graphite, corundum, silicon nitride

Graphite: Presolar graphite grains (Amari *et al* 1990, 1993; Hoppe *et al* 1995) probably originated from all four potential sources listed above. The isotopic ratio $^{12}\text{C}/^{13}\text{C}$ varies among the analyzed single round grains by a factor ~ 3500 from ~ 2 to ~ 7300 and, based on the distribution of $^{12}\text{C}/^{13}\text{C}$ ratios, the grains can be

assigned to four groups with the distribution different for grains of different effective density.

It is primarily the presence of anomalous noble gases that points to an origin for a significant number of grains from novæ and from carbon stars (Amari *et al* 1995): Ne-E(L), monoisotopic ^{22}Ne present in about 30% of the grains (Nichols *et al* 1994), in all likelihood is the decay product of ^{22}Na ($t_{1/2} = 2.6$ year) thought to be synthesized in novæ and supernovæ, while the presence of s-process-Kr and -Xe (Amari *et al* 1995) shows the need for a contribution from carbon stars.

Other unusual isotopic compositions have been found in nitrogen contained in the graphite grains as well as trace O, Mg, Si, K, Ca and Ti. A remarkable number of grains show large ^{26}Mg excesses inferred to arise from decay within the grains of now extinct ^{26}Al ($t_{1/2} = 0.7$ Ma). Inferred $^{26}\text{Al}/^{27}\text{Al}$ ratios range up to values as high as 0.1 (orders of magnitude higher than the “canonical value” of 5×10^{-5} generally considered typical of the early solar system: see review by MacPherson *et al* 1995). Also found are the decay products of other extinct radionuclides: ^{41}Ca ($t_{1/2} = 0.1$ Ma) and ^{44}Ti ($t_{1/2} \sim 60$ year; Görres *et al* 1998) which show up in a number of grains in the form of large excesses of ^{41}K and ^{44}Ca (Amari *et al* 1996a; Nittler *et al* 1996). Large silicon isotopic anomalies found in some grains (Hoppe *et al* 1995), together with the former presence of ^{44}Ti and ^{41}Ca clearly point to an origin from supernovæ for these grains as for the SiC grains of type X (Amari and Zinner 1997). They also point, however, to the need for complex mixing processes in supernova ejecta so that nuclides produced in the inner regions of the supernova end up being trapped in carbonaceous materials originating farther out (Amari and Zinner 1997).

Aluminum oxide (corundum): Presolar oxides were first discovered in 1992 (Huss *et al* 1992; Hutcheon *et al* 1994). In the meantime about 100 presolar corundum grains have been identified plus one spinel (MgAl_2O_4) grain and two of a composition intermediate between those of corundum and spinel (Nittler 1997). About half of the grains analyzed for Mg show large excesses of ^{26}Mg corresponding to initial $^{26}\text{Al}/^{27}\text{Al}$ ratios of up to 0.016. In addition, they show large variations in the isotopic composition of oxygen based on which most grains can be assigned to one of four groups (Nittler 1997; Nittler *et al* 1997).

Some recently identified corundum grains do not fit into any of the previously defined groups and may have a supernova origin (Nittler *et al* 1998; Choi *et al* 1998), but the most likely sources of the vast majority of corundum grains are red giant stars (Nittler 1997). It is worthy of note, however, that the detailed compositions of oxygen measured in presolar grains in the laboratory span a much wider range than spectroscopical observations of stars (Zinner 1997). They also support the need to include in stellar evolution calculations the effects of “hot bottom burning” in

asymptotic giant branch stars (Boothroyd *et al* 1994; 1995) and have even pointed to the need to include an additional “extra mixing” process called “cool bottom processing” (Wasserburg *et al* 1995; Nittler *et al* 1997). Interestingly, it is also possible to draw conclusions from the isotopic composition of presolar corundum grains concerning galactic chemical evolution and the age of the galaxy (Nittler and Cowsik 1997).

Silicon nitride: Only very few grains of silicon nitride have been identified so far (Nittler *et al* 1995; Amari and Zinner 1997). They bear similarities to SiC grains of type X (section 3) with which they probably share an origin from supernovæ. Characteristic isotopic features are excesses relative to solar of ^{28}Si and ^{15}N , both excesses and deficits of ^{13}C and extremely high inferred $^{26}\text{Al}/^{27}\text{Al}$ (up to 0.2).

3. Silicon carbide

3.1 General features and light elements

The origin of the presolar silicon carbide grains is the most clear-cut of all presolar phases. For the vast majority of grains (the “mainstream” grains) an origin from carbon stars is indicated (Hoppe *et al* 1994; Hoppe and Ott 1997). The same probably holds true for subtypes A, B, Y and Z (Hoppe and Ott 1997). Only for the type X grains a different origin, namely from supernovæ, is indicated (Amari and Zinner 1997; Hoppe and Ott 1997). An overview of the subtypes is given in table 2 (adapted from Hoppe and Ott 1997).

Among the arguments for the carbon star origin of most SiC grains is that the range of $^{12}\text{C}/^{13}\text{C}$ observed in individual mainstream grains is similar to the range observed in the atmospheres of such stars (Alexander 1993; Hoppe *et al* 1994; Hoppe and Ott 1997), and the fact that the heavy trace elements show the signature of the slow neutron capture (s-) process of nucleosynthesis (Lewis *et al* 1990; Hoppe and Ott 1997). The latter is thought to occur in the He burning shell of Red Giant stars during the asymptotic giant branch (AGB) phase, with transport of He shell material to the surface by “third dredge up” episodes (Hoppe and Ott 1997; Lattanzio and Boothroyd 1997; Gallino *et al* 1997). The observed nitrogen isotopic compositions, the detection of extinct ^{26}Al in the form of ^{26}Mg excesses, as well as the presence of almost pure ^{22}Ne (Ne-E(H)), which, as the s-process nuclides, is thought to originate from the He-burning shell are consistent with this interpretation (Gallino *et al* 1990; Hoppe and Ott 1997; Gallino *et al* 1997).

Carbon and nitrogen: Carbon and nitrogen isotopic compositions are characterized by $^{12}\text{C}/^{13}\text{C}$ ratios between 2 and 7000 (solar system: 89) and $^{14}\text{N}/^{15}\text{N}$ ratios from 7 to 19000 (solar system: 272), i.e.,

Table 2. Isotopic signatures of the light to intermediate-mass elements (C to Ti) in single SiC mainstream grains. Data for X grains and the solar system C- and N-isotopic compositions are shown for comparison. Adapted from Hoppe and Ott (1997).

Group	Ab. ^a (%)	¹² C/ ¹³ C	¹⁴ N/ ¹⁵ N	²⁶ Al/ ²⁷ Al ^b	Si	Ti ^c
Mainstream	87–94	10–100	50–19000	10 ^{−5} –10 ^{−2}	Slope 1.34 line	V-shape
Type A	2	2–3.5	50–600	10 ^{−3} –10 ^{−2}	Slope 1.34 line	?
Type B	2–5	3.5–10	5–12000	10 ^{−4} –0.06	Slope 1.34 line	V-shape
Type Y	1–2	100–260 ^d	400–5000	10 ^{−4} –10 ^{−3}	Slope 0.35 line	⁵⁰ Ti excess ^e
Type Z	0–3	8–180	1100–19000	10 ^{−3}	Depletion in ²⁹ Si ^e ; ³⁰ Si-rich side of slope 1.34 line	?
X grains	1	18–7000	13–250 ^f	0.02–0.6 ^g	²⁸ Si excess ^e (up to 5x)	^{49,50} Ti excesses ^e
Solar system		89	272			

^a Ab.: Abundance. Ranges refer to abundances observed in different size separates.

^b Approximate ranges.

^c Isotopic pattern as predominantly observed.

^d Observed range. The more general definition is ¹²C/¹³C > 100.

^e Relative to solar system isotopic composition.

^f Observed range. The more general definition is isotopically heavy N (¹⁴N/¹⁵N < 272).

^g Observed range. The more general definition is ²⁶Al/²⁷Al > 0.01.

both ratios vary by more than three orders of magnitude (figure 1). The mainstream grains are marked by ¹²C/¹³C = 10–100 and ¹⁴N/¹⁵N = 50–19000. Most of them (70%) have enrichments in ¹³C and ¹⁴N with ¹²C/¹³C ratios between 40 and 80 and ¹⁴N/¹⁵N ratios between 500 and 5000. The opposite signature is shown by the X grains, most of which are characterized by enrichments in ¹²C and ¹⁵N.

Magnesium and aluminum: Many (≈ 50%) of the SiC grains have large excesses in ²⁶Mg and the

lack of clear ²⁶Mg excesses in the others may be, at least in part, due to contamination with Mg of solar system (terrestrial) origin (Hoppe and Ott 1997). Excesses in ²⁶Mg are attributed to the *in situ* decay of radioactive ²⁶Al because (i) ²⁵Mg/²⁴Mg ratios are normal (typically within 10%; cf. Huss *et al* 1997), and (ii) excesses in ²⁶Mg can be very large (Mg sometimes is virtually monoisotopic ²⁶Mg). The inferred initial ²⁶Al/²⁷Al ratios range from ≈ 10^{−5} to 10^{−2} for the mainstream grains (table 2). The highest abundance of radiogenic ²⁶Mg is observed for the X grains which have ²⁶Al/²⁷Al ratios of 0.02 to 0.6. While the ²⁶Al/²⁷Al ratios of the subgroup Y and Z grains are indistinguishable from the typical mainstream grains, the ratio tends to be slightly higher (up to 0.06) in grains with low ¹²C/¹³C (subgroups A and B).

Silicon: Deviations of the ²⁹Si/²⁸Si ratios from normal, i.e. δ²⁹Si values, are between −750 and +240‰ and likewise δ³⁰Si values range from −770 to +510‰ (figure 2). As in the case of carbon and nitrogen, the Si-isotopic compositions of the X grains are distinct from those of the mainstream grains. The range covered by the mainstream grains is much smaller, and, while the X grains are depleted in ²⁹Si and ³⁰Si, most mainstream grains are enriched in the heavy Si isotopes falling in figure 2 along a line with slope 1.34 (Hoppe *et al* 1994). Grains that lie to the ³⁰Si-rich side of the mainstream Si correlation line make up the subgroups Y and Z with the latter much more common among smaller (< 2 μm) SiC grains. Y grains fall on a line with slope 0.35, while most Z grains are depleted in ²⁹Si and ³⁰Si.

The scatter of the Si data along the slope 1.34 correlation line suggests a simple two component mixing scenario for most of the grains. This view, however, is incompatible with the expectations from current AGB star models. In AGB stars Si is affected

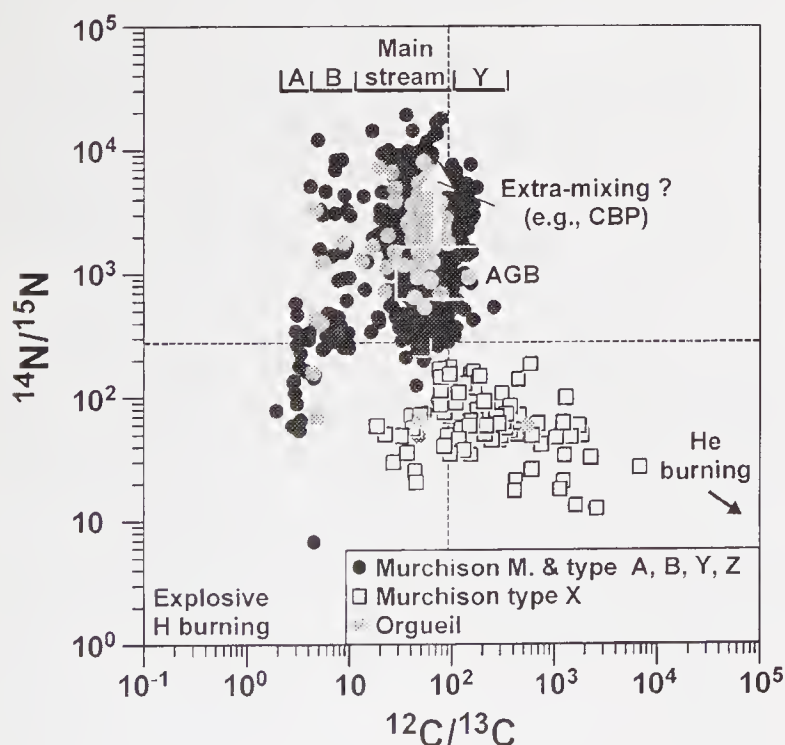


Figure 1. Carbon and nitrogen isotopic compositions in individual silicon carbide grains (figure from review by Hoppe and Ott 1997, see there for primary references). Different subtypes of grains (table 2) are marked by different symbols. Also indicated are the effects of several nucleosynthesis processes (see discussion in Hoppe and Ott 1997).

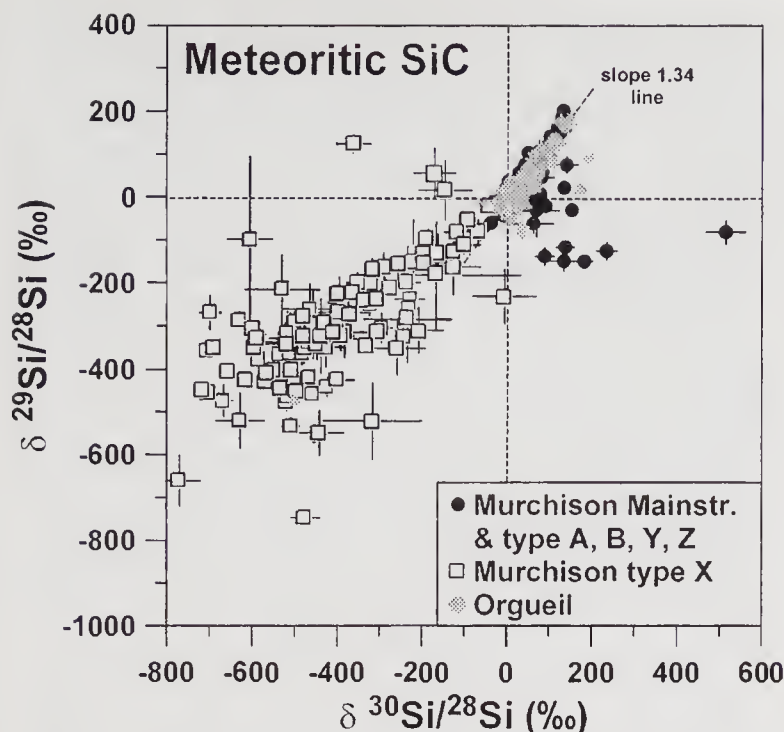


Figure 2. Silicon isotopic composition in individual silicon carbide grains (figure from review by Hoppe and Ott 1997, see there for primary references). The ratios shown are δ -values, i.e. deviations from the normal composition in permil. X grains are strongly enriched in ^{28}Si , i.e. they show large negative δ -values. Mainstream grains fall into a more limited range along a line with slope 1.34 (see text for discussion).

by the s-process in the He shell, leading to enrichments of ^{29}Si and ^{30}Si (Gallino *et al* 1990, 1994; Brown and Clayton 1992). With conditions considered typical for the He shell of AGB stars the production of ^{30}Si is larger than that of ^{29}Si and the Si isotopic composition is expected to evolve along a line with slope between 0.3 and 0.5 (in the $\delta^{29}\text{Si}$ vs. $\delta^{30}\text{Si}$ representation of figure 2), inconsistent with the slope 1.34 line of the mainstream grains. The currently preferred interpretation of the line is that it reflects the galactic chemical evolution of the Si isotopes and represents a range of Si starting compositions of a large number of AGB stars and not the effects of the internal stellar nucleosynthesis (Timmes and Clayton 1996).

Calcium and titanium: Measurements on bulk samples (Amari *et al* 1996b) show excesses in the heavy Ca isotopes with $\delta^{42}\text{Ca}$ values up to 40‰, $\delta^{43}\text{Ca}$ values up to 70‰, and $\delta^{44}\text{Ca}$ values up to 60‰, where $\delta^i\text{Ca}$ is the per mil deviation from the solar system $^i\text{Ca}/^{40}\text{Ca}$ ratio. This is qualitatively compatible with the s-process in the He shell of AGB stars (Gallino *et al* 1990), although there remain problems in detail (Hoppe and Ott 1997). The large ^{44}Ca excesses ($\delta^{44}\text{Ca}$ up to 19000‰) observed in X grains (Amari *et al* 1992; Hoppe *et al* 1996; Nittler *et al* 1996) are presumably from the *in situ* decay of ^{44}Ti and are taken as an indicator of their supernova origin.

Ti is the most abundant trace element contained in the SiC grains after N, Al, and O. Most grains have excesses in all isotopes relative to ^{48}Ti , expressing a V-

shape isotopic pattern (Hoppe and Ott 1997). Such a pattern is qualitatively consistent with predictions for AGB stars where Ti is affected by the s-process in the He shell (Gallino *et al* 1994). However, the observed spread in Ti-isotopic compositions is larger than models predict for mixing of s-process Ti with unprocessed envelope material. Hence the data contradict any single star model and, in order to explain the Si data, a large number of parent stars with different initial Ti-isotopic compositions and different degrees of He shell dredge-up are required (Gallino *et al* 1994; Hoppe and Ott 1997).

3.2 Heavy trace elements and s-process nucleosynthesis

The most conspicuous feature in the isotopic compositions of heavy elements is the relative overabundance of the isotopes that are solely or predominantly produced in the s-process (figures 3 and 4). Compared to isotope abundance anomalies found for heavy elements in FUN Ca-Al-rich inclusions, effects in SiC are larger by orders of magnitude (Begemann 1993; Zinner 1997). As a result, correction for mass-dependent fractionation in nature or during analysis, which is critical in the CAIs, is of no importance in presolar SiC. It is also important to realize that the heavy trace elements yield information of a different kind than the lighter, major constituents of SiC. For C and N, e.g., a wide range of individual compositions exists (figure 1), essentially all of which are quite different from pure compositions produced in a single process of nucleosynthesis. As a consequence, it is possible in these cases to infer the processes involved

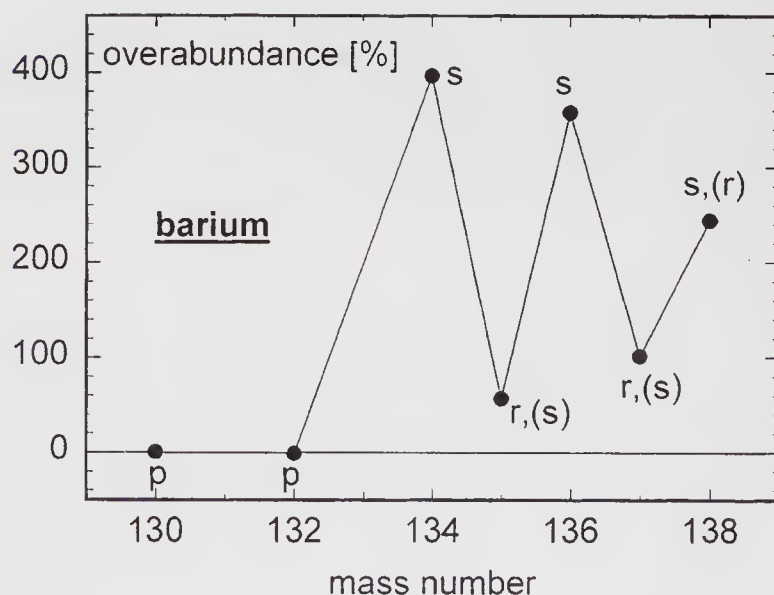


Figure 3. Most extreme composition of Ba measured in a "bulk SiC" separate (Prombo *et al* 1993). Also indicated are the nucleosynthesis processes responsible for the production of the various isotopes. Compared to the normal composition, those produced solely in the s-process ($^{134,136}\text{Ba}$) are five-fold enriched relative to those with no s-process contribution ($^{130,132}\text{Ba}$).

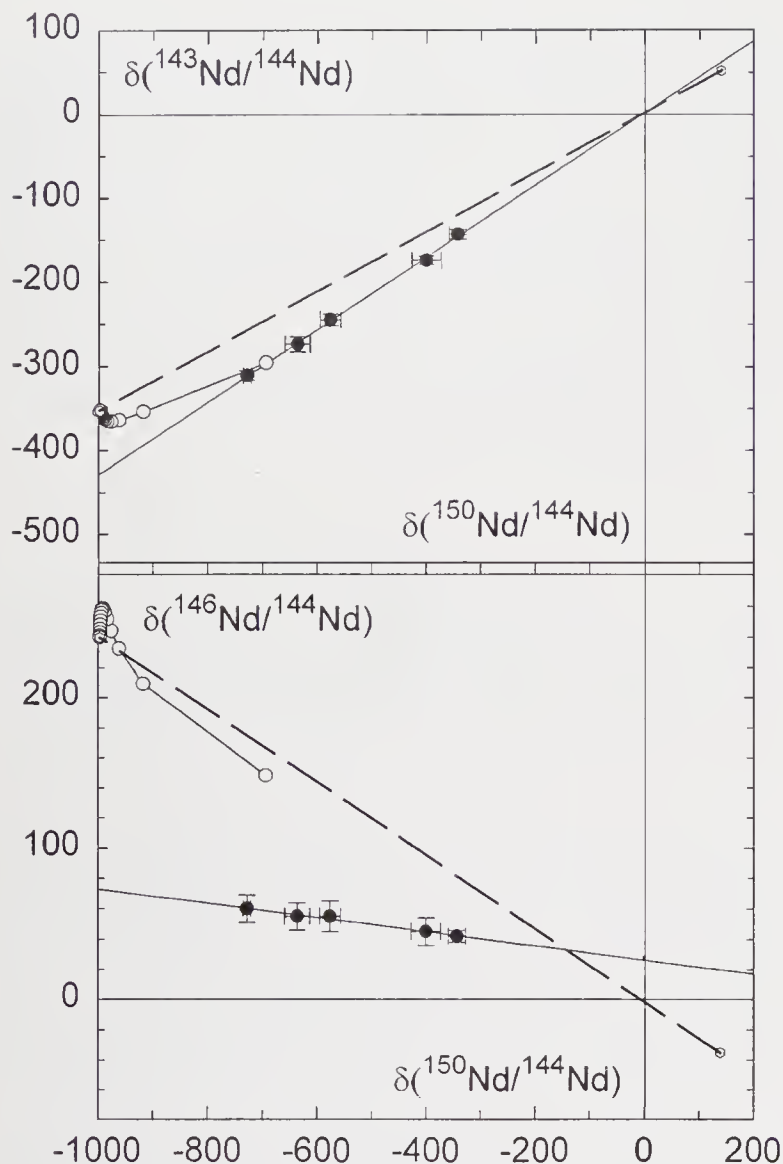


Figure 4. Nd compositions in SiC separates (full circles) as measured by Richter (1995). The data are shown as δ -values (deviation from normal in permil). Extension of the correlation lines defined by the data points to $\delta(^{150}\text{Nd}/^{144}\text{Nd}) = -1000\%$ (no ^{150}Nd , this isotope is not produced in the s-process) defines the “experimental” s-process composition. The dashed line is a mixing line between new calculations for s-process-Nd (left) and the starting composition of Nd in an AGB star envelope (R Gallino, pers. comm.). Also shown is the expected development (open circles moving towards left) of the Nd composition in the envelope due to the addition of He shell matter starting at the time when the envelope gets carbon-rich (R Gallino, pers. comm.).

and – with the input from nucleosynthesis calculation predictions – further infer the extent of mixing (see review by Zinner 1997). By contrast, the isotopic patterns found for the heavy elements allow us to infer the extent of mixing as well as the compositions of the s-process components proper, which, in turn, yield constraints on the physical conditions (neutron exposure, neutron density, temperature and mass density) during the process.

While the s-process signature was first seen in the noble gases (Srinivasan and Anders 1978; Ott *et al* 1988; Lewis *et al* 1990), later also non-volatile elements with the signature of the s-process were discovered (Hoppe and Ott 1997). Measurements of ensembles of

SiC grains by thermal ionization mass spectrometry (Ba, Sr, Nd, Sm, Dy) and ion probe (partial spectra of Ba, Nd and Sm) have been performed, and by now the s-process “SiC bulk” composition of seven heavy trace elements in SiC has been firmly established (Hoppe and Ott 1997). As an example the most extreme measured composition of Ba in “SiC bulk” (Prombo *et al* 1993) is shown in figure 3, where, compared to normal Ba, the ratio of s-process-only nuclides ^{134}Ba and ^{136}Ba to nuclides not produced in the s-process (^{130}Ba , ^{132}Ba) is enhanced by a factor of 5. An important new development is the application of laser resonance ionization mass spectrometry for the study of s-process elements in single SiC grains. So far data by this method have been obtained for the relatively abundant elements Zr and Mo as well as for Sr (Nicolussi *et al* 1997, 1998a, 1998b).

Several of the isotopic ratios in the s-process components of elements for which data are available from the “bulk SiC” measurements are sensitive to the physical parameters that characterize the s-process. Based on the approach of the classical model (a phenomenological approach in which the physical parameters are held constant; see Käppeler *et al* 1989, 1990) “effective” values for neutron exposure, neutron density and mass density have been calculated from the bulk SiC measurements (Richter 1995; Hoppe and Ott 1997). In this approach, the neutron exposure τ_0 inferred from the $^{138}\text{Ba}/^{136}\text{Ba}$ ratio in bulk SiC as well as in SiC grain size fractions is distinct from the one that characterizes the solar system abundance distribution ($0.14\text{--}0.17\text{ mb}^{-1}$ vs. 0.30 mb^{-1} for $kT = 30\text{ keV}$). The difference largely persists even if the data are interpreted in the framework of a “more realistic” stellar model that takes into account changes in the physical parameters during thermal pulses in AGB stars (Gallino *et al* 1993).

Neutron density, temperature and mass density effect isotopic ratios, where branchings in the s-process occur, i.e. where there is effective competition between neutron capture and β -decay. Using the approach of the classical model, Richter (1995) has estimated from the Nd isotopic ratios (^{147}Nd branching) in bulk SiC the effective neutron density as $3.2 \times 10^8\text{ cm}^{-3}$, similar to what has been inferred from the normal (solar) abundance ratio of the s-only isotopes ^{148}Sm and ^{150}Sm (Wisshak *et al* 1993). An interesting case is that of ^{163}Dy , which is stable under normal conditions, but under stellar (plasma) conditions can decay into ^{163}Ho via bound-state β -decay (Takahashi and Yokoi 1987; Jung *et al* 1992). Based on the electron-density and temperature dependency of the decay rate given by Takahashi and Yokoi (1987) and using “standard” values for temperature and neutron density in the classical approach, Richter (1995) has estimated from his data for the ^{163}Dy branching in bulk SiC samples the electron density. The result implies an upper

limit for the mass density at the s-process site of $3.3 \times 10^3 \text{ g/cm}^{-3}$.

On a general level, the isotopic ratios inferred for the s-process components in bulk or grain size separated bulk samples of SiC follow the “classical model” for the main component of the s-process (Clayton 1983; Käppeler *et al* 1989). Some deviations have been noted in early work (Ott and Begemann 1990; Richter *et al* 1992, 1993; Prombo *et al* 1993), but to a large extent seem to have been caused by errors in the measured neutron capture cross sections (Gallino *et al* 1993; Hoppe and Ott 1997; Zinner 1997). They have largely disappeared in cases where these have been re-measured (Wisshak *et al* 1993; Voss *et al* 1994; Toukan *et al* 1995).

Questions remain, on a more refined level, however. In the case of Nd, as an example, the latest cross section measurements have largely eliminated the earlier discrepancies between model predictions and compositions derived from SiC measurements (up to more than 40%; Richter *et al* 1993), and both sets of data now claim an accuracy on the order of per cent. On that level, discrepancies do remain, as shown in figure 4, where the s-process endpoint of mixing lines defined by different measurements (Richter *et al* 1993) clearly misses the model predictions both of the classical and the stellar model approach (Gallino 1997, pers. comm.). It has been suggested (Hoppe and Ott 1997) that we are not dealing with a simple two-component system in the case of the measured compositions and the situation may be complex with contributions from the s-process (G component), matter of normal composition (solar system material in the “bulk” samples) and AGB star envelope material (N component), with the composition of the latter not really known. However, this does not solve the puzzle. As current understanding of heavy element nucleosynthesis goes, isotopes like ^{143}Nd , ^{144}Nd and ^{146}Nd contain contributions from only s- and r-process (not counting the minor p-process contributions). The isotopic ratios of these isotopes are well-defined for both components since none is affected by branchings, and hence all possible compositions can lie only on well defined mixing lines between s- and r-Nd (including “normal” Nd and also Nd-N, which are just two cases of specific s/r mixing ratios). As a result, the discrepancies between predictions and measurements must have their origin in problems with either the cross section or SiC grain measurements or in our understanding of basic heavy element nucleosynthesis.

Farther-reaching information than via “bulk SiC” measurements can be obtained via the analysis of single SiC grains (Nicolussi *et al* 1997; 1998a; 1998b), and the available data show large variations both in the composition of the s-process components where their composition is influenced by branchings as well as in the extent of mixing of s-process material with unprocessed envelope material. The Mo data

(Nicolussi *et al* 1998a) largely reflect the latter effect. As far as the Zr data (Nicolussi *et al* 1997) are concerned, their interpretation is complicated by the fact that there is no truly pure r- or p-isotope, from the abundance of which to unequivocally infer the extent of mixing. The abundance of ^{96}Zr , which is traditionally a pure r-isotope, but can be made in the s-process at high neutron densities (branching at ^{95}Zr with $t_{1/2} = 64\text{d}$), records both mixing and the effective neutron density, which both enter in the stellar model calculations and are difficult to disentangle. It is clear from the data, however, that some grains show extreme ^{96}Zr depletions which are not predicted to occur by the stellar model. The most interesting element for the description of the s-process for which single grain data exist at present is strontium, however, where the $^{88}\text{Sr}/^{86}\text{Sr}$ abundance ratio traces the branching at ^{85}Kr . Compared to bulk and grain size separate analyses (Prombo *et al* 1992; Podosek *et al* 1998) the single grain data (Nicolussi *et al* 1998b) show much larger variations in $^{88}\text{Sr}/^{86}\text{Sr}$, but as in the case of ensembles of grains, $^{87}\text{Sr}/^{86}\text{Sr}$ in the single grains analyzed so far is indistinguishable from the normal isotopic ratio.

3.3 Age of interstellar SiC

The abundances of nuclides produced by cosmic-ray induced spallation reactions should enable us to derive an age for presolar grains. This has been pioneered by Tang and Anders (1988) who recognized that spallation on the abundant target element silicon should lead to a noticeable enhancement of the rare Ne isotope ^{21}Ne . Based on their approach the latest Ne data for interstellar SiC yield presolar ages between 10 and 130 Ma, increasing with grain size (Lewis *et al* 1994). But there are a number of assumptions that enter into this approach (Hoppe and Ott 1997): the exact composition of the base Ne-E(H) to which spallation Ne would be added, the production rate for ^{21}Ne in the interstellar medium (itself a function of the flux and spectrum of galactic cosmic rays), the possibility of a dilution effect (Lewis *et al* 1994) and the exact amount of recoil loss of spallation Ne produced in μm -sized grains. Recent experiments (Ott and Begemann 1997) indicate that such loss could approach 100%. These authors suggest that the variations in Ne composition observed between different grain size separates (Lewis *et al* 1990, 1994) have a nucleo-synthetic rather than spallogenic origin, but they also point to the possibility that more reliable ages could be obtained via spallogenic ^{126}Xe produced on abundantly present Ba and REE.

4. Presolar diamond

Diamond, the nominally most abundant identified presolar phase in meteorites (table 1), was the first for

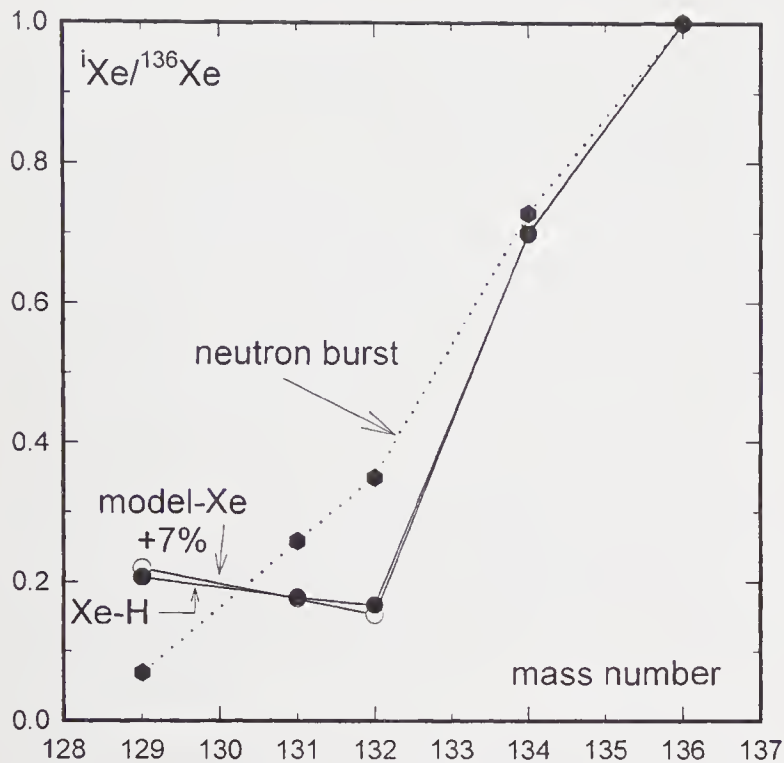


Figure 5. Comparison of the composition of Xe-H (Huss and Lewis 1994a, filled circles) with predictions of the neutron burst model (Howard *et al* 1992, dotted line with filled diamonds) and the early separation model (Ott 1996, open circles). Xe of the early separation model consists of “average” r-process xenon separated after about 2 hours from precursors yet to decay into Xe isotopes, with an admixture of 7% (at ^{136}Xe) of fully developed r-Xe.

which there was a hint in the form of the anomalous Xe-HL component (Reynolds and Turner 1964) and it was the first presolar phase in meteorites that was actually identified (Lewis *et al* 1987). Nevertheless, it is still the most enigmatic, a fact that may be caused by its low trace element content and by our inability to analyze individual diamond grains, which consist of only a few thousand atoms each. For this reason we cannot even be sure what fraction of the diamonds really is presolar (see section 1).

4.1 Isotopic features

As a whole, carbon in meteoritic nanodiamond is isotopically normal ($^{12}\text{C}/^{13}\text{C} \sim 92$), and, while nitrogen has a $^{14}\text{N}/^{15}\text{N}$ ratio that is ca. 50% higher than solar, until very recently the noble gases were the only elements with clearly identified unusual isotopic features of, in all likelihood, nucleosynthetic origin. Most conspicuous is Xe-HL, with about a factor of two enhancements of the light (p-process only) and heavy (r-process only) isotopes (Huss and Lewis 1994a). Puzzling are two facts: a) the close association of the excesses in the light and heavy isotopes and b) the exact ratio of the excesses in the various isotopes: neither do the p-only isotopes ^{124}Xe and ^{126}Xe occur in the “average” p-process ratio as defined by the solar system abundances, nor do excess ^{134}Xe and ^{136}Xe (as well as the excesses in $^{129,131,132}\text{Xe}$) occur in the

“average” r-process ratio (Ott 1996) – otherwise ^{134}Xe and ^{136}Xe would show the same relative enhancement and also ^{124}Xe and ^{126}Xe would show equal enhancements. A “neutron burst” occurring in a supernova (Heymann and Dziczkaniec 1979; Clayton 1989; Howard *et al* 1992) has long been considered the most likely source of the heavy isotope enrichment, but the agreement between predicted Xe compositions from that model and observations has been poor (Ott 1996; figure 5). An alternative model has been suggested (Ott 1996) because of this, among other things, which suggests that within hours after termination of an “average” r-process, before complete decay of the radioactive precursors from the process into stable end products, an early separation occurred. With the addition of a few per cent of fully decayed precursors, the model provides an exact match to the Xe-H spectrum (figure 5; Ott 1996). The model also successfully predicts the observed virtual absence of Ba-H ($\text{Ba-H}/\text{Xe-H} < 10^{-3}$; Lewis *et al* 1991). Further support for the model may come from new analyses of tellurium in diamond separates (Richter *et al* 1998), where a component has been identified that – as predicted – consists of virtually ^{128}Te and ^{130}Te only. However, the two isotopes do not occur in the predicted ratio, which has led to the suggestion that the idea of an “average r-process source” may have to be abandoned (Richter *et al* 1998). In addition, it is not at all apparent that any of the three possible separation processes discussed would work on the required time scale after the explosion of a supernova (see discussion in: Ott 1996; Richter *et al* 1998). A further important observation which may tell us about the origin of the anomalies (Cameron 1998) is the apparent absence of an enhancement of p-process-only ^{120}Te , so apparently, unlike in Xe, there is no “L component” accompanying Te-H.

4.2 New studies of gas release properties

Xe-HL is not the only xenon component present in separates of presolar diamonds. Two additional components have been identified (Huss and Lewis 1994a): Xe-P3 released at lower temperature than Xe-HL and Xe-P6 released at higher temperature (each, as Xe-HL, accompanied by characteristic components in the other noble gases). Extending previous detailed work on meteoritic diamonds from various meteorites (Huss *et al* 1994a; 1994b), we are currently in the process of detailed studies of gas release profiles from nanodiamonds from the Murchison meteorite and comparison with artificial nanodiamonds, hoping to learn more about the actual siting of the gases in the diamonds and hoping this might also tell us something about the diamonds proper. Below is a short summary and at times speculative interpretation of preliminary results.

First, similar to previously reported observations (Verchovsky and Pillinger 1994) in vacuum pyrolysis we observe a low temperature release of volatiles besides the noble gases, primarily CO, accompanying the release of Xe-P3 and accounting for about 15% of total diamond C (Zadnik and Ott 1998). Second, in our experiments gas release is found to be virtually identical in vacuum and in hydrogen atmospheres of 0.1 and 1000 mbar (Zadnik and Ott 1998; in oxygen, of course the diamonds combust), which confirms earlier conclusions (Huss and Lewis 1994b) that the release of P3 gases does not significantly depend on the nature of the surroundings.

Third, the release of xenon implanted into artificial nanodiamonds as low energy ions with energies of 250 eV and 1.2 keV is very similar to the release of the P3 component (Zadnik and Ott 1998; Koscheev *et al* 1998) and its temperature dependence can be described by the formalism developed for volume diffusion or by a “chemical erosion model” (where the grains are eroded starting from the outside; cf. Reynolds *et al* 1978) with activation energies of 1.2 eV and 0.5 eV (Koscheev *et al* 1998), respectively. Since the range of the ions in the implantation experiment is about the size of the diamonds, it is concluded that the implanted Xe is probably not surface- but rather volume-sited (Koscheev *et al* 1998). By analogy, this would then hold for the P3 component, too. If true, it seems unlikely that Xe-HL and Xe-P6 could be contained in the same type of grains as Xe-P3. More likely all those components differ not in the type of location within their carrier (as advocated, e.g., by Huss and Lewis 1994b) but rather in the type of their carriers, may they be different types of diamonds or different phases altogether. Given that there is only one Xe atom per several millions of diamond grains, there is ample room for different carriers in the diamond separates, provided they meet the physical and chemical criteria characteristic of the diamonds: acid resistance, combustibility and small size. An interesting observation during the gas release experiments (Zadnik and Ott, unpublished) is that the Xe-HL carrier seems more difficult to combust after being first pyrolyzed to 1200°C.

The abundance in and release from nanodiamonds of P3 gases may be our best handle on the temperature history of these objects. Our approach (Koscheev *et al* 1998; Zadnik and Ott 1998) differs, however, from that of Huss and Lewis (1994b). While these authors conclude that the abundance in nanodiamonds of P3 gases is a function of the maximum temperature they experienced (only), we conclude from the fact that the gas release data nicely plot on Arrhenius plots, that combinations of temperature and time are recorded. If this can be confirmed, a useful property of this thermometer/chronometer is the relative independence of environmental conditions (unless oxidizing) and the comparably low activation

energy (Zadnik and Ott 1998) which facilitates extrapolation from laboratory data to relevant temperatures. For example, a preliminary estimate based on this approach and assuming that Murchison diamonds still contain 90% of their initial endowment of Xe-P3, suggests that they cannot have been exposed to temperatures higher than 100°C for more than $\sim 10^3$ years – or some equivalent combinations of temperature and time (Zadnik and Ott 1998). The same limit probably applies to the host meteorite itself, given the fact that – like presolar SiC (Alexander *et al* 1990) – the individual diamonds are distributed in the meteorites rather homogeneously (Banhart *et al* 1998).

5. Concluding remarks

Carbon, the structural element of most of the surviving presolar grains identified in meteorites, and all heavier elements are the products of nucleosynthesis in stars. It is important to note that the interstellar material from which the solar system formed, must have had contributions from a variety of stellar sources, with the sum of these contributions yielding the composition that we define as “normal”. The “safe” identification via large isotope abundance anomalies thus will not identify presolar grains that show isotopic signatures typical at the time and location of solar system formation. What we do identify rather are “circumstellar” grains that formed from a single stellar source and the isotopic composition of which is dominated by (a) special process(es) of nucleosynthesis.

While this may be a reason that no additional presolar grain types have yet been identified, another may be that – following the lead of the isotopically anomalous noble gases – only acid-resistant phases have been isolated so far: diamond, SiC and graphite as actual carriers of these gases and corundum and silicon nitride by the pure chance that they too are chemically resistant and ended up in the same separates as did presolar silicon carbide. It has been rightly noted (Nittler 1997) that in the identified presolar grains there is a surprising lack relative to the carbonaceous phases of presolar silicates/oxides. *In situ* search for silicates has been unsuccessful so far, but, apart from the fact that even in the most primitive meteorites silicates may have largely a solar system origin, this may be a problem related to small grain sizes and progress along these lines will have to await the advent of a new generation of ion microprobes with higher spatial resolution (Zinner 1997). In the meantime, another promising approach to tracing down acid-soluble presolar grains – currently employed in the search for the carrier of excess ^{54}Cr in primitive meteorites – may be that of stepwise dissolution of minerals and analysis of the

solutions (Rotaru *et al* 1992; Podosek *et al* 1997; Ott *et al* 1997).

Acknowledgements

My thanks go to Peter Hoppe, who provided figures 1 and 2; to Roberto Gallino for providing unpublished calculations of s-process Nd; and to Gary Huss and Larry Nittler for constructive reviews.

References

- Alexander C M O' D 1993 Presolar SiC in chondrites: how variable and how many sources?; *Geochim. Cosmochim. Acta* **57** 2869–2888
- Alexander C M O' D, Swan P and Walker R M 1990 *In situ* measurement of interstellar silicon carbide in two CM chondrite meteorites; *Nature* **348** 715–717
- Amari S and Zinner E 1997 Supernova grains from meteorites; in *Astrophysical Implications of the Laboratory Study of Presolar Materials*, (eds) T J Bernatowicz and E Zinner (AIP Conf. Proc 402) pp. 287–305
- Amari S, Anders E, Virag A and Zinner E 1990 Interstellar graphite in meteorites; *Nature* **345** 238–240
- Amari S, Hoppe P, Zinner E and Lewis R S 1992, Interstellar SiC with unusual isotopic compositions: grains from a supernova?; *Astrophys. J.* **394** L43–L46
- Amari S, Hoppe P, Zinner E and Lewis R S 1993 The isotopic compositions and stellar sources of meteoritic graphite grains; *Nature* **365** 806–809
- Amari S, Lewis R S and Anders E 1995 Interstellar grains in meteorites: III. Graphite and its noble gases; *Geochim. Cosmochim. Acta* **59** 1411–1426
- Amari S, Zinner E and Lewis R S 1996a ^{41}Ca in presolar graphite of supernova origin; *Astrophys. J.* **470** L101–L104
- Amari S, Zinner E and Lewis R S 1996b Ca and Ti isotopic compositions of size-separated SiC fractions from the Murchison meteorite; *Lunar Planet. Sci.* **27** 23–24
- Banhart F, Lyutovich Y, Braatz A, Jäger C, Henning T, Dorschner J and Ott U 1998 Presolar diamond in unprocessed Allende; *Meteoritics Planet. Sci.* **33** (Suppl.) A12
- Begemann F 1993 Isotope abundance anomalies and the early solar system: MuSiC vs. FUN; in *Origin and Evolution of the Elements* Cambridge University Press, pp. 517–526
- Bernatowicz T J and Zinner E (eds) 1997 *Astrophysical Implications of the Laboratory Study of Presolar Materials* (AIP Conf. Proc. 402) pp. 750
- Bernatowicz T, Fraundorf G, Tang M, Anders E, Wopenka B, Zinner E and Fraundorf P 1987 Evidence for interstellar SiC in the Murray carbonaceous meteorite; *Nature* **330** 728–730
- Black D C and Pepin R O 1969 Trapped neon in meteorites – II; *Earth Planet. Sci. Lett.* **6** 395–405
- Boothroyd A I, Sackmann I-J and Wasserburg G J 1994 Predictions of oxygen isotope ratios in stars and of oxygen-rich interstellar grains in meteorites; *Astrophys. J.* **430** L77–L80
- Boothroyd A I, Sackmann I-J and Wasserburg G J 1995 Hot bottom burning in asymptotic giant branch stars and its effect on oxygen isotopic abundances; *Astrophys. J.* **442** L21–L24
- Brown L E and Clayton D D 1992 SiC particles from asymptotic giant branch stars: Mg burning and the s-process; *Astrophys. J.* **392** L79–L82
- Cameron A G W 1998 Two cradles for the heavy elements; *Nature* **391** 228–231
- Choi B-G, Huss G R and Wasserburg G J 1998 Oxygen, magnesium, calcium, and titanium isotopes in asymptotic giant branch and supernova oxides; *Meteoritics Planet. Sci.* **33** (Suppl.) A32
- Clayton D D 1983 Principles of stellar evolution and nucleosynthesis; (Chicago, USA: The University of Chicago Press), pp. 612
- Clayton D D 1989 Origin of heavy xenon in meteoritic diamonds; *Astrophys. J.* **340** 613–619
- Gallino R, Busso M, Picchio G and Raiteri C M 1990 On the astrophysical interpretation of isotope anomalies in meteoritic silicon carbide grains; *Nature* **348** 298–302
- Gallino R, Raiteri C M and Busso M 1993 Carbon stars and isotopic Ba anomalies in meteoritic SiC grains; *Astrophys. J.* **410** 400–411
- Gallino R, Raiteri C M, Busso M and Matteucci F 1994 The puzzle of silicon, titanium, and magnesium anomalies in meteoritic silicon carbide grains; *Astrophys. J.* **430** 858–869
- Gallino R, Busso M and Lugaro M 1997 Neutron capture nucleosynthesis in AGB stars; in *Astrophysical Implications of the Laboratory Study of Presolar Materials*, (eds) T J Bernatowicz and E Zinner (AIP Conf. Proc 402) pp. 115–153
- Görres J, Meißner J, Schatz H, Stech E, Tischhauser P, Wiescher M, Bazin D, Harkewicz R, Hellström M, Sherrill B, Steiner M, Boyd R N, Buchmann L, Hartmann D H and Hinnefeld J D 1998 Half-life of ^{44}Ti as a probe for supernova models; *Phys. Rev. Lett.* **80** 2554–2557
- Heymann D and Dziczkaniec M 1979 Xenon from intermediate zones of supernovae; *Proc. Lunar Planet. Sci. Conf.* **10** 1943–1959
- Hoppe P and Ott U 1997 Mainstream silicon carbide grains from meteorites; in *Astrophysical Implications of the Laboratory Study of Presolar Materials*, (eds) T J Bernatowicz and E Zinner (AIP Conf. Proc 402) pp. 27–58
- Hoppe P, Amari S, Zinner E, Ireland T and Lewis R S 1994 Carbon, nitrogen, magnesium, silicon, and titanium isotopic compositions of single interstellar silicon carbide grains from the Murchison carbonaceous chondrite; *Astrophys. J.* **430** 870–890
- Hoppe P, Amari S, Zinner E and Lewis R S 1995 Isotopic compositions of C, N, O, Mg, and Si, trace element abundances, and morphologies of single circumstellar graphite grains in four density fractions from the Murchison meteorite; *Geochim. Cosmochim. Acta* **59** 4029–4056
- Hoppe P, Strebel R, Eberhardt P, Amari S and Lewis R S 1996 Type II supernova matter in a silicon carbide grain from the Murchison meteorite; *Science* **272** 1314–1316
- Howard W M, Meyer B S and Clayton D D 1992 Heavy-element abundances from a neutron burst that produces Xe-H; *Meteoritics* **27** 404–412
- Huss G R 1997 The survival of presolar grains in solar system bodies; in *Astrophysical Implications of the Laboratory Study of Presolar Materials* (eds) T J Bernatowicz and E Zinner (AIP Conf. Proc 402) pp. 721–748
- Huss G R and Lewis R S 1994a Noble gases in presolar diamonds I: Three distinct components and their implications for diamond origins; *Meteoritics* **29** 791–810
- Huss G R and Lewis R S 1994b Noble gases in presolar diamonds II: Component abundances reflect thermal processing; *Meteoritics* **29** 811–829
- Huss G R, Hutcheon I D, Wasserburg G J and Stone J 1992 Presolar (?) corundum in the Orgueil meteorite; *Lunar Planet. Sci.* **23** 563–564
- Huss G R, Hutcheon I D and Wasserburg G J 1997 Isotopic systematics of presolar silicon carbide from the Orgueil (CI) chondrite: implications for solar system formation and stellar nucleosynthesis; *Geochim. Cosmochim. Acta* **61** 5117–5148
- Hutcheon I D, Huss G R, Fahey A J and Wasserburg G J 1994 Extreme ^{26}Mg and ^{17}O enrichments in an Orgueil corundum: identification of a presolar oxide grain; *Astrophys. J.* **425** L97–L100

- Jung M, Bosch F, Beckert K, Eickhoff H, Folger H, Franzke B, Gruber A, Kienle P, Klepper O, Koenig W, Kozuharov C, Mann R, Moshhammer R, Nolden F, Schaaf U, Soff G, Spädtke P, Steck M, Stöhlker Th and Sümmerer K 1992 First observation of bound-state β -decay; *Phys. Rev. Lett.* **69** 2164–2167
- Käppeler F, Beer H and Wisshak K 1989 S-process nucleosynthesis – nuclear physics and the classical model; *Rep. Prog. Phys.* **52** 945–1013
- Käppeler F, Gallino R, Busso M, Picchio G and Raiteri C M 1990 S-process nucleosynthesis: classical approach and asymptotic giant branch models for low-mass stars; *Astrophys. J.* **354** 630–643
- Koscheev A P, Gromov M D, Herrmann S and Ott U 1998 Mass fractionation and thermal release from nanodiamonds of low-energy implanted xenon; *Meteoritics Planet. Sci.* **33** (Suppl.) A87–A88
- Lattanzio J C and Boothroyd A I 1997 Nucleosynthesis of elements in low to intermediate mass stars through the AGB phase; in *Astrophysical Implications of the Laboratory Study of Presolar Materials* (eds) T J Bernatowicz and E Zinner (AIP Conf. Proc 402) pp. 85–114
- Lewis R S, Tang M, Wacker J F, Anders E and Steel E 1987 Interstellar diamonds in meteorites; *Nature* **326** 160–162
- Lewis R S, Amari S and Anders E 1990 Meteoritic silicon carbide: pristine material from carbon stars; *Nature* **348** 293–298
- Lewis R S, Huss G R and Lugmair G 1991 Finally, Ba & Sr accompanying Xe-HL in diamonds from Allende; *Lunar Planet. Sci.* **22** 807–808
- Lewis R S, Amari S and Anders E 1994 Interstellar grains in meteorites: II. SiC and its noble gases; *Geochim. Cosmochim. Acta* **58** 471–494
- MacPherson G J, Davis A M and Zinner E K 1995 The distribution of aluminum-26 in the early solar system – a reappraisal; *Meteoritics* **30** 365–386
- Nichols R H Jr, Kehm K, Brazzle R, Amari S, Hohenberg C M and Lewis R S 1994 Ne, C, N, O, Mg, and Si isotopes in single interstellar graphite grains: multiple stellar sources for Neon E(L); *Meteoritics* **29** 510–511
- Nicolussi G K, Davis A M, Pellin M J, Lewis R S, Clayton R N and Amari S 1997 s-process zirconium in presolar silicon carbide grains; *Science* **277** 1281–1283
- Nicolussi G K, Pellin M J, Lewis R S, Davis A M, Amari S and Clayton R N 1998a Molybdenum isotopic composition of individual presolar silicon carbide grains from the Murchison meteorite; *Geochim. Cosmochim. Acta* **62** 1093–1104
- Nicolussi G K, Pellin M J, Lewis R S, Davis A M, Clayton R N and Amari S 1998b Strontium isotopes in single presolar silicon carbide grains; *Meteoritics Planet. Sci.* **33** (Suppl.) A116–A117
- Nittler L R 1997 Presolar oxide grains in meteorites; in *Astrophysical Implications of the Laboratory Study of Presolar Materials* (eds) T J Bernatowicz and E Zinner (AIP Conf. Proc 402) pp. 59–82
- Nittler L R and Cowsik R 1997 Galactic age estimates from O-rich stardust in meteorites; *Phys. Rev. Lett.* **78** 175–178
- Nittler L R, Hoppe P, Alexander C M O 'D, Amari S, Eberhardt P, Gao X, Lewis R S, Strebel R, Walker R M and Zinner E 1995 Silicon nitride from supernovae; *Astrophys. J.* **453** L25–L28
- Nittler L R, Amari S, Zinner E, Woosley S E and Lewis R S 1996 Extinct ^{44}Ti in presolar graphite and SiC: proof of a supernova origin; *Astrophys. J.* **462** L31–L34
- Nittler L R, Alexander C M O 'D, Gao X, Walker R M and Zinner E 1997 Stellar sapphires: the properties and origins of presolar Al_2O_3 in meteorites; *Astrophys. J.* **483** 475–495
- Nittler L R, Alexander C M O 'D, Wang J and Gao X 1998 Meteoritic oxide grain from supernova found; *Nature* **393** 222
- Ott U 1996 Interstellar diamond xenon and timescales of supernova ejecta; *Astrophys. J.* **463** 344–348
- Ott U and Begemann F 1990 Discovery of s-process barium in the Murchison meteorite; *Astrophys. J.* **353** L57–L60
- Ott U and Begemann F 1997 Spallation recoil and the age of presolar meteorite grains; *Meteoritics Planet. Sci.* **32** A102–A103
- Ott U, Begemann F, Yang J and Epstein S 1988 s-process krypton of variable isotopic composition in the Murchison meteorite; *Nature* **332** 700–702
- Ott U, Specht S and Podosek F A 1997 An exploratory ion probe search for ^{54}Cr -rich grains in Orgueil; *Lunar Planet. Sci.* **28** 1053–1054
- Podosek F A, Ott U, Brannon J C, Neal C R, Bernatowicz T J, Swan P and Mahan S E 1997 Thoroughly anomalous chromium in Orgueil; *Meteoritics Planet. Sci.* **32** 617–627
- Podosek F A, Prombo C A, Amari S and Lewis R S 1998 s-process Sr isotopic compositions in presolar SiC from the Murchison meteorite; *Astrophys. J.* in press
- Prombo C A, Podosek F A, Amari S and Lewis R S 1992 s-process Sr and Ba in SiC from Murchison series KJ; *Lunar Planet. Sci.* **23** 1111–1112
- Prombo C A, Podosek F A, Amari S and Lewis R S 1993 s-process Ba isotopic composition in presolar SiC from the Murchison meteorite; *Astrophys. J.* **410** 393–399
- Reynolds J H and Turner G 1964 Rare gases in the chondrite Renazzo; *J. Geophys. Res.* **69** 3263–3281
- Reynolds J H, Frick U, Neil J M and Phinney D L 1978 Rare-gas-rich separates from carbonaceous chondrites; *Geochim. Cosmochim. Acta* **42** 1775–1797
- Richter S 1995 Massenspektrometrische Untersuchungen von interstellarer Materie und Bedingungen im s-Prozeß der Nukleosynthese (in German); Ph. D. thesis, Johannes Gutenberg-Universität, Mainz
- Richter S, Ott U and Begemann F 1992 s-process isotope anomalies: neodymium, samarium, and a bit more of strontium; *Lunar Planet. Sci.* **23** 1147–1148
- Richter S, Ott U and Begemann F 1993 s-process isotope abundance anomalies in meteoritic silicon carbide: new data; in *Nuclei in the Cosmos*, Proc. Sec. Int. Symp. on Nuclear Astrophysics (eds) F Käppeler und K Wisshak (Bristol, UK: IOP Publishing Ltd.) pp. 127–132
- Richter S, Ott U and Begemann F 1998 Tellurium in pre-solar diamonds as an indicator for rapid separation of supernova ejecta; *Nature* **391** 261–263
- Rotaru M, Birck J-L and Allègre C J 1992 Clues to early solar system history from chromium isotopes in carbonaceous chondrites; *Nature* **358** 465–470
- Srinivasan B and Anders E 1978 Noble gases in the Murchison meteorite: possible relics of s-process nucleosynthesis; *Science* **201** 51–56
- Takahashi K and Yokoi K 1987 Beta-decay rates of highly ionized heavy atoms in stellar interiors; *Atomic Data and Nuclear Data Tables* **36** 375–409
- Tang M and Anders E 1988 Interstellar silicon carbide: how much older than the solar system?; *Astrophys. J.* **335** L31–L34
- Timmes F X and Clayton D D 1996 Galactic evolution of silicon isotopes: application to presolar SiC grains from meteorites; *Astrophys. J.* **472** 723–741
- Toukan K A, Debus K, Käppeler F and Reffo G 1995 Stellar neutron capture cross sections of Nd, Pm, and Sm isotopes; *Phys. Rev.* **C51** 1540–1550
- Verchovsky A B and Pillinger C T 1994 Chemical reactions occurring during pyrolysis of presolar diamonds and release patterns of light nitrogen and noble gases; *Meteoritics* **29** 543–544

- Voss F, Wisshak K, Guber K, Käppeler F and Reffo G 1994 Stellar neutron capture cross section of the Ba isotopes; *Phys. Rev.* **C50** 2582–2601
- Wasserburg G J, Boothroyd A I and Sackmann J-I 1995 Deep circulation in red giant stars: a solution to the carbon and oxygen isotope puzzles?; *Astrophys. J.* **447** L37–L40
- Wisshak K, Guber K, Voss F and Käppeler F 1993 Neutron capture in $^{148,150}\text{Sm}$: a sensitive probe of the s-process neutron density; *Phys. Rev.* **C48** 1401–1419
- Zadnik M G and Ott U 1998 Studies of (not only) noble gas release from presolar diamond; *Meteoritics Planet. Sci.* **33** (Suppl.) A170
- Zinner E 1997 Presolar material in meteorites: an overview; in *Astrophysical Implications of the Laboratory Study of Presolar Materials* (eds) T J Bernatowicz and E Zinner (AIP Conf. Proc 402) pp. 3–26
- Zinner E, Tang M and Anders E 1987 Large isotopic anomalies of Si, C, N and noble gases in interstellar silicon carbide from the Murray meteorite; *Nature* **330** 730–732
- Zinner E, Amari S, Wopenka B and Lewis R S 1995 Interstellar graphite in meteorites: isotopic compositions and structural properties of single graphite grains from Murchison; *Meteoritics* **30** 209–226

The triggered origin of the solar system

HARRI A T VANHALA

*Department of Terrestrial Magnetism, Carnegie Institution of Washington, 5241 Broad Branch Road NW,
Washington DC 20015-1305, USA
e-mail: harri@dtm.ciw.edu*

The scenario of the triggered origin of the solar system suggests that the formation of our planetary system was initiated by the impact of an interstellar shock wave on a molecular cloud core. The strength of this scenario lies in its ability to explain the presence of short-lived radionuclides in the early solar system. According to the proposal, the radioactivities were produced in a stellar source, transported into the molecular cloud core by a shock wave and mixed into the collapsing system during the interaction between the shock wave and the core. We examine the viability of the scenario by presenting results from recent numerical simulations. The calculations show that molecular cloud cores can be triggered into collapse by the impact of a shock wave propagating at the velocity of $10\text{--}45\text{ km s}^{-1}$. Some of the shock wave material incident on the core, typically 10–20%, can be injected into the collapsing system. The time scale of the process is $\sim 10^4\text{--}10^5$ years, sufficiently short for the survival of the short-lived radioactivities. The simulations therefore confirm the viability of the scenario of the triggered origin of the solar system.

1. Introduction

Studies of primitive meteoritic material have revealed the presence of short-lived radioactivities in the early solar system. In the last few years, the group of short-lived radionuclides detected in meteorites has grown to include ^{26}Al , ^{36}Cl , ^{41}Ca , ^{53}Mn , ^{60}Fe , ^{107}Pd , ^{129}I , ^{182}Hf , and ^{244}Pu (see reviews by Cameron 1993, Wasserburg *et al* 1994, and Podosek and Nichols 1997). The mean lifetimes of the isotopes range from 1.5×10^5 years (^{41}Ca) to 1.18×10^8 years (^{244}Pu). Particularly important for our present discussion are the shortest-lived (half-life < 10 Ma) of these isotopes, especially ^{41}Ca and ^{26}Al . Their presence in the early solar system requires their introduction into the presolar material at most 1 Ma before their incorporation into the meteoritic inclusions.

The short time interval has led to the idea of the triggered origin of the solar system (Cameron and Truran 1977; Cameron 1993; Wasserburg *et al* 1994; Boss 1995; Cameron *et al* 1995, 1997; Boss and Foster 1997). According to this scenario, the radioactivities

were produced in stellar interiors and transported to the molecular cloud core by an interstellar shock wave. The shock wave triggered the collapse of the core and deposited freshly synthesized radioactivities into the system. Possible stellar sources of radioactivities include supernovae (Cameron *et al* 1995, 1997), AGB stars (Cameron 1993; Wasserburg *et al* 1994), novae (Gehrz *et al* 1993) and Wolf-Rayet stars (Arnould *et al* 1997). The proposal for the triggered origin of the solar system is one aspect of the more general idea of assisted star formation (Elmegreen 1998).

Recent efforts to explain the presence of the short-lived radioactivities in the early solar system by local production through irradiation of molecular cloud or solar nebula material by energetic particles (Clayton and Jin 1995a, 1995b; Shu *et al* 1996, 1997) have encountered difficulties (Bateman *et al* 1996; Clayton and Jin 1995b; Ramaty *et al* 1996; Sahijpal *et al* 1998), and external seeding of the radionuclides remains an attractive explanation. The viability of the triggered origin scenario can be explored through

Keywords. Hydrodynamics; ISM; molecular clouds; shock waves; solar system; stars formation; short-lived radionuclides.

numerical simulations: by studying the processes involved in the impact of an interstellar shock wave on a molecular cloud core, the probability of assisted collapse can be estimated. In the following, we shall describe the numerical studies examining the issue and provide a synthesis of the main results. We are especially interested in addressing the following questions:

- Can the collapse of a molecular cloud core be induced by the impact of an interstellar shock wave?
- Is the time scale of the process sufficiently short for the survival of the radioactivities?
- Can radioactivities carried by the shock wave be injected into the collapsing system?

These questions will be addressed in sections 2, 3, and 4, respectively. Section 5 discusses other aspects of triggered star formation, while section 6 summarizes the results and discusses future directions.

2. Triggered collapse of molecular cloud cores

The key issue in the examination of the viability of the triggered origin scenario is to determine whether shock waves can cause molecular cloud cores to collapse. In addition to being crucial for the discussion of the origin of the solar system, the possibility of assisted collapse may have important consequences for the general star formation theory (Elmegreen 1998). Interstellar space is a violent, evolving place, and it is important to know whether interstellar shock waves are generally destructive or whether they can assist in the star formation process.

The early simulations of the interaction between shocks and molecular clouds were principally concerned with high-velocity (supernova) shock waves impacting molecular clouds or traveling through ambient interstellar material (Nittman *et al* 1982; Heathcote and Brand 1983; Krebs and Hillebrandt 1983; Różycka and Tenorio-Tagle 1987; Bedogni and Woodward 1990; Stone and Norman 1992; Klein *et al* 1994; Mac Low *et al* 1994; Xu and Stone 1995). The studies employed a variety of simulation methods and used both two-dimensional (2D) and three-dimensional (3D) codes. The basic result of these studies is the complete destruction of the clouds by Rayleigh-Taylor (RT) and Kelvin-Helmholtz (KH) instabilities created at the contact surface between the shock wave and the cloud. The fragmentation of the clouds was found to occur at all scales, down to the resolution of the code (Klein *et al* 1994). The clouds were typically destroyed in a few cloud crushing times t_{cc} , where t_{cc} determines the time for the shock wave to cross through the cloud. It is defined as $t_{cc} \equiv (\chi_{icm})^{1/2} R_c / v_{shock}$, where χ_{icm} is the ratio of the cloud density to the density of the intercloud medium, R_c is the radius

of the cloud and v_{shock} is the velocity of the shock wave (Klein *et al* 1994). Strong magnetic fields may be able to prevent the cloud from being completely destroyed (Mac Low *et al* 1994), but this avenue has not been fully explored.

Since the high-velocity shock wave calculations did not include self-gravity, the results are not directly applicable to the question of triggered collapse. Instead, they are useful in describing cloud shredding by high-velocity shock waves, such as in observed supernova remnants, and discussing the instabilities created during the interaction between a shock wave and a molecular cloud.

The problem of triggered collapse has been addressed directly by recent studies using three-dimensional hydrocode calculations (Boss 1995), two-dimensional piecewise-parabolic method (PPM) simulations (Foster and Boss 1996, 1997; Boss and Foster 1998), and three-dimensional smoothed particle hydrodynamics (SPH) calculations (Cameron *et al* 1997; Vanhala and Cameron 1998). These studies concentrated on moderately slow ($10\text{--}50\text{ km s}^{-1}$) shock waves impacting centrally condensed, self-gravitating molecular cloud cores. The cores had Gaussian, Bonnor-Ebert or relaxed power-law density profiles, while their masses ranged from 1 to 10 solar masses and their radii from ~ 0.05 to $\sim 0.2\text{ pc}$.

Apart from the simulation methods themselves, the calculations also differed in their choice of thermodynamics. The hydrocode and the PPM calculations employed either an isothermal or an adiabatic equation of state, while the SPH calculations used a method called variable γ thermodynamics (Vanhala and Cameron 1998). In this equation of state solver, pressure and specific internal energy are calculated at a desired density and temperature, and the derivatives of thermodynamic quantities are derived from these properties. As a result, the adiabatic exponent γ ($[d\log P/d\log \rho]_{ad}$) does not have a single value but varies as a function of density and temperature (figure 1). At the typical molecular cloud temperature of 10 K and density of $10^{-21}\text{ g cm}^{-3}$, the value of γ is $5/3$, but as the temperature rises and molecules and atoms are excited, dissociated and ionized, its value changes between 1 and $5/3$. The SPH code also included cooling due to molecules, atoms and dust, as well as magnetic effects through magnetic pseudo-fluid.

The basic result of the simulations is that the molecular clouds can be triggered into collapse if the momentum of the shock wave is sufficient to compress the core to the point of collapse, but not so high that it will tear the cloud apart. Foster and Boss (1996) found that the critical momentum, which divides the cases which induce collapse and those which do not, is $0.1 M_{\odot} \text{ km s}^{-1}$ for a 10 K, $1 M_{\odot}$ cloud, and that it scales as the mass of the cloud times its sound speed.

If the properties of the shock wave are calculated from the Rankine-Hugoniot jump conditions (e.g.,

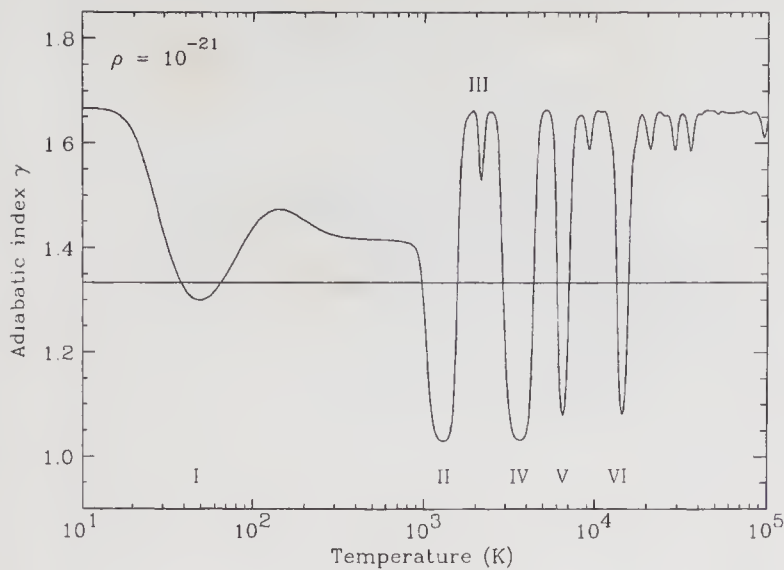


Figure 1. The adiabatic exponent γ as a function of temperature at the typical molecular cloud density of $10^{-21} \text{ g cm}^{-3}$. The major features are marked by Roman numerals I–VI, and they correspond to the excitation (I) and dissociation (II) of hydrogen molecules, the dissociation of CO molecules (III), the ionization of hydrogen atoms (IV), and the single (V) and double (VI) ionization of helium atoms. The smaller wiggles at high temperatures are due to multiple ionizations of C, N, and O atoms. The line at $\gamma = 4/3$ marks the boundary between stable ($\gamma > 4/3$) and unstable ($\gamma < 4/3$) systems. An equilibrium mix between the ortho and para states of hydrogen is assumed.

Draine and McKee 1993), the behavior of the system can be divided into three groups according to the shock velocity (Vanhala and Cameron 1998). During the impact of a low-velocity shock wave ($v_s < 20 \text{ km s}^{-1}$), the core is compressed by a factor of ~ 10 but it usually bounces back and is torn apart. Intermediate-velocity shocks ($20 \text{ km s}^{-1} < v_s < 45 \text{ km s}^{-1}$) compress and stretch the core and may cause it to collapse, while high-velocity shocks ($v_s > 45 \text{ km s}^{-1}$) destroy the core.

The 20 km s^{-1} velocity limit for successful triggering is due to the post-shock temperature becoming sufficiently high to destroy the principal coolants, molecular hydrogen and carbon monoxide, at this point (Cameron *et al* 1997). At velocities higher than this, the gas remains hot and the pressure exerted on the core is sufficient to compress it to the point of collapse. At lower velocities, the coolants survive, the post-shock flow cools efficiently and the pressure is usually insufficient to trigger collapse. Successful collapse in the variable γ SPH simulations is therefore achieved through the combined effect of momentum and post-shock gas pressure, while in the isothermal PPM calculations momentum alone is able to cause sustained collapse. The SPH calculations agree with the results of Woodward (1976), who discussed the importance of high post-shock pressure at the surface of the cloud in the context of cloud compression caused by spiral density waves.

Figure 2 shows a sequence of images leading to triggered collapse. The pre-impact core (figure 2a) has

a peak density of $7.35 \times 10^{-17} \text{ g cm}^{-3}$, with the core joining smoothly to the background gas in a bell-shaped density profile. The velocity of the approaching shock front is 25 km s^{-1} , resulting in a density jump of 22 and a post-shock temperature of 3650 K. Upon impact, the shock wave first compresses the core in a planar manner (figure 2b), then settles to a bow shock around the core (figure 2c). The facing side of the core is compressed further, while the material at the edges is stripped away (figure 2d). The core is finally stretched to a thin filament (figure 2e), the head of which goes into collapse, while the tail merges into the post-shock flow (figure 2f). The maximum density in the collapsing region at the end of the simulation is $1.72 \times 10^{-11} \text{ g cm}^{-3}$, 2.4×10^6 times the original core density.

The results of the simulations depend on the evolutionary stage of the pre-impact core. According to the SPH simulations, well-evolved cores (central density $> \text{a few } \times 10^{-17} \text{ cm}^{-3}$) can be triggered at lower velocities than less evolved cores, and they can also withstand higher shock speeds without being destroyed. The mass of the core has a similar effect: the most massive systems may be pushed to collapse by low-velocity shocks even if they are weakly evolved. The evolutionary stage of the core also influences the end result of triggered collapse. If the core is assumed to have evolved into its pre-impact state under the control of ambipolar diffusion, cores at later evolutionary stages have higher central densities and smaller radii at the time of impact. In this case, the result is the collapse of a single mass concentration. If the core is weakly evolved, the maximum density in the core is smaller and the radius larger. Upon impact, the compressed system may fragment and form a multiple star system.

Figure 3 shows the result of an SPH simulation run leading to the formation of a binary system. The central density in the pre-impact core (figure 3a) is $7.49 \times 10^{-19} \text{ g cm}^{-3}$, about one hundredth of the initial peak density in the case shown in figure 2. The velocity of the shock wave is 10 km s^{-1} , resulting in a density jump of 16 and a post-shock temperature of 1337 K. The shock wave compresses the massive ($\sim 20 M_\odot$) core rapidly to the point of collapse (figure 3b). As figure 3(c) shows, the core has fragmented during compression and formed two centers of collapse. Figure 3(d) shows the density profile along the line connecting the fragments and proves the binary nature of the system. The mass of the primary (the right-side clump in figure 3c) and the secondary (left) are 1.67 and 1.52 solar masses, respectively. This case is also an example of a very massive core being pushed to collapse by a low-velocity shock wave.

The outcome of the simulations is also sensitive to the thermodynamics employed. This is demonstrated by calculations using identical initial conditions and differing only in the value of the adiabatic exponent

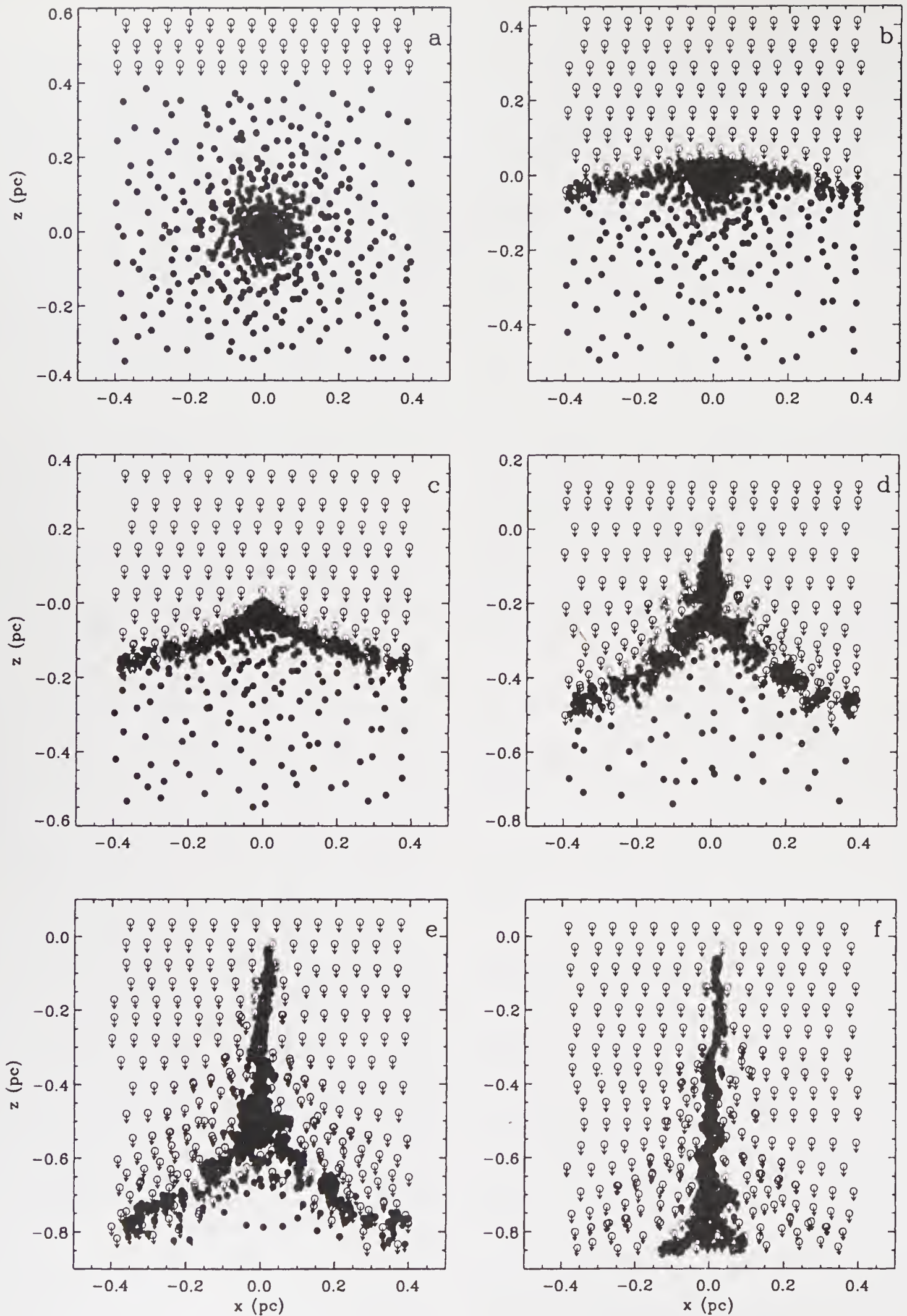


Figure 2. The interaction between the shock wave and the molecular cloud core in a 3D SPH simulation run with 4496 particles in the core (filled circles) and 7772 in the shock wave (open circles). The initial peak density in the core is $7.35 \times 10^{-17} \text{ g cm}^{-3}$. The shock approaches from the $+z$ direction with a velocity of 25 km s^{-1} . The system is shown in the xz plane with the units in parsecs. The different frames correspond to $t = 0$ years (a), 21,000 years (b), 27,000 years (c), 42,000 years (d), 57,000 years (e) and 70,000 years (f). The head of the filament in frame (f) is collapsing, and the peak density is $1.72 \times 10^{-11} \text{ g cm}^{-3}$.

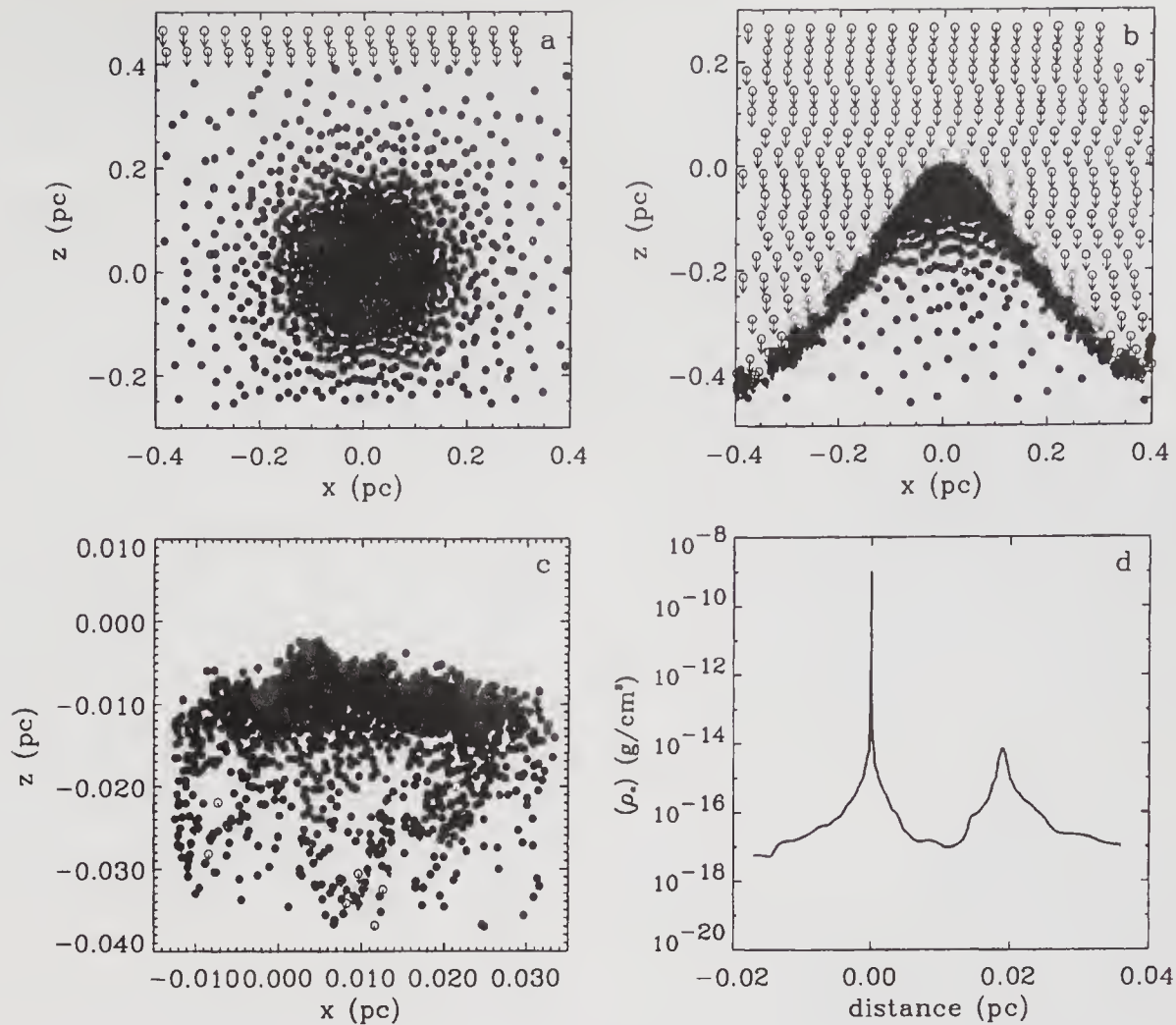


Figure 3. Results from a 3D SPH simulation run leading to the formation of a binary system. The system has 20,000 particles in the core (filled circles) and 9,000 in the shock wave (open circles). The initial peak density in the core is $7.49 \times 10^{-19} \text{ g cm}^{-3}$, and the velocity of the shock wave approaching from $+z$ direction is 10 km s^{-1} . The system is shown in the xz plane with the units in parsecs. The frames correspond to $t = 0$ (a) and $t = 128,000$ years (b). Frame (c) zooms into the fragmented, collapsing region and frame (d) shows the density profile in the system along the line connecting the two fragments. The peak density of the primary fragment is $2.28 \times 10^{-9} \text{ g cm}^{-3}$ and of the secondary $8.76 \times 10^{-15} \text{ g cm}^{-3}$.

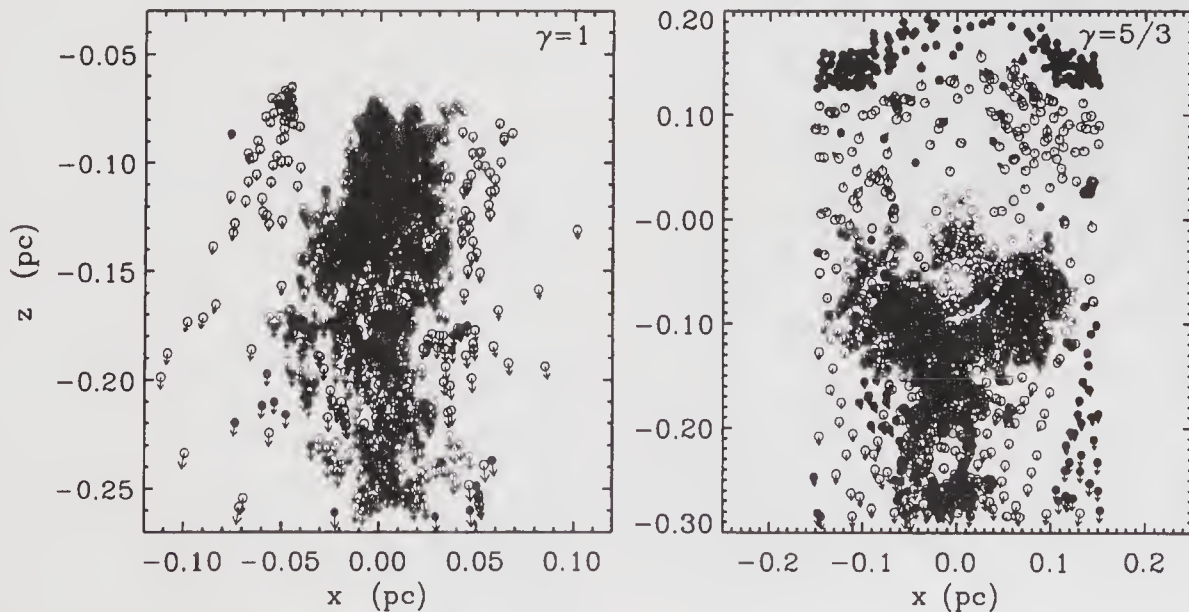


Figure 4. Results from 3D SPH simulation runs studying the effect of thermodynamics. The initial conditions in the two runs are identical except for the choice of thermodynamics: isothermal (left frame) and adiabatic ($\gamma = 5/3$). The former case leads to the collapse of the molecular cloud core, the latter to cloud shredding through instabilities. The system is shown in the xz plane with the units in parsecs. The open circles denote cloud particles and the filled circles the shock flow material.

(figure 4): a shock with $\gamma = 5/3$ (figure 4 right panel) results in the destruction of the cloud, while $\gamma = 1$ (figure 4 left panel) pushes the core into collapse

(Foster and Boss 1996; Vanhala and Cameron 1998). In the former case, RT and KH instabilities develop at the contact surface between the core and the shock

wave, and they destroy the cloud in a manner similar to the high-velocity shock waves described above. A strong shock develops at the facing side of the core, and some of the shocked material is reflected back towards the origin of the shock wave. In the $\gamma = 1$ case, the high compression in the isothermal shock front quickly compresses the core to the point of collapse. The difference between the two cases can be interpreted as the difference between high-velocity shock waves where the molecular coolants are destroyed and lower-velocity ones where the molecules survive and cool the gas rapidly, corresponding to the $\gamma = 5/3$ and $\gamma = 1$ cases, respectively (Foster and Boss 1996). This is especially true for purely momentum-driven collapse; if the collapse also requires high post-shock pressure (as is the case in the variable γ SPH calculations), higher shock velocities may be needed to drive the core into collapse. The stability of the core is also affected by the choice of the equation of state, and this may be another reason for the differences between the two cases (see the discussion below).

Calculations performed with a variable γ further demonstrate the crucial role of thermodynamics: sustained collapse is found to take place only when the temperature in the compressed core rises above ~ 27 K (Cameron *et al* 1997; Vanhala and Cameron 1998). This is the temperature where the adiabatic exponent first falls below the stability value of $\gamma = 4/3$ (see figure 1) and the molecular cloud core becomes unstable against collapse (e.g., Low and Lynden-Bell 1976; Tohline 1981; Whitworth 1981). If the temperature remains lower than this, the core rebounds from the maximum compression and fails to collapse. However, the temperature at which γ falls below $4/3$ is very sensitive to the state of hydrogen in molecular clouds (Cameron *et al* 1997). In the SPH calculations, an equilibrium mix between the ortho and para states of molecular hydrogen is assumed, and the temperature limit stated above applies to these conditions. Recent measurements of the ortho-para ratio in interstellar space tend to confirm the validity of this assumption (Smith *et al* 1997 and references therein), but the distribution between the ortho and para states may vary in different environments according to the presence of suitable catalysts and may also be affected by the passage of shock waves (Timmermann 1998). The sensitivity of our results on thermodynamics stresses the need for a more thorough investigation of this aspect of the problem.

3. The time scale of triggered collapse

The second test of the triggered origin scenario is to determine whether the time scale for assisted collapse is sufficiently short for the survival of the radioactivities. The mean life of the shortest-lived of the

detected radionuclides, ^{41}Ca , is 150,000 years. In order for this isotope to survive in the early solar system, the time scale from its production to its incorporation into the meteoritic inclusions must be less than a few of its mean lives.

The numerical simulations indicate that the time scale of the triggered collapse of the molecular cloud core from the first approach of the shock wave to the collapse of the system is $\sim 10^4$ to $\sim 10^5$ years (Foster and Boss 1996; Vanhala and Cameron 1998). Travel time from the most distant object considered as a candidate for the stellar source of the radioactivities, a supernova explosion occurring at the distance of a few parsecs, is a few $\times 10^4$ years (Cameron *et al* 1997). Combined, this results in a time interval from the production of the radioactivities to the collapse of the core of roughly 150,000 years, the mean life of ^{41}Ca . Injection may continue for a longer period of time (see section 4), but even in this case, the time scale is expected to be only a few mean lives of ^{41}Ca . The simulations therefore confirm that the short time scale of the formation of the solar system implied by the short-lived radionuclides can be explained by the scenario of the triggered origin of the solar system.

4. Injection of radioactivities into the collapsing core

The third test of the triggered origin scenario is to determine whether radioactivities carried by the shock wave can be injected into the collapsing molecular cloud core. The simulations have provided preliminary answers to this question, but the details of the problem require further study.

Boss (1995) found that about $0.01 M_{\odot}$ of shock wave material was mixed into the collapsing $\sim 1 M_{\odot}$ protostellar core in his calculations. He estimated the injection efficiency – defined as the amount of shock wave material injected into the collapsing system compared with that originally incident on it – to be $\sim 50\%$.

The higher resolution 2D PPM simulations of Foster and Boss (1997) found that shock wave material is injected into the molecular cloud core through Rayleigh-Taylor fingers, when shocked material gathers on the surface of the cloud and penetrates into the core in finger-like structures. Injection was found to take place at a roughly constant rate for about 0.7 Ma, continuing long after the central regions have gone into collapse. Of the total amount of material incident on the core, about 10–20% is retained in the collapsing system. The injection efficiency does not decrease significantly even if the radioactivities are lagging far behind the immediate shock front (Boss and Foster 1998). The calculations also found that dust grains appear not to decouple much from the gas but follow the behavior of the main

flow instead. The steady injection rate implies that no temporal heterogeneities are expected in the abundances of deposited short-lived radioactivities in the early solar system. On the other hand, since the calculations suggest that most of the material is injected preferentially in the outer half (by mass) of the collapsing system, spatial heterogeneities may be possible. However, the resolution of the calculations is too small (the smallest grid size was ~ 50 AU) to make any concrete conclusions on the possible existence of heterogeneities – either spatial or temporal – and more detailed calculations are required to examine this aspect of the problem.

When using an isothermal equation of state, the 3D SPH calculations reproduce the 2D PPM results, down to the injection efficiency of 19% (Vanhala and Cameron 1998). Figure 5 shows the development of the RT fingers at the surface of the molecular cloud core during the impact of the shock wave in the 3D SPH simulations. The result is essentially the same as in the calculations of Foster and Boss (1997): material accumulates at the surface of the core, and the clumps penetrate into the core in finger-like structures. The case shown in figure 5 eventually leads to the system shown in the left panel of figure 4 some 235,000 years after the first approach of the shock wave. Note that the injection occurs more rapidly in the SPH case (~ 0.2 Ma) than in the PPM case (~ 0.7 Ma). This implies that the injection rate depends on the details of the calculations, and more work is required to constrain the likely time scales for injection.

In contrast with the isothermal calculations described above, SPH simulations using the variable γ scheme found no evidence of mixing in the cases leading to collapse (Vanhala and Cameron 1998). Mixing is found to take place during the impact of low-velocity ($v_s < 20 \text{ km s}^{-1}$) shock waves, but in these cases collapse is not usually initiated. Vanhala and Cameron (1998) explain the lack of evidence for mixing in their variable γ calculations in terms of buoyancy and entropy effects: when a hot, shocked gas bubble tries to penetrate into the cool core, it slows down and is reaccelerated towards the surface, and large-scale mixing is prohibited. Fluid instabilities at the interface between the core and the penetrating bubble are expected to induce dynamically driven mixing, but this occurs only in a shallow layer at the surface of the core and at scales the calculations are unable to resolve. With the continuing arrival of shocked material at the core, the surface mixing continues and the mixing layer becomes subject to erosion, creating a larger-scale manifestation of the small-scale behavior. The erosion of the core seen in figure 2 may be due to this effect.

How can the differences in the results regarding injection given by the different calculations be reconciled? The common property of all cases showing evidence for injection is the (nearly) isothermal nature

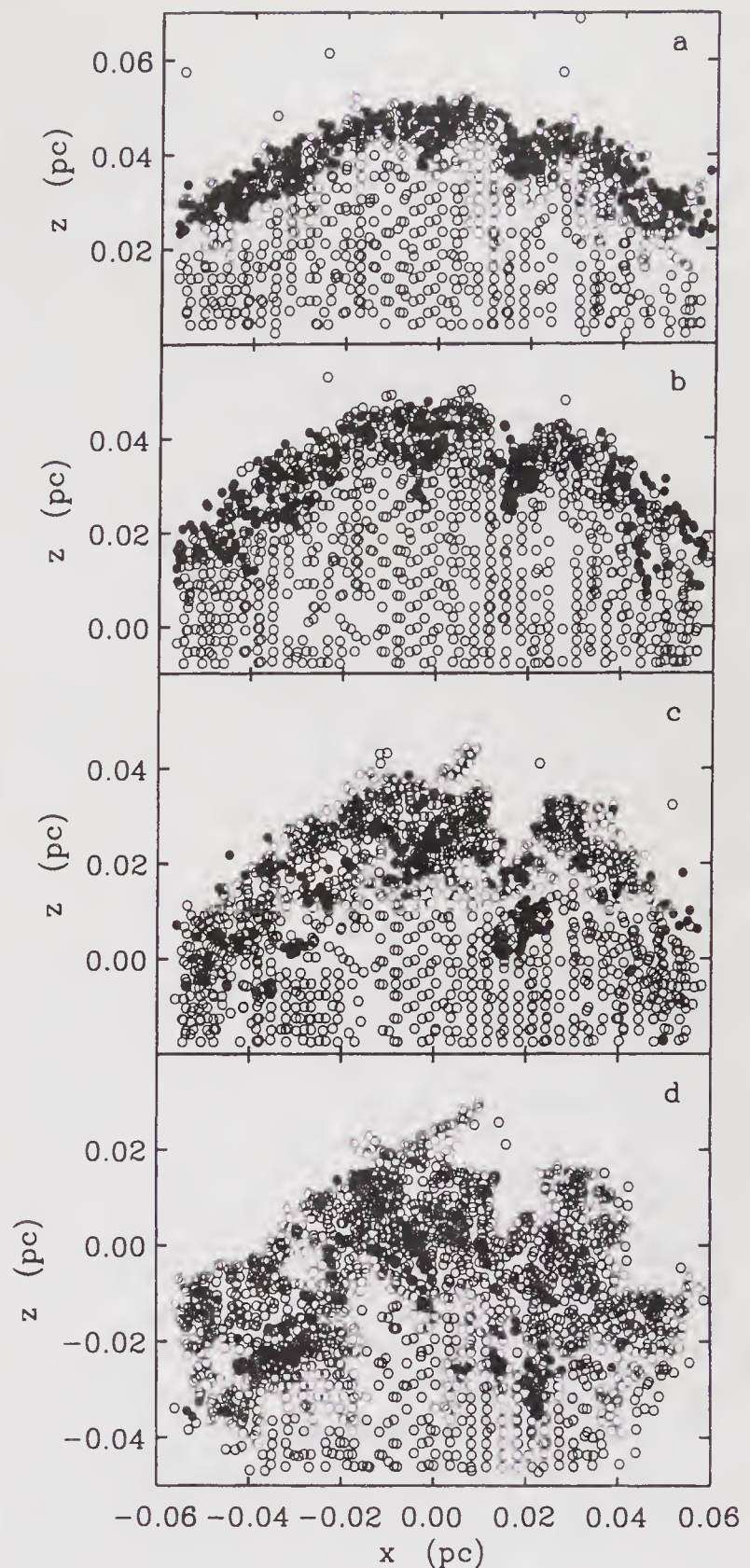


Figure 5. Injection of shock wave material in the 3D SPH simulations using an isothermal equation of state. The system is shown in the xz plane at $t = 3,000$ years (a), 4,500 years (b), 10,900 years (c) and 30,200 years (d). Shock wave material collects on the surface of the core and penetrates into it in finger-like structures.

of the shock wave. The requirement for successful injection therefore appears to be that the hot shocked gas must cool rapidly behind the immediate shock front, resulting in shocks that are either isothermal or nearly so. In the latter case, there may be a high-temperature post-shock region, but its size is fairly small, and the temperatures in the post-shock gas

return rapidly to the pre-shock values. As described in section 2, the requirement for sustained collapse in the SPH calculations using variable γ thermodynamics is that the principal coolants must be destroyed in the shock front and the post-shock gas must remain hot for sufficient pressure to be exerted on the core. Consequently, the RT-style mixing found in the isothermal calculations appears to be difficult in these cases. Instead, a more likely method of mixing shock wave material into the core during the impact of a higher-velocity shock wave may be the dynamically driven instabilities discussed above. It is also possible that in rapidly cooling shock waves the finite-size high-temperature, high-pressure region is able to push the core into collapse, and injection occurs through RT-fingers when the cooler post-shock material arrives to the core. Clearly, the question of injection is very complicated, and more detailed studies exploring issues such as thermodynamics, shock thickness, and cooling are needed for a more comprehensive answer regarding the mixing of shock wave material into the collapsing molecular cloud core.

5. Other aspects of triggered star formation

The viability of the scenario of the triggered origin of the solar system can be examined through the evidence contained in primitive meteoritic material and by numerical simulations studying the processes involved in triggered collapse. Since the solar system is thought to be just one example of more general (assisted) star formation, further evidence for triggered star formation may be obtained through astronomical observations. Identifying the triggered origin of a young stellar object is difficult, however, since once initiated, the collapse and the further evolution of the protostellar system are expected to follow similar paths in both the triggered and unassisted case, with the possible exception of the angular momentum contained in the collapsing system (Cameron *et al* 1997). Furthermore, by the time the triggered young star can be detected, the shock wave that initiated its formation is expected to have slowed down and dispersed into the surrounding medium. Catching a triggering event in action is therefore very difficult, and the evidence for assisted star formation is mostly circumstantial. In this section, we shall provide some general arguments for the prevalence of triggered star formation and give a few examples where these processes are thought to have occurred.

In the light of the basic result of the simulations described in section 2 – that shock waves with velocities of $10\text{--}45\text{ km s}^{-1}$ are capable of triggering collapse – the natural question is: what sources of shocks are there in interstellar space? Not surprisingly, there are many events capable of creating shocks of the required magnitude.

Supernova explosions occurring in the immediate vicinity of a molecular cloud are highly destructive, but as the expansion wave plows into the surrounding medium, it slows down. Using momentum conservation calculations, Cameron *et al* (1997) estimate that the supernova shock wave slows down to $25\text{--}45\text{ km s}^{-1}$ within 3–5 parsecs, but the distance may be even more, depending on the density of the ambient material. Foster and Boss (1996) estimate higher benevolent supernova distances – 14–19 pc – based on an estimate of the cooling of the supernova remnant from the adiabatic to isothermal phase during its expansion into low-density ambient medium. Other possible sources of shocks in connection with evolved stars include the ejection of a planetary nebula from an asymptotic giant branch star (Cameron 1993; Wasserburg *et al* 1994), novae (Gehrz *et al* 1993) and Wolf-Rayet winds from massive stars (Arnould *et al* 1997). In these three cases, the source must be located in the vicinity of the molecular cloud.

An important source of shocks in molecular clouds are the young stars associated with them. Young stellar objects are observed to drive bipolar outflows from their vicinity into the surrounding medium (Lada 1985; Fukui *et al* 1993). Even though the mechanism for the creation of these outflows is still under debate, they are now thought to be a natural phase in the pre-main-sequence evolution of young stellar objects. The outflows typically reach velocities of $10\text{--}100\text{ km s}^{-1}$ (Fukui *et al* 1993). The fastest flows can therefore disrupt nearby cores, while the lower-velocity ones are capable of triggering collapse. The shocks created by the outflows are usually bow shocks (Fukui *et al* 1993), and further work is required to understand what effect this deviation from the planar structure of the shock wave may have to the results described in section 2.

Other possible triggering events include collisions between molecular clouds (see review by Elmegreen 1998) and ionized gas flows (Elmegreen and Lada 1977). In the latter case, ultraviolet radiation from hot massive stars ionizes nearby cloud material and accelerates gas to the sound velocity of hydrogen, $\sim 10\text{ km s}^{-1}$. These flows can therefore assist in the collapse of well-evolved or very massive molecular cloud cores.

Despite the difficulties in determining the triggered origin of young stellar objects, there are a few cases where assisted star formation appears to be the best explanation for the observed properties of the system. One of the most striking examples is the NICMOS image of NGC 2264 IRS in the Cone Nebula in Monoceros, where the wind from a B2 star is thought to have triggered the formation of six young stellar objects seen at the projected distance of $\sim 4000\text{ AU}$ from the central object (Thompson *et al* 1998). Other suggested examples of triggered star formation include the R association CMa R1, which lies on the edge of an old supernova remnant (Herbst and

Assousa 1977), the Upper Scorpius OB association (Walter *et al* 1994), and the dust globule ESO 210-6A in the Gum nebula (Schwartz 1977; Graham and Elias 1983; Graham and Heyer 1989).

On a grander scale, interactions between galaxies often compress pre-existing molecular clouds or make them collide with each other, in this manner triggering massive star formation (e.g., Higdon and Wallin 1997). Another example of large-scale triggering has been found in the radio galaxy NGC 5128 (Cen A), where a radio jet impacts an adjacent cloud and triggers star formation (Graham 1998).

Assisted star formation appears to be an important feature of stellar evolution on all scales, from the formation of individual stars to the massive starbursts in interacting galaxies. Even though the mechanisms behind the triggering of the various objects may be different, the basic idea is the same: molecular cloud matter is compressed by an outside agent to the point of collapse. However, determining the importance of assisted star formation quantitatively would require statistics of triggered objects vs. those formed through unassisted collapse, and at present sufficient data are not available. Instead, the more indirect evidence presented here and elsewhere (see Cameron *et al* 1997), can be used to suggest that assisted star formation may be more common than previously thought.

6. Summary and future directions

The numerical simulations studying the triggered origin of the solar system have shown that a molecular cloud core can be triggered into collapse by the impact of an interstellar shock wave traveling at the velocity of $10\text{--}45\text{ km s}^{-1}$. The time scale of the process ($\sim 10^4\text{--}10^5$ years) is sufficiently short to accommodate for the survival of the shortest-lived radioactivities detected in the early solar system. Preliminary calculations of mixing of the shock wave material into the collapsing system suggest that radioactivities can be injected through instabilities at the contact surface between the core and the shocked material. More detailed calculations are required to understand the details of the injection process, however.

Further work incorporating more physical ingredients is required to strengthen the conclusions presented in this paper. Effects which may influence the results but which have been ignored in the calculations described here include the full treatment of magnetic effects, the alignment of the rotation axis of the core with respect to the approaching shock front and the detailed structure of the shock wave. The last of these effects is especially interesting, since the structure of the shock wave may significantly influence the mixing of shock wave material into the core. The planar structure of the shock wave assumed by

the calculations described in section 2 is a good choice for exploratory calculations, since it makes no assumptions about the origin of the shock wave, and the results are therefore applicable to all shock waves propagating at the studied velocity. In a more realistic situation, however, the inhomogeneities present in the molecular cloud material are expected to cause the shock wave to deviate from the basic planar structure. The event responsible for the creation of the shock may also leave its signature on the shock wave. Calculations exploring different shock structures may therefore eventually provide clues to what might be the most likely source for the shock wave that triggered the formation of the solar system.

Acknowledgements

The author thanks A P Boss, A G W Cameron, P N Foster and J N Goswami for valuable comments and discussions during the preparation of this manuscript. This work was supported by NASA Origins of Solar Systems grant NAG5-4306.

References

- Arnould M, Paulus G and Meynet G 1997 Short-lived radionuclide production by non-exploding Wolf-Rayet stars; *Astron. Astrophys.* **321** 452–464
- Bateman N P T, Parker P D and Champagne A E 1996 On the production of ^{26}Al in the early solar system by low-energy oxygen cosmic rays; *Astrophys. J. Lett.* **472** L119–L122
- Bedogni R and Woodward P R 1990 Shock wave interactions with interstellar clouds; *Astron. Astrophys.* **231** 481–498
- Boss A P 1995 Collapse and fragmentation of molecular cloud cores. II. Collapse induced by stellar shock waves; *Astrophys. J.* **439** 224–236
- Boss A P and Foster P N 1997 Triggering presolar cloud collapse and injecting material into the presolar nebula; in *Astrophysical Implications of the Laboratory Study of Presolar Materials* (eds) T J Bernatowicz and E Zinner (Woodbury: AIP) pp. 649–664
- Boss A P and Foster P N 1998 Injection of short-lived isotopes into the presolar cloud; *Astrophys. J. Lett.* **494** L103–L106
- Cameron A G W 1993 Nucleosynthesis and star formation; in *Protostars and Planets III*, (eds) E H Levy and J I Lunine (Tucson: University of Arizona Press), pp. 47–73
- Cameron A G W and Truran J W 1977 The supernova trigger for formation of the solar system; *Icarus* **30** 447–461
- Cameron A G W, Höflich P, Myers, P C and Clayton D D 1995 Massive supernovae, Orion gamma rays, and the formation of the solar system; *Astrophys. J. Lett.* **447** L53–L57
- Cameron A G W, Vanhala H and Höflich P 1997 Some aspects of triggered star formation; in *Astrophysical Implications of the Laboratory Study of Presolar Materials* (eds) T J Bernatowicz and E Zinner (Woodbury: AIP), pp. 665–693
- Clayton D D and Jin L 1995a Gamma rays, cosmic rays, and extinct radioactivity in molecular clouds; *Astrophys. J.* **451** 681–699
- Clayton D D and Jin L 1995b A new interpretation of ^{26}Al in meteoritic inclusions; *Astrophys. J. Lett.* **451** L87–L91
- Draine B T and McKee C F 1993 Theory of interstellar shocks; *Ann. Rev. Astron. Astrophys.* **31** 373–432

- Elmegreen B G 1998 Observations and theory of dynamical triggers for star formation; in *Origins of Galaxies, Stars, Planets and Life* (eds) C E Woodward, H A Thronson and M Shull) (*Astr. Soc. Pacific*) in press
- Elmegreen B G and Lada C J 1977 Sequential formation of subgroups in OB associations; *Astrophys. J.* **214** 725–741
- Foster P N and Boss A P 1996 Triggering star formation with stellar ejecta; *Astrophys. J.* **468** 784–796
- Foster P N and Boss A P 1997 Injection of radioactive nuclides from the stellar source that triggered the collapse of the presolar nebula. *Astrophys. J.* **489** 346–357
- Fukui Y, Iwata T, Mizuno A, Bally J and Lane A P 1993 Molecular outflows; in *Protostars and Planets III* (eds) E H Levy and J I Lunine (Tucson: University of Arizona Press), pp. 603–639
- Gehrz R D, Truran J W and Williams R E 1993 Classical Novæ contributions to the interstellar medium; in *Protostars and Planets III* (eds) E H Levy and J I Lunine (Tucson: University of Arizona Press) pp. 75–95
- Graham J A 1998 Shocked gas and star formation in the Centaurus A radio galaxy; *Astrophys. J.* **502** 245–252
- Graham J A and Elias J H 1983 Herbig-Haro objects in the dust globule ESO 210-6A; *Astrophys. J.* **272** 615–626
- Graham, J A and Heyer M H 1989 Young stars of low mass in the Gum nebula; *Publ. Astron. Soc. Pacific* **101** 573–587
- Heathcote S R and Brand P W J L 1983 The state of clouds in a violent interstellar medium; *Mon. Not. R. Astron. Soc.* **203** 67–86
- Herbst W and Assousa G E 1977 Observational evidence for supernova-induced star formation: Canis Major R1; *Astrophys. J.* **217** 473–487
- Higdon J L and Wallin J F 1997 Wheels of fire. III. Massive star formation in the “double-ringed” ring galaxy AM 0644-741; *Astrophys. J.* **474** 686–700
- Klein R I, McKee, C F and Colella P 1994 On the hydrodynamic interaction of shock waves with interstellar clouds. I. Nonradiative shocks in small clouds; *Astrophys. J.* **420** 213–236
- Krebs J and Hillebrandt W 1983 The interaction of supernova shockfronts and nearby interstellar clouds; *Astron. Astrophys.* **128** 411–419
- Lada C J 1985 Cold outflows, energetic winds, and enigmatic jets around young stellar objects; *Ann. Rev. Astron. Astrophys.* **23** 267–317
- Low C and Lynden-Bell D 1976 The minimum Jeans mass or when fragmentation must stop; *Mon. Not. R. Astron. Soc.* **176** 367–390
- Mac Low, M-M, McKee C F, Klein R I, Stone J M and Norman M L 1994 Shock interactions with magnetized interstellar clouds. I. Steady shocks hitting nonradiative clouds; *Astrophys. J.* **433** 757–777
- Nittman J, Falle S A E G and Gaskell P H 1982 The dynamical destruction of shocked gas clouds; *Mon. Not. R. Astron. Soc.* **201** 833–847
- Podosek F A and Nichols Jr R H 1997 Short-lived radionuclides in the solar nebula; in *Astrophysical Implications of the Laboratory Study of Presolar Materials* (eds) T J Bernatowicz and E Zinner (Woodbury: AIP) pp. 617–647
- Ramaty R, Kozlovsky B and Lingenfelter R E 1996 Light isotopes, extinct radioisotopes, and gamma-ray lines from low-energy cosmic-ray interactions; *Astrophys. J.* **456** 525–540
- Różycka M and Tenorio-Tagle G 1987 The hydrodynamics of clouds overtaken by supernova remnants. II. Attrition shocks, condensation and ejection of clouds; *Astron. Astrophys.* **176** 329–337
- Sahijpal S, Goswami J N, Davis A M, Grossman L and Lewis R S 1998 A stellar origin for the short-lived nuclides in the early solar system. *Nature* **391** 559–561
- Schwartz R D 1977 Evidence of star formation triggered by expansion of the Gum nebula; *Astrophys. J. Lett.* **212** L25–L26
- Shu F H, Shang H and Lee T 1996 Toward an astrophysical theory of chondrites; *Science* **271** 1545–1552
- Shu F H, Shang H, Glassgold A E and Lee T 1997 X-rays and fluctuating X-winds from protostars; *Science* **277** 1475–1479
- Smith M D, Davis C J and Lioure A 1997 The ortho and para fractions of molecular hydrogen in protostellar outflows and Herbig-Haro objects; *Astron. Astrophys.* **327** 1206–1214
- Stone J M and Norman M L 1992 The three-dimensional interaction of a supernova remnant with an interstellar cloud; *Astrophys. J. Lett.* **390** L17–L19
- Thompson R I, Corbin M R, Young E and Schneider G 1998 NGC 2264 IRS: Evidence for triggered star formation; *Astrophys. J. Lett.* **492** L177–L179
- Timmermann R 1998 Ortho-H₂/para-H₂ ratio in low-velocity shocks; *Astrophys. J.* **498** 246–255
- Tohline J E 1981 The collapse to equilibrium of rotating, adiabatic spheroids. I. Protostars; *Astrophys. J.* **248** 717–726
- Vanhala H A T and Cameron A G W 1998 Numerical simulations of triggered star formation. I. Collapse of dense molecular cloud cores; *Astrophys. J.* **508** 291–307
- Walter F M, Vrba F J, Mathieu R D, Brown A and Myers P C 1994 X-ray sources in regions of star formation. V. The low mass stars of the Upper Scorpius association; *Astron. J.* **107** 692–719
- Wasserburg G J, Busso M, Gallino R and Raiteri C M 1994 Asymptotic giant branch stars as a source of short-lived radioactive nuclei in the solar nebula; *Astrophys. J.* **424** 412–428
- Whitworth A 1981 Global gravitational stability for one-dimensional polytropes; *Mon. Not. R. Astron. Soc.* **195** 967–977
- Woodward P R 1976 Shock-driven implosion of interstellar gas clouds and star formation; *Astrophys. J.* **207** 484–501
- Xu J and Stone J M 1995 The hydrodynamics of shock-cloud interactions in three dimensions; *Astrophys. J.* **454** 172–181

Short-lived nuclides in the early solar system

J N GOSWAMI

*Physical Research Laboratory, Ahmedabad 380 009, India
e-mail: goswami@prl.ernet.in*

Isotopic records in meteorites provide evidence for the presence of several short-lived nuclides in the early solar system with half-lives varying from 10^5 to $\sim 8 \times 10^7$ years. Most of the nuclides with longer half-life ($>10^7$ years) are considered to be products of stellar nucleosynthesis taking place over long time scales in our galaxy. However, for the relatively shorter-lived nuclides, two possibilities exist; they could be products of energetic particle interactions taking place in a presolar or early solar environment, or, they could have been produced in a stellar source and injected into the protosolar molecular cloud just prior to its collapse. The presently available data appear to support the latter case and put a stringent constraint of less than a million years for the time scale for the collapse of the protosolar molecular cloud to form the Sun and some of the first solar system solids. This short time scale also suggests the possibility of a triggered origin for the solar system with the very process of injection of the short-lived nuclides acting as the trigger for the collapse of the protosolar molecular cloud. Fossil records of the short-lived nuclides in meteorites also provide very useful chronological information on the early solar system processes like the time scale for nebular processing, the time scales for differentiation and for metal/silicate fractionation within planetesimals. The currently available data suggest a time scale of a few million years for nebular processing and a relatively short time scale of about ten million years within which differentiation, melting and recrystallization in some of the planetesimals took place.

1. Introduction

Isotopic studies of meteorites have provided evidence for the presence of several short-lived nuclides in the material from which the solar system objects have formed. The half-life of these nuclides varies from $\sim 10^5$ years (^{41}Ca) to 8.2×10^7 years (^{244}Pu), and they provide extremely useful information on the time scales of various processes taking place during the early evolutionary history of the solar system (Wasserburg 1985; Podosek and Swindle 1988; Podosek and Nichols 1997). These radionuclides can be considered as “now-extinct” nuclides for all practical purposes, and their one time presence in the early solar system is inferred from the observed excess in their daughter nuclide concentrations in different meteorite samples. Such samples must have incorporated the short-lived nuclides “live” at the time of their formation and *in situ* decay of these nuclides give

rise to the observed excess. ^{129}I (half-life ~ 16 Ma) is the first short-lived nuclide whose one time presence in the early solar system was inferred from the observed excess of ^{129}Xe in the meteorite Richardton (Reynolds 1960; Jeffreys and Reynolds 1961). This was followed by the discovery of fission Xe from ^{244}Pu (half-life ~ 82 Ma; Rowe and Kuroda 1965). A major breakthrough in the field took place with the discovery of excess ^{26}Mg from the decay of ^{26}Al having a half-life of less than a million year (7×10^5 years) in Ca-Al-rich refractory Inclusions (CAIs) of the Allende meteorite (Lee *et al* 1976, 1977). The CAIs are considered to be some of the first solar system solids to have formed in the solar nebula, the gas and dust cloud surrounding the nascent Sun (e.g., see, Grossman 1980). Since then, the presence of a large number of short-lived nuclides in the early solar system has been established and these are listed in table 1. In a few cases, experimental data only provide

Keywords. Meteorites; solar system; short-lived nuclides; Sun; energetic particles; stellar sources.

Table 1. *Short-lived nuclides in the early solar system.*

Nuclide	Half-life (Ma)	Daughter nuclide	Initial abundance	Ref.	Stellar production site ¹
⁴¹ Ca	0.1	⁴¹ K	$\sim 1.5 \times 10^{-8}$ (⁴¹ Ca/ ⁴⁰ Ca)	[1]	SN, AGB, WR
²⁶ Al	0.7	²⁶ Mg	$\sim 5 \times 10^{-5}$ (²⁶ Al/ ²⁷ Al)	[2]	SN, N, AGB, WR
⁶⁰ Fe	1.5	⁶⁰ Ni	$\sim 4 \times 10^{-9}$ (⁶⁰ Fe/ ⁵⁶ Fe)	[3]	SN, AGB
			$\sim 2 \times 10^{-8*}$	[4]	
⁵³ Mn	3.7	⁵³ Cr	$\sim 4.4 \times 10^{-5}$ (⁵³ Mn/ ⁵⁵ Mn)	[5]	SN
			$\sim 4.7 \times 10^{-6}$, $\sim 10^{-5*}$	[4]	
¹⁰⁷ Pd	6.5	¹⁰⁷ Ag	$\sim 2 \times 10^{-5}$ (¹⁰⁷ Pd/ ¹⁰⁸ Pd)	[6]	SN, AGB, WR
			$\sim 4.5 \times 10^{-5*}$		
¹⁸² Hf	9	¹⁸² W	$\sim 2 \times 10^{-4}$ (¹⁸² Hf/ ¹⁸⁰ Hf)	[7]	SN
¹²⁹ I	16.7	¹²⁹ Xe	$\sim 10^{-4}$ (¹²⁹ I/ ¹²⁷ I)	[8]	SN
²⁴⁴ Pu	82	α , SF ⁺	$\sim 7 \times 10^{-3}$ (²⁴⁴ Pu/ ²³⁸ U)	[9]	SN
⁹⁹ Tc [#]	0.21	⁹⁹ Ru	$\sim 10^{-4}$ (⁹⁹ Tc/ ⁹⁹ Ru)	[10]	AGB, WR
³⁶ Cl [#]	0.3	³⁶ Ar	$\sim 1.4 \times 10^{-6}$ (³⁶ Cl/ ³⁵ Cl)	[11]	SN, AGB, WR
²⁰⁵ Pb [#]	15	²⁰⁵ Tl	$\sim 3 \times 10^{-4}$ (²⁰⁵ Pb/ ²⁰⁴ Pb)	[12]	AGB, WR
⁹² Nb [#]	35	⁹² Zr	$\sim 2 \times 10^{-5}$ (⁹² Nb/ ⁹³ Nb)	[13]	SN

¹: SN = supernova; N = nova; AGB = Asymptotic Giant Branch star; WR = Wolf-Rayet star

*: extrapolated value at the time of formation of CAI

+ : SF = spontaneous fission products

: suggestive evidence is present; needs confirmation

[1] Srinivasan *et al* (1994, 1996); [2] Lee *et al* (1977); see also MacPherson *et al* (1995) [3] Shukolyukov and Lugmair (1993a, b) and Lugmair *et al* (1995); [4] Lugmair *et al* (1995) and Lugmair and Shukolyukov (1988); [5] Birck and Allegre (1985); [6] Kelly and Wasserburg (1978), see also Chen and Wasserburg (1996); [7] Lee and Halliday (1995, 1996) and Harper and Jacobsen (1996); [8] Jeffreys and Reynolds (1961), see also Hohenberg *et al*, this volume; [9] Rowe and Kuroda (1965) and Hudson *et al* (1988); [10] Yin *et al* (1992); [11] Murty *et al* (1997); [12] Chen and Wasserburg (1987); [13] Harper (1996).

weak to strong hints for their presence, and these need to be confirmed by more refined experiments.

All the short-lived nuclides present in the early solar system could be products of stellar nucleosynthesis taking place in different stellar sites (table 1). In fact, the relatively longer-lived and high-mass nuclides (¹⁸²Hf, ¹²⁹I and ²⁴⁴Pu) are distinct products of rapid neutron capture (r-process) nucleosynthesis taking place during supernova explosions. However, in the case of the shorter-lived nuclides like ⁴¹Ca, ²⁶Al, ⁶⁰Fe, ⁵³Mn, and ¹⁰⁷Pd, two possible sources have been suggested. They could be freshly synthesized nuclides from a single stellar source (e.g. a supernova, an asymptotic giant branch (AGB) star, a Wolf-Rayet (W-R) star) that were injected into the protosolar cloud just prior to its collapse. Alternatively, they could be products of energetic particle interactions taking place either in the protosolar molecular cloud (prior to its collapse) or later in the solar nebula following the formation of the Sun. Identification of the most plausible source of the short-lived nuclides is important if we wish to use them as time markers of the early solar system processes. For example, if they are of stellar origin, their initial presence in meteorites provides a constraint on the time scale for the collapse of the protosolar molecular cloud; the nuclide with the shortest half-life providing the most stringent constraint. On the other hand, if these nuclides are produced by energetic particles from an active early

Sun interacting with gas and dust in the solar nebula, they can serve as time markers only for early solar system processes and not for presolar processes. Further, if the short-lived nuclides were indeed freshly synthesized products from a specific stellar source, the possibility exists that the very process of their injection could have also triggered the collapse of protosolar molecular cloud leading to the formation of the solar system. In this paper we shall briefly outline the developments taking place in this field of research and discuss some new results that allow us to identify the most plausible source(s) of the short-lived nuclides, particularly those with half-life <10 Ma, and the constraints they impose on the time scales for the formation of the Sun and some of the first solar system objects. Earlier developments in this field have been reviewed by Wasserburg (1985), Podosek and Swindle (1988), Cameron (1993) and Podosek and Nichols (1997).

2. Meteoritic evidence for the presence of short-lived nuclides in the early solar system

The case for the presence of a short-lived nuclide in the early solar system is based on the presence of excess abundance of its daughter nuclide in samples of meteorites. The case for its presence is strengthened if one can show that the excess in the daughter nuclide

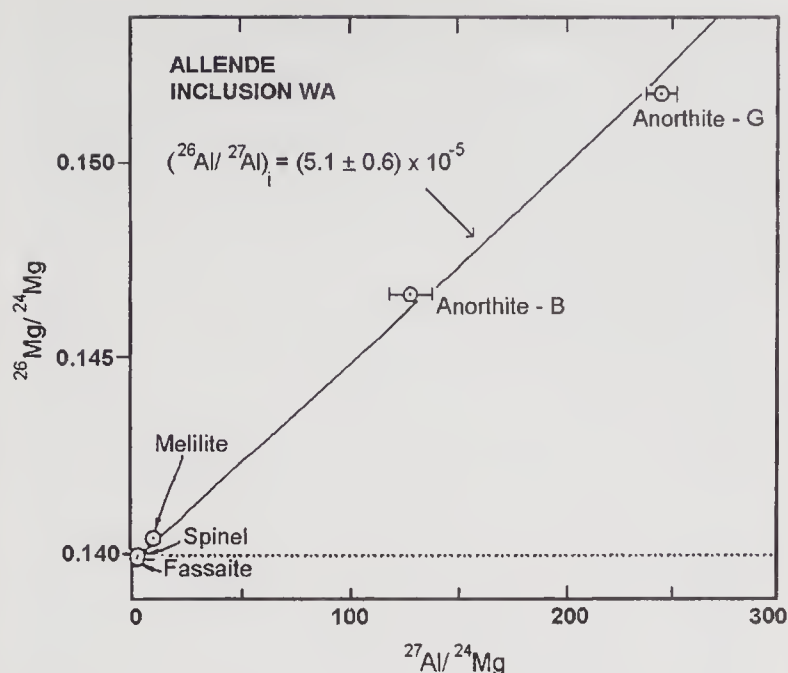


Figure 1. Magnesium isotopic ratio, $^{26}\text{Mg}/^{24}\text{Mg}$, measured in different refractory mineral phases in the Allende Ca-Al-rich refractory inclusion WA, plotted as a function of their $^{27}\text{Al}/^{24}\text{Mg}$ ratios. The dotted line represents the reference (normal) $^{26}\text{Mg}/^{24}\text{Mg}$ ratio of 0.13932. The linear correlation of excess $^{26}\text{Mg}/^{24}\text{Mg}$ with $^{27}\text{Al}/^{24}\text{Mg}$ ratio indicates that the excess in ^{26}Mg is related to Al and resulted from *in situ* decay of ^{26}Al initially present in these refractory phases at the time of their formation in the early solar system [from Lee *et al* 1977].

abundance (e.g. ^{26}Mg in the case of ^{26}Al or ^{41}K in the case of ^{41}Ca) is also correlated with the abundance of the parent element (e.g. aluminum or calcium in these cases). Such a correlation is clearly evident in figure 1, where we show the data for Mg-Al isotopic compositions measured in different refractory phases of an Allende CAI (WA) by Lee *et al* (1977). The $^{26}\text{Mg}/^{24}\text{Mg}$ ratios in the phases with high Al/Mg ratio are distinctly above the normal value of 0.13932 and the excess clearly correlates with the measured $^{27}\text{Al}/^{24}\text{Mg}$ ratios in the phases. In fact this correlation can be expressed by a linear relationship as follows:

$$\begin{aligned} \left[\frac{^{26}\text{Mg}}{^{24}\text{Mg}} \right]_m &= \left[\frac{^{26}\text{Mg}}{^{24}\text{Mg}} \right]_i + \left[\frac{^{26}\text{Al}}{^{24}\text{Mg}} \right]_i \\ &= \left[\frac{^{26}\text{Mg}}{^{24}\text{Mg}} \right]_i + \left[\frac{^{26}\text{Al}}{^{27}\text{Al}} \right]_i \times \left[\frac{^{27}\text{Al}}{^{24}\text{Mg}} \right]_m \end{aligned}$$

the subscripts “*m*” and “*i*” stand for “measured” and “initial”, respectively. The intercept of the correlation line gives the value of initial $^{26}\text{Mg}/^{24}\text{Mg}$, and the slope, the value for initial $^{26}\text{Al}/^{27}\text{Al}$, at the time of formation of the analyzed object. As can be seen from figure 1, the initial value of $^{26}\text{Al}/^{27}\text{Al}$ at the time of formation of the Allende CAI WA was inferred to be 5×10^{-5} .

The discovery of ^{26}Al was followed by that of ^{107}Pd (half-life = 6.5 Ma; Kelly and Wasserburg 1978; see also Chen and Wasserburg 1996) in iron meteorites. An excess of ^{107}Ag that correlates with the abundance of Pd was found for several iron meteorites and the best initial value for $^{107}\text{Pd}/^{108}\text{Pd}$ at the time of formation of

these meteorites was inferred to be 2×10^{-5} . ^{53}Mn (half life = 3.7 Ma) was the next short-lived nuclide whose presence in Allende CAIs was inferred from the presence of excess ^{53}Cr and an initial $^{53}\text{Mn}/^{55}\text{Mn}$ ratio of 4.4×10^{-5} (at the time of CAI formation) was estimated from the data (Birck and Allègre 1985). However, recent studies of Mn-Cr isotopic systematics in differentiated meteorites and chondrules (Lugmair and Shukolyukov 1998; Nyquist *et al* 1997) suggest that the inferred initial could be an over-estimate by almost a factor of five. This aspect will be discussed at length in a later section. It is important to note here that the presence of all the short-lived nuclides (see, table 1) in the early solar system cannot be established from a study of the same suite of samples (e.g., the CAIs or the differentiated meteorites). The problem is related to both the time scales of processes and the chemistry of the samples. The shorter-lived nuclides like ^{41}Ca and ^{26}Al , belonging to the refractory group of elements, will be primarily incorporated into the early forming refractory solids like the Ca-Al-rich Inclusions (CAIs). However, incorporation of the longer-lived nuclides of elements like Fe, Mn and Pd will be inhibited by the refractory nature of the CAIs, and even if present, the abundance of these nuclides in CAIs will be extremely low, making detection of the decay products of the radioactive species of these elements very difficult. On the other hand, both ^{41}Ca and ^{26}Al will decay significantly by the time of formation of non-refractory silicates and metals present in ordinary chondrites and differentiated meteorites, and these meteorites will primarily host the relatively longer-lived nuclides. In table 1, we have included extrapolated values for the initial abundances of some of the longer-lived nuclides at the time of CAI formation along with the actual value obtained from studies of samples of differentiated meteorites.

There has been a spurt of activity in this field in the nineties and evidence has been obtained to establish the presence of three new short-lived nuclides (^{60}Fe , ^{41}Ca , ^{182}Hf) in the early solar system. Weak to strong hints have also been found for the possible presence of three additional radionuclides (^{99}Tc , ^{92}Nb , ^{36}Cl). The presence of the short-lived nuclide ^{60}Fe (half-life = 1.5 Ma) in the early solar system has been established from the observed excess in its decay product, ^{60}Ni , in bulk samples of several differentiated meteorites (Shukolyukov and Lugmair 1993a,b). The excess in ^{60}Ni also correlates with the abundance of ^{56}Fe in the samples. However, the correlation appears to be disturbed when one considers data for mineral separates. This was attributed to possible elemental fractionation taking place during or following the decay of ^{60}Fe within these objects, which makes it difficult to infer an accurate value for the initial $^{60}\text{Fe}/^{56}\text{Fe}$ from this data set. However, later studies of Mn-Cr isotopic systematics in the same set of meteorites showed them to be coeval and a value of $\sim 4 \times 10^{-9}$

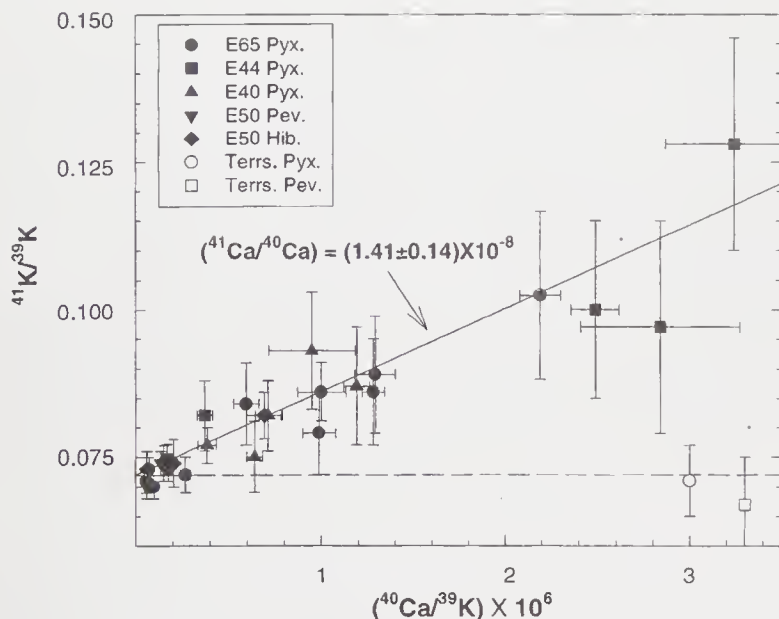


Figure 2. Potassium isotopic ratio, $^{41}\text{K}/^{39}\text{K}$, measured in refractory oxides (hibonite = Hib; perovskite = Pev) and silicate (pyroxene [fassaite] = Pyx) phases in several Ca-Al-rich refractory inclusions (E40, E44, E50, E65) from the Efremovka meteorite, plotted as a function of their $^{40}\text{Ca}/^{39}\text{K}$ ratios. The dotted line represents the reference (normal) $^{41}\text{K}/^{39}\text{K}$ ratio of 0.072; data for terrestrial fassaite and perovskite fall along this line [from Srinivasan *et al* 1996].

has been inferred for the initial abundance of $^{60}\text{Fe}/^{56}\text{Fe}$ at the time of formation of these differentiated meteorites belonging to the eucrite group (Lugmair *et al* 1995).

Search for the presence of the short-lived nuclide ^{41}Ca (half-life $\sim 10^5$ years) in meteorite samples was carried out both at Caltech, USA, and at Max Planck Institute für Chemie, Mainz, Germany, during the eighties. While the results obtained at Mainz were negative, Hutcheon *et al* (1984) from Caltech suggested that the data obtained by them from the study of Allende CAIs provide a possible hint for the presence of this nuclide in the early solar system. The first conclusive proof for the presence of this nuclide in the early solar system was provided by the results obtained at the Physical Research Laboratory, Ahmedabad, India, from a study of several CAIs from the primitive carbonaceous meteorite, Efremovka (Srinivasan *et al* 1994). The CAIs found in the Efremovka meteorite are considered to be more pristine and much well preserved than the CAIs in the Allende meteorite, based on petrographic and trace element data (Nazarov *et al* 1982, 1984). Mg-Al isotopic studies of these objects carried out by us (Goswami *et al* 1994) confirmed this suggestion and led to the choice of the Efremovka CAIs to look for possible excess of ^{41}K due to decay of ^{41}Ca . The data shown in figure 2 clearly demonstrate that the measured values of $^{41}\text{K}/^{39}\text{K}$ in many of the analyzed samples are higher than the normal value of 0.072. Further, this excess also correlates well with the measured $^{40}\text{Ca}/^{39}\text{K}$ ratio in the analyzed phases indicating that the excess ^{41}K is due to *in situ* decay of ^{41}Ca that got incorporated at the

time of formation of the Efremovka CAIs. Later studies provided additional evidence for the presence of ^{41}Ca in other Efremovka CAIs as well as in refractory hibonite (Ca-Al-oxide) grains from the carbonaceous chondrite Murchison and from one Allende CAI (Srinivasan *et al* 1996; Sahijpal *et al* 1998). The best value for the initial $^{41}\text{Ca}/^{40}\text{Ca}$, at the time of formation of the CAIs, is estimated to be $\sim 1.5 \times 10^{-8}$. ^{41}Ca is the shortest-lived nuclide among the now-extinct nuclides whose initial presence in the early solar system have been established from meteorite studies (table 1). As discussed later, the presence of ^{41}Ca in early solar system objects imposes very important constraint on the formation time scale of these objects.

^{182}Hf is the most recent entry into the list of the short-lived nuclides that were present in the early solar system. ^{182}Hf (half-life = 9 Ma) decays to ^{182}W ; while Hf has an affinity for silicates, W prefers to go with metals. This makes the Hf-W isotopic system most ideal to infer time scales of silicate/metal fractionation taking place during differentiation in meteorite parent bodies (planetesimals) and in the Moon and planets like the Earth and Mars. The presence of ^{182}Hf in the early solar system has been inferred from the lower value of the measured $^{182}\text{W}/^{184}\text{W}$ ratio in iron meteorites (by about 4ε units; ε = parts per ten thousands), compared to the measured ratios in samples of carbonaceous chondrites (Lee and Halliday 1995, 1996; Harper and Jacobsen 1996). This deficit is interpreted as due to fractionation and segregation of metal (W) during differentiation taking place in the parent bodies of iron meteorites prior to significant decay of ^{182}Hf . Although a correlation of excess ^{182}W with the abundance of the parent element (Hf) is yet to be established, the indirect evidences are robust enough to conclude that ^{182}Hf was indeed present in the early solar system. The initial $^{182}\text{Hf}/^{180}\text{Hf}$ inferred from the available data is $\sim 2 \times 10^{-4}$.

3. Sources of the short-lived nuclides

All the short-lived nuclides present in the early solar system are generally considered to be of stellar origin (table 1). However, there have been suggestions that some of them, particularly the ones with shorter half-life, could be produced by energetic particle interactions with gas and dust in the protosolar molecular cloud or later in the solar nebula. In fact there has also been a suggestion that these nuclides could have had a "fossil" origin and were transported to the solar nebula by circumstellar dust that incorporated these nuclides at the time of their formation in stellar/supernova envelopes (Clayton 1982). In this scenario, one cannot consider these nuclides as time markers of early solar system processes. However, the isotopic systematics and other characteristics observed in the analyzed CAIs are not consistent with this scenario; a

detailed discussion of this aspect can be found in Podosek and Swindle (1988) and MacPherson *et al* (1995). We believe that the meteorite data argue strongly for the “live” presence of the short-lived nuclides in the early solar system and shall try to pinpoint the most plausible source(s) of these nuclides.

3.1 Production of short-lived nuclides by energetic particles

The possibility of production of the short-lived nuclide ^{26}Al by energetic particles from an active early Sun interacting with gas and dust in the solar nebula was proposed soon after the discovery of ^{26}Al (Heymann and Diczkaniec 1976). However, the flux of solar energetic particles (SEP) needed to match the initial $^{26}\text{Al}/^{27}\text{Al}$ ratio (5×10^{-5}) turned out to be extremely high (more than 10^5 times the contemporary flux), and ad-hoc features in the energy spectrum of the SEP had to be invoked to avoid co-production of other isotopic anomalies. Several different scenarios for SEP irradiation of nebular gas and dust were proposed subsequently to match the initial abundance of ^{26}Al in the early solar system (Clayton *et al* 1977; Lee 1978; Heymann *et al* 1978). The inadequacy of these models was immediately evident following the discovery of the short-lived nuclide ^{53}Mn , when it was shown that the same set of model parameters for SEP cannot produce appropriate amounts of ^{26}Al and ^{53}Mn to match the meteorite data (Wasserburg and Arnould 1987). We have now completed an in-depth study of this problem by considering SEP production of the four short-lived nuclides ^{26}Al , ^{36}Cl , ^{41}Ca and ^{53}Mn . We have ignored shelf-shielding of SEP particles by nebular gas and dust to maximize production. Micron- to millimeter-sized grains of solar composition, and following a power-law size-distribution, are considered

as targets. The results obtained by us (see figure 3) clearly demonstrate that no combination of flux enhancement factor and irradiation duration can lead to co-production of ^{26}Al with any of the other three nuclides in appropriate amounts to match the meteorite data; production of ^{26}Al in the required amount leads to overproduction of all the other three nuclides by almost an order of magnitude. It may however be noted that the nuclides, ^{41}Ca , ^{36}Cl and ^{53}Mn , may be co-produced at the required level if we consider an irradiation duration of about one million years and a flux enhancement factor of $\sim 10^4$, compared to the contemporary long-term averaged SEP flux [$N(E > 10 \text{ MeV}) = 100 \text{ protons cm}^{-2} \text{ s}^{-1}$] deduced from lunar sample studies. Further, if the lower initial abundance of ^{53}Mn proposed by Lugmair and Shukolyukov (1998) is indeed correct, production of ^{53}Mn is feasible even with a lower flux enhancement factor that will not lead to any significant production of ^{41}Ca and ^{26}Al . We finally note that SEP irradiation cannot produce the short-lived nuclide ^{60}Fe that has a half-life intermediate between those of ^{26}Al and ^{53}Mn .

A completely different model for the energetic particle production of the short-lived nuclides in the protosolar molecular cloud fragment itself has been proposed a few years back (Clayton 1994). This proposal is based on the observation of enhanced flux of gamma rays from a star forming region in the Orion molecular cloud that suggests the presence of an enhanced flux of low energy heavy ions in this molecular cloud complex (Bloemen *et al* 1994). The protosolar molecular cloud fragment must have been a part of such a molecular cloud complex, prior to its collapse to form the solar system. Thus, the gas and dust in the protosolar cloud could have been irradiated by energetic particles present in such a cloud complex. Although the proposal looks attractive, detailed calculations

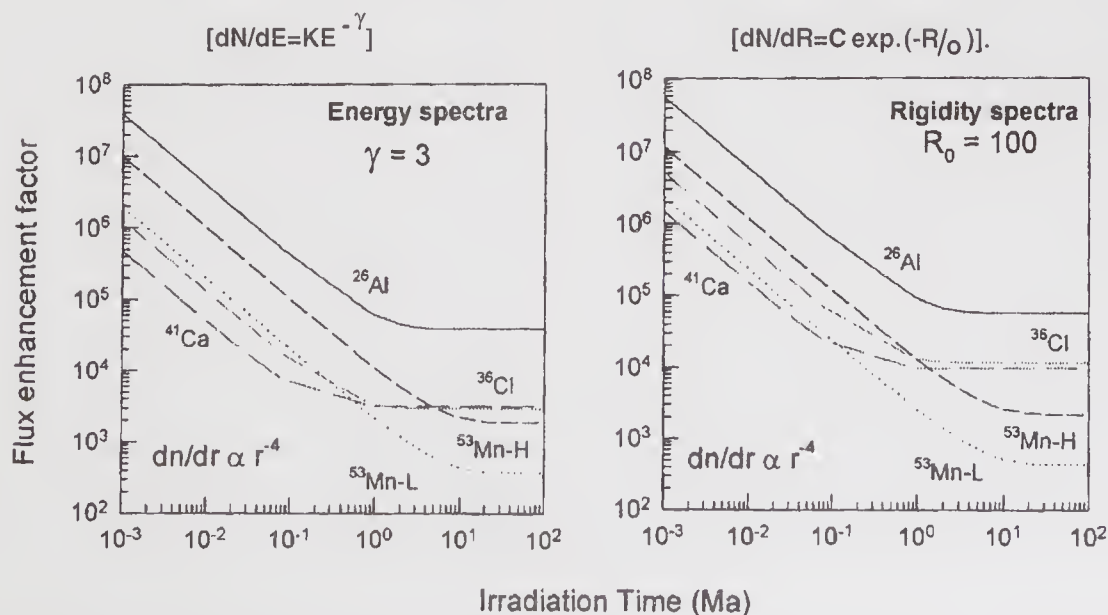


Figure 3. Enhancement factor in solar energetic particle (SEP) flux, relative to its long-term averaged value of $N(>10 \text{ MeV}) = 100 \text{ protons cm}^{-2} \text{ s}^{-1}$, required to explain the initial abundances of several short-lived nuclides in the early solar system, plotted as a function of SEP irradiation duration. Two values for initial abundance of ^{53}Mn are used (see table 1 and text). Results are presented for SEP flux representation both in kinetic energy [$dN/dE = KE^{-\gamma}$] and rigidity [$dN/dR = c \exp(-R/R_0)$].

(Clayton and Jin 1995a; Ramaty *et al* 1996), that considered various compositions for the irradiating particles as well as for the irradiated components, showed that it has the same drawback as in the SEP irradiation models; matching of the meteorite data for initial abundance of ^{26}Al leads to overproduction of both ^{41}Ca and ^{53}Mn . A self-consistent solution that can account for the meteorite data for the short-lived nuclides, ^{41}Ca , ^{26}Al , and ^{53}Mn , could not be obtained in both the energetic particle irradiation models.

Several variants of the SEP irradiation model have also been proposed in recent years. These include production by anomalous cosmic rays in the early solar system (Clayton and Jin 1995b) and the fluctuating X-wind model that proposes both formation and irradiation of CAIs very close to the proto-Sun (Shu *et al* 1997; Lee *et al* 1998). As in the earlier models for SEP irradiation, these models also fail to co-produce the short-lived nuclides in amounts that will match the meteorite observations. This shortcoming of all the irradiation models has more to do with the relevant nuclear reaction cross sections and abundance of the target elements rather than the irradiation scenarios proposed. Since the target composition is well defined (close to “solar” composition in all the scenarios) and the reaction cross-sections are well known, the relative productions of the different short-lived nuclides cannot be changed much by varying the fluxes and energy spectra of the interacting particles. Further, all the irradiation models fail to produce the short-lived nuclide ^{60}Fe (see however, Lee *et al* 1998). We shall now consider the case for a stellar origin for these short-lived nuclides.

3.2 A stellar origin for the short-lived nuclides

Injection of freshly synthesized material from one or more stellar source(s) into the protosolar molecular cloud fragment has remained the favourite hypothesis to explain the presence of the short-lived nuclides in the early solar system. We have noted earlier that the three relatively longer-lived, high-mass radionuclides, ^{182}Hf , ^{129}I and ^{244}Pu , are exclusively produced via rapid neutron capture (r-process) nucleosynthesis during supernova events. The initial abundances of these nuclides in the early solar system are determined by the contribution from continuous galactic nucleosynthesis and may be inferred from the known supernova rate in our galaxy and the yields of these nuclei during supernova events (e.g., see Wasserburg *et al* 1996). The possibility that continuous galactic nucleosynthesis could perhaps also contribute some fraction towards the inventory of the other short-lived nuclides like ^{107}Pd , ^{53}Mn and ^{60}Fe present in the early solar system cannot be ruled out (Wasserburg *et al* 1996). Nonetheless, the emphasis in this field of research at present is to identify a single stellar source that can hopefully account for all the short-lived nuclides with

mean life <10 Ma that were present in the early solar system.

Three specific stellar objects have been proposed as possible source for the short-lived nuclides ^{41}Ca , ^{36}Cl , ^{26}Al , ^{60}Fe , ^{53}Mn and ^{107}Pd present in the early solar system (table 1). These are:

- A thermally pulsing asymptotic giant branch (TP-AGB) star,
- a type-II supernova (SN), and
- a non-exploding Wolf-Rayet (W-R) star.

One can check the viability of any one of these stellar objects being the source of the short-lived nuclides in the early solar system by adopting the following approach: • calculate the yield of each radionuclide and its stable counterpart (e.g., ^{26}Al and ^{27}Al or ^{41}Ca and ^{40}Ca) during nucleosynthesis taking place in the stellar source, • choose two parameters, the “free-decay time interval”, defining the time elapsed between the synthesis of these nuclides in the stellar source and their final incorporation into the analyzed early solar system solids, and the “dilution factor”, i.e., the dilution of the freshly synthesized stellar material with preexisting material in the protosolar molecular cloud and in the intervening medium between the stellar source and the protosolar molecular cloud that are devoid of the short-lived species, and • look for a self-consistent set of parameters that will yield initial abundances of the nuclides consistent with the meteorite observations (table 1).

The possibility that a TP-AGB star could be the source of the short-lived nuclides present in the early solar system has been discussed at length by Cameron (1993). Yields of the short-lived nuclides, ^{41}Ca , ^{36}Cl , ^{26}Al , ^{60}Fe , and ^{107}Pd , during the TP-AGB stage for a three solar mass star have been evaluated by Wasserburg *et al* (1994, 1995) and Gallino *et al* (1996). Their results suggest that a self-consistent solution is possible if one considers a free-decay time interval of $\sim 6 \times 10^5$ years and a dilution factor of $\sim 10^4$. These calculations also predict the presence of the radionuclides, ^{205}Pb (half-life = 15 Ma) and ^{135}Cs (half-life = 2.3 Ma) in the early solar system; the presently available upper limit estimate for the initial abundance of ^{205}Pb in meteorites (Chen and Wasserburg 1987) is not inconsistent with these predictions. A major problem with the TP-AGB star as a source is its inability to synthesize ^{53}Mn . Further, there are some uncertainties in estimating the neutron source function responsible for producing the nuclides ^{41}Ca , ^{36}Cl , ^{60}Fe and ^{107}Pd . The chance association of a TP-AGB star with a molecular cloud complex also appears to be small (Kastner and Myers 1994); however, over the life-time of a molecular cloud complex the possibility of such an association could be quite significant.

Cameron *et al* (1995) have examined the case of a massive (>25 solar mass) supernova as a source of the short-lived nuclides in the early solar system by

considering the yields of these nuclides during supernova events (Woosley and Weaver 1995). In principle, a supernova could be a source for several short-lived nuclides (^{41}Ca , ^{36}Cl , ^{26}Al , ^{60}Fe and ^{53}Mn) present in the early solar system. However, ^{26}Al is under-produced and a self-consistent dilution factor for all the nuclides cannot be achieved; the distance of the supernova from the protosolar cloud is estimated to be $\sim 4\text{--}10$ parsec in this model. To overcome the problem of underproduction of ^{26}Al , Cameron *et al* (1995) suggested that the supernova could be associated with a very massive star (>60 solar masses) which has already gone through the Wolf-Rayet stage. In such a case, ^{26}Al , produced and ejected during the W-R stage is subsequently picked up by the fast moving supernova ejecta. Unfortunately, the dynamics of supernova explosion and mixing of supernova ejecta with surrounding medium are not well understood at present. It is also difficult to ascertain accurately the production of ^{107}Pd during a massive SN event.

The possibility that a Wolf-Rayet star could be the source for the short-lived nuclides in the early solar system was initially proposed by Dearborn and Blake (1985, 1988). More recently Arnould *et al* (1997a,b) have considered the case for a non-exploding W-R star (>60 solar mass) as a source of these nuclides. They could obtain a self-consistent solution for only a couple of nuclides (^{41}Ca and ^{36}Cl) with a dilution factor of a few thousands and a very short free-decay time interval of 2×10^5 years. ^{26}Al is underproduced, ^{60}Fe is extremely underproduced and like in the case of a TP-AGB star, a W-R star cannot produce ^{53}Mn . An interesting feature of this model is the prediction of an initial abundance of ^{205}Pb in the early solar system, which is even higher than the presently inferred upper limit estimate from meteorite data. As in the case of the other stellar sources, the dynamics of interaction of W-R ejecta with its surrounding environment is not well understood.

Even though there are problems associated with all the three stellar objects considered above, they appear to be a better choice than energetic particle production as the source of the short-lived nuclides present in the early solar system. As already noted, co-production of ^{41}Ca , ^{26}Al and ^{53}Mn , in the required amounts to match the meteorite data is not possible in the latter case and productions of ^{60}Fe and ^{107}Pd are negligible. The possibility that a stellar object could be the source of the short-lived nuclides is also supported by the recent observations made by us (Sahijpal *et al* 1998) that suggest a strong correlation in the presence of the two short-lived nuclides, ^{41}Ca and ^{26}Al , in early solar system objects. This can be seen in figure 4, where we plot the inferred initial abundances of $^{26}\text{Al}/^{27}\text{Al}$ and $^{41}\text{Ca}/^{40}\text{Ca}$ for samples from three different meteorites. The close correlation in the presence/near-absence of ^{26}Al and ^{41}Ca is clearly evident. When present, the initial abundances of $^{26}\text{Al}/^{27}\text{Al}$ and $^{41}\text{Ca}/^{40}\text{Ca}$ are

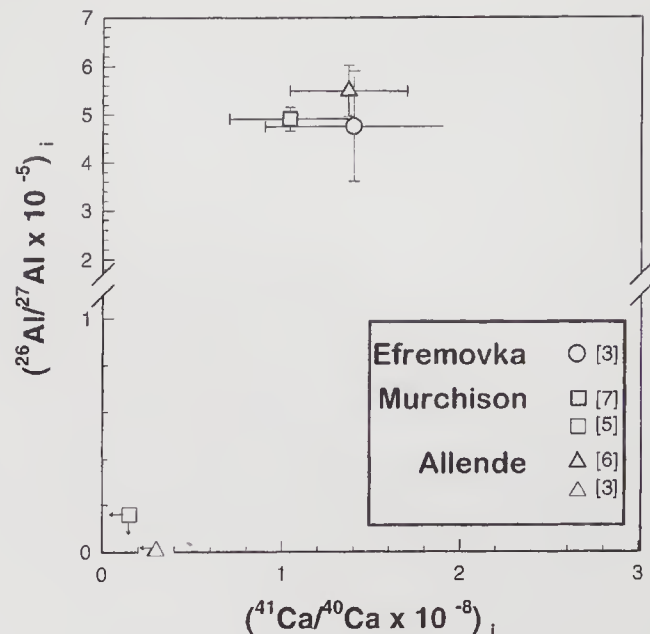


Figure 4. A plot of initial abundances of $^{26}\text{Al}/^{27}\text{Al}$ and $^{41}\text{Ca}/^{40}\text{Ca}$ in a set of refractory oxide phase (hibonite: $\text{CaAl}_{12-2X}\text{Mg}_X\text{Ti}_X\text{O}_{19}$) from three carbonaceous meteorites, Murchison, Allende and Efremovka. The number of analyses performed to obtain the initial abundance in each case is given within parenthesis. Data taken from Sahijpal *et al* (1998).

close to their canonical values of 5×10^{-5} and 1.5×10^{-8} , respectively. This observation indicates that these two nuclides were derived from a single source and followed the same pathways in the solar nebula before getting incorporated in the analyzed early solar system solids. Since *co-production of these two nuclides in the required amount is not possible in any of the irradiation models*, our data strongly suggest a stellar source for these nuclides.

The choice of the most plausible stellar source is made difficult as none of them could account for the whole suite of short-lived nuclides with mean life <10 Ma. TP-AGB star is an interesting possibility only if ^{53}Mn can be accounted by energetic particle production or contribution from continuous galactic nucleosynthesis. It should be noted that our data on correlation between the presence of ^{26}Al and ^{41}Ca do not rule out their possible production by energetic particle interactions; however, if it were there, this contribution has to be much smaller compared to that coming from a stellar source. In this context, an accurate knowledge of the initial abundance of ^{53}Mn in the early solar system has become very important. As noted earlier if the revised initial abundance of $\sim 10^{-5}$ for $^{53}\text{Mn}/^{55}\text{Mn}$, proposed recently by Lugmair and Shukolyukov (1998), is indeed correct, the possibility that ^{53}Mn was produced by energetic particle interactions without concurrently producing much of ^{41}Ca and ^{26}Al cannot be ruled out. However, if we can rule out both energetic particle production as well as contribution from galactic nucleosynthesis as possible sources of ^{53}Mn , a supernova remains the most viable source for the short-lived nuclides present in the early solar system. While the case for a Wolf-Rayet star as a

source is not very promising, a precise determination of the initial abundance of ^{205}Pb in the early solar system can clinch the choice between a TP-AGB and a W-R star.

4. Short-lived nuclides and time scales for early solar system processes

4.1 Time scale for the formation of the Sun

A stellar origin for the short-lived nuclides puts a very strong constraint on the time scale for the collapse of the protosolar molecular cloud that led to the formation of the Sun and some of the first solar system solids. Obviously, the most stringent constraint comes from ^{41}Ca , the nuclide with the shortest half-life (10^5 years), whose presence in early solar system solids suggests that this time scale is less than a million years. As already noted, a self-consistent solution that can explain the meteorite data for several of the short-lived nuclides requires this time interval to be $\sim 6 \times 10^5$ years with a TP-AGB star as a source and an even lower value of $\sim 2 \times 10^5$ years with a W-R star as a source. The short collapse time scale would imply a very dense protosolar molecular cloud with number density of hydrogen molecule, $n(\text{H}_2)$, $> 10^4 \text{ cm}^{-3}$. This short time scale also suggests the possibility for a triggered collapse of the protosolar molecular cloud with the stellar source responsible for production and injection of the short-lived nuclides itself acting as the trigger. In fact recent numerical simulation studies of this problem have shown that the dynamics of such a collapse appears to be highly probable within the time scale constraints placed by the data for the short-lived nuclides (Boss 1995; Foster and Boss 1997; Vanhala and Cameron 1998; Vanhala 1998).

4.2 Formation of early solar system solids and time scale for nebular processing

Meteoritic material is composed of several distinctly different types of objects that were perhaps formed at different epochs during the early evolutionary history of the solar system. The Ca-Al-rich refractory objects (CAIs), representing some of the first formed solids in the solar system, are found primarily in primitive carbonaceous chondrites. As already noted the initial presence of the short-lived nuclide ^{41}Ca in CAIs indicate that ^{41}Ca was still extant in the solar nebula at the time of CAI formation, and they must have formed within a million years of protosolar cloud collapse.

Another more ubiquitous object found in all chondritic meteorites is chondrule, the tens of micron to few millimeter sized spheroids that represent quickly crystallizing molten silicate droplets. The chondrules are generally considered to have formed in the solar

nebula during some high temperature processes (e.g., see, Grossman 1988). Even after a prolonged search, the initial presence of the short-lived nuclide ^{26}Al was found only in a small set of chondrules from a specific class of meteorites, the unequilibrated ordinary chondrites (Russel *et al* 1996, 1997; Kita *et al* 1998). Further, the measured initial abundance of $^{26}\text{Al}/^{27}\text{Al}$ in the chondrules are lower than the value of 5×10^{-5} measured in CAIs, and ranges between $< 10^{-6}$ and 2×10^{-5} . If we attribute this difference in the initial abundance of ^{26}Al to late formation of chondrules, it will imply that the chondrule formation started within a million years after the formation of the CAIs and continued for at least five million years when the chondrules devoid of ^{26}Al were formed. However, this chronological interpretation is based on the assumption that the initial abundance of $^{26}\text{Al}/^{27}\text{Al}$ was the same at both the CAI and chondrule forming zone(s) in the solar nebula. It is difficult to uniquely prove this assumption, particularly in view of the fact that many of the CAIs also have lower than normal initial abundance of $^{26}\text{Al}/^{27}\text{Al}$ or are devoid of ^{26}Al . However, the differences seen among the CAIs are generally attributed to secondary processes affecting these objects and the data are not inconsistent with the assumption of a uniform initial $^{26}\text{Al}/^{27}\text{Al}$ ratio in the CAI-forming zone (e.g., see MacPherson *et al* 1995). A very detailed study of Mn-Cr isotopic systematics in a set of meteorites belonging to the eucrite group has also shown that the initial $^{53}\text{Mn}/^{55}\text{Mn}$ ratio in the eucrite forming zone was rather uniform (Lugmair and Shukolyukov 1998). In the discussion that follows, we shall assume a uniform distribution of the short-lived nuclides in the meteorite-forming zone of the solar nebula. If the chondrules are indeed nebular products, the lower abundance as well as the absence of ^{26}Al in them would suggest a time scale of several million years during which nebular processing must have been active in the early solar system (Russel *et al* 1996). This time scale, however, contradicts the time scale of less than a million years for the formation of larger (km-sized) objects, inferred from analytical studies of evolution of small objects in the solar nebula (e.g., see Wiedenschilling 1988), and an even shorter time scale of $< 10^5$ years within which the millimeter-sized CAIs are expected to spiral in towards the Sun (Wiedenschilling 1977). Thus, one would require a very special mechanism to store the CAIs until chondrule formation is complete so that both of them could be incorporated together in the carbonaceous chondrites. The only other possibility is secondary processes affecting the chondrules leading to exchange/redistribution of Mg isotopes that resulted in the lower initial $^{26}\text{Al}/^{27}\text{Al}$ values. However, the very low-grade metamorphism suffered by the unequilibrated ordinary chondrites makes this proposition rather unlikely. A solution to this problem is an important challenge in the field of planetary sciences.

4.3 Time scale for the formation and differentiation of planetesimals

The meteorites belonging to achondrite, stony-iron and iron groups are derived from planetesimals (meteorite parent bodies) that have undergone extensive melting and differentiation. Initial presence of ^{107}Pd (half-life = 6.5 Ma) has been established in the iron and stony-iron groups of meteorites (Kelly and Wasserburg 1978; see also Chen and Wasserburg 1996). In addition, the basaltic achondrites belonging to the eucrite sub-group contain evidence for the presence of the two short-lived nuclides, ^{60}Fe and ^{53}Mn , having half-lives of 1.5 Ma and 3.7 Ma, respectively (Shukolyukov and Lugmair 1993a,b; Lugmair *et al* 1995; Lugmair and Shukolyukov 1998). If we compare the value of initial $^{53}\text{Mn}/^{55}\text{Mn}$ ratio of $\sim 4.4 \times 10^{-5}$ for the CAIs (Birck and Allègre 1985) with the value of $\sim 5 \times 10^{-6}$ reported for the eucrites (Lugmair and Shukolyukov 1998), it will imply a time interval of ~ 12 Ma between the formation of the CAIs and the eucrites, that are believed to be a product of widespread melting and differentiation taking place on large (hundreds of km-sized) planetesimals. However, absolute U-Pb ages of CAIs and basaltic achondrites belonging to the angrite group (Manhès *et al* 1988; Lugmair and Galer 1992; Göpel *et al* 1994) suggest a shorter time interval between their formation, even though the initial $^{53}\text{Mn}/^{55}\text{Mn}$ in angrite is much lower ($\sim 10^{-6}$) than that measured in the eucrites indicating that formation of eucrites preceded that of angrites. It has been suggested by Lugmair and Shukolyukov (1998) that the initial abundance of ^{53}Mn determined in CAI may be affected by intrinsic isotopic anomalies in chromium present in the carbonaceous chondrites (note that ^{53}Mn decays to ^{53}Cr and presence of ^{53}Mn is inferred from measurement of the abundances of Cr isotopes). Based on data for both ^{60}Fe and ^{53}Mn in eucrites along with the data for absolute age of CAIs and differentiated meteorites, Lugmair and Shukolyukov (1998) suggest a time scale of ~ 6 Ma for the time interval between the formation of CAIs and the eucrites. This time scale is in close agreement with the very recent report of the possible presence of ^{26}Al in the Piplia-Kalan eucrite with an initial $^{26}\text{Al}/^{27}\text{Al}$ value of $\sim 7 \times 10^{-7}$ (Srinivasan *et al* 1998), suggesting a time difference of ~ 5 Ma between the formation of the CAIs and the eucrites.

The iron meteorites are supposed to be representative of Fe-Ni cores of large planetesimals and thus the presence of the short-lived nuclide ^{107}Pd in them allows us to constrain the time scale for core formation in such planetesimals. Similarly, the presence of short-lived nuclides in stony-iron meteorites, which contain both silicate and metal phases, allow us to infer the time scale for magmatism and differentiation in such objects. Although relative time scale with respect to CAI formation cannot be deduced from the data on

initial abundance of ^{107}Pd in these meteorites, the spread in the inferred initial $^{107}\text{Pd}/^{108}\text{Pd}$ in them (Chen and Wasserburg 1996) suggests a time scale of ~ 12 Ma for the formation of these meteorites. This would suggest that large-scale magmatism, differentiation and crystallization of Fe-Ni core in asteroidal-sized bodies must have been complete within this time scale.

The recent discovery of deficit in $^{182}\text{W}/^{184}\text{W}$ ratio in iron meteorites relative to carbonaceous chondrites also supports a small time scale for differentiation in meteorite parent bodies. The measured deficit of a few parts per ten thousand in the $^{182}\text{W}/^{184}\text{W}$ ratio has been attributed by Lee and Halliday (1995) to the onset of silicate-metal fractionation in the parent bodies of iron meteorites prior to any significant decay of ^{182}Hf . The observed deficit in the initial ratio corresponds to a time scale of only a few million years within which silicate/metal fractionation in these objects was nearly complete. In fact, additional data obtained by the same group also suggest that accretion, differentiation and core formation in the parent body of the HED (howardite, eucrite and diogenite) meteorites took place within a time scale of ~ 10 Ma (Lee and Halliday 1996).

In summary, the data for the short-lived nuclides in meteorites suggest a very short time-scale of less than a million years within which the protosolar molecular cloud collapsed to form the Sun and some of the first solar system solids like the Ca-Al-rich inclusions (CAIs). The time scale of nebular processing, as inferred from the isotopic data for CAIs and chondrules is several million years, which is difficult to accommodate in the current models of the evolution of small objects in the solar nebula. The available data also suggest that the formation of the basaltic achondrites, that involved large scale melting and differentiation of meteorite parent bodies (planetesimals), as well as of iron meteorites, that involved formation and crystallization of metallic cores within planetesimals, took place within the first ten million years in the history of the solar system.

Even though our understanding of the processes leading to the formation and early evolution of the solar system has increased considerably in recent years, there are several aspects that need further attention. These include: (i) confirmation of the presence of the short-lived nuclides ^{36}Cl , ^{99}Tc , ^{205}Pb , ^{92}Nb , for which weak to strong hints are presently available; such data will provide additional constraints to pinpoint the source of the short-lived nuclides present in the early solar system, (ii) identification of isotopic anomalies in diagnostic nuclides that will provide information on possible contribution towards the inventory of the short-lived nuclides in the early solar system from energetic particle production; Lee *et al* (1998) have recently proposed that ^{50}V and ^{138}La could be two potential nuclides in this regard, (iii) a precise determination of initial $^{53}\text{Mn}/^{55}\text{Mn}$ abundance

at the time of CAI formation so that the conflict between Mn-Cr and U-Pb isotopic systematics in estimating the time scale for melting and differentiation of the parent bodies of the achondrites can be resolved, (iv) need for better stellar evolution and nucleosynthesis models to pinpoint plausible stellar source(s) of the short-lived nuclides and further analytical and observational studies related to the possibility of a triggered origin of the solar system.

Acknowledgement

I am grateful to A Boss, A G W Cameron, D D Clayton, A Davis, I D Hutcheon, R Gallino, R Lingenfelter, G Lugmair, K Marti, R Ramaty, F Shu, H Vanhala, G J Wasserburg and E Zinner for discussions on various aspects of the formation and early evolution of the solar system. I acknowledge with thanks the inputs and comments received from S V S Murty, and S Sahijpal in preparing this article.

References

- Arnould M, Paulus G and Meynet G 1997a Short-lived radionuclide production by non-exploding Wolf-Rayet stars; *Astron. Astrophys.* **321** 452–465
- Arnould M, Meynet G and Paulus G 1997b Wolf-Rayet stars and their nucleosynthetic signatures in meteorites; *Astrophysical implications of the laboratory study of presolar materials* (eds) T J Bernatowicz and E Zinner (Woodbury: AIP), pp. 179–202
- Birck J L and Allègre C J 1985 Evidence for the presence of ^{53}Mn in the early solar system; *Geophys. Res. Lett.* **12** 745–748
- Bloemen H, Wijnands R, Bennet K, Diehl R, Hermsen W, Lichti G, Morris D, Ryan J, Schonfelder V, Strong A W, Swanenburg B N, de Vries C and Winkler C 1994 COMPTEL observations of the Orion complex: Evidence for cosmic-ray induced gamma-ray lines; *Astron. Astrophys.* **281** L5–L8
- Boss A P 1995 Collapse and fragmentation of molecular cloud cores. II. Collapse induced by stellar shock waves; *Astrophys. J.* **439** 224–236
- Cameron A G W 1993 Nucleosynthesis and star formation; *Protostars and planets III* (eds) E H Levy and J I Lunine (Tucson: Univ. of Arizona Press), pp. 47–73
- Cameron A G W, Höflich P, Myers P C and Clayton D D 1995 Massive supernovae, Orion gamma rays, and the formation of the solar system; *Astrophys. J. Lett.* **447** L53–L57
- Chen J H and Wasserburg G J 1987 A search for evidence of extinct lead 205 in iron meteorites; *Lunar Planet. Sci.* **XVIII** 165–166
- Chen J H and Wasserburg G J 1996 Live ^{107}Pd in the early solar system and implications for planetary evolution; *Earth Processes: Reading the isotopic code* (eds) A Basu and S Hart, *AGU Geophys. Mon. Ser.* **95**, pp 1–20
- Clayton D D 1982 Cosmic chemical memory: A new astronomy; *Q. J. R. Astron. Soc.* **23** 174–212
- Clayton D D 1994 Production of ^{26}Al and other extinct radionuclides by low-energy heavy cosmic rays in molecular clouds; *Nature* **368** 222–224
- Clayton D D and Jin L 1995a Gamma rays, cosmic rays, and extinct radioactivity in molecular cloud; *Astrophys. J.* **451** 681–699
- Clayton D D and Jin L 1995b A new interpretation of ^{26}Al in meteoritic inclusions; *Astrophys. J. Lett.* **451** L87–L91
- Clayton D D, Dwek E and Woosley S E 1977 Isotopic anomalies and proton irradiation in the early solar system; *Astrophys. J.* **214** 300–315
- Dearborn D S P and Blake J B 1985 On the source of the ^{26}Al observed in the interstellar medium; *Astrophys. J. Lett.* **288** L21–L24
- Dearborn D S P and Blake J B 1988 Possible contributions by Wolf-Rayet stars to the protosolar nebula: Extinct radioactivities, or grains of truth from Wolf-Rayet stars? *Astrophys. J.* **332** 305–312
- Foster P N and Boss A P 1997 Injection of radioactive nuclides from the stellar source that triggered the collapse of the presolar nebula; *Astrophys. J.* **489** 346–357
- Gallino R, Busso M, Arlandini C, Lugaro M and Straniero O 1996 Neutron captures in low-mass AGB stars; *Mem. S.A. It.* **67** 761–774
- Göpel C, Manhès G and Allègre C J 1994 U-Pb systematics of phosphates from equilibrated ordinary chondrites; *Earth Planet. Sci. Lett.* **121** 153–171
- Goswami J N, Srinivasan G and Ulyanov A A 1994 Ion microprobe studies of Efremovka CAIs: I. Magnesium isotope composition; *Geochim. Cosmochim. Acta* **58** 431–447
- Grossman J 1988 Formation of chondrules; *Meteorites and the early solar system* (eds) J F Kerridge and M S Matthews (Tucson: Univ. of Arizona Press), pp. 680–696
- Grossman L 1980 Refractory inclusions in the Allende meteorite; *Ann. Rev. Earth Planet. Sci.* **8** 559–608
- Harper C L Jr 1996 Evidence for ^{92}Nb in the early solar system and evaluation of a new p-process cosmochronometer from $^{92}\text{Nb}/^{92}\text{Mo}$; *Astrophys. J.* **466** 437–456
- Harper C L Jr and Jacobsen S B 1996 Evidence for ^{182}Hf in the early solar system and constraints on the timescale of terrestrial accretion and core formation; *Geochim. Cosmochim. Acta* **60** 1131–1153
- Heymann D and Dziczkaniec M 1976 Early irradiation of matter in the solar system: Magnesium (proton, neutron) scheme; *Science* **191** 79–81
- Heymann D, Dziczkaniec M, Walker A, Huss G and Morgan J A 1978 Effects of proton irradiation on a gas phase in which condensation take place. I. Negative ^{26}Mg anomalies and ^{26}Al ; *Astrophys. J.* **225** 1030–1044
- Hohenberg C M, Brazzle R H, Pravdivtseva O V and Meshik A P 1998 The I-Xe chronometer (this volume)
- Hudson G B, Kennedy B M, Podosek F A and Hohenberg C M 1988 The early solar system abundance of ^{244}Pu as inferred from the St. Severin chondrite; *Proc. Lunar Planet. Sci. Conf.* **19** 547–557
- Hutcheon I D, Armstrong J T and Wasserburg G J 1984 Excess ^{41}K in Allende CAI: A hint reexamined; *Meteoritics* **19** 243–244
- Jeffreys P M and Reynolds J H 1961 Origin of excess ^{129}Xe in stone meteorites; *J. Geophys. Res.* **66** 3582–3583
- Kastner J H and Myers P C 1994 An observational estimate of the possibility of encounters between mass-losing evolved stars and molecular clouds; *Astrophys. J.* **421** 605–614
- Kelly W R and Wasserburg G J 1978 Evidence for the existence of ^{107}Pd in the early solar system; *Geophys. Res. Lett.* **5** 1079–1082
- Kita N T, Nagahara T, Togashi S and Morishita Y 1998 New evidence of aluminium-26 from a ferrous-oxide-rich chondrule in Semarkona (LL3.0); *Meteor. Planet. Sci.* **33** A83–A84
- Lee D C and Halliday A N 1995 Hafnium-tungsten chronometry and the timing of terrestrial core formation; *Nature* **378** 771–774
- Lee D C and Halliday A N 1996 Hf-W Isotopic evidence for rapid accretion and differentiation in the early solar system; *Science* **274** 1876–1879

- Lee T 1978 A local proton irradiation model for isotopic anomalies in the solar system; *Astrophys. J.* **219** 217–226
- Lee T, Papanastassiou D A and Wasserburg G J 1976 Demonstration of ^{26}Mg excess in Allende and evidence for ^{26}Al ; *Geophys. Res. Lett.* **3** 109–112
- Lee T, Papanastassiou D A and Wasserburg G J 1977 Aluminium-26 in the early solar system: Fossil or fuel? *Astrophys. J.* **211** 107–110
- Lee T, Shu F H, Shang H, Glassgold A E and Rehm K E 1998 Protostellar Cosmic rays and extinct radioactivities in meteorites; *Astrophys. J.* in press
- Lugmair G W and Shukolyukov A 1998 Early solar system timescales according to ^{53}Mn - ^{53}Cr systematics; *Geochim. Cosmochim. Acta* (in press)
- Lugmair G W and Galer S J G 1992 Age and isotopic relationship among the angrites Lewis Cliff 86010 and Angra Dos Reis; *Geochim. Cosmochim. Acta* **56** 1673–1694
- Lugmair G W, Shukolyukov A and MacIsaac Ch 1995 The abundance of ^{60}Fe in the early solar system; *Nuclei in the Cosmoc III* (eds) M Busso *et al* (AIP), pp. 591–594
- MacPherson G J, Davis A M and Zinner E K 1995 The distribution of aluminium-26 in the early solar system : A reappraisal; *Meteoritics* **30** 365–386
- Manhès G, Göpel C and Allègre C J 1988 Systematique U-Pb dans les inclusions refractaires d'Allende: le plus vieux matériau solaire; *C.R. ATP Planetol.* (in French) 323–327
- Murty S V S, Goswami J N and Shukolyukov Yu A 1997 Excess ^{36}Ar in the Efremovka meteorite: A strong hint for the presence of ^{36}Cl in the early solar system; *Astrophys. J. Lett.* **475** L65–L68
- Nazarov M A, Ulyanov A A, Korina M I and Kolesov G M 1982 Efremovka CAIs: Major and trace element chemistry; *Lunar Planet. Sci.* **XIII** 584–585
- Nazarov M A, Korina M I, Ulyanov A A, Kolesov G M and Sherbovsky E Ya 1984 Minerology, petrology and chemical composition of Ca and Al-rich inclusions of Efremovka meteorite; *Meteoritika* (in Russian) **43** 49–66
- Nyquist L, Lindstorm D, Shih C-Y, Wiesmann H, Mittlefehldt D, Wentworth S and Martinez R 1997 Mn-Cr systematics of chondrules from the Bishunpur and Chainpur meteorites; *Lunar Planet. Sci. Conf.* **XXVIII** 1033–1034
- Podosek F A and Swindle T D 1988 Extinct nuclides; *Meteorites and the early solar system* (eds) J F Kerridge and M S Matthews (Tucson: Univ. of Arizona Press), pp. 1093–1113
- Podosek F A and Nichols Jr R H 1997 Short-lived radionuclides in the solar nebula; *Astrophysical Implications of the laboratory study of presolar materials* (eds) T J Bernatowicz and E Zinner (Woodbury: AIP), pp. 617–647
- Ramaty R, Kozlovsky B and Lingenfelter R E 1996 Light isotopes, extinct radioisotopes and gamma ray lines from low energy cosmic ray interactions; *Astrophys. J.* **456** 525–540
- Reynolds J H 1960 Determination of the age of the elements; *Phys. Res. Lett.* **4** 8–10
- Rowe M W and Kuroda P K 1965 Fissiogenic Xe from the Pasamonte meteorite; *J. Geophys. Res.* **70** 709–714
- Russell S S, Srinivasan S, Huss G R, Wasserburg G J and MacPherson G J 1996 Evidence for wide spread ^{26}Al in the solar nebula and constraints for nebula time scales; *Science* **273** 575–762
- Russell S S, Huss G R, MacPherson G J and Wasserburg G J 1997 Early and late chondrule formation: New constraints for solar nebula chronology from $^{26}\text{Al}/^{27}\text{Al}$ in unequilibrated ordinary chondrites; *Lunar Planet. Sci.* **28** 1209–1210
- Sahijpal S, Goswami J N, Davis A M, Grossman L and Lewis R S 1998 A stellar origin for the short-lived nuclides in the early Solar System; *Nature* **391** 559–561
- Shu F H, Shang H, Glassgold E and Lee T 1997 X-rays and fluctuating X-wind from protostars; *Science* **277** 1475–1479
- Shukolyukov A and Lugmair G W 1993a Live iron-60 in the early solar system; *Science* **259** 1138–1142
- Shukolyukov A and Lugmair G W 1993b ^{60}Fe in eucrites; *Earth Planet. Sci. Lett.* **119** 159–166
- Srinivasan G, Ulyanov A A and Goswami J N 1994 ^{41}Ca in the early solar system; *Astrophys. J. Lett.* **431** L67–L70
- Srinivasan G, Sahijpal S, Ulyanov A A and Goswami J N 1996 Ion microprobe studies of Efremovka CAIs: II. Potassium isotope composition and ^{41}Ca in the early solar system; *Geochim. Cosmochim. Acta* **60** 1823–1835
- Srinivasan G, Goswami J N and Bhandari N 1998 Search for extinct aluminium-26 in the Piplia Kalan eucrite; *Meteor. Planet. Sci.* **33** A148–A149
- Vanhala H A T 1998 The triggered origin of the solar system (this volume)
- Vanhala H A T and Cameron A G W 1998 Numerical simulations of triggered star formation. I. Collapse of dense molecular cloud cores; *Astrophys. J.* (in press)
- Wasserburg G J 1985 Short-lived nuclei in the early solar system; *Protostars and planets II* (eds) D C Black and M S Matthews (Tucson: Univ. of Arizona Press), pp. 703–737
- Wasserburg G J and Arnould M 1987 A possible relationship between extinct ^{26}Al and ^{53}Mn in meteorites and early solar system; *Lecture notes in physics 287, 4th workshop on nuclear astrophysics* (eds) W Hillebrandt *et al* (Heidelberg: Springer-Verlag) pp. 262–276
- Wasserburg G J, Busso M, Gallino R and Raiteri C M 1994 Asymptotic giant branch stars as a source of short-lived radioactive nuclei in the solar nebula; *Astrophys. J.* **424** 412–428
- Wasserburg G J, Gallino R, Busso M, Goswami J N and Raiteri C M 1995 Injection of freshly synthesized ^{41}Ca in the early solar nebula by an asymptotic giant branch star; *Astrophys. J. Lett.* **440** L101–L104
- Wasserburg G J, Busso M and Gallino R 1996 Abundances of actinides and short-lived nonactinides in the interstellar medium: Diverse supernova sources for the *r* processes; *Astrophys. J. Lett.* **466** L109–L113
- Woosley S E and Weaver T A 1995 The evolution and explosion of massive stars. II. Explosive hydrodynamics and nucleosynthesis; *Astrophys. J. (Suppl.)* **101** 181–235
- Weidenschilling S J 1977 Aerodynamics of solid bodies in the solar nebula; *Mon. Not. R. Astron. Soc.* **180** 57–70
- Weidenschilling S J 1988 Formation processes and time scales for meteorite parent bodies; *Meteorites and the early solar system* (eds) J F Kerridge and M S Matthews (Tucson: Univ. of Arizona Press), pp 348–371
- Yin Q, Jagoutz E and Wanke H 1992 Re-Search for extinct ^{99}Tc and ^{98}Tc in the early solar system; *Meteoritics* **27** 310

The I-Xe chronometer

C M HOHENBERG, R H BRAZZLE, O V PRAVDIVTSEVA and A P MESHNIK

Department of Physics and McDonnell Center for Space Sciences, Washington University, St. Louis, MO 63130, USA

e-mail : cmh@radon.wustl.edu

^{129}Xe , from the decay of the now-extinct 16.7 Ma ^{129}I , accumulates in iodine-bearing sites and since most iodine host phases are secondary, the I-Xe system is typically a chronometer for post-formational processes. The validity of the I-Xe chronometer is confirmed by comparison with Pb-Pb ages on phosphate and feldspar separates from twelve meteorites. Phosphate separates are found to be concordant with Pb-Pb for all six samples in which useful I-Xe data were obtained. Feldspar is a better iodine host than apatite in H chondrites, typically providing good I-Xe isochrons. These too are concordant with the Pb-Pb ages of the corresponding phosphates for five out of six feldspar separates. The exception is Allegan whose feldspar yields one of the oldest I-Xe ages observed, similar to those for CI and CM magnetites. We attribute this to a more primary mineralization, predating the secondary phosphate from which the comparison Pb-Pb age was obtained. Absolute I-Xe ages, found using the reported Pb-Pb age of Acapulco phosphate provide an absolute I-Xe age of 4.566 ± 0.002 Ga for both Shallowater and Bjurböle irradiation standards. This allows relative I-Xe ages to be interpreted in the context of absolute ages.

1. Introduction

Live ^{129}I incorporated into solid matter in the early solar system will reside exclusively at iodine-bearing mineral sites. Subsequent *in situ* decay of ^{129}I results in the daughter $^{129*}\text{Xe}$ (asterisk denoting iodine derived) at these sites where the ratio of $^{129*}\text{Xe}$ to stable ^{127}I , observed today, is a record of the $^{129}\text{I}/^{127}\text{I}$ ratio at the time of isotopic closure. The short 16.7 Ma half-life of ^{129}I provides a rapidly changing initial $^{129}\text{I}/^{127}\text{I}$ ratio and forms the basis for a sensitive early solar system chronometer, one that is easy to apply and capable of high precision.

Reactor neutron irradiation of a meteorite sample converts stable ^{127}I to $^{128*}\text{Xe}$ by neutron capture ($^{127}\text{I} + n, \gamma \rightarrow ^{128*}\text{Xe} + \beta$). Now there are two iodine-derived Xe isotopes at these sites: $^{128*}\text{Xe}$, from n-capture of ^{127}I , and $^{129*}\text{Xe}$, from the decay of radioactive ^{129}I . If no Xe loss or subsequent iodine contamination has occurred, $^{129*}\text{Xe}$ will reside there in fixed proportion with recently created $^{128*}\text{Xe}$. This

provides a clock that can be read by simply measuring isotope ratios; isotopic dilution or other techniques to determine elemental concentrations are not required.

The association between $^{128*}\text{Xe}$ and $^{129*}\text{Xe}$ can be studied in exquisite detail by stepwise heating of the sample to progressively higher temperatures. Whether these isotopes are released by diffusion, by migration of dislocations or by disruption, the less retentive iodine-bearing sites will yield their gases at lower temperatures and the more retentive sites at the higher temperature steps, providing site delineation on the basis of thermal properties. Figure 1(a) is a three-isotope correlation plot for the Shallowater enstatite achondrite. At temperatures above the point where enstatite begins to release Xe we see linear mixing between normal trapped Xe, represented here at the lower left by OC-Xe (Lavielle and Marti 1992), and a single iodine-derived component to the upper right with $^{128*}\text{Xe}$ in fixed proportion with radiogenic $^{129*}\text{Xe}$. These higher temperature fractions release more than 95% of the total iodine-derived Xe.

Keywords. Chronometry; age dating; I-Xe; extinct radionuclides.

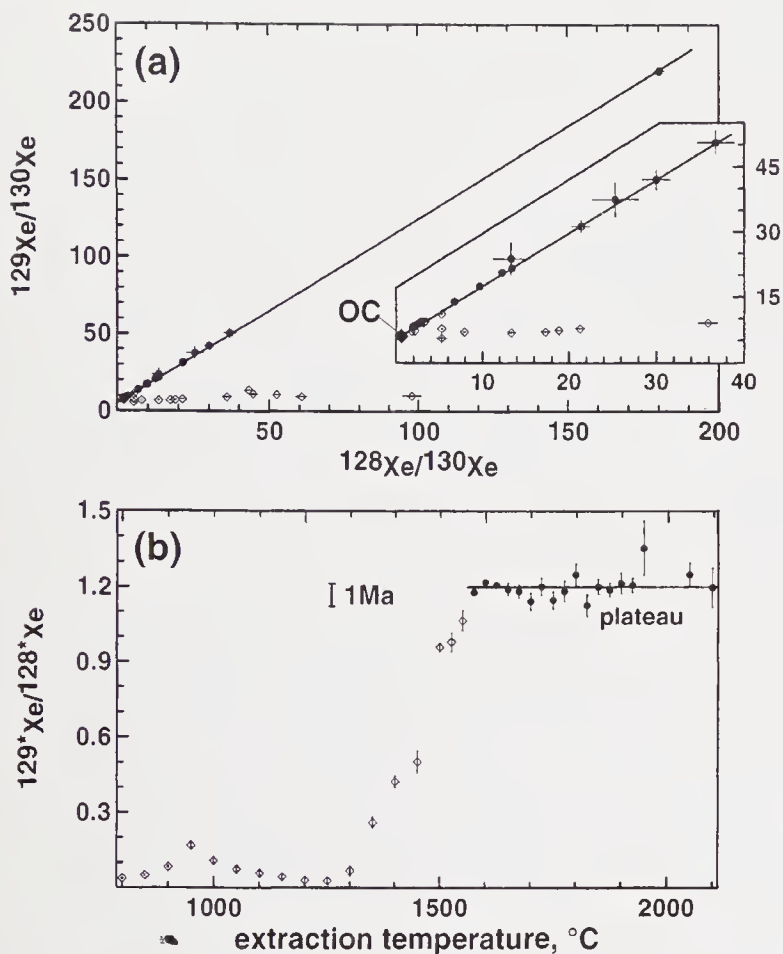


Figure 1. Two different representations of the I-Xe data for the Shallowater reference sample. The upper figure is a standard I-Xe isochron showing lower temperature extractions (open symbols) which release iodine-derived $^{128*}\text{Xe}$ not accompanied by the full complement of radiogenic $^{129*}\text{Xe}$. However, more than 95% is released in the eighteen higher temperature steps (closed symbols) $>1500^\circ\text{C}$. These fractions define a linear isochron ($^{128*}\text{Xe}$ and $^{129*}\text{Xe}$ in constant proportion), representing mixtures of OC trapped (Lavielle and Marti 1992) and iodine-derived Xe (upper-right) and demonstrating constant initial iodine ($^{127}\text{I}/^{129}\text{I})_0$ at these dominant iodine-bearing sites. The lower figure is a plateau plot, similar to those typically used in ^{39}Ar - ^{40}Ar dating, where we show a bar representing a 1 Ma age interval. The $^{129*}\text{Xe}/^{128*}\text{Xe}$ ratio shown for the iodine-derived component is found by removing the trapped component using all of the ^{130}Xe . Both plots demonstrate a 1σ apparent precision of about 80,000 yr. from slope uncertainty in the upper figure and scatter about the plateau in the lower figure.

In figure 1(b) we have subtracted the trapped component so that the ratio of iodine-derived $^{129*}\text{Xe}$ and $^{128*}\text{Xe}$ are displayed as an age plateau plot, similar to that commonly used for ^{39}Ar - ^{40}Ar dating. As can be seen in both figures, $^{128*}\text{Xe}$, unaccompanied by a full complement of $^{129*}\text{Xe}$, is released at the lower steps, reflecting losses of radiogenic xenon (or superficial iodine contamination). Above 1500°C these two contributions are released in fixed proportion, shown in figure 1(a) as a linear mixing line and in figure 1(b) as points defining the plateau. An isochron plot (figure 1a) is generally the more useful analytical tool since no assumptions about the composition of trapped Xe are needed. The measured isotope ratios themselves define the linear array and its constant

slope demonstrates a constant ratio of $^{128*}\text{Xe}$ and $^{129*}\text{Xe}$ in the temperature extractions defining the line. The value of this slope is proportional to initial iodine, the ratio of radioactive ^{129}I and stable ^{127}I at the time of xenon closure. As this ratio is time dependent, the correlation line of figure 1(a) is an isochron whose slope provides the time of closure, changing by a factor of 2 for each 15.6 Ma difference in closure time. Since we cannot experimentally determine the value for initial iodine at any known time in the past, we cannot use I-Xe method (by itself) as an absolute chronometer, but we can compare initial iodine in different iodine hosts and derive the relative times of isotopic closure. Shallowater, with eighteen different temperature steps defining the isochron and plateau portion of figures 1(a and b), respectively, has an age uncertainty of about 80,000 year, both from the standard deviation of the isochron slope and the standard deviation on the plateau.

The slope of the I-Xe isochron, a direct measure of the ratio of the daughter $^{129*}\text{Xe}$ to iodine-derived $^{128*}\text{Xe}$, actually equals initial iodine ($^{129}\text{I}/^{127}\text{I}) \equiv \mathbf{R}_0$ divided by the neutron capture probability for ^{127}I . However, effective neutron capture cross sections are nearly impossible to accurately calculate, requiring integration of the appropriate excitation function over the specific neutron energy spectra for each irradiation, never known with sufficient precision to be useful. If a reference standard is included with each irradiation, then the ratio of the two values for initial iodine is simply the ratio of the slopes of the two isochrons, with the neutron capture probabilities conveniently canceling. The time difference between isotope closure, the I-Xe age of the sample relative to the standard, is therefore equal to the mean life of ^{129}I times the natural log of the ratio of the measured slopes. Variations in the neutron fluence (and hence variations in the capture probability) are minimized by continuous rotation of the irradiation capsule and monitored by flux wires. Maximum fluence variations, typically 1–2 percent, correspond to an age uncertainty of about 0.2 to 0.4 Ma.

It is difficult to measure meteoritic iodine at ppb levels by conventional methods such as INAA, but low iodine concentrations can be determined from the neutron-produced $^{128*}\text{Xe}$ in I-Xe dating. Neutron capture by ^{127}I shows large contributions from resonance capture by epithermal neutrons. In order to determine actual values for initial iodine, a KI irradiation monitor was prepared and the neutron capture probability directly measured by isotopic dilution for the Valecitos-1 irradiation. By referencing all irradiations to the value for initial iodine \mathbf{R}_0 , thus determined for Bjurböle $(1.095 \pm .029) \times 10^{-4}$ (Hohenberg and Kennedy 1980), initial iodine ratios can be found for all other samples. Since initial iodine is the ratio of radiogenic $^{129*}\text{Xe}$ to stable ^{127}I , and the $^{129*}\text{Xe}$ concentration is measured directly, the iodine concentration

Table 1. *Relative I-Xe ages, absolute I-Xe ages, Pb-Pb ages (Göpel et al 1994), and iodine concentrations for phosphate and feldspar separates.*

Sample	(weight, mg)	$I_{\text{total}}/I_{\text{corr}}$ (ppb) ⁺	Absolute I-Xe ages, Ga	Relative I-Xe ages, Ma	Pb-Pb ages, Ga
Irradiation monitors					
Shallowater	43/43	4.566 ± 0.002	≡ 0	—	—
L4 Bjurböle	(63.01)	18/14	4.566 ± 0.002	−0.46 ± 0.15	—
Phosphate separates					
H4 Beaver Creek	(0.95)	1.0/0.2	4.569 ± 0.005	−3 ± 4	—
H4 Phum Sambo	(5.08)	0.34/—	—	—	—
H4 St. Marguerite	(0.87)	0.9/0.7	4.567 ± 0.006	−1 ± 6	4.5630 ± 0.0006
H5 Allegan	(7.64)	no apatite	—	—	4.5563 ± 0.0008
H5 Richardton	(5.23)	2.3/—	Disturbed	—	4.5534 ± 0.0006
H6 Guarena	(0.31)	—	—	—	4.5056 ± 0.0005
H6 Kernouve	(0.39)	3.6/1.1	4.523 ± 0.006	43 ± 6	4.5214 ± 0.0005
L6 Bruderheim	(26.6)	(~ 17/13)	Shocked ?	(~ 85)	—
L6 Modoc	(4.84)	7.0/6.2	4.509 ± 0.004	57 ± 8	—
L6 Walters	(9.09)	3.7/2.4	4.512 ± 0.004	54 ± 4	—
LL6 St. Severin	(2.72)	—	—	—	4.5571 ± 0.0015
Acapulco	(2.16)	39/39	≡ 4.557 ± 0.002	8.8 ± 0.2	4.557 ± 0.002
Feldspar separates					
H4 Phum Sambo	(1.17)	65/60	4.567 ± 0.002	−0.9 ± 0.1	—
H4 St. Marguerite	(0.23)	128/128	4.567 ± 0.002	−0.7 ± 0.4	—
H5 Allegan	(1.47)	2.4/2.1	4.573 ± 0.003	−6.9 ± 1.4	—
H5 Richardton	(1.35)	119/60	4.558 ± 0.002	8.2 ± 0.5	—
LL6 St. Severin	(2.25)	1.8/0.2	4.558 ± 0.004	8.0 ± 3.2	—
Acapulco	(9.58)	1.3/1.2	4.562 ± 0.003	3.8 ± 1.5	—

⁺ Iodine concentrations, normalized to iodine concentrations inferred for Bjurböle by isotope dilution (Hohenberg and Kennedy 1980), are determined both from total ¹²⁸Xe and that correlated with ¹²⁹Xe.

is also determined. Recently the Shallowater enstatite achondrite has been adopted as the preferred irradiation standard. This is because Shallowater has a more precise I-Xe isochron than Bjurböle, its iodine host phase is known (Kehm *et al* 1994) and its I-Xe age consequently better understood. With nearly the same I-Xe age (Bjurböle predates Shallowater by ~ 500,000 yr., table 1), R_0 for Shallowater is 1.072×10^{-4} so that the value for initial iodine R_0 in any sample is then given by:

$$R_0 \equiv (^{129}\text{I}/^{127}\text{I})_0 = (1.072 \times 10^{-4})e^{-\Delta t/\tau},$$

where Δt is the I-Xe age relative to Shallowater and τ is the 23 Ma mean life of ¹²⁹I. Since ¹²⁹I has decayed to ¹²⁹Xe, the initial iodine isotopic ratio equals the ¹²⁹Xe/¹²⁷I ratio observed today. The iodine concentration is therefore simply the measured concentration of ¹²⁹Xe divided by R_0 , with appropriate conversion factors to yield grams/gram. Iodine concentrations found in this manner are independent of the effective neutron capture cross sections, other than those reviewed by Hohenberg and Kennedy (1980). Iodine concentrations given in table 1 consist of two values: one is based upon the correlated ¹²⁹Xe/¹²⁸Xe ratio (given by the slope of the isochron) and measures the iodine currently associated with ¹²⁹Xe, that is iodine residing in the more retentive sites. The other value is based upon the total ¹²⁸Xe measured for the whole

sample, yielding total iodine. Since these are based upon observed neutron effects in each sample, rather than that predicted from estimated cross sections, iodine concentrations should be as accurate as the measured Xe concentrations (typically 10%) and, of course, the original isotopic dilution experiment which established R_0 for Bjurböle. The iodine concentrations in table 1 show that nearly all of the iodine is still associated with radiogenic ¹²⁹Xe, demonstrating that it was intimately associated with short-lived ¹²⁹I, remaining to this day in fixed proportion with its daughter. As also can be seen in the table, feldspar is generally richer in iodine than phosphate, especially among the H chondrites.

2. I-Xe dating in the context of meteorite metamorphism

Excess ¹²⁹Xe from the decay of extinct ¹²⁹I was discovered in the Richardton meteorite by Reynolds in 1959 (Reynolds 1960). The method for I-Xe dating of meteorites, discussed above, was developed shortly after that (Fish and Goles 1962). Despite the fact that a large number of meteorites have been dated by the I-Xe method (more than 80), there is not a general agreement that these apparent ages are meaningful, or even if the I-Xe system is a chronometer at all (Jordan

et al 1980; Swindle and Podosek 1988). It is not that I-Xe ages were discordant with other radiochronometers because few, if any, chronometers could reliably measure age intervals of a few million years. The major reason for distrust stems from observations that the measured I-Xe ages seldom seem to correlate with other accepted chemical/physical indicators of ongoing meteoritic metamorphism. One might think that the degree of metamorphism must provide at least some measure of fine-scale chronology, yet except for the enstatite meteorites, petrographic classification does not even vaguely correlate with measured whole-rock I-Xe "ages" (Kennedy 1981; Swindle and Podosek 1988). Many reasons have been proposed for this apparent discrepancy. Some of these conclude that it may be isotopic heterogeneity, not time, that is responsible for the observed range in initial iodine observed among meteorites (Jordan *et al* 1980; Crabb *et al* 1982). If so, the I-Xe system would not be a chronometer. It has also been proposed that live ^{129}I may have never existed in the solar system at all. In this model the daughter product ^{129}Xe would have survived in refractory pre-solar grains as a distinct Xe component which was never fractionated from iodine, preserving the observed I-Xe relationship (Clayton 1975). Verification of the I-Xe clock is therefore essential if I-Xe ages are to be accepted as meaningful, properly interpreted and used with confidence. It has proven difficult to directly compare I-Xe ages with other chronometers. Only recently have any other chronometers provided a precision similar to I-Xe, some are not subject to the same closure conditions as I-Xe (e.g. K-Ar) and most have different host minerals in bulk material. Nevertheless, this is a task whose time has come and this work represents that effort.

Formation and evolution of meteorites is more complex than expressed by the major mineralogy, at least as far as iodine geochemistry is concerned. Secondary processes such as aqueous alteration and thermal metamorphism play major roles in the redistribution of iodine in meteorites and final assimilation of iodine in the host lattice structures. Knowledge of the specific iodine host phases among primary and secondary minerals is essential for the understanding of every I-Xe age. For instance, the refractory CAI inclusions in Allende are largely composed of minerals similar to those predicted to be the first condensates from the primitive solar nebula. Yet the major iodine host minerals in these objects are sodalite and nepheline, phases produced during post-formational alteration (Meeker *et al* 1983). Iodine in chondrules also seems to be located in alteration products, yet many of these inclusions and many chondrules from Allende have excellent I-Xe isochrons (Swindle *et al* 1988). It is then clear that the iodine hosts could not have been isotopically closed at the time of nebular condensation because the iodine had yet to be incorporated. The I-Xe ages for these objects must therefore have nothing

to do with their formation, referring instead to the time of aqueous alteration or post-formational metamorphism when the iodine migrated into its final host phases. In fact, most identified iodine carriers in meteorites are secondary minerals (sodalite, nepheline, phosphate) and unidentified very fine-grained dispersed phases (Kehm *et al* 1994). Therefore, closure of the I-Xe system seldom occurs at major mineralization, but responds instead to the post-formational processes responsible for the secondary iodine-bearing phases (Brazzle *et al* 1994; Brazzle *et al* 1997). Notable exceptions here are the enstatite meteorites where the iodine is clearly associated with the major mineral enstatite (or micro-inclusions within it; Crabb and Anders 1982; Kehm *et al* 1994). For these meteorites, the I-Xe ages do group by petrographic grade (Swindle and Podosek 1988; Kehm *et al* 1994). To summarize, the I-Xe system is not in general a chronometer of primary mineralization. With most iodine hosts secondary, the I-Xe system holds great promise for providing a record of post-formational metamorphism. However this also means that care must be taken in comparing the I-Xe clock with another chronometer for purposes of verification. Proper comparisons must be made on single mineral systems where the hosts phases and closure conditions are the same for both clocks.

3. Verification of the I-Xe clock

The work of Göpel *et al* (1994) provides an extensive database of Pb-Pb ages for phosphate separates from ordinary chondrites. Since chlorapatite is a potential carrier of iodine, phosphates are a good place to start for direct, single mineral, comparisons between the I-Xe and Pb-Pb chronometers. Phosphate is relatively low in abundance, diminishing in grain size in the lower petrographic grades, so bulk mineral separation methods are needed to recover usable quantities. Furthermore, since phosphate separates contain both apatite and merrillite, and only apatite is a likely iodine host, the first task is to demonstrate that I-Xe ages derived from bulk phosphate separates are the same as those derived from pure apatite.

Acapulco is a unique meteorite in many respects, including a high abundance of phosphate with relatively large grain size, providing a means for comparing the I-Xe records of individual apatite grains with that observed for bulk phosphate mineral separates. A collection of the larger phosphate grains were hand-picked for individual study, neutron-irradiated at the University of Missouri Research reactor, and divided individually into apatites and merrillites on the basis of their SEM EDX spectra. A collection of nine apatite grains and eight merrillite grains, ranging in mass from 2 to 13 μg , were measured individually by laser volatilization and mass spectrometry. Results from

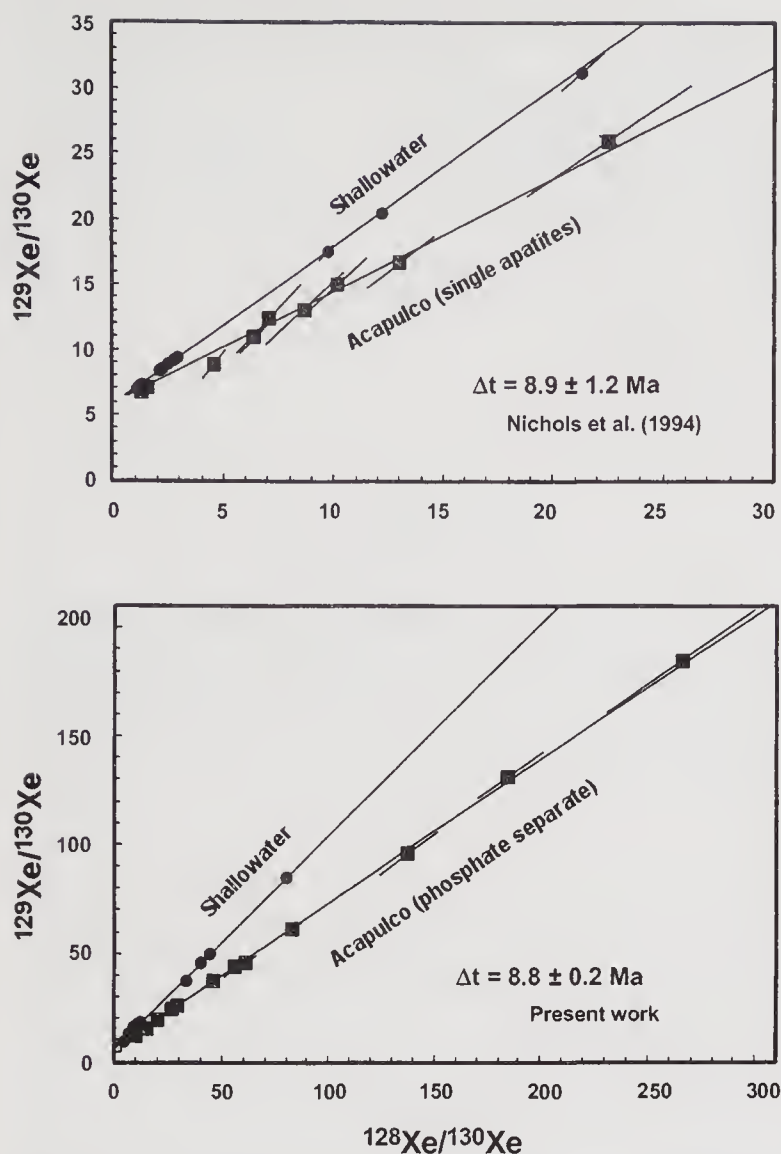


Figure 2. I-Xe isochrons for two different samples of neutron-irradiated Acapulco phosphate. The upper graph shows the Xe released from individual large apatite grains by total laser volatilization (Nichols *et al* 1994); the lower graph shows the results of stepwise heating bulk phosphate separates (present work). Acapulco phosphate contains essentially no uncorrelated iodine. The I-Xe ages are the same for both samples demonstrating that the I-Xe method works on phosphate separates. The presence of $\sim 50\%$ merrillite, which contains no iodine, grain-size differences, and the possible presence of other minor phases have no affect on the I-Xe isochron. The I-Xe isochron of Shallowater is included for reference.

that study show that the merrillites contain neither iodine-produced ^{128}Xe nor radiogenic ^{129}Xe whereas each apatite grain contains both iodine-derived isotopes, collectively forming a single I-Xe isochron. This isochron is indistinguishable from the one formed by bulk Acapulco phosphate separates (figure 2 and Nichols *et al* 1994), demonstrating correct assessment of the carrier phase (apatite) in the bulk separate and simultaneous closure of the individual apatite grains.

Phosphate separates from Acapulco, and the other meteorites reported here, are made by magnetic and density separations (Göpel *et al* 1994). Although the non-magnetic fraction, typically phosphate and feldspar, could have been further separated at this time using heavy liquids, bromoform, the heavy liquid of choice, contains heavy halogens which would contaminate

the sample with iodine-produced ^{128}Xe . Therefore, for the samples prepared in St. Louis, the heavy liquid separation step was delayed until after the neutron irradiation.

Typically 20 g of meteorite is gently crushed, sieved into grain sizes between 37 and 75 microns, and magnetically separated using a Frantz Isodynamic Magnetic Separator. The fraction that is non-magnetic at 1.6 amps, typically 1–20 mg, is sealed under vacuum in a quartz tube for neutron irradiation at the University of Missouri Research Reactor, where it receives about $2 \times 10^{19} \text{ n/cm}^2$. The irradiation capsule itself is flooded with water from the pool for cooling and the capsule is rotated continuously for uniformity of the integrated flux, monitored by three types of flux wires (Co-doped Al, Ni and Zr). The maximum neutron fluence spatial variations recorded by these flux wires are typically 1–2 per cent. A sample of the I-Xe reference standard, Shallowater enstatite, is included with each irradiation. After irradiation the separates were density separated with bromoform, transferred into a platinum boat using a pipette with the last methanol wash, allowed to dry, weighed, and loaded into the side arm of the sample tree. The xenon was then extracted by stepwise heating to progressively higher temperatures in a pre-outgassed open tungsten coil resistance heater (Hohenberg 1980). Blanks are low and are of little consequence in these studies, either in amount or in composition, matching within statistics that of typical trapped Xe components; most of the measurement uncertainties are dominated by statistical errors.

Figure 2 shows the I-Xe isochron for a phosphate separate from Acapulco. As with Shallowater, the lower temperature extractions from the Acapulco phosphate separate show some superficial iodine not correlated with radiogenic ^{129}Xe , but these fractions release only minor amounts ($< 1\%$) of the total iodine-derived ^{128}Xe . The higher temperature extractions, releasing essentially all of the iodine-derived Xe, define an excellent linear I-Xe isochron with error bars that are generally smaller than the symbols (apparent precision, 0.2 Ma). For comparison, the I-Xe isochron for the Shallowater standard, irradiated along with Acapulco, is included. The difference in slope indicates that the apatites in Acapulco closed for xenon $8.8 \pm 0.2 \text{ Ma}$ after closure of the Shallowater enstatite standard and 9.25 Ma later than the Bjurböle standard. Setting this time to be $4.557 \pm 0.002 \text{ Ga}$, the Pb-Pb age reported for Acapulco phosphates (Göpel *et al* 1994), establishes an absolute calibration for I-Xe ages as pointed out by Nichols *et al* (1994). The absolute I-Xe ages of Shallowater and Bjurböle defined by this normalization are $4.566 \pm 0.002 \text{ Ga}$. This absolute calibration does not take into account the possibility of systematic uncertainties of phosphate Pb-Pb ages due to common lead corrections (Tera and Carlson 1997) although, as will be shown, the work reported

here does support the relative Pb-Pb ages reported by Göpel *et al* (1994).

It is worth emphasizing here that more than 99% of the iodine in Acapulco phosphate resides in fixed proportion with radiogenic ^{129}Xe , shown in all of the different temperature fractions making up the isochron. This demonstrates that essentially all of iodine in Acapulco apatite resides in fixed proportion with ^{129}Xe , confirming that the ^{129}Xe was derived by *in situ* decay from live ^{129}I , effectively ruling out the possibility that this ^{129}Xe could have arrived as dead ^{129}I in SUNOCONS, as proposed by Clayton (1975). Having established one time marker with Acapulco phosphate, the relative closure times measured by I-Xe and Pb-Pb chronometers in other phosphate separates can be compared.

Phosphate separates were prepared for twelve meteorite samples, six of these in St. Louis and another six, including Acapulco, in the Paris laboratory of Christa Göpel. These included three H4, two H5, two H6, three L6, one LL6 meteorites and Acapulco, and ranged in mass from about 0.3 to 9.09 mg, but included a Bruderheim phosphate sample of 26.6 mg. Some of the samples obtained from Paris were quite small (< 1 mg), and were prepared using heavy liquids prior to neutron irradiation, although there is no evidence that heavy halogen contamination was a problem. The samples prepared in St. Louis avoided this potential problem and ranged in mass from nearly 3 to 9.1 mg, excluding the large Bruderheim sample. Results from analysis of these samples are shown in table 1. Details of the I-Xe analysis for each of these samples are given in Brazzle *et al* (1998), and the original data are reported in Brazzle (1997).

Acapulco chlorapatites carry a relatively large amount of iodine but many of the phosphate separates reported here have low iodine abundances and comparisons of I-Xe and Pb-Pb chronometers in these are not as precise as for Acapulco phosphate. These data when considered individually can be used to test individual concordancy or discordancy between the apparent I-Xe age and the corresponding Pb-Pb age interval for separates with appreciable iodine (or consistency and inconsistency for samples with lower iodine contents and consequently less precision). When viewed collectively, the data are much more definitive, delineating the underlying framework of concordance or discordance with the Pb-Pb clock. Figure 3 shows the I-Xe isochron plot for neutron-irradiated phosphates from the H6 meteorite Kernouve together with the Shallowater isochron from the same irradiation and a dashed line corresponding to the Acapulco isochron. A third line has been drawn in the position of an I-Xe isochron with the 35.6 Ma age difference determined from the different Pb-Pb ages of Kernouve and Acapulco phosphates. Although the error bars on the data points are large, and an isochron poorly defined, the line shown does intersect

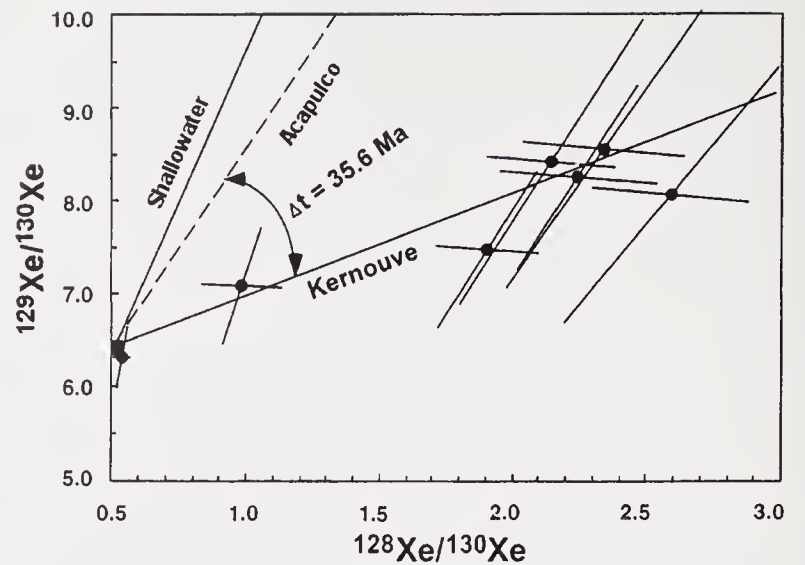


Figure 3. I-Xe structure of Kernouve phosphate with Shallowater and Acapulco phosphate isochrons for reference. The Pb-Pb age difference between Acapulco and Kernouve phosphates (indicated) agrees with a best fit isochron through trapped Xe, demonstrating consistency between the I-Xe and Pb-Pb age intervals for these samples.

most of the data points. This indicates an I-Xe age relative to Acapulco phosphate that is consistent with the Pb-Pb age difference reported by Göpel *et al* (1994). The actual Kernouve isochron, a best fit to the data, indicates closure 34.2 ± 6 Ma after Acapulco phosphate, the relatively large error reflecting the low iodine content. A similar plot, with slightly better precision, is shown for St. Marguerite (H4) phosphate in figure 4 indicating closure at nearly the same time as Shallowater, 10 Ma before Acapulco phosphate. Most I-Xe isochrons pass within errors of normal trapped Xe, taken here to be represented by OC-Xe, the trapped Xe component observed in Forest Vale (Lavielle and Marti 1992). In the case of St. Marguerite phosphate, the free fit isochron does not pass through normal trapped Xe within errors and so both the free fit line and one forced through OC were considered. The stated uncertainty of the I-Xe age for St. Marguerite phosphate therefore includes both statistical errors and the age difference between the free fit and forced isochrons. The I-Xe age uncertainties for both Kernouve and St. Marguerite may appear to be significant but, when the relative age differences of these two samples is considered (three half-lives of ^{129}I), the data are good enough. The I-Xe ages relative to Acapulco phosphate for both of these samples are consistent, indeed concordant, with those measured by Pb-Pb.

Beaver Creek (H4) has a relatively long cosmic ray exposure age and a low iodine content, requiring corrections for cosmic ray spallation contributions. Removal of the relatively minor amounts of spallation from ^{128}Xe and ^{129}Xe , and normalizing to spallation-corrected ^{130}Xe , results in an acceptable isochron and some additional uncertainties due to the spectral decomposition, expressed in the error limits on the

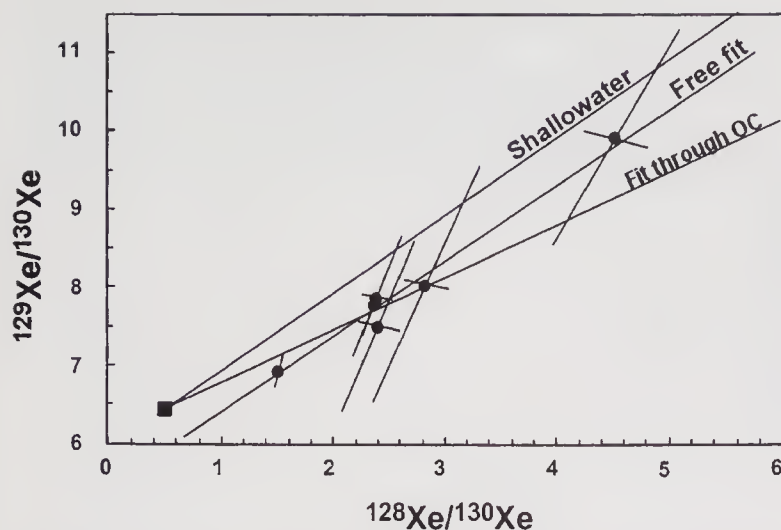


Figure 4. I-Xe structure for St. Marguerite phosphate with the Shallowater reference isochron. The St. Marguerite data by themselves do not pass through normal trapped Xe. Two lines are shown: one forced through OC and the other a free fit to the data. The relative I-Xe age of St. Marguerite phosphate (1 ± 6 Ma before Shallowater; 10 ± 6 Ma before Acapulco phosphate) includes errors computed from both statistical errors and the difference of the two slopes and agrees within errors with the relative Pb-Pb age.

derived I-Xe age. The derived I-Xe age of 3 ± 4 Ma before Shallowater (12 ± 4 Ma before Acapulco phosphate), and absolute I-Xe age of 4.569 ± 0.005 Ga for Beaver Creek, agrees with typical Pb-Pb and I-Xe ages of other H4 meteorites, substantially older than the H5s and H6s (table 1). Even though a Pb-Pb age for Beaver Creek phosphate has not been determined, the entire range of Pb-Pb ages for phosphates from other H4 meteorites is only 3 Ma (Göpel *et al* 1994), less than the uncertainty on the Beaver Creek I-Xe age. We therefore conclude that the I-Xe and Pb-Pb ages for Beaver Creek phosphate are concordant. For Phum Sambo the extremely low iodine content (0.34 ppb) of the phosphate prevents a meaningful isochron from being obtained but the data are not inconsistent with isochrons for typical H4 meteorites (~ 10 Ma before Acapulco phosphate). It will be shown later that Phum Sambo feldspar does produce a good isochron, one in excellent agreement with the Pb-Pb ages of these meteorites.

There are phosphate separates that fail to produce I-Xe isochrons even when sufficient iodine exists for good measurements and Richardton (H5) phosphate is one of these, seeming to have a disturbed I-Xe system (figure 5). Since the linear I-Xe isochron itself defines the composition of initial iodine and establishes its uniformity, samples that yield no isochron conversely show that iodine and ^{129}Xe are no longer associated. It is known that shock disturbs the I-Xe system (Caffee *et al* 1982) and many H5 meteorites, including Richardton, show mineralogical evidence of significant shock (Stöffler *et al* 1991; Evensen *et al* 1979; Taylor and Heymann 1969; Pravdivtseva *et al* 1998). We can plausibly attribute this disturbance to

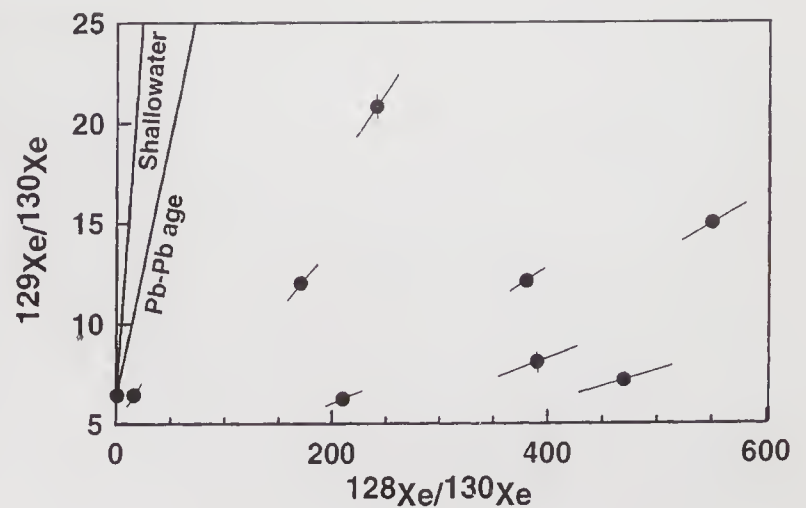


Figure 5. Richardton H5 phosphate has a disturbed I-Xe system and shows some mineralogical signs of shock (stage S3, Stöffler *et al* 1991). Its phosphate has fifty times less iodine than its feldspar. Although Richardton phosphate seems disturbed, Richardton feldspar (figure 9) shows a relatively good I-Xe isochron.

shock but, regardless of its cause, the I-Xe system of Richardton phosphate contains no discernable age information. However, like Phum Sambo, the feldspar separate from Richardton does provide an excellent I-Xe isochron and, as will be shown, the I-Xe ages of the feldspar separates from both Phum Sambo and Richardton are concordant with the relative Pb-Pb ages. It is known that Bruderheim suffered a major shock event ~ 500 Ma ago. Its I-Xe system also shows disturbance at all but the highest temperature fractions. The three highest temperature points, corresponding to the peak release of a largely degassed phosphate separate, do provide a model I-Xe age for Bruderheim (a line through these points and trapped Xe) that is consistent with the I-Xe ages of the other L6 meteorites, Modoc and Walters, and with the Pb-Pb age of the L6 Marion.

I-Xe isochrons of moderate quality are found for phosphates from the L6 meteorites Modoc and Walters by forcing the isochron through trapped Xe (figure 6). Nevertheless, they indicate closure of the I-Xe system of these two L6 meteorites at about the same time, 41.4 ± 8.0 and 42.2 ± 1.6 Ma, respectively, after closure of Acapulco apatite. The data for Walters shown in figure 6 actually resolve by temperature into two isochrons, differing in age by a few Ma, suggesting different closure times for two different populations of phosphates in this meteorite. While there are no Pb-Pb ages for phosphates from these two meteorites, there is for the L6 meteorite Marion, whose Pb-Pb age is 45.7 ± 2.2 Ma after Acapulco phosphates (Göpel *et al* 1994). The Pb-Pb age for Marion, the trend of Pb-Pb ages observed in ordinary chondrites (Göpel *et al* 1994), and the two similar I-Xe ages for phosphates from Modoc and Walters is suggestive. It leads one to conclude that the L6 phosphates are similar in both Pb-Pb and I-Xe ages (at least within the uncertainties shown here), and

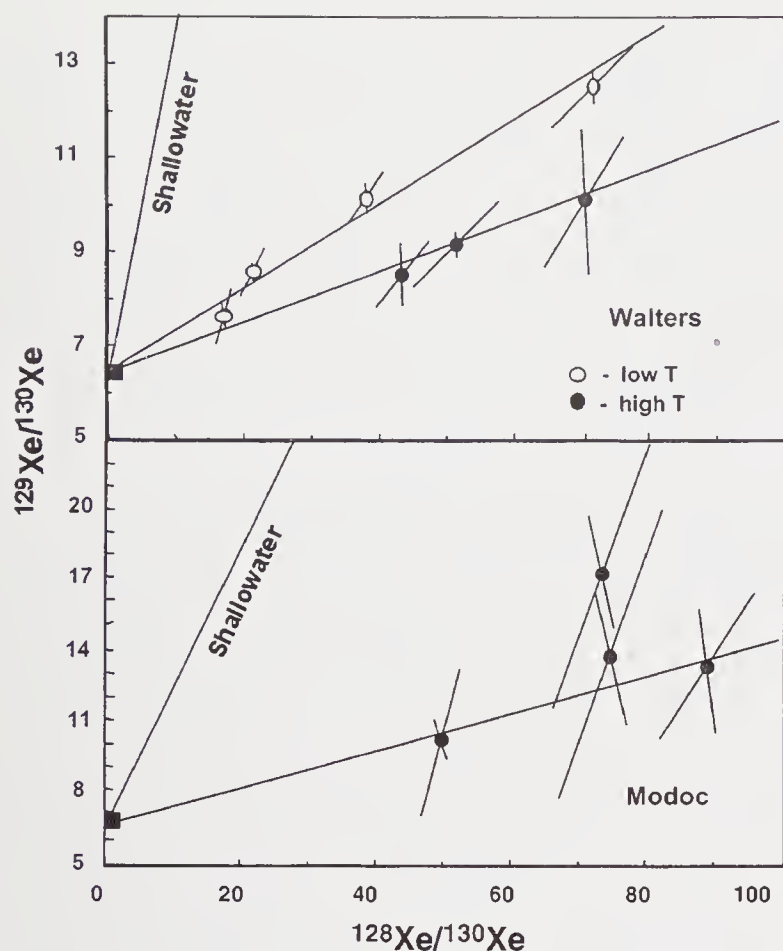


Figure 6. I-Xe isochron plots for Modoc and Walters phosphate, both L6 meteorites. Two populations of phosphate seem to be present for Walters, defining lower temperature (open symbols) and higher temperature (closed symbols) isochrons, which differ in age by about 8 Ma. Using an average value to compare with Pb-Pb ages of these separates, an I-Xe age of 54 ± 4 Ma, relative to Shallowater, is obtained for Walters. If the rather poorly defined array of points for Modoc is interpreted as an isochron (forced through trapped, OC), the corresponding I-Xe age relative to Shallowater is 57 ± 8 Ma. When referenced to Acapulco phosphate, the ages are 42 ± 4 and 44 ± 8 Ma for Walters and Modoc, respectively, essentially the same as the Pb-Pb age interval for the L6 Marion.

that there is general concordancy between the I-Xe and Pb-Pb clocks for these objects.

Results for all of the meteorites for which I-Xe age information is obtained is shown in table 1 and figure 7. The solid line in the figure is the line of concordancy between the I-Xe and Pb-Pb ages; the relative ages are shown with respect to Acapulco phosphate, the best I-Xe isochron. Beaver Creek phosphate is included, with an I-Xe age of 11.8 ± 4 Ma before Acapulco, similar to the other H4 meteorites, and a range of Pb-Pb ages spanning the other H4 phosphates (size of the plotted point). If we also include the L6 meteorites Modoc and Walters, there are six phosphate separates that lie on the line of concordancy (defined by one of them, Acapulco). The uncertainties associated with Bruderheim L6 phosphate (not shown in the figure) make it less important, but it too is consistent with the other L6s. The implied concordancy between I-Xe and Pb-Pb clocks is indeed impressive: six phosphate separates are concordant,

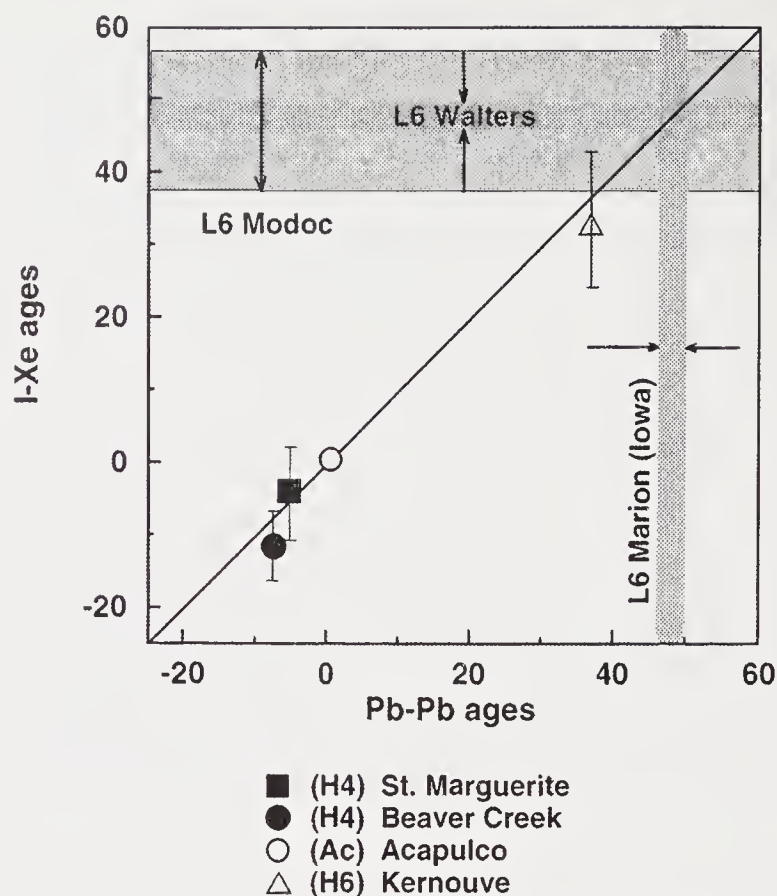


Figure 7. Summary of all I-Xe and Pb-Pb phosphate age intervals relative to Acapulco. The lack of precision of some I-Xe isochrons is due to the low iodine content of most of these phosphates, but the short half-life of ^{129}I offsets this. The age span in this figure is more than three half-lives so that large uncertainties in slope are not very important. The two L6 meteorites (Modoc and Walters) have no corresponding Pb-Pb ages, but their I-Xe ages are basically identical and agree with the Pb-Pb age of phosphate from the L6 Marion. This is taken to demonstrate agreement between the two clocks. Phosphates from all six meteorites lie on the line of concordancy. Although some I-Xe systems are disturbed (Bruderheim and Richardton, present work) and do not yield isochrons, there are no discordant I-Xe ages.

one (Bruderheim) is consistent and there are no discordant samples.

The major limitation on the direct comparisons between I-Xe and Pb-Pb ages in meteoritic phosphates is the generally low iodine content of phosphate. Other minerals, especially in the H-chondrites, are better iodine hosts than apatite. The final step in sample preparation for this work is a density separation which yields both phosphate (high-density) and feldspar (low-density) fractions. The feldspar separates, analyzed during the course of this work, carry large amounts of iodine, in many cases much more than the phosphate separates. Feldspars fractions from all of the H chondrites in this study yield very good I-Xe isochrons (not true of the L or LL chondrites where the iodine apparently resides in other phases). From figure 4 we saw that St. Marguerite phosphate has a rather poorly defined I-Xe isochron but the feldspar separate (figure 8), which contains two orders of magnitude more iodine than the phosphate, provides an excellent I-Xe isochron, as does Richardton (figure 9), whose phosphate showed a

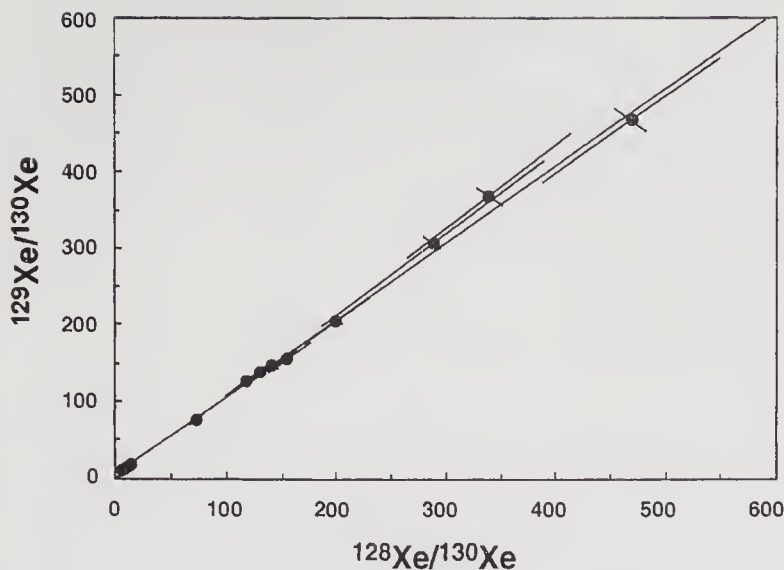


Figure 8. I-Xe isochron for St. Marguerite feldspar. St. Marguerite feldspar is 150 times richer in iodine than its phosphate and it yields an I-Xe isochron that is indistinguishable in age, yet ten times as precise as that produced by its phosphate. This suggests that the relative I-Xe ages of feldspar separates may track the relative Pb-Pb ages of phosphate separates, providing additional samples for I-Xe and Pb-Pb comparisons. Feldspars from H chondrites are richer in iodine than phosphates and have better isochrons. However, feldspar from Acapulco is somewhat older than its phosphate, predating it by a few Ma, but this is small compared with the ~50 Ma span of relative ages considered here.

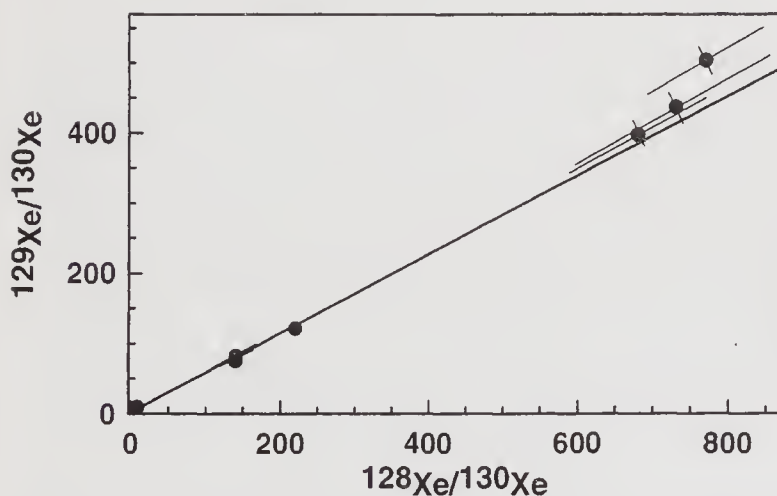
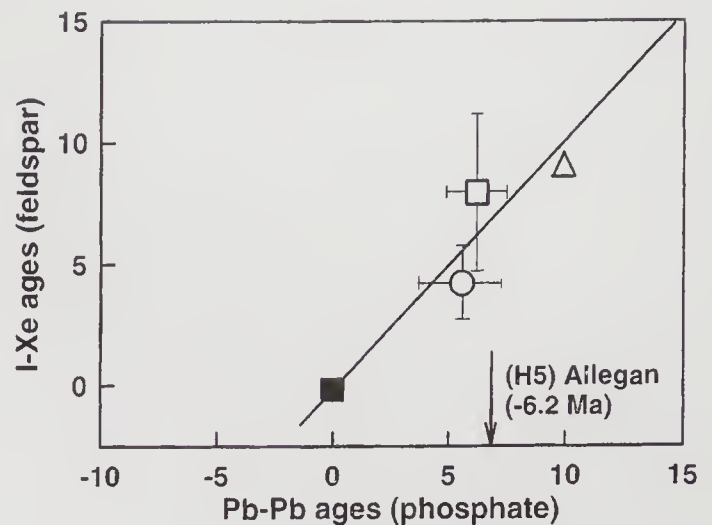


Figure 9. I-Xe isochron for Richardton feldspar, consisting of the seven highest temperature extractions. While the point most enriched in radiogenic ^{129}Xe is off the isochron by about 3σ , it may reflect some of the shock effects shown in figure 5 and the other points define a nice isochron. The relative I-Xe age of Richardton feldspar, relative to St. Marguerite feldspar, is nearly identical to the difference in the Pb-Pb ages of their phosphate separates.

disturbed I-Xe structure. Acapulco, Phum Sambo, St. Marguerite, Richardton, St. Severin and Allegan feldspars all provide good I-Xe isochrons, but what do we know in general about the relative chronology of feldspar and phosphate? The I-Xe ages of St. Marguerite feldspar and phosphate are the same within the relative measured precision of a few Ma. The I-Xe age of Acapulco feldspar, while not as precise as that of its phosphate and differing from it by a few



■ (H4) St. Marguerite, (H4) Phum Sambo
○ (Ac) Acapulco
△ (H5) Richardton
□ (LL6) St. Severin

Figure 10. Summary of I-Xe and Pb-Pb age intervals of feldspar separates relative to St. Marguerite feldspar (St. Marguerite feldspar has a better isochron than Acapulco feldspar, so is used as the reference sample). Feldspar separates from five meteorites lie on the line of concordancy defined by equal age differences, relative to St. Marguerite, for Pb-Pb phosphate separates. The Phum Sambo point is superimposed on the St. Marguerite point and indistinguishable from it. One sample, Allegan, does not lie on this line. The absolute I-Xe age of Allegan feldspar is the same as I-Xe ages for Orgueil and Murchison magnetites (Lewis and Anders 1975), among the oldest reported ages. This suggests that while Allegan phosphate is secondary, its feldspar may be from a more primary period of mineralization.

million years, is nevertheless similar on the time scale of age differences between these samples. Given the generally low iodine content of phosphate, it is fortunate for this study that the I-Xe age intervals for feldspar seem to be similar to those for isotopic closure in the corresponding phosphate. Comparing the I-Xe ages of feldspar with the Pb-Pb ages for phosphate can provide a useful check for general concordancy between the two systems. However, we must bear in mind that these are not identical systems and some differences may exist.

Table 1 gives the I-Xe ages of the feldspar separates from all the H-chondrites (the only meteorite class where feldspar is observed to be a major iodine host phase), Richardton feldspar, Acapulco feldspar and St. Severin feldspar. Acapulco feldspar seems to have closed 4.8 Ma before its phosphate, although the I-Xe age of Acapulco feldspar is less precise than its phosphate, and less precise than that of St. Marguerite feldspar. On the other hand, feldspar and phosphate in St. Marguerite closed at the same time, and its feldspar I-Xe age is the most precise of all feldspar separates studied here. For this reason we have selected St. Marguerite feldspar as our reference

sample for relative feldspar I-Xe ages. There is excellent agreement between the I-Xe ages of feldspar and Pb-Pb ages of phosphate separates from Acapulco, Phum Sambo, St. Severin, and Richardton, relative to St. Marguerite (figure 10). Note that feldspar from the H4 meteorite Phum Sambo has the same I-Xe age as feldspar from the H4 St. Marguerite, identical with its phosphate. Given the limited range of Pb-Pb ages observed for H4 meteorites (Göpel *et al* 1994), which lie within the plotted symbol, both Phum Sambo and St. Marguerite show concordant I-Xe and Pb-Pb ages.

The only meteorite that does not show concordancy between Pb-Pb age intervals for phosphate and I-Xe age intervals for feldspar is Allegan which has an I-Xe age 6.2 Ma before St. Marguerite and a Pb-Pb age 6.7 Ma after St. Marguerite (off of the plotted area in figure 10). Although the reason for this is not clear, the absolute I-Xe age for Allegan feldspar, calibrated by the Pb-Pb age of Acapulco phosphate, is 4.573 ± 0.002 Ga, the same absolute I-Xe age as those of Murchison and Orgueil magnetites (Lewis and Anders 1975), among the oldest I-Xe ages. Allegan is also the only meteorite studied whose phosphate contains no detectable iodine (all merrillite, no apatite) and its feldspar significantly predates both its phosphate formation and secondary alteration in CV meteorites. The old ages of the Allegan feldspar and CI/CM magnetite separates plausibly reflects primary rather than secondary origin for these minerals.

Taken as a whole, the feldspar data strongly reinforce the phosphate data, providing confirmation that the I-Xe system is not only a valid chronometer but one with a record that is both reliable and interpretable. The I-Xe data alone, for both phosphates and feldspars, show the same regular sequence of decreasing age with petrographic type for the H-meteorites observed for Pb-Pb by Göpel *et al* (1994). Models invoking nebular heterogeneity of iodine have persistently been proposed as counter-explanations of early I-Xe results but the degree of heterogeneity required are extreme (two orders of magnitude), contradicting the observed homogeneity for nuclides with even shorter half life (^{26}Al), and require local homogeneity (constant $(^{129}\text{I}/^{127}\text{I})_0$ at closure). Since there is no longer indication of discordancy for the I-Xe chronometer there is no longer any necessity to invoke such explanations. In fact, the converse is true. Samples involved in this comparison: Acapulco, Kernouve, St. Marguerite, Beaver Creek, St. Severin, Phum Sambo, Richardton, Bruderheim, Modoc and Walters, are from a diverse group of parent bodies. This suggests isotopic uniformity for iodine over a substantial part of the nebula. In summary, these studies have demonstrated that the I-Xe system is a chronometer with consistent agreement with Pb-Pb on single mineral systems. It is not compromised by isotopic heterogeneity in the early solar system and,

since most iodine host phases are secondary minerals, I-Xe can provide a close look at meteorite evolution in the early solar system. Being sensitive to post-formational processes, the I-Xe clock is capable of providing a high-resolution record of meteorite evolution not accessible with other chronometers.

4. Summary and conclusions

The I-Xe and Pb-Pb clocks have been compared in single mineral systems to test the validity and reliability of the I-Xe system as a chronometer. In all phosphate separates where I-Xe isochrons are obtained (7 of 12 separates) the relative I-Xe closure ages agree with the relative Pb-Pb ages. The relative I-Xe ages agree with the relative Pb-Pb ages in all feldspar except Allegan. A suite of 12 distinct mineral separates (7 phosphates and 5 feldspars) has I-Xe ages that agree with previously measured Pb-Pb ages. Concordancy shown between the Pb-Pb and I-Xe systems demonstrates that differences observed in initial iodine are strictly due to radioactive decay and that the I-Xe system is indeed a reliable chronometer.

Absolute I-Xe ages can be found by normalization of the I-Xe irradiation standards with the reported Pb-Pb age of Acapulco phosphate. This leads to an absolute I-Xe age of 4.566 ± 0.002 Ga for both Bjurböle and Shallowater (the error is largely due to the Pb-Pb age of Acapulco phosphate; Bjurböle predates Shallowater by 0.46 ± 0.15 Ma, well within the normalization error). Most iodine hosts are secondary minerals so the I-Xe system is generally a chronometer for post-formational processes. For this reason there will generally be differences in the closure ages among different iodine-bearing hosts. Whole-rock I-Xe ages are therefore subject to misinterpretation, being a superposition of many phases, as shown by the historical record of I-Xe dating. When performed on single mineral systems the I-Xe chronometer can be a powerful tool for the study of the post-formational record and meteorite evolution. Allegan has a very old I-Xe age, equal to the oldest previously measured I-Xe ages (Orgueil and Murchison magnetite, Lewis and Anders 1975) leading to the suggestion that these may reflect primary, rather than secondary, mineralization. Normalization of I-Xe ages through Acapulco phosphate, however, leads to a problem. We have tested I-Xe relative ages against Pb-Pb and have confirmed their validity. However, the absolute I-Xe ages, which come from Acapulco normalization, suggest closure of Allegan feldspar and the CM/CI magnetites at about 4.573 Ga. This is significantly older (by ~ 7 Ma) than the 4.566 ± 0.002 Ga age of "normal" CAIs, reported by Manhés *et al* (1988). It is difficult to accept an absolute chronology in which magnetite and feldspar predate normal CAIs. This encourages us to further test absolute age normalization by using other

calibration samples, and to explore the possibility of systematic (few Ma) bias of some of the reported Pb-Pb ages. While neither of these would affect the concordancy between relative I-Xe and Pb-Pb ages reported here, they might confirm or refine the absolute I-Xe age calibration.

Acknowledgements

We would like to thank Christa Göpel for use of her superb Pb-Pb data, and for all of the help she provided both teaching and performing mineral separations. We thank Glenn MacPherson, NMNH, Christa Göpel and Kurt Marti for providing most of our samples, and Tim Swindle for assistance with some of the irradiations. We have special appreciation of the University of Missouri Research Reactor staff for their help, and the State of Missouri for its support through Reactor Sharing grants. This work was supported in part by NASA grant NAG5-4173. We also would like to thank NASA for the award of its Graduate Education Fellowship that provided support for Robert Brazzle during the course of this work.

References

- Brazzle R H, Göpel C, Nichols R N, Kehm K and Hohenberg C M 1994 Time frame for secondary processing through I-Xe chronometry (abstr.); *Meteoritics* **29** 448
- Brazzle R H 1997 Concordance of I-Xe and Pb-Pb ages in single mineral systems; Ph. D. Thesis, Washington University, St. Louis
- Brazzle R H, Meshik A P and Hohenberg C M 1997 Comparing iodine-xenon and lead-lead chronometers in single mineral systems: verification and interpretation of the iodine-xenon clock (abstr.); *Meteoritics* **32** 20–21
- Brazzle R H, Pravdivtseva O V, Meshik A P and Hohenberg C M 1998 Verification and interpretation of the I-Xe chronometer; *Geochim. Cosmochim. Acta* (submitted)
- Caffee M W, Hohenberg C M, Horz F, Hadson B, Kennedy B M, Podosek F A and Swindle T D 1982 Shock disturbance of the I-Xe system; *J. Geophys. Res.* **87** A318–A330
- Clayton D D 1975 Extinct radioactivities: Trapped residuals of presolar grains; *Astrophys. J.* **199** 765–769.
- Crabb J and Anders E 1982 On the siting of noble gases in E-chondrites; *Geochim. Cosmochim. Acta* **46** 2351–2361.
- Crabb J, Lewis R S and Anders E 1982 Extinct ^{129}I in C3 chondrites; *Geochim. Cosmochim. Acta* **46** 2511–2526
- Evensen N M, Carter S R, Hamilton P J, O'Nions R K and Ridley W I 1979 A combined chemical-petrological study of separated chondrules from the Richardton meteorite; *Earth Planet. Sci. Lett.* **42** 223–236
- Fish R A and Goles G G 1962 Ambient xenon: A key to the history of meteorites; *Nature* **196** 27–31
- Göpel C, Manhès G and Allègre C J 1994 U-Pb systematics of phosphates from equilibrated ordinary chondrites; *Earth Planet. Sci. Lett.* **121** 153–171
- Hohenberg C M 1980 High sensitivity pulse-counting mass spectrometer system for noble gas analysis; *Rev. Sci. Instrum.* **51**(8) 1075–1082
- Hohenberg C M and Kennedy B M 1980 I-Xe dating: intercomparisons of neutron irradiations and reproducibility of the Bjurböle standard; *Geochim. Cosmochim. Acta* **45** 251–256
- Jordan J, Kirsten T and Richter H 1980 $^{129}\text{I}/^{127}\text{I}$: A puzzling early solar system chronometer; *Z. Naturforsch.* **35a** 145–170
- Kehm K, Hohenberg C M and Nichols R H Jr 1994 Xenon isotopic measurements in Shallowater: *in situ* pulsed laser volatilization and the search for the carrier of radiogenic ^{129}Xe ; *Lunar Planet. Sci.* **XXV** 683–684.
- Kennedy B M 1981 *K-Ar and I-Xe gas retention ages of enstatite chondrite meteorites*, Ph. D. thesis, Washington Univ., Saint Louis, pp 298
- Lavielle B and Marti K 1992 Trapped xenon in ordinary chondrites; *J. Geochem. Res.* **97** 875–881
- Lewis R S and Anders E 1975 Condensation time of the solar nebula from extinct ^{129}I in primitive meteorites; *Proc. Natl. Acad. Sci. U.S.A.* **72** 268–273
- Manhès G, Göpel C and Allègre C J 1988 Systematique U-Pb dans les inclusions refractaires d'Allende: le plus vieux matériau solaire, *C. R. ATP Planetol.* 323–327
- Meeker G P, Wasserburg G J and Armstrong J T 1983 Replacement textures in CAI and implications regarding planetary metamorphism; *Geochim. Cosmochim. Acta* **47** 707–721
- Nichols R H, Hohenberg C M, Kehm K, Kim Y and Marti K 1994 I-Xe Studies of the Acapulco meteorite: Absolute I-Xe ages of individual phosphate grains and the Bjurböle standard; *Geochim. Cosmochim. Acta* **58** 2553–2561
- Pravdivtseva O P, Hohenberg C M and Brazzle R H 1998 Isotopic record of shock metamorphism in the Richardton H5 chondrite; *Meteoritics and Planet. Sci.* **33** A126–A127
- Reynolds J H 1960 Determination of the age of the elements; *Phys. Rev. Lett.* **4** 8–10
- Stoffler D, Klaus K and Scott E R D 1991 Shock metamorphism of ordinary chondrites; *Geochim. Cosmochim. Acta* **55** 3845–3867
- Swindle T D and Podosek F A 1988 Iodine-xenon dating; in *Meteorites and the Early Solar System* (eds) J F Kerridge and M S Matthews, (Tucson) pp. 1127–1146
- Swindle T D, Caffee M W and Hohenberg C M 1988 I-Xe studies of Allende inclusions: Eggs and the pink angel; *Geochim. Cosmochim. Acta* **52** 2215–2227
- Taylor G J and Heymann D 1969 Shock, reheating and the gas retention ages of chondrites; *Earth Planet. Sci. Lett.* **7** 151–161
- Tera F and Carlson R W (1997) Reexamining the U-Pb chronology of the early solar system; *Lunar Planet. Sci.* **XXVII** 1425–1426

Noble gas components in planetary atmospheres and interiors in relation to solar wind and meteorites

K MARTI and K J MATHEW

*Department of Chemistry, University of California, San Diego, La Jolla, CA 92093-0317, USA
e-mail: marti@ucsd.edu*

We discuss observed xenon isotopic signatures in solar system reservoirs and possible relationships. The predominant trapped xenon component in ordinary chondrites (OC) is OC-Xe and its isotopic signature differs from Xe in ureilites, in carbonaceous chondrites, in the atmospheres of Earth and Mars, and in the solar wind. Additional minor Xe components were identified in type 3 chondrites and in the metal phase of chondrites. The OC-Xe and ureilite signatures are both consistent with varying mixtures of HL-Xe and slightly mass fractionated solar-type Xe. Xenon in the Martian atmosphere is found to be strongly mass fractionated by 37.7‰ per amu, relative to solar Xe, favoring the heavy isotopes. Xenon in SNC's from the Martian mantle show admixture of solar-type Xe, which belongs to an elementally strongly fractionated component. The origin of the isotopic signatures of Ne and Xe in the terrestrial atmosphere are discussed in the light of evidence that the Xe isotopic fractionations in the Martian and terrestrial atmospheres are consistent. However, in the terrestrial atmospheric Xe component excesses are observed for ^{132}Xe and also for $^{129,131}\text{Xe}$, relative to fractionated solar Xe. The suggested chemically fractionated fission Xe component (CFF-Xe) seems to closely match the above excesses. We discuss models of origin for planetary volatiles and possible processes driving their evolution to present day compositions.

1. Observed noble gas components

The origin of terrestrial and planetary volatiles and the mechanisms driving their evolution to present day compositions are still poorly understood. Since noble gases are chemically inert, they can be expected to provide the most tractable clues for an understanding. Although several sources for the initial planetary atmospheres have been suggested, many models start with an acquisition of primitive solar nebular gases that are either altered by a variety of possible mechanisms or augmented by late-stage veneers and mantle outgassing. Ozima *et al* (1998) recently reviewed some possible relationships. A comparison of the elemental abundances of noble gases in chondritic meteorites (type 3 to CI) and planetary atmospheres to the solar abundances (figure 1) shows the large depletion of noble gases on the inner planets.

Among the noble gases, the isotopic signatures of Xe, due to its nine stable isotopes, give a wealth of

information on the origin and evolution of observed components. Table 1 presents a summary of the Xe isotopic abundances as observed in several solar system reservoirs.

2. Xenon isotopic signatures in meteorites

Trapped noble gases in chondrites provide valuable clues regarding the origin and evolution of the solar nebula (Levskii *et al* 1971; Alaerts *et al* 1979; Lavielle and Marti 1992; Huss *et al* 1996). The relative elemental abundance patterns are rather similar in all classes of chondrites (Marti 1967; Heymann and Mazor 1968). Mixing models have been considered in some detail (Lavielle and Marti 1992; Huss *et al* 1996) and variable mixing ratios of solar-type Xe (possibly slightly mass fractionated) and HL-Xe (as observed in pre-solar diamonds) have been very successful in accounting for observed meteoritic components.

Keywords. Noble gases; isotopic composition; planetary atmospheres; xenon.

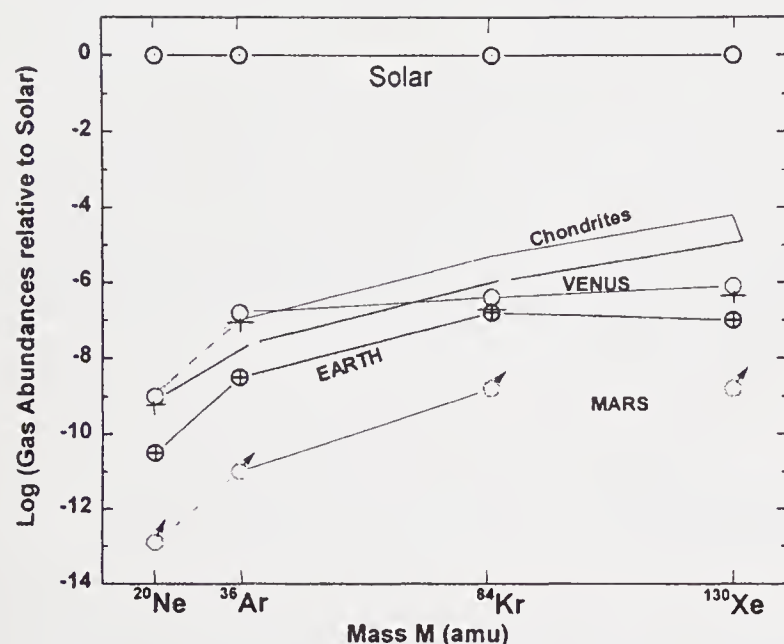


Figure 1. This figure shows noble gas abundances in planetary atmospheres relative to the sun (abundance curves are normalized to Si). For comparison the range of chondritic abundances (type 3 to CI) are shown. The gross depletion of noble gases compared to the solar abundances is apparent, and also the similarity between the observed elemental patterns of Earth and Mars. Solar and planetary data are from Pepin (1991), chondritic data from Marti (1967).

Lavielle and Marti (1992) observed consistency for all isotopes using two-component mixtures in OC-Xe, in ureilite-Xe, in oxidized residues from unequilibrated chondrites as well as in Q-Xe, as observed in unequilibrated and carbonaceous chondrites, respectively (Schelhaas *et al* 1990; Wieler *et al* 1992), except

for Xe signatures observed in planetary atmospheres. Therefore, references to meteoritic reservoirs of heavy noble gases using the traditional term “planetary” gases (Signer and Suess 1963) must now be considered misleading and should be avoided.

In contrast to xenon in carbonaceous chondrites, trapped xenon in ureilites was interpreted to represent a single uniform component (Wilkening and Marti 1976). The first detailed investigation of carriers of heavy noble gases in H chondrites was carried out by Moniot (1980). As previously observed for carbonaceous chondrites, carbon-rich residues obtained by HCl/HF demineralization were found to contain a large fraction of the trapped Xe in these chondrites. Moniot (1980) observed that Xe in the oxidized residue of Dimmitt displayed isotopic anomalies characterized by simultaneous excesses of the heavy and light isotopes, termed HL-Xe (R O Pepin and D Phinney, 1978). The OC-Xe signature (Lavielle and Marti 1992) is consistent with residue data of Moniot (1980). Schelhaas *et al* (1990) studied Xe in several chondrites and observed minor HL-Xe components in all cases of type 3.6 and lower. Carriers of Xe components with the S-Xe isotopic signature (SiC) were also observed in type 3 chondrites (Huss 1990). Wieler *et al* (1992) obtained isotopic signatures of Q-Xe in the Allende and Murchison carbonaceous chondrites by the CSSE-technique. Their Q-Xe data agree with OC-Xe isotopic signatures, but do not agree with either Xe in bulk carbonaceous chondrites (AVCC), or Kenna-type Xe (Wilkening and Marti 1976). A range of isotopic compositions was reported for

Table 1. Isotopic composition of various solar system xenon components. Also listed are the 95% confidence limits on the isotopic ratios.

Component [Ref.]*	$^{124}\text{Xe}/^{130}\text{Xe}$	$^{126}\text{Xe}/^{130}\text{Xe}$	$^{128}\text{Xe}/^{130}\text{Xe}$	$^{129}\text{Xe}/^{130}\text{Xe}$	^{130}Xe	$^{131}\text{Xe}/^{130}\text{Xe}$	$^{132}\text{Xe}/^{130}\text{Xe}$	$^{134}\text{Xe}/^{130}\text{Xe}$	$^{136}\text{Xe}/^{130}\text{Xe}$
Earth Atmos. [1]	0.02337 ±8	0.02186 5	0.46922 19	6.48503 271	1.0	5.21551 50	6.60982 64	2.56341 46	2.17569 112
Mars Atmos. [2]	0.0230 ±13	≡ 0.021	0.4728 69	15.562 41	1.0	5.180 17	6.529 21	2.585 11	2.269 16
Chond.: OC-Xe [3]	0.0286 ± 3	0.0255 2	0.511 2	6.420 11	1.0	5.060 8	6.174 11	2.344 5	1.963 4
Unequi. [4]	0.0287 ± 4	0.0254 3	0.510 2	6.380 12	1.0	5.038 7	6.135 9	2.318 7	1.942 6
Q-Xe [5]	0.0283 ± 4	0.0252 3	0.509 2	6.387 31	1.0	5.049 18	6.165 23	2.342 9	1.959 9
Urei.: Kenna [6]	0.0289 ± 3	0.0254 2	0.508 2	6.358 15	1.0	5.027 10	6.136 11	2.313 6	1.916 6
Solar: Pesyan. [7]	0.0280 ± 18	0.0259 17	0.508 4	6.369 13	1.0	4.986 10	6.087 12	2.234 6	1.803 5
12001 [8]	0.0290 ± 7	0.0259 9	0.5038 28	6.354 17	1.0	4.988 11	6.062 16	2.239 8	1.818 6
CSSE** [9]	0.0294 ± 7	0.0255 8	0.510 5	6.273 42	1.0	4.980 17	6.020 33	2.207 9	1.797 6

* References to the published data are [1] Valkiers *et al.* (1998); [2] Mathew *et al.* (1998); [3] Lavielle and Marti (1992); [4] Huss *et al.* (1996); [5] Wieler *et al.* (1992); [6] Wilkening and Marti (1976); [7] Kim and Marti (1992); [8] Eberhardt *et al.* (1972); [9] Wieler and Baur (1994).

** CSSE solar-Xe composition is the weighted average of the first two acid etch steps of the lunar ilmenite 71501. These steps are assumed to be free from spallation component.

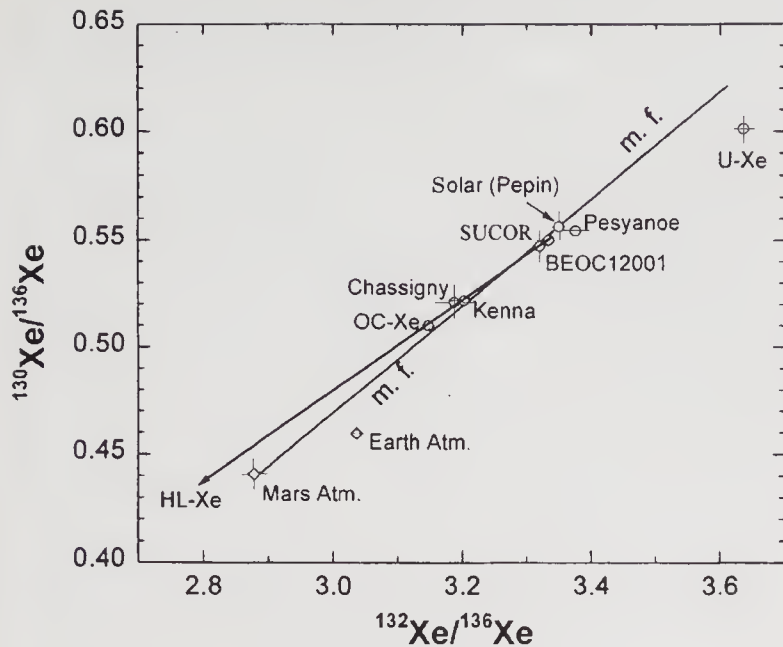


Figure 2. Isotopic relationships between Xe reservoirs of the solar system. Different estimates for the solar Xe signatures, obtained from lunar samples and from meteorites, show only small variations. Observed meteoritic Xe signatures can be explained as a result of the superposition of HL-Xe (of pre-solar origin) with solar Xe or slightly mass fractionated solar Xe. The terrestrial atmospheric Xe composition, however, does not plot on this trend. Also note that the mass fractionation trend through solar Xe misses the proposed U-Xe composition.

enstatite chondrites (Crabb and Anders 1981) which overlap the OC-Xe composition.

Separated metal of Forest Vale (and other chondrites) reveals yet another isotopically distinct xenon component: (FVM-Xe; Marti *et al* 1989). In a detailed study, Huss *et al* (1996) confirmed that a single trapped component, modified by nebular heating and mixing with additional components, was acquired by all classes of chondrites. Their implied correlation of second-order differences with other evidence for nebular processing requires that the mixing process with components initially carried by pre-solar grains must have been established prior to processes responsible for formation of the different chondrite classes.

3. Noble gas components on Mars

The trapped nitrogen in the SNC meteorites ALH84001, EET79001, and Zagami is consistent with the signatures of heavy Martian atmospheric nitrogen component (Becker and Pepin 1984; Marti *et al* 1995; Murty and Mohapatra 1997; Mathew *et al* 1998) but the heaviest component observed so far is $\delta^{15}\text{N} \leq 282\%$, considerably lower than that measured by Viking. ALH84001 data also show a nitrogen component which is isotopically light ($\delta^{15}\text{N} \leq -21\%$), presumably reflecting a mantle component. Furthermore, ALH84001 reveals two distinct Xe components, suggesting also a mantle-derived Martian component and an atmospheric component (Mathew *et al* 1998).

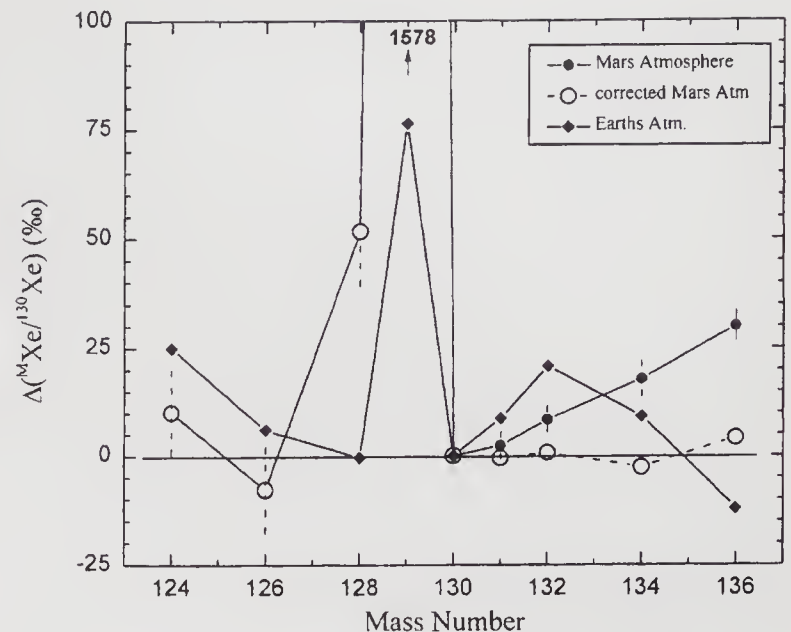


Figure 3. Deviations in ‰ of the measured Martian atmospheric composition from mass fractionated solar Xe (37.7‰ per amu). Also shown are the fission corrected (fission contribution at ^{136}Xe is 2.5%) Martian atmospheric composition (Mathew *et al* 1998) with respect to this fractionated solar Xe. The composition of the terrestrial atmospheric Xe is shown for comparison.

The isotopic signature of the second Xe component is consistent with solar-type, as previously observed in Chassigny (Ott 1988). When comparing these signatures with those of other components, xenon in the Martian atmosphere is found to be strongly fractionated by 37.7‰ per amu, relative to solar Xe, favoring the heavy isotopes. The isotopic composition of Xe in the Martian atmosphere may have been modified by outgassing of fission Xe, mainly due to ^{244}Pu , assuming a chondritic $^{244}\text{Pu}/^{238}\text{U}$ ratio applies to Mars. However, a detailed study of this component (Mathew *et al* 1998) indicates only a minor contribution (2.5% at ^{136}Xe). Possibly a significant portion of such fission components was retained in the Martian interior. The fission-corrected Martian atmospheric Xe plots close to the fractionation line inferred for terrestrial Xe, as shown in figure 3. For Martian atmosphere, Swindle *et al* (1986) also inferred a composition similar to terrestrial atmospheric Xe. The $\Delta = 0$ line in figure 3 corresponds to a 37.7‰ per amu fractionation of solar Xe. ^{129}Xe excesses due to decay of extinct ^{129}I are observed on both planets and the concentrations per gram planet mass are rather similar.

4. Terrestrial noble gas reservoirs

Large $^{40}\text{Ar}/^{36}\text{Ar}$ ratios (^{40}Ar of radiogenic origin) in mantle material compared to atmospheric ratios have been interpreted as evidence for early catastrophic degassing (Ozima 1975). Ne in the Earth's mantle is characterized by excesses on $^{21,22}\text{Ne}$, produced by (α, n) reactions. However, nucleogenic production is

negligible for ^{20}Ne . The isotopic signatures of He and Ne in mantle materials clearly distinguish two regions: the well mixed mid-ocean ridge basalt (MORB) source has a fairly constant $^3\text{He}/^4\text{He}$ ratio of $8R_a$ (where R_a is the atmospheric ratio of 1.39×10^{-6} ; Lupton 1983); the ocean island basalt (OIB) source, on the other hand, is characterized by higher $^3\text{He}/^4\text{He}$ ratios compared to MORB (as high as $35R_a$). This is attributed to a higher time integrated $(\text{U}+\text{Th})/^3\text{He}$ ratio in MORB compared to OIB and is consistent with a higher $(\text{U}+\text{Th})/^22\text{Ne}$ ratio. Since the high $^{20}\text{Ne}/^{22}\text{Ne}$ ratios observed in OIB and MORB samples cannot be explained by nuclear processes, the existence of a reservoir of solar like Ne seems required (e.g. Honda *et al* 1991). The highest $^{20}\text{Ne}/^{22}\text{Ne}$ ratios observed so far are ~ 13 . Considering that atmospheric contamination and minor shifts due to nucleogenic ^{22}Ne would lower the observed $^{20}\text{Ne}/^{22}\text{Ne}$ ratios, the measured Ne data are compatible with the solar-type Ne ratio measured on the moon. Whether this reservoir represents primordial solar Ne in the mantle (e.g. Honda *et al* 1991; Burnard *et al* 1997), or whether the solar-like isotopic composition of He and Ne could result from subducted interplanetary dust particles (e.g. Allègre *et al* 1993; Anderson 1993) is a matter of debate. In either case, there is clear evidence that the atmospheric signature does not simply derive from mantle outgassing through time, but that the mantle was isolated early on (Lupton 1983; Sarda *et al* 1988; Honda *et al* 1991). The isotopic compositions of Ar, Kr, and Xe in the mantle are poorly constrained, because of the omnipresence of atmospheric contamination (e.g. Farley and Poreda 1993; Farley and Craig 1994). Recently, Burnard *et al* (1997) analyzed gases trapped in individual vesicles in the volatile-rich basaltic glass “popping rock”. They conclude that all of the ^{36}Ar may have been of atmospheric origin adhering to the surface of the samples, and that the $^{40}\text{Ar}/^{36}\text{Ar}$ ratio of the upper mantle is $> 40,000$. Based on these results, they suggest that the non-radiogenic noble gas inventory of the Earth’s mantle may be approximately solar in composition. They speculate that gases in the Earth’s proto-planet were degassed by collisions during the accretionary period and that the mantle gases were acquired from the solar wind during the final stages of the Earth’s formation.

Isotopic studies of Xe in SNC meteorites have shown that terrestrial atmospheric Xe apparently no longer is unique in the solar system. Nevertheless its composition has been a major unsolved question. The first clear recognition of non-atmospheric Xe in terrestrial samples came from the analysis of CO_2 well gases with excesses of ^{129}Xe originating from the decay of ^{129}I (e.g. Butler *et al* 1963; Phinney *et al* 1978). Presently, it appears that mantle Xe is characterized by excesses on mass ^{129}Xe , as well as some fission excesses on $^{131}\text{--}^{136}\text{Xe}$ (e.g. Allègre *et al* 1986, 1987; Poreda and Farley 1992; Kunz *et al* 1998).

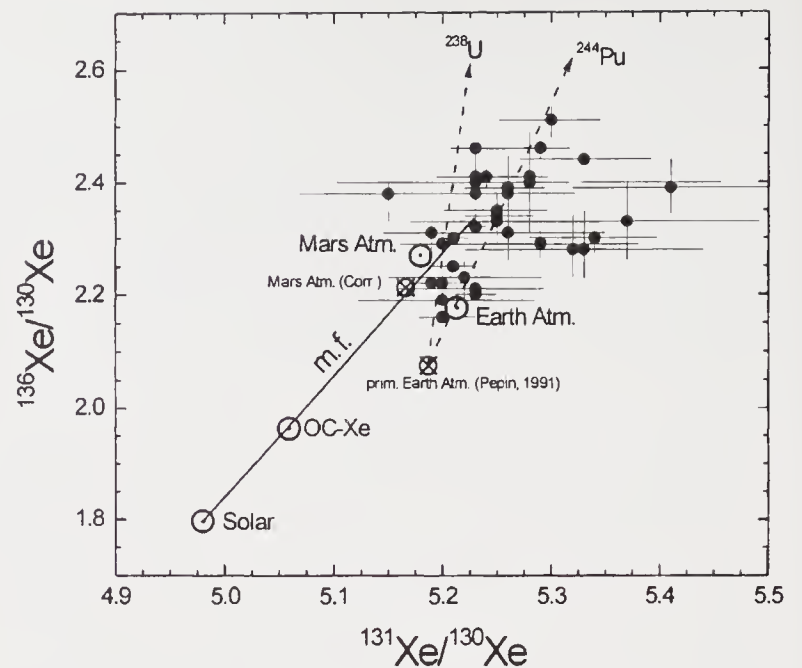


Figure 4 $^{136}\text{Xe}/^{130}\text{Xe}$ vs. $^{131}\text{Xe}/^{130}\text{Xe}$ data of MORB samples. Data from Kunz *et al* (1998). Solar Xe is from Wieler and Baur (1994), OC-Xe from Lavielle and Marti (1992) and Mars atmospheric composition from Mathew *et al* (1998). Prim. Earth atmosphere is the ^{244}Pu -fission corrected composition deduced by Pepin (1991), and Mars Atm. (Corr.) is the Martian atmospheric composition corrected for ^{244}Pu -derived Xe (inferred from a comparison of the measured Martian atmospheric signature with solar Xe fractionated by 37.7‰ per amu; Mathew *et al* 1998).

However, the abundance and isotopic composition of primordial mantle Xe is not known. Xe measurements in SNC meteorites by Mathew *et al* (1998) indicate that fission-corrected Martian atmospheric Xe is compatible with mass fractionated solar Xe (figure 3). A comparison of this Xe isotopic composition with terrestrial atmospheric Xe reveals excesses on $^{131,132}\text{Xe}$ in the Earth’s atmosphere. Interestingly, these excesses are consistent with an Xe component called CFF-Xe (chemically fractionated fission; e.g. Shukolyukov *et al* 1994) (figure 2). This latter component is due to the fast diffusion of fission fragments from the parent U-bearing mineral into adjacent mineral phases, where the fragments subsequently decay.

Recent experimental work has focused on the characterization of Xe components in the mantle (Burnard *et al* 1997; Kunz *et al* 1998). Kunz *et al* (1998) claim that ^{244}Pu -derived fission Xe has been identified in the Earth’s mantle. However, their data interpretation is clearly biased, first because the trapped Xe is assumed to be a primitive (^{244}Pu fission-free) atmospheric component and, second, their data (figure 4) are not compatible with their inferred two-component mixture.

5. Other proposed components

In addressing relationships among solar system xenon components it is important to define the initial isotopic composition. The composition of primitive

U-Xe was derived empirically (Takaoka 1972; Pepin and Phinney 1978; Pepin 1991). Some supporting evidence has also come forth (Michel and Eugster 1994). Based on this hypothetical primitive solar system component (U-Xe), it is possible to construct models involving mass-fractionation (due to e.g. solar EUV driven hydrodynamic escape (Pepin 1991), or due to giant impacts (Benz and Cameron 1990; Pepin 1997)), and a later addition of ^{244}Pu and/or ^{238}U fission produced Xe, to account for the present atmospheric Xe composition. A problematic aspect of such models is that different starting materials are required for each planet. For Venus the isotopic signatures are not known, therefore the difference is in the initial elemental abundance of the noble gases. In applying this model to Mars, Pepin (1991) had to assume a CI carbonaceous chondrite-like Xe composition. On the other hand, based on multivariate correlation analysis of terrestrial atmospheric Xe, and of Xe components in separated phases of carbonaceous chondrites, it was inferred that primitive Xe must have been similar to solar Xe rather than U-Xe (Igarashi 1995).

The recent Xe isotopic studies in SNC meteorites by Mathew *et al* (1998) indicate that fission corrected Martian atmospheric Xe is mass fractionated solar Xe (figure 3). The fractionation is 37.7‰/amu, very similar to the fractionation observed for terrestrial Xe, when compared to solar Xe. The only exceptions are excesses of $^{128,129}\text{Xe}$, which most likely result from (n,γ)-reactions on ^{127}I and from decay of ^{129}I . This implies that for Mars the signatures of OC-Xe (Lavielle and Marti 1992) and U-Xe (Pepin 1991; Pepin and Phinney 1978) cannot represent the starting composition before mass fractionation occurred. This seems to conflict with the assumption made by Pepin (1991). As figure 2 shows, the signature of terrestrial Xe can be related to U-Xe by mass fractionation, but the Martian atmospheric Xe signature and meteoritic components are not compatible with mass-fractionated U-Xe.

These observations lend some appeal to an alternative model for the origin of terrestrial atmospheric Xe. It was suggested that the terrestrial Xe isotopic signature represents a mixture of mass-fractionated solar Xe and CFF Xe (e.g. Shukolyukov *et al* 1994). This latter component is due to a fast diffusion of fission fragments (Sn, Sb, Te, I, Se) from the parent U-bearing mineral into adjacent mineral phases, where the fragments subsequently decay into Xe and other isotopes. This results in an isotopic composition which depends on the half-lives and the chemical properties of the fission fragments. CFF Xe has been identified in U-free inclusions of samples from the natural reactor in Okelobondo, in the southern extension of the Oklo deposit (Meshik *et al* 1997). It is characterized by large excesses on ^{132}Xe (as well as excesses on $^{129,131}\text{Xe}$) which results in a pattern that cannot be produced by total yields in known fission

reactions. The excesses observed by Kunz *et al* (1998) in their samples agree in part with CFF-Xe rather than ^{244}Pu -fission Xe.

6. Models of atmospheric evolution

Mechanisms which can cause fractionation involve among others adsorption (e.g. Bernatowicz and Podosek 1986), ion implantation from plasmas (e.g. Bernatowicz and Fahey 1986; Ponganis *et al* 1997), Jean's escape and hydrodynamic escape (e.g. Pepin 1991, 1997), and gravitational capture followed by hydrodynamic escape (e.g. Ozima and Zahnle 1993). Also a setting for low energy ion implantation (Ponganis *et al* 1997) has been suggested: During the T-Tauri phase of the proto-sun the solar nebula was being swept by intense solar wind and strong flare activities. Elemental and isotopic fractionation will occur in solar wind sputtering and photochemical escape (Jakosky *et al* 1994). During the brief period ($\sim 10^6$ years) of the T-Tauri phase of the proto-sun, the solar nebula probably was being swept up by an intense solar wind with a mass loss rate of $dM/dt \sim 10^{-7}-10^{-6} M_{\text{sun}} \text{ year}^{-1}$ (Bachiller 1996). This was probably accompanied by strong flare activities (Feigelson *et al* 1993) which also contributed to the grain irradiation effect. However, the penetration of the solar particles should at first be limited to the inner edge and boundary layer of the solar nebula. This scenario is compatible with Wetherill's (1981) suggestion that, because of the blocking effect, the condensed grains forming Venus should be affected more severely by primordial solar wind implantation than Earth and Mars. However, models predict that the "implantation surface" or the stagnation point between the T-Tauri wind and the inner edge of the solar nebula should progress outward to reach the condensation zones of asteroids and eventually of icy planetesimals orbiting in the Uranus and Neptune region (Ip 1984).

It is not clear whether the solar nebula was completely clear of gas during the T-Tauri phase. Even if there was little gas in the dust disk, the sputtering effect of the solar wind particles should be effective in generating a gas cloud (Ip 1995). The subsequent ionization effect of the solar UV radiation and the charge-exchange process between the T-Tauri wind and the neutral gas will lead to a situation similar to that of solar wind interactions with comets, Venus and Mars, in which the interplanetary magnetic fields are compressed (or draped) ahead of the ionospheres of these planetary bodies. This is the region in which solar wind ion sputtering and implantation of the condensed grains will be most effective. Shu *et al* (1996) have also called attention to the potential importance of this thin boundary layer in producing chondrules.

In addition to Xe, the Ne isotopic signature is probably a good choice for a search of evolutionary

signatures in an early atmosphere: There is an established difference in isotopic composition between mantle Ne and atmospheric Ne. For the $^{20}\text{Ne}/^{22}\text{Ne}$ ratio, the difference is not due to nuclear reactions. A knowledge of $^{20}\text{Ne}/^{22}\text{Ne}$ ratios in the early atmosphere would therefore represent a very significant tool in characterizing and understanding the processes that ultimately formed the atmosphere.

The heavy solar system wide bombardment documented in lunar age data rapidly decreased ~ 3.8 Ga ago and if the late accretion of material was a significant process in establishing the Ne isotopic composition of the atmosphere, there might be a record in old terrestrial rocks. It is also conceivable that isotopic fractionation due to hydrodynamic escape has decreased the $^{20}\text{Ne}/^{22}\text{Ne}$ ratio to a value < 9.80 and that the atmospheric ratio evolved through time by mixing with degassed mantle gases. Existing model calculations on simple two-reservoir mixing processes (e.g. Marty and Allè 1994; Porcelli and Wasserburg 1994) are consistent with low $^{20}\text{Ne}/^{22}\text{Ne}$ ratios, including ratios as low as Ne-A (traditionally called planetary type Ne) observed in some meteorites. Obviously, a difficulty to the detection of low atmospheric $^{20}\text{Ne}/^{22}\text{Ne}$ ratios is the separation of nucleogenic Ne components which need to be resolved, as these are pronounced for ^{22}Ne .

Alternatively, the detection of trapped $^{20}\text{Ne}/^{22}\text{Ne}$ ratios > 9.8 would indicate that the primordial terrestrial atmospheric Ne contained a solar-type component. Hydrodynamic escape of Ne requires H escape fluxes considerably larger than presently supplied to the terrestrial exosphere by solar extreme-ultraviolet radiation. The decline of this radiation from an early T-Tauri stage through time is poorly constrained. Pepin (1992) assumed mean decay time of 9×10^7 years, implying that hydrodynamic escape essentially stops after ~ 400 Ma. Alternatively, Feigelson *et al* (1993) suggested a power law decay with time which holds over the entire stellar age, and which would imply that hydrodynamic escape was active longer than in Pepin's model. Indeed, Pepin (1997) also invokes late hydrodynamic escape driven by H_2 escape fluxes just intense enough to lift Ne out of the atmosphere to explain the atmospheric Ne isotopic composition in a new version of his model.

The presence of solar-type Xe in the Martian interior, apparently in a reservoir which is elementally strongly fractionated may offer a new approach to studying the relationships between an atmospheric reservoir and the components stored in the interiors of terrestrial planets.

Acknowledgements

We acknowledge helpful discussions with W H Ip, R Lingenfelter and J N Goswami and useful sugges-

tions by two anonymous reviewers. Research supported by NASA grant NAG5-4543.

References

- Alaerts L, Lewis R S and Anders E 1979 Isotopic anomalies of noble gases in meteorites and their origins. IV. C3 (Ornans) carbonaceous chondrites; *Geochim. Cosmochim. Acta* **43** 1421–1432
- Allègre C J, Sarda P, and Staudacher T 1993 Speculations about the cosmic origin of He and Ne in the interior of the Earth; *Earth Planet. Sci. Lett.* **117** 229–233
- Allègre C J, Staudacher T, and Sarda P 1986/87 Rare gas systematics: formation of the atmosphere, evolution and structure of the Earth's mantle; *Earth Planet. Sci. Lett.* **81** 127–150
- Anderson D L 1993 Helium-3 from the mantle: Primordial signal or cosmic dust?; *Science* **261** 170–176
- Bachiller R 1996 Bipolar molecular outflows from young stars and protostars; *Ann. Rev. Astron. Astrophys.* **34** 111–154
- Benz W and Cameron A G W 1990 Terrestrial effects of the giant impact; in *Origin of the Earth* (eds) H E Newsom and J H Jones (Oxford Univ. Press) pp. 61–67
- Becker R H and Pepin R O 1984 The case for a Martian origin of the shergottites: Nitrogen and noble gases in EETA 79001; *Earth Planet. Sci. Lett.* **69** 225–242
- Bernatowicz T J and Fahey A J 1986 Xe isotopic fractionation in a cathodeless glow discharge; *Geochim. Cosmochim. Acta* **50** 445–452
- Bernatowicz T J and Podosek F A 1986 Adsorption and isotopic fractionation of Xe; *Geochim. Cosmochim. Acta* **50** 1503–1507
- Burnard P, Graham D, and Turner G 1997 Vesicle-specific noble gas analyses of “popping rock”: Implications for primordial noble gases in Earth; *Science* **276** 568–571
- Butler W A, Jeffery P M, Reynolds J H, and Wasserburg G J 1963 Isotopic variations in terrestrial xenon; *J. Geophys. Res.* **68** 3283–3291
- Crabb J and Anders E 1981 Noble gases in E-chondrites; *Geochim. Cosmochim. Acta* **45** 2443–2464
- Eberhardt P, Geiss J, Graf H, Gröglér N, Mendia M D, Mörgeli M, Schwaller H, Stettler A, Krähenbühl U and von Gunten H R 1972 Trapped solar wind noble gases in Apollo 12 lunar fines 12001 and Apollo 11 breccia 10046; *Proc. Lunar Planet. Sci. Conf.* **3rd** 1821–1856
- Farley K A and Craig H 1994 Atmospheric Argon contamination of ocean island basalt olivine phenocrysts; *Geochim. Cosmochim. Acta* **58** 2509–2517
- Farley K A and Poreda R J 1993 Mantle Neon and atmospheric contamination; *Earth Planet. Sci. Lett.* **114** 325–339
- Feigelson E D, Casanova S, Montmerle T and Guibert J 1993 Rosat X-ray study of the Chamaeleon I dark cloud. I. The stellar population; *Astrophys. J.* **416** 623–646
- Honda M, McDougall I, Patterson D B, Doulgeris A and Clague D A 1991 Possible solar noble-gas component in Hawaiian basalts; *Nature* **349** 149–151
- Heymann D and Mazor E 1968 Noble gases in unequilibrated ordinary chondrites; *Geochim. Cosmochim. Acta* **32** 1–19
- Huss G R 1990 Ubiquitous interstellar diamond and SiC in primitive chondrites: abundances reflect metamorphism; *Nature* **347** 159–162
- Huss G R, Lewis R S and Hemkin S 1996 The “normal planetary” noble gas component in primitive chondrites: Compositions, carrier, and metamorphic history; *Geochim. Cosmochim. Acta* **60** 3311–3340
- Igarashi G 1995 Primitive xenon in the Earth; in *Volatiles in the earth and solar system* (ed) K A Farley (American Institute of Physics) pp. 70–80

- Ip W H 1984 Magnetic field amplification in the solar nebula through interaction with the T-Tauri wind; *Nature* **312** 625–626
- Ip W H 1995 Cosmic ray acceleration by protostellar winds in the Orion molecular complex; *Astron. Astrophys.* **300** 283–288
- Jakosky B M, Pepin R O, Johnson R E and Fox J L 1994 Mars atmospheric loss and isotopic fractionation by solar-wind-induced sputtering and photochemical escape; *Icarus* **111** 271–288
- Kim J S and Marti K 1992 Solar-type xenon: Isotopic abundances in Pesyanoe; *Proc. Lunar Planet. Sci. Conf.* **22** 145–151
- Kunz J, Staudacher T and Allègre C J 1998 Plutonium-fission xenon found in earth's mantle; *Science* **280** 877–880
- Lavielle B and Marti K 1992 Trapped xenon in ordinary chondrites; *J. Geophys. Res. (Planets)* **97** 20875–20881
- Levskii L K, Fedorova I V and Yakovleva S Z 1971 Distribution of inert gases in chondrites; *Geokhimiya* **5** 515–522
- Lupton J E 1983 Terrestrial inert gases: Isotope tracer studies and clues to primordial components in the mantle; *Annu. Rev. Earth Planet. Sci.* **11** 371–414
- Marti K 1967 Trapped xenon and the classification of chondrites; *Earth Planet. Sci. Lett.* **2** 193–196
- Marti K, Kim J S, Lavielle B, Pellas P and Perron C 1989 Xenon in chondritic metal; *Z. Naturforsch.* **44a** 963–967
- Marti K, Kim J S, Thakur A N, McCoy T J and Keil K 1995 Signatures of the Martian Atmosphere in glass of the Zagami meteorite; *Science* **267** 1981–1984
- Marty B and Allè P 1994 Neon and Argon isotopic constraints on Earth-atmosphere evolution; in *Noble Gas Geochem. Cosmochem.* (ed. Matsuda J.) (Terra Scientific Publishing Company) pp. 191–204
- Mathew K J, Kim J S and Marti K 1998 Martian atmospheric and indigenous components of xenon and nitrogen in the Shergotty, Nakhla, and Chassigny group meteorites; *Meteorit. Planet. Sci.* **33** 655–664
- Meshik A, Hohenberg C, Kehm K, Swan P, and Dymkov Yu 1997 Chemically fractionated fission (CFF) Xe in Okelobondo (zone 13 of Oklo): Implications for the origin of terrestrial xenon; *Lunar Planet. Sci.* **28** 943–944
- Michel Th and Eugster O 1994 Primitive xenon in diogenites and Plutonium-244-fission xenon ages of a diogenite, a howardite and eucrites; *Meteoritics* **29** 593–606
- Moniot R K 1980 Noble-gas-rich separates from ordinary chondrites; *Geochim. Cosmochim. Acta* **44** 253–271
- Murty S V S and Mohapatra R K 1997 Nitrogen and heavy noble gases in ALH84001: Signatures of ancient Martian atmosphere; *Geochim. Cosmochim. Acta* **61** 5417–5428
- Ott U 1988 Noble gases in SNC meteorites: Shergotty, Nakhla, Chassigny; *Geochim. Cosmochim. Acta* **52** 1937–1948
- Ozima M 1975 Ar isotopes and Earth-atmosphere evolution models; *Geochim. Cosmochim. Acta* **39** 1127–1140
- Ozima M and Zahnle K 1993 Mantle degassing and atmospheric evolution – noble gas view; *Geochem. J.* **27** 185–200
- Ozima M, Wieler R, Marty B and Podosek F A 1998 Comparative studies of solar, Q-gases and terrestrial noble gases, and implications on the evolution of the solar nebula; *Geochim. Cosmochim. Acta* **62** 301–314
- Pepin R O 1997 Evolution of Earth's noble gases: consequences of assuming hydrodynamic loss driven by giant impact; *Icarus* **126** 148–156
- Pepin R O 1992 Origin of noble gases in the terrestrial planets; *Ann. Rev. Earth Planet. Sci.* **20** 389–430
- Pepin R O 1991 On the origin and early evolution of terrestrial planet atmospheres and meteoritic volatiles; *Icarus* **92** 2–79
- Pepin R O and Phinney D 1978 Components of xenon in the solar system; Univ. of Minnesota Space Science Center
- Phinney D, Tennyson J and Frick U 1978 Xenon in CO₂ well gas revisited; *J. Geophys. Res.* **83** 2313–2319
- Ponganis K V, Graf T, and Marti K 1997 Isotopic fractionation in low-energy ion implantation; *J. Geophys. Res. (Planets)* **102** 19335–19343
- Porcelli D and Wasserburg G J 1994 A unified model for terrestrial rare gases; in *Volatiles in the earth and solar system* (ed) K A Farley (American Institute of Physics) pp. 56–69
- Poreda R J and Farley K A 1992 Rare gases in Samoan xenoliths; *Earth Planet. Sci. Lett.* **113** 129–144
- Sarda P, Staudacher T and Allègre C J 1988 Neon isotopes in submarine basalts; *Earth Planet. Sci. Lett.* **91** 73–88
- Schelhaas N, Ott U and Begemann F 1990 Trapped noble gases in unequilibrated ordinary chondrites; *Geochim. Cosmochim. Acta* **54** 2869–2882
- Shu F H, Shang H and Lee T 1996 Toward an astrophysical theory of chondrites; *Science* **271** 1545–1552
- Shukolyukov Yu A, Fugzan M M, Assonov S S, Koloskov M V, Fisenko A V and Semenova L F 1994 Xe and Kr isotope anomalies in Sikhote-Alin' iron meteorite inclusions; *Geokhimiya* **10** 1379–1392 (translation: *Geochemistry International* **31**(5) 1–14)
- Signer P and Suess H E 1963 Rare gases in the sun, in the atmosphere, and in meteorites; in *Earth Science and Meteorites* (eds) J Geiss and E D Goldberg (Amsterdam: North-Holland) pp. 241–272
- Takaoka N 1972 An interpretation of general anomalies of xenon and the isotopic composition of primitive xenon; *Mass Spectrosc.* **20** 287–302
- Valkiers S, Aregbe Y, Taylor P D P and De Bièvre P 1998 A primary xenon isotopic standard with SI traceable values for isotopic composition and molar mass; *Int. J. Mass Spectr. and Ion Processes* **173** 55–63
- Wetherill G W 1981 Solar wind origin of ³⁶Ar on Venus; *Icarus* **46** 70–80
- Wieler R and Baur H 1994 Krypton and xenon from the solar wind and solar energetic particles in two lunar ilmenites of different antiquity; *Meteoritics* **29** 570–580
- Wieler R, Anders E, Baur H, Lewis R S and Signer P 1992 Characterisation of Q-gases and other noble gas components in the Murchison meteorite; *Geochim. Cosmochim. Acta* **56** 2907–2921
- Wilkening L L and Marti K 1976 Rare gases and fossil particle tracks in the Kenna ureilite; *Geochim. Cosmochim. Acta* **40** 1465–1473

Studies of modern and ancient solar energetic particles

R C REEDY

Mail Stop D436, Los Alamos National Laboratory, Los Alamos, NM 87545, USA
e-mail: rreedy@lanl.gov

Modern solar energetic particles (SEPs) have been studied for about 50 years by satellites and ground-based observations. These measurements indicate much about the nature of SEPs but cover too short a period to quantify the probabilities of very large solar particle events. Many SEPs have high enough energies to make nuclides in material in which they interact. Radionuclides measured in lunar samples have been used to extend the record about SEPs back several million years. Some new measurements of modern SEPs during the last solar cycle and new results for nuclides made by SEPs in lunar samples are presented and their implications discussed. Both the modern and ancient records need to be improved, and methods to get a better understanding of solar energetic particles discussed. The fluxes of SEPs during the last million years show an increasing trend when averaged over shorter radionuclide half-lives.

1. Introduction

There are many types of particles in the solar system. Most, such as those in the solar wind, have energies below an MeV and must be observed directly, either now in space or as implanted species in certain solar-system materials. However, more energetic particles, like galactic-cosmic-ray (GCR) particles and solar energetic particles (SEPs), can interact with solar-system matter and produce nuclides. These “cosmogenic” nuclides allow us to study the energetic particles that made them as well as the history of the material in which the nuclides were made (e.g., Reedy *et al* 1983). GCR particles ($E \sim 1\text{--}10$ GeV) penetrate deep into matter and make many nuclides. The nature of GCR particles is fairly well known.

Solar energetic particles occur very rarely and are accelerated to high energies by various processes involving the Sun. The peak fluxes during a solar particle event (SPE) last only a few hours, and an SPE lasts only for a few days to a week or two. SEPs have energies from ~ 1 MeV to hundreds and occasionally thousands of MeV with the flux usually dropping fairly rapidly with increasing energy (Smart and Shea 1989). The nuclei in an SPE are $\approx 98\%$ protons (Smart and Shea 1989), with a proton/ α -particle ratio of ~ 50

(Goswami *et al* 1988) and with small amounts of heavier nuclei (Tylka *et al* 1997). Before direct measurements of SEPs by spacecraft in the mid-1960s, some observations since 1942 were made using Earth-based instruments that detected ionization, neutrons, or radio disturbances caused by SEPs (Shea and Smart 1995). A few SPEs have very high fluxes and event-integrated fluences that are serious radiation hazards in space (Shea and Smart 1996).

Most SEPs are stopped in less than a centimeter of solid matter. SEPs can induce nuclear reactions that produce high concentrations of certain nuclides near the very surface, such as in cosmic dust, meteoroids, and lunar samples (Reedy and Arnold 1972). Nuclides made by SEPs have been observed in many extra-terrestrial samples and are often called solar-cosmic-ray-produced nuclides. Many SEP-produced nuclides have been observed in lunar samples (e.g., Reedy and Marti 1991; Rao *et al* 1994). When cross sections to unfold the lunar data are available, these SEP-produced nuclides have been used to infer the average fluxes of SEPs over various time periods determined by the half-life of the radionuclide or the surface exposure age of the lunar sample. Such fossil records enable us to study the long-term record of SEPs during the last 10^7 years. This paper reviews SEPs and what is

Keywords. Solar energetic particles; cosmogenic nuclides; lunar rocks.

Table 1. *Solar-proton integral fluxes during the last four solar cycles.*

Time period	Data source	Flux references	R_0 (MV)	Integral		Fluxes [#]	
				E>10	E>30	E > 60	E > 100
1986–1996	Several	This work	≈65	≈152	≈31	– [‡]	– [‡]
1976–1986	GSFC	Goswami <i>et al</i> 1988	40	63	5	0.6	~0.2 [‡]
1976–1986		Feynman <i>et al</i> 1990	57	52	8.6	– [‡]	– [‡]
1965–1975	SPME	Reedy 1977	90	92	30	8	– [‡]
1965–1975		Feynman <i>et al</i> 1990	86	64	20	– [‡]	– [‡]
1954–1964	²² Na [@] , ⁵⁵ Fe	Reedy 1977	100	≈378	≈136	≈59	≈26
1954–1996		(See text)	83	≈171	≈50	≈19	≈7

[#] Omnidirectional fluxes in protons cm⁻² s⁻¹; energies in MeV.

[‡] Not measured (1965–1973), not reported (1973–1986), or not determined (1986–1996).

[@] Using an older set of cross sections slightly different from newer ones.

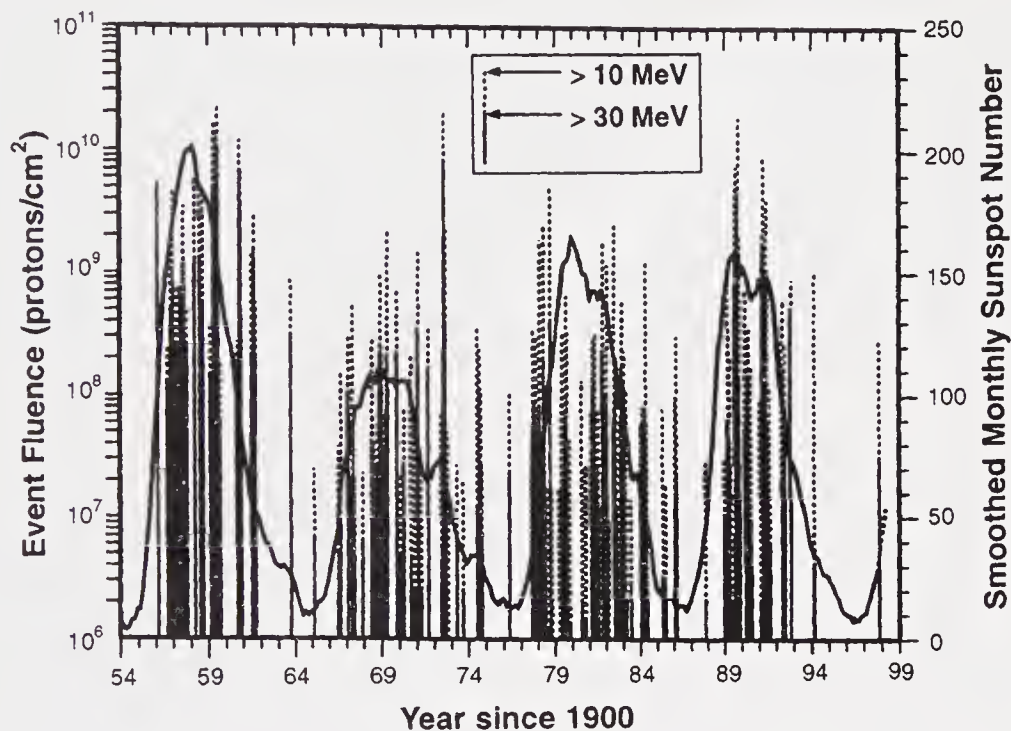


Figure 1. The event-integrated proton fluences >10 and >30 MeV near the Earth for solar particle events (vertical solid and dashed bars) and the smoothed monthly sunspot number (continuous curve) are shown as a function of time since 1954.

known about them from both modern measurements of SEPs and the fossil record with SEP-produced nuclides in lunar samples. Suggestions for further studies that will provide a better understanding of SEPs, both modern and ancient, are also presented.

2. Modern measurements

Table 1 lists average SEP fluxes for the four solar cycles from 1954 to 1996 for protons above four energies from 10 to 100 MeV and the approximate values of the characteristic rigidity, R_0 . The parameter R_0 determines the shape for an exponential rigidity spectrum, $dJ/dR = k \times \exp(-R/R_0)$, where k is a constant and R is the particle's rigidity (momentum per unit charge). The event-integrated fluences for SPEs from 1954 to 1997 are shown in figure 1 along with the smoothed monthly sunspot number, an indicator of the level of solar activity. A solar cycle extends between consecutive minima of the smoothed sunspot number

and is usually about eleven years long. The event-integrated fluences of SEPs have been compiled in detail by several authors for SPEs since 1954 until 1987 (e.g., Reedy 1977; Goswami *et al* 1988; Feynman *et al* 1990; Shea and Smart 1990).

The average fluxes from 1954 to 1964, solar cycle 19, are based on indirect measurements of relative SPE fluences and activities of ²²Na (half life = 2.6 years) and ⁵⁵Fe (half life = 2.7 years) in lunar rocks (Reedy 1977). These results for 1954–1964 need to be calculated again using better estimates of the relative SPE fluences for that period and newer cross sections for the nuclear reactions making ²²Na (e.g., Sisterson *et al* 1996). Preliminary calculations (e.g., Sisterson *et al* 1996) indicate that the average fluxes for 1954–1964 will be smaller than those calculated by Reedy (1977).

There are two sets of solar-proton average fluxes using different instruments given in table 1 for the two solar cycles from 1965 to 1986. For both of these 11-year solar cycles, there are some disagreements for the fluxes averaged over the solar cycle as estimated by

these various groups. These results suggest that these average fluxes are usually good to $\sim 30\%$. For SPEs with very high fluxes, measured fluxes could be more uncertain because of dead-time effects (e.g., Tylka *et al* 1997). Measurements during times with many very-high-energy protons could be affected by protons entering through the sides or collimators of detector systems (e.g., Reeves *et al* 1992). Some work needs to be done to check these fluxes and to try to reduce their uncertainties. The event-integrated fluences of Reedy (1977) and Goswami *et al* (1988) are used for the 1954–1996 averages in tables 1 and 2 and in figure 1 for 1954 to 1996. The average fluxes for solar cycles 20 and 21 (1965–1986) are much less than those for solar cycle 19. This variation among SEP fluxes for individual solar cycles makes it hard to get good estimates for the long-term average fluxes of SEPs.

The values for the solar cycle 22, 1986–1996, are preliminary ones from databases for energetic-particle instruments on the GOES and IMP–8 satellites. The fluences for some of the larger events have been published for GOES (Shea and Smart 1992) and IMP–8 (Feynman *et al* 1993) data. There are some differences in the event-integrated fluences for SPEs in these data sets, and averages, when available, were usually adopted here. For three of the four largest events in 1989, the event-integrated fluences of Reeves *et al* (1992) >10 MeV are within 50% of those from the other two data sets. The >10 MeV fluence for the other event (29th September 1989) in Reeves *et al* (1992) is about twice those of the others. Event-integrated proton fluences for the largest events during this last solar cycle are among the largest observed during the last five decades (Reeves *et al* 1992; Feynman *et al* 1993; Shea and Smart 1992, 1994). These data show that solar cycle 22 needs to be included in any study predicting SEP fluences in

space, such as was done recently by Feynman *et al* (1993).

The fluences for the 11th November 1997 solar particle event, especially >30 MeV, are very preliminary values from peak fluxes >10 MeV in the database for the GOES satellites at geosynchronous orbit. A more complete set of intensities of event-integrated fluences and average fluxes of SEPs from 1954 until 1998 is being prepared (Reedy *et al* 1998).

As shown in figure 1, the largest SPEs since 1954 had event-integrated proton fluences $\lesssim 3 \times 10^{10}$ protons cm^{-2} for energies >10 MeV. Solar particle events of this size are serious radiation hazards to people, spacecraft, and instruments in deep space, especially away from the Earth's atmosphere and strong geomagnetic field (Shea and Smart 1996). It is hard to set good limits on huge SPEs using the present sets of direct measurements of SEPs. Other records for SEPs, such as nuclides made by SEPs in lunar samples, have been used to extend our database for the average fluxes of SEPs.

3. Ancient records

The best records of solar energetic particles in the past are some nuclides made by SEPs and preserved in the top layers of lunar samples. SEP-produced nuclides have been studied since the first lunar samples returned by Apollo 11 in 1969. These nuclides represent various time periods in the past (see table 2), as determined by the mean-life of a radionuclide and/or the surface exposure age of the lunar sample. The interpretations of the depth-versus-concentration profiles of nuclides made by SEPs in lunar rocks and cores have provided average fluxes and spectral shapes of solar protons for various time periods back to ~ 5 Ma.

Table 2. Average solar-proton fluxes[†] for various time periods.

Time period	Data source	Flux References	Integral		Fluxes [#]	
			E > 10	E > 30	E > 60	E > 100
1954–1996	Modern	(See text)	171	50	19	7
10^4 year	^{14}C	Jull <i>et al</i> 1998	$\sim 103^\dagger$	42	17	7
0.2 Ma	$^{41}\text{Ca}^*$	Fink <i>et al</i> 1998	$\sim 200^\dagger$	≈ 56	≈ 16	≈ 4
0.3 Ma	$^{81}\text{Kr}^*$	Reedy and Marti 1991	$\sim 160^\dagger$	$\sim 48^\dagger$	~ 15	~ 4
0.5 Ma	^{36}Cl	Reedy and Nishiizumi 1998	$\sim 70^\dagger$	30	12	≈ 5
1 Ma	$^{26}\text{Al}^\oplus$	Kohl <i>et al</i> 1978	70	25	9	3
1 Ma	$^{26}\text{Al}, ^{10}\text{Be}^\oplus$	Nishiizumi <i>et al</i> 1995	100	26	7	2
1 Ma	$^{26}\text{Al}, ^{10}\text{Be}$	Michel <i>et al</i> 1996	55	24	11	5
1 Ma	$^{26}\text{Al}, ^{10}\text{Be}$	Fink <i>et al</i> 1998	89	32	12	4
2 Ma	^{21}Ne	Rao <i>et al</i> 1994	68	21	6	2
5 Ma	^{53}Mn	Kohl <i>et al</i> 1978	70	25	9	3

[†]As noted in the text, the fluxes $J(>10 \text{ MeV})$ and spectral shapes are not well determined using profiles of cosmogenic nuclides measured in lunar samples.

[#]Omnidirectional fluxes in protons $\text{cm}^{-2} \text{s}^{-1}$; energies in MeV.

[†]Energy is below main reaction thresholds.

* Need some (^{41}Ca) or many (^{81}Kr) key cross sections.

[⊕] Using older sets of cross sections slightly different from newer ones.

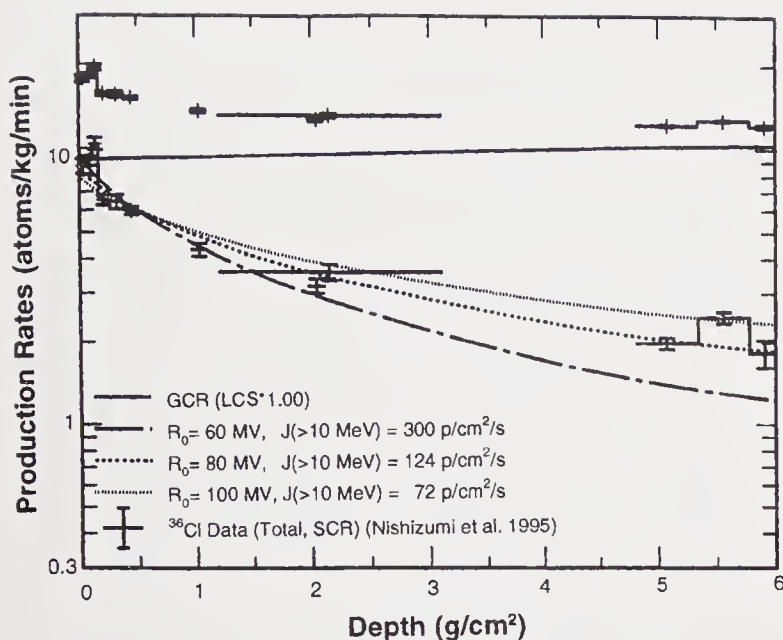


Figure 2. Measured ^{36}Cl activities (top symbols); calculated GCR production rates (solid line); inferred solar-proton ^{36}Cl production rates (lower symbols); and three sets of best fit production rates for various solar-proton exponential-rigidity spectral shapes (R_0) and integral fluxes $>10 \text{ MeV}$ (lower curves) as a function of depth in lunar rock 64455.

One of the first results from measuring SEP-produced nuclides in lunar samples using either several radionuclides with different half-lives (e.g., Kohl *et al* 1978) or one nuclide in samples of different surface ages (e.g., Bhandari *et al* 1976) was that the fluxes of SEPs over various time periods during the past few million years were not very different. One major question (e.g., Reedy and Marti 1991) has been whether there have been any changes in the past fluxes of SEPs.

It should be noted that, even a few years ago, not many cross sections existed for unfolding the records of most SEP-produced radionuclides, such as ^{14}C (half-life = 5730 years) and ^{36}Cl (half-life = 0.3 Ma). Recently, several groups have measured most of the needed cross sections (e.g., Michel *et al* 1996; Sisterson *et al* 1996, 1997a,b; Jull *et al* 1998).

3.1 The SEP record in lunar samples

The energies of solar energetic particles are low enough that most SEPs are slowed down and stopped by ionization energy losses in the top centimeter or so of solid matter before inducing a nuclear reaction (Reedy and Arnold 1972). The flux of SEPs drops rapidly with depth, so that the concentrations of SEP-produced nuclides decrease rapidly with increasing depth. These nuclides are also made by GCR-particles with a production profile that increases slowly with increasing depths to depths of tens of centimeters (Reedy and Arnold 1972).

An example of the concentration-versus-depth profile of a radionuclide in a lunar sample is shown at the top of figure 2 for ^{36}Cl measured in lunar rock

64455 (Nishiizumi *et al* 1995). The decrease in the concentration of ^{36}Cl in the top few g cm^{-2} (about a centimeter) is characteristic of production by SEPs. The solid curve near the top of figure 2 is the GCR production profile of ^{36}Cl calculated by J Masarik (priv. comm., 1997) using the LAHET Code System (LCS); see Reedy and Nishiizumi (1998) for details. LCS is a series of Monte Carlo codes, including the LAHET (Los Alamos High Energy Transport) and MCNP (Monte Carlo N-Particle) codes, that numerically simulate the production, transport, and interactions of particles in matter. Subtracting the GCR contribution from the measured concentrations, one gets the contribution from SEPs, which are shown in figure 2 as the lower set of symbols and lines. For ^{36}Cl , the SEP-produced component is about the same as the GCR one near the very surface of rock 64455 but drops rapidly to low values at the rock's bottom at 6 g cm^{-2} , which is about 2.2 cm for the 2.74 g cm^{-3} density of rock 64455.

The SEP profile is converted to the incident flux and spectral shape of SEPs (assumed to be protons) using cross sections for the main nuclear reactions making ^{36}Cl from the major target elements. Most (about 95%) ^{36}Cl is made from calcium, such as the $^{40}\text{Ca}(p,n4p)^{36}\text{Cl}$ reaction, with the remaining ^{36}Cl made from potassium, titanium, and iron. Accurate cross sections for the production of ^{36}Cl from calcium and potassium have only been recently measured. The cross sections of Sisterson *et al* (1997b) were used to interpret the SEP profile for ^{36}Cl (Reedy and Nishiizumi 1998).

The incident spectral shape of SEPs was assumed to be that for an exponential in rigidity with R_0 the spectral-shape parameter (given above in section 2). Other spectral shapes, such as power laws in energy or rigidity, did not give better fits. Because both the flux, J , and spectral shape, R_0 , are variable, it is possible that more than one set of (R_0 , J) fits the data. As shown in figure 2, three sets of (R_0 , J) give reasonable fits to the SEP profiles for ^{36}Cl in 64455. The one with the largest fraction of low-energy protons, $R_0 = 60 \text{ MV}$, fits the near-surface points better, but the harder ($R_0 = 80$ and 100 MV) spectra are better for the deeper points in figure 2. However, a slight ($\sim 5\%$) increase in the GCR component would move the deepest points determined for the SEP component lower, to near the calculated curve for 60 MV , while a decrease in the GCR component would yield a best fit near $R_0 = 100 \text{ MV}$.

The measured ^{36}Cl profiles in lunar core 15008 and lunar rock 74275 have also been studied (Reedy and Nishiizumi 1998). For $R_0 = 100 \text{ MV}$, the best-fit integral fluxes for energies above 10 MeV , $J(>10 \text{ MeV})$, are $124 \text{ protons cm}^{-2} \text{ s}^{-1}$ for 15008 and $95 \text{ protons cm}^{-2} \text{ s}^{-1}$ for 74275, higher than the same spectral shape for 64455. The best fit $J(>10 \text{ MeV})$ for ^{36}Cl in these three lunar samples varied and the values of R_0 also varied. However, most of these fits gave the integral fluxes

given for ^{36}Cl in table 2. There is much scatter in the fluxes $J(>10\text{ MeV})$ and some spread in $J(>100\text{ MeV})$, but most fits had fluxes $J(>30\text{ MeV})$ and $J(>60\text{ MeV})$ close to those in table 2.

The results for a given nuclide or set of nuclides can also vary, as indicated in table 2 for the four sets of results using ^{26}Al (half-life = 0.7 Ma) and ^{10}Be (half-life = 1.5 Ma), depending on the sample measured or the interpretation procedure. However, the fluxes $J(>30\text{ MeV})$ and $J(>60\text{ MeV})$ vary less than $J(>10\text{ MeV})$. The reasons for these variations need to be examined. The uncertainties in the SEP fluxes determined with cosmogenic nuclides are not well determined and need to be better characterized.

3.2 Factors affecting the interpretation of the SEP record

Lunar samples are very well suited for studies of the fossil records of SEPs, having been in a known orbit on a body with no atmosphere and very weak magnetic fields. Meteorites are not used for such studies because of their generally-unknown orbits and fairly-large amounts of ablation that remove the outer surfaces where nuclides are made by SEPs.

Only lunar samples with a well-documented record on the lunar surface should be used for studies of SEPs in the past. Their exposure histories need to be well known. The best lunar rocks are ones with a simple cosmic-ray exposure history since they were placed on the lunar surface from a great depth in the Moon by an impact. Lunar cores should not have been recently disturbed by micrometeorite impact induced gardening or astronaut activities. The orientation of the sample on the Moon's surface should be known as well as the location of any objects (such as boulders and mountains) that could shield the sample from cosmic-ray particles.

The cosmogenic-nuclide measurements should be used to test the lunar-sample's exposure history. The activities of radionuclides and concentrations of stable nuclides can be compared to the expected production rates, especially in the deeper subsamples. Several measurements of nuclides that are made readily by SEPs in subsamples at and near the bottom of a lunar rock would provide a check that the rock was not flipped over at some time during its surface exposure (e.g., Nishiizumi *et al* 1995).

The many subsamples used for analysis should be for a wide range of depths (with many near the surface) and from a surface with a known location, shape, and orientation (best if horizontal) on the Moon's surface. All parts of each subsample should have the same range of depths below the surface. A slice should have the same depths for the entire area and not have variable thicknesses.

The depth of each subsample below the surface needs to be known in units of the grams of material

above the subsample per unit area (g cm^{-2}). For many samples, this requires a good knowledge of the density of the sampled material. Rock densities vary, with rock 64455 being 2.74 g cm^{-3} and rock 74275 being 3.36 g cm^{-3} . Densities for lunar cores should be the ones related to sampling, such as the compacted density of 1.65 g cm^{-3} used for samples of 15008.

The composition of each subsample should be known for the target elements making the SEP-produced nuclides of interest. Usually there is little elemental variation among subsamples, but occasionally there can be some variability in composition. Usually the analyses assume an average composition and no variation among subsamples. If elemental production rates are known, the measured activities of each subsample could be adjusted to the average composition.

The measured concentrations need to be corrected to get that due only to SEPs. The main correction usually is for the production of that nuclide by GCR particles. Corrections for GCR production can be made and tested if one has a deep sample where SEP production is negligible, in which case a GCR production profile is needed to correct the samples closer to the surface. In many samples, such deep subsamples are not available (e.g., the small rock 64455) or were not taken. In those cases, good models for GCR production, such as LCS, are needed. Most GCR models are for a slab geometry. Some 3-D calculations done with LCS for hemispheric rocks on top of the lunar surface show that the GCR production rates vary depending on the size of the rock but that the shape of the profile as a function of depth is similar to that for a slab geometry (Reedy and Masarik 1995).

For ^{41}Ca (half-life = 0.1 Ma) and possibly ^{36}Cl , production by neutron-capture reactions with thermal neutrons needs to be considered (Fink *et al* 1998). Neutron-capture production of ^{36}Cl is not expected to be important in samples like 74275 and 15008 with high concentrations of neutron-capturing elements like Fe and Ti. In 64455 with its low Ti and Fe, it was estimated that 30 ppm of Cl would contribute ~ 0.5 atoms $\text{min}^{-1}\text{ kg}^{-1}$ of ^{36}Cl .

In some cases, such as ^{10}Be and ^{26}Al in 74275, corrections need to be made for pre-exposure production before being brought to the lunar surface. There can be some uncertainty in the time and depth of the previous exposure and in the rock's orientation at depth (e.g., Fink *et al* 1998).

Production by solar alpha particles for most solar-proton-produced nuclides is expected to be much less than 10% of the total SEP production (Reedy 1998). The main exception is 76-kyr ^{59}Ni , which is made in low yields by protons because nickel is very rare in lunar samples but readily made by the $^{56}\text{Fe}(\alpha, n)^{59}\text{Ni}$ reaction (Lanzerotti *et al* 1973).

The incident solar protons are usually assumed to have an exponential-rigidity spectral shape, which works fairly well for most modern measurements (e.g.,

Reeves *et al* 1992). However, it has not been shown that this is the best shape for unfolding SEP records. An exponential in rigidity generally gives good fits to the fossil SEP profiles. Other simple spectral shapes, such as power laws in energy or rigidity, generally do not give better fits to SEP-produced nuclides.

Often, as above for ^{36}Cl , a fairly-wide range of spectral shapes can give good fits. Several radionuclides, especially ^{10}Be , have been shown to be sensitive to the spectral shape of solar protons (Nishiizumi *et al* 1988). The low concentrations of SEP-produced ^{10}Be measured in lunar rocks require that the incident SEPs not have many high energy particles (e.g., Nishiizumi *et al* 1988; Fink *et al* 1998). Thus, recently, ^{10}Be and ^{26}Al have often been used together to get the average SEP flux over the last ~ 1 Ma (e.g., Michel *et al* 1996; Fink *et al* 1998).

Almost all calculations have used the slab or hemispherical geometries with the SEP model of Reedy and Arnold (1972). Calculations using an irregular shape for rock 68815 (Russ and Emerson 1980) gave results not very different than those using the Reedy-Arnold model. Some 3-D calculations using Monte Carlo codes, such as the LAHET code (Masarik and Reedy 1996), should be done of solar protons irradiating irregularly-shaped lunar rocks.

Most models used for production of nuclides by solar protons (e.g., Reedy and Arnold 1972) only consider the slowing and stopping of the protons by ionization energy losses. LCS calculations showed that production by secondary neutrons is not important except for very hard ($R_0 \gtrsim 200$ -MV) solar-proton spectra (Masarik and Reedy 1996). The relations used for the slowing of protons in matter are well determined. Thus the calculated fluxes of SEP particles as a function of depth in a lunar sample should be good for interpreting SEP records.

For some nuclides [e.g., ^{41}Ca and ^{81}Kr (half-life = 0.2 Ma)], there is still a need for the measurement of more cross sections for the main proton reactions making these SEP-produced nuclides. Some cross sections for proton reactions making some SEP-produced nuclides (e.g., neon) need to be checked with some additional measurements. Measurements of cross sections for neutron-induced reactions are needed to help get better calculated production rates for GCR particles, which are mainly neutrons in lunar samples.

Some systematic studies are needed where many SEP-produced nuclides are studied in a few good rocks (e.g., 68815 and 64455) or cores (such as 15008). Any trend in SEP fluxes determined from several nuclides in a given sample would eliminate most of the effects due to the sample and help to study the other effects. A best fit for the SEPs making one or several nuclides could also be determined using several lunar samples, such as was done above for ^{36}Cl in lunar rocks 64455 and 74275 and lunar core 15008.

3.3 Summary of the SEP fossil record

Lunar SEP-produced nuclides give only an average flux of solar protons over the radionuclide's mean-life or the sample's surface-exposure age. While the uncertainties in these average fluxes are not well characterized, these fluxes are known well enough (better than a factor of two) to be of much value in studies of lunar samples and ancient solar energetic particles. Better average fluxes of SEPs in the past should be determined as soon as some of the factors above are better understood and improved models, such as for GCR production, are developed. There exist many good profiles for SEP-produced nuclides that should be re-examined. Profiles of some SEP-produced nuclides not often measured (e.g., ^{41}Ca and ^{81}Kr) should be measured in suitable lunar samples.

The integral fluxes $J(>30 \text{ MeV})$ and $J(>60 \text{ MeV})$ are better determined than $J(>10 \text{ MeV})$, as indicated in fits to individual profiles (as for ^{36}Cl above) and by the smaller spread among results in table 2 for the last ~ 1 –5 Ma. The trend for $J(>30 \text{ MeV})$ and $J(>60 \text{ MeV})$ fluxes in table 2 suggests that the average flux of SEPs over the last few million years is less than that for more recent periods, including the last four solar cycles (1954–1997).

4. Conclusions

Both the modern and ancient records for SEPs have been briefly reviewed above. The SEP record from 1954 to 1964 is fairly uncertain with reported SPE fluences often differing by factors of several earth-based measurements need to be examined to give good fluences, especially relative ones. These data sets can then be used with lunar short-lived radioactivity measurements, as in (Reedy 1977), to check the absolute fluences and average fluxes for this period. The modern record is fairly good since 1965, although several reports of event-integrated fluences (e.g., Goswami *et al* 1988; Feynman *et al* 1990) differ for some events by $\sim 50\%$ or more. More data sets that can be used to get modern SPE fluences need to be studied to improve the recent record. The measurements of SEPs since 1987 need to be carefully analyzed to get average SEP fluxes and SPE fluences for this period of several very large solar particle events.

We are getting a better understanding of the fossil record with new measurements of SEP-produced nuclides in lunar rocks and of the nuclear-reaction cross sections for making these nuclides. Better models to correct for production by GCR particles are also being developed. Average SEP fluxes for the nuclides in table 2 have recently become or should soon be known better than previously.

High intensities of solar energetic particles are serious radiation hazards in space. Modern and ancient measurements together have been used to show that

huge solar particle events (event-integrated fluences $\gtrsim 10^{11}$) should be very rare (Reedy 1996). However, the record for SEPs is not complete. More work is needed to improve our understanding of both the modern and ancient records of solar energetic particles.

Acknowledgements

I thank J N Goswami and other colleagues at PRL for inviting me to the 'Isotopes in the Solar System' Conference, for suggesting the subject of solar energetic particles, and for their past influences on my work in this research area. I thank T Cleghorn, H Sauer, and A Tylka for their help in locating fluences for solar particles during the last solar cycle and K Nishiizumi and J N Goswami for comments on much of what is presented here. Some of the ideas presented here resulted from discussions with many colleagues including R Belian, D Fink, G Herzog, T Jull, G Reeves, and J Sisterson. This work was supported by NASA and done under the auspices of the U.S. Dept. of Energy.

References

- Bhandari N, Bhattacharya S K and Padia J T 1976 Solar proton fluxes during the last million years, In *Proc. 7th Lunar Planet. Sci. Conf.* (New York, USA: Pergamon Press) pp. 513–523
- Feynman J, Armstrong T P, Dao-Gibner L and Silverman S 1990 New interplanetary proton fluence model; *J. Spacecraft Rockets* **27** 403–410
- Feynman J, Spitale G and Wang J 1993 Interplanetary proton fluence model: JPL 1991; *J. Geophys. Res.* **98** 13281–13294
- Fink D, Klein J, Middleton R, Vogt S, Herzog G F and Reedy R C 1998 ^{41}Ca , ^{26}Al , and ^{10}Be in lunar basalt 74275 and ^{10}Be in the double drive tube 74002/74001; *Geochim. Cosmochim. Acta* **62** 2389–2402
- Goswami J N, McGuire R E, Reedy R C, Lal D and Jha R 1988 Solar flare protons and alpha particles during the last three solar cycles; *J. Geophys. Res.* **93** 7195–7205
- Jull A J T, Cloudt S, Donahue D J, Sisterson J M, Reedy R C and Masarik J 1998 ^{14}C depth profiles in Apollo 15 and 17 cores and lunar rock 68815; *Geochim. Cosmochim. Acta* (in press)
- Kohl C P, Murrell M T, Russ III G P, and Arnold J R 1978 Evidence for the constancy of the solar cosmic ray flux over the past ten million years: ^{53}Mn and ^{26}Al measurements; In *Proc. 9th Lunar Planet. Sci. Conf.* (New York, USA: Pergamon Press) pp. 2299–2310
- Lanzerotti L J, Reedy R C and Arnold J R 1973 Alpha particles in solar cosmic rays over the last 80,000 years; *Science* **179** 1232–1234
- Masarik J and Reedy R C 1996 Monte Carlo simulation of cosmogenic nuclide production by solar cosmic rays; *Meteorit. Planet. Sci.* **31** A84–A85
- Michel R, Leya I and Borges L 1996 Production of cosmogenic nuclides in meteoroids: accelerator experiments and model calculations to decipher the cosmic ray record in extra-terrestrial matter; *Nucl. Instrum. Methods Phys. Res.* **B113** 434–444
- Nishiizumi K, Imamura M, Kohl C P, Nagai H, Kobayashi K, Yoshida K, Yamashita H, Reedy R C, Honda M and Arnold J R 1988 ^{10}Be profiles in lunar surface rock 68815; In *Proc. 18th Lunar Planet. Sci. Conf.* (New York, USA: Cambridge University Press) pp. 79–85
- Nishiizumi K, Kohl C P, Arnold J R, Finkel R C, Caffee M W, Masarik J and Reedy R C 1995 Final results of cosmogenic nuclides in lunar rock 64455; In *Lunar and Planetary Science XXVI* (Houston, USA: Lunar and Planetary Institute) pp. 1055–1056
- Rao M N, Garrison D H, Bogard D D and Reedy R C 1994 Determination of the flux and energy distribution of energetic solar protons in the past 2 Ma using lunar rock 68815; *Geochim. Cosmochim. Acta* **58** 4231–4245
- Reedy R C and Arnold J R 1972 Interaction of solar and galactic cosmic-ray particles with the moon; *J. Geophys. Res.* **77** 537–555
- Reedy R C 1977 Solar proton fluxes since 1956; In *Proc. 8th Lunar Sci. Conf.* (New York, USA: Pergamon Press) pp. 825–839
- Reedy R C, Arnold J R, and Lal D 1983 Cosmic-ray record in solar system matter; *Annu. Rev. Nucl. Part. Sci.* **33** 505–537
- Reedy R C and Marti K 1991 Solar-cosmic-ray fluxes during the last ten million years; In *The Sun in Time* (Tucson, USA: U. Arizona Press) pp. 260–287
- Reedy R C and Masarik J 1995 Cosmogenic-nuclide depth profiles in lunar rocks; In *Lunar and Planetary Science XXVI* (Houston, USA: Lunar and Planetary Institute) pp. 1153–1154
- Reedy R C 1996 Constraints on solar particle events from comparisons of recent events and million-year averages; In *Solar Drivers of Interplanetary and Terrestrial Disturbances* (ASP Conf. Series Vol. 95) pp. 429–436
- Reedy R C 1998 Cosmogenic nuclides produced by solar alpha particles; In *Lunar and Planetary Science XXIX* (Houston, USA: Lunar and Planetary Institute) Abstract #1701
- Reedy R C and Nishiizumi K 1998 Factors affecting the interpretation of solar-proton-produced nuclides and some chlorine-36 results; In *Lunar and Planetary Science XXIX* (Houston, USA: Lunar and Planetary Institute) Abstract #1698
- Reedy R C *et al* 1998 Intensities of solar particle events; *Space Sci. Rev.* in preparation
- Reeves G D, Cayton T E, Gary S P and Belian R D 1992 The great solar energetic particle events of 1989 observed from geosynchronous orbit; *J. Geophys. Res.* **97** 6219–6226
- Russ III G P and Emerson M T 1980 ^{53}Mn and ^{26}Al evidence for solar cosmic ray constancy – an improved model for interpretation; In *The Ancient Sun* (New York, USA: Pergamon Press) 387–399
- Shea M A and Smart D F 1990 A summary of major solar proton events; *Solar Phys.* **127** 297–320
- Shea M A and Smart D F 1992 Recent and historical solar proton events; *Radiocarbon* **34** 255–262
- Shea M A and Smart D F 1994 Significant proton events of solar cycle 22 and a comparison with events of previous solar cycles; *Adv. Space Res.* **14** (10)631–(10)638
- Shea M A and Smart D F 1995 History of solar proton event observations; *Nucl. Phys. B (Proc. Suppl.)* **39a** 16–25
- Shea M A and Smart D F 1996 Overview of the effects of solar-terrestrial phenomena on man and his environment; *Nuovo Cimento* **19c** 945–952
- Sisterson J M, Schneider IV R J, Beverding A, Gans C S, Kim K, Englert P A J, Castaneda C, Vincent J and Reedy R C 1996 Short-lived cosmogenic radionuclide production in lunar rocks; improved estimates for the solar proton flux in recent solar cycles; In *Lunar and Planetary Science XXVIII* (Houston, USA: Lunar and Planetary Institute) pp. 1207–1208

- Sisterson J M, Kim K, Beverding A, Englert P A J, Caffee M, Jull A J T, Donahue D J, McHargue L, Castaneda C, Vincent J and Reedy R C 1997a Measurement of proton production cross sections of ^{10}Be and ^{26}Al from elements found in lunar rocks; *Nucl. Instrum. Methods Phys. Res. B* **123** 324–329
- Sisterson J M, Nishiizumi K, Caffee M W, Imamura M, and Reedy R C 1997b Revised ^{36}Cl production rates in lunar rock 64455 using new cross section measurements; In *Lunar and Planetary Science XXVIII* (Houston, USA: Lunar and Planetary Institute) pp. 1329–1330
- Smart D F and Shea M A 1989 Solar proton events during the past three solar cycles; *J. Spacecraft Rockets* **26** 403–415
- Tylka A J, Dietrich W F and Boberg P R 1997 Probability distributions of high-energy solar-heavy-ion fluxes from IMP-8; *IEEE Trans. Nucl. Sci.* **44** 2140–2149

Interpretation of cosmogenic nuclides in meteorites on the basis of accelerator experiments and physical model calculations

R MICHEL and S NEUMANN

Center for Radiation Protection and Radioecology, University Hannover, Am Kleinen Felde 30, D-30167 Hannover, Germany

e-mail: michel@mbox.zsr.uni-hannover.de

Cosmogenic nuclides in extraterrestrial matter provide a wealth of information on the exposure and collision histories of small objects in space and on the history of the solar and galactic cosmic radiation. The interpretation of the observed abundances of cosmogenic nuclides requires detailed and accurate knowledge of their production rates. Accelerator experiments provide a quantitative basis and the ground truth for modeling cosmogenic nuclide production by measurements of the relevant cross sections and by realistic simulations of the interaction of galactic protons with meteoroids under completely controlled conditions, respectively. We review the establishment of physical model calculations of cosmogenic nuclide production in extraterrestrial matter on the basis of such accelerator experiments and exemplify this approach by presenting new experimental and theoretical results for the cosmogenic nuclide ^{44}Ti . The model calculations describe all aspects of cosmogenic nuclide production and allow the determination of long-term solar and galactic cosmic ray spectra and a consistent interpretation of cosmogenic nuclides in extraterrestrial matter.

1. Introduction

In the solar system, one observes two types of natural medium- and high-energy corpuscular radiation, the solar cosmic radiation (SCR) and the galactic cosmic radiation (GCR). SCR particles are emitted during energetic solar events from the sun and consist on the average of 98% protons and 2% α -particles (Goswami *et al* 1988). Their spectral distributions and intensities vary from event to event, typical energies going up to a few hundred MeV/n. GCR particles come from outside the solar system. They are injected into the interstellar medium by supernova explosions and are accelerated stochastically by complicated processes (Bryant *et al* 1992) and occasionally attain extreme energies up to 10^{21} eV. GCR consists of 87% protons, 12% α -particles and 1% heavier ions which show similar energy spectra when compared as function of energy per nucleon (Alsmiller *et al* 1972). Mean GCR

energies are a few GeV/n. GCR spectra are modulated by interaction of GCR particles with the solar magnetic field and thus depend on the solar activity. Typical SCR and GCR proton spectra at 1 A.U. are shown in figure 1. For both, SCR and GCR spectra, suitable mathematical parameterizations exist.

For SCR particles, it is convenient to describe the differential flux density $\partial J/\partial R$ as function of the rigidity R . R is the relativistic momentum of the particle over its charge. This means for SCR protons

$$\frac{\partial J_{p,\text{SCR}}}{\partial R} = J_{0,\text{SCR}}(4\pi, E_p > 10 \text{ MeV}) \cdot \exp(-R/R_0) \quad (1)$$

with a characteristic rigidity, R_0 [MV], and a 4π -integral flux density of protons with energies E_p above 10 MeV, $J_{0,\text{SCR}}(4\pi, E_p > 10 \text{ MeV})$ [$\text{cm}^{-2} \text{ s}^{-1}$].

The energy-differential flux densities of GCR spectra $\partial J_{\text{GCR}}/\partial E$ can be parameterized according to

Keywords. Cosmogenic nuclides; meteorites; simulation experiments; cross sections; modeling of production rates.

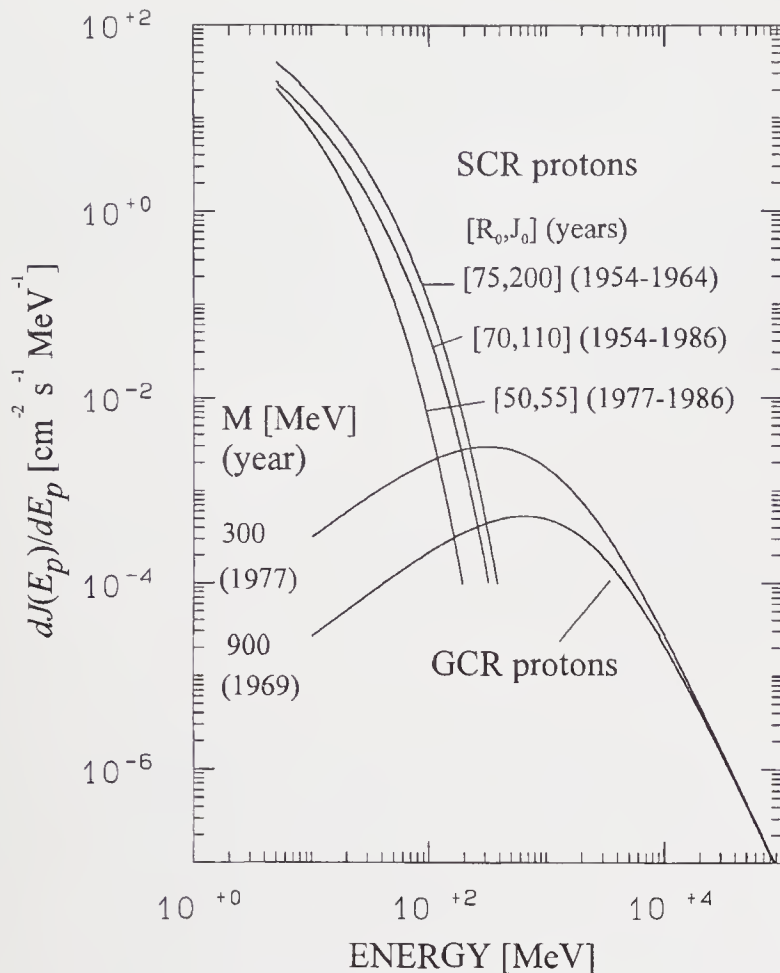


Figure 1. Free space GCR proton spectra at 1 A.U. for times of a quiet (1977) and an active sun (1969) and average SCR proton spectra for three periods from 1954 to 1986. SCR spectra can be parameterized for individual flares as well as for time-averaged spectra by exponentially falling rigidity spectra (McGuire and von Rosenvinge 1984) characterized by a characteristic rigidity, R_0 [MV], and a 4π integral flux density of protons with energies above 10 MeV, $J_0(4\pi, E > 10 \text{ MeV})$ [$\text{cm}^{-2} \text{ s}^{-1}$]. Rigidities of the observed flare spectra show a much broader range (20 MV – 150 MV) than shown here for solar cycle averaged SCR spectra (Shea and Smart 1990). According to Castagnoli and Lal (1980), GCR spectra can be characterized by only one parameter M [MeV] which describes the modulation by the solar magnetic field of GCR particles when entering the solar system. M is equivalent to the energy a GCR particle loses when penetrating into the solar system to a given heliocentric distance.

Castagnoli and Lal (1980) using a modulation parameter M [MeV] which represents the energy loss which a particle undergoes when it enters the solar system and propagates to a certain heliocentric distance. For GCR protons one obtains

$$\frac{\partial J_{p,\text{GCR}}}{\partial E_p} = c \cdot \frac{E_p \cdot (E_p + 2m_p \cdot c^2) \cdot (E_p + x + M)^{-2.65}}{(E_p + M) \cdot (E_p + 2m_p \cdot c^2 + M)} \quad (2)$$

with $x = 780 \cdot \exp(-2.5 \cdot 10^4 E_p)$ and $c = 1.244 \cdot 10^6 \text{ cm}^{-2} \text{ s}^{-1} \text{ MeV}^{-1}$. For heavier GCR particles analogous parameterizations exist.

In the solar system, SCR and GCR interact with cosmic dust, meteoroids, asteroids, comets and lunar and planetary surfaces, thereby producing a wide range of stable and radioactive nuclides (table 1). These so-

called cosmogenic nuclides have found manifold applications. On Earth, they are produced by interactions with the atmosphere and these cosmogenic nuclides are incorporated in the large scale environmental processes. There they act as natural tracers for use in archaeology, hydrology, glaciology, climatology, and other environmental sciences (Finkel and Suter 1993). Cosmogenic nuclides produced *in situ* in the earth's crust have a high potential for studying processes like erosion, deglaciation (Lal 1986; Lal *et al* 1987) and to date individual events e.g. impacts of extraterrestrial objects (Nishiizumi *et al* 1991b).

Investigations of cosmogenic nuclides in extraterrestrial matter allow us to study the history of the matter exposed to SCR and GCR particles as well as the dependence on time of the spectral distribution of SCR and GCR over time scales of millions of years (Geiss *et al* 1962; Lal 1972). Cosmogenic nuclides in extraterrestrial matter provide a past record which cannot be retrieved by any other means. Already these very first reviews demonstrated the scientific potential of cosmogenic nuclides in extraterrestrial matter. The

Table 1. List of cosmogenic nuclides in meteorites with half-lives above 0.5 month and their target elements.

Nuclide	Half-life	Main target elements
^{48}V	0.0438 a	Ti, Fe, Ni
^{51}Cr	0.0759 a	Fe, Ni
^{37}Ar	0.096 a	Ca, Ti, Fe, Ni
^7Be	0.146 a	C, O, Mg, Al, Si, S*, P*, Ca, Ti, Fe, Ni
^{58}Co	0.194 a	Fe^{\S} , Ni
^{56}Co	0.213 a	Fe, Ni
^{46}Sc	0.230 a	Ti, Fe, Ni
^{57}Co	0.743 a	Fe, Ni
^{54}Mn	0.855 a	Fe, Ni, Mn
^{22}Na	2.6 a	Mg, Al, Si, Ca, Ti, Fe, Ni
^{55}Fe	2.7 a	Mn, Fe, Ni
^{60}Co	5.26 a	Co^{\S} , Ni
^3H	12.3 a	C, O, Mg, Al, Si, S*, P*, Ca, Ti, Fe, Ni
^{44}Ti	59.2 a	Ti, Fe, Ni
^{32}Si	133 a	Ca, Ti, Fe, Ni
^{39}Ar	269 a	Ca, Ti, Fe, Ni
^{14}C	5.73 ka	O, Mg, Al, Si, S*, P*, Ca, Ti, Fe, Ni
^{59}Ni	75 ka	Fe^{\S} , Ni
^{41}Ca	103 ka	Ca^{\S} , Ti, Fe, Ni
^{81}Kr	210 ka	Rb, Sr, Y, Zr
^{36}Cl	300 ka	Cl^{\S} , Ca, Ti, Fe, Ni
^{26}Al	716 ka	Mg, Al, Si, S*, P*, Ca, Ti, Fe, Ni
^{60}Fe	1.5 Ma	Ni
^{10}Be	1.51 Ma	C, O, Mg, Al, Si, S*, P*, Ca, Ti, Fe, Ni
^{53}Mn	3.7 Ma	Fe, Ni
^{129}I	15.7 Ma	Te^{\S} , Ba, REE
^{40}K	1.28 Ga	Ca, Ti, Fe, Ni
He	stable	C, O, Mg, Al, Si, S*, P*, Ca, Ti, Fe, Ni
Ne	stable	Na, Mg, Al, Si, S*, P*, Ca, Ti, Fe, Ni
Ar	stable	Cl^{\S} , Ca, Fe, Ni
Kr	stable	Br^{\S} , Rb, Sr, Y, Zr
Xe	stable	Te^{\S} , I^{\S} , Ba^{\S} , REE

Note: Special relevance of target elements (exclusively or also) with respect to production of cosmogenic nuclides by neutron capture (§) or by α -induced reactions (§) are indicated. Elements marked with (*) are only relevant in iron meteorites or the metal phase of stony irons.

exploitation of this potential, however, suffered for a long time from large experimental and theoretical uncertainties due to limited analytical techniques as well as due to crude and empirical modeling.

Shortly after the discovery of the first cosmogenic radionuclide (^3H) in meteoritic material (Begemann *et al* 1957; Fireman and Schwarzer 1957), the whole variety of cosmogenic radio nuclides measurable in meteorites became evident (Ehmann and Kohman 1958; Shedlovsky 1960; Arnold *et al* 1961). These investigations used radiochemical techniques to extract the whole suite of cosmogenic radionuclides from hundreds of grams or even kilograms of meteoritic materials to allow for the detection of their decay with the measuring techniques available at that time.

Stable cosmogenic nuclides in extraterrestrial matter were observed as positive isotopic abundance anomalies in rare gases (Begemann *et al* 1957; Ebert and Wänke 1957; Gentner and Zähringer 1957; Voshage and Hintenberger 1959; Hoffmann and Nier 1958; Eberhardt and Eberhardt 1960; Signer and Nier 1960). The advantage of using mass spectrometry to determine cosmogenic rare gases was that different cosmogenic nuclides could be measured in single samples with masses of the order of hundred milligrams with an accuracy of the order of 3% and 1–2% if absolute concentrations or isotopic ratios were considered, respectively. This measuring technique also allowed to distinguish depth and size effects of cosmogenic nuclide production rates and to establish empirical shielding corrections to improve the determination of CR exposure ages (Signer and Nier 1962; Eberhardt *et al* 1966; Marti 1967; Schultz and Signer 1976; Eugster 1988; Eugster and Michel 1995).

Cosmogenic radionuclides were not efficiently used due to a lack of sensitive and accurate measuring methods. Some improvements were made for special radionuclides. Thus, the application of γ - γ -coincidence techniques to measure nuclides such as ^{26}Al , ^{22}Na and ^{60}Co allowed for a nondestructive analysis in samples of a few tens of grams (Anders 1960; Herpers *et al* 1967). In addition, radiochemical neutron activation analysis was used to determine ^{53}Mn in 100 mg samples of meteorites and lunar surface materials (Herpers *et al* 1967). These achievements together with further technical improvements caused by the need to analyze cosmogenic nuclides in small aliquots of the lunar samples from the Apollo Missions provided a wealth of information on stable and radioactive cosmogenic nuclides in extraterrestrial matter, see (Reedy *et al* 1983; Vogt *et al* 1990) for reviews.

A break-through in the measurement of long-lived cosmogenic radionuclides, however, was only obtained when accelerator mass spectrometry (AMS) was first used for the measurement of ^{36}Cl in meteorites (Nishiizumi *et al* 1979). Today, AMS allows the determination of radionuclides such as ^{10}Be , ^{14}C , ^{26}Al , ^{36}Cl , ^{53}Mn , ^{60}Fe , ^{59}Ni , and ^{129}I in 100 mg samples. Using

sophisticated chemical separation schemes (Vogt and Herpers 1988), AMS measurements can be performed on many of these nuclides simultaneously from one individual sample. AMS is sensitive enough to even allow for the determination of cosmogenic nuclides in individual grains of cosmic dust (Nishiizumi *et al* 1991a) and to investigate *in situ* produced cosmogenic nuclides in terrestrial surface samples (Lal 1986, Lal *et al* 1987); see (Finkel and Suter 1993) for further references. Today, the advanced measuring techniques allow for the determination of the whole suite of stable and long-lived cosmogenic nuclides in a single sample of 500 mg combining rare gas mass spectrometry and AMS by *consortia* studies by different laboratories.

With respect to the short-lived radionuclides with half-lives between a few days and several decades, measuring techniques also have improved. Large volume semiconductor detectors in low-background active and passive shields are used to measure about 10 radionuclides in a single sample of freshly fallen meteorites; this however requires masses of the order of 100 g (Bhandari *et al* 1989; Jenniskens *et al* 1994; Murty *et al* 1998). Even depth profiles of cosmogenic nuclides in different fragments of a meteorite are measured. Though such measurements often have some drawbacks due to the statistical uncertainties involved and the problem of determination of detector efficiencies for large-volume samples, relatively short-lived cosmogenic radionuclides such as ^{44}Ti with half-life of 59.2 years (Ahmad *et al* 1998), provide the only means to reconstruct the intensity and spectral distribution of cosmic ray particles on time scales up to a few hundred years (Bonino *et al* 1994, 1995; Neumann *et al* 1997a).

This paper deals with the interpretation of cosmogenic nuclides in meteorites on the basis of physical model calculations of their production rates. It reviews some aspects of the development of such models and describes the present state of the art. A general procedure is described to develop model calculations from basic physical principles, using accelerator experiments to measure the relevant nuclear reaction data and to validate such model calculations by simulation experiments. Since simulation experiments are performed under controlled conditions, they yield ground truth for the modeling of cosmogenic nuclides production in space. Besides the review aspect of this work, it presents new data for the cosmogenic nuclide ^{44}Ti and describes the general procedures to perform physical model calculations and to interpret cosmogenic nuclide abundances on the basis of such model calculations.

2. Physical models of cosmogenic nuclide production

The production rates of cosmogenic nuclides in meteorites (and other objects) depend on size and

bulk chemical composition of the meteoroid, on the shielding depth and the chemical composition of a sample in it, on spectral distribution, composition and intensity of the solar (SCR) and galactic (GCR) cosmic radiation and on the exposure history of the meteoroid. Except for bulk and sample chemical compositions, all these parameters are unknown for a given meteorite and must be reconstructed. To decipher the cosmic ray records in meteorites it is thus necessary to determine the long-term spectral distributions and intensities of the cosmic radiation, to reconstruct the preatmospheric shapes of the meteoroids and the location of the samples in it and to untangle their exposure histories. For such interpretations reliable model calculations of production rates of cosmogenic nuclides are a basic requirement. During recent years, physical models of cosmogenic nuclide production without free parameters have been developed (Michel *et al* 1989b, 1991, 1995a, 1996; Bhandari *et al* 1993; Leya 1997; Leya *et al* 1995, 1996; Masarik and Reedy 1993, 1994; Reedy and Masarik 1994) that describe all relevant aspects of cosmogenic nuclide records in extraterrestrial matter.

Physical models of cosmogenic nuclide production in extraterrestrial matter were preceded by a large number of empirical and semi-empirical models of cosmogenic nuclide production rates. It would by far exceed the scope of this paper to give a complete review on such models. We therefore refer here to earlier surveys and discussions of such models (Reedy 1987; Michel *et al* 1991, 1995a) and refrain here from a critical discussion of empirical and semi-empirical models.

In physical models of cosmogenic nuclide production, the production rates P of a cosmogenic nuclide i are calculated as the sum of the production rates by SCR and GCR

$$P_i = P_{i,\text{SCR}} + P_{i,\text{GCR}}. \quad (3)$$

Due to their relatively low energies of less than a few 100 MeV/n, SCR primaries produce only negligible amounts of secondary particles whose influence mostly can be neglected in SCR model calculations. SCR ^4He particles can also be neglected because of their low abundances. Only in rare cases, e.g. ^{57}Co , ^{58}Co , and ^{59}Ni , ^4He -induced reactions have to be taken into account. Thus, the production rate of a cosmogenic nuclide i by irradiation with a SCR proton spectrum characterized by its spectral parameters J_0 and R_0 can be calculated straight forward via

$$P_{i,\text{SCR}}(R, d, c_b, c_s, J_0, R_0) = N_L \cdot \sum_j \frac{c_{s,j}}{A_j} \cdot \int \sigma_{i,j,p}(E_p) \cdot \frac{\partial J_{p,\text{SCR}}}{\partial E_p}(E_p, d, R, c_b, J_0, R_0) dE_p \quad (4)$$

with R being a shape parameter (radius) of the irradiated object, d being the depth of a sample inside the object and N_L Avogadro's number. The bulk chemical

composition $c_b = \{c_{b,j}, j = 1, \dots, m\}$ determines the transport of particles and their resulting spectra (in case of GCR calculations also the production and transport of secondary particles). The sample chemical composition $c_s = \{c_{s,j}, j = 1, \dots, n\}$ is the vector of chemical abundances of those elements contributing to the production of the particular cosmogenic nuclide. The depth dependent spectra $\partial J_{p,\text{SCR}}/\partial E_p$ can be calculated considering electronic stopping and nuclear attenuation of the primary particles in an irradiated body with bulk chemical composition c_b taking into account the actual irradiation geometry. Due to their low energies the depth scales of SCR interactions are restricted to the outer surfaces of the irradiated objects or to small objects. 15 g cm^{-2} may be a good estimate of the maximum depth relevant for SCR interactions irradiating an infinite plane. In a number of publications this model has been used and there is an agreement in the way of the calculational procedures as well as in the results obtained for the depth- and size-dependent SCR spectra (Reedy and Arnold 1972; Michel and Brinkmann 1980; Michel *et al* 1982; Bhattacharya and Bhandari 1975). The differences in production rates between SCR model calculations reported so far exclusively depend on the availability of reliable and high accuracy cross sections of the underlying nuclear reactions.

For the interaction of GCR particles with matter, energies up to 10 GeV/n have to be considered. The particle spectra inside an irradiated object are followed by intra- and inter-nuclear cascade calculations using Monte Carlo techniques which also take into account an accurate description of the spectra of secondary particles (Armstrong and Alsmiller 1971; Michel *et al* 1991, 1995a; Masarik and Reedy 1993, 1994; Reedy and Masarik 1994). The secondary particles, in particular neutrons, are produced in significant amounts during the high-energy interactions of the primaries and dominate the GCR production of cosmogenic nuclides in meteorites and planetary surfaces.

The depth scales on which GCR interactions occur extend to several hundreds of g cm^{-2} , a typical interaction length of GCR primaries in stony material being about 100 g cm^{-2} . Except for situations with extremely deep shielding, such as in the terrestrial underground, non-hadronic particles (such as electrons and muons) can be neglected as a source of cosmogenic nuclide production. Further, since the production of secondary complex particles such as ^2H , ^3H , ^3He , and ^4He is lower by orders of magnitude than the production of secondary protons and neutrons (Koch 1989), calculation of secondary GCR production of cosmogenic nuclides can be restricted to proton- and neutron-induced reactions.

In addition to protons, GCR consists of 8% ^4He and 1% heavier nuclei (Alsmiller *et al* 1972), the spectra of all GCR particles being about the same if the energy is measured in energy per nucleon. This

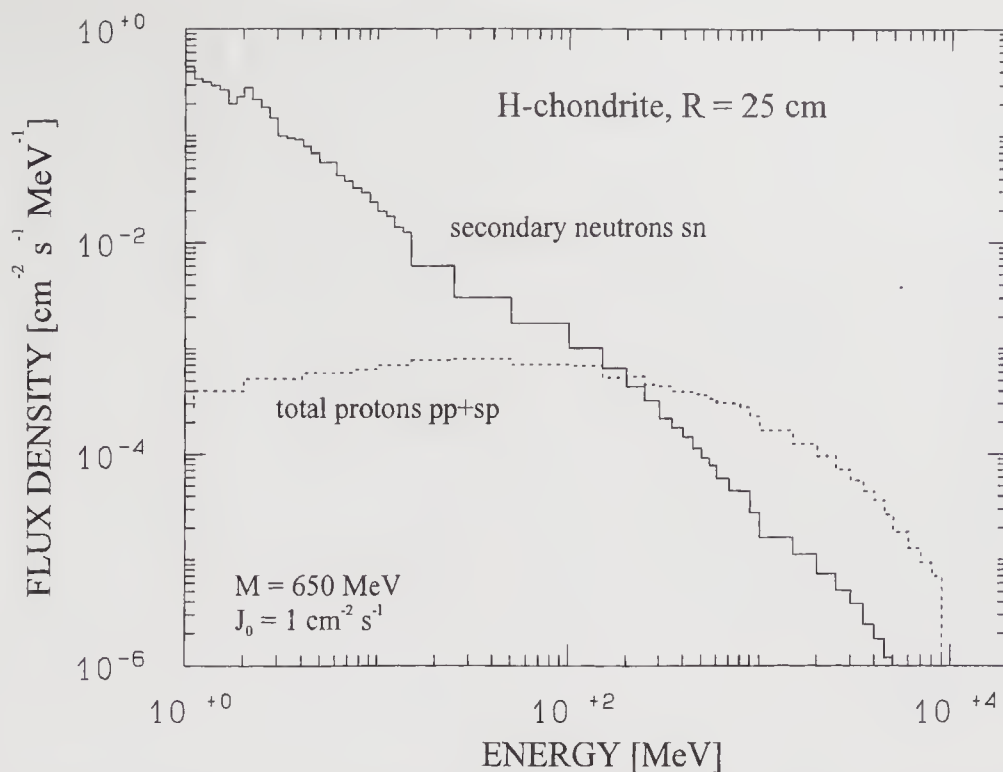


Figure 2. GCR spectra of total (= primary + secondary) protons and secondary neutrons in the center of a H-chondrite with a radius of 25 cm calculated by HETC within the HERMES code system. For the calculations a primary GCR proton spectrum with a modulation parameter $M = 650$ MeV was assumed. The data are normalized to a flux density of primary particles of $J_0 = 1 \text{ cm}^{-2} \text{ s}^{-1}$.

again facilitates the calculation of GCR production rates since the production of secondary nucleons depends in good approximation only on the total energy dissipated in an irradiated object. Only for special cases, e.g. ^{57}Co , ^{58}Co and ^{59}Ni , production by ^4He particles must be considered explicitly. In general, it is sufficient to consider particles heavier than protons only approximately by the number of primary nucleons in a GCR spectrum which differs from the number of primary protons in it (Michel *et al* 1991; Leya 1997).

Since the GCR production by primary protons and by secondary protons and neutrons depends linearly on the number of primary GCR nucleons with energies above 10 MeV, $J_{0,\text{GCR}}$, which itself is unambiguously connected to the modulation parameter M of the GCR proton spectrum, one can write:

$$P_{i,\text{GCR}}(R, d, c_b, c_s, M) = J_{0,\text{GCR}}(M) \cdot (P_{i,\text{GCR},pp} + P_{i,\text{GCR},sp} + P_{i,\text{GCR},sn}) \quad (5)$$

with $P_{i,\text{GCR},x}$ being the production rates due to a unit flux density of primary protons, secondary protons and secondary neutrons for $x = pp, sp, sn$ respectively. In the context of analyzing cosmogenic nuclides in meteorites one has to consider that M and hence $J_{0,\text{GCR}}$ depend on the mean distance from the sun and on helio-latitude of the orbit of an object in space.

The $P_{i,\text{GCR},x}$ can be calculated in analogy to equation 4 as folding integrals of the spectra of primary and secondary GCR particles at the location of a sample inside the irradiated body and of the cross

sections of the underlying nuclear reactions for $x = pp, sp, sn$ according to

$$P_{i,\text{GCR},x}(d, R, c_s, c_b, M) = N_L \cdot \sum_j \frac{C_{s,j}}{A_j} \cdot \int \sigma_{i,j,x}(E_x) \cdot \frac{\partial J_x}{\partial E_x}(E_x, d, R, c_b, M) dE_x. \quad (6)$$

Note that the spectra $\partial J_x / \partial E_x(E_x, d, R, c_b, M)$ are normalized to unit flux density of primary GCR nucleons. The depth and size dependent spectra of primary and secondary GCR nucleons $\partial J_x / \partial E_x(E_x, d, R, c_b, M)$ can be calculated using Monte Carlo codes such as HETC within the HERMES code system (Cloth *et al* 1988) or LAHET (Prael and Lichtenstein 1989) which both originated from HET developed in the sixties by Armstrong and Chandler (1972). In principle, these codes also allow for the direct calculation of residual nuclide production. However, as demonstrated e.g. by a recent *International Model and Code Intercomparison for Medium Energy Activation Yields* organized by NEA/OECD, all available codes at best are capable of predicting residual nuclide cross sections with average deviations of a factor of two (Michel and Nagel 1997). Often, however, such deviations even exceed factors of ten. Medium-energy codes are much more capable of calculating the nucleon spectra of secondary particles resulting from medium energy nuclear reactions including their transport in matter, e.g. (Filges *et al* 1992). Moreover, the spectra resulting from HETC and LAHET were found to be in good agreement as far as GCR model calculations for meteorites and the lunar surface are concerned

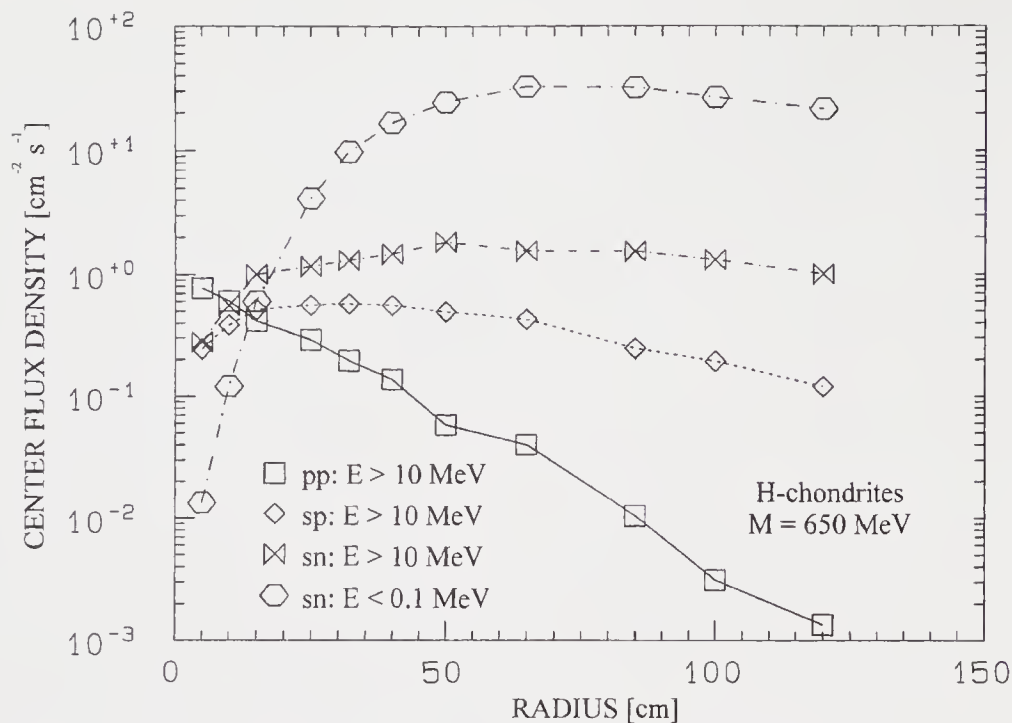


Figure 3. Flux densities of primary and secondary GCR particles in the center of H-chondrites irradiated by a $M = 650$ MeV GCR proton spectrum.

(Michel *et al* 1991, 1995a; Armstrong and Alsmiller 1971; Masarik and Reedy 1993).

Such Monte Carlo calculations can describe particle transport down to 1 MeV for charged particles and to 20 MeV for neutrons. For protons this is sufficient since Coulomb repulsion prevents charged particles of lower energies to induce nuclear reactions. However, since neutrons of all energies can produce nuclear interactions, transport codes designed for low-energy neutrons such as MORSE (Emmet 1975) or MCNP (Briesmeister 1993) have to be coupled to HETC or LAHET to follow the neutrons down to thermal energies and to obtain the entire neutron spectra.

Using the spectra calculated in this way it is then possible to reliably calculate GCR production rates of cosmogenic nuclides with high accuracy of better than 10% provided cross sections for the production of cosmogenic nuclide by proton- and neutron-induced reactions are available.

In figure 2 we show GCR proton and neutron spectra in the center of a H-chondrite with a radius of 25 cm and in figure 3, the dependence of center flux densities on meteoroid radii for the same meteorite class. Only in cosmic dust and presolar grains the built-up of secondary particles can be neglected. Already in meteoroids with radii of 5 cm production by GCR secondaries becomes significant and in objects with radii between 40 and 50 cm the internuclear cascade is fully developed and secondary particles, in particular neutrons, dominate. Significant thermal and epithermal neutron fields, however, are relevant only in larger objects; in smaller ones leakage through the surface prevents their built-up. For example, the production of ^{60}Co which is mainly due to $^{59}\text{Co}(n,\gamma)^{60}\text{Co}$ has, in the center of H-chondrites, its maximum at a radius of about 85 cm. Up to a radius of 30 cm, it

is below 10% of the maximum center production rate (Fanenbruck *et al* 1994).

It has to be emphasized that proton and neutron flux densities have different dependence on depth and size, a fact which emphasizes the importance to describe adequately the decrease of center production rates for large meteoroid radii (c.f. Michel *et al* 1995a).

3. Cross sections for the production of cosmogenic nuclides

Up to the middle of the seventies the situation for cross sections of proton induced reactions was very unsatisfactory; see Michel *et al* (1995b) for a discussion. Therefore, systematic and comprehensive investigations were started by the first author and various collaborators in order to measure all relevant cross sections for the production of cosmogenic nuclides in extraterrestrial matter. After an early phase of experiments at KFA/Jülich, UCL/Louvain La Neuve and IPN/Orsay, (Michel *et al* 1985b and references therein), at CERN/Geneve (Michel *et al* 1989c) and at LANL/Los Alamos (Michel *et al* 1995b), a general experimental routine was evolved to determine excitation functions from thresholds up to 2.6 GeV by combining experiments at LNS/Saclay, TSL/Uppsala and PSI/Villigen covering the energy ranges from 2.6 GeV to 200 MeV, from 180 MeV to 70 MeV and below 70 MeV, respectively, (Bodemann *et al* 1993, Michel *et al* 1995b, 1997a, Schiek *et al* 1996a and references therein).

During the past two decades the target elements C, N, O, Mg, Al, Si, Ca, Ti, Mn, Fe, Co, Ni, Cu, Nb, Sr, Y, Zr, Nb, Ba and Au have been investigated. Residual radionuclides and stable rare gas isotopes

were measured after irradiation by AMS, γ -spectrometry and by conventional mass spectrometry covering most relevant cross sections for the production of cosmogenic nuclides. A collaboration of up to 13 institutes at Ahmedabad, Bordeaux, Köln, Hannover, Jülich, Mainz, New Brunswick, Philadelphia, Uppsala and Zürich contributed to these investigations. In 1997, the database covered nearly 550 target/product combinations with about 15,000 cross sections. It is available in EXFOR format (McLane 1996) at the Nuclear Data Bank of NEA/OECD/Paris or from the Nuclear Data Center of IAEA/Vienna. A complete review of all related references including the relevant EXFOR numbers may be found elsewhere (Michel *et al* 1997a). Large number of targets have been irradiated and stored for the measurement of long-lived and stable nuclides in the future. Recent analyses covered the production of long-lived radionuclides such as ^{14}C (Neupert 1996), ^{36}Cl (Schiekel *et al* 1994, 1996b; Sudbrock *et al* 1997), ^{41}Ca and ^{129}I (Schnabel *et al* 1996, 1997) and of stable rare gas isotopes (Leya *et al* 1998b; Gilabert *et al* 1998a; Neumann *et al* 1997b).

In figure 4 we give a survey on the cross sections for the production of ^{44}Ti from the relevant target elements titanium, iron and nickel and present a large number of new measurements. These data nearly completely satisfy the data needs of cross sections for the proton induced production of ^{44}Ti . ^{44}Ti was measured by using Ge and Si detector by measuring the 67.85 keV and 78.38 keV γ -transitions of ^{44}Ti , having γ -intensities of 94.4% and 96.2%, respectively; (see Gloris 1998; Sudbrock 1997 for details). Only a few earlier measurements by other authors exist (Brodzinski *et al* 1971a, 1971b; Dropesky and O'Brien 1972; Honda and Lal 1964; Raisbeck and Yiou 1977b). The cross sections of Brodzinski *et al* (1971a, 1971b) deviate considerably from those measured by our collaboration.

Though our various collaborations established most of the existing cross section data base for the production of cosmogenic nuclides, significant contributions by a few other groups must be mentioned. The Bordeaux group investigated the production of rare gas isotopes from various target elements (Regnier *et al* 1982, and references therein) and Raisbeck and Yiou measured cross sections for long-lived radionuclides (Raisbeck and Yiou 1977a). During recent years, Sisterson and coworkers also performed systematic measurements at various accelerators in order to improve the availability of cross sections for interpretation of SCR effects (Sisterson *et al* 1992a, 1992b, 1994, 1997).

For neutron-induced reactions the situation is much worse. In spite of the fact that secondary neutrons dominate the production of cosmogenic nuclides, there is an extreme lack of experimental cross sections. Only for capture reactions of thermal and epithermal

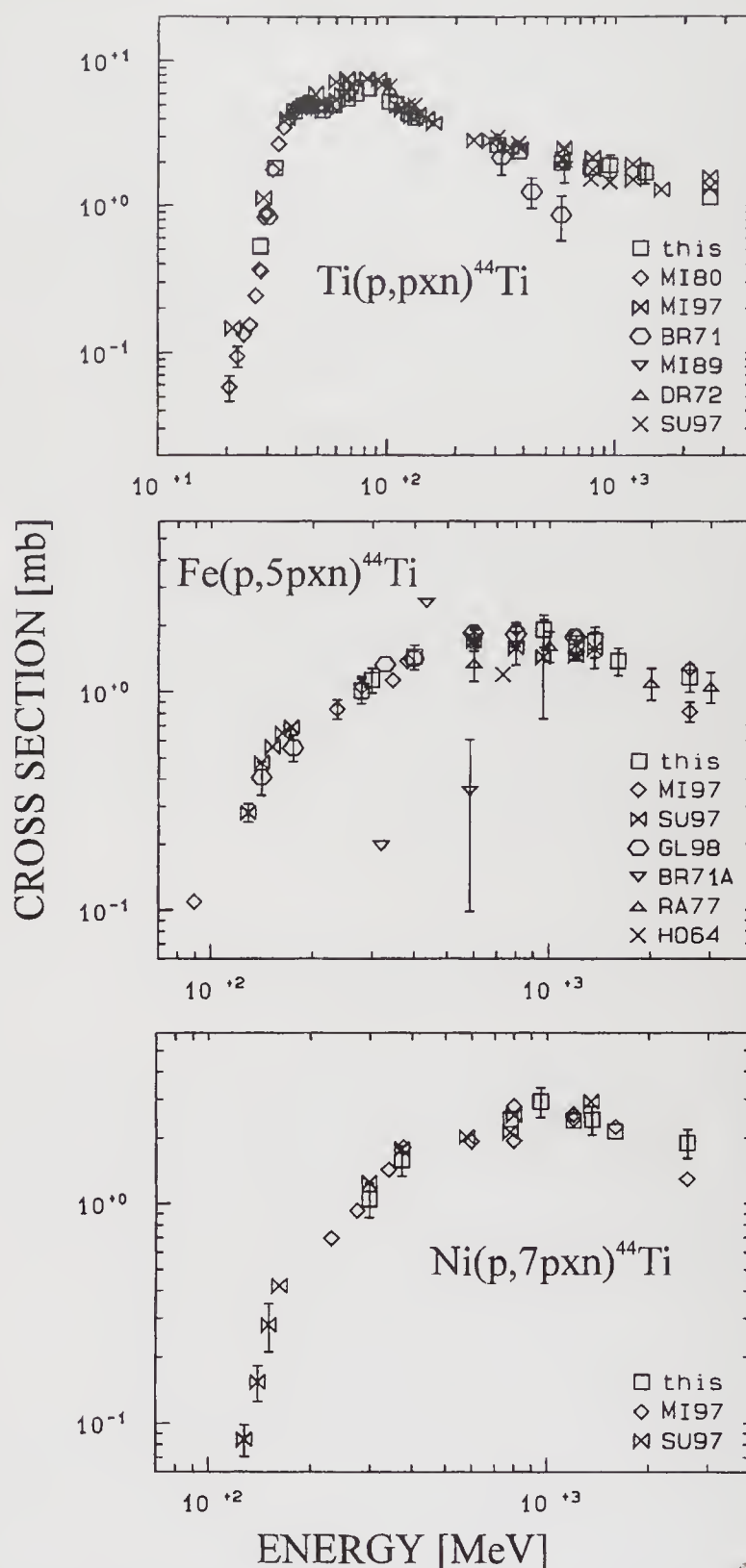


Figure 4. Cross sections for the proton-induced production of ^{44}Ti from Ti, Fe and Ni. Except for a few measurements by other authors [BR71 (Brodzinski *et al* 1971a); BR71A (Brodzinski *et al* 1971b); DR72 (Dropesky and O'Brien 1972); RA77 (Raisbeck and Yiou 1977b); HO64 (Honda and Lal 1964)] the data are from work of our group: this and MI80 (Michel and Brinkmann 1980); MI89 (Michel *et al* 1989c); MI97 (Michel *et al* 1997a); SU97 (Sudbrock 1997); GL98 (Gloris 1998).

neutrons the data base is acceptable and physical model calculations can be reliably performed (Fanenbruck *et al* 1994). Generally, most available data are for energies equal to or below 14.7 MeV; and only a few investigations went up to 30 MeV. There are two reports on measurements of cross sections of neutron-induced reactions relevant for the production of

cosmogenic nuclides below 30 MeV (Reedy *et al* 1979; Lavielle *et al* 1990). Above 30 MeV, there is nearly a complete lack of production cross sections; only a few measurements of production cross sections for cosmogenic nuclides exist (Nakamura *et al* 1992). Therefore, the only first hand sources of neutron cross sections at medium energies are nuclear reaction models. As mentioned above, however, these models and codes describe the production of residual nuclides by nuclear reactions at best within a factor of two (Michel and Nagel 1997).

This causes uncertainties in the *a priori* GCR model calculations even if one uses the available high-quality proton cross sections. Also the assumption of equal proton and neutron cross sections which is frequently made does not hold even at medium energies (Michel *et al* 1998) and systematic measurements of neutron cross sections are just about to start (Neumann *et al* 1997c). The application of theoretical neutron cross sections in model calculations calls for validation of the calculational methods and/or for other means to obtain information about the required neutron cross sections.

4. Simulation of GCR interactions with meteoroids

Such validations can be obtained from thick-target experiments which provide at the same time a solution of the problem of missing neutron cross sections. Simulation experiments on Earth, in which thick targets are irradiated under controlled conditions by medium- and high-energy protons or ^4He nuclei and in which the production of residual nuclides in the thick targets are directly measured, have for a long time been regarded as a tool to directly measure cosmogenic nuclide production rates. However, it turned out that most such experiments could not satisfy this expectation, see (Michel *et al* 1985a, 1989a) for critical reviews of the historical development. A breakthrough was achieved several years ago (Michel *et al* 1985a, 1989a) when simulation experiments with 600 MeV protons were performed at the CERN synchrocyclotron, during which an isotropic irradiation of artificial stony meteoroids with radii of 5, 15 and 25 cm was performed for the first time by complex movements of the targets during irradiation. However, the production rates measured in these experiments turned out to be too low by factors between two and ten compared to those observed in real meteorites. This was due to the fact that 600 MeV was too low an energy to simulate the mean GCR proton spectra whose average proton energy is above 1 GeV. The underestimate of the production rates in the 600 MeV simulation experiments was thus due to the dependence of secondary particle multiplicities on primary particle energy. In spite of this limitation, these experiments demon-

strated that even in small meteoroids GCR production of cosmogenic nuclides is dominated by secondary particles, mostly neutrons.

At Laboratoire National Saturne (LNS) at CEN Saclay/France this problem was overcome. Two simulation experiments were performed at the SATURNE synchrotron of LNS in which an artificial stony meteoroid made of gabbro with a radius of 25 cm and an artificial iron meteoroid made of steel with a radius of 10 cm were isotropically irradiated with 1.6 GeV protons. This energy matches the average GCR proton energy during times of quiet sun such as the Maunder Minimum (Castagnoli and Lal 1980). The isotropic irradiation was achieved by four simultaneous movements during irradiation. By two translational movements (up/down and left/right) the artificial meteoroids were exposed to a parallel proton "rain" covering their total cross sections. In this parallel proton beam the artificial meteoroids were rotated around two perpendicular axes. During effective beam-on-target times of 282.1 h and 125.7 h, respectively, the artificial stony and iron meteoroid received proton fluences of $1.3 \times 10^{14} \text{ cm}^{-2}$ and $2.4 \times 10^{14} \text{ cm}^{-2}$, that are approximately equivalent to 1.6 and 3.0 Ma exposure of real meteoroids in space. The measured production rates matched those observed in real meteorites within 10% (Michel *et al* 1995a; Leya 1997; Leya *et al* 1998b).

Inside the artificial stony and iron meteoroids, several thousands of thin targets of most cosmochemically relevant target elements were irradiated and production rate depth profiles of all the relevant cosmogenic nuclides (> 500 target/product combinations) were measured using γ -spectrometry as well as accelerator and rare gas mass spectrometry. A theoretical analysis of the experimental production rates was performed using depth- and size-dependent spectra of primary and secondary particles calculated by the HERMES code system (Cloth *et al* 1988) and experimental and theoretical thin-target cross sections of the underlying nuclear reactions. However, these *a priori* calculations were found to reproduce the experimental production rates in the 600 MeV and 1600 MeV simulation experiments only within 40% on the average. Since the cross sections of proton-induced reactions are considered to be of high reliability, the discrepancies between experimental and *a priori* calculated production rates was attributed to the poor quality of the neutron cross sections used.

A solution of this problem, however, can be derived from the thick-target experiments themselves. The experimental production rates measured in the thick-target experiments performed at different energies and with different meteoroid radii and bulk chemical compositions contain information of the neutron-induced production which can be extracted if the proton-induced production can be reliably calculated and subtracted from the experimental ones; see

(Michel 1998) for a complete list of up-to-date references. As discussed elsewhere in detail (Michel *et al* 1996; Leya 1997; Leya and Michel 1997) it is possible to adjust the *a priori* neutron excitation functions by taking into account all available experimental data by an energy dependent least squares fit using the code STAY'SL (Perey 1977) modified by Matzke (1979). Using this method a self-consistent set of cross sections of the underlying neutron-induced reactions was established (Leya and Michel 1997). With those new neutron cross sections, it is possible to describe by *a posteriori* model calculations simultaneously all data from the simulation experiments with an accuracy better than 10% (Michel *et al* 1996, 1997b; Leya 1997; Leya *et al* 1998a).

As an example, in figure 5 we present the production rates of ^{44}Ti from titanium, iron and nickel measured in the artificial iron meteoroid together with the results of *a posteriori* model calculations. Further examples of experimental depth profiles in the artificial meteoroids and of *a priori* and *a posteriori* model calculations may be found elsewhere (Michel *et al* 1993, 1994, 1995a, 1996, 1997b; Leya 1997; Leya and Michel 1997). A comprehensive publication of all the results obtained for radionuclides is presently under preparation (Leya *et al* 1998b). For rare gases only a small part of the results were published up to now (Wieler *et al* 1992; Weber and Begemann 1992; Mathews *et al* 1994; Gilabert *et al* 1994, 1996, 1997). The majority of results still remains to be published.

As has been shown elsewhere (Michel *et al* 1996) the proton and neutron spectra inside the artificial meteoroids irradiated isotropically with 1.6 GeV protons are a good approximation of the actual spectra in meteoroids. However, there remain distinct differences caused by the monoenergetic protons in the simulation experiments and the continuous spectrum of GCR primaries in space. Therefore, production rates obtained from simulation experiments cannot directly be used for the interpretation of cosmogenic nuclide abundances in meteorites. In order to derive reliable production rates of cosmogenic nuclides in meteoroids one has to calculate the primary and secondary GCR spectra inside a meteoroid starting from continuous and realistic free-space GCR spectra and then to calculate production rates using the same proton and neutron cross sections used in the *a posteriori* calculations of the production rates in the artificial meteoroids.

5. Cosmogenic nuclides in meteorites

Given the good agreement obtainable between the experimental and *a posteriori* theoretical production depth profiles in the artificial meteoroids irradiated by 0.6 GeV and 1.6 GeV protons, it is possible to calculate for a given GCR proton spectrum the production

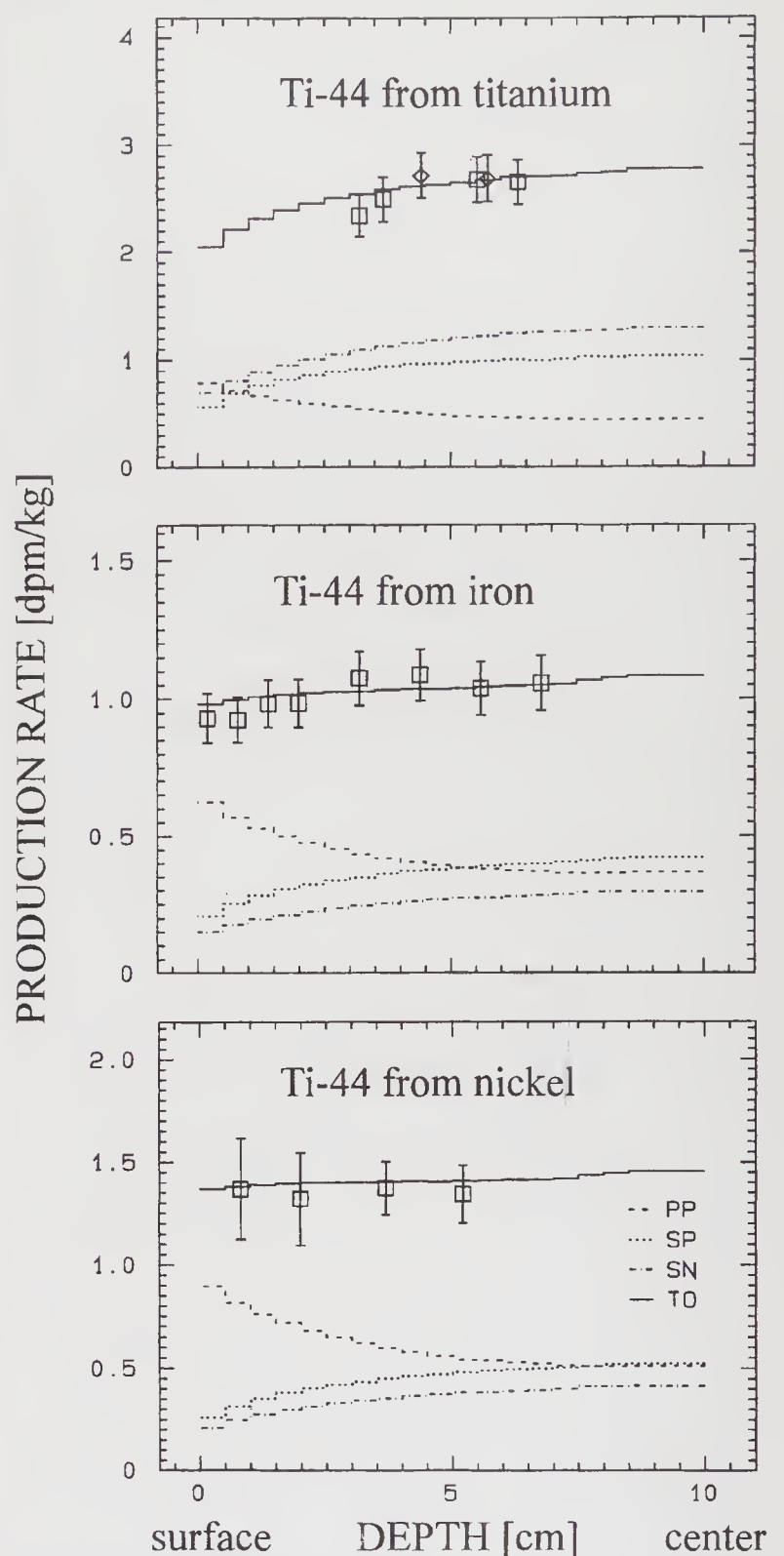


Figure 5. Depth profiles for the production of ^{44}Ti from Ti, Fe and Ni in an artificial iron meteoroid with a radius of 10 cm irradiated isotropically with 1.6 GeV protons. The theoretical production rates are from *a posteriori* calculations using the experimental proton cross sections shown in figure 3 and neutron excitation functions extracted from thick-target simulation experiments. For the theoretical production rates the total production as well as those due to primary protons, secondary protons and secondary neutrons are distinguished.

rates in real stony and iron meteoroids in space with the same claim of accuracy for each of the target/product combinations investigated in the terrestrial simulation experiments.

Since the production rates of cosmogenic nuclides strongly depend on the spectral distribution of primary SCR and GCR particles, e.g. (Michel *et al*

1982, 1991), one first has to determine the long-term SCR and GCR spectra in order to calculate their dependencies on depth in and size of a meteoroid.

The dependence on the GCR modulation parameter of GCR production rates in meteorites is largest for cosmogenic nuclides which are preferably produced by low-energy secondary particles. Consequently, the dependence on modulation decreases in the sequence ^{53}Mn , ^{26}Al , ^{21}Ne , ^{10}Be . The center production rates in an undifferentiated stony meteoroid with a radius of 40 cm of these nuclides differ by factors of 3.1, 2.3, 1.6 and 1.5, respectively, for modulation parameters between 300 MeV and 900 MeV (Michel *et al* 1991; Leya 1997).

The dependence of ^{44}Ti production rates on solar modulation is in-between those of ^{26}Al and ^{21}Ne as a consequence of the large mass difference between ^{44}Ti and its most important target element iron. But, it is not a real low-energy product and therefore not very sensitive to solar modulation. The production rates in the center of a 40 cm radius H-chondrite are calculated to be 0.92, 1.05, 1.09, 1.27, and 1.63 dpm kg $^{-1}$ for modulation parameters M of 900, 650, 620, 450, and 300 MeV, respectively, the production rate for $M = 300$ MeV being 1.8 times larger than for $M = 900$ MeV. Within the range of relevant parameters the dependence of ^{44}Ti production rates as function of integral number of primary GCR protons can well be approximated by a linear function.

Having calculated the dependence of production rates on solar modulation, long-term GCR spectra can be derived by fitting theoretical GCR production rate depth profiles of long-lived radionuclides to those ones observed in extraterrestrial matter provided that the abundances of stable cosmogenic rare gases indicate that the exposure ages are long enough to make sure that the radionuclides are in saturation. Such experimental data exist for ^{10}Be , ^{14}C , ^{26}Al , ^{36}Cl , and ^{53}Mn in the lunar surface and in a number of well investigated meteorites as e.g. Knyahinya, St. Severin, and Keyes. We used for this purpose ^{26}Al in Knyahinya (Michel *et al* 1996; Leya 1997). Figure 6 shows the best GCR production rate depth profile of ^{26}Al in Knyahinya describing the experimental data by Graf *et al* (1990). The long-term GCR spectrum has a mean flux density of primary GCR nucleon $J_{0,\text{GCR}} = 4.06 \text{ cm}^{-2} \text{ s}^{-1}$ which is equivalent to $J_{0,\text{GCR},\text{pp}} = 2.62 \text{ cm}^{-2} \text{ s}^{-1}$ and to a GCR modulation parameter $M = 620$ MeV in the meteoroid orbits. In figure 7 the long-term spectrum is compared with the range of observed and deduced integral GCR spectra. This figure also demonstrates that the flux densities of the individual spectra are hardly changing around 10 MeV $J_{0,\text{pp}}(E > 10 \text{ MeV})$ and that, consequently, $J_{0,\text{pp}}(E > 10 \text{ MeV})$ is a better choice to characterize a GCR spectrum than $J_{0,\text{pp}}(E > 1 \text{ GeV})$.

The determination of $J_{0,\text{GCR}}$ at the same time fixes the production rates of ^{26}Al in meteorites of all sizes

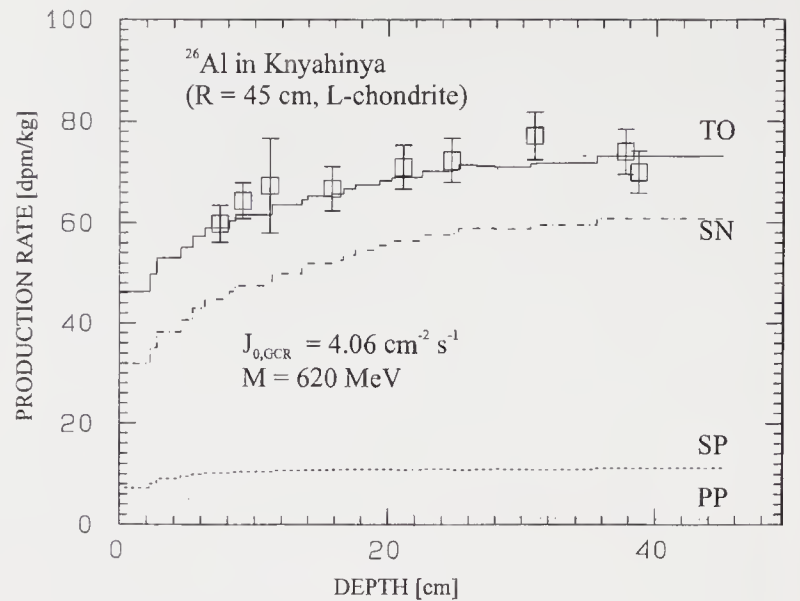


Figure 6. Modeling of ^{26}Al in Knyahinya is used to determine the 4π integral flux density of GCR nucleons. The resulting value $J_{0,\text{GCR}} = 4.06 \text{ cm}^{-2} \text{ s}^{-1}$ is equivalent to a GCR proton spectrum with a modulation parameter of 620 MeV. The experimental data are from Graf *et al* (1990).

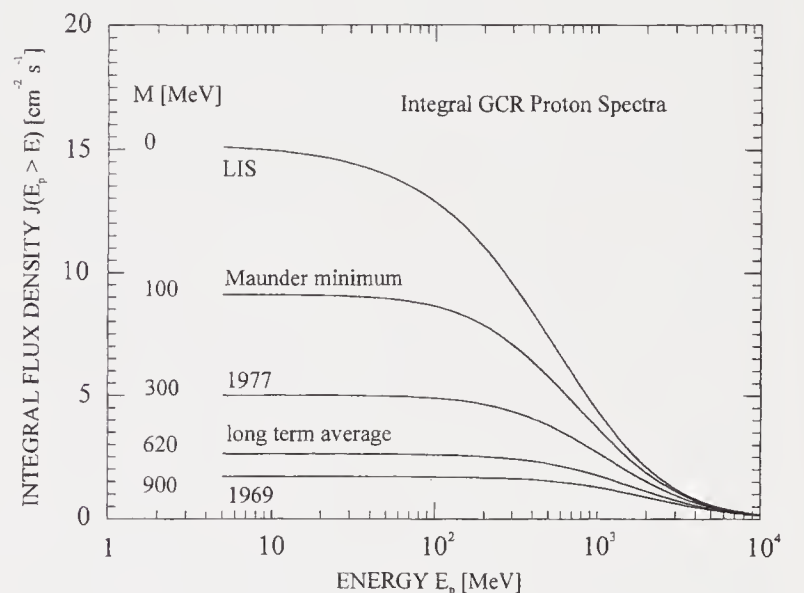


Figure 7. The long-term averaged GCR proton spectrum with a modulation parameter $M = 620$ MeV compared to observed spectra and to spectra derived by Castagnoli and Lal (1980) for the local interstellar spectrum (LIS) and for the Maunder minimum.

and chemical compositions and in the lunar surface. The production rate depth profiles calculated for H-chondrites are shown in figure 8. Provided that the GCR stayed constant as function of time the calculation of production rates of other cosmogenic nuclides is fixed at the same time.

As shown elsewhere (Michel *et al* 1996; Leya 1997; Neupert 1996), the depth profiles of ^{10}Be , ^{14}C , ^{26}Al , ^{36}Cl , ^{41}Ca and ^{53}Mn measured in stony and iron meteorites and in the lunar surface, adjusted for orbit dependence of GCR spectra and intensities, can also be described with this GCR spectrum. Thus, one can conclude that the GCR flux was constant during the last ten million years and had a spectrum with a

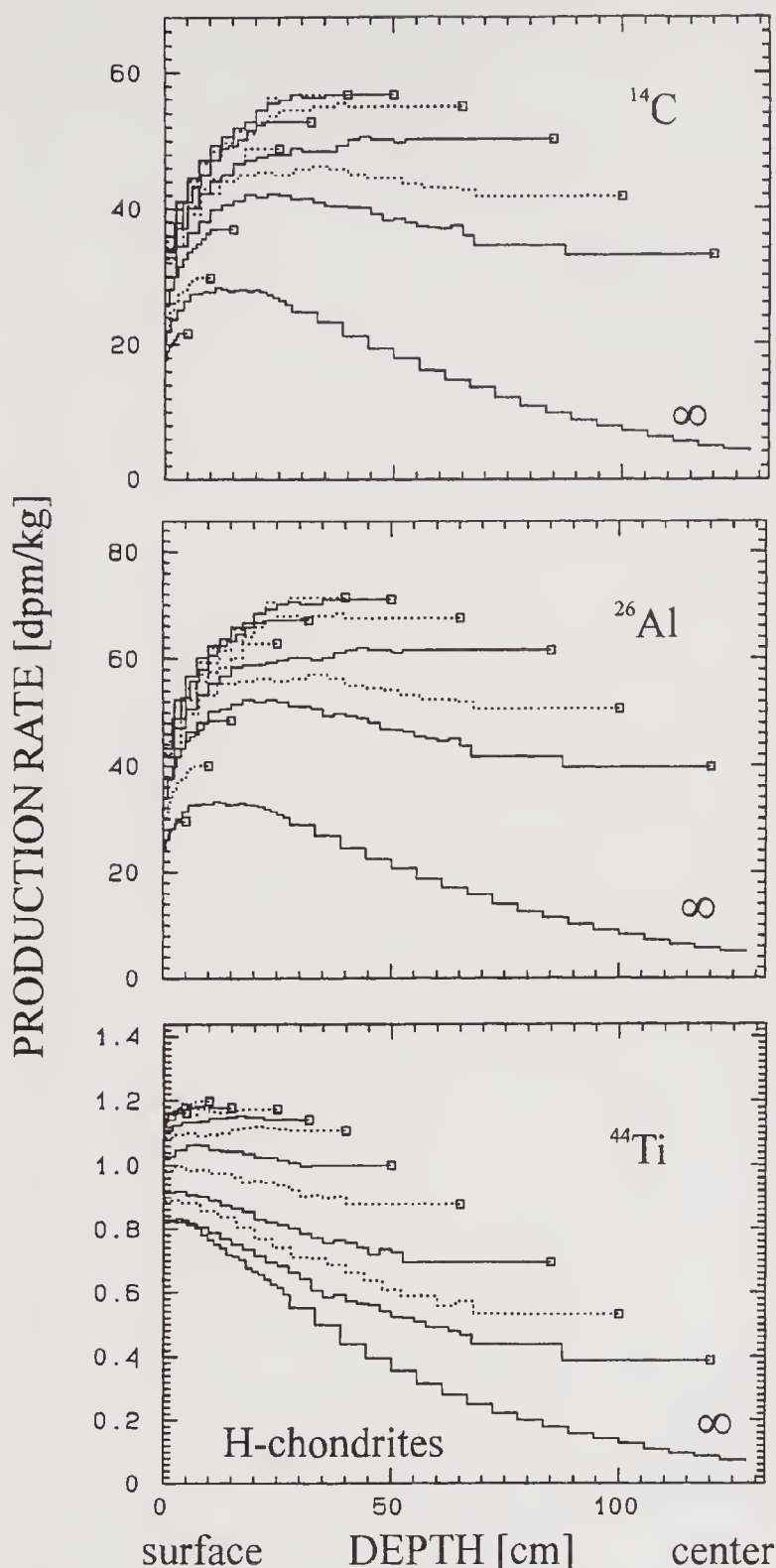


Figure 8. GCR production rates of ^{14}C , ^{26}Al and ^{44}Ti in H-chondrites for the long-term averaged GCR spectrum.

modulation parameter of $M = 620$ MeV. Changes on smaller time scales as seen in the terrestrial ^{14}C record do not show up in the long-lived radionuclides with half-lives exceeding 5 ka. There are, however, indications on short-term changes on a time scale of a few decades as deduced by Bonino *et al* (1994, 1995) from the analysis of ^{44}Ti in stony meteorites. An extension of the time scale up to 50 million years would be possible by analyzing ^{129}I in stony meteorites. However, since the nuclear data needed for such an analysis are still incomplete the analysis of ^{129}I in extraterrestrial matter is still ambiguous (Schnabel *et al* 1997).

Since the model calculations are based on the evaluation of equation 6 and since the total production rates are a sum of elemental production rates, elemental composition of different meteoroid classes or individual objects can easily be taken into account. Also the dependence of production rates on bulk chemical composition, which was observed in stony irons by Begemann and Schultz (1988) and Jentsch and Schultz (1996), is easily accounted for by individual calculation of the respective depth- and size-dependent spectra in different matrices (Michel *et al* 1990; Masarik and Reedy 1994; Leya 1997; Leya *et al* 1998b). At present, our model calculations cover the cosmogenic nuclides ^{10}Be , ^{14}C , ^{26}Al , ^{36}Cl , ^{41}Ca , ^{53}Mn as well as He, Ne, Ar, Kr and Xe isotopes with an accuracy $<10\%$ for production rates and $<3\%$ for production rate ratios and allows a complete interpretation of cosmogenic nuclides in stony and iron meteorites and lunar surface materials.

The determination of long-term SCR spectra is more complicated than for GCR spectra. SCR effects have been clearly distinguished in lunar surface samples for a wide variety of cosmogenic nuclides; e.g. (Finkel *et al* 1971; Bhandari *et al* 1976; Kohl *et al* 1978; Rao *et al* 1994). Only recently, a depth profile with a clear signature of SCR interactions was reported in meteorites by Nishiizumi *et al* (1990). There is, however, further evidence for a more general presence of SCR contributions to cosmogenic nuclide production in small meteoroids (Michel *et al* 1982; Michel and Stück 1984) and in the outermost surface of meteorites where material from close to the preatmospheric surface luckily survived atmospheric transit (Lal and Marti 1977).

In order to determine long-term SCR spectra, theoretical SCR production rates have to be fitted to “experimental” SCR production rates in order to find the best set of SCR spectral parameters describing the latter data. However, “experimental” SCR production rates do not exist. They have to be calculated by subtraction of a GCR contribution which itself is not accessible experimentally but has to be derived from GCR model calculations which at best can be validated by comparison with experimental GCR production rates measured at much larger depths where SCR contributions are negligible. Thus, the extraction of experimental SCR data is only possible if reliable GCR model calculations are at hand.

There are two more difficulties when interpreting SCR effects in lunar surface material and meteorites. First, there is no unambiguous determination of SCR spectral parameters since the spectra depend on two parameters, R_0 and J_0 , and only best fit combinations can be obtained as demonstrated by Rao *et al* (1994) after a proper analysis of GCR production rates is performed. Secondly, there is the problem that such analyses have to take into account space erosion, i.e. the change of the outermost surface of an object in

space by CR sputtering and by impact of cosmic dust and micrometeorites.

But mainly the lack of high-quality cross sections led to a number of widely disagreeing determinations of long-term SCR parameters (Finkel *et al* 1971; Kohl *et al* 1978; Bhandari *et al* 1976; Reedy and Marti 1991). Uncertainties about erosion rates of extraterrestrial matter in space just added to ambiguities of these determinations. Since short-lived cosmogenic radionuclides are not affected by such uncertainties, SCR effects observed for such nuclides can be consistently described taking into account actual flare data (Bodemann 1993). Our determination of long-term averaged SCR spectral parameters from ^{26}Al and ^{53}Mn depth profiles in lunar rocks yielded long-term averaged SCR parameters $J_{0,\text{SCR}} = 55 \text{ cm}^{-2} \text{ s}^{-1}$ and $R_0 = 125 \text{ MV}$ (Bodemann 1993; Michel *et al* 1996). As discussed elsewhere in detail (Michel *et al* 1996) our model calculations on the basis of the long-term SCR and GCR spectra given above reproduce the production rates of ^{10}Be and ^{26}Al in the Salem meteorite reported by Nishiizumi *et al* (1990) and exclude smaller values for long-term-averaged rigidities of SCR spectra.

There is still a discrepancy with respect to long-term SCR parameters derived from investigations of ^3He , ^{21}Ne , ^{22}Ne , and ^{38}Ar in lunar rocks 68815 and 61016 by Rao *et al* (1994). These authors concluded that long-term SCR spectra with $J_{0,\text{SCR}} = 66 \text{ cm}^{-2} \text{ s}^{-1}$ and $R_0 = 85 \text{ MV}$ are needed to fit the experimental data, parameters which cannot explain the observed ^{26}Al profiles (Michel 1998). Whether there is a long-term change in SCR and consequently GCR parameters or whether this discrepancy is merely due to unreliable cross sections is still open. This problem can be settled after remeasuring the respective cross sections which is underway (Leya *et al* 1998b; Gilabert *et al* 1998b; see also Reedy, this volume).

Some conclusions about the production of cosmogenic nuclides in stony meteoroids may be drawn here. There is evidence from the simulation experiments and from model calculations for real meteoroids in space that the elemental production rates of different target elements contributing to the production of a particular cosmogenic nuclide do not have identical depth and size dependences. Therefore, empirical corrections of production rates for different chemical compositions derived from meteorite data have inherent uncertainties since they neglect such dependencies. Physical model calculations and the general approach described here allow calculations of more reliable production rates for different meteorite classes.

For determination of the production rates of stable cosmogenic nuclides, usually constant production rate ratios of a stable and radioactive nuclide have to be assumed. Our model calculations show, however, that quite often, correlations between production rates of different cosmogenic nuclides deviate from linearity.

Thus, the fundamental assumptions of dating methods have to be scrutinized by physical model calculations as it was done e.g. for the $^{81}\text{Kr}/\text{Kr}$ method by Gilabert *et al* (1996, 1997). This can be done by calculation of production rates of the respective nuclide after careful measurement and analysis of the relevant cross sections and thick-target production rates from simulation experiments. Moreover, such a procedure is applicable to arbitrary meteorite classes. For He, Ne, Ar and Kr this was demonstrated with good success (Michel *et al* 1995a; Herpers *et al* 1995; Knauer *et al* 1995; Leya 1997; Leya *et al* 1995, 1996; Neupert 1996; Weigel *et al* 1997) and also the results for Xe are promising (Gilabert *et al* 1994).

Extreme deviations from constant production rate ratios are observed e.g. for the nuclide pair ^{26}Al and ^{10}Be (figure 9), the production modes of which differ strongly because of different energies at which these nuclides are produced. ^{26}Al is a low-energy product in stony meteorites while ^{10}Be is a high-energy one. This is, however, an advantage since the location of measured ^{10}Be and ^{26}Al data in an ^{26}Al versus ^{10}Be plot of production rates allows to constrain meteoroid size and sample shielding depth (Neupert 1996; Neupert *et al* 1997; Merchel *et al* 1997; Scherer *et al* 1997). Combining such information with rare gas data, in particular with the dependence of shielding parameters $^3\text{He}/^{21}\text{Ne}$ and $^{22}\text{Ne}/^{21}\text{Ne}$ and production rates on radius and depth allows the determination of the exposure history of a meteorite: the radius of the meteoroid, sample shielding depths, exposure and terrestrial age and the decision about pairing of different finds and complex exposure histories.

The exposure age can be derived both from radius and depth assignment or from the theoretical dependence of rare gas production rates on shielding parameters, which for medium sized meteoroids (25 to 50 cm radius) agree well with those obtained from semi-empirical models (Eugster 1988). For larger radii the empirical shielding depth correlations of production rates do not hold. It is to be noted that for smaller radii the production of cosmogenic nuclides by SCR particles has also to be considered (Michel *et al* 1995a) which often shows up in ^{26}Al but not in ^{10}Be . In addition, due to the availability of the relevant elemental production rates, by physical model calculations, the differentiated meteorites can also be dated with respect to their exposure ages with similar accuracy (Weigel *et al* 1997).

The knowledge about radius and shielding depth is also crucial for the determination of terrestrial ages e.g. via ^{14}C . Figure 8 shows the production rates of ^{14}C in H-chondrites. For radii between 5 and 50 cm these production rates vary by up to a factor of three. For calculating a terrestrial age from a measured ^{14}C specific activity the proper saturation activity has to be derived on the basis of size and shielding information obtained from other cosmogenic nuclides

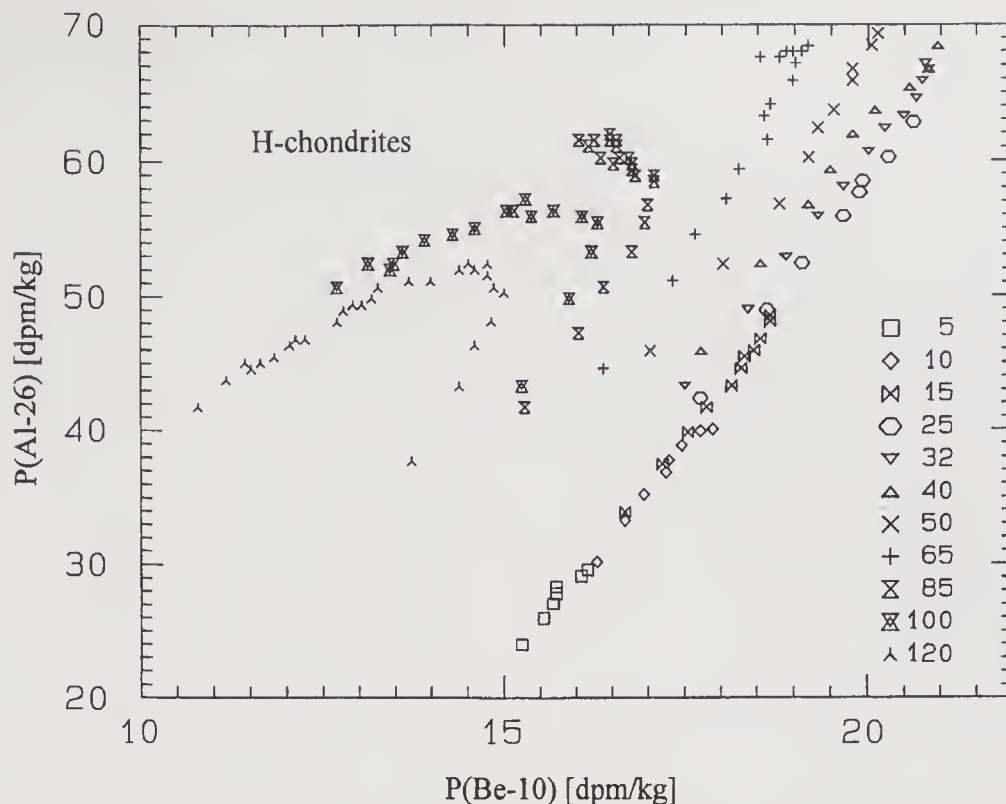


Figure 9. Correlation of ^{26}Al and ^{10}Be production rates in H-chondrites for the long-term averaged GCR spectrum.

measured in the same sample, which are then interpreted by physical model calculations.

Considering the achievements made so far in the measurement and interpretation of cosmogenic nuclides in extraterrestrial matter, some future goals, both experimental and theoretical ones, can be defined. From the experimental point of view an extension of the cosmogenic nuclide coverage during measurement of any sample is desirable. This stresses the importance of consortium studies as a regular approach.

The time scales on which GCR spectra are investigated can be extended from about 10 Ma to 50 Ma by analysis of ^{129}I . Further, analyses of ^{59}Ni in lunar samples would be highly desirable since they provide the only means to derive long term spectra of energetic solar ^4He particles.

Though our physical model calculations also adequately describe cosmogenic nuclide production in iron meteoroids (Leya 1997), an extension of the model calculations to $^{41}\text{K}/^{40}\text{K}$ -dating of iron meteorites is desirable. In this context, it has to be mentioned that for iron meteorites one faces particular problems since contributions to cosmogenic nuclide production by trace elements such as sulfur and phosphorus are significant (Leya 1997). Here further cross section data are needed.

For a further development of the model calculations, improvement in cross section data for the production of nuclides such as ^3H , ^{53}Mn , ^{60}Fe , ^{129}I and of rare gas isotopes is the major task. Some systematic work in this direction is underway for proton-induced reactions and, hopefully, may begin soon for neutron-induced ones in the near future.

6. Conclusions

Making systematic use of accelerators to measure the cross sections relevant for the production of cosmogenic nuclides and to simulate the irradiation conditions which a meteoroid undergoes in space, it was possible to establish a physical model without free parameters which describes all aspects of the production of cosmogenic nuclides by solar and galactic cosmic ray particles. Further extension and development of this model exclusively rest on the improvement of our knowledge about the nuclear reactions underlying the production of cosmogenic nuclides.

Acknowledgement

This work was partially supported by the German Science Foundation. The first author is grateful to a large number of colleagues for collaboration over a time period of two decades. Also the opportunity to use a wide variety of accelerators and to enjoy the skill and assistance of the accelerator staff is gratefully acknowledged. Without the collaborators and the accelerator staff the maturity of physical model calculations obtained today would not have been achieved.

References

- Ahmad I, Bonino G, Castagnoli G C, Fischer S M, Kutschera W and Paul M 1998 Three-laboratory measurement of the ^{44}Ti half-life; *Phys. Rev. Lett.* **80** 2550–2553

- Alsmiller R G, Santoro R T, Barish J and Claiborne H C 1972 Shielding of manned space vehicles against protons and α -particles; *ORNL-RSIC* **35**
- Anders E 1960 The record in meteorites-II On the presence of aluminum-26 in meteorites and tektites; *Geochim. Cosmochim. Acta* **19** 53-62
- Armstrong T W and Alsmiller R G Jr 1971 Calculation of cosmogenic radionuclides in the moon and comparison with Apollo measurements; *Proc. 2nd Lunar Sci. Conf.* **2** 1729-1745
- Armstrong T W and Chandler K C 1972 HETC-A high energy transport code; *Nucl. Sci. Eng.* **49** 110
- Arnold J R, Honda M and Lal D 1961 Record of cosmic-ray intensity in the meteorites; *J. Geophys. Res.* **66** 3519-3531
- Begemann F, Geiss J and Hess D C 1957 Radiation age of a meteorite from cosmic-ray-produced ^3He and ^3H ; *Phys. Rev.* **107** 540-542
- Begemann F and Schultz L 1988 The influence of bulk composition on the production rate of cosmogenic nuclides in meteorites; *LPSC XIX* 51-52
- Bhandari N, Bhattacharya S K and Padia J T 1976 Solar proton fluxes during the last million years; *Proc. Lunar Sci. Conf.* **VII** 513-523
- Bhandari N, Bonino G, Callegari E, Castagnoli G C, Mathew K J, Padia J T and Queirazza G 1989 The Torino, H6, meteorite shower; *Meteoritics* **24** 29-34
- Bhandari N, Mathew K J, Rao M N, Herpers U, Bremer K, Vogt S, Wölfl W, Hofmann H-J, Michel R, Bodemann R and Lange H-J 1993 Depth and size dependence of cosmogenic nuclide production rates in stony meteoroids; *Geochim. Cosmochim. Acta* **57** 2361-2375
- Bhattacharya S K and Bhandari N 1975 Effects of exposure conditions on cosmic-ray records in lunar rocks; *Proc. Lunar Sci. Conf.* **VI** 1901-1912
- Bodemann R 1993 Zur Wechselwirkung der solaren kosmischen Strahlung mit extraterrestrischer Materie-Messung von Wirkungsquerschnitten und Modellrechnungen; Thesis, Universität Hannover
- Bodemann R, Lange H-J, Michel R, Schiek T, Rösel R, Herpers U, Hofmann H-J, Dittrich B, Suter M, Wölfl W, Holmqvist B, Condé H and Malmberg P 1993 Production of Residual Nuclides by Proton-Induced Reactions on C, N, O, Mg, Al and Si; *Nucl. Instr. Meth. Phys. Res.* **B82** 9-31
- Bonino G, Castagnoli G C, Taricco C and Bhandari N 1994 Cosmogenic Ti-44 in meteorites and century scale solar modulation; *Adv. Space Res.* **14** 783-786
- Bonino G, Castagnoli G C, Bhandari N and Taricco C 1995 Behaviour of the heliosphere over prolonged solar quiet periods by Ti-44 measurements in meteorites; *Science* **270** 1648-1650
- Briesmeister J F 1993 MCNP-A general Monte Carlo N-particle transport code, version 4A; A-12625-M, LANL, Los Alamos pp. 693
- Brodzinski R L, Rancitelli L A, Cooper J A and Wogman N A 1971a High-energy proton spallation of titanium; *Phys. Rev.* **C4** 1250-1257
- Brodzinski R L, Rancitelli L A, Cooper J A and Wogman N A 1971b High-energy proton spallation of iron; *Phys. Rev.* **C4** 1257-1265
- Bryant D A, Powell G I and Perry C H 1992 The origin of high-energy cosmic rays; *Nature* **356** 582-583
- Castagnoli G and Lal D 1980 Solar modulation effects in terrestrial production of Carbon-14; *Radiocarbon* **22** 133-159
- Cloth P, Filges D, Neef R D, Sterzenbach G, Reul Ch, Armstrong T W, Colborn B L, Anders B and Brückmann H 1988 HERMES-High Energy Radiation Monte-Carlo Elaborate System; JUEL-2203
- Dropesky B J and O'Brien H A 1972 LANL Report LA-5120-PR
- Eberhardt P and Eberhardt A 1960 Neon und andere Edelgase in Steinmeteoriten; *Helv. Physica Acta* **33** 593-594
- Eberhardt P, Eugster O, Geiss J and Marti K 1966 Rare gas measurements in 30 stone meteorites; *Z. Naturforsch.* **21a** 414-426
- Ebert K H and Wänke H 1957 Ueber die Einwirkung der Höhenstrahlung auf Eisenmeteorite; *Z. Naturforsch.* **12a** 766-773
- Ehmann W D and Kohman T P 1958 Cosmic ray induced radioactivities in meteorites - II. ^{26}Al , ^{10}Be and ^{60}Co , aerolites, siderites and tektites; *Geochim. Cosmochim. Acta* **14** 364-369
- Emmett M B 1975 The MORSE Monte Carlo radiation code system; ORNL-4972
- Eugster O 1988 Cosmic-ray production rates for He-3, Ne-21, Ar-38, Kr- and Xe-126 in chondrites based on Kr-81-Kr exposure ages; *Geochim. Cosmochim. Acta* **52** 1649-1662
- Eugster O and Michel T 1995 Common asteroid break-up events of eucrites, diogenites and howardites and cosmic-ray production rates for noble gases in achondrites; *Geochim. Cosmochim. Acta* **59** 177-199
- Fanenbruck O, Lange H-J and Michel R 1994 On the production of cosmogenic nuclides by low-energy neutrons; *Meteoritics* **29** 465
- Filges D, Cloth P and Theis D 1992 Improvements and perspectives of INC-models in the medium- and high-energy range; *Proc. Int. Symp. on Nuclear Data Evaluation Methodology* (ed) C Dunford, World Scientific Publishing Co., Singapore, pp. 535-542
- Finkel R C, Arnold J R, Imamura M, Reedy R C, Fruchter J S, Loosli H H, Evans J C, Delany A C 1971 Depth variation of cosmogenic nuclides in a lunar rock and lunar soil; *Proc. 2nd Lunar Sci. Conf.* **2** 1773-1789
- Finkel R C and Suter M 1993 AMS in the Earth sciences: Techniques and applications; *Adv. Anal. Chem.* **1** 1-114
- Fireman E L and Schwarzer D 1957 Measurement of ^6Li , ^3He and ^3H in meteorites and its relation to cosmic radiation; *Geochim. Cosmochim. Acta* **11** 252-262
- Geiss J, Oeschger H and Schwarzer U 1962 The history of cosmic radiation as revealed by isotopic changes in the meteorites and on the Earth; *Space Sci. Rev.* **1** 197-223
- Gentner W and Zähringer J 1957 Argon und Helium als Kernreaktionsprodukte in Meteoriten; *Geochim. Cosmochim. Acta* **11** 60-71
- Gilabert E, Lavielle B, Simonoff G N, Rösel R, Herpers U, Neumann S, Lüpke M and Michel R 1994 Cosmogenic nuclide production of Kr and Xe in chondrites: The simulation experiment LNS 172; *Meteoritics* **29** 468
- Gilabert E, Lavielle B, Schiek Th, Herpers U, Neumann S and Michel R 1996 Measurements and modeling the production of Kr and Xe in simulation experiments of an artificial iron meteoroid; *Meteor. & Planet. Sci.* **31A** 50-51
- Gilabert E, Lavielle B, Schiek Th, Herpers U, Neumann S, Leya I and Michel R 1997 Measurements and modeling the production of krypton and xenon in a simulation experiment of an artificial iron meteoroid: application to the chondrite Knyahinya; *Meteor. & Planet. Sci.* **32A** 47
- Gilabert E, Lavielle B, Neumann S, Gloris M, Michel R, Sudbrock F and Herpers U 1998a Cross sections for the proton-induced production of krypton isotopes from Rb, Sr, Y, and Zr for energies up to 1600 MeV; *Nucl. Instr. Meth. Phys. Res. B* (in press)
- Gilabert E, Lavielle B, Neumann S, Gloris M, Michel R, Sudbrock F and Herpers U 1998b New cross-section measurements of proton-induced production of helium, neon, and argon in iron and nickel in the energy range from 159 to 1600 MeV; *Meteor. & Planet. Sci.* **33A** 58-59
- Gloris M 1998 *Protonen-induzierte Restkernproduktion in schweren Elementen bei mittleren Energien*; Thesis, Universität Hannover

- Goswami J N, McGuire R E, Reedy R C, Lal D and Jha R 1988 Solar flare protons and alpha particles during the last three solar cycles; *J. Geophys. Res.* **A93** 7195–7205
- Graf Th, Signer P, Wieler R, Herpers U, Sarafin R, Fieni S V, Pellas P, Bonani G, Suter M and Wölfl W 1990 Cosmogenic nuclides and nuclear tracks in the chondrite Knyahinya; *Geochim. Cosmochim. Acta* **54** 2511–2520
- Herpers U, Herr W and Wölfl R 1967 Determination of cosmic-ray-produced nuclides ^{53}Mn , ^{45}Sc and ^{26}Al in meteorites by neutron activation and gamma coincidence spectroscopy; In *Radioactive Dating and Methods of Low-level Counting IAEA, Vienna* pp. 199–205
- Herpers U, Vogt S, Bremer K, Hofmann H-J, Suter M, Wölfl W, Wieler R, Lange H-J and Michel R 1995 Cosmogenic nuclides in differentiated Antarctic meteorites: Measurements and model calculations; *Planet. & Space Sci.* **43** 545–556
- Hoffmann J H and Nier A O 1958 Production of helium in iron meteorites by the action of cosmic rays; *Phys. Rev.* **112** 2112–2117
- Honda M and Lal D 1964 Spallation cross section for long-lived radionuclides in iron and light nuclei, *Nucl. Phys.* **51** 363–368
- Jenniskens P, Betlem H, Betlem J, Barifaijo E, Schlüter T, Hampton C, Laubenstein M, Kunz J and Heusser G 1994 The Mbale meteorite shower; *Meteoritics* **29** 246–254
- Jentsch O and Schultz L 1996 Cosmogenic noble gases in silicate inclusions of iron meteorites: Effects of bulk chemical composition on elemental production rates; *J. Royal Soc. Western Australia* **79** 67–71
- Knauer M, Neupert U, Michel R, Bonani G, Dittrich-Hannen B, Hajdes I, Ivy-Ochs S, Kubik P W and Suter M 1995 AMS Measurement of the long-lived radionuclides ^{10}Be , ^{14}C , ^{26}Al ; *Meteorites from Hot and Cold Deserts*, Proc. of a Workshop on “Meteorites in Hot and Cold Deserts”, Nördlingen, July 20–22, 1994, LPI Techn. Rep. 95-02 1995, The Lunar and Planetary Institute, Houston, pp. 38–42
- Koch K M 1989 *Experimente zur Messung von doppelt-differentiellen Produktionsquerschnitten für geladene Teilchen zur Absicherung von Rechenmodellen für die Beschreibung von Wechselwirkungen hochenergetischer Protonen mit Materie*; JÜL-2296
- Kohl C P, Murrell M T, Russ G P, Arnold J R 1978 Evidence for the constancy of the solar cosmic ray flux over the past ten million years: Mn-53 and Al-26 measurements; *Proc. Lunar Planet. Sci. Conf.* **IX** 2299–2310
- Lal D 1972 Hard rock cosmic ray archaeology; *Space Sci. Rev.* **14** 3–102
- Lal D 1986 On the study of continental erosion rates and cycles using cosmogenic Be-10 and Al-26 and other isotopes; *Dating young sediments* (eds) A J Hurford, E Jaeger, J A M Ten Cate, Proc. Workshop, Beijing China, Sept. 1985, CCOP Technical Secretariat, Bangkok, pp. 285–297
- Lal D and Marti K 1977 On the flux of low-energy particles in the solar system: The record in St. Severin meteorite; *Nuclear Track Detection* **1** 127–130
- Lal D, Nishiizumi K and Arnold J R 1987 *In situ* cosmogenic ^3H , ^{14}C and ^{10}Be for determining the net accumulation and ablation rates of ice sheets; *J. Geophys. Res.* **92** 4947–4952
- Lavielle B, Sauvageon H, Bertin P 1990 Cross sections for Neon and Krypton isotopes produced by Neutrons; *Workshop on Cosmogenic Nuclide Production Rates* (eds) P A J Englert, R C Reedy, R Michel, LPI Tech Rep 90-05, Lunar and Planetary Institute, Houston, pp 65–69
- Leya I, 1997 *Modellrechnungen zur Beschreibung der Wechselwirkungen galaktischer kosmischer Teilchenstrahlung mit Stein- und Eisenmeteoroiden, Dünntargetbestrahlungen und Dicktargetexperimente*; Thesis, Universität Hannover
- Leya I and Michel R 1997 Determination of neutron cross sections for nuclide production at intermediate energies by deconvolution of thick-target production rates; *Società Italiana di Fisica* (eds) G Reffo, A Ventura and C Grandi, pp. 1463–1467
- Leya I, Lange H-J, Michel R, Meltzow B, Herpers U, Busemann H, Wieler R, Dittrich-Hannen B, Suter M and Kubik P W 1995 A physical model of cosmogenic nuclide production in stony and iron meteoroids on the basis of simulation experiments; *Meteoritics* **30** 536
- Leya I, Lange H-J, Michel R, Meltzow B, Herpers U, Sudbrock F, Busemann H, Wieler R, Dittrich-Hannen B, Suter M and Kubik P W 1996 Model calculations for the production of cosmogenic nuclides in stony and iron meteoroids by galactic-cosmic-ray particles; *Meteoritics* **31A** 80
- Leya I, Lange H-J, Lüpke M, Neupert U, Daunke R, Fanenbruck O, Michel R, Rösel R, Meltzow B, Schiekel Th, Sudbrock F, Herpers U and Filges D 1998a Simulation of the interaction of GCR protons with meteoroids – On the production of radionuclides in thick gabbro and steel targets irradiated isotropically with 1.6 GeV protons; *Meteor. & Plan. Sci.* (submitted)
- Leya I, Baur H, Busemann H, Wieler R, Gloris M, Neumann S, Michel R, Herpers U 1998b Cross sections for the proton induced production of He and Ne isotopes from magnesium, aluminum and silicon; *Nucl. Instr. Meth. Phys. Res. B* **145** 449
- Marti K 1967 Mass-spectrometric detection of cosmic-ray-produced ^{81}Kr in meteorites and the possibility of Kr-Kr-dating; *Phys. Rev. Lett.* **18** 264–266
- Masarik J and Reedy R C 1993 Production profiles of nuclides by galactic-cosmic-ray particles in the tops of lunar rocks; *Meteoritics* **28** 391–392
- Masarik J and Reedy R C 1994 Effects of bulk composition on nuclear production processes in meteorites; *Geochim. Cosmochim. Acta* **58** 5307–5317
- Mathews K J, Rao M N, Weber H, Dragovitsch P, Peiffer F and Michel R 1994 Xenon production cross sections at high energies and production rates of Xenon isotopes in small meteorites based on simulation experiments; *Nucl. Instr. Meth. Phys. Res.* **B94** 449–474
- Matzke M 1979 Unfolding by least-squares methods: SAND-II, STAY'SL; *Proc. 3rd ASTM-Euratom Symp. on Reactor Dosimetry, Ispra* 721–731
- McGuire R E and von Rosenvinge T T 1984 The energy spectra of solar energetic particles; *Adv. Space Res.* **4** 117–125
- McLane V 1996 *EXFOR systems manual: Nuclear reaction data exchange manual*; BNL-NCS-6330
- Merchel S, Herpers U, Neumann S, Michel R, Kubik P-W, Suter M, Faestermann D, Knie K, Korschinek G, Scätz T and Bhandari N 1997 Depth profiles of long-lived cosmogenic radionuclides in Mbale; *Meteor. & Planet. Sci.* **32A** 90
- Michel R 1998 SATURNE – An intense source of galactic cosmic ray particles; *Proc. Les 20 ans de Saturne 2* Paris, May 3–4, World Scientific Publishing (in press)
- Michel R and Brinkmann G 1980 On the depth dependent production of Radionuclides ($44 < A < 59$) by solar protons in extraterrestrial matter; *J. Radioanal. Chem.* **59** 467–510
- Michel R and Stück R 1984 On the production of cosmogenic nuclides in meteorites by primary galactic particles: Cross sections and model calculations; *Lunar Planet. Sci. Conf. XIV, Part 2; J. Geophys. Res.* **B89** Suppl. 673–684
- Michel R and Nagel P 1997 *International codes and model intercomparison for intermediate energy activation yields*; NSC/DOC 97 -1, NEA/OECD, Paris
- Michel R, Brinkmann G and Stück R 1982 Solar cosmic ray produced nuclides in meteorites; *Earth Planet. Sci. Lett.* **59** 33–48; *ibid* **64** (1983) 174
- Michel R, Dragovitsch P, Englert P, Peiffer F, Stück R, Theis S, Begemann F, Weber H, Signer P, Wieler R, Filges D and Cloth P 1985a On the depth-dependance of spallation

- reactions in a spherical thick diorite target homogeneously irradiated by 600 MeV protons simulation of production of cosmogenic nuclides in small meteorites; *Nucl. Instr. Meth. Phys. Res.* **B16** 61–82
- Michel R, Peiffer F and Stück R 1985b Measurement and hybrid model analysis of integral excitation functions for proton-induced reactions on vanadium, manganese and cobalt up to 200 MeV; *Nucl. Phys.* **A441** 617–639
- Michel R, Peiffer F, Theis S, Begemann F, Weber H, Signer P, Wieler R, Cloth P, Dragovitsch P, Filges D and Englert P 1989a Production of stable and radioactive nuclides in thick stony targets $R = 15$ and 25 cm isotropically irradiated with 600 MeV protons simulation of production of cosmogenic nuclides in meteorites; *Nucl. Instr. Meth. Phys. Res.* **B42** 76–100
- Michel R, Cloth P, Dragovitsch P and Filges D 1989b On the production of cosmogenic nuclides in meteoroids by galactic protons; *Lunar Planet. Sci.* **XX** 693–694
- Michel R, Dittrich B, Herpers U, Schiffmann T, Cloth P, Dragovitsch P and Filges D 1989c Proton-induced spallation at 600 MeV; *Analyst* **114** 287–293
- Michel R, Dragovitsch P and Filges D 1990 On the dependence of cosmogenic nuclide production rates in meteoroids on bulk chemical composition; *Meteoritics* **25** 386–387
- Michel R, Dragovitsch P, Dagge G, Cloth P and Filges D 1991 On the production of cosmogenic nuclides in extraterrestrial matter by galactic protons; *Meteoritics* **26** 221–242
- Michel R, Lüpke M, Herpers U, Filges D, Dragovitsch P, Wölfli W, Dittrich B and Hofmann H-J 1993 Simulation of the interactions of galactic cosmic ray protons by isotropic irradiation of a thick stony target with 1.6 GeV protons; *J. Radioanal. Nucl. Chem.* **169** 13–25
- Michel R, Lange H-J, Lüpke M, Herpers U, Rösel R, Filges D, Cloth P and Dragovitsch P 1994 Measurement and modeling of radionuclide production in thick spherical targets irradiated isotropically with 1600 MeV protons; *Proc. Int. Conf. Nucl. Data for Sci. & Tech.* (ed) J K Dickens, May 9–13, 1994, Gatlinburg, Tennessee, USA; American Nuclear Society, Inc, La Grange Park, Illinois, pp. 377–379
- Michel R, Lange H-J, Lüpke M, Herpers U, Rösel R, Suter M, Dittrich-Hannen B, Kubik P W, Filges D and Cloth P 1995a Simulation and modeling of the interaction of galactic protons with stony meteoroids; *Planet. & Space Sci.* **43** 557–572
- Michel R, Gloris M, Lange H-J, Leya I, Lüpke M, Herpers U, Dittrich-Hannen B, Rösel R, Schiekel Th, Filges D, Dragovitsch P, Suter M, Hofmann H-J, Wölfli W, Kubik P W, Wieler R and Signer P 1995b Nuclide production by proton-induced reactions on elements $6 \leq Z \leq 29$ in the energy range from 800 to 2600 MeV; *Nucl. Instr. Meth. Phys. Res.* **B103** 183–222
- Michel R, Leya I and Borges L 1996 Production of cosmogenic nuclides in meteoroids – Accelerator experiments and model calculations to decipher the cosmic ray record in extraterrestrial matter; *Nucl. Instr. Meth. Phys. Res.* **B113** 434–444
- Michel R, Bodemann R, Busemann H, Daunke R, Gloris M, Lange H-J, Klug B, Krins A, Leya I, Lüpke M, Neumann S, Reinhardt H, Schnatz-Büttgen M, Herpers U, Schiekel Th, Sudbrock F, Holmqvist B, Condé H, Malmberg P, Suter M, Dittrich-Hannen B, Kubik P-W and Synal H-A 1997a Cross sections for the production of residual nuclides by low- and medium-energy protons from the target elements C, N, O, Mg, Al, Si, Ca, Ti, Mn, Fe, Co, Ni, Cu, Sr, Y, Zr, Nb, Ba and Au; *Nucl. Instr. Methods in Phys. Res.* **B129** 153–193
- Michel R, Gloris M, Krins A, Leya I, Reinhardt H, Herpers U, Schiekel Th, Sudbrock F, Holmqvist B, Condé H, Malmberg P, Suter M, Kubik P-W, Synal H-A and Filges D 1997b Thin-target and thick-target experiments as basis for the modelling of nuclide production at medium energies; *Proc. 2nd Int. Conf. on Accelerator-Driven Technologies and Applications* (ed) H Condé, Kalmar, Schweden, Uppsala University, Gotab, Stockholm, pp. 448–454
- Michel R, Gloris M, Neumann S and Leya I 1998 Neutron cross sections for physical model calculations of cosmogenic nuclide production rates; *Meteor. & Planet. Sci.* **33A** 108
- Murty S V S, Bhandari N, Suthar K M, Clement C J, Bonino G and Castagnoli G C 1998 Cosmogenic effects in Mbale, L5/6 chondrite; *Meteor. & Planet. Sci.* submitted
- Nakamura T, Sugita H, Imamura M, Uwamino Y, Shibata S, Nagai H, Tabanatake M and Kobayashi K 1992 Measurement of long-lived ^{10}Be , ^{14}C and ^{26}Al production cross sections for 10–40 MeV neutrons by accelerator mass spectrometry; *Nuclear Data for Science and Technology* (ed) S M Qaim, Springer Verlag, Berlin, pp. 714–716
- Neumann S, Leya I and Michel R 1997a The influence of solar modulation on short-lived cosmogenic nuclides in meteorites with special emphasis on ^{44}Ti ; *Meteor. & Planet. Sci.* **32A** 98
- Neumann S, Gloris M, Michel R, Gilibert E, Lavielle B, Schiekel T and Herpers U 1997b Measurement and calculation of proton-induced integral cross sections of stable krypton isotopes for energies up to 1.6 GeV on Rb, Sr and Y; *Conf. Proc. on Nuclear Data for Science and Technology* (eds) G Reffo, A Ventura and C Grandi Società Italiana di Fisica, Bologna, **59** pp. 1519–1521
- Neumann S, Michel R, Sudbrock F, Herpers U, Malmberg P, Jonsson O, Holmqvist B, Condé H, Kubik P W and Suter M 1997c A new facility at the The Svedberg Laboratory for activation experiments with medium energy neutrons; *Conf. Proc. on Nuclear Data for Science and Technology*, (eds) G Reffo, A Ventura and C Grandi, Società Italiana di Fisica, Bologna, **59** pp. 379–383
- Neupert U 1996 *Langlebige kosmogene Radionuklide in Meteoriten aus heißen und kalten Wüsten-Messung von natürlichen Vorkommen, Dünntargetwirkungsquerschnitten und Dicktargetproduktionsraten zur Rekonstruktion von Bestrahlungsgeschichten* Thesis, Universität Hannover
- Neupert U, Michel R, Leya I, Neumann S, Scherer P, Bonani G, Hajdas I, Ivy-Ochs S, Kubik P-W and Suter M 1997 Ordinary chondrites from the Acfer region: A study of exposure histories; *Meteor. & Planet. Sci.* **32A** 47–48
- Nishiizumi K, Arnold J R, Elmore D, Ferraro R D, Gove H E, Finkel R C, Beukens R P, Chang K H and Kilius L R 1979 Measurements of Cl-36 in antarctic meteorites and antarctic ice using a van de Graaff accelerator; *Earth Planet. Sci. Lett.* **45** 285–292
- Nishiizumi K, Nagai H, Imamura M, Honda M, Kobayashi K, Sharma P, Wieler R, Signer P, Goswami J N, Reedy R C and Arnold J R 1990 Solar cosmic ray produced nuclides in Salem meteorite; *Meteoritics* **25** 392
- Nishiizumi K, Arnold J R, Fink D, Klein J, Middleton R, Brownlee D E and Maurette M 1991a Exposure history of individual cosmic particles; *Earth Planet. Sci. Lett.* **104** 315–324
- Nishiizumi K, Kohl C P, Shoemaker S M, Arnold J R, Klein J, Fink D and Middleton R 1991b *In situ* Be-10-Al-26 exposure ages at meteor crater, Arizona; *Geochim. Cosmochim. Acta* **55** 2699–2703
- Perey F G 1977 *Least-squares dosimetry unfolding: The program STAY'SL*; ORNL/TM-6062, ENDF-254, NEA Data Bank, Gif-sur-Yvette
- Prael R and Lichtenstein H 1989 *User guide to LCS: The LAHET code system*; Los Alamos Rep. UR-89-3014
- Raisbeck G M and Yiou F 1977a The Be-10 problem revisited; *XV Int. Cosmic Ray Conf. Plovdiv* **2** 203–207
- Raisbeck G M and Yiou F 1977b Cross sections for spallation production of Ti-44 : Application to determining cosmic ray acceleration time; *XV Int. Cosmic Ray Conf. Plovdiv* **2** 112–115
- Rao M N, Garrison D H, Bogard D D and Reedy R C 1994 Determination of the flux and energy distribution of

- energetic solar protons in the past 2 Myr using lunar rock 68815; *Geochim. Cosmochim. Acta* **58** 4231–4245
- Reedy R C and Arnold J R 1972 Interaction of solar and galactic cosmic-ray particles with the moon; *J. Geophys. Res.* **77** 537–555
- Reedy R C, Herzog G F and Jessberger E K 1979, The reaction $\text{Mg}(n,\alpha)\text{Ne}$ at 14.1 and 14.7 MeV: Cross sections and implications for meteorites; *Earth Planet. Sci. Lett.* **44** 341–348
- Reedy R C, Arnold J R and Lal D 1983 Cosmic-ray record in solar system matter; *Ann. Rev. Nucl. Part. Sci.* **33** 505–537
- Reedy R C 1987 Meteorites, Cosmic ray record; *Encyclopedia Physical Science Technology* **8** 197–226
- Reedy R C and Marti K 1991 Solar-cosmic-ray fluxes during the last ten million years; *The sun in time* (eds) C P Sonett, M S Giampapa and M S Matthews, Uni. of Arizona Press, Tucson, AZ, pp. 260–287
- Reedy R C and Masarik J 1994 Cosmogenic-nuclide depth profiles in the lunar surface; *Lunar Planet. Sci.* **XXV** 1119–1120
- Regnier S, Lavielle B, Simonoff M and Simonoff G N 1982 Nuclear reactions in Rb, Sr, Y and Zr targets; *Phys. Rev.* **C26** 931–943
- Scherer P, Schultz L, Neupert U, Knauer M, Neumann S, Leya I, Michel R, Mokos J, Lipschutz M E, Metzler K, Suter M and Kubik P-W 1997 Alan hills 88019: An Antarctic H-chondrite with a very long terrestrial age; *Meteor. & Planet. Sci.* **32** 769–773
- Schickel Th, Rösler R, Herpers U, Leya I, Gloris M, Michel R, Dittrich-Hannen B, Kubik P W, Synal H-A and Suter M 1994 Cross sections for the p-induced production of longlived radionuclides for the interpretation of cosmogenic nuclides; In, *Proc. Int. Conf. Nuclear Data for Sci. & Tech.*, (ed) J K Dickens, May 9–13, Gatlinburg, Tennessee, USA; American Nuclear Society, Inc, La Grange Park, Illinois pp. 344–346
- Schickel Th, Sudbrock F, Herpers U, Gloris M, Lange H-J, Leya I, Michel R, Dittrich-Hannen B, Synal H-A, Suter M, Kubik P W, Blann M and Filges, D 1996a Nuclide production by proton-induced reaction on elements $6 < Z < 49$ in the energy range from 200 MeV to 400 MeV; *Nucl. Instr. Meth. Phys. Res.* **B114** 91–119
- Schickel T, Sudbrock F, Herpers U, Gloris M, Leya I, Michel R, Synal H A and Suter M 1996b On the production of ^{36}Cl by high energy protons in thin and thick targets; *Nucl. Instr. Meth. Phys. Res.* **B113** 484–489
- Schnabel Ch, Synal H-A, Suter M, Michel R, Gloris M, Leya I and Herpers U 1996 Determination of proton-induced cross sections and production rates of ^{129}I from Te in the medium energy range; *Radiocarbon* **38** 107–108
- Schnabel Ch, Gartenmann P, Lopez-Guitierrez J M, Dittrich-Hannen B, Suter M, Synal H-A, Leya I, Gloris M, Michel R, Sudbrock F and Herpers U 1997 Determination of proton-induced production cross sections and production rates of ^{129}I and ^{41}Ca ; *Conf. Proc. on Nuclear Data for Science and Technology* (eds) G Reffo, A Ventura and C Grandi, Società Italiana di Fisica, Bologna, **59** pp. 1559–1561
- Schultz L and Signer P 1976 Depth dependence of spallogenic helium, neon and argon in the St. Severin chondrite; *Earth Planet. Sci. Lett.* **30** 191–199
- Shea M A and Smart D F 1990 A summary of major solar proton events; *Solar Phys.* **127** 297–399
- Shedlovsky J P 1960 Ph.D. Thesis, Princeton University
- Signer P and Nier A O 1960 The distribution of cosmic-ray-produced rare gases in iron meteorites; *J. Geophys. Res.* **65** 2947–2963
- Signer P and Nier A O 1962 The measurement and interpretation of rare gas concentrations in iron meteorites; *Researches on meteorites* (ed) C B Moore, Wiley, pp. 7–35
- Sisterson J M, Jull A J T, Donahue D J, Koehler A M, Reedy R C and Englert P A J 1992a Cross section for production of carbon-14 from oxygen and silicon: Implications for cosmogenic production rates; *Meteoritics* **26** 395–396
- Sisterson J M, Koehler A M, Jull A J T, Donahue D J, McHargue L and Reedy R C 1992b Cross section measurements for the production of ^{14}C and ^{10}Be : Improved estimates for cosmogenic nuclide production rates; *Lunar Planet. Sci.* **XXIII** 1305–1306
- Sisterson J M, Jull A J T, Beverding A, Koehler A M, Castaneda A C, Vincent J, Donahue D J, Englert P A J, Gans C, Young J and Reedy R C 1994 Proton production cross section of C-14 from silicon and oxygen: Implications for cosmic-ray studies; *Proc. 6th Int. Conf. on Accelerator Mass Spectrometry, Nucl. Instr. Meth. Phys. Res.* **B92** 510–512
- Sisterson J M, Kim K, Beverding A, Englert P A J, Caffee M, Jull A J T, Donahue D J, McHargue L, Castaneda C, Vincent J and Reedy R C 1997 Measurement of proton cross sections of ^{10}Be and ^{26}Al from elements found in lunar rocks; *Nucl. Instr. Meth. Phys. Res.* **B123** 324–329
- Sudbrock F 1997 *Experimentelle und theoretische Studien zur Restkernproduktion bei Spallations- und Fragmentationsreaktionen* Thesis, Universität zu Köln
- Sudbrock F, Berkle A, Herpers U, Neupert U, Gloris M, Leya I, Michel R, Synal H-A, Kubik P W, Bonani G and Suter M 1997 Cross sections for the proton-induced production of the long-lived radionuclides Be-10, C-14 and Cl-36 measured via accelerator mass spectrometry; *Conf. Proc. on Nuclear Data for Science and Technology*, (eds) G Reffo, A Ventura and C Grandi, Società Italiana di Fisica, Bologna, **59** pp. 1534–1536
- Vogt S and Herpers U 1988 Radiochemical separation techniques for the determination of long-lived radionuclides in meteorites by means of accelerator-mass-spectrometry; *Fresenius Z. Anal. Chem.* **331** 186–188
- Vogt S, Herzog G F and Reedy R C 1990 Cosmogenic nuclides in extraterrestrial matter; *Rev. Geophys.* **28** 253–275
- Voshage H and Hintenberger H 1959 Massenspektrometrische Isotopenhäufigkeitsmessungen an Kalium aus Eisenmeteoriten und das Problem der Bestimmung der ^{41}K - ^{40}K -Strahlungsalter; *Z. Naturf.* **16A** 1042–1053
- Weber K H W and Begemann F 1992 On the production of Ar and Ne isotopes from target elements Ca and K; *Meteoritics* **27** 305
- Weigel A, Neumann S, Eugster O and Michel R 1997 Noble gas isotopic abundances in Acapulcoites and Lodranites Acapulco, ALH 81187, ALH 81261, ALH 84190, LEW 86220, LEW 88280 and QUE 93148; *LPSC XXVIII The Lunar and Planetary Science Institute, Houston*
- Wieler R, Signer P, Rösler R, Herpers U, Lüpke M, Lange H-J and Michel R 1992 On the production of He, Ne and Ar isotopes from Mg, Al, Si, Ca, Fe and Ni in an artificially irradiated meteoroid; *Meteoritics* **27** 315–316



Group photograph of the conference participants.



The Plenary speakers (clockwise from top: Profs. D Lal, G J Wasserburg, D E Maier-Reimer, R J Delmas and R K O'Nions).



Participants in the Panel Discussion (Profs. F Begemann, N Bhandari and S Krishnaswami and the plenary speakers).



Views of the Conference and Poster sessions.



Views of Registration and social events.

List of Participants

- G S Agarwal** Physical Research Laboratory, Navrangpura, Ahmedabad 380 009, India.
gsa@prl.ernet.in
- Masood Ahmad** National Geophysical Res. Inst., Isotope Geochemistry Div., Uppal Road, Hyderabad 500 007, India.
postmast@csngri.ren.nic.in
- Iqbal Ahmed** Physical Research Laboratory, Navrangpura, Ahmedabad 380 009, India.
- R Agnihotri** Physical Research Laboratory, Navrangpura, Ahmedabad 380 009, India.
rajesh@prl.ernet.in
- Peter G Appleby** Mathematical Sciences, University of Liver Pool, Liver Pool, U.K.
appleby@liverpool.ac.uk
- K Asha** Atomic Minerals Division, Dept. of Atomic Energy, Begumpet, Hyderabad 500 016, India.
- N M Ashok** Physical Research Laboratory, Navrangpura, Ahmedabad 380 009, India.
ashok@prl.ernet.in
- R N Athavale** National Geophysical Res. Inst., Uppal Road, Hyderabad 500 007, India.
postmast@csngri.ren.nic.in
- S Balakrishnan** Pondicherry University, Dept. of Earth Sciences, Kalapet, Pondicherry 605 014, India.
sbknxfes@uor.ernet.in
- D M Banerjee** Delhi University, Geology Dept., Delhi 110 007, India.
csec@doe.ernet.in
- Santanu Banerjee** Dept of Geological Sciences, Jadavpur University, Calcutta 700 032, India.
- M Baskaran** Texas A&M University, Dept. of Oceanography, Galveston, 5007 Univ. Avenue TX 77551 U.S.A.
baskaran@tamug.tamu.edu
- F Begemann** Max Planck Institut Fur Chemie, Postfach 3060, Mainz 55020, Germany.
- M I Bhat** Wadia Inst. of Himalayan Geology, 33, General Mahadeo Singh Road, Dehradun 248 001, India.
wihg@iasdl01.vsnl.net.in
- S K Bhattacharya** Physical Research Laboratory, Navrangpura, Ahmedabad 380 009, India.
bhatta@prl.ernet.in
- N Bhandari** Physical Research Laboratory, Navrangpura, Ahmedabad 380 009, India.
bhandari@prl.ernet.in
- K S Baliyan** Physical Research Laboratory, Navrangpura, Ahmedabad 380 009, India.
baliyan@prl.ernet.in
- Ravi Bhushan** Physical Research Laboratory, Navrangpura, Ahmedabad 380 009, India.
bhushan@prl.ernet.in
- R N Bhutani** Physical Research Laboratory, Navrangpura, Ahmedabad 380 009, India.
rajneesh@prl.ernet.in
- R S Bindu** Osaka City University, Faculty of Geosciences, Sugimoto, Sumiyoshi-Ku, Osaka 558, Japan.
bindu@sci.osaka-cu.ac.jp
- G Bonino** Dipartimento Di Fisica, Generale Dell Universita, Via P. Giuria 1, Torino 10125, Italy.
bonino@to.infn.it
- D V Borole** National Institute of Oceanography, Dona Paula, Goa 403 004, India.
dnyan@csnio.ren.nic.in
- John Cantle** Shiva Chem Technologies (I) Pvt. Ltd., Hyderabad 500 029, India.
- Cini Castagnoli** Istituto Di Cosmogeofisic, Corse Fiume 4, 10133 Torino, Italy.
cini@icg.to.infn.it
- Tikam Chabria** Dept. of Atomic Energy, Atomic Mineral Division, Begumpet, Hyderabad 500 016, India.
dir@amdhyd.ernet.in
- S S Chakraborty** Physical Research Laboratory, Navrangpura, Ahmedabad 380 009, India.
subrata@prl.ernet.in
- S Chakraborty** University of California, Dept. of Chemistry, 0356 San Diego, La Jolla CA 92093 U.S.A.
schakrab@chem.ucsd.edu
- Rakesh Chandra** Wadia Inst. of Himalayan Geology, 33, General Mahadeo Singh Rd, Dehradun 248 001, India.
wihg@iasdl01.vsnl.net.in
- T Chandrasekhar** Physical Research Laboratory, Navrangpura, Ahmedabad 380 009, India.
chandra@prl.ernet.in
- Allan R Chivas** School of Geosciences, University of Wollongong, Northfields Avenue, Wollongong NSW 2522, Australia.
a.chivas@uow.edu.au
- A K Choudhary** R.N.A.R, College Road, Sobarsa Chowk, Samastipur 848 101, India.
- Thomas M Church** University of Delaware, College of Marine Studies, Robinson Hall, Newark DE 19716-3501 U.S.A.
tchurch@udel.edu
- T K Dalai** Physical Research Laboratory, Navrangpura, Ahmedabad 380 009, India.
tarunk@prl.ernet.in
- Anirban Das** Physical Research Laboratory, Navrangpura, Ahmedabad 380 009, India.
anirban@prl.ernet.in

- Dr (Smt) Radha R Das** Atomic Minerals Division, Dept. of Atomic Energy, 1/C, Chemistry Lab., Begumpet, Hyderabad 500 016, India.
- P S Datta** Nuclear Research Laboratory, Indian Agricultural Res. Inst., Pusa, New Delhi 110 012, India.
- A M Dayal** National Geophysical Res. Inst., Uppal Road, Hyderabad 500 007, India.
postmast@csngri.res.nic.in
- R Delmas** Centre National De La Recherche, Sci. Domaine Universitaire, Lgge 64, Rue Moliere, Saint Martin De Heres 38402 France.
delmas@glaciog.grenet.fr
- M P Deomurari** Physical Research Laboratory, Navrangpura, Ahmedabad 380 009, India.
- M R Deshpande** Physical Research Laboratory, Navrangpura, Ahmedabad 380 009, India.
mrd@prl.ernet.in
- R D Deshpande** Physical Research Laboratory, Navrangpura, Ahmedabad 380 009, India.
deshpand@prl.ernet.in
- M H Dixit** Physical Research Laboratory, Navrangpura, Ahmedabad 380 009, India.
dixit@prl.ernet.in
- Amit Dubey** Physical Research Laboratory, Navrangpura, Ahmedabad 380 009, India.
amit@prl.ernet.in
- K Dutta** Physical Research Laboratory, Navrangpura, Ahmedabad 380 009, India.
koushik@prl.ernet.in
- Mitsuru Ebihara** Tokyo Metropolitan Univ., Dept. Chemistry Fac. Sci., Hachioji, Tokyo 192 03 Japan.
ebihara-mitsuru@c.metro-u.ac.jp
- J M Edmond** Massachusetts Inst. of Technology, Dept. of Earth Atmospheric and Cambridge, Ma 02139 U.S.A.
jedmond@mit.edu
- D Elmore** Director, Prime Lab, Purdue Univ., 1396 Physics Bldg. West Lafayette, IN 47907-1396, U.S.A.
elmore@primelab.physics.purdue.edu
- R J Francey** CSIRO, Div. Atmospheric Research, Private Mail Bag 1, Aspendale, Victoria 3195 Australia.
rjf@dar.csiro.au
- Raja S Ganeshram** Woods Hole Oceanographic Inst., Clarke 4; Ms 25, 360, Woods Hole Road, Woods Hole, MA 02543-1541 U.S.A.
rganeshram@whoi.edu
- P Ghosh** Physical Research Laboratory, Navrangpura, Ahmedabad 380 009, India.
pghosh@prl.ernet.in
- Parthasarathi Ghosh** Indian Statistical Inst., Dept. of Geology, 203, B. T. Road, Calcutta 700 035, India.
res001@isical.ernet.in
- Subhashis Ghosh** Geological Survey of India, Geochronology & Isotope Division, 15 A&B Kyd Street, Calcutta 700 016, India.
gsi@gems.vsnl.net.in
- K Gopalan** National Geophysical Res. Inst., Uppal Road, Hyderabad 500 007, India.
postmast@csngri.res.nic.in
- Anurag Gosain** Wadia Inst. of Himalayan Geology, 33, General Mahadeo Singh Road, Dehradun 248 001, India.
wihg@giadsl01.vsnl.net.in
- J N Goswami** Physical Research Laboratory, Navrangpura, Ahmedabad 380 009, India.
goswami@prl.ernet.in
- Francis E Grousset** Universite Bordeaux 1, Dept. Geologie Et Oceanographie, Avenue Des Facultes, 33405 Talence-Cedex France.
grousset@geocean.u-bordeaux.fr
- K R Gupta** Dept. of Science and Technology, Earth Science Division Technology Bhavan, New Delhi 110 016, India.
dst@srneted.ernet.in
- S N Gupta** Geological Survey of India, Geochronology & Isotope Division 15 A&B Kyd Street Calcutta 700 016, India.
gsi@gems.vsnl.net.in
- S K Gupta** Physical Research Laboratory, Navrangpura, Ahmedabad 380 009, India.
skgupta@prl.ernet.in
- S Hamilton** Atomic Minerals Div., North Western Region, Uniaragarden, Jln Road, Jaipur 302 004, India.
- Gary Hancock** Division of Water Resources, CSIRO, GPO Box 1666, Canberra, Act 2601 Australia.
gary.hancock@cbr.clw.csiro.au
- Charles L Harper** John Templeton Foundation, Two Radnor Corporate Center, Suite 320, 100 Matsonford Road, Radnor, Pa 19087 U.S.A.
harper@templeton.org
- Charles M Hohenberg** Washington University, Dept. of Physics, St Louis, MO 63130 U.S.A.
cmh@radon.wustl.edu
- Youngsook Huh** 42-44 Carleton Street E34-166, MIT Cambridge, MA 02139 U.S.A.
yhuh@mit.edu
- N Hussain** College of Marine Studies, The Graduate College of Marine Sci., Robinson Hall, Newark, De 19716-3501 U.S.A.
najid@brahms.udel.edu
- R H Jadeja** Physical Research Laboratory, Navrangpura, Ahmedabad 380 009, India.
rashmi@prl.ernet.in
- A K Jain** University of Roorkee, Dept. of Earth Sciences, Roorkee 247 667, India.
earth@rurkiu.ernet.in
- M Jain** Delhi University, Dept. of Geology, Delhi 110 007, India.
- R A Jani** Physical Research Laboratory, Navrangpura, Ahmedabad 380 009, India.
rajani@prl.ernet.in

- M. Jayananda** Bangalore University, Geology Dept., Jnanabharati, Bangalore 560 056, India.
bang@sirneteb.ernet.in
- D. Jagadheesha** Physical Research Laboratory, Navrangpura, Ahmedabad 380 009, India.
jagadish@prl.ernet.in
- U De S Jayawardena** Faculty of Engineering, Dept of Civil Engineering, University of Peradeniya, Peradeniya, Srilanka.
upali@soils.pdn.ac.lk
- U C Joshi** Physical Research Laboratory, Navrangpura, Ahmedabad 380 009, India.
joshi@prl.ernet.in
- N Juyal** Physical Research Laboratory, Navrangpura, Ahmedabad 380 009, India.
navin@prl.ernet.in
- S Kailas Bhabha** Atomic Research Centre, Nuclear Physics Division, Trombay, Bombay 400 085, India.
kailas@magnum.barctl.ernet.in
- E M Kolesnikov** Isotope Geochronology Lab., Geological Faculty, Moscow State University, Moscow 119 899 Russia.
mike@pcrt762.cs.msu.su
- C Krishna** Indian Institute of Technology, B-224, R P Hill, Kharagpur 721 302, India.
- P Krishnamurthy** Dept. of Atomic Energy, Atomic Mineral Division, Begumpet, Hyderabad 500 016, India.
- R V Krishnamurthy** Western Michigan University, Dept. of Geology Rood Hall, Kalamazoo, MI 49008 U.S.A.
r.v.krishnamurthy@wmich.edu
- S Krishnaswami** Physical Research Laboratory, Navrangpura, Ahmedabad 380 009, India.
swami@prl.ernet.in
- Teh Lung Ku** Univ. of Southern California, Dept. of Earth Sci., Los Angeles CA 90089-0740 U.S.A.
rku@usc.edu
- Anil Kumar** National Geophysical Res. Inst. Uppal Road Hyderabad 500 007, India.
postmast@csngri.ren.nic.in
- U Saravana Kumar** Bhabha Atomic Research Center, Isotope Division, Mumbai 400 085, India.
- B Kumar** National Geophysical Res. Inst., Uppal Road, Hyderabad 500 007, India.
postmast@csngri.ren.nic.in
- S L Kusumgar** Physical Research Laboratory, Navrangpura, Ahmedabad 380 009, India.
skusum@prl.ernet.in
- L Labyerie** Centre Des Faibles Radioactivities, Domaine Du CNRS 91198 Gif Sur Yvette, France.
labyerie@cfr.cnrs-gif.fr
- Devendra Lal** Scripps Inst. of Oceanography, GRD 0220, La Jolla, CA 92093 0220 U.S.A.
dlal@ucsd.edu
- Vivek Laul** Mohanlal Sukhadia University, Dept. of Geology, Udaipur 313 002, India.
- P. Lefort** Institut Dolomieu, C N R S., Grenoble, 38301 Grenoble, France.
patrick.lefort@ujf-grenoble.fr
- D E Maier Reimer** Max Planck Institut Fur Meteorologie, Hamburg 13, Germany.
maier-reimer@dkrz.de
- A K Mallick** Director G & I G Division, Geological Survey of India, 15 A&B, Kyd Street, Calcutta 700 016, India.
gsi@gems.vsnl.net.in
- Oliver K Manuel** Univ of Missouri, Dept. of Chemistry, 142 Schrenk Hall, MO 65401, Rolla U.S.A.
om@umr.edu
- K Marhas** Physical Research Laboratory, Navrangpura, Ahmedabad 380 009, India.
jitti@prl.ernet.in
- K Marti** University of California, Dept. of Chemistry 0317, 9500 Gilman DR, San Diego, La Jolla, CA 92093-0317 U.S.A.
kmarti@ucsd.edu
- Bernard Marty** C.R.P.G. 15 Rue Notre-Dame Des Pauvres, B. P. 20, 54501 Vandœuvre Nancy Cedex, France.
bmarty@crpg.cnrs-nancy.fr
- Jun-Ichi Matsuda** Osaka University 1-1, Machikane-Yama, Toyonaka-Shi, Osaka 560, Japan.
matsuda@ess.sci.osaka-u.ac.jp
- R Mahajan** Physical Research Laboratory, Navrangpura, Ahmedabad 380 009, India.
mahajan@prl.ernet.in
- Aninda Mazumdar** Delhi University, Dept. of Geology, Delhi 110 007, India.
- R Michel** Center for Radiation Protection and Radioecology, University of Hannover, Am Kleinen Felde 30, D-30167 Hannover Germany.
michel@mbox.zsr.uni-hannover.de
- P Mishra** Physical Research Laboratory, Navrangpura, Ahmedabad 380 009, India.
- R K Mohapatra** Physical Research Laboratory, Navrangpura, Ahmedabad 380 009, India.
ratana@prl.ernet.in
- W S Moore** University of South Carolina, Dept. of Geological Sci., SC 29208 South Carolina, U.S.A.
moore@epoch.geol.sc.edu
- M E A Mondal** Physical Research Laboratory, Navrangpura, Ahmedabad 380 009, India.
- U Morgenstern** Institute of Geological and Nuclear Science Ltd., P.O. Box 31312, Lower Hutt, New Zealand.
U.Morgenstern@gns.cri.nz
- S V S Murty** Physical Research Laboratory, Navrangpura, Ahmedabad 380 009, India.
murty@prl.ernet.in
- Satya Murthy** Shiva Chem Technologies, Hyderabad 500 029, India.
- A Sathy Naidu** Institute of Marine Science, University of Alaska, Fairbanks, Alaska, 99701-1080 U.S.A.
ffsan@aurora.alaska.edu

- Pothuri Divakar Naidu** National Institute of Oceanography, Dona Paula, Goa 403 004, India.
sdivak@sci.shizuoka.ac.jp
- S W A Naqvi** C. O. D. National Inst. of Oceanography, Dona Paula, Goa 403 004, India.
naqvi@csnio.ren.nic.in
- V N Nijampurkar** Physical Research Laboratory, Navrangpura, Ahmedabad 380 009, India.
nijam@prl.ernet.in
- Y Nozaki** University of Tokyo, Ocean Research Inst., Nakano-Ku, Tokyo 164, Japan.
nozaki@ori.u-tokyo.ac.jp
- R K O'Nions** University of Oxford, Dept. of Earth Sci., Parks Road, Oxford OX1 3PR, UK.
keith.onions@earth.ox.ac.uk
- Ulrich Ott** M. P. I. Fur Chemie, Postfach 3060, Mainz 55020, Germany.
ott@mpch-mainz.mpg.de
- J T Padia** Physical Research Laboratory, Navrangpura, Ahmedabad 380 009, India.
padia@prl.ernet.in
- V M Padmakumari** National Geophysical Res. Inst., Uppal Road, Hyderabad 500 007, India.
postmast@csngri.ren.nic.in
- K Pandarinath** Physical Research Laboratory, Navrangpura, Ahmedabad 380 009, India.
- Anand Kumar Pandey** Wadia Inst. of Himalayan Geology, 33, General Mahadeo Singh Road, Dehradun, 248 001, India.
wihg@iasdl01.vsnl.net.in
- Kanchan Pandey** Physical Research Laboratory, Navrangpura, Ahmedabad 380 009, India.
kanchan@prl.ernet.in
- B K Pandey** Dept. of Atomic Energy, Atomic Mineral Division, Begumpet, Hyderabad 500 016, India.
- R K Pant** Wadia Inst. of Himalayan Geology 33, General Mahadeo Singh Road, Dehradun 248 001, India.
wihg@iasdl01.vsnl.net.in
- G V C Pantulu** National Geophysical Res. Inst., Uppal Road, Hyderabad 500 007, India.
postmast@csngri.ren.nic.in
- Sushma Prasad** Physical Research Laboratory, Navrangpura, Ahmedabad 380 009, India.
- D J Patil** National Geophysical Res. Inst., Uppal Road, Hyderabad 500 007, India.
postmast@csngri.ren.nic.in
- Della Monica Patrizia** Istituto Di Cosmogeofisica, Cs. Fiume 4, 10100 Torino, Italy.
patrizia@icg.to.iutut.it
- Prabha Kumari** 15-A, National Road, Dehradun 248 001, India.
- B N Prabhu** Mass Spectrometry Lab., KDMIP, O.N.G.C. Dehradun 248 195, India.
ongc@iasdl01.vsnl.net.in
- V K Rai** Physical Research Laboratory, Navrangpura, Ahmedabad 380 009, India.
rai@prl.ernet.in
- V Rajamani** Jawaharlal Nehru University, School of Environment Science, New Delhi 110 067, India.
vrm@jnuniv.ernet.in
- S Rajan** Geological Survey of India, Geologist, Marine Wing, Edappally, Cochin 682 024, India.
- Rama Y-4**, Sector 9, C.B.D. New Bombay 400 614, India.
- S Ramadurai** T.I.F.R., Astrophysic Group, Homi Bhabha Road, Bombay 400 005, India.
durai@tifrvax.tifr.res.in
- M Ramakrishnan** Airborne Min. Surveys & Explo. Wing, Geological Survey of India, Vasudha Bhavan, Kumaraswamy Layout, Bangalore 560 078, India.
- R Ramesh** Physical Research Laboratory, Navrangpura, Ahmedabad 380 009, India.
r.ramesh@prl.ernet.in
- R Rengarajan** Physical Research Laboratory, Navrangpura, Ahmedabad 380 009, India.
rajan@prl.ernet.in
- R Rangarajan** National Geophysical Research Institute, Uppal Road, Hyderabad 500 007, India.
postmast@csngri.ren.nic.in
- D K Rao** Physical Research Laboratory, Navrangpura, Ahmedabad 380 009, India.
kamesh@prl.ernet.in
- M N Rao** Planetary Science Group, NASA/Johnson Space Center, Building 31, Houston, Texas 77058 U.S.A.
m.n.raol@jsc.nasa.gov
- S M Rao** Bhabha Atomic Research Center. Head, Isotope Division, Trombay, Bombay 400 085, India.
smrao@magnum.barct.1.ernet.in
- Y J Bhaskar Rao** National Geophysical Research Institute, Uppal Road, Hyderabad 500 007, India.
postmast@csngri.ren.nic.in
- B G A Rao** Physical Research Laboratory, Navrangpura, Ahmedabad 380 009, India.
anand@prl.ernet.in
- N V C Rao** 3-4-1007/1 (Upstairs), Batkatpura Bus Depot Lane, Hyderabad 500 027, India.
- M Rao** National Institute of Oceanography, G.O.D., Dona Paula, Goa 403 004, India.
- S S Rathore** Mass Spectrometry Lab., KDMIP, O.N.G.C., Kaulagarh Road, Dehradun 248 195, India.
ongc@iasdl01.vsnl.net.in
- Piyoosh Rautela** Wadia Institute of Himalayan Geology, 33, General Mahadeo Singh Road, Dehradun 248 001, India.
wihg@iasdl01.vsnl.net.in
- J S Ray** Physical Research Laboratory, Navrangpura, Ahmedabad 380 009, India.
ranjan@prl.ernet.in
- S B Ray** Geologist, Geological Survey of India, Unit-VIII Bhubaneswar 751 012, India.

- D V Reddy** National Geophysical Res. Inst., Uppal Road, Hyderabad 500 007, India.
postmast@csngri.ren.nic.in
- Robert C Reedy** Los Alamos National Lab., Mail Stop D 436, Los Alamos, NM 87545 U.S.A.
rreedy@lanl.gov
- A B Roy** Mohanlal Sukhadia University, Dept. of Geology, Udaipur 313 001, India.
- S Sinha Roy** 5, Indira Nagar, P.O. Durgapura, Jaipur 302 018, India.
- Shushanta Sarangi** Dept. of Applied Geology, Indian School of Mines, Dhanbad 826 004, India.
cme@ismine.ernet.in
- P K Saraswati** Dept. of Earth Sciences, Indian Institute of Technology, Powai, Bombay 400 076, India.
pratul@zircon.geos.iitb
- M M Sarin** Physical Research Laboratory, Navrangpura, Ahmedabad 380 009, India.
sarin@prl.ernet.in
- S B Sahijpal** Physical Research Laboratory, Navrangpura, Ahmedabad 380 009, India.
- A Sarkar** Physical Research Laboratory, Navrangpura, Ahmedabad 380 009, India.
ashish@prl.ernet.in
- Amitabha Sarkar** Geological Survey of India, Geochronology and Isotope Geology, 29 Jawaharlal Nehru Road, Calcutta 700 016, India.
gsi@gems.vsnl.net.in
- Anindya Sarkar** Indian School of Mines, Dept. of Applied Geology, Dhanbad 826 004, India.
cme@ismine.ernet.in
- Gautam Sarkar** Geological Survey of India, 27, Jawaharlal Nehru Road, Calcutta 700 016, India.
gsi@gems.vsnl.net.in
- M Satishkumar** Dept. of Geosciences, Osaka City University, Sugimoto 3-3-138, Sumiyoshi-Ku Osaka 558 Japan.
satish@sci.osaka-cu.ac.jp
- D R Schink** Texas A & M University, Dept. of Oceanography, College Station, Texas 77843 U.S.A.
dschink@astra.tamu.edu
- Ludolf Schultz** Max Planck Institut Fur Chemie, Otto Hahn Institut, Postfach 3060, D-55020 Mainz, Germany.
schultz@mpch-mainz.mpg.de
- S K Sengupta** Geological Survey of India, Technical and Co-ordination Div., 5th North Bye Lane, Zoo Narengi Rd, Gauwahati 781 021, India.
- K K Sharma** Wadia Institute of Himalayan Geology, 33, General Mahadeo Singh Road, Dehradun 248 001, India.
wihg@giadl01.vsnl.net.in
- P. Sharma** Purdue University, Prime Lab., 1396 Physics Building, West Lafayette, IN 47907-1396, U.S.A.
sharma@primelab.purdue.edu
- Mukul Sharma** M.P.I. Fur Chemie, Postfach 3060, Mainz 55020, Germany.
msharma@geobar.mpch-mainz.mpg.de
- V G Shah** Physical Research Laboratory, Navrangpura, Ahmedabad 380 009, India.
vgshah@prl.ernet.in
- S D Sharma** National Geophysical Res. Inst., Uppal Road, Hyderabad 500 007, India.
postmast@csngri.ren.nic.in
- J. P. Shrivastava** Delhi University, Geology Dept., Delhi 110 007, India.
- P N Shukla** Physical Research Laboratory, Navrangpura, Ahmedabad 380 009, India.
- A D Shukla** Physical Research Laboratory, Navrangpura, Ahmedabad 380 009, India.
anilds@prl.ernet.in
- R N Singh** C-MMACS, National Aerospace Laboratories, Belur Campus, Bangalore 560 037, India.
- Sandeep Singh** University of Roorkee, Dept. of Earth Sciences, Roorkee 247 667, India.
earth@rurkiu.ernet.in
- Surinder Singh** Gurunanak Dev University, Dept. of Physics, Amritsar 143 005, India.
- A K Singal** Physical Research Laboratory, Navrangpura, Ahmedabad 380 009, India.
asingal@prl.ernet.in
- S K Singh** Physical Research Laboratory, Navrangpura, Ahmedabad 380 009, India.
sunil@prl.ernet.in
- A K Singhvi** Physical Research Laboratory, Navrangpura, Ahmedabad 380 009, India.
singhvi@prl.ernet.in
- N M Sinha** Physical Research Laboratory, Navrangpura, Ahmedabad 380 009, India.
nirjhari@prl.ernet.in
- D K Sinha** Dept. of Atomic Energy, Atomic Mineral Division, Begumpet, Hyderabad 500 016, India.
- A K Sinha** Wadia Institute of Himalayan Geology, 33, General Mahadeo Singh Road, Dehradun 248 001, India.
wihg@giadl01.vsnl.net.in
- U K Sinha** B.A.R.C., Isotope Division, Trombay, Bombay 400 085, India.
- Devesh K. Sinha** Dept. of Geology, Banaras Hindu University, Varanasi 221 005, India.
- M S Sisodia** J.N.V. University, Dept. of Geology, Jodhpur 342 001, India.
root@mbmec.ren.nic.in
- B L K Somayajulu** Physical Research Laboratory, Navrangpura, Ahmedabad 380 009, India.
soma@prl.ernet.in
- B Sreenivas** National Geophysical Res. Inst., Geochronology Division, Uppal Road, Hyderabad 500 007, India.
postmast@csngri.ren.nic.in
- Neptune Srimal** Geological Survey of India, Geochronology and Isotope Geology, 15 A&B Kyd Street, Calcutta 700 016, India.
neptune@giadl01.vsnl.net.in

- G Srinivasan** Physical Research Laboratory, Navrangpura, Ahmedabad 380 009, India.
sринi@prl.ernet.in
- M S Srinivasan** Banaras Hindu University, Dept. of Geology, Varanasi 221 005, India.
- K V Subbarao** Indian Institute of Technology, Dept. of Earth Sciences, Powai, Mumbai 400 076, India.
subbu@zircon.geos.iitb.ernet.in
- B S Sukhija** National Geophysical Res. Inst., Uppal Road, Hyderabad 500 007, India.
postmast@csngri.res.nic.in
- K M Suthar** Physical Research Laboratory, Navrangpura, Ahmedabad 380 009, India.
- Tim Swindle** University of Arizona, Lunar and Planetary Lab., Tucson, AZ 85721 U.S.A.
tmswindl@ccit.arizona.edu
- Carla Taricco** Instituto Di Geocosmofisica, Corso Fiume 4, Torino 10133, Italy.
carla@icg.to.infn.it
- V C Tewari** Wadia Institute of Himalayan Geology 33 General Mahadeo Singh Road, Dehradun 248 001, India.
wihg@gasdl01.vsnl.net.in
- M Thiemens** Univ. of California, Dept. of Chemistry 0317, 9500 Gilman DR. San Diego, CA 92093 U.S.A.
mht@chem.ucsd.edu
- J V Thomas** Physical Research Laboratory, Navrangpura, Ahmedabad 380 009, India.
jvthomas@prl.ernet.in
- J R Trivedi** Physical Research Laboratory, Navrangpura, Ahmedabad 380 009, India.
jtrivedi@prl.ernet.in
- M N Vahia** T.I.F.R., Homi Bhabha Road, Mumbai 400 005, India.
vahia@tifrvax.tifr.res.in
- Harri Vanhala** Carnegie Inst. of Washington 5241 Broad Branch Road, N. W., Washington DC 20015 1305 U.S.A.
harri@dtm.ciw.edu
- Hari Om Vats** Physical Research Laboratory, Navrangpura, Ahmedabad 380 009, India.
vats@prl.ernet.in
- V S Venkatavaradan** Director, Nehru Planetarium, Dr. Annie Besant Road, Worli, Bombay 400 018, India.
- T R Venkatesan** Physical Research Laboratory Navrangpura Ahmedabad 380 009, India.
tearve@prl.ernet.in
- S P Verma** Centro De Investigacion En Energia, Apartado Postal 34, Temixco, MOR 62580, Mexico.
spv@mazatl.cie.unam.mx
- B Vijayagopal** National Geophysical Res. Inst., Uppal Road, Hyderabad 500 007, India.
postmast@csngri.res.nic.in
- H S Virk** Gurunanak Dev University, Dept. of Physics, Amritsar 143 005, India.
- G. J. Wasserburg** Div. of Geol. and Planet. Sci., Caltech, Mail Code 170-25, Pasadena, CA 91125, U.S.A.
isotopes@gps.caltech.edu
- Rainer Wieler** Eth Zurich Isotopengeologie, No C61, CH-8092 Zurich, Switzerland.
wieler@erdw.ethz.ch
- D N Yadav** Birbal Sahni Institute of Paleobotany, 53, University Road, Lucknow 226 007, India.
bsip@bsip.sirnetd.ernet.in
- M G Yadava** Physical Research Laboratory, Navrangpura, Ahmedabad 380 009, India.
myadava@prl.ernet.in
- Jongmann Yang** Ewha Womans University, Dept. of Physics, Seoul 120-750 Korea.
jyang@mm.ewha.ac.kr

